REVIEW OF THE VKI DOCTORAL RESEARCH

2020 - 2021



von Karman Institute for Fluid Dynamics

Front cover: Oxidation of pure titanium sample in air plasma
Picture of Andra Fagnani

©2021 by the von Karman Institute for Fluid Dynamics
Waterloosesteenweg 72, B-1640 Sint-Genesius-Rode
To order: https://www.vki.ac.be

ISBN 978-2-87516-164-2

D/2021/0238/734, T. Magin, Editor-in-Chief

The contents of this book are the property of the von Karman Institute for Fluid Dynamics. No part of this book may be reproduced or distributed in any form of by any means, or stored in a database or retrieval system, without the prior written permission from the Publisher.

PREFACE

The twelve symposium on the doctoral research of the von Karman Institute for Fluid Dynamics took place online during the period March 1 to 3, 2021. The doctoral students present the progress of their research work carried out in the three departments: Aeronautics and Aerospace, Environmental and Applied Fluid Dynamics, Turbomachinery and Propulsion. The first-year students have presented a poster on their research plans and some preliminary results, while the most advanced students have proposed a presentation followed by a session of questions.

This event was attended by the faculty of the von Karman Institute, as well as by colleagues from universities and industrial partners. The Symposium is open to external attendees free of charge. In addition to the presentations of the PhD candidates, we had the pleasure to welcome three prominent keynote lecturers who open each day the Symposium:

- Dr. Graham V. Candler, McKnight Presidential Chair, Distinguished McKnight University Professor, Russell J. Penrose Professor, Associate Department Head, Aerospace Engineering & Mechanics, University of Minnesota, USA, "*Simulation of Hypersonic Transition and High-Speed Turbulence with CFD,"*
- Prof. Steven L. Brunton, James B. Morrison Endowed Career Development Professor in Mechanical Engineering, Adjunct Associate Professor, Applied Mathematics, University of Washington, USA, "*Machine learning for Fluid Mechanics,"*
- Prof. Frank Eulitz, Professor and Head of the Turbomachinery and Propulsion Department, von Karman Institute for Fluid Dynamics, Belgium, "*Turbomachinery Power for Decarbonization - Trends and Perspectives."*

This year, the best presentation award has been attributed to Fabio Pino for his research on "Prospects in machine learning-based flow control for liquid metal coating" We would like to congratulate him on this achievement. Due to the COVID-19 situation, the symposium had to be organized online and the poster session was replaced by a pitch session.

This proceedings volume contains 51 papers, which are divided into the following topics: Aerothermochemistry, Aerothermodynamics, Rarefied and Plasma Flows, Aeroacoustics, Liquid Metal and Industrial Flows, Environmental Flows and Safety, Liquid and Solid Propulsion, Shape Optimization, Turbine Aerodynamics and Heat Transfer, Compressor Aerodynamics and Heat Transfer, Instrumentation and Measurement Techniques, Liquid and Solid Propulsion, Shape Optimization.

We would like to emphasize that this publication serves as a tool for communication and aims to enhance exchange between the doctoral candidates, the faculty, and external attendees. The annual publication of their results in proceedings is of crucial importance to the VKI research providing a thorough review of the different activities within the three departments.

As such, the doctoral candidate students play a key role in strengthening the expertise in experimental research, computational methods, and physical modelling. In addition to basic research, works carried out at the von Karman Institute often leads to implementation of real-life industrial applications critical to the fluid dynamics community.

Andrea Fagnani Fabio Pino Phd Representatives	Thierry Magin Professor	Christelle Debeer Organizer / Editor

The contribution of all VKI members who helped with this event is deeply acknowledged in particular the faculty, library and printing office staff.

TABLE OF CONTENTS

Editorial notes i

Table of contents iii

AEROTHERMOCHEMISTRY

Enrico ANFUSO (first year PhD) 3
Investigation of aerothermodynamic phenomena of aerospace flight in ground testing facilities

Michele CAPRIATI 5
Heat flux characterization of an under-expanded/supersonic plasma jet over a catalytic probe

Andrea FAGNANI 13
Comprehensive characterization of the aero-thermo-mechanical response of space debris materials to atmospheric entry plasmas

David HENNEAUX 27
A high-order level-set method to follow the gas-liquid interface of melting materials

Francisco TORRES HERRADOR 37
Understanding the graphitization process of carbon fibers

AEROTHERMODYNAMICS

Daniel Gabor KOVACS (first year PhD) 49
Experimental investigation of space debris fragmentation during re-entry

Ray VANDENHOECK 51
Massively parallel and robust high-order methods for transitional hypersonic flow modelling on unstructured grids

Ali Can ISPIR 63
Simulation of supersonic mixing of alternative fuels for air-breathing engines based on data mining techniques

Fabio Miguel PEREIRA MORGADO (first year PhD) 69
Multi-disciplinary modelling of the aerothermodynamically-induced fragmentation of re-entering bodies

RAREFIED AND PLASMA FLOWS

Maxim VAN CAPPELLEN 73
The intercardinal Lagrangian-Eulerian scheme: solving kinetic equations with quadrature-based moment methods fast, accurate and realizable

Giuseppe Matteo GANGEMI (first year PhD) 83
Development of a high order fluid solver for air plasma sheath

Pedro JORGE (first year PhD) 85
Development of gas-surface interaction models from continuum to rarefied flow regimes

Pietro PARODI (first year PhD) 87
Modeling and simulation of air plasmas using particle methods applied to air-breathing electric propulsion

Firas BEN AMEUR 89
Development of high-order adaptative algorithms for simulating magnetic reconnection processes with uncertainty quantification

Louis REBOUL 113
Fluid modeling of low-temperature partially-magnetized plasmas in the presence of sheaths: numerical issues for the simulation of instabilities and comparison with kinetic simulations

Vincent GIANGASPERO 125
Modeling strategy for blackout analysis of re-entry phases in space exploration mission

AEROACOUSTICS

Joachim DOMINIQUE 135
A wall pressure fluctuations model beneath turbulent boundary layer using artificial neural network

Kartik VENKATRAMAN 145
Numerical investigation of vertical axis wind turbine noise under uniform flow conditions

LIQUID METAL AND INDUSTRIAL FLOWS

David BARREIRO-VILLAVERDE 153
Modal analysis of the liquid-gas interaction in jet wiping

Fabio PINO 163
Prospects in machine learning-based flow control for liquid metal coating

Matilde FIORE 175
Thermal turbulence modelling of liquid metal flows via data analysis and machine learning

Aude LECARDONNEL 189
Experimental characterization of evaporation heat exchangers using low global warming potential fluids

Tommaso CARLESI (first year PhD) 201
Development of an advanced experimental technique to measure turbulent heat flux in liquid metals

Yohanna HENROTEL (first year PhD) 203
Modelisation of heat and mass transfer in multiphase heat exchangers core

Wassim ABDEL NOUR (first year PhD) 205
Topological optimization of a multiphasic heat exchanger manifold

ENVIRONMENTAL FLOWS AND SAFETY

Loreline FAUGIER 209
Elaboration of numerical and experimental models for airflow in a subway station

Tom LAURIKS 219
Application of improved CFD modeling for prediction and mitigation of traffic-related air pollution hotspots in a realistic urban street

Abdelhafidh MOUMEN 233
On the application of background-oriented Schlieren on the ballistics field

Baris KALE 247
Implementation of a generalized actuator disk model into the Weather Research and Forecasting (WRF) model for high-fidelity simulations of wind turbine wakes

Benoit FOLOPPE (first year PhD) 259
Multi-fidelity modeling of offshore wind energy systems including mesoscale variability at wind turbine scale: an application to wind farm control for grid balancing

Emmanuel GILLYNS (first year PhD) 261
Wind turbine wakes impact on the dynamics of high-voltage cables for fatigue assessment and optimization

Pierrette ATIKPO (first year PhD) 263
Near-field pollutant dispersion due to explosions

Adithya VEMURI (first year PhD) 265
Weather predictions for offshore wind energy: Case of extreme events

Gert-Jan GLABEKE (first year PhD) 267
Assessment and optimization of LIDAR Doppler velocimetry for complex atmospheric flows

Konstantinos VRATSINIS (first year PhD) 269
Prediction of potential future bearing failures

LIQUID AND SOLID PROPULSION

Domenico FIORINI 273
Dynamic contact angle analysis using inverse methods

Aysu ÖZDEN (first year PhD) 265
Advanced numerical schemes for high-speed deflagration and detonation

Bora Orcun CAKIR (first year PhD) 287
Design and Analysis of a novel high-supersonic aircraft concept

SHAPE OPTIMIZATION

Tom DE BRUYN 291
Aero-elastic tailoring of composite turbomachinery blades through gradient-based optimisation: harmonic solvers

Luca ZAMPINI 297
Elliptic mesh generation for industrial shape optimization

Romain POLETTI (first year PhD) 307
Real-time optimization of bio-inspired wings using the deformable overset method and machine learning

Thanh-Son TRAN (first year PhD)..... 309
Inlet distortion mitigation through gradient-based optimization

TURBINE AERODYNAMICS AND HEAT TRANSFER

Gustavo LOPES..... 313
Adaptation of a transonic linear cascade to investigate purge and secondary flow effects on the aerodynamics of high-speed low-pressure turbines

Mizuki OKADA 323
PIV measurement of rim seal flows in a high-speed turbine rig

Antonio Federico TORRE 333
Experimental investigation of the aerodynamics of a single-stage high-speed low-pressure turbine

Gonçalo GRANJAL CRUZ (first year PhD)..... 343
Improvement of measurement accuracy using Bayesian inference - Application to low speed UHBR fan

COMPRESSOR AERODYNAMICS AND HEAT TRANSFER

Riccardo TORACCHIO 347
Steady and unsteady numerical characterization of the stable operating range of a highly-loaded low-pressure compressor stage

Cedric BABIN..... 359
Measurement setup and strategy for shrouded stator cavity flow characterization in high speed axial compressor facility

Federico BERTELLI (first year PhD) 371
The role of turbulence length scales on the aerodynamics of internal flow passages

INSTRUMENTATION AND MEASUREMENT TECHNIQUES

Bart BROUWERS..... 375
Monitoring of flow mechanics in cohesive sediment layers

Muhsin Can AKKURT..... 387
Ray-tracing based PIV of turbulent flows in roughened circular channels

AEROTHERMOCHEMISTRY

Investigation of aerothermodynamic phenomena of aerospace flight in ground testing facilities

Enrico Anfuso

Aeronautics and Aerospace Department, von Karman Institute for Fluid Dynamics, Belgium, anfuso@vki.ac.be

Supervisor: Olivier Chazot

Mysuposition (e.g. Associate Professor), Aeronautics and Aerospace Department, von Karman Institute for Fluid Dynamics, Belgium, chazot@vki.ac.be

Abstract

Thermal Protection Systems are vital to protect vehicles during atmospheric entry. The design and development of TPS are performed in ground testing facilities capable to reproduce the complex hypersonic flight. However, even though ground testings have been conducted for over 50 years, our knowledge of the phenomena is still limited. Testing conditions need to be better addressed for a truthful flight-to-ground extrapolation, and engineers resort to safety factors to determine the head shield thickness, at the expense of reduced mass of embarked payload.
This work focuses on improving the characterization of testing conditions of two facilities at the Von Karman Institute (VKI): the Longshot and Plasmatron. The former produces flow at high Reynolds and Mach numbers for short testing time, suitable for aerodynamic studies. The latter is usually operated in subsonic regime providing long duration heating test for aerothermochemistry investigations.

Laser absorption spectroscopy is applied to determine free stream density, temperature, and velocity of the shock-tunnel as well as to check possible thermal non-equilibrium effect (e.g. vibrational freezing) due to the rapid expansion in the nozzle. Results are then compared with those of the typical rebuilding procedures and uncertainties assessed through a robust Uncertainty Quantification (UQ) analysis.
Chemical models and plasma jet instabilities affect the characterization of the testing conditions of the facility. The impact of the kinetic models is studied using UQ analysis and optical emission spectroscopy while the influence of the jet unsteadiness employing data-driven methods. A recent study has shown that the unsteady nature of the plasma jet may lead to discrepancies between steady-state simulations and time-averaged results of experiments. Data-driven techniques represent therefore a powerful tool to treat experimental data and assess the relevance of steady-state simulation.
Finally, supersonic plasma conditions are achieved with a new convergent-divergent nozzle design and manufactured at the VKI. An experimental campaign will be carried out to characterize the thermo-chemical state of the jet in different regions of the flow field (free-stream, shock layers, and boundary layer edge) using optical emission spectroscopy. Then, a big effort will be directed to extend and develop flight-to-ground extrapolation methodologies to duplicate shear, pressure and heat flux in the stagnation region and at off-stagnation points.

Heat flux characterization of an under-expanded/supersonic plasma jet over a catalytic probe

Michele Capriati

Aeronautics and Aerospace Department, von Karman Institute for Fluid Dynamics, Belgium, michele.capriati@vki.ac.be
CMAP - Centre de Mathmatiques Appliques - Ecole Polytechnique, Inria Saclay - Ile de France, France

Supervisor: Thierry Magin

Associate Professor, Aeronautics and Aerospace Department, von Karman Institute for Fluid Dynamics, Belgium, magin@vki.ac.be

University Supervisor: Pietro Congedo

Head of the PLATON project-team in CMAP Laboratory (INRIA Saclay Ile-de-France, Ecole Polytechnique), France, pietro.congedo@inria.fr

Abstract

An under-expanded/supersonic air plasma flow over a catalytic probe is numerically simulated. Surface heat flux and pressure, as well as shock stand-off distance, shows good agreement with the experimental values. A characterization of the error associated to the numerical grid is also performed.

Keywords: Under-expanded flows, plasma flows, discretization errors, gas-surface interaction

1. Introduction

The von Karman Institute Plasmatron facility is used for the characterization of materials exposed to a high-enthalpy plasma environment. It is particularly helpful to predict the behaviour of Thermal-Protection Material (TPM). TPM are used in atmospheric entry applications to protect the vehicle from the extremely demanding conditions to which it is subject: it experiences tremendous heat load and mass lost.
The in-ground subsonic plasma flow duplicates the in-flight highly reactive boundary layer when the local heat transfer simulation constrains are respected[1]. This principle is exploit to study the catalytic or ablative behaviour of the TPM by measuring heat fluxes, recession rates and surface temperatures.
When the flow is subsonic, the recession experienced by the sample is almost constant along its angular direction. To explore the effects of the shape change of the probe, a supersonic plasma experimental campaign has been recently conducted at the VKI. The supersonic flow was achieved by mounting a sonic nozzle at the end of the plasma torch. It expands the gas to choked condition. By adequately lowering down the chamber pressure it is possible to further expand the gas, allowing to reach supersonic Mach number.
The experimental campaign was simulated using the US3D flow solver [2]. The catalytic behaviour of the surface was modeled using the gas-surface interaction module present in MUTATION++[3].
We propose a strategy to determine the temperature at the inlet of the nozzle, by matching the surface heat flux experimentally reported. The structure of the flow is analyzed and compared to the experimentally observed one: the under-expanded gas accelerates through an expansion fan and interacts with the probe generating a normal shock. The jet appears to to be highly dissociated; the atoms recombine on the catalytic surface, increasing the experienced heat flux by their diffusive quota.
Furthermore a characterization of the numerical error on the prediction of heat flux and pressure is performed. It is essential to estimate the numerical precision of the prediction for a given computational budget.
The article is structure as follow: in section 2) the gas equations are presented, as well as the description of the catalytic boundary condition and of the

flow solver; in section 3) the strategy to determine the numerical error is given; in section 4) the details of the supersonic experimental campaign are reported; in section 5) the numerical grids and the boundary condition are shown; and finally in section 6) the numerical result are discussed.

2. Governing equations and flow solver

The gas is a mixture of n_s chemical reacting species in thermal equilibrium. The flow is described by the Navier-Stokes equations:

$$\frac{\partial \rho_i}{\partial t} + \nabla \cdot (\rho_i \mathbf{u} + \mathbf{j}_i) = \dot{\omega}_i, \quad \forall i \in S, \tag{1}$$

$$\frac{\partial \rho \mathbf{u}}{\partial t} + \nabla \cdot (\rho \mathbf{u} \cdot \mathbf{u} + p\bar{\bar{I}} + \bar{\bar{\tau}}) = \mathbf{0}, \tag{2}$$

$$\frac{\partial \rho E}{\partial t} + \nabla \cdot (\rho \mathbf{u} H + \bar{\bar{\tau}}\mathbf{u} + \mathbf{q}) = 0. \tag{3}$$

Symbol S stands for the set of species indices, ρ_i is the partial density of species i, $\mathbf{u}$ is the mass-averaged mixture velocity, $\mathbf{j}_i$ the diffusion mass flux of species i, $\dot{\omega}_i$, its chemical production/destruction rate, p, the thermodynamic pressure of the mixture, $\bar{\bar{\tau}}$, the viscous stress tensor, E, the total energy, $H = E + p/\rho$, the total enthalpy, and $\mathbf{q}$, the total heat flux.
Thermodynamics properties are obtained using the NASA polynomials [4]. Diffusion mass fluxes are computed using the Stephan-Maxwell equations, while viscosity and thermal conductivity are based on Chapman-Enskog solution of the Boltzmann Eq. [5; 6]. Chemical production rates $\dot{\omega}$ for species i are computed using finite-rate chemistry, with reaction rate coefficients taken from [7]. The library MUTATION++ [8] provides the closure to the models above mentioned to the flow solver.

2.1. Gas-Surface Interaction

GSI phenomena can be expressed as a boundary condition imposed to the Navier-Stokes equations, when dealing with a chemically reactive surface. It returns to the CFD solver the surface state computed by solving balance equations in an infinitesimal volume containing both the gas and material phases. When the surface temperature is user-defined (isothermal condition), the surface state is defined by means of the species partial densities.
For a catalytic material, the surface mass balance for each species i reads:

$$\dot{\omega}_i^s = \mathbf{j}_i \cdot \mathbf{n}, \quad \forall i \in S \tag{4}$$

Versor $\mathbf{n}$ is the normal to the surface. It can be computed using phenomenological or finite-rate chemistry models. The different fidelity models for chemical closures are available in MUTATION++ [3]. In this work we used a phenomenological model. The gas state near the interface is obtained by solving the system (4) using a Newton method and the surface state is returned to the CFD solver.
When the temperature at the wall is unknown, an additional energy balance must be applied. Such a balance is also available in MUTATION++, but was not used in this work.
Phenomenological models were first introduced to describe the catalytic behaviour of a surface in hypersonic simulations [9]. They are widely used in the hypersonic community because of their simplicity, they only require the definition of the probability that a macroscopic reaction takes place:

$$\gamma_i^{rea} = \frac{\mathcal{N}_i^{rea}}{\mathcal{N}_i} \tag{5}$$

where $\mathcal{N}_i^{rea}$ is the number flux of species i subject to the reaction and $\mathcal{N}_i = n_i \sqrt{k_b T_s/(2\pi m_i)}$, the number flux of species i impinging the surface. Symbol k_b stands for Boltzmann's constant, T_s the surface temperature, and m_i, the mass of species i. A fully catalytic behavior is obtained when the probability γ approaches unity; whereas a non-catalytic behavior is reached when γ is equal to zero. The chemical production rate reads:

$$\dot{\omega}_i^s = m_i \gamma_i^{rea} \mathcal{N}_i. \tag{6}$$

2.2. US3D flow solver

US3D is a three-dimensional finite-volume flow solver developed at the University of Minnesota for aerodynamic/hypersonic applications [2]. The code uses an unstructured grid, the numerical fluxes are computed in this work according to the modified Steger-Warming scheme [10] with a MUSCL approach to obtain second-order accuracy. The Data Parallel Line Relaxation (DPLR [11]) ensures rapid convergence to steady-state. US3D is highly scalable and efficient, making it possible to solve very large problems on parallel computers in a cost-effective manner. We have coupled US3D to MUTATION++ by means of *User defined routines* available in the code for the closure of: I) Transport (viscosity, thermal conductivity, diffusive fluxes), II) Gas chemistry, III) Multitemperature energy transfer terms IV) Gas-Surface interaction.

3. Numerical error determination

The numerical error associated to the discretization of the physical domain (discretization error, ϵ_ϕ) can be evaluated by performing a systematic grid refinement[12]. It can be represented by an exponential function:

$$\epsilon_\phi \approx \delta_{\mathrm{RE}} = \phi_\mathrm{i} - \phi_0 = \alpha h_\mathrm{i}^p. \tag{7}$$

The quantity ϕ_i is a flow quantity of interest at the grid refinement i, ϕ_0, the estimate of the exact solution, α, a constant to be determined, h_i, the typical cell size and p is the observed order of grid convergence. To represent the density of the grids using a single parameter the numerical grids have to be geometrically similar: grid parameters, such as deviation from orthogonality, skewness, etc. should remain constant.
In most of the application the 'exact' solution of the quantity of interest cannot be analytically computed; in these cases, it can be estimate by minimizing the standard deviation, σ, between the numerical solutions and the fit low:

$$\phi_\mathrm{i} = \phi_0 + \alpha h_\mathrm{i}^p, \tag{8}$$

the minimum number of grids (n_g) required is 4.
A positive value of order of convergence (p) implies a monotonic convergence, in contrast a negative value a monotonic divergence. In practical applications, it is not always possible to fall into the monotonic convergence range. In such scenario, others ways to characterize the numerical error are given in literature:

$$\sigma_1 = \alpha h_\mathrm{i}, \tag{9}$$

$$\sigma_2 = \alpha h_\mathrm{i}^2, \tag{10}$$

or

$$\sigma_{12} = \alpha_1 h_\mathrm{i} + \alpha_2 h_\mathrm{i}^2, \tag{11}$$

one should choose the one the best fit the data, *i.e* the one with the lowest standard deviation.
Eca proposed to compute the uncertainty associated to the numerical prediction [12]:

$$U_\phi(\phi_\mathrm{i}) = \begin{cases} F_\mathrm{s}\epsilon_\phi(\phi_\mathrm{i}) + \sigma + |\phi_\mathrm{i} - \phi_\mathrm{fit}|, & \text{if } \sigma < \Delta_\phi \\ 3\frac{\sigma}{\Delta_\phi}(\epsilon_\phi(\phi_\mathrm{i}) + \sigma + |\phi_\mathrm{i} - \phi_\mathrm{fit}|), & \text{otherwise} \end{cases} \tag{12}$$

where $\Delta_\phi = (\phi_\mathrm{i}^{\max} - \phi_\mathrm{i}^{\min})/(n_\mathrm{g} - 1)$ is a data range parameter and F_s is a safety factor equal to 1.25 if $0.5 \leq p < 2.1$ and $\sigma < \Delta_\phi$, and to 3 otherwise.

4. Experimental campaign

An experimental campaign was conducted at the von Karman Institute to characterize the response of a material exposed to an air plasma flow. When the flow is subsonic, the sample experiences a quasi-uniform recession. To investigate the effects arising from shape changing, the flow was accelerated to supersonic conditions. To this end, a sonic nozzle was mounted at the exit of the plasma torch to expand the gas to choked conditions. It was chosen a reservoir pressure of 165hPa and a chamber one of 5.5 hPa, resulting in a flow highly under-expanded. The Plasmatron was supplied with a power of 600 kW. The sonic nozzle has an exit diameter of 35 mm and the probe is placed at a distance of 75mm from the exit of the nozzle. The probe induces a shock that interacts with the expansion fan and the boundary layer, as one can see from fig.1. A calorimeter probe is used to characterize the heat flux and a Pitot probe for the stagnation pressure; they are, respectively 4.48 MW/m^2 and 26 hPa. Uncertainty on the heat flux is about the 10% while for pressure measurements is about the 0.25% of the full scale, *i.e.* 0.5 hPa. Two runs were performed to assess the repeatability of the test. The probes have a nose radius of 25 mm with a 15 mm cylinder.

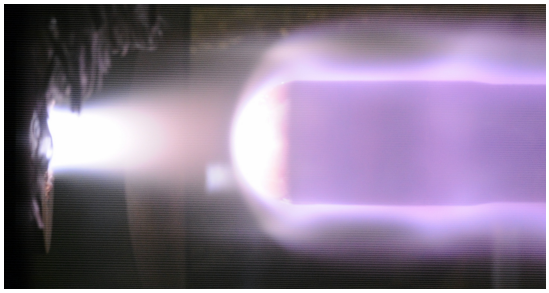

Figure 1: Under-expanded air jet over the catalytic probe.

5. Numerical domain and boundary conditions

The computational domains is represented in fig. 2: from the left to the right I) exit of plasma torch/nozzle inlet, II) sonic nozzle surface, III) expansion chamber and IV) probe. Particular attention was posed to well capture the shock to have reliable results on the probe surface: as one can see in figure 3 the grid is almost aligned to the shock and the cells are stretched in the shock direction. The four grids listed table 1 are obtained by doubling the number of the nodes in the x direction starting from the coarsest mesh (number

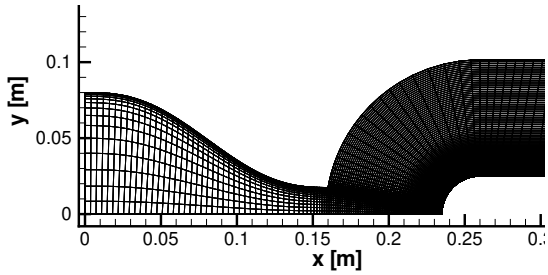

Figure 2: Numerical domain: from the left to the right I) exit of plasma torch/nozzle inlet, II) sonic nozzle surface, III) expansion chamber and IV) probe. Mesh number 2 on table 1.

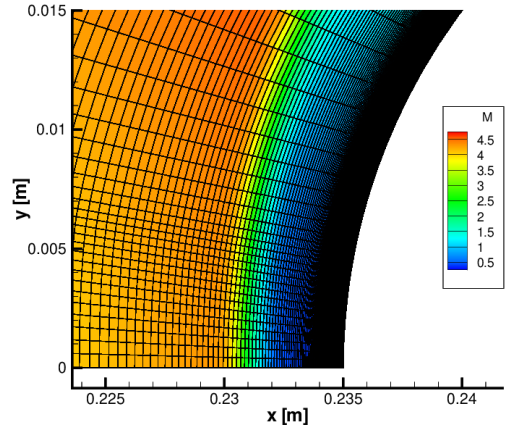

Figure 3: Zoom of the numerical domain: grid aligned to the shock and stretched in the direction of the shock.

4) to the finest one (number 1). A number of four was chosen to compute the numerical error on surface heat flux and pressure, following the procedure reported in section 3. The boundary condition applied to the simulation are the following:

- nozzle inlet: pressure of 165 hPa and a mass flow of 6 g/s; the value of inlet temperature is determined through an iterative procedure to match the experimental heat flux; the chemical composition was assumed at equilibrium,
- nozzle surface: isothermal condition, with temperature equal to 1500 K,
- chamber free surface: an inlet condition is prescribed for numerical stability; it is characterized by a small velocity (1m/s), room temperature and a chamber pressure of 5.5 hPa,
- probe: isothermal/catalytic surface with a temperature of 350K and a recombination probability for oxygen equal to 0.12 and for nitrogen to 0.7, as suggested by Bellas [13].

Table 1: Used meshes: index, number of cells, length of first cell on the stagnation point (Δy), ratio of characteristic lengths ($h_i = \Delta y_i/\Delta y_1$)

Mesh index	cells	Δy	h_i
1	23710	4.9e-07	1
2	11855	9.8e-7	2
3	5960	2.0e-6	4.1
4	2987	4.16e-6	8.5

All the other surfaces are characterized by a symmetry boundary condition.

6. Simulation results

The experimental camping, described in section 4, was simulated using the US3D flow solver. A 5 species air mixture was used (N2, O2, NO, N, O), whose reaction rates constant were taken from [7]. Purpose of the numerical analysis is to:

- determine the condition at the inlet of the nozzle in terms of temperature;
- characterize the numerical error for a given computational budget (number of cells used) and compute the associated uncertainty;
- predict stagnation point observable: heat flux and stagnation pressure;
- describe the flow structure.

6.1. Exit plasma torch temperature determination

A pressure of 165 hPa and a mass flux of 6g/s was experimentally measured at the exit of the plasma torch/inlet of the nozzle. Unlike these quantities, the value of the temperature is not experimentally observable. Generally it is numerically re-built using the ICP code: magnetohydrodynamics equations are solved for a given power supplied to the Plasmatron and of its efficiency. Results of the simulation are the input for the VKI boundary layer code, that provides an estimate of the heat flux on the surface. The efficiency is iterated until the heat flux is accurately predicted: in such a way it is possible to re-build the conditions at the exit of the plasma torch.
The procedure adopted within this work is slightly different: we propose to iterate directly on the inlet

temperature, without solving magnetohydrodynamics equations, until the experimental heat flux is matched. For this procedure the mesh 2 in table 1 was chosen as it exhibits a good time for converging to steady-state (≈8h, on 16 cores).
A value of inlet temperature equal to 6950K predicts an heat flux of 4.53 MW/m^2 and a pressure of 2653 hPa on the stagnation point, in good agreement with the experimental data. Thus, it was chosen for the simulations.

6.2. Numerical error determination

The four numerical grids in table 1 were used to characterize the numerical error for a given computational budget (number of cells) and to compute the associated uncertainty, as described in section 3.
The distribution of the heat flux and of the pressure as function of the probe angle is given in Fig.4 and 5, respectively: as the gas expands along the probe surface both the quantities decreases. The results shown are obtained with the finest mesh.

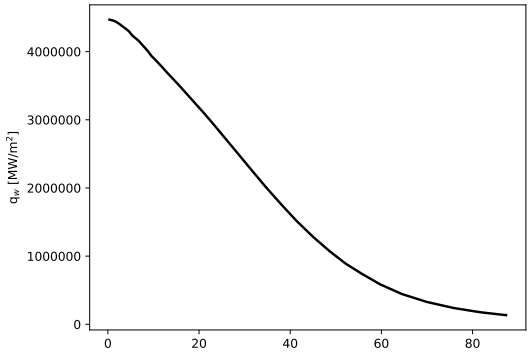

Figure 4: Heat flux around the probe as function of the angle for the finest mesh.

Their values on the stagnation point are shown in table 2 for the four numerical grids. Equation (7)

Table 2: Heat flux and pressure on the stagnation point for the four grids in table 2

Mesh index	q_w [MW/m^2]	p [Pa]
1	4.46	2638
2	4.53	2653
3	4.65	2663
4	4.81	2566

was adopted to characterize the numerical error on the

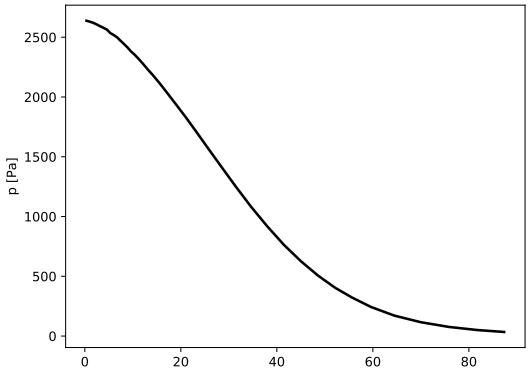

Figure 5: Pressure around the probe as function of the angle for the finest mesh.

heat flux. The fitted curve is plotted in Fig. 6, a convergence order $p = 0.5312$ ensure to have a monotonic convergence; the coefficient α is equal to 0.16 MW/m^2, the standard deviation, σ, to 0.0097, and the 'exact' value, ϕ_0, to 4.30 MW/m^2. The uncertainty associated to the first grid is 0.22 MW/m^2. This estimate is within the experimental uncertanties, *i.e.* 4.48 ± 0.448 MW/m^2. Equation (7) was predicting nega-

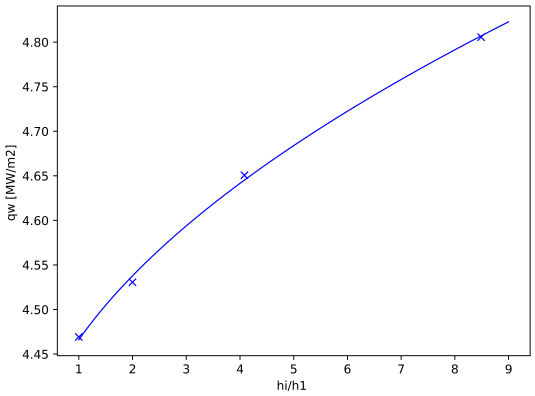

Figure 6: Heat flux as function of grid refinement, numerical results with cross, fitting with solid line.

tive values of order of convergence for the pressure; thus, a second order fitting was performed, Eq. (11). The values of the two coefficients are, respectively, $\alpha_1 = -4.03$ Pa and $\alpha_2 = 28.82$ Pa, the standard deviation, σ, is equal to 1.28, and the 'exact' value, ϕ_0, to 2612.63 Pa. The uncertainty associated to the first grid is 3.25 Pa. This values is slightly higher than the experimental value, *i.e.* 25 ± 0.5 hPa. To better understand why the pressure is not in the monotonic convergence, one can take a look to Fig. 8: mesh 4 is the only

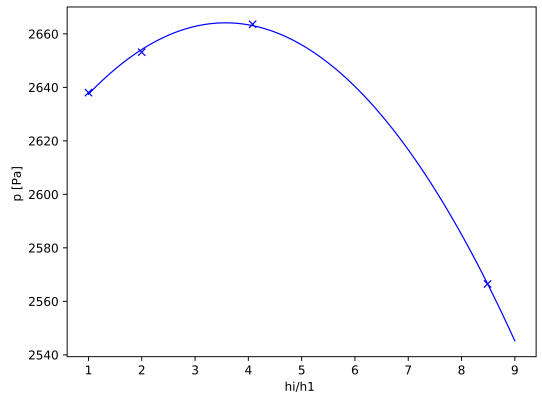

Figure 7: Pressure as function of grid refinement, numerical results with cross, fitting with solid line.

mesh whose cells are not stretched in the shock directions, it is well known in the hypersonic community that this generally leads to ill-behaving predictions of surface properties.

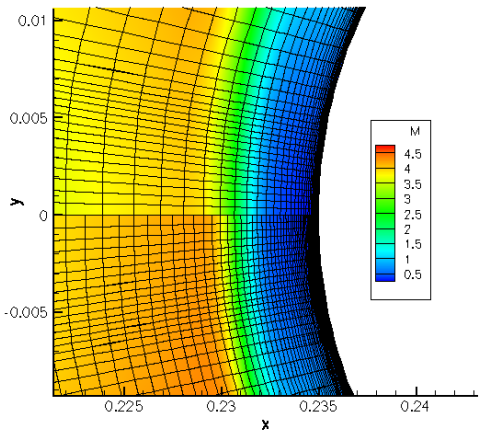

Figure 8: Zoom of mesh 4 (top) and mesh 3 (bottom): mesh 4 is the first mesh whose cells are not stretched in the shock direction.

6.3. *Fluid structure*

The flowfield solution obtained with the finest mesh is shown in Fig. 9. The flow is highly under-expanded. In fact, it is characterized by a total pressure ratio, $\eta_0 = p_0/p_{\text{chamber}} = 30$; the gas expands in the nozzle to an exit pressure of ≈ 8200 Pa, corresponding to an exit pressure ratio, $\eta_{exit} = p_{exit}/p_{\text{chamber}} = 15$. Thus, it continues its expansion in the chamber. From the figure, the Prandtl Meyer expansion fan in well visible at the nozzle exit, as well as the typical barrel shape shock structure, typical of this configuration. The flow develops until it reaches the probe: a normal shock is generated and it interacts with the barrel shock and the boundary layer. After that the gas undergoes strong velocity gradients to align the streamline to the probe geometry.

The probe is positioned relatively close to the nozzle exit: the normal shock prevents the traditional Mach disk to be formed.

A comparison between the solution of the simulation

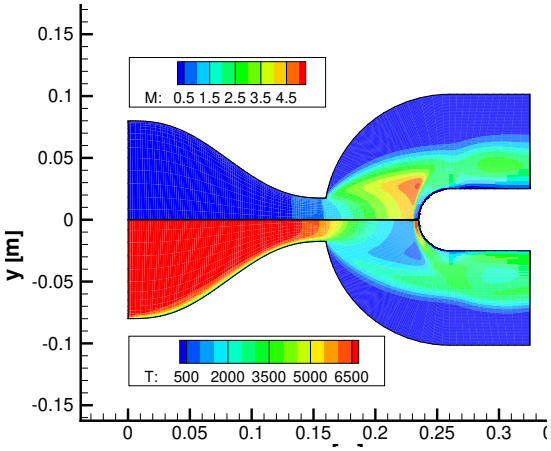

Figure 9: Structure of the under-expanded jet: expansion fan, barrel shape shock, and normal shock. Mach number on the top, temperature on the bottom. Results obtain with mesh 1 in table 1

and a picture of the experiment is given in Fig. 10. This comparison is quantitative as the camera was not perfectly aligned to the sample; furthermore an Abel inversion of the photo should be performed to have the same 2D numerical field. One can notice the higher temperature of the jet core at the exit of the nozzle that decreases as the gas expand and the shock developing in front of the probe, whose intensity decreases moving along the probe.

Quantitative comparison can be done on the position of the shock, shown in Fig. 11: the experimental image was taken with a camera with resolution 0.114 mm/pixel; considering the surface position to be at pixel 301 and the shock one at pixel 272, a stand-off distance of 3.3 mm is observed. From the simulation the stand-off distance is computed at half of the temperature jump ($T \approx 4060$ K), corresponding to a value of 3.8 mm: the simulation predicts a value of stand-off distance 0.5 mm greater.

The jet is dominated by dissociated species, as shown in Fig. 12: nitrogen partially recombines in the nozzle boundary layer. Greater recombination occurs in the boundary layer of the catalytic probe, whose surface

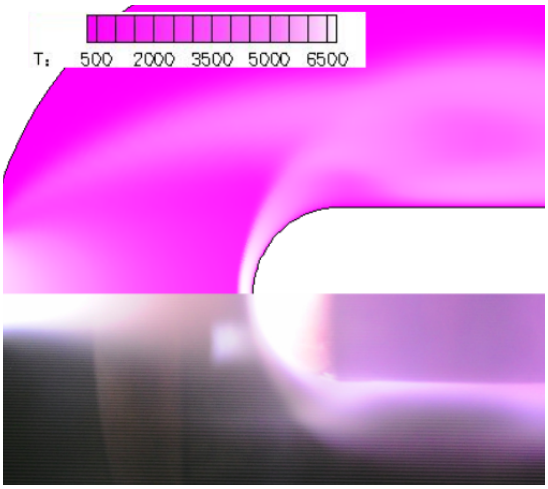

Figure 10: Qualitative comparison between the numerical temperature field (top) and the experimental one(bottom): I) hot jet core, and II) normal shock.

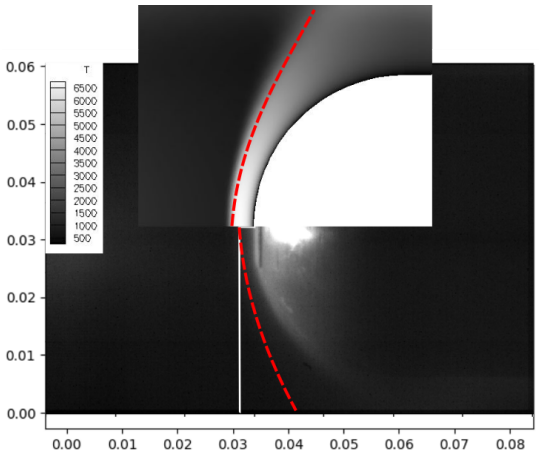

Figure 11: Quantitative comparison between the numerical stad-off distance (top) and the experimental one (bottom).

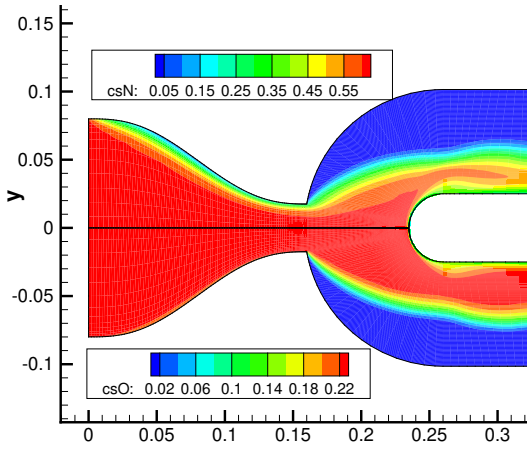

Figure 12: Mass fraction field: atomic nitrogen (top), and atomic oxygen (bottom).

chemical activity promotes recombination. The trend can be better appreciated by looking at Fig. 13: it represents the species distribution in the probe boundary layer, along the stagnation line. The surface chemical activity drives the diffusion of atomic species to the probe where they recombine; molecules diffuse in the opposite direction. It is observed that this catalytic activity almost double the heat flux experienced by the probe.

7. Conclusion

An experimental campaign carried out at the von Karman was simulated. It consists of an under-expanded/supersonic air plasma flow over a catalytic probe. The US3D flow solver was used to perform the simulations. It has been shown that is possible to numerically re-built the temperature at the inlet of the sonic nozzle by matching the heat flux.
Four different meshes, obtained by doubling the nodes in the x direction were used to estimate the numerical error for a given computational budget. An uncertainty on the numerical prediction was computed.
Results relative to the surface (heat flux and pressure) showed good agreement with the experimental values. The flow structure was discussed and compared with the experimental one; the shock stand-off distance is predicted to be 0.5mm further than the experimental value.
In the future a uncertainty analysis will be performed on the test case: the idea is to reduce the computational cost of the simulation by building a multi-fidelity surrogate model.

Acknowledgments

Authors acknowledge the Air Force Office of Scientific Research (AFOSR) for supporting the work under the grant FA9550-18-1-0209.

References

[1] A. F. Kolesnikov, Conditions of simulation of stagnation point heat transfer from a high-enthalpy flow, Fluid Dynamics 28 (1993) 131–137.
[2] G. V. Candler, H. B. Johnson, I. Nompelis, V. M. Gidzak, P. K. Subbareddy, M. Barnhardt, Development of the us3d code for advanced compressible and reacting flow simulations.

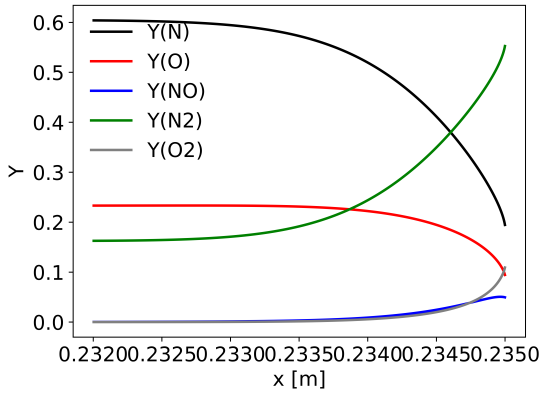

Figure 13: Chemical composition in the probe boundary layer, results along the stagnation line.

[3] G. Chatzigeorgis, A. Viladegut, P. Barbante, O. Chazot, T. Magin, A. Turchi, Development of catalytic and ablative gas-surface interaction models for the simulation of reacting gas mixtures, in: 23rd AIAA Computational Fluid Dynamics Conference, 2017. doi:10.2514/6.2017-4499.

[4] S. Gordon, J. McBride, Thermodynamic Data to 20,000 K For Monatomic Gases, Tech. Rep. 1999-208523, NASA (1999).

[5] J. H. Ferziger, H. G. Kaper, Mathematical theory of transport processes in gases, American Journal of Physics 41 (4) (1973) 601–603.

[6] T. E. Magin, G. Degrez, Transport algorithms for partially ionized and unmagnetized plasmas, Journal of Computational Physics 198 (2) (2004) 424–449.

[7] C. Park, R. L. Jaffe, H. Partridge, Chemical-kinetic parameters of hyperbolic earth entry, Journal of Thermophysics and Heat Transfer 15 (1) (2001) 76–90.

[8] J. B. Scoggins, V. Leroy, G. Bellas-Chatzigeorgis, B. Dias, T. E. Magin, Mutation++: Multicomponent thermodynamic and transport properties for ionized gases in c++, SoftwareX 12 (2020) 100575.

[9] R. Goulard, On catalytic recombination rates in hypersonic stagnation heat transfer, Journal of Jet Propulsion 28 (11) (1958) 737–745.

[10] J. L. Steger, R. Warming, Flux vector splitting of the inviscid gasdynamic equations with application to finite-difference methods, Journal of Computational Physics 40 (2) (1981) 263–293.

[11] M. J. Wright, G. V. Candler, D. Bose, Data-parallel line relaxation method for the navier-stokes equations, AIAA Journal 36 (9) (1998) 1603–1609.

[12] L. Ea, M. Hoekstra, A procedure for the estimation of the numerical uncertainty of cfd calculations based on grid refinement studies, Journal of Computational Physics 262 (2014) 104–130.

[13] G. Bellas-Chatzigeorgis", "development of advanced gas-surface interaction models for chemically reacting flows for re-entry conditions", Ph.D. thesis, Politecnico di Milano (2001).

Comprehensive characterization of the aero-thermo-mechanical response of space debris materials to atmospheric entry plasmas

Andrea Fagnani

Aeronautics and Aerospace Department, von Karman Institute for Fluid Dynamics, Belgium, andrea.fagnani@vki.ac.be

Supervisor: Olivier Chazot

Head of Department and Professor, Aeronautics and Aerospace Department, von Karman Institute for Fluid Dynamics, Belgium, chazot@vki.ac.be

University Supervisor: Annick Hubin

Professor at Department of Materials and Chemistry, Vrjie Universiteit Brussel, Belgium, annick.hubin@vub.be

Abstract

The number of space debris in Earth's orbit has drastically increased over the last decades, leading to a major concern about future sustainability for the space environment. Moreover, on-ground casualty risk requirements are nowadays imposed by space agencies worldwide, demanding innovative cost-effective strategies to ensure safe disposal of space objects upon uncontrolled re-entry. Combined theoretical, numerical and experimental research is then required to improve our understanding of the complex gas/surface interaction and material response of space debris materials in atmospheric entry flows. In this paper, we review the high-enthalpy ground testing capabilities at the von Karman Institute for Fluid Dynamics, combining novel techniques with tools inherited from the sound expertise on thermal protection systems testing to pave the way for space debris material experimentation.

Keywords:
Space debris, aerothermochemistry, plasma wind tunnels

1. Introduction

Satellites orbiting Earth offer unrivalled possibilities for research and commercial applications; however, space activities over the last decades have left more than 20000 objects in orbit which are no longer functional, namely, space debris [1]. Their number is predicted to increase exponentially in the future and, due to their hypervelocity motion, collision with existing and new missions can lead to a catastrophic break up, generating even more debris in a cascade effect known as the Kessler syndrome [2]. Space debris, mitigation guidelines [3], suggested by the United Nations in 2007, were embraced by the European Commission and implemented by the European Space Agency (ESA) through the Clean Space Initiative. These measures aim at reducing the generation of new debris, limiting the break-up probability, requiring passivation procedures and implementing disposal strategies, such as re-orbiting and de-orbiting at the end-of-life [4]. Moreover, on average over the past decade, an object with mass above 800 kg has re-entered the atmosphere every week [5]. As often witnessed during these events, ground recoveries are the clear testimony of non-demisability of some spacecraft components [6]. As a result, space agencies and nations have discussed requirements to limit the on-ground casualty risk for future missions. Compliance to this requirement can be safely achieved through controlled re-entry and ground impact over large unpopulated areas. Yet, this solution has major consequences at system level, possibly requiring a full redesign of the spacecraft and leading to higher mass and thus increased mission cost [7]. Among the alternative strategies, the Design for Demise (D4D) refers to all measures taken in the design of a space object to increase the potential for demise, i.e. complete degradation, upon an uncontrolled re-entry at the end-of-

life. The latter, in turn, has the advantage to be cost effective (e.g., no additional propellent is needed) and features less stringent design requirements [8]. Thus, the ultimate goal of the D4D is the ability to correctly predict the complex multi-physical and multi-scale response of space materials to the extreme conditions of atmospheric entry, so as to guarantee, at a design level, their complete degradation. Yet, as it will be further detailed later on, this estimation is a complex task and current scientific capabilities do not allow such predictive characterizations [9]. Hence, D4D demands a strong research effort in modeling, numerical simulations and experimental activities.

1.1. Aerothermal phenomena of demising metals and silicates

During atmospheric entry, the bow shock formed in front of the spacecraft travelling at hypersonic speed produces a high-temperature plasma ($T \approx 10000$ K). A material submitted to such temperatures will undergo a series of degradation phenomena, which are generically known as ablation [10]. If the latter proceeds until the entire material mass is consumed, demise of the component has occurred. This process can be regarded as a multi-physics gas-surface interaction phenomenon. In the materials of interest for this work, the aerothermal heating of the material induces melting and formation of gas-liquid and liquid-solid interfaces. The liquid layer may be removed by surface shear forces, imposed by the surrounding flow, or by thermo-chemical phenomena such as evaporation. Injection of vapour into the boundary layer, in turn, affects the aerodynamic heat transfer and the gas-phase chemistry [11], producing a coupled flow-material problem. Additionally, molecular species dissociate due to the extreme temperatures, recombine in the boundary layer and diffuse towards the surface. At the wall, heterogeneous chemistry occurs, including catalysis, nitridation and oxidation. The latter is of paramount importance in the survivability of metallic components due to the high melting points of most metallic oxides, as already documented in the literature [9].

1.2. Ground testing and experimental data demands

The aspiration for a cleaner and more sustainable future for the space environment, allowing to benefit both from its scientific and economical applications, advocates for a revolutionary effort in the design of new demisable systems.

Ground testing in plasma wind-tunnels is currently the only affordable possibility for both material qualification and validation of material response codes [12]. Due to the multiplicity of the phenomena involved in the space debris demise, however, ground reproduction of a full re-entry scenario seems infeasible. The leading path is then represented by a model development strategy based on consistent wind tunnel experiments. The latter, then, must be able to correctly isolate each critical phenomenon. However, a withstanding challenge in high-enthalpy facilities experimentation is the correct scaling of all the driving physical phenomena [13]. For the specific case of multiphase melting-ablation, this challenge is hardly addressed in the existing literature.

Leveraging on the strong expertise of the VKI in the ground testing of reusable [14] and ablative [10] thermal protection systems, in this work we propose to adapt and improve existing tools and complement them with novel capabilities, chiefly blending numerical models and advanced data processing techniques, to provide a consistent framework to carry out state-of-the-art experimentation on space debris materials. The goal is to improve the ground testing reliability and reducing uncertainties to develop new thermo-chemical ablation models.

2. VKI Plasmatron facility

The VKI Plasmatron is the world's largest Inductively Coupled Plasma (ICP) facility, equipped with a 160 mm diameter torch powered by a high-frequency, high-power, high-voltage (400 kHz, 1.2 MW, 2 kV) electric generator. The flow regime is typically subsonic, although sonic and supersonic flow conditions can also be achieved by means of a nozzle configuration. As the gas is heated by electromagnetic induction, the main advantage of ICP torches with respect to arc-jet heaters is the high purity of the plasma flows, due to the absence of chemical pollution associated to the erosion of the electrodes. A copper water-cooled probe, holding a 14 mm copper calorimeter in the center of the front face, is used to calibrate the plasma flow conditions. The Cold Wall (CW) ($T_{\mathrm{cw}} = 350$K) stagnation point heat flux ($\dot{q}_{\mathrm{cw}}$) is determined by the cooling water mass flow, controlled by a calibrated rotameter, and the inlet/outlet temperature difference, measured by two type-E thermocouples. A water-cooled Pitot probe is used to perform dynamic pressure (p_{dyn}) measurements. The pressure line is connected to a Validyne variable reluctance pressure transducer and a voltage demodulator amplifies the

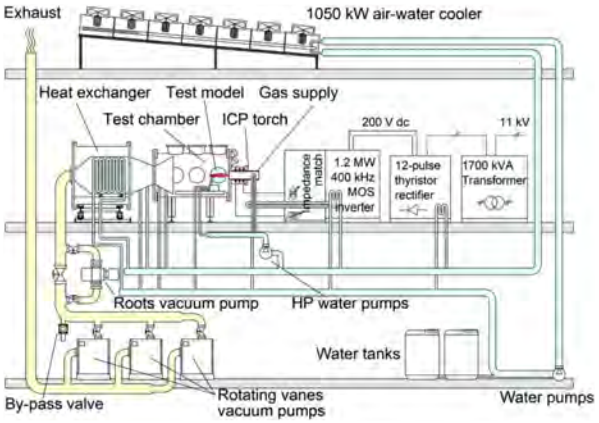

Figure 1: Schematic of the VKI Plasmatron facility.

signal. Validyne and amplifier are calibrated prior to the test by means of a Betz water manometer. An absolute pressure transducer (Memberanovac DM 12, Leybold Vacuum) measures the static pressure (p_s) in the Plasmatron test chamber. As the plasma jet is low subsonic ($Ma \approx 0.1$), the static pressure can be assumed constant in the whole test chamber. The gas mass flow rate ($\dot{m}_{gas}$) supplied to the torch is monitored through a calibrated gas rotameter, while the Plasmatron control system allows to record the electric power ($\mathbb{P}_{el}$) supplied to the induction coil.

2.1. Need for accurate free-stream characterization

To ensure repeatability of the test conditions and to provide accurate data for flow and material response simulations, the correct characterization of the plasma flow conditions is of significant relevance. Flow conditions, in fact, provide the necessary scaling parameters for extrapolation to flight [13] and the required input data for the numerical simulation of the experimental material response [12]. Due to the extreme temperatures of the gas, direct measurements of all the necessary physical quantities is often infeasible. To this purpose, experimental and numerical tools must be chiefly combined in order to determine the quantities of interest. Different techniques for enthalpy determination in plasma facilities can be found in the literature, however they can show significant discrepancies, failing to produce accurate and reproducible results [15].

Traditionally, for the VKI Plasmatron facility, the process combines intrusive experimental measurements at stagnation point (heat flux and dynamic pressure), with numerical simulations of the chemical non equilibrium boundary layer [13], fed with non-dimensional parameters describing the boundary layer edge quantities [15]. This procedure, however, relies on several assumptions which can affect its accuracy. The rebuilt boundary layer edge enthalpy can be very sensitive to the definition of the catalytic coefficient γ, which describes the recombination of atomic species at the wall. Empirical data for copper catalysis in air plasma available in the literature show a significant spread, which inevitably reflect on the accuracy of the technique [15]. Secondly, the procedure relies on some parameters extracted from a full Navier-Stokes simulation of the test environment in local thermodynamic equilibrium (VKI ICP code [16; 14]), describing the boundary layer edge hydrodynamic quantities [15]. This, in turn, relies on the assumption of the ICP torch induction efficiency ($\eta = 50\%$), and variations in the actual value of this parameter can also affect the rebuilt edge enthalpy. Finally, the procedure relies on the assumption of Local Thermodynamic Equilibrium at the boundary layer edge, which still lacks a more exhaustive validation.

3. Experimental plasma free-stream investigation by means of optical emission spectroscopy

Following the work of Le Quang [17], we set-up an optical emission spectroscopy system, able to provide spatially resolved light emission measurement. A full data processing suite has been recently developed to retrieve locally resolved gas temperature measurements. In particular, we use absolute spectroscopic measurements of atomic lines of oxygen and nitrogen, along with spectral fitting of rovibronic transition of

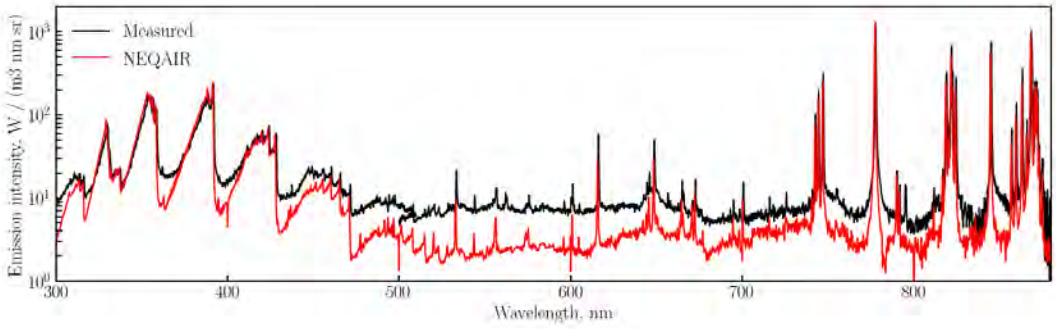

Figure 2: Example of comparison between measured and simulated local plasma radiation in absolute units from the ultraviolet to the near infrared along the jet axis (p_s = 100mbar, T = 7243K).

molecular systems (CN, N_2^+, N_2 and NO mainly) in absolute intensity to retrieve local gas flow temperatures, under the assumption of LTE conditions. For further details about the techniques, the reader is addressed to ref. [18; 19].

Fagnani et al. [18] compared the experimental data to the plasma jet simulated temperatures, allowing to determine critical parameters to provide the correct numerical rebuilding. The technique has revealed very powerful to consolidate the enthalpy rebuilding methodology applied to the VKI Plasmatron facility. However, we found critical issues in the measurement set-up, deriving from chromatic aberrations effects in the optical imaging system. This could significantly affect the measurement results. Here, we characterize the phenomenon experimentally and we implement an effective solution to provide chromatic aberration free spectroscopic measurements.

3.1. Chromatic aberration free spectroscopic measurements

An optical system generally includes a number of reflecting and/or refracting surfaces which can alter the direction of optical rays. The rays leaving an object point can be converged to another point in space, forming an optical image. Optical aberrations, however, may alter the formation of the image, leading to a blurring effect. In particular, chromatic aberration results due to the different index of refraction of the material constituting the optical system for different wavelengths. Since the focal length of a lens is dependent on the index of refraction, polychromatic light from a point object fails to image at a single a point [20]. In particular, since spectroscopy aims at resolving polychromatic light in wavelength, it can be strongly affected by chromatic aberrations.

It was found that the original spectrographic set-up for the free-stream characterization, employing a fused silica plano-convex lens for imaging, was affected by strong chromatic aberrations. Measurements were carried out to characterize the phenomenon and the set-up was updated with new optical components to overcome the issue. A procedure was finally established to verify the chromatic aberration free measurements.

3.1.1. Measurement of chromatic aberration

For a simple imaging system, like a thin lens, the object position p, the image position q and the focal length f_λ are related by the law

$$\frac{1}{p} + \frac{1}{q} = \frac{1}{f_\lambda}, \tag{1}$$

and the focal length of a thin lens can be approximated as [20]

$$\frac{1}{f_\lambda} = (n_\lambda - 1)\left(\frac{1}{R_1} + \frac{1}{R_2}\right) \tag{2}$$

where n_λ is the index of refraction as a function of wavelength, while R_1 and R_2 are the radii of the two convex surfaces. It can be seen that, since the focal length depends on wavelength, for a fixed object position p, the image distance also varies with wavelength. However, since the lens is used for magnification purposes, then $p >> q$ and measuring chromatic aberration effects on the image plane would require to resolve very small variation of q. Yet, if the optical system is employed backwards, placing a light source in the image plane, the variation of the object position p (which now becomes the image) with wavelength is largely amplified. To this purpose, a set of three lasers with red, green and blue (r, g, b) light were connected to the spectrograph by means of a fibre optic and shoot

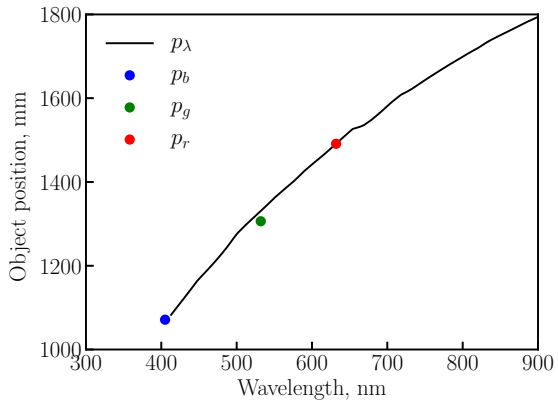

(a)

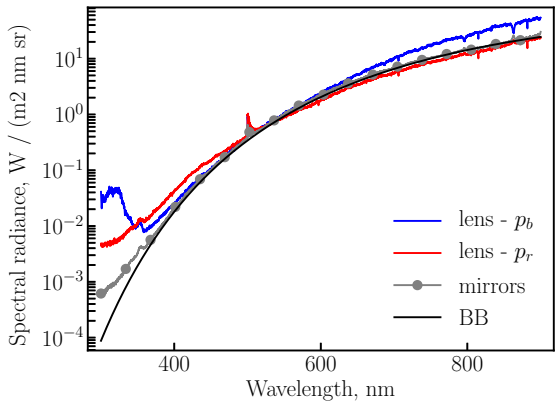

(b)

Figure 3: (a) Measured positions of the object focal plane for a fixed image position at different wavelengths agree well with the theoretical predictions. (b) Chromatic aberration effects are clearly shown when cross-checking the measurement with a known radiation source. Mirrors allow to avoid chromatic aberrations over the whole spectral range.

backwards on the light path. Hence, if the optical system is focused on the red light, the image position will be

$$q_\mathrm{r} = \frac{1}{1/f_\mathrm{r} - 1/p_\mathrm{r}}. \tag{3}$$

Then, the object position of an image source of light with wavelength λ at a distance q_red can be computed as

$$p_\lambda = \frac{1}{1/f_\lambda - 1/q_\mathrm{r}}. \tag{4}$$

Once the refractive index of fused silica and geometric specifications of lens (R_1 and R_2) are known from the manufacturer, p_λ can be computed. The three lasers are now shoot backwards on the light path of the spectrograph and the position p_r, p_g and p_b are measured as the mean distance between close and far focus. Fig. 3(a) shows that measured positions follow well the theoretical prediction p_λ. We can notice a significant chromatic aberration in the optical system, leading to $\sim$ 40 cm distance between the focal planes of red and blue components of light. Viceversa, this means that the image of a polychromatic light source at position p_r will be highly defocused on the image plane at distance q_r for wavelength components in the blue light.

3.1.2. Validation of the chromatic aberration free measurements

Since mirrors work with light reflection instead of refraction, their focal length is independent of wavelength and thus they do not suffer from chromatic aberrations. The optical set-up was updated, substituting the plano-convex lens with a periscope including a planar and a spherical UV-enhanced aluminium mirrors. Performing the same focal plane measurements described in the previous section confirmed that the optical system is now free from chromatic aberrations. To further validate the new set-up, a blackbody source with known temperature was placed on the object plane and measurements were performed using both the lens and mirror optical imaging systems. Fig. 3(b) clearly shows the chromatic aberration effects. In the case of the lens, when the blackbody and calibration sources are placed on the focal plane for red light (solid red curve), the measured radiance overlaps with the Planck curve on the red, while it overshoots on the blue. Viceversa, when blackbody and calibration source are placed on the focal plane of the blue light (solid blue curve), the measured radiance agrees with the Planck curve on the blue but overshoots on the red. When the optical imaging system is replaced with

mirrors, and the blackbody and calibration source are placed on the unique focal plane, then the measured radiance agrees with the Planck curve over the whole spectral range. The residual mismatch for $\lambda < 350$ nm is attributed to the very weak signal of the blackbody source at $T = 1773$ K, for which the signal to noise ratio becomes too low for a good measurement.

4. Experimental methods for ablation characterization

A schematic of the experimental setup for in situ ablation measurements can be found in Fig. 4. Two-colour pyrometry provides direct information of the material's surface temperature. Furthermore, in combination with broadband radiometry, the total directional emissivity can be measured in situ, at high temperature and in a time-resolve fashion. Such information is critical for accurate numerical simulations, as radiation is the primary means of cooling at extreme re-entry conditions. Test models can be additionally instrumented with high-temperature type-K and type-B thermocouples, in order to monitor the temperature evolution in specific points. Moreover, infrared thermography allows to determine surface temperature maps over the entire sample material, while high-speed camera imaging provides information about the material surface recession rate. Further details on the latter techniques are provided hereafter.

4.1. 3D temperature map reconstruction on an ablating surface

In this context, IR thermography is a valuable technique to perform temperature measurements in high-enthalpy facilities, because it is a non-intrusive optical technique, characterized by high sensitivity, low response time and it is fully two dimensional. However, while infrared data are available in the form of 2D images, the observed test object surface is often non-planar and the precise spatial reconstruction of the temperature maps becomes a critical task. Optical calibration techniques have already been introduced in IR thermography by Le Sant [21; 22; 23] and Cardone et al. [24]. These techniques adopt calibration targets or specifically designed control points on the investigated object, along with perspective projection models [25], to establish a relationship between the points of the observed surface and the image pixels, thus enabling the reconstruction of 3D temperature maps from the 2D thermal image. In addition, these procedures also allow to correct for the angular dependence

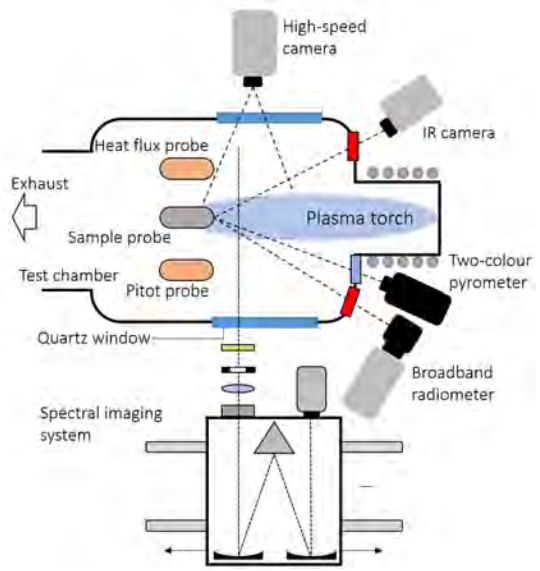

Figure 4: Snapshot of the two-dimensional unsteady heat transfer simulation used to extract $\partial \dot{q}_r / \partial r(x,t)$ for the correction on the one-dimensional solver.

of the material emissivity, since the angle of view with respect to the object surface normal can be easily computed [26]. In the VKI Plasmatron facility, however, the test material sample can undergo significant surface recession due to ablation phenomena which occur when interacting with the high-temperature, chemically reacting plasma flow. Hence a traditional optical calibration procedure with a static target, in which the initial test object shape is known and kept constant for the entire test time, is no longer correct. Instead, an improved procedure is needed to allow the dynamic tracking of the test object shape in time. In the present work, we introduce a novel experimental methodology which allows to accurately reconstruct the surface temperature maps onto ablating surfaces [27]. Moreover, a specific procedure, comparing the emissivity-independent temperature measurement, provided by the two-colour pyrometer, with the calibrated IR camera signal was developed to provide a time-resolved and temperature-dependent in situ measurement of the in-band emissivity. Once this coefficient is determined, the IR camera frame intensity can be corrected accordingly, hence providing an accurate temperature measurement.

4.2. Time-resolved surface recession and sample shape measurements

As already introduced in section 1.1, as the material sample is exposed to the plasma flow, melting-

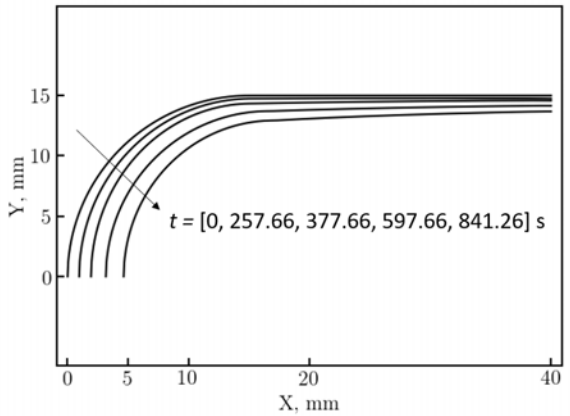

(a)

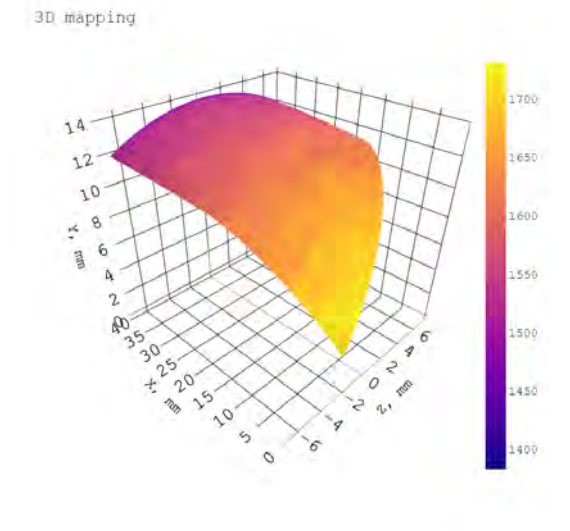

(b)

Figure 5: (a) Fitted shapes of the test sample material, starting from the edge detection applied to the HSC frames, at different times during the test. Notice the significant ablation around the stagnation region (∼ 5mm) as well as in the lateral region (∼ 1.2mm), which result in a considerable shape change. (b) Example of 3D reconstruction of the temperature map (temperature units in Kelvin). Notice the ablated sample geometry.

ablation phenomena result in recession and shape change of the test material. Hence, the initial test object geometry evolves in time in a hardly predictable manner. While the calibration parameters found with the optical calibration procedure are still valid, the object shape is no longer the initial one and the coordinates of the test object surface points in the real world frame R become unknown. To this purpose, we propose to exploit an additional measurement to infer the object shape. The Phantom 7.1 CMOS high-speed camera (Vision Research, Wayne, New Jersey, USA), featuring a 200 mm focal length lens, is adopted for the in-situ recession analysis of the ablating test sample. A calibration chessboard, placed at the initial sample location, provides the necessary pixel to length calibration and an acquisition rate of 10 Hz is used. Edge detection algorithms, available in the OpenCV library are then applied to the recorded frames. Once the edge pixels are located, the measured shape is fitted with a combination of elliptical and linear shape functions. Finally, under the assumption of axisymmetry, the three-dimensional object shape can be easily inferred from the observed two-dimensional projection. This procedure allows to retrieve the position of the sample surface points in time. Exploiting the precise synchronization between the IR camera and the high-speed camera, the time-dependent test object shape can be projected onto the IR camera image frame, by means of the previously described optical calibration model, allowing three-dimensional temperature maps reconstructions on the ablating surface 5(b).

5. Material response simulations

Experimental and numerical capabilities must be also combined to correctly estimate the material response of the material sample exposed to the plasma flow. This capability reveals to be a crucial aspect in the design of valuable experiments, able to produce reliable and repeatable data for model development. For instance, surface temperature and recession rate should be estimated before the test to adequately adapt the experimental instrumentation to capture the observed phenomena. Test conditions, as far as heat flux and static pressure are concerned, should be chosen following a rigorous approach, in order to highlight and possibly isolate different demise mechanisms, e.g., evaporation, melting and shear ablation. Hence, our approach follows a systematic procedure, which aims at including simulation tools at

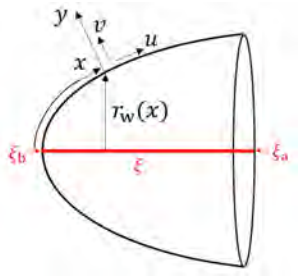

Figure 6: Sketch of the reference frame used to write the liquid layer equations.

the experiment design level, trying to optimize the test configuration for each specific condition.

5.1. Numerical approach

The melting of the slab is a phase change problem, characterized by discontinuities in the thermophysical properties at material melting temperature. In such case, the integral form of the energy conservation, along with the equation of state expressing the temperature dependence of the enthalpy, contain all the physical information needed to determine the evolution of the phases [28]. The enthalpy method has been used by Dias et al. [29; 30] to investigate meteor ablation and by Fagnani et al. [31] to study erosion of the arc jet electrodes with a shear ablation model initially developed by Bethe and Adams [11].

Considering a one-dimensional slab, as represented in Fig. 6, the homogeneous energy conservation writes

$$\begin{cases} \frac{d}{dt}\int_\Omega H + \oint_{\partial\Omega} \dot{\mathbf{q}}\cdot\mathbf{n} = 0 \\ H(\xi, t=0) = H(T_0) \\ \dot{\mathbf{q}}(\xi_a, t)\cdot\mathbf{n}_a = 0 \\ \dot{\mathbf{q}}(\xi_b, t)\cdot\mathbf{n}_b = \dot{q}_b(t), \end{cases} \tag{5}$$

where H is the enthalpy per unit volume, $\dot{\mathbf{q}}$ is the heat flux and $\mathbf{n}$ is the unit vector and ξ is the axial coordinate. We consider an adiabatic boundary condition at ξ_a. A more detailed explanation on the boundary condition $\dot{q}_b(t)$ is presented later in the next section. Following the approach presented by Alexiades [28], the integral form of the energy equation is discretised by means of a finite-volume method in the computational domain. The equation of state provides the thermodynamic closure, giving the material enthalpy as a function of temperature.

5.2. Surface mass and energy balances

Considering the particular case of space debris material samples exposed to high-temperature plasma flows, when subjected to aerodynamic heat transfer, pressure gradients and shear forces, they will form a flowing liquid layer. Considering the reference frame depicted in Fig. 6, under common boundary layer assumptions, the conservation of mass and momentum around the stagnation point reduce to the following [32; 11]

$$\begin{cases} \frac{1}{x}\frac{\partial(xu)}{\partial x} + \frac{\partial v}{\partial y} = 0 \\ \frac{\partial}{\partial y}(\mu\frac{\partial u}{\partial y}) = \frac{dp_w}{dx}. \end{cases} \tag{6}$$

The latter system is then integrated in the liquid layer thickness δ to provide the normal recession velocity due to the motion of the molten layer

$$v_{\text{melt}} = \int_0^\delta 2\cdot\left[\int_0^y \left(\frac{\tau'_w + p''_w(\eta-\delta)}{\mu(\eta)}\right)d\eta\right]dy, \tag{7}$$

where τ_w and p_w are the tangential shear stress and pressure.

As far as the evaporation boundary condition is concerned, $\mathcal{B}'$ tables are widely used in the aerospace community to estimate the evaporation mass loss rate as a function of temperature and pressure for thermal protection materials [12]. In this case, surface mass and energy balances at thermodynamic equilibrium couple the atmosphere of interest with the ablating surface, as sketched in Fig. 7, with an imaginary thin control volume fixed to the receding wall.

Considering the conservation of the element mass, the non dimensional mass blowing rate writes [31]

$$\mathcal{B}' = \frac{y^{\text{gp}}_{k,\text{e}} - y^{\text{gp}}_{k,\text{w}}}{y^{\text{gp}}_{k,\text{w}} - y^{\text{cp}}_{k,\text{w}}}. \tag{8}$$

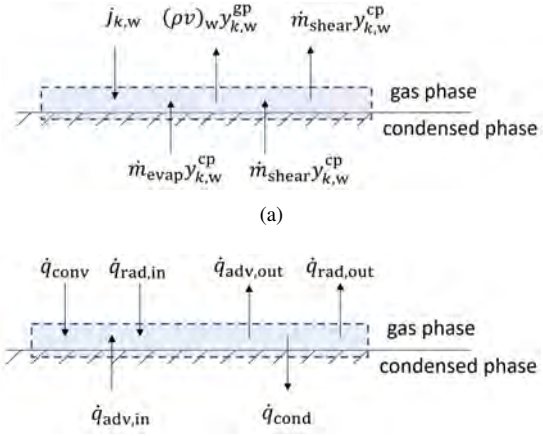

Figure 7: Schematic of the surface mass (a) and energy (b) balances for an infinitesimally thin control volume, fixed to the ablating surface.

The gas phase equilibrium composition $y^{\mathrm{gp}}_{k,\mathrm{w}}$ of the multiphase system is computed with the MUTATION++ library [33], allowing to obtain $\mathcal{B}'$ tables as a function of the surface temperature and pressure. Once the ablating mass flux $\dot{m} = \dot{m}_{\mathrm{evap}} + \dot{m}_{\mathrm{shear}}$ is computed, one can determine the recession speed as

$$\dot{s}_{\mathrm{w}} = \frac{\dot{m}}{\rho^{\mathrm{cp}}_{\mathrm{w}}}. \tag{9}$$

Considering now the control volume sketched in fig. 7(b), under common transfer coefficient assumptions [12], the surface energy balance yields

$$\begin{aligned} \dot{q}_{\mathrm{cond}} &= -k\nabla T \cdot \hat{\mathbf{n}} = \\ &= \rho_{\mathrm{e}} u_{\mathrm{e}} c_h (h^{\mathrm{gp}}_{\mathrm{r}} - h^{\mathrm{gp}}_{\mathrm{w}}) - \sigma\varepsilon(T^4_{\mathrm{w}} - T^4_{\mathrm{amb}}) \\ &- \dot{m}_{\mathrm{evap}}(h^{\mathrm{gp}}_{\mathrm{w}} - h^{\mathrm{cp}}_{\mathrm{w}}) \end{aligned} \tag{10}$$

where $\hat{\mathbf{n}}$ is the outgoing normal to the boundary. In particular, we can notice that $\dot{q}_{\mathrm{adv,out}} - \dot{q}_{\mathrm{adv,in}} = \dot{m}_{\mathrm{evap}}(h^{\mathrm{gp}}_{\mathrm{w}} - h^{\mathrm{cp}}_{\mathrm{w}})$, i.e., the ablated energy due to shear forces does not contribute to the net balance, since by assumption it does not undergo any phase change. Hence, once the multiphase equilibrium and surface mass balance are computed, $h^{\mathrm{gp}}_{\mathrm{w}}$ and $\dot{m}_{\mathrm{evap}} = \mathcal{B}' \cdot \rho_{\mathrm{e}} u_{\mathrm{e}} C_h$ are known, and the conductive flux $\dot{q}_{\mathrm{cond}}$ at the boundary can be computed. This can be directly exploited as a boundary flux to update the solution at the following time step. The solver has been verified against analytical solution for transient heat conduction, one- and two-phase melting and similar ablative material response codes.

6. Preliminary results

6.1. Quartz ablation

We tested a 25 mm radius hemispherical sample, with a 25 mm long cylinder. The sample was made of grade 2 natural quartz glass, produced by proQuarz GmbH (Mainz, Germany). The density is specified to be $2200\,\mathrm{kg\,m^{-3}}$, while the rated impurity content ranges between 20 and 40 ppm, and the OH content is around 150 ppm. The material sample was glued to an alumina-silica insulator by means of a high-temperature quartz-ceramic bond (Aremco 668) and held by a graphite support to a water-cooled probe holder.

The material thermophysical properties, necessary for the material response simulations, are taken from Wray et al. [34] and Urbain et al. [35] in terms of thermal conductivity and viscosity, respectively, and the thermodynamic properties from Mac Bride et al. [36].

A preliminary test was performed in air plasma, allowing $\sim$ 200 s of exposure to the flow, and compared to the 1D material response simulations based on the thermochemical ablation tables approach. The measured cold-wall heat flux was $\dot{q}_{\mathrm{cw}} = 2632 \pm 263\,\mathrm{kW\,m^{-2}}$, while the dynamic pressure was $p_{\mathrm{dyn}} = 36.8 \pm 4\,\mathrm{Pa}$. Following the procedure reported by the authors in [18], the measured free-stream temperatures, by means of the spectral imaging system, allowed to retrieve a calibrated effective electric power of $\mathcal{P}_{\mathrm{el,eff}} \approx 140\,\mathrm{kW}$. This value, along with the measured chamber static pressure and inlet gas mass flow rate, is used as an input to run the VKI ICP code. The two-dimensional CFD simulations provided an estimated boundary layer thickness of $\delta_{\mathrm{e}} = 4.89\,\mathrm{mm}$ on the stagnation line, with an edge temperature of $T_e = 7245\,\mathrm{K}$, corresponding to a specific enthalpy of $h_{\mathrm{e}} = 38.47\,\mathrm{MJ\,kg^{-1}}$. The estimated radial velocity gradient at the boundary layer edge was $\beta_e = 4061\,\mathrm{s^{-1}}$. The VKI Boundary Layer code is run using these values as edge conditions, both for a Fully-Catalytic (FC) and a Non-Catalytic (NC) wall, with a surface temperature of $T_w = 350\,\mathrm{K}$. The computed stagnation point heat fluxes are $\dot{q}_{\mathrm{w,FC}} = 2644\,\mathrm{kW\,m^{-2}}$ and $\dot{q}_{\mathrm{w,NC}} = 1520\,\mathrm{kW\,m^{-2}}$, respectively. We notice how the fully-catalytic value is close to the cold-wall measured value, as expected for the highly-catalytic copper surface [37]. As highlighted in section 1, silica is a particularly inert material, typically showing a low catalytic efficiency to oxygen and nitrogen recombination. Hence, the non-catalytic heat transfer coefficient is computed as

$$\rho_e u_e c_{\mathrm{h,NC}} = \frac{\dot{q}_{\mathrm{w,NC}}}{h_{\mathrm{e}} - h_{\mathrm{e}}} = 39.57 \times 10^{-3}\,\mathrm{kg\,m^{-2}\,s^{-1}}. \tag{11}$$

Finally the VKI ICP code simulation provides an estimate of the wall shear stress gradient $\tau'_{\mathrm{w}} = 213.9\,\mathrm{Pa\,m^{-1}}$ and pressure double gradient $p''_{\mathrm{w}} = -162\,587\,\mathrm{Pa\,m^{-2}}$ at the stagnation point, which are needed to compute the mass removal due to shear ablation.

We computed the one-dimensional material response using the pre-computed $\mathcal{B}'$-tables to estimate the material evaporation and the non-catalytic heat transfer coefficient for the surface energy balance (see eq. 10). Fig.8(a) compares the experimental results with the simulated time evolution of the surface temperature. The measured evolution of the surface temperature in the stagnation region is obtained

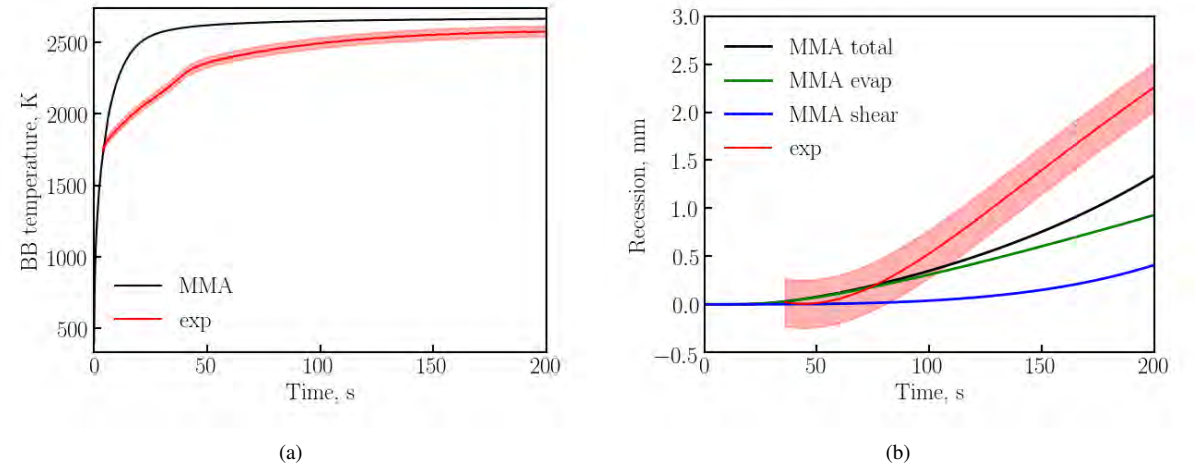

(a) (b)

Figure 8: (a) Comparison between the experimental stagnation point temperature with the one computed by the material response code. (b) Comparison of the experimental and computed stagnation point recession, highlighting the evaporation and shear ablation contributions in the latter.

by correcting the radiometric measurement with a total emissivity value of 0.3. The simulated material's surface temperature shows both a faster transient behaviour and a larger peak temperature (2660 K) with respect to the measured values.

As far as the stagnation point recession is concerned, the frame-by-frame analysis of the HSC images allowed to extract the time evolution of the test sample shape. The recession profile is then interpolated with a third order polynomial for better comparison with the numerical simulations. From Fig. 8(b)The computed values show initial agreement with the measured quantities around $t = 50\,\mathrm{s}$. As time evolves, however, the measured recession is increasingly underestimated by the computation. Moreover, we can notice how the evaporative mass flux is the largest contribution to the overall recession for the whole simulated time. Yet, as heat diffuses in the material, the material viscosity decreases and the shear ablation contribution becomes more important.

7. Titanium oxidation in air plasma

We tested a 15 mm radius hemispherical sample, with a 25 mm long cylinder. The sample was made of grade 2 titanium (maximum impurity contents of 0.3% Fe, 0.25% O, 0.08 C, 0.03% N and 0.015% H), produced by Melotte NZ (Zonhoven, Belgium). The material sample was glued to an alumina-silica insulator by means of a high-temperature MgO bond (Aremco 571) and held by a graphite support to a water-cooled probe holder. The sample was exposed for $\sim$ 70s in air plasma at $p_s = 100$mbar, cold-wall heat flux of $\dot{q}_{cw} = 1556 \pm 156\,\mathrm{kW\,m^{-2}}$ and a dynamic pressure of $p_{dyn} = 14 \pm 2\,\mathrm{Pa}$.

Fig. 9(b) shows the recorded surface temperature around the stagnation point. From the ratio between two-color pyrometry and broadband radiometry, an total angular emissivity of $\varepsilon \sim 0.7$ could be retrieved, which is in agreement with literature values [38]. Fig. 9(a) shows a comparison of the pre- and post-test sample conditions, highlighting the significant oxidation on the surface. Preliminary surface analysis results carried out at the SURF labs at VUB showed that TiO_2 is the primary compound found in the oxide layer, while nitrides are absent. As a result of the absence of nitridation effects, we plan to perform tests in nitrogen gas, which may allow to isolate surface reactions from melting-ablation. This would be of great importance for model validation based on ground experiments.

8. Conclusions and future work

Ground testing of space debris metallic and silicate materials requires improvements in the existing ground testing capabilities. In this paper we reviewed and updated critical procedures in the VKI Plasmatron set-up and data processing techniques, which allow to perform more consistent and repeatable measurements. As far as the flow characterization is concerned, locally resolved emission spectroscopy and an advanced data processing suite allows to perform lo-

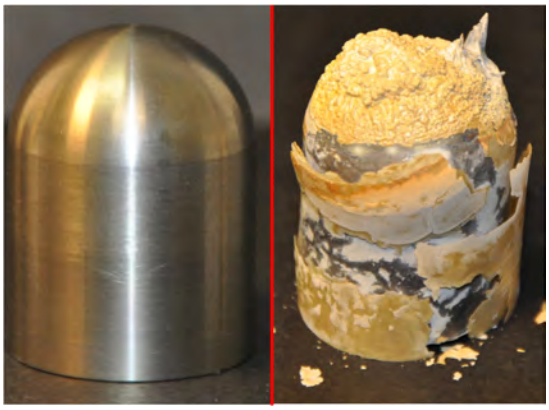

(a)

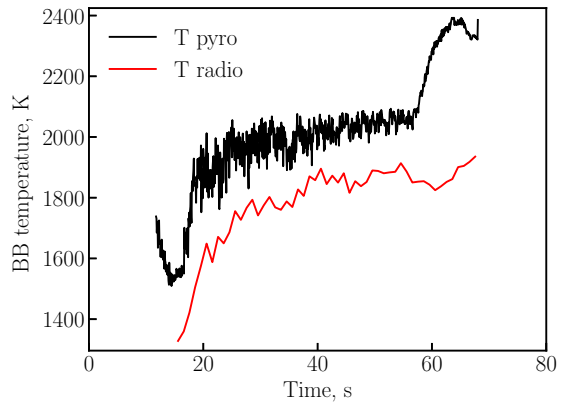

(b)

Figure 9: (a) Pre- and post-test visual inspection of the titanium grade-2 sample showed significant oxidation (TiO_2) on the surface. (b) Experimental surface temperature at stagnation point from 2-color pyrometer and broadband radiometer.

cal gas temperature measurement. Chromatic aberration effects were found and experimentally characterized in the existing set-up. Substitution of the optical imaging system with mirror components revealed critical in avoiding this undesirable effect. On the material investigation level, simulation tools, able to estimate melting and recession for evaporation and shear stresses, are being introduced at the experiment design level. The in situ material response characterization, featuring traditional techniques such as pyrometry, radiometry and high-speed camera imaging, has been improved with 3D temperature map reconstruction techniques, combined with recession measurement on an ablating surface. We presented preliminary experimental results of ablation of a quartz sample and oxidation of a titanium sample in air plasma.

Acknowledgement

The author would like to acknowledge B. Helber and D. Le Quang for the precious experimental support, B. Dias for the fruitful discussions and teaching about the melting-ablation modelling and K. Baert for the preliminary surface analysis of the titanium sample. F. Torres Herrador is acknowledged for the useful review and comments.

References

[1] H. Klinkrad, Space Debris, Vol. 60 of Springer Praxis Books, Springer Berlin Heidelberg, 2006. doi:10.1007/3-540-37674-7.
URL http://link.springer.com/10.1007/3-540-37674-7

[2] D. J. Kessler, N. L. Johnson, J. C. Liou, M. Matney, Kessler Syndrome-AAS Paper.pdf, Advances in the Astronautical Sciences.
URL https://pdfs.semanticscholar.org/2276/55e022441d1379dfdc395173ed2e776d54ee.pdf

[3] United Nations Office For Outer Space Affairs, Committee on the Peaceful Uses of Outer Space, Space Debris Mitigation Guidelines of the Committee on the Peaceful Uses of Outer Space, United Nations Publication (2010) 1arXiv:SalesNo.E.99.I.17.
URL http://www.unoosa.org/pdf/publications/st{_}space{_}49E.pdf

[4] ESA Space Debris Mitigation WG, ESA Space Debris Mitigation Compliance Verification Guidelines (1.0) (2015) 1–95.

[5] S. Lemmens, Q. Funke, H. Krag, On-ground casualty risk reduction by structural design for demise, Advances in Space Research 55 (11) (2015) 2592–2606. doi:10.1016/j.asr.2015.02.017.
URL http://dx.doi.org/10.1016/j.asr.2015.02.017

[6] Y. Prevereaud, Contribution à la modélisation de la rentrée atmosphérique des débris spatiaux, Université de Toulouse, 2014.

[7] S. Heinrich, J. Martin, J. Pouzin, Satellite design for demise thermal characterisation in early re-entry for dismantlement mechanisms, Acta Astronautica 158 (2019) 161–171. doi:10.1016/j.actaastro.2018.03.021.
URL https://doi.org/10.1016/j.actaastro.2018.03.021

[8] P. M. Waswa, M. Elliot, J. A. Hoffman, Spacecraft Design-for-Demise implementation strategy & decision-making methodology for low earth orbit missions, Advances in Space Research 51 (9) (2013) 1627–1637. doi:10.1016/j.asr.2012.11.020.
URL http://dx.doi.org/10.1016/j.asr.2012.11.020

[9] Y. Prévereaud, J. L. Vérant, M. Balat-Pichelin, J. M. Moschetta, Numerical and experimental study of the thermal degradation process during the atmospheric re-entry of a TiAl6V4 tank, Acta Astronautica 122 (2016) 258–286. doi:10.1016/j.actaastro.2016.02.009.
URL http://dx.doi.org/10.1016/j.actaastro.2016.02.009

[10] B. Helber, Material Response Characterization of Low-density Ablators in Atmospheric Entry Plasmas, 2016.

[11] H. A. Bethe, M. C. Adams, A Theory for the Ablation of Glassy Materials, Journal of the Aerospace Sciences 26 (6) (1959) 321–328. doi:10.2514/8.8080.
URL http://arc.aiaa.org/doi/10.2514/8.8080

[12] B. Helber, A. Turchi, J. B. Scoggins, A. Hubin, T. E. Magin, Experimental investigation of ablation and pyrolysis processes of carbon-phenolic ablators in atmospheric entry plasmas, International Journal of Heat and Mass Transfer 100 (2016) 810–824. doi:10.1016/j.ijheatmasstransfer.2016.04.072.
URL http://dx.doi.org/10.1016/j.ijheatmasstransfer.2016.04.072

[13] P. F. Barbante, O. Chazot, Flight extrapolation of plasma wind tunnel stagnation region flowfield, Journal of Thermophysics and Heat Transfer 20 (3) (2006) 493–499. doi:10.2514/1.17185.

[14] D. Vanden Abeele, G. Degrez, Efficient computational model for inductive plasma flows, AIAA journal 38 (2) (2000) 234–242. doi:10.2514/3.14402.

[15] A. Viladegut, O. Chazot, Empirical modeling of copper catalysis for enthalpy determination in plasma facilities, Journal of Thermophysics and Heat Transfer 34 (1) (2020) 26–36. doi:10.2514/1.T5683.

[16] G. Degrez, D. V. Abeele, P. Barbante, B. Bottin, Numerical simulation of inductively coupled plasma flows under chemical non-equilibrium, International Journal of Numerical Methods for Heat and Fluid Flow 14 (4) (2004) 538–558. doi:10.1108/09615530410532286.

[17] D. Le Quang Huy, Spectroscopic Measurements of Sub- and Supersonic Plasma Flows for the Investigation of Atmospheric Re-entry Shock Layer Radiation., von Karman Institute for Fluid Dynamics, 2015.

[18] A. Fagnani, D. Le Quang Huy, B. Helber, S. Demange, A. Turchi, O. Chazot, A. Hubin, Investigation of a Free-Stream Air Plasma Flow by Optical Emission Spectroscopy and Comparison to Magnetohydrodynamics Simulations, in: AIAA Scitech 2020 Forum, American Institute of Aeronautics and Astronautics, Reston, Virginia, 2020, pp. 1–15. doi:10.2514/6.2020-0382.
URL https://arc.aiaa.org/doi/10.2514/6.2020-0382

[19] C. O. Laux, T. G. Spence, C. H. Kruger, R. N. Zare, Optical diagnostics of atmospheric pressure air plasmas, Plasma Sources Science and Technology 12 (2) (2003) 125–138. doi:10.1088/0963-0252/12/2/301.

[20] F. L. Pedrotti, L. M. Pedrotti, L. S. Pedrotti, Introduction to Optics, Introduction to Opticsdoi:10.1017/9781108552493.

[21] Y. Le Sant, M. C. Merienne, Image resection method applied to mapping techniques, ICIASF Record, International Congress on Instrumentation in Aerospace Simulation Facilities (1995) 1–8.

[22] Y. Le Sant, B. Deleglise, Y. Mebarki, An automatic image alignment method applied to pressure sensitive paint measurements, in: ICIASF'97 Record. International Congress on Instrumentation in Aerospace Simulation Facilities, IEEE, 1997, pp. 57–65. doi:10.1109/ICIASF.1997.644658.
URL http://ieeexplore.ieee.org/document/644658/

[23] Y. Le Sant, M. Marchand, P. Millan, J. Fontaine, An overview of infrared thermography techniques used in large wind tunnels, Aerospace Science and Technology 6 (5) (2002) 355–366. doi:10.1016/S1270-9638(02)01172-0.

[24] G. Cardone, A. Ianiro, G. Dello Ioio, A. Passaro, Temperature maps measurements on 3D surfaces with infrared thermography, Experiments in Fluids 52 (2) (2012) 375–385. doi:10.1007/s00348-011-1225-9.

[25] J. Heikkila, Geometric camera calibration using circular control points, IEEE Transactions on Pattern Analysis and Machine Intelligence 22 (10) (2000) 1066–1077. doi:10.1109/34.879788.
URL http://ieeexplore.ieee.org/document/879788/

[26] G. M. Carlomagno, G. Cardone, Infrared thermography for convective heat transfer measurements, Vol. 49, 2010. doi:10.1007/s00348-010-0912-2.

[27] A. Fagnani, B. Helber, O. Chazot, Infrared temperature measurements on 3D objects with surface recession, in: Proceedings of the 2020 International Conference on Quantitative InfraRed Thermography, QIRT Council, 2020, pp. 1–10. doi:10.21611/qirt.2020.059.
URL http://qirt.org/archives/qirt2020/papers/059.pdf

[28] V. Alexiades, A. D. Solomon, Mathematical Modeling Of Melting And Freezing Processes, CRC Press, 1992.

[29] B. Dias, F. Bariselli, A. Turchi, A. Frezzotti, P. Chatelain, T. Magin, Development of a melting model for meteors, in: AIP Conference Proceedings, Vol. 1786, 2016, p. 160004. doi:10.1063/1.4967661.
URL http://aip.scitation.org/doi/abs/10.1063/1.4967661

[30] B. Dias, A. Turchi, E. C. Stern, T. E. Magin, A model for meteoroid ablation including melting and vaporization, Icarus 345 (November 2019) (2020) 113710. doi:10.1016/j.icarus.2020.113710.
URL https://doi.org/10.1016/j.icarus.2020.113710

[31] A. Fagnani, B. Helber, O. Chazot, Evaluation of Probe-Material Thermal Interaction in Plasma Wind Tunnel Tests by Means of IR Thermography and Thermal Inverse Modellingdoi::10.13009/EUCASS2019-4138TH.

[32] H. Schlichting, K. Gersten, Boundary-Layer Theory, 9th Edition, Springer Berlin Heidelberg, Berlin, Heidelberg, 2017. doi:10.1007/978-3-662-52919-5.
URL http://link.springer.com/10.1007/978-3-662-52919-5

[33] J. B. Scoggins, V. Leroy, G. Bellas-Chatzigeorgis, B. Dias, T. E. Magin, Mutation++: MUlticomponent Thermodynamic

And Transport properties for IONized gases in C++, SoftwareX 12. arXiv:2002.01783, doi:10.1016/j.softx.2020.100575.

[34] K. L. Wray, T. J. Connolly, Thermal conductivity of clear fused silica at high temperatures, Journal of Applied Physics 30 (11) (1959) 1702–1705. doi:10.1063/1.1735040.

[35] G. Urbain, Y. Bottinga, P. Richet, Viscosity of liquid silica, silicates and alumino-silicates, Geochimica et Cosmochimica Acta 46 (6) (1982) 1061–1072. doi:10.1016/0016-7037(82)90059-X.

[36] B. J. Mcbride, S. Gordon, M. A. Reno, Thermodynamic Data for Fifty Reference Elements, Nasa Technical Memorandum (2001) 44.

[37] F. Panerai, Aerothermochemistry Characterization of Thermal Protection Systems, no. February, 2012.

[38] N. Milošević, I. Aleksić, Thermophysical properties of solid phase Ti-6Al-4V alloy over a wide temperature range, International Journal of Materials Research 103 (6) (2012) 707–714. doi:10.3139/146.110678.

A high-order level-set method to follow the gas-liquid interface of melting materials

Henneaux David

Aeronautics and Aerospace Department, von Karman Institute for Fluid Dynamics, Belgium, david.henneaux@vki.ac.be

Supervisor: Magin Thierry

Professor, Aeronautics and Aerospace Department, von Karman Institute for Fluid Dynamics, Belgium, magin@vki.ac.be

University Supervisor: Chatelain Philippe

Professor, Institute of Mechanics, Materials and Civil Engineering, Université catholique de Louvain, Belgium, philippe.chatelain@uclouvain.be

Abstract

The application of emerging sharp interface high-order methods to complex flow problems like the interaction between a gas and a melt layer is strongly linked with the ability of representing interfaces dynamics with high accuracy. In this work, we propose to develop efficient and high-order reinitialization and extension strategies for the level-set method in the framework of the discontinuous Galerkin method (DGM).

Keywords: level-set, high-order, discontinuous Galerkin, two-phase flows

1. Context and motivations

Recently, different unstructured high-order methods have emerged. These methods offer the possibility of combining the geometrical flexibility of finite volume or finite element methods with the high precision of finite difference or spectral methods. The algorithms and the theoretical foundation behind the most mature methods of this kind, like the discontinuous Galerkin methods, are now well-established. In the context of computational fluid dynamics, active research is still conducted in order to extend and apply those promising methods to complex flow situations. One of those, which is the subject of the present work, is about immiscible two-phase flows separated by a phase interface. More precisely, our interest is about predicting the interaction between atmospheric air and metallic melt layer occurring during the ablation of re-entering space debris. The main challenge associated to such situations is to be able to preserve the high resolution of high-order methods in the vicinity of the interface where decisive physical phenomena take place, like the shear removal or evaporation in our particular example. We propose to achieve this by means of a so-called extended discontinuous Galerkin method [1].

In addition of being able to capture discontinuous solutions across phase interfaces, a method to represent and follow this interface is also required. As the interface position and geometrical quantities will be inferred from this representation, the order of convergence of the global approach will of course be influenced by the accuracy with which the interface is located. For reasons explained in Sec. 2, our method of choice is the level-set method discretized by a classical DGM. The objective of the present work is to develop and implement high-order reinitialization (Sec. 3) and extension (Sec. 4) strategies associated to the level-set method.

2. Description of the level-set method and its discretization with a DGM

A brief overview of the idea behind the level-set method, the properties that a level-set function needs to satisfy and the equations that govern its evolution are first given in this section. General algorithms employed in this work to handle different aspects of the

level-set method are then presented.

2.1. The representation of moving interfaces

A large collection of fluid situations involve the presence of moving interfaces, the most common situation being the interaction between two fluid phases. In many of such situations, in addition to predicting the dynamics of quantities in the different phases and their coupling across the interface, a method is needed to describe the motion of the interface itself. Two different approaches can be identified in that regard: interface tracking and interface capturing methods. In the first set of methods, the interface is explicitly represented by a function (e.g. marker particles method) or by deforming the grid such that it conforms with the interface position. In the class of interface capturing methods, the interface is represented implicitly by a function defined on all the domain. To this class belong the volume-of-fluid (VOF) method and the level-set (LS) method. For the applications targeted in this work that might involve important interface distortions, a pure Eulerian method is desirable in order to use a fixed grid. Second, an interface capturing method is better adapted to deal with complex interfacial motions like merger, folding and break-up. The choice was therefore made to use the level-set method because it can handle topology changes of the interface automatically and it allows for a straightforward calculation of interfacial geometrical quantities [2]. In addition, the level-set method was the best candidate to develop an unfitted/ extended discontinous Galerkin method [3; 4] as it does not need any interface reconstruction.

2.2. Governing equation and properties

The level-set method first proposed in [5] relies on two central embeddings: (i) the embedding of the $d-1$ dimensional interface Γ as the zero level-set of a d dimensional function φ defined over the entire domain Ω, (ii) the embedding (or extension) of the interface's velocity $\mathbf{v}_\Gamma$ to this higher dimensional level-set function [6].

2.2.1. Interface representation

By definition, the interface is implicitly identified by the zero iso-contour of the level-set function $\varphi : \mathbb{R}^d \to \mathbb{R}$ for all time t, i.e.

$$\Gamma(\mathbf{x},t) = \left\{ \mathbf{x} \in \mathbb{R}^d \,|\, \varphi(\mathbf{x},t) = 0 \right\} , \quad \forall t . \tag{1}$$

The normal vector $\mathbf{n}_\Gamma$ to the interface and the interface curvature κ_Γ can then be obtained as

$$\mathbf{n}_\Gamma(\mathbf{x},t) = \frac{\nabla\varphi(\mathbf{x},t)}{\|\nabla\varphi(\mathbf{x},t)\|} , \quad \kappa_\Gamma(\mathbf{x},t) = \nabla\cdot\left(\frac{\nabla\varphi(\mathbf{x},t)}{\|\nabla\varphi(\mathbf{x},t)\|}\right) , \quad \forall \mathbf{x} \in \Gamma(\mathbf{x},t) . \tag{2}$$

Away from the interface front, the level-set function needs also to be specified and it is usually defined as the signed distance to the interface, i.e.

$$\varphi(\mathbf{x},t) = \begin{cases} \mathrm{dist}(\mathbf{x},\Gamma(\varphi)) , & \mathbf{x} \in \Omega_1 , \\ 0 , & \mathbf{x} \in \Gamma , \\ -\mathrm{dist}(\mathbf{x},\Gamma(\varphi)) , & \mathbf{x} \in \Omega_2 , \end{cases}$$
$$\text{with:} \quad \mathrm{dist}(\mathbf{x},\Gamma(\varphi)) = \min_{\mathbf{x}_{\Gamma,cp} \,:\, \varphi(\mathbf{x}_{\Gamma,cp})=0} \left\| \mathbf{x} - \mathbf{x}_{\Gamma,cp} \right\| , \tag{3}$$

where $\mathbf{x}_{\Gamma,cp}(\mathbf{x},t) \in \Gamma(\mathbf{x},t)$ is the closest point belonging to the interface from the point $\mathbf{x}$. Defining the level-set as a signed distance function has interesting properties, namely that it is almost everywhere differentiable and that its gradients satisfy the eikonal equation,

$$\|\nabla\varphi(\mathbf{x})\| = 1 , \quad \mathbf{x} \in \mathbb{R}^d . \tag{4}$$

The level-set function, initially defined as a signed distance function, may lose its distance property due to advection. This can be troublesome for two main reasons: (i) the gradient of the level-set may become very steep in case the level-set function becomes disturbed and the computation of the normal may lead to numerical instabilities, (ii) the level-set function may become too flat to accurately determine the position of the iso-0. That is why the so-called reinitialization procedure to recover the signed distance property of the level-set, detailed in Sec. 3, may be necessary.

2.2.2. Interface motion

In order to update the position of the interface at every time step, the level-set advection equation needs to be solved:

$$\frac{\partial\varphi(\mathbf{x},t)}{\partial t} + \mathbf{v}_{\mathrm{ext}}(\mathbf{x},t)\cdot\nabla\varphi(\mathbf{x},t) = 0 , \quad \forall \mathbf{x} \in \mathbb{R}^d ,$$
$$\varphi(\mathbf{x},t=0) = \varphi^0(\mathbf{x}) , \tag{5}$$

where $\mathbf{v}_{\mathrm{ext}}$ is the extended advection velocity which should, in the limit as one approaches the zero level-set, smoothly yield the velocity of the interface $\mathbf{v}_\Gamma$, i.e.

$$\lim_{\mathbf{x}\to\mathbf{x}_\Gamma} \mathbf{v}_{\mathrm{ext}}(\mathbf{x}) = \mathbf{v}_\Gamma(\mathbf{x}_\Gamma) , \quad \mathbf{x} \in \Omega , \ \mathbf{x}_\Gamma \in \Gamma . \tag{6}$$

Beyond that requirement, different approaches can be considered to extend the velocity to every points away from the interface. The approach used in this work is described in Sec. 4.

2.3. Discretization with a discontinuous Galerkin method

Equation (5) is first rewritten in conservative form:

$$\frac{\partial \varphi}{\partial t} + \nabla \cdot (\mathbf{v}_{\text{ext}} \varphi) = \varphi \nabla \cdot \mathbf{v}_{\text{ext}} \, . \tag{7}$$

Since an extended velocity is used in the domain, this velocity field will not necessarily be divergence free and therefore the source term on the right hand side of Eq. (7) has to be taken into account. The DG spatial discretization of this equation on a discretized domain $\Omega = \cup \Omega_m$ with the set of element interfaces $I = \cup I_i$ is then formulated as:

Find $\boldsymbol{\varphi}^h \in \mathcal{V}^h$ such that

$$\begin{aligned} \sum_{\Omega_m \in \Omega} \mathbf{M}_m \frac{\mathrm{d}\boldsymbol{\varphi}_m^h}{\mathrm{d}t} = & \sum_{\Omega_m \in \Omega} \int_{\Omega_m} \nabla^h \mathbf{w}_m^h \cdot \left(\boldsymbol{\varphi}_m^h \mathbf{v}_{\text{ext}}^h \right) \mathrm{d}V \\ & - \sum_{I_i \in I} \int_{I_i} \left([\mathbf{w}_i^h] \cdot \mathbf{n}_{I_i} \right) \mathcal{H}(\boldsymbol{\varphi}_m^{h,+}, \boldsymbol{\varphi}_m^{h,-}, \mathbf{n}_{I_i}) \, \mathrm{d}S \\ & + \sum_{\Omega_m \in \Omega} \int_{\Omega_m} \mathbf{w}_m^h \left(\boldsymbol{\varphi}_m^h \nabla^h \cdot \mathbf{v}_{\text{ext}}^h \right) \mathrm{d}V \, , \end{aligned} \tag{8}$$

in which $\mathbf{M}$ is the mass matrix, $\boldsymbol{\varphi}^h$ and $\mathbf{w}^h$ are the approximated discrete level-set solution and test functions, respectively, both expressed as linear combinations of some polynomial shape functions forming a base for the finite dimensional space $\mathcal{V}^h$. The convective numerical flux function is taken as an upwind flux:

$$\mathcal{H}(\varphi^+, \varphi^-, \mathbf{n}) = \begin{cases} \varphi^- \, v_n & \text{if } v_n > 0 \, , \\ \varphi^+ \, v_n & \text{if } v_n \leq 0 \, , \end{cases} \qquad \text{where } v_n = \mathbf{v}_{\text{ext}} \cdot \mathbf{n} \tag{9}$$

The resulting system of ODE's reads under a compact form as

$$\mathbf{M} \frac{\mathrm{d}\boldsymbol{\varphi}^h}{\mathrm{d}t} = \mathcal{R}(\boldsymbol{\varphi}^h, \mathbf{v}_{\text{ext}}) \, , \tag{10}$$

where $\mathcal{R}$ is the residual associated to the spatial terms of Eq. (8). It is integrated in time with an explicit or implicit time-stepping scheme. For explicit time integration, multi-stage Runge-Kutta schemes can be selected. When implicit time marching is chosen, multi-step (BDF) or multi-stage (ESDIRK) schemes are available. The distinction is made between these two approaches in Algorithm 1 to highlight when the reinitialization and extension procedures are called. It has to be noted that the pseudo-algorithm for the implicit schemes assumes a single stage scheme. In case several stages are used, the non-linear iterations are performed at every stages.

2.4. General algorithm for reinitialization and velocity extension

An overview of the general algorithm for the level-set advection used in this work is presented in Algorithm 2, followed by an overview of the different steps concerning the reinitialization and the extension of the velocity. At this stage, it is important to mention that the reinitialization and extension of the velocity procedures developed in this work are based on a direct geometrical approach, in opposition to the main other class of PDE-based methods. The different steps involved in the process are detailed in the following sections.

Before going further, it is also important to note that a narrow-band technique has been implemented in order to restrict the procedures mentioned above to the elements crossed by the iso-0 of the level-set as well as their neighbors (which can be defined based on the adjacent edges or vertices). This reduces significantly the computational efforts and allows to avoid considering the level-set in regions where it may be singular. The comparison between a reinitialized level-set field computed all over the domain and on a narrow-band region is presented in Fig. 1.

3. Reinitialization

3.1. Theory

Three main approaches exist in the literature to reinitialize the level-set function in order to recover its signed distance property. The first one is to stand at each computational mesh point, find the corresponding closest point on the interface and assign to the level-set the signed distance between the mesh point and the closest point on the front [2]. This approach directly uses the definition of the level-set function given by Eq. (3) and is the one used in this work. The second approach is to solve the eikonal Eq. (4). Very efficient methods like the Fast Marching Method [7] and the Fast Sweeping Method [8] have been designed for that purpose. The last possibility is to convert the static eikonal equation into a time-dependent hyperbolic PDE whose steady-state solution returns the signed distance function [9], or to reformulate the equation as a minimization problem and solve an elliptic equation [10].

3.2. Implementation

The reinitialization strategy that has been implemented is largely based on the work of Saye [11] in

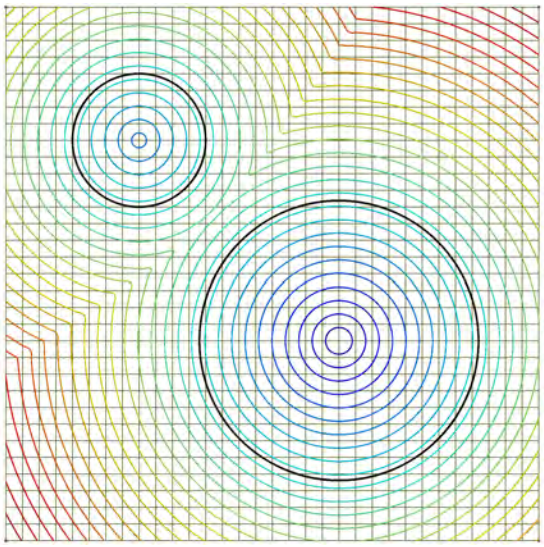

(a) Iso-contours of a level-set field defined all over the domain, iso-0 in black.

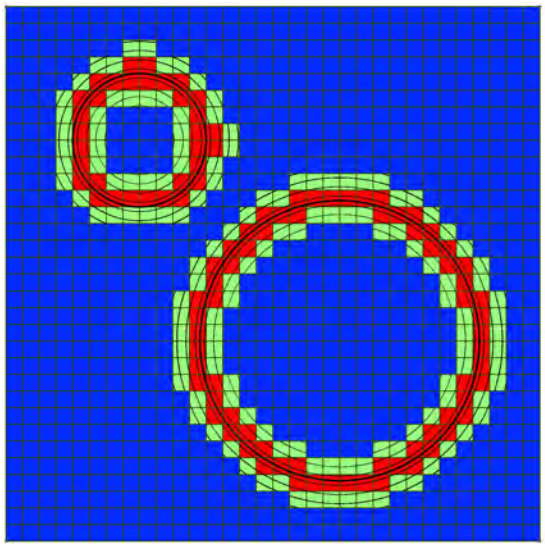

(b) Iso-contours of a level-set field defined only in a narrow-band region, thick black line is the iso-0. Blue elements belong to the far field, the red ones are the cut elements and the green ones the cut-neighbors; those last two categories forming the narrow-band.

Figure 1: Comparison between the full domain and the narrow-band strategy on a dual-circle configuration.

Algorithm 1 Advection of the level-set φ^t to the next time step φ^{t+1} based or not on the fluid state $\mathbf{U}$

procedure MoveLevelSet($\varphi^t, \Delta t, \mathbf{U}$)
  $k = 0$, $\varphi_k^* \leftarrow \varphi^t$
  If Explicit Scheme **do**
    $\mathbf{v}_{\text{ext},k}^* \leftarrow \texttt{ReinitExtend}(\varphi_k^*, \mathbf{U})$ ▷ Algorithm 2
    $\mathcal{R}_k \leftarrow \mathcal{R}(\varphi_k^*, \mathbf{v}_{\text{ext},k}^*)$
    For $k = 1, ..., \text{nbStages} - 1$ **do**
      $\varphi_k^* = \varphi^t + \alpha_k \Delta t \mathbf{M}^{-1} \mathcal{R}(\varphi_{k-1}^*, \mathbf{v}_{\text{ext},k-1}^*)$
      $\mathbf{v}_{\text{ext},k}^* \leftarrow \texttt{ReinitExtend}(\varphi_k^*, \mathbf{U})$ ▷ Algorithm 2
      $\mathcal{R}_k \leftarrow \mathcal{R}(\varphi_k^*, \mathbf{v}_{\text{ext},k}^*)$
    end do
    $\varphi^{t+1} \leftarrow \varphi^t + \sum_{k=0}^{\text{nbStages-1}} \gamma_k \Delta t \mathbf{M}^{-1} \mathcal{R}_k$
  end if
  If Implicit Scheme **do** ▷ NB: for single stage scheme
    While $\left\| \mathcal{R}_{\text{implicit}}(\varphi_k^*, \mathbf{v}_{\text{ext},k}^*) \right\| > \text{tol}$ **do** ▷ $\mathcal{R}_{\text{implicit}}$: $\mathcal{R}$ + temporal contribution
      $\mathbf{v}_{\text{ext},k}^* \leftarrow \texttt{ReinitExtend}(\varphi_k^*, \mathbf{U})$ ▷ Algorithm 2
      $\varphi_{k+1}^* \leftarrow \texttt{SolveSystem}(\varphi_k^*, \mathbf{v}_{\text{ext},k}^*)$ ▷ Solve non-linear system with damped inexact Newton
      $k \leftarrow k + 1$
    end do
    $\varphi^{t+1} \leftarrow \varphi_k^*$
  end if
  If Reinitialization **do**
    $\varphi_{\text{reinit}} \leftarrow \texttt{ReinitExtend}(\varphi^{t+1}, \mathbf{U})$ ▷ Algorithm 2
    $\varphi^{t+1} \leftarrow \varphi_{\text{reinit}}$ ▷ Level-set at the next time step replaced by reinitialized field
  end if
end procedure

Algorithm 2 Main steps for the reinitialization and extension of the velocity based on a direct geometric approach

1: **procedure** ReinitExtend(φ, $\mathbf{U}$)
2: cloudPts ← `SampleLevelSet`(φ, sampleStrategy) ▷ Generate cloud of points sampling the LS: Sec. 3.2
3: searchTree ← `CreateSearchTree`(cloudPts) ▷ Create search tree from the cloud of points
4: $\mathbf{x}_{\Gamma,cp}, \varphi_{\text{reinit}}$ ← `ComputeClosestPoint`(φ, cloudPts, searchTree) ▷ Compute closest points ∀ nodes: Sec. 3.2
5: $\mathbf{v}_{\text{ext}}$ ← `ComputeExtendedVelocity`($\varphi, \mathbf{x}_{\Gamma,cp}$, $\mathbf{U}$) ▷ Compute extended velocity ∀ nodes: Sec. 4.2
6: **end procedure**

which a procedure for high-order closest point calculations to implicitly defined surfaces is presented. This new implementation extends the original one available in the discontinuous Galerkin Argo platform[1] based on the work of Marchandise [2]. The main contributions of the present work are:

- the implementation of Saye's strategy into a discontinuous Galerkin framework and its adaptation to work on arbitrary unstructured meshes;
- the creation of interface sampling points using either a recursive contouring algorithm [13] or a high-order quadrature for implicitly defined surfaces on quadrilateral elements [14];
- the dynamic building of narrow-band region offering the possibility to restrict the operations on a reduced set of elements.

The different steps involved in the reinitialization procedure are described below.

1. A global *set of sampling points approximating the interface* identified by Eq. (1) is first generated. This is accomplished by using one of the two following approaches:
   - *Recursive contouring algorithm* [13]: the elements crossed by the iso-0 of the level-set are divided recursively (with a chosen recursion level) into sub-elements and the vertices of the subdivided elements are collected. Since those vertices does not belong to the iso-0 of the level-set, they are "projected" onto the zero level-set with a simple Newton method. If the projected point does not move outside of the element that is considered, it is added to the global set of sampling points `cloudPts`; otherwise it is discarded.
   - *Saye's quadrature* [14]: a quadrature rule for the surface integration over the interface is computed for each element cut by the iso-0, which provides a set of points that lie exactly on the iso-0 and that are added to the global set of sampling points `cloudPts`.
2. The sampling points are then stored in a Approximate Nearest Neighbor (ANN) *search tree* [15] denotded by `searchTree` after.
3. For each computational mesh point $\mathbf{x}_q$, a *high-order computation of closest points* on the interface is finally applied. First, the previously created search tree is used to find the closest point $\mathbf{x}_{\Gamma,cp,\text{guess}}$ in the set of sampling points. Then, this point is used as a guess for the Newton's method applied on a minimum distance constrained optimization problem with the constraint that the final "polished" closest point $\mathbf{x}_{\Gamma,cp}$ be on the iso-0 of the level-set φ (as proposed in [11]). This is formulated as follows:

$$\begin{aligned} &\text{minimize} \quad d(\mathbf{x}) = \frac{1}{2}\left\|\mathbf{x}-\mathbf{x}_q\right\|^2 , \\ &\text{subject to} \quad \varphi(\mathbf{x}) = 0 , \end{aligned}$$

which, by virtue of the method of Lagrange, can be recast as:

$$\nabla L(\mathbf{x},\lambda) = 0 , \quad \text{with: } L(\mathbf{x},\lambda) = \frac{1}{2}\left\|\mathbf{x}-\mathbf{x}_q\right\|^2 + \lambda\varphi(\mathbf{x}) ,$$

with the Lagrangian L and the Lagrange coefficient λ. The resulting non-linear system is then solved with an iterative Newton's method. An important point to highlight here is the fact that all the operations are usually performed in the parametric coordinates in a FEM framework. The non-linear system to be solved is therefore expressed in terms of the derivatives with respect to the parametric coordinates $\boldsymbol{\xi}$ thanks to the mapping $\mathbf{x}(\boldsymbol{\xi})$:

$$\nabla_{(\boldsymbol{\xi},\lambda)} L(\mathbf{x}(\boldsymbol{\xi}),\lambda) = 0 , \tag{11}$$

[1] Argo is a proprietary code developed by the Belgian research center Cenaero. Details can be found in [12].

and its linearization around a certain point $(\boldsymbol{\xi}, \lambda)$ leads to the linear system giving the Newton's steps $(\Delta\boldsymbol{\xi}, \Delta\lambda)$ at each iteration:

$$\begin{bmatrix} \nabla^2_{\xi\xi} L(\boldsymbol{\xi}, \lambda) & \nabla_{\xi}\varphi(\boldsymbol{\xi}) \\ \nabla^T_{\xi}\varphi(\boldsymbol{\xi}) & 0 \end{bmatrix} \begin{bmatrix} \Delta\boldsymbol{\xi} \\ \Delta\lambda \end{bmatrix} = - \begin{bmatrix} \nabla_{\xi} L(\boldsymbol{\xi}, \lambda) \\ \varphi(\boldsymbol{\xi}) \end{bmatrix} \tag{12}$$

where the gradient of the Lagrangian with respect to $\boldsymbol{\xi}$ can be expressed based on the Jacobian matrix of the mapping between parametric and physical coordinates $\mathbf{J}_{\text{map}}$

$$\nabla_{\xi} L(\boldsymbol{\xi}, \lambda) = \mathbf{J}^T_{\text{map}}(\mathbf{x}(\boldsymbol{\xi}) - \mathbf{x}_q) + \lambda \nabla_{\xi}\varphi(\boldsymbol{\xi}) \,, \tag{13}$$

while the Hessian of the Lagrangian with respect to $\boldsymbol{\xi}$ is computed by finite differences for simplicity

$$\nabla^2_{\xi\xi} L(\boldsymbol{\xi}, \lambda) = \frac{\nabla_{\xi} L(\boldsymbol{\xi} + \epsilon, \lambda + \epsilon) - \nabla_{\xi} L(\boldsymbol{\xi}, \lambda)}{\epsilon} \,. \tag{14}$$

Assuming that $\nabla_{\xi} L(\boldsymbol{\xi}^0, \lambda^0) \approx 0$, the initial value for the Lagrange multiplier is specified as:

$$\lambda^0 = - \frac{\mathbf{J}^T_{\text{map}}(\mathbf{x}^0 - \mathbf{x}_q) \cdot \nabla^T_{\xi}\varphi(\boldsymbol{\xi}^0)}{\left\| \nabla_{\xi}\varphi(\boldsymbol{\xi}^0) \right\|^2} \tag{15}$$

For some elements, this iterative procedure, starting from a guess point inside a given element, may converge to a solution which would be located in another adjacent element. As the level-set function is represented by piecewize polynomial functions, the process is stopped if the iterate is located outside of the element above a prescribed margin. In this situation, the Newton's procedure is applied on the neighbouring elements.

3.3. Verification test case: the dual-circle

For the numerical results to follow, the error between the computed solution, φ^h, and the analytical solution, φ, is given in the $L2$-norm as:

$$E_{L2} = \int_{\Omega} (\varphi^h - \varphi)^2 \, \mathrm{d}V \,,$$

where Ω refers to the narrow-band region (as the test cases presented in this work have been conducted with the narrow-band strategy).
A test case from [16] is selected to illustrate the convergence rate of our reinitialization procedure. It consists of two circles of different radii with iso-contours initially specified by an exponential function. The

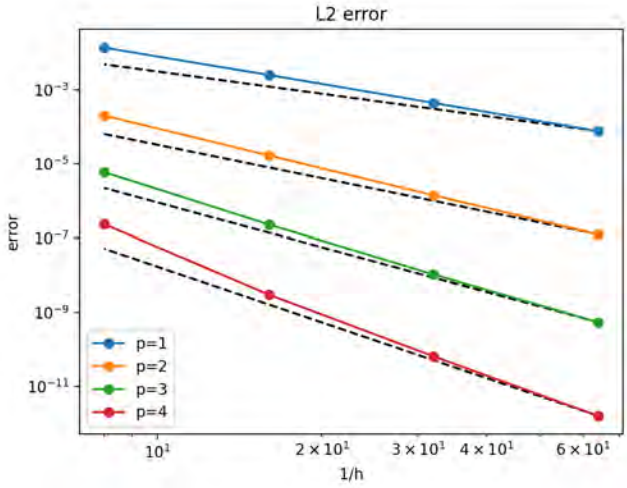

Figure 2: L2-convergence study about the reinitialization of the dual-circle test case. Dashed lines indicate theoretical convergence rates.

reinitizalied level-set iso-contour field is shown in Fig. 1b while the errors graph for different combinations of interpolation orders and mesh sizes is presented in Fig. 2. As expected, when the errors are computed excluding singularities regions, the convergence rate follows the theoretical rate $p + 1$.

4. Extension of the interfacial velocity

4.1. Theory

The most direct approach to define the velocity $\mathbf{v}_{\text{ext}}$ in Eq. (5) away from the interface is to use the underlying fluid velocity $\mathbf{u}_{\text{fluid}}$ itself:

$$\mathbf{v}_{\text{ext}}(\mathbf{x}, t) = \mathbf{u}_{\text{fluid}}(\mathbf{x}, t) \,. \tag{16}$$

Doing so, a (very) frequent reinitialization is needed as the level-set function will quickly loose its signed-distance property. In many applications however, the velocity field $\mathbf{v}_{\text{ext}}$ with which the level-set is advected makes sense only at the interface. In this case, a dedicated technique to build the extended velocity in the domain from the interface is required. This technique should be designed such that the extended velocity match the interface velocity (as specified by Eq. (6)). Another desirable feature is that it moves the neighbouring level-sets in such a way that the signed distance property is preserved. This can be achieved by extrapolating the interface velocity in the domain, i.e. for each grid point, the value of the interface velocity

at the closest point on the front is used as the extension velocity at that point, as suggested in [17]:

$$\mathbf{v}_{\text{ext}}(\mathbf{x}, t) = \mathbf{v}(\mathbf{x}_{\Gamma,cp}, t) \, . \tag{17}$$

It can be shown that Eq. (17) is equivalent to the solution of the following equations:

$$\begin{aligned} \nabla \mathbf{v}_{\text{ext}}(\mathbf{x}, t) \cdot \nabla \varphi(\mathbf{x}, t) = 0 \qquad & \mathbf{x} \in \Omega \, , \\ \mathbf{v}_{\text{ext}}(\mathbf{x}, t) = \mathbf{v}_{\Gamma}(\mathbf{x}, t) \qquad & \mathbf{x} \in \Gamma \, , \end{aligned} \tag{18}$$

which ensures that the extended velocity, starting from the interface, remains constant along the normal direction. One the most common (and fastest) method to solve Eq. (18) directly is based on the Fast Marching Method and was proposed in [18; 19]. Finally, it is also possible to reformulate Eq. (18) as a hyperbolic ([20]) or elliptic ([21]) PDE. It can be shown that under the extended velocity field obtained either from Eq. (17) or Eq. (18), the level set function remains a signed distance function for all times, assuming that both $\mathbf{v}_{\text{ext}}$ and φ are smooth. Thus, at least theoretically, extending the velocity in this way would eliminate the need for reinitialization, and hence improve the accuracy of the resulting computation.
In this work, a direct geometrical approach based on Eq. (17) is used.

4.2. Implementation

The implementation allows flexibility about the way the interface velocity can be obtained. In the case the level-set is not transported by an external fluid velocity field, the first option is to directly specify the norm of the interface velocity that will depend on the position along the interface. The two other possibilities have been included in order to be able to simulate two-phase flows without or with phase transition: it is possible to give to the interface velocity the velocity of one of the two phases or to compute the velocity from a pre-defined solver accounting for example for phase transition.
From an algorithmic point of view, the position of the closest point on the interface computed during the reinitialization is first retrieved for each mesh point. The fluid states from the single-phase flow or from both sides of the interface in case of two-phase flow are then interpolated onto the closest point with the help of the shape functions and the nodal values in the element to which the closest point belongs. The normal and the curvature computed before are also available there. From these quantities, the velocity on the iso-0 can be entirely determined and then extended to the mesh point with Eq. (17).

4.3. Verification test case: the rotating circle

The test case chosen here comes from [22]. It is about the motion of a circular contour of radius 1 centered initially at $(0.0, 1.25)$ in a flow field which is rotating around the point $(0.0, 0.0)$ outside the circle. The velocity field has an angular velocity equal to 1 and is given in Cartesian coordinates by

$$\mathbf{v}(\mathbf{x}) = (-y, x) \, .$$

The problem is discretized on the domain $\Omega = (-3, 3)^2$ on structured meshes with different mesh sizes. The implicit multi-step ESDIRK43 time-stepping scheme is chosen with $\Delta t = 5e{-}4$. The exact solution can be found using standard rotational transformation depending on time. Reinitialization every 100 times is performed. In Fig. 3a, the initial velocity field and the position of the iso-0 are represented. In Fig. 3b, the iso-contours of the level-set over the narrow-band at the final time are drawn as well as the iso-contours of the extended velocity field. As we can observe, the velocity iso-contours are straight and seem to be normal to the iso-0, indicating that the velocity of the iso-0 is correctly extended to the mesh points. This is partially confirmed on the convergence graph in Fig. 4 where the error between the analytical expression of the level-set at the final time and the computed solution follows the expected trend for the interpolation orders $p = 1$ and $p = 2$. However, for $p = 3$, the convergence seems to "saturate" on the finest mesh. It is not clear which could be the exact cause of this behavior. However, we can point out the possible influence that might have the current treatment of the elements entering the narrow-band at every time steps. Because the narrow-band evolves as time passes, new elements are frequently added and removed from the narrow-band. When an element is added at one time step, reinitialization is done in this element in order to assign a correct value of the level-set. However, at the previous times, the value of the level-set associated to this element was set to +1 or -1 because it was belonging to the far field elements. When a high-order time-stepping scheme is used, it is required to provide solutions from previous time steps in case of multi-step schemes and previous sub-time steps in case of multi-stage ones. If we simply apply those temporal schemes in the elements that appear in the narrow-band, we will run into troubles because we will consider the value for the level-set fixed to +1 or -1 from the previous time steps. To avoid this problem, we only considered multi-stage schemes and we update the narrow-band outside of the loop on the

different stages. Doing so, the order of the temporal scheme could be artificially decreased locally. And preliminary studies have clearly shown that for unsteady problems, the choices of the time step and the order of the selected time-stepping scheme can have a dominant effect on the resulting convergence rate.

5. Conclusions and upcoming work

We have described the different steps of a high-order level-set reinitialization and extension methodology. Two test cases were selected to demonstrate the accuracy of the procedure. This represents an important piece in the more global and currently ongoing development of a sharp interface two-phase flows solver whose purpose is to produce high-fidelity simulations of the gas-liquid interactions that occur during the ablation of metallic space debris.
The next steps toward applying the results of the present work to real case studies are described in details below.

5.1. Level-set

Concerning the level-set method itself, three elements requires some further developments:

- *investigate the saturation of the convergence rate for unsteady problems*: as already discussed in Sec 4.3, the convergence rate of the methods put in place applied to unsteady problems involving extension of the velocity does not match the theoretical rate. Further investigations are needed to identify the possible causes of this limitation;

- *improve robustness of closest point search procedure*: with the guess points given as an input to the Newton's method that are very frequently close to the final closest point on the interface, the iterative process converges usually quickly. If the solution is located in an element different from the one to which the guess point belongs, the procedure is applied on the adjacent elements, which reinforces the robustness of the approach. Despite this, it might happen that the procedure is not able to find the exact (up to approximation errors) closest point on the interface. As proposed in [11], a constrained gradient-based descent mechanism can be added as a back-up to Newton's method. Safeguarded Newton's strategies are also possible;

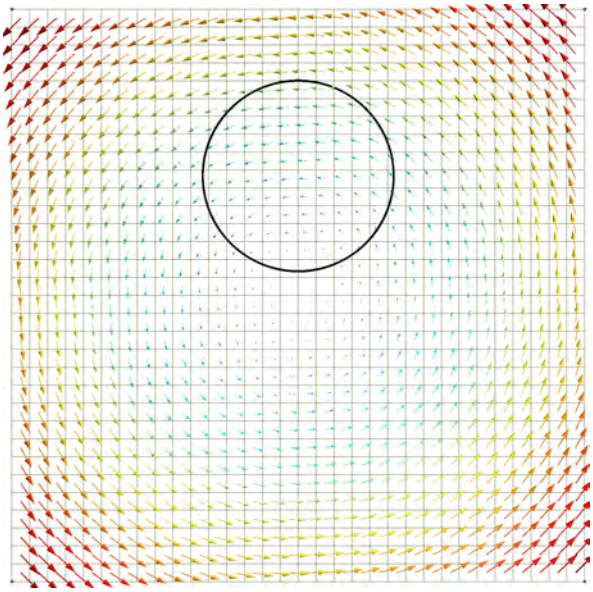

(a) Initial velocity field and position of the iso-0 for the rotating circle test case.

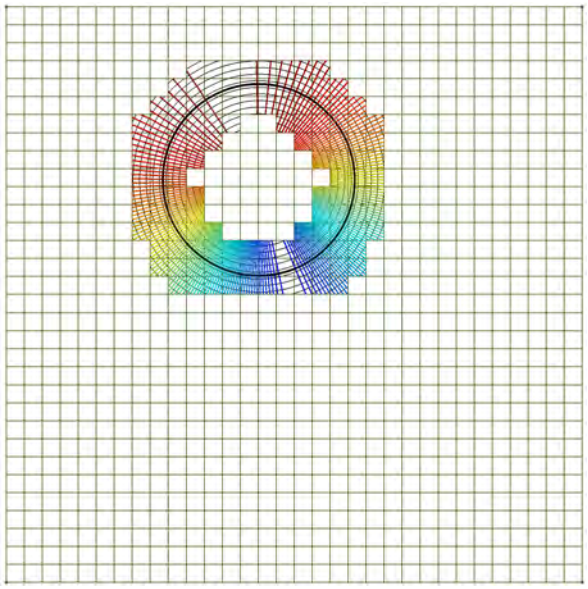

(b) Iso-contours of the extended velocity field in color which are perpendicular to the iso-contours of the level-set on the narrow-band.

Figure 3: Comparison between the full domain and the narrow-band strategy on a dual-circle configuration.

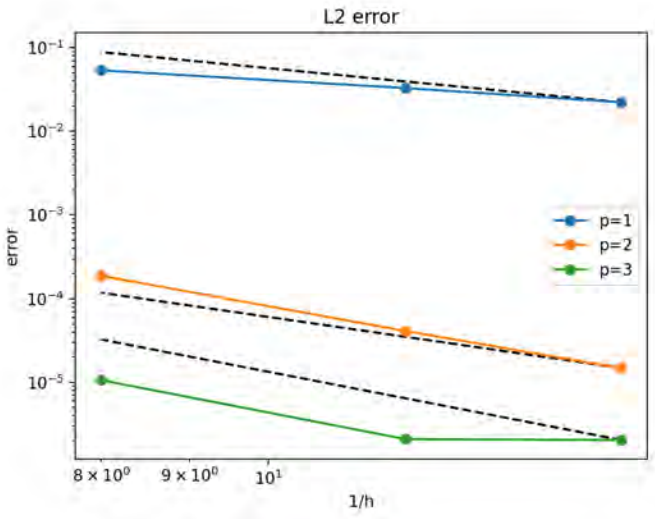

Figure 4: L2-convergence study about the advection and velocity extension of the rotating circle test case. Dashed lines indicate theoretical convergence rates.

- *smooth/filter secondary quantities*: it is well known that a direct evaluation of the normal and a fortiori the curvature from the DG polynomial may lead to oscillating results. This is due to the amplification of the small jumps in the level-set representation at the element interfaces when gradients of the level-set are computed. Since the interface velocity can depend on the local normal and curvature, it is important to smooth these oscillations as much as possible. One way to do so in the DG framework is to incorporate neighbouring element information in a way that effectively dampens the influence of the high-order modes present in the DG discretization. This can be achieved by means of different approaches, like using the concept of the partition of unity method [23] or the $P_N P_M$-reconstruction [24].

5.2. Coupling between level-set and XDG methods

In this work, the combined use of the level-set method and the XDG method has not been studied as the focus was put on the development of methodologies specific to the level-set method. However, we can formulate a few comments about the coupling with the XDG method that has already been used in previous work [1]. The coupling used up to now is based on an explicit approach where the level-set and the governing equations discretized by the XDG method are solved in a separate way. To improve the accuracy, an implicit coupling will also be considered in the future. With this approach, the level-set advection is incorporated into the iteration process for solving the flow equations at every time step [25]. As temporal integration of the equations is carried out with a moving interface, a correction term accounting for this movement is needed to compute the numerical fluxes across the interface [26].

Acknowledgments

My doctoral work is supported by the Fonds de la Recherche Scientifique (FNRS) of Belgium, under a FRIA grant. I would like to thank Pierre Schrooyen and Larbi Arbaoui from Cenaero with whom I had very interesting discussions about the level-set method and its implementation in the Argo code.

References

[1] D. Henneaux, P. Schrooyen, B. Ricardo Barros Dias, A. Turchi, P. Chatelain, T. Magin, Extended discontinuous galerkin method for solving gas-liquid compressible flows with phase transition, in: AIAA AVIATION 2020 FORUM, 2020, p. 2971.

[2] E. Marchandise, Simulation of three-dimensional two-phase flows : coupling of a stabilized finite element method with a discontinuous level set approach, Ph.D. thesis, Universite catholique de Louvain (2006).

[3] P. Schrooyen, J.-S. Cagnogne, N. Poletz, K. Hillewaert, A high-order extended discontinuous galerkin method for moving immersed interface problem, in: XDMS Conference, Umea, 2017.

[4] P. Schrooyen, L. Arbaoui, J.-S. Cagnone, N. Poletz, K. Hillewaert, A high-order extended discontinuous galerkin method to treat hydrodynamics problems, in: ECCM-ECFD Conference, Glasgow (UK), 2018.

[5] S. Osher, J. A. Sethian, Fronts propagating with curvature-dependent speed: algorithms based on hamilton-jacobi formulations, Journal of computational physics 79 (1) (1988) 12–49.

[6] J. A. Sethian, P. Smereka, Level set methods for fluid interfaces, Annual review of fluid mechanics 35 (1) (2003) 341–372.

[7] J. A. Sethian, A fast marching level set method for monotonically advancing fronts, Proceedings of the National Academy of Sciences 93 (4) (1996) 1591–1595.

[8] Y.-H. R. Tsai, L.-T. Cheng, S. Osher, H.-K. Zhao, Fast sweeping algorithms for a class of hamilton–jacobi equations, SIAM journal on numerical analysis 41 (2) (2003) 673–694.

[9] M. Sussman, A level set approach for computing solutions to incompressible two-phase flow, Ph.D. thesis, UCLA - Computational and Applied Mathematics (1994).

[10] T. Utz, F. Kummer, M. Oberlack, Interface-preserving level-set reinitialization for dg-fem, International Journal for Numerical Methods in Fluids 84 (4) (2017) 183–198.

[11] R. Saye, High-order methods for computing distances to implicitly defined surfaces, Communications in Applied Mathematics and Computational Science 9 (1) (2014) 107–141.

[12] K. Hillewaert, Development of the discontinuous galerkin method for high-resolution, large scale cfd and acoustics in industrial geometries, Ph.D. thesis, Universit catholique de Louvain (2013).
[13] J.-F. Remacle, N. Chevaugeon, E. Marchandise, C. Geuzaine, Efficient visualization of high-order finite elements, International Journal for Numerical Methods in Engineering 69 (4) (2007) 750–771.
[14] R. Saye, High-order quadrature methods for implicitly defined surfaces and volumes in hyperrectangles, SIAM Journal on Scientific Computing 37 (2) (2015) A993–A1019.
[15] S. Arya, D. M. Mount, N. S. Netanyahu, R. Silverman, A. Y. Wu, An optimal algorithm for approximate nearest neighbor searching fixed dimensions, Journal of the ACM (JACM) 45 (6) (1998) 891–923.
[16] L. Anumolu, M. F. Trujillo, Gradient augmented reinitialization scheme for the level set method, International Journal for Numerical Methods in Fluids 73 (12) (2013) 1011–1041.
[17] R. Malladi, J. A. Sethian, B. C. Vemuri, Shape modeling with front propagation: A level set approach, IEEE transactions on pattern analysis and machine intelligence 17 (2) (1995) 158–175.
[18] D. Adalsteinsson, J. A. Sethian, The fast construction of extension velocities in level set methods, Journal of Computational Physics 148 (1) (1999) 2–22.
[19] D. L. Chopp, Another look at velocity extensions in the level set method, SIAM Journal on Scientific Computing 31 (5) (2009) 3255–3273.
[20] D. Peng, B. Merriman, S. Osher, H. Zhao, M. Kang, A pde-based fast local level set method, Journal of computational physics 155 (2) (1999) 410–438.
[21] T. Utz, F. Kummer, A high-order discontinuous galerkin method for extension problems, International Journal for Numerical Methods in Fluids 86 (8) (2018) 509–518.
[22] T. Utz, Level set methods for high-order unfitted discontinuous galerkin schemes, Ph.D. thesis, Technische Universität (2018).
[23] R. Saye, Implicit mesh discontinuous galerkin methods and interfacial gauge methods for high-order accurate interface dynamics, with applications to surface tension dynamics, rigid body fluid–structure interaction, and free surface flow: Part ii, Journal of Computational Physics 344 (2017) 683–723.
[24] S. Fechter, Compressible multi-phase simulation at extreme conditions using a discontinuous galerkin scheme, Ph.D. thesis, Universitat Stuttgart (2015).
[25] M. Smuda, F. Kummer, On a marching level-set method for extended discontinuous galerkin methods for incompressible two-phase flows, arXiv preprint arXiv:2010.08417.
[26] F. Kummer, B. Müller, T. Utz, Time integration for extended discontinuous galerkin methods with moving domains, International Journal for Numerical Methods in Engineering 113 (5) (2018) 767–788.

Understanding the graphitization process of carbon fibers

Francisco Torres Herrador

Aeronautics and Aerospace Department, von Karman Institute for Fluid Dynamics, Belgium, fratorhe@vki.ac.be

Supervisor: Olivier Chazot

Head of Department and Professor, Aeronautics and Aerospace Department, von Karman Institute for Fluid Dynamics, Belgium, chazot@vki.ac.be

Supervisor: Thierry Magin

Professor, Aeronautics and Aerospace Department, von Karman Institute for Fluid Dynamics, Belgium, magin@vki.ac.be

University Supervisor: Kevin M. Van Geem

Professor, Laboratory for Chemical Technology (LCT), Faculty of Engineering and Architecture, Ghent University, Belgium, kevin.VanGeem@UGent.be

University Supervisor: Julien Blondeau

Professor, Thermo and Fluid dynamics (FLOW), Faculty of Engineering, Vrije Universiteit Brussel, Belgium, jublonde@vub.ac.be

Abstract

Thermal conductivity of carbon fibers is one of the major properties influencing heat transfer in thermal protection systems of spacecraft. Recent experiments have shown that the thermal conductivity of carbon fiber materials permanently increases up to four times after being submitted to high temperatures. The cause of this increase, yet to be completely understood, may be related to their graphitization. We investigate the microstructural changes that occur in the carbon fibers which lead to such an increase of thermal conductivity. We proposed the following approach: i) the investigation of the process of graphitization from molecular dynamics, and ii) experimental studies on samples submitted to plasma wind tunnel testing. Preliminary results show that the graphitization process occurs in the time-scale of a typical plasma wind tunnel test in a region within $\sim$ 1 cm from the surface. Molecular dynamics simulations show good agreement with x-ray diffraction experiments. The combination of numerical simulations and experiments lead us to a better understanding of the graphitization process which is key for a better understanding of the evolution of the thermal conductivity of carbon fiber in high temperature conditions.

Keywords: carbon/phenolic, thermal degradation, thermal analysis

1. Introduction

Nowadays, most Thermal Protection Systems (TPS) of spacecraft are carbon/phenolic ablators. These composite materials are made of a carbon fiber preform which is then impregnated with a phenolic resin. This mixture provides a low-density, poorly conductive material ideal for atmospheric entry scenarios. These materials have made possible missions such as Stardust [1] or Mars Science Laboratory (MSL) [2; 3] using the Phenolic Impregnated Carbon Ablator (PICA) from NASA. One encounters examples of carbon/phenolic materials both in industry (PICA-X^{TM} from SpaceX, ASTERM^{TM} from Airbus) and other government agencies (ZURAM® from DLR).

TPS is a critical system in a spacecraft: its failure would be fatal. Therefore, large safety factors are often applied in order to compensate for the uncertainties, to ensure mission success. However, new mod-

els have been developed in recent years which allow to accurately simulate the aerothermal environment of the spacecraft during atmospheric entry [4; 5], thus reducing sources of uncertainty coming from the modeling. However, these advanced models require accurate material characterization. In particular, the thermal conductivity of the carbon fiber preform is one of the major contributors to the heat transfer within the TPS [6].

We have characterized the thermal conductivity of the pre-charred ZURAM® material, which is CALCARB® with the char from the phenolic resin. Laser Flash Analysis (LFA) of the material up to 2800 °C were performed at Forschungszentrum Jlich (Germany). In these measurements (Fig. 1), the conductivity of different samples was measured up to a certain maximum temperature (continuous line), and then it was measured again in the cool-down phase (dashed line). This showed that as the thermal conductivity of the samples that reached temperatures higher than 2000 °C showed a permanent increase up to four times higher. In the particular case of CALCARB® material, this occurs at temperatures higher than 2000 °C because this is the temperature at which the fibers are treated during manufacturing.

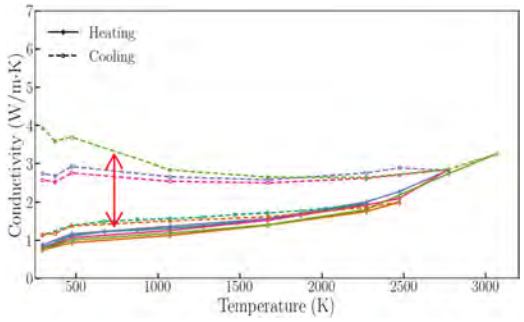

Figure 1: Conductivity measurements of pre-charred ZURAM®. A permanent increase of thermal conductivity can be observed (heat up phase (solid line), and cool down phase (dashed line).

Such a non-negligible increase on thermal conductivity requires a better understanding for several reasons: 1) we need to understand the time-scale of this phenomenon to understand if it can occur during flight, 2) accurately reproduce plasma wind tunnel experiments, in which samples are submitted to heating and cool down [7–9], 3) improve fundamental understanding on the behavior of carbon materials. In addition, future sample return missions (to Mars) or a more intensive launching frequency may require the re-use of ablative TPS materials. Such scenario would require in-depth understanding of this phenomenon and its effects.

Literature pointed out that this increase of conductivity is due to the graphitization of the carbon fibers [10; 11]. Graphitization is a process by which carbon atoms re-arrange themselves into a graphite-*like* structure. Due to the re-arrangement of the carbon atoms in a more regular pattern and reducing the inter-layer spacing, the phonon transport is more efficient, thus increasing the macroscopic quantity of thermal conductivity [12; 13].

One finds two main studies of graphitization in literature: at the atom scale, or on the consequent change on thermal conductivity. At atom scale, several works focused on understanding how to simulate this effect using molecular dynamics [14–17], or observing this effect by means of techniques such as Raman Spectra or X-Ray Diffraction [11; 13; 18; 19]. In addition, some experiments have been performed on similar materials (carbon blacks) to understand the time-scale of the phenomenon [20; 21]. On the effect of the thermal conductivity, we highlight the work of Pradere [22] in which several types of carbon fibers were analyzed up to 3000 °C, providing data that shows the effect of heat treatments on the thermal conductivity.

In this work, we intend to merge those two perspectives and achieve a more complete explanation of this process. To do so, we propose the following approach: **i)** simulate the graphitization process and its correspondence to the real phenomenon by comparing X-ray diffraction graphs (Section 4.3), **ii)** Experimental observations by means of plasma wind tunnel testing and Raman spectroscopy to understand the timescale of the phenomenon (Section 4.1).

2. Materials and methods

2.1. Facilities

In the context of this work, we have made use of two facilities: the VKI plasma wind tunnel (Plasmatron) and a Raman microscope. In the following, we provide a brief description on each of them focusing on the relevant information for the current work.

2.1.1. Plasma wind tunnel: VKI Plasmatron

In order to simulate entry conditions, the VKI uses its 1.2 MW coupled inductive plasma wind tunnel. This unique facility is capable of generating a subsonic high enthalpy plasma flow characteristic of a

planetary entry. Due to the use of an induction coil, the generated plasma is highly pure. This facility also allows the use of different testing gases to simulate different environments. In the current work, the testing gas used was nitrogen in order to avoid oxidation reactions. The cold heat flux was targeted to be (2.5 MW), this would heat up the sample up to temperatures higher than 2000 °C. This is important since CALCARB® CBCF 18-2000 is treated at 2000 °C during manufacturing (Section 2.2).

2.1.2. Raman microscope

The setup used is a commercially available Raman Microscope LabRam HR Evolution (HORIBA Scientific). This device uses a solid state laser (532 nm) and a CCD detector (spectral resolution $< 1\,\mathrm{cm}^{-1}$, lateral resolution 0.5 µm, axial resolution 2 µm).

The working principle of Raman spectrometry is based on the Raman scattering [23]. Typically, when a molecule gets excited by a laser, its vibrational state will pass to a virtual energy state, and then return to its ground state in an elastic process known as Rayleigh scattering. However, in a small percentage of the cases (10^{-7}), the molecule will return to a higher vibrational state. In such case, the frequency of the emitted photon will be different from the absorbed. This inelastic process is known as Raman scattering, in Stokes mode. If instead, the molecule is already at a higher vibrational state and then returns to its original ground state, we have anti-Stokes Raman scattering (Fig. 2). This means that the difference in wavelength (or frequency) between the absorbed and emitted photons (Raman shift) provides information on the interatomic bounds, leading to a unique fingerprint for each molecule.

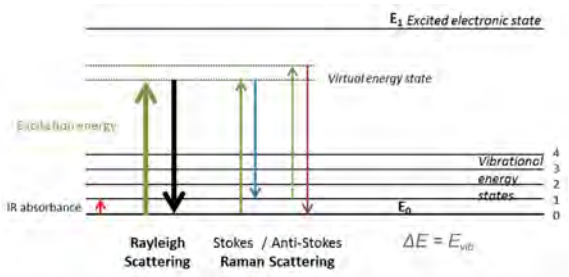

Figure 2: Principle of operation of a Raman microscope

2.1.3. X-Ray Diffraction

Another technique that has been used to analyze these carbon fibers is X-Ray Diffraction (XRD). In this technique, an x-ray beam is shot on the surface of the material at an angle ω and, if the location of the atoms satisfies Bragg's Law (Eq. (1)), the diffracted beam will be of a constructive type and a signal will be detected by the detector. The detector is located at an angle $\theta = 2\omega$. Bragg's Law states that a signal will be obtained if the phase shift between the rays is a multiple n of the inter-planar distance d. In this work, these experiments were carried using an apparatus Siemens D5000, with an X-ray source $CuK\alpha$ with $h\nu = 8047.8\,\mathrm{eV}$ and $\lambda = 0.154\,\mathrm{nm}$.

$$2d\sin\theta = n\lambda \tag{1}$$

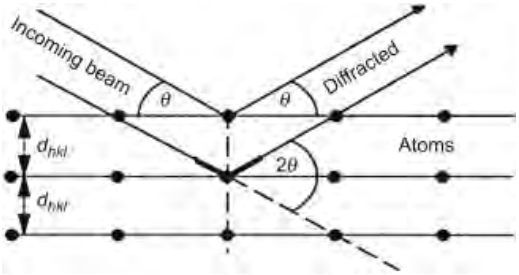

Figure 3: Schematic of working principle of XRD (From [24]).

2.2. Material and sample preparation

The material used to perform these experiments is CALCARB® CBCF 18-2000. This material is made of short carbon fibers (length ~ 500 µm) product of the pyrolysis of rayon. These fibers are arranged with a certain preferential plane, while in the other axes the fibers are distributed more randomly, thus CALCARB® material is often considered orthotropic. The manufacturer (Mersen Ltd.) pre-treats the batches of CALCARB® at high temperatures (~ 2000 °C) in order to ensure its thermal stability. However, as it will be seen in the following, this thermal stability may not hold at temperatures exceeding the Heat Treatment Temperature (HTT).

The material is provided in slabs ($20\,\mathrm{cm}^3 \times 20\,\mathrm{cm}^3 \times 5\,\mathrm{cm}^3$) which are then cut into the required shapes for testing. In this case, the sample was cut into a 50 mm diameter hemispherical shape typically used at the VKI Plasmatron (Fig. 4) [25–27]. The sample was instrumented with several thermocouples: most of them were located in the central thermal plug, whereas some others were located axially outside the plug. The actual location of the TC was determined using X-Ray tomography.

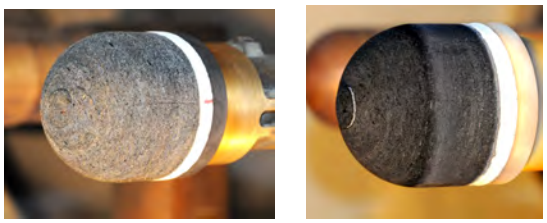

(a) Before (b) After

Figure 4: Photographs of sample mounted in the Plasmatron facility. Test conditions: Nitrogen, cold-wall heat-flux 2.5 MW · m^{-2}, p_s of 100 mbar, duration 30 s.

The sample was submitted to a heat-flux of 2.5 MW · m^{-2} in a nitrogen environment with a chamber static pressure of 100 mbar for 30 s. Then, the sample cooled down by re-radiating the heat. A slight change in color can be observed on the sample surface due to the coke formation from the interaction of the nitrogen gas and the carbon surface (Fig. 4b)

Temperature was recorded using two type-B thermocouples ($T_{\max}$ = 2050 K, TC1 and TC2) and type-K TC for the other TCs ($T_{\max}$ = 1500 K). Surface temperature (T_s) was also recorded using a two-color pyrometer and an infrared camera (not described here).

After this pre-treatment, the sample was cut at the different TC locations in the shape of disks (~ 1 mm) to be analyzed using Raman spectroscopy. An additional sample was extracted from outside the thermal plug as depicted in Fig. 6 in a slice perpendicular to the flow direction.

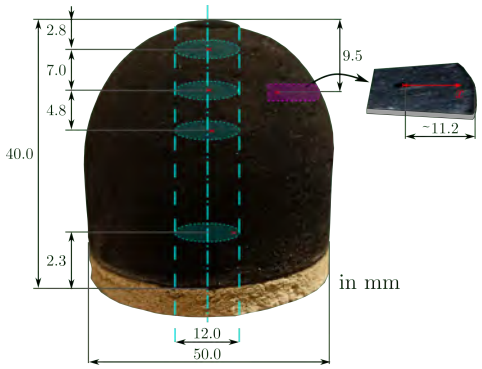

Figure 6: Post heat treatment sample preparation. The ellipses show the TC locations that were analysed, see the following sections

Moreover, a sample from CALCARB® CBCF 18-2000 which was not submitted to the plasma wind tunnel heat-treatment was also analyzed as a reference, hereafter referred as *preform*.

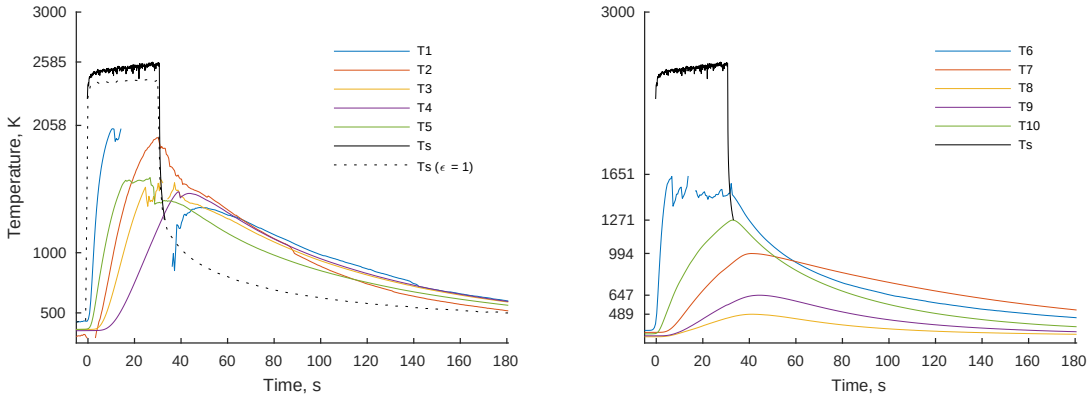

Figure 5: Temperature measurements during the plasma wind tunnel test for sample preparation: 2 type-B thermocouples ($T1$ and $T2$) and 3 type-K thermocouples ($T3$ to $T5$) located in the sample (locations in Fig. 6), as well as a two-color pyrometer T_s. The surface temperature T_s evolves as expected: a very fast rise, followed by a slight rise during test time at constant heat flux and a slower decrease during cooldown. Both type-B thermocouples (T1 and T2) provided a reliable signal until their temperature limit (close to 2050 K).

3. Numerical Tools

In the context of this work, we have used different computational tools for the different parts: analysis of the experimental results (Ramanpy) and simulation of the graphitization process (LAMMPS). In the following sections, we provide a brief description of each tool. Useful references are provided for the interested reader.

3.1. Ramanpy

We have developed an in-house utility to post-process Raman (or XRD) data, `Ramanpy`[1]. This code, written in Python, uses the non-linear fitting package `lmfit` to perform optimization tasks. The user only needs to define an input file with the ranges for the expected peaks, and the code will fit them using Lorentzian functions. Moreover, the code implements smoothing technique based on the Savitzky-Golay filter which is used to smooth curves without the shift found in a typical moving average. In addition to the fitted parameters, the code also returns the 95 % confidence interval for each variable, and other statistics of interest. The code has specific functions to compute the quantities of interest for the analyses of the carbon materials presented here (I_R, peak width, peak location, etc.), but it can be easily extended to other materials by means of its object-oriented programming structure.

[1] https://github.com/Fratorhe/ramanpy

3.2. Large-scale Atomic/Molecular Massively Parallel Simulator

The Large-scale Atomic/Molecular Massively Parallel Simulator (LAMMPS) is a classical Molecular Dynamics (MD) simulation software developed by Sandia Labs [28]. In classical MD the interactions between atoms/molecules are simulated using potentials (force fields). These potentials are then integrated at every time-step to obtain the acceleration, velocity, and position of each atom using a Verlet-*like* numerical scheme. System properties (i.e. total energy, temperature, pressure, etc) are obtained from the aforementioned variables. The main benefit from using LAMMPS is that its modular design allows the user to use different types of potentials, and to extract any atom or system property anytime. It should be pointed out that, in general, MD simulations use periodic boundary conditions in each direction, thus reducing the large computational cost of simulating systems with many atoms.

Computational cost largely depends on the number of atoms and on the type of potential used. MD is mostly CPU intensive type of problem due to the need of computing the forces between each pair of atoms. As an order of magnitude, preliminary simulations carried out in this work with 10000 atoms, took $\sim$ 8 h in a typical 8-processor desktop computer.

4. Results

4.1. Raman

The CALCARB® CBCF 18-2000 samples described in Section 2.2 were analyzed using Raman Spectroscopy. For the locations where higher temperatures were achieved more measurements were performed whereas for the locations where temperature was not as high, less repetitions were taken. In any case, at least three repetitions were carried out for each location in order to ensure that the results had statistical significance.

For each measurement, a Raman spectrum was obtained (Fig. 7). In this kind of spectrum, one can distinguish several peaks. Each peak is due to changes in the vibrational state of the atoms and the consequent release of photons. However, for the current work, we define two peak types: G and D, for the ordered (graphite-like) and the disordered (amorphous) carbon structure respectively [11; 18]. The relative intensity of these peaks (intensity ratio, $I_R = I_D/I_G$) is a quantitative measure of the state of the material, thus values of $I_R > 1.2$ would indicate an amorphous material, while $I_R \sim 0.3$ would indicate a highly graphitized material.

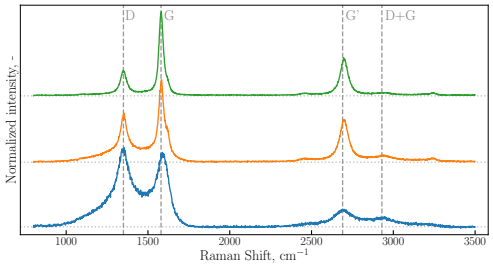

Figure 7: Typical Raman spectra obtained for 3 different locations. It can be seen that the I_R between the D and G peaks varies. For each spectrum, the intensities are normalized with respect to its highest value.

Figure 8 shows the measured values of the I_R for the different samples described in Section 2.2. It can be seen that for the untreated sample (blue, preform) that the material as received presents already certain graphitization $I_R \sim 1.2$, this is mainly due to the HTT to which the fibers are submitted during the manufacturing process.

We should also observe the I_R at the different thermocouple locations. First the location TC4, which was the deepest TC, shows an I_R similar to the one obtained in the case of the untreated preform sample.

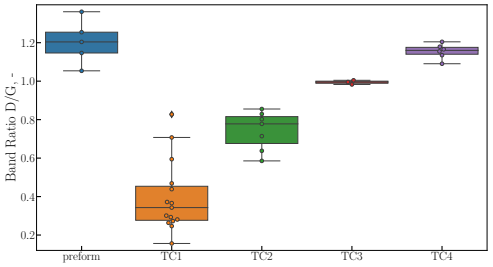

Figure 8: I_R computed for the reference preform and the different TC locations.

However, as we get closer to the surface, the I_R reduces from the $I_R \sim 1.2$ obtained for TC4, to an average of $I_R \sim 0.3$ for the case of TC1. We also observe that for TC locations closer to the surface, the dispersion on the values for the I_R becomes larger. This could be to due to different factors: i) since the largest temperature gradients are produced near the surface, at slight different locations, different temperatures may be achieved, thus different I_R, ii) the fibers did not have enough time to achieve their final graphitized state, or iii) some locations may not achieve the same graphitized state if the location probed is within a grain border.

The sample that was extracted from the side of the carbon fiber preform was also analyzed. In this case, the interest was to understand how the graphitization evolves in depth for a continuous sample. The sample measured 11.2 mm from the TC location to the external surface. Raman measurements were performed at several locations along the radial direction from the TC to the external part of the sample. It can be seen that until 8000 µm the I_R shows similar values to the preform Fig. 9), or to TC3 and TC4 explained before. There is also an outlier at $x = 5500$ µm with an $I_R \sim 1.4$. However, as we get closer to the surface, in the region starting at $x = 8000$ µm, that the I_R quickly decreases down to the values encountered at TC1, in relatively small region of 2 mm. After, one enters in the coking zone generated from the interaction of carbon with the nitrogen testing gas, again losing the graphitized structure hence obtaining larger values of I_R comparable to the reference preform.

These results indicate that the locations closer to the surface achieved high temperatures such that the internal structure of the carbon fibers passed from an amorphous state to a much higher graphite-like state. In addition, it shows that for a typical Plasmatron test conditions (duration and heat-flux) the carbon fibers

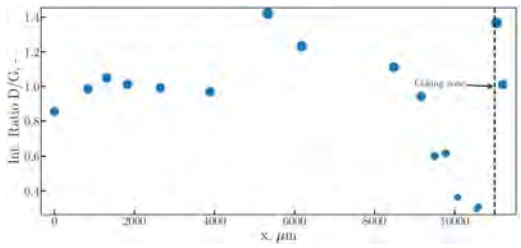

Figure 9: I_R along a perpendicular line to the flow within the preform material. The TC depicted in Fig. 6 is located at the origin. It can be seen that the graphitization occurs within 3 mm from the surface.

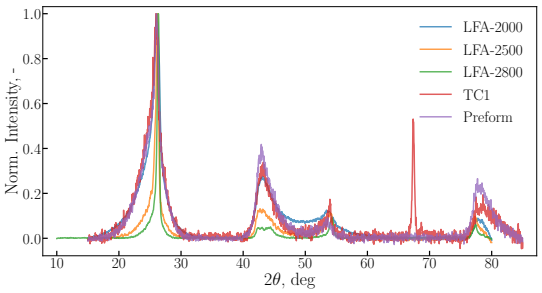

Figure 10: XRD results for the different samples.

undergo relevant micro-structural changes.

4.2. X-Ray Diffraction

Several carbon fiber samples were analyzed on XRD (Fig. 10). As a general overivew, four main peaks can be observed which roughly correspond to the 2θ angles 26,43,55,78° for all the samples tested. An additional peak for TC1 was observed at 68°, but this was later attributed to a piece of thermocouple that remained inside the sample.

It can be observed that Preform, LFA-2000 and TC1 provided the same results. These samples were respectively: the carbon fiber preform as received, a disk used to measure with LFA up to 2000 °C (see Fig. 1) and, the top sample from the sample treated in Plasmatron (see Fig. 6). It was expected that the results for Preform and LFA-2000 were very similar since the pretreatment temperature of the preform was 2000 °C as well, so no further changes were expected. However, the TC1 sample was submitted to the plasma flow and a larger degree of graphitization was expected. This change was actually observed in the Raman measurements (Section 4.1). It is possible that XRD could not observe this change due to the thickness of the sample, or to the irregularities on the surface, which made it difficult to perform measurements.

The remaining two samples (LFA-2500 and LFA-2800) were also disks used in LFA (see Fig. 1), but in these cases the maximum temperatures were 2500 °C and 2800 °C, respectively. It be seen that as the temperature increases, the main peak at 26° becomes much narrower. This indicates an important change in the degree of graphitization of the material.

4.3. Simulation of the graphitization process

As explained in Section 1, the graphitization process can be simulated by means of Molecular Dynamics (MD). We followed the procedure established by de Tomas et al. [14; 15]. This procedure starts with a simple cubic lattice of carbon atoms such that the density corresponds to the one being studied. This structure is very unstable and collapses, with a rapid temperature increase. An NVE with thermostat is applied to avoid the simulation getting too unstable. Then, an NVT is applied to quench the process and decrease the temperature to room temperature. This is followed by another NVT for equilibration of the amorphous structure, allowing it to stabilize and minimize its energy. Finally, the structure is annealed at the desired temperature for a long period of time (> 100 ps) in order to obtain the graphitized carbon.

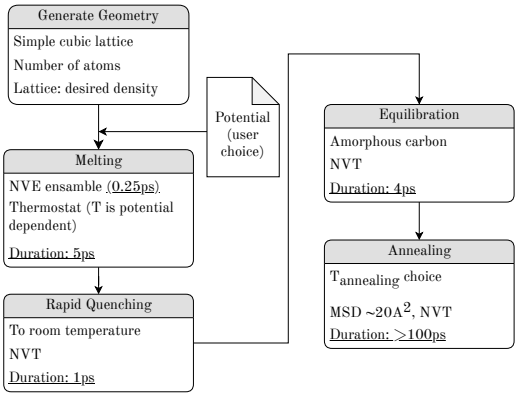

Figure 11: Steps for the simulation of graphitization of carbon as defined in [14]

A very extensive review of carbon potentials (force fields) was performed by De Tomas [16] focusing on their capability to simulate the the graphitization process. It was found that each potential gives relatively different results. On this ongoing work, we have tested different potentials such as Tersoff or EDIP to reproduce the result of de Tomas [14]. An example

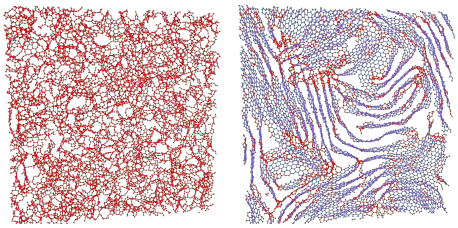

(a) Amorphous (b) Graphitized

Figure 12: Slices of a 100 000 atoms graphitization simulation using EDIP potential. In purple, the atoms which are in a graphite structure, in red the ones that are not.

for the amorphous and graphitized structures using the EDIP potential [29] can be seen in Fig. 12.

In addition, one can also simulate X-ray diffraction using LAMMPS. The method was developed by Coleman et al [30]. We have applied this method to the structures shown in Fig. 12, and the results are depicted in Fig. 13.

The variation in intensity shown in the amorphous (orange) is due to absence of any crystalline structure and this produced a broadening of the signal. Instead, the annealed structure (blue) has three main peaks corresponding to 21,43,78° which are in qualitatively agreement with the results obtained experimentally (see Fig. 3).

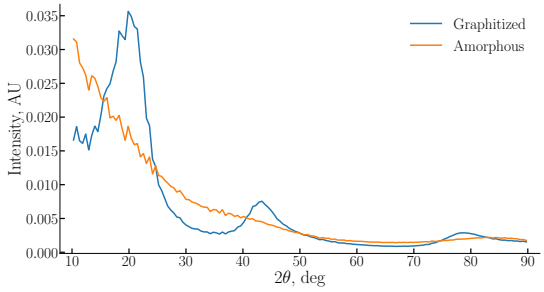

Figure 13: Simulation of XRD diffractogram using LAMMPS for amorphous and annealed structures.

5. Conclusion

This work presented an overview of the effort being carried out to understand the graphitization process and its effects on material properties.

Raman spectroscopy has been used to characterize samples from plasmatron experiments using the intensity band ratio I_R. We have observed that the graphitization process occurs in typical duration of Plasmatron experiments.

We have performed preliminary MD simulations to understand the evolution of a carbon material from an amorphous to a graphitized state. These simulations are also the basis for thermal conductivity calculations currently being carried out. In addition, XRD has been simulated and compared to the experimental results with good qualitative agreement.

Acknowledgments

The research of F. Torres-Herrador is supported by SB PhD fellowship 1S58718N of the Research Foundation Flanders (FWO). The LFA measurements on pre-charred ZURAM® shown in this work were performed for VKI at the Forschungszentrum Jülich (GE) under the ESA contract no. 4000122914/18/NL/KML (AblaNTIS). The ESA technical officer, Heiko Ritter, and Dr. Gerald Pintsuk from Jülich are acknowledge for their support in defining and performing the experiments, respectively. We would like to thank F. Panerai (UIUC) and N.N. Mansour (NASA Ames) for fruitful discussion. Advice given by C. de Tomas has been a great help on the MD simulations. We would like to thank A. Turchi and B. Helber (VKI) for their useful suggestions. P. Collin (VKI) is acknowledged for his valuable help as Plasmatron operator. A. Hubin and K. Baert (VUB) are acknowleged for her help on Raman microscopy. I would like to thank A. Fagnani for the useful comments on this manuscript.

References

[1] D. Kontinos, M. Stackpoole, Post-Flight Analysis of the Stardust Sample Return Capsule Earth Entry, in: 46th AIAA Aerospace Sciences Meeting and Exhibit, American Institute of Aeronautics and Astronautics, Reno, Nevada, 2008. doi:10.2514/6.2008-1197.
URL https://arc.aiaa.org/doi/abs/10.2514/6.2008-1197

[2] K. T. Edquist, B. R. Hollis, C. O. Johnston, D. Bose, T. R. White, M. Mahzari, Mars Science Laboratory Heat Shield Aerothermodynamics: Design and Reconstruction, Journal of Spacecraft and Rockets 51 (4) (2014) 1106–1124. doi:10.2514/1.A32749.
URL https://doi.org/10.2514/1.A32749

[3] C. Szalai, E. Slimko, P. Hoffman, Mars Science Laboratory Heatshield Development, Implementation, and Lessons Learned, in: Journal of Spacecraft and Rockets, Vol. 51, 2014, pp. 1167–1173. doi:10/f6ftx5.
URL https://doi.org/10.2514/1.A32673

[4] J. B. E. Meurisse, J. Lachaud, F. Panerai, C. Tang, N. N. Mansour, Multidimensional material response simulations of a full-scale tiled ablative heatshield, Aerospace Science and Technology 76 (2018) 497–511. doi:10/gc4pgh.

URL http://www.sciencedirect.com/science/article/pii/S1270963817323179

[5] P. Schrooyen, K. Hillewaert, T. E. Magin, P. Chatelain, Fully implicit Discontinuous Galerkin solver to study surface and volume ablation competition in atmospheric entry flows, International Journal of Heat and Mass Transfer 103 (2016) 108–124. doi:10.1016/j.ijheatmasstransfer.2016.07.022.
URL http://www.sciencedirect.com/science/article/pii/S0017931015310127

[6] M. Rivier, J. Lachaud, P. M. Congedo, Ablative thermal protection system under uncertainties including pyrolysis gas composition, Aerospace Science and Technology 84 (2019) 1059–1069. doi:10/ggd9mz.
URL http://www.sciencedirect.com/science/article/pii/S127096381831472X

[7] J. Lachaud, A. Martin, I. Cozmuta, B. Laub, Ablation Test Case 1, in: 4th Ablation Workshop, Albuquerque, New Mexico, 2011.

[8] J. Lachaud, A. Martin, T. van Eekelen, I. Cozmuta, Ablation Test Case 2, in: 5th Ablation Workshop, Lexingotn, Kentucky, 2012.

[9] T. van Eekelen, I. Cozmuta, A. Martin, J. Lachaud, Ablation Test Case 3, in: 6th Ablation Workshop, Illinois, 2014.

[10] A. Gupta, S. R. Dhakate, P. Pal, A. Dey, P. K. Iyer, D. K. Singh, Effect of graphitization temperature on structure and electrical conductivity of poly-acrylonitrile based carbon fibers, Diamond and Related Materials 78 (2017) 31–38. doi:10/gb43wn.
URL http://www.sciencedirect.com/science/article/pii/S0925963517300195

[11] M. B. Vzquez-Santos, E. Geissler, K. Lszl, J.-N. Rouzaud, A. Martnez-Alonso, J. M. Tascn, Comparative XRD, Raman, and TEM Study on Graphitization of PBO-Derived Carbon Fibers, The Journal of Physical Chemistry C 116 (1) (2012) 257–268. doi:10/b345b5.
URL https://doi.org/10.1021/jp2084499

[12] J. Che, T. an, W. Deng, W. A. Goddard, Thermal conductivity of diamond and related materials from molecular dynamics simulations, The Journal of Chemical Physics 113 (16) (2000) 6888–6900, publisher: American Institute of Physics. doi:10.1063/1.1310223.
URL https://aip.scitation.org/doi/10.1063/1.1310223

[13] L. G. Canado, K. Takai, T. Enoki, M. Endo, Y. A. Kim, H. Mizusaki, A. Jorio, L. N. Coelho, R. Magalh£es-Paniago, M. A. Pimenta, General equation for the determination of the crystallite size La of nanographite by Raman spectroscopy, Applied Physics Letters 88 (16) (2006) 163106. doi:10/cmf3rc.
URL https://aip.scitation.org/doi/abs/10.1063/1.2196057

[14] C. de Tomas, I. Suarez-Martinez, N. A. Marks, Graphitization of amorphous carbons: A comparative study of interatomic potentials, Carbon 109 (2016) 681–693. doi:10/gcz65k.
URL http://www.sciencedirect.com/science/article/pii/S0008622316306790

[15] C. de Tomas, I. Suarez-Martinez, F. Vallejos-Burgos, M. J. Lpez, K. Kaneko, N. A. Marks, Structural prediction of graphitization and porosity in carbide-derived carbons, Carbon 119 (2017) 1–9. doi:10/gbhgvk.
URL http://www.sciencedirect.com/science/article/pii/S0008622317303615

[16] C. de Tomas, A. Aghajamali, J. L. Jones, D. J. Lim, M. J. Lpez, I. Suarez-Martinez, N. A. Marks, Transferability in interatomic potentials for carbon, Carbon 155 (2019) 624–634. doi:10/gf8kgt.
URL http://www.sciencedirect.com/science/article/pii/S0008622319307675

[17] K. Li, H. Zhang, G. Li, J. Zhang, M. Bouhadja, Z. Liu, A. A. Skelton, M. Barati, ReaxFF Molecular Dynamics Simulation for the Graphitization of Amorphous Carbon: A Parametric Study, Journal of Chemical Theory and Computation 14 (5) (2018) 2322–2331. doi:10/gdgqff.
URL https://doi.org/10.1021/acs.jctc.7b01296

[18] A. C. Ferrari, Raman spectroscopy of graphene and graphite: Disorder, electronphonon coupling, doping and nonadiabatic effects, Solid State Communications 143 (1) (2007) 47–57. doi:10/b686ms.
URL http://www.sciencedirect.com/science/article/pii/S0038109807002967

[19] M. B. Vzquez-Santos, A. Martnez-Alonso, J. M. D. Tascn, J.-N. Rouzaud, E. Geissler, K. Lszl, Complementary X-ray scattering and high resolution imaging of nanostructure development in thermally treated PBO fibers, Carbon 49 (9) (2011) 2960–2970. doi:10.1016/j.carbon.2011.03.013.
URL http://www.sciencedirect.com/science/article/pii/S0008622311001898

[20] T. Gruber, T. W. Zerda, M. Gerspacher, Raman studies of heat-treated carbon blacks, Carbon 32 (7) (1994) 1377–1382. doi:10/cxv32b.
URL http://www.sciencedirect.com/science/article/pii/0008622394901252

[21] T. W. Zerda, T. Gruber, Raman Study of Kinetics of Graphitization of Carbon Blacks, Rubber Chemistry and Technology 73 (2) (2000) 284–292. doi:10/c36ddn.
URL https://www.rubberchemtechnol.org/doi/abs/10.5254/1.3547591

[22] C. Pradere, J. C. Batsale, J. M. Goyhnche, R. Pailler, S. Dilhaire, Thermal properties of carbon fibers at very high temperature, Carbon 47 (3) (2009) 737–743. doi:10/d73c23.
URL http://www.sciencedirect.com/science/article/pii/S0008622308006015

[23] P. J. Larkin, Infrared and Raman Spectroscopy, Elsevier, 2018. doi:10.1016/C2015-0-00806-1.
URL https://linkinghub.elsevier.com/retrieve/pii/C20150008061

[24] J. Epp, 4 - X-ray diffraction (XRD) techniques for materials characterization, in: G. Hbschen, I. Altpeter, R. Tschuncky, H.-G. Herrmann (Eds.), Materials Characterization Using Nondestructive Evaluation (NDE) Methods, Woodhead Publishing, 2016, pp. 81–124. doi:10.1016/B978-0-08-100040-3.00004-3.
URL https://www.sciencedirect.com/science/article/pii/B9780081000403000043

[25] B. Helber, Material response characterization of low-density ablators in atmospheric entry plasmas, Ph.D. thesis, Vrije Universiteit Brussel (2016).

[26] B. Helber, O. Chazot, T. Magin, A. Hubin, Ablation of Carbon Preform In the VKI Plasmatron, in: 43rd AIAA Thermophysics Conference, American Institute of Aeronautics and Astronautics, 2012.
URL http://arc.aiaa.org/doi/abs/10.2514/6.2012-2876

[27] B. Helber, F. Torres Herrador, V. Leroy, A. Turchi, O. Chazot, T. E. Magin, Experiments of the ZURAM carbon-phenolic ablator for test case definition and material code validation., in: 9th Ablation Workshop, Bozeman, Montana USA, 2017.

[28] S. Plimpton, Fast Parallel Algorithms for Short-Range Molecular Dynamics, Journal of Computational Physics

117 (1) (1995) 1–19. doi:10.1006/jcph.1995.1039.
URL http://www.sciencedirect.com/science/article/pii/S002199918571039X

[29] N. A. Marks, Generalizing the environment-dependent interaction potential for carbon, Physical Review B 63 (3) (2000) 035401, publisher: American Physical Society. doi:10.1103/PhysRevB.63.035401.
URL https://link.aps.org/doi/10.1103/PhysRevB.63.035401

[30] S. P. Coleman, D. E. Spearot, L. Capolungo, Virtual diffraction analysis of Ni symmetric tilt grain boundaries, Modelling and Simulation in Materials Science and Engineering 21 (5) (2013) 055020, publisher: IOP Publishing. doi:10.1088/0965-0393/21/5/055020.
URL https://doi.org/10.1088%2F0965-0393%2F21%2F5%2F055020

AEROTHERMODYNAMICS

Experimental investigation of space debris fragmentation during re-entry

Dániel Gábor Kovács

Aeronautics and Aerospace Department, von Karman Institute for Fluid Dynamics, Belgium, kovacs@vki.ac.be

Supervisor: Olivier Chazot

Full Professor and Head of the Department, Aeronautics and Aerospace Department, von Karman Institute for Fluid Dynamics, Belgium, chazot@vki.ac.be

Promoter: Gaëtan Kerschen

Professor, Department of Aerospace and Mechanical Engineering, Université de Liège, Belgium, g.kerschen@ulg.ac.be

Abstract

Nowadays, besides the goal of enabling ecological and more economical space access, the accumulation of space debris is rising environmental and safety problems. By 2021 the number of debris objects larger than 1 cm orbiting around Earth is almost reaching 1,000,000. The impact of these remains with other objects can give birth to additional detritus enlarging the chance of further collisions. The United Nations has enacted guidelines for the mitigation of space debris by promoting their reentry for better use of the space environment. Risk assessments must be performed in order to accurately predict the demiseability of the objects to avoid causing damage on the ground or any harm to the population. The aerothermal effects determining the fragmentation and the ablation of these bodies are highly dependent on the trajectory and the aerodynamic characteristics, given that their correct estimation is required to precisely assess the demiseability.

The present Ph.D. project is going to address the fragmentation phenomenon occurring during the atmospheric re-entry, the aerodynamics of the fragmented bodies, and the associated thermodynamics and heat transfer by the means of experimental tools. As a first step, an extensive literature survey will take place to establish the state of the art. Relevant flight trajectories and generic models are to be identified from the literature and with the application of the VKI Trajectory code, yielding flight and test conditions. Investigations will be performed in the VKI Longshot gun tunnel and in the H-3 blow down wind tunnel. In order to simulate accurately the breakup phenomenon, besides the similarity of the aerodynamic non-dimensional numbers, an appropriate scaling must be identified for the mechanical properties. Free-flight and stationary model measurement techniques will be applied in the Longshot wind tunnel to study the breakup and the separation process, and the interaction of the fragments. Based on the trajectory of the fragments their aerodynamic properties will be retrieved, and the application of temperature sensitive paint on stationary models would allow the identification of the surface heat-fluxes. Tests are to be performed in the H-3 wind tunnel using stationary models equipped with internal balances, flow visualization, and infrared thermography. This will allow the investigation of specific points of the breakup trajectory in terms of aerodynamics, flow topology and shock interactions, and hot-spots and heat-fluxes. Following the interpretation and the validation of the measurements, a methodology for extrapolating the wind tunnel test results to flight conditions must be identified.

Keywords: hypersonic, space debris, re-entry, aerothermodynamics, fragmentation, proximal bodies, free-flight

Massively Parallel and Robust High-Order Methods for Transitional Hypersonic Flow Modelling on Unstructured Grids

Ray Vandenhoeck

Aeronautics and Aerospace Department, von Karman Institute for Fluid Dynamics, Belgium, vandenhoeck@vki.ac.be

Supervisor: Andrea Lani

Aeronautics and Aerospace Department, von Karman Institute for Fluid Dynamics, Belgium, lani@vki.ac.be
Centre for Mathematical Plasma Astrophysics, KU Leuven, Belgium

University Supervisor: Johan Steelant

Professor, Department of Mechanical Engineering, KU Leuven, Belgium, johan.steelant@kuleuven.be
ESA/ESTEC, The Netherlands

Abstract

This work presents the development of the first high-order Flux Reconstruction (FR) solver for flows governed by the compressible Reynolds-Averaged Navier-Stokes (RANS) equations including Laminar-Turbulent Transition (LTT). The solver is fully implicit and implemented in the open-source COOLFluiD platform. The Spalart-Allmaras model, the $k-\tilde{\omega}$ Shear Stress Transport (SST) model and the Langtry-Menter Local Correlation-Based Transition Model (LCTM) are implemented. Some modifications are made to the original $k-\omega$ SST model in order to obtain more robust and stable simulations. In particular, the natural logarithm of ω is transported and the equations are transformed accordingly. The solver is verified both in fully turbulent flow as well as in several transitional flow cases. The results of the verification cases are compared to references from the literature and good agreement is found in all cases. Finally, it was shown that the FR method obtains accurate results on very coarse meshes, with a considerably larger first element height (y_1^+), i.e. up to $y_1^+ \simeq 10$, than state-of-the-art finite volume solvers without wall-extended functions.

Keywords: Computational Fluid Dynamics, High-Order, Flux Reconstruction, Laminar-Turbulent Transition, Local Correlation-Based Transition Model, Langtry-Menter

1. Introduction

In recent years, Computational Fluid Dynamics (CFD) codes have been used for increasingly complex applications in an ever expanding plethora of application fields. As a consequence, CFD methods are required to obtain accurate results faster and for increasingly more sophisticated physical models. In the last few decades, significant progress has been made in the development of efficient high-order Finite Element (FE)-type CFD methods that can potentially offer an answer to the steep rise in the requirements imposed on CFD methods. High-order FE-type methods, as opposed to the traditionally used low-order Finite Volume (FV) method, can obtain arbitrary high orders while still keeping a compact stencil, making these methods particularly well-suited for parallel High-Performance Computing (HPC). Additionally, high-order FE-type methods exhibit a higher accuracy per Degree of Freedom (DoF) as compared to their low-order counterparts. However, high-order FE-type methods are generally less robust and more involving to implement than low-order FV methods. Additionally, they typically need special treatment in order to obtain stable results, especially when discontinuities are present in the flow field.

In order to accurately resolve the effects of turbulence, Large Eddy Simulations (LES) or Direct Numerical Simulations (DNS) offer sufficient accuracy. However these methods are computationally costly and as such can hardly be used within a realistic time

frame for complex geometries that lead to meshes with a large number of cells, or when several hundreds or thousands of simulations need to be made for a particular case. In those cases, the Reynolds-Averaged Navier-Stokes (RANS) equations are typically solved with one of the many turbulence models and corresponding closures available in the literature. This approach sacrifices accuracy, but greatly reduces computational cost.

In many applications, the onset and length of Laminar-Turbulent Transition (LTT) have a profound impact on the quantities of interest. For example in the case of high-speed vehicles, the heat flux on the thermal protection system of the vehicle is determined in large part by the flow regime. As a consequence, it is paramount in the design of such vehicles to accurately predict the onset and length of LTT. Unfortunately not many CFD-compatible LTT models for the RANS equations are available in literature. One reason for this is that transition is caused by a multitude of physical mechanisms: natural transition caused by Tollmien-Schlichting waves, crossflow instability, bypass transition, and separation-induced transition. Furthermore, methods based on the stability equations, such as the e^n method as proposed in [1], are typically not suited for general CFD applications, especially with complex geometries, as they require non-local operations and prior knowledge of the global geometry. One of the few transition models for the RANS equations available in the literature that only contains local operations and as such is well-adapted to massively parallel CFD codes, is the Langtry-Menter Local Correlation-Based Transition Model (LCTM). This model is outlined in [2; 3; 4; 5]. It triggers transition by comparing the local vorticity Reynolds number with a transported critical momentum thickness Reynolds number in order to avoid non-local operations.

The present paper discusses the development of a fully-implicit FR solver for flows governed by the RANS equations, including LTT. The FR solver can solve the compressible RANS equations with the Spalart-Allmaras turbulence model, the $k-\tilde{\omega}$ SST turbulence model and the Langtry-Menter LCTM. This is implemented within COOLFluiD[1], an open-source framework for multi-physics modeling and simulations [6; 7; 8].

First, chapter 2 presents the system of equations to be solved, i.e. the compressible RANS equations with the Spalart-Allmaras model, the $k-\tilde{\omega}$ SST turbulence model and Langtry-Menter LCTM. Next, chapter 3 gives a concise overview of the FR method. Chapter 4 gives an overview of the implementation of the present solver. Finally, chapter 5 presents several verification test cases. More specifically, flat plate cases are studied for a fully turbulent flow with the Spalart-Allmaras and $k-\tilde{\omega}$ SST turbulence models and for a transitional flow with different free stream turbulence intensities with the $k-\tilde{\omega}$ SST turbulence model and Langtry-Menter LCTM.

[1] https://github.com/andrealani/COOLFluiD/wiki

2. Governing Equations

The present work considers the compressible RANS equations, also commonly referred to as the Favre-averaged Navier-Stokes equations. In order to model LTT, the Langtry-Menter LCTM is also incorporated, which build upon the $k-\tilde{\omega}$ SST model. First, the RANS equations with the $k-\tilde{\omega}$ SST model are presented in section 2.1. Next, the Spalart-Allmaras model is briefly described in section 2.2. Finally, the Langtry-Menter model is discussed in section 2.3.

2.1. RANS with the $k-\tilde{\omega}$ SST Model

The present $k-\tilde{\omega}$ SST model corresponds in essence to the SST-2003 model found in [9; 10]. However, instead of the variable ω, the natural logarithm $\tilde{\omega} = \ln\omega$ is transported and the equations are transformed accordingly. This was first proposed in [11] for the DG method. However in [11], this approach was not applied to the SST-2003 model, but to the Wilcox $k-\omega$ model found in [12].

It was found that when using the original $k-\omega$ SST-2003 model with FR, the steep increase of ω near a wall leads to instabilities, with the positivity of ω not being preserved when resolving the steep gradient with high-order polynomials. Since the distribution of $\tilde{\omega}$ near the wall is much smoother and does not exhibit a steep gradient, the instability disappears when transporting $\tilde{\omega}$ instead. Furthermore, transporting $\tilde{\omega}$ inherently guarantees the positivity of ω. The system of equations constituting the compressible RANS equations with the $k-\tilde{\omega}$ SST model can be written as follows:

$$\frac{\partial\rho}{\partial t} + \frac{\partial}{\partial x_j}(\rho u_j) = 0, \tag{1}$$

$$\frac{\partial(\rho u_i)}{\partial t} + \frac{\partial}{\partial x_j}(\rho u_j u_i) = \frac{\partial\tilde{\tau}_{ji}}{\partial x_j} - \frac{\partial p}{\partial x_i}, \tag{2}$$

$$\frac{\partial(\rho e_0)}{\partial t} + \frac{\partial}{\partial x_j}(\rho u_j h_0) = \frac{\partial}{\partial x_j}(u_i\tilde{\tau}_{ij} - \mathcal{q}_j) - P + \beta^*\rho k e^{\tilde{\omega}}, \tag{3}$$

$$\frac{\partial(\rho k)}{\partial t}+\frac{\partial}{\partial x_j}(\rho u_j k) = P-\beta^*\rho k e^{\tilde{\omega}}+\frac{\partial}{\partial x_j}\left((\mu+\sigma_k\mu_t)\frac{\partial k}{\partial x_j}\right), \tag{4}$$

$$\frac{\partial(\rho\tilde{\omega})}{\partial t}+\frac{\partial}{\partial x_j}(\rho u_j\tilde{\omega}) = \frac{\rho\hat{\gamma}}{\mu_t}e^{-\tilde{\omega}}P-\beta\rho e^{\tilde{\omega}}+ (\mu+\sigma_\omega\mu_t)\frac{\partial\tilde{\omega}}{\partial x_k}\frac{\partial\tilde{\omega}}{\partial x_k}+\frac{\partial}{\partial x_j}\left((\mu+\sigma_\omega\mu_t)\frac{\partial\tilde{\omega}}{\partial x_j}\right)+ 2(1-F_1)\rho\sigma_{\omega2}e^{-\tilde{\omega}}\frac{\partial k}{\partial x_j}\frac{\partial\tilde{\omega}}{\partial x_j}, \tag{5}$$

where the following relations apply:

$$P = \min\left(\tau_{ij}\frac{\partial u_i}{\partial x_j}, 10\beta^*\rho e^{\tilde{\omega}}k\right), \tag{6}$$

$$p = (\tilde{\gamma}-1)\rho\left(e_0-\frac{u_k u_k}{2}\right),\ q_j = -\left(\frac{\mu}{\mathrm{Pr}}+\frac{\mu_t}{\mathrm{Pr}_t}\right)\frac{\partial h}{\partial x_j}, \tag{7}$$

$$\tau_{ij} = 2\mu_t\left(S_{ij}-\frac{1}{3}\frac{\partial u_k}{\partial x_k}\delta_{ij}\right)-\frac{2}{3}\rho k\delta_{ij}, \tag{8}$$

$$\tilde{\tau}_{ij} = 2\mu\left(S_{ij}-\frac{1}{3}\frac{\partial u_k}{\partial x_k}\delta_{ij}\right)+\tau_{ij}, \tag{9}$$

$$\mu_t = \frac{\rho a_1 k}{\max\left(a_1 e^{\tilde{\omega}},\sqrt{2S_{ij}S_{ij}}F_2\right)},\ S_{ij} = \frac{1}{2}\left(\frac{\partial u_i}{\partial x_j}+\frac{\partial u_j}{\partial x_i}\right), \tag{10}$$

$$F_1 = \tanh\left(\min\left(\max\left(\frac{\sqrt{k}}{\beta^* e^{\tilde{\omega}}d},\frac{500\mu}{\rho e^{\tilde{\omega}}d^2}\right),\frac{4\rho\sigma_{\omega2}k}{CD_{k\omega}d^2}\right)^4\right), \tag{11}$$

$$CD_{k\omega} = \max\left(2\rho\sigma_{\omega2}\frac{\partial k}{\partial x_j}\frac{\partial\tilde{\omega}}{\partial x_j},10^{-10}\right), \tag{12}$$

$$F_2 = \tanh\left(\max\left(2\frac{\sqrt{k}}{\beta^* e^{\tilde{\omega}}d},\frac{500\mu}{\rho e^{\tilde{\omega}}d^2}\right)^2\right), \tag{13}$$

where $\tilde{\gamma}$ is the adiabatic index, taken constant as 1.4, d is the wall distance, Pr the Prandtl number taken constant as 0.72 and Pr_t the turbulent Prandtl number taken constant as 0.9.

The constants used in the present model are shown in table 1. For the blended constants the following general relation applies:

$$\varphi = F_1\varphi_1+(1-F_1)\varphi_2. \tag{14}$$

Table 1: $k-\tilde{\omega}$ SST model constants

$\hat{\gamma}_1$	σ_{k1}	$\sigma_{\omega1}$	β_1	a_1
5/9	0.85	0.5	0.075	0.31
$\hat{\gamma}_2$	σ_{k2}	$\sigma_{\omega2}$	β_2	β^*
0.44	1.0	0.856	0.0828	0.09

2.1.1. Notes on the $k-\tilde{\omega}$ SST model equations

Compared to the reference in [11], an extra term appears in equation 5:

$$2(1-F_1)\rho\sigma_{\omega2}e^{-\tilde{\omega}}\frac{\partial k}{\partial x_j}\frac{\partial\tilde{\omega}}{\partial x_j}. \tag{15}$$

This term comes from the SST-2003 model while not being present in the Wilcox model. It should be noted that this term is also transformed from the original term in [9; 10] to transport $\tilde{\omega}$.

Furthermore, it should be noted that in equation 5 the term:

$$(\mu+\sigma_\omega\mu_t)\frac{\partial\tilde{\omega}}{\partial x_k}\frac{\partial\tilde{\omega}}{\partial x_k}, \tag{16}$$

appears when transforming the diffusive term in equation 5 to transport $\tilde{\omega}$.

Finally, a note on positivity preservation is made. Since $\tilde{\omega}$ is transported, the positivity of ω is automatically satisfied. However k could still reach negative values, especially in the transient of simulations. As such, k is replaced in the equations above by $\bar{k}$:

$$\bar{k} = \max(k,0). \tag{17}$$

2.2. RANS with the Spalart-Allmaras Model

The Spalart-Allmaras turbulence model, as presented in [13; 14], adds one equation to the system of equations to be solved, instead of the two additional equations of the $k-\tilde{\omega}$ SST model. This equation transports a working variable $\tilde{\nu}$, which is used to locally determine the turbulent eddy viscosity μ_t. This transport equation is written as follows:

$$\frac{\partial(\rho\tilde{\nu})}{\partial t}+\frac{\partial}{\partial x_j}(\rho u_j\tilde{\nu}) = c_{b1}\tilde{S}\rho\tilde{\nu}(1-f_{t2})+\frac{c_{b2}\rho}{\sigma}\frac{\partial\tilde{\nu}}{\partial x_i}\frac{\partial\tilde{\nu}}{\partial x_i} -\rho\left(c_{w1}f_w-c_{b1}\frac{f_{t2}}{\kappa^2}\right)\left(\frac{\tilde{\nu}}{d}\right)^2-\frac{\nu+\tilde{\nu}}{\sigma}\frac{\partial\rho}{\partial x_i}\frac{\partial\tilde{\nu}}{\partial x_i}+ \left(\frac{\partial}{\partial x_j}\left(\frac{\rho(\nu+\tilde{\nu})}{\sigma}\frac{\partial\tilde{\nu}}{\partial x_j}\right)\right), \tag{18}$$

where the following relations apply:

$$\tilde{S} = \Omega+\frac{\tilde{\nu}}{\kappa^2 d^2}f_{v2},\quad \Omega = \sqrt{2\Omega_{ij}\Omega_{ij}}, \tag{19}$$

$$\Omega_{ij} = \frac{1}{2}\left(\frac{\partial u_i}{\partial x_j}-\frac{\partial u_j}{\partial x_i}\right),\ f_{v2} = 1-\frac{\chi}{1+\chi f_{v1}}, \tag{20}$$

$$\chi = \frac{\tilde{\nu}}{\nu},\ f_{v1} = \frac{\chi^3}{\chi^3+c_{v1}^3},\ f_w = g\left(\frac{1+c_{w3}^6}{g^6+c_{w3}^6}\right)^{\frac{1}{6}}, \tag{21}$$

$$g = r+c_{w2}(r^6-r),\ r = \min\left(\frac{\tilde{\nu}}{\tilde{S}\kappa^2 d^2},10\right), \tag{22}$$

$$f_{t2} = c_{t3}\exp\left(-c_{t4}\chi^2\right),\quad \mu_t = \rho\tilde{\nu}f_{v1}. \tag{23}$$

This eddy viscosity is taken into account in the stress tensor $\tilde{\tau}_{ij}$ used in the momentum and energy equations, respectively equations 2 and 3. It should be noted that in the Spalart-Allmaras model, the k-contributions in equations 2 and 3 disappear.

The constants used in the present model are shown in table 2.

Table 2: Spalart-Allmaras model constants

c_{b1}	c_{w2}	c_{t3}	σ	c_2	c_{v1}
0.1355	0.3	1.2	2/3	0.7	7.1
c_{b2}	c_{w3}	c_{t4}	κ	c_3	c_{w1}
0.622	2	0.5	0.41	0.9	$\frac{c_{b1}}{\kappa} + \frac{1+c_{b2}}{\sigma}$

2.2.1. Notes on the Spalart-Allmaras model equation

In order to avoid negative values of $\tilde{S}$, $\tilde{S}$ is limited as follows, as proposed in [14]:

$$\tilde{S} = \begin{cases} \Omega + \frac{\Omega(c_2^2\Omega + c_3\bar{S})}{(c_3 - 2c_2)\Omega - \bar{S}}, & \bar{S} < -c_{v2}\Omega, \\ \Omega + \bar{S}, & -c_{v2}\Omega \leq \bar{S}, \end{cases} \tag{24}$$

where

$$\bar{S} = \frac{\tilde{\nu}}{\kappa^2 d^2} f_{v2}. \tag{25}$$

Furthermore, in order to preserve the positivity of $\tilde{\nu}$, it is limited as follows: $\bar{\tilde{\nu}} = \max(\tilde{\nu}, 0)$.

2.3. RANS with the Langtry-Menter LCTM

The Langtry-Menter model used in the present work corresponds to the SST-2003-LM2009 model found in [5; 15]. The Langtry-Menter LCTM adds two equations to the RANS equations with the $k - \tilde{\omega}$ SST model and modifies the k-equation given in equation 4. These equations, one to transport the intermittency γ, and one the transport the momentum thickness Reynolds number $\tilde{\mathrm{Re}}_{\theta t}$, are written as follows:

$$\frac{\partial(\rho\gamma)}{\partial t} + \frac{\partial}{\partial x_j}(\rho u_j \gamma) = F_l c_{a1} \rho S \sqrt{\gamma F_{os}}(1 - c_{e1}\gamma) - c_{a2}\rho\Omega\gamma F_t(c_{e2}\gamma - 1) + \frac{\partial}{\partial x_j}\left(\left(\mu + \frac{\mu_t}{\sigma_f}\right)\frac{\partial\gamma}{\partial x_j}\right), \tag{26}$$

$$\frac{\partial\left(\rho\tilde{\mathrm{Re}}_{\theta t}\right)}{\partial t} + \frac{\partial}{\partial x_j}(\rho u_j \tilde{\mathrm{Re}}_{\theta t}) = c_{\theta t}\frac{\rho}{t}\left(\mathrm{Re}_{\theta t}^{eq} - \tilde{\mathrm{Re}}_{\theta t}\right)(1 - F_{\theta t}) + \frac{\partial}{\partial x_j}\left(\sigma_{\theta t}(\mu + \mu_t)\frac{\partial\tilde{\mathrm{Re}}_{\theta t}}{\partial x_j}\right), \tag{27}$$

where the following relations apply:

$$F_l = F_{l1}(1 - F_{sl}) + 40F_{sl}, \tag{28}$$

$$F_{sl} = \exp\left(-\left(\frac{\mathrm{Re}_\omega}{200}\right)^2\right), \quad \mathrm{Re}_\omega = \frac{\rho e^{\tilde{\omega}} d^2}{\mu}, \tag{29}$$

$$F_{os} = \max(F_{os2} - F_{os3}, 0),\ F_t = \exp\left(-\left(\frac{R_T}{4}\right)^4\right), \tag{30}$$

$$F_{os1} = \frac{\mathrm{Re}_V}{2.193\mathrm{Re}_{\theta c}},\ F_{os3} = \max\left(1 - \left(\frac{R_T}{2.5}\right)^3, 0\right), \tag{31}$$

$$F_{os2} = \min(\max(F_{os1}, F_{os1}^4), 2),\ \mathrm{Re}_V = \frac{\rho S d^2}{\mu}, \tag{32}$$

$$R_T = \frac{\rho k}{\mu e^{\tilde{\omega}}},\ S = \sqrt{2S_{ij}S_{ij}},\ t = \frac{500\mu}{\rho U^2},\ U = \sqrt{u_k u_k}, \tag{33}$$

$$F_{\theta t} = \min\left(\max\left(F_w \exp\left(-\left(\frac{d}{\delta}\right)^4\right), 1 - \left(\frac{c_{e2}\gamma - 1}{c_{e2} - 1}\right)^2\right), 1\right), \tag{34}$$

$$\delta = \frac{375\Omega\mu\tilde{\mathrm{Re}}_{\theta t} d}{\rho U^2},\ F_w = \exp\left(-\left(\frac{\mathrm{Re}_\omega}{10^5}\right)^2\right), \tag{35}$$

$$\mathrm{Re}_{\theta t}^{eq} = \begin{cases} (1173.51 - 589.428Tu + \\ 0.2196Tu^{-2})F(\lambda_\theta), & Tu \leq 1.3, \\ 331.5(Tu - 0.5658)^{-0.671}F(\lambda_\theta), & 1.3 < Tu, \end{cases} \tag{36}$$

$$F(\lambda_\theta) = \begin{cases} 1 + \left(12.986\lambda_\theta + 123.66\lambda_\theta^2 + \right. \\ \left. 405.689\lambda_\theta^3\right)\exp\left(-\left(\frac{Tu}{1.5}\right)^{1.5}\right), & \lambda_\theta \leq 0, \\ 1 + 0.275(1 - \exp(-35\lambda_\theta))\cdot \\ \exp\left(-\frac{Tu}{0.5}\right), & 0 < \lambda_\theta, \end{cases} \tag{37}$$

$$\mathrm{Re}_{\theta t}^{eq} = \frac{\rho U \theta_t}{\mu}, \quad \lambda_\theta = \frac{\rho\theta_t^2}{\mu}\frac{dU}{ds}, \tag{38}$$

$$Tu = 100\sqrt{\frac{2}{3}\frac{k}{U^2}}, \quad \frac{dU}{ds} = \frac{u_m u_n}{U^2}\frac{\partial u_m}{\partial x_n}. \tag{39}$$

The new k-equation that replaces equation 4 in the Langtry-Menter model is written as follows:

$$\frac{\partial(\rho k)}{\partial t} + \frac{\partial}{\partial x_j}(\rho u_j k) = \gamma_{eff} P + \frac{\partial}{\partial x_j}\left((\mu + \sigma_k\mu_t)\frac{\partial k}{\partial x_j}\right) - \min(\max(\gamma_{eff}, 0.1), 1)\beta^*\rho k e^{\tilde{\omega}}, \tag{42}$$

where the following relations apply:

$$\gamma_{eff} = \max(\gamma, \gamma_{sep}),\ F_{ra} = \exp\left(-\left(\frac{R_T}{20}\right)^4\right), \tag{43}$$

$$\gamma_{sep} = \min\left(s_1 \max\left(0, \frac{\mathrm{Re}_V}{3.235\mathrm{Re}_{\theta c}} - 1\right)F_{ra}, 2\right)F_{\theta t}. \tag{44}$$

Furthermore, the blending factor F_1 of the SST model is modified in the following way, where F_1' is the blending coefficient computed in equation 11:

$$F_1 = \max(F_1', F_3),\ F_3 = \exp\left(-\left(\frac{R_y}{120}\right)^8\right),\ R_y = \frac{\rho d\sqrt{k}}{\mu}. \tag{45}$$

$$F_{l1} = \begin{cases} 39.8189 - 119.27 \cdot 10^{-4}\tilde{\mathrm{Re}}_{\theta t} - 132.567 \cdot 10^{-6}\tilde{\mathrm{Re}}_{\theta t}^2, & \tilde{\mathrm{Re}}_{\theta t} < 400, \\ 263.404 - 123.939 \cdot 10^{-2}\tilde{\mathrm{Re}}_{\theta t} + 194.548 \cdot 10^{-5}\tilde{\mathrm{Re}}_{\theta t}^2 - 101.695 \cdot 10^{-8}\tilde{\mathrm{Re}}_{\theta t}^3, & 400 \leq \tilde{\mathrm{Re}}_{\theta t} < 596, \\ 0.5 - 3 \cdot 10^{-4}(\tilde{\mathrm{Re}}_{\theta t} - 596), & 596 \leq \tilde{\mathrm{Re}}_{\theta t} < 1200, \\ 0.3188, & 1200 \leq \tilde{\mathrm{Re}}_{\theta t}, \end{cases} \tag{40}$$

$$\mathrm{Re}_{\theta c} = \begin{cases} -396.035 \cdot 10^{-2} + 10120.656 \cdot 10^{-4}\tilde{\mathrm{Re}}_{\theta t} - 868.23 \cdot 10^{-6}\tilde{\mathrm{Re}}_{\theta t}^2 + 696.506 \cdot 10^{-9}\tilde{\mathrm{Re}}_{\theta t}^3 - 174.105 \cdot 10^{-12}\tilde{\mathrm{Re}}_{\theta t}^4, & \tilde{\mathrm{Re}}_{\theta t} \leq 1870, \\ \tilde{\mathrm{Re}}_{\theta t} - \left(593.11 + 0.482\left(\tilde{\mathrm{Re}}_{\theta t} - 1870\right)\right), & 1870 < \tilde{\mathrm{Re}}_{\theta t}, \end{cases} \tag{41}$$

The constants used in the present model are shown in table 3.

Table 3: Langtry-Menter model constants

c_{a1}	c_{e1}	$c_{\theta t}$	σ_f
2	1	0.03	1
c_{a2}	c_{e2}	s_1	$\sigma_{\theta t}$
0.06	50	2	2

2.3.1. Notes on the Langtry-Menter model equations

From equations 36, 37, and 38 it is not possible to obtain $\mathrm{Re}_{\theta t}^{eq}$ explicitly, which is needed in the transport equation of $\tilde{\mathrm{Re}}_{\theta t}$, given in equation 27. In order to obtain $\mathrm{Re}_{\theta t}^{eq}$, the Newton-Raphson method is used by iterating over θ_t. The equation being solved iteratively is written as follows:

$$0 = \mathrm{Re}_{\theta t}^{eq}\left(Tu, F(\lambda_\theta(\theta_t))\right) - \frac{\rho U \theta_t}{\mu}. \tag{46}$$

Convergence of the Newton-Raphson method is said to be reached when either 10 iterations are performed, or when:

$$|\theta_n - \theta_{n-1}| < 10^{-6}\theta_{n-1}. \tag{47}$$

The initial value of θ_t is the following:

$$\theta_0 = \frac{\mu}{\rho U}\mathrm{Re}_{\theta t}^{eq}(Tu, F(\lambda_\theta) = 1). \tag{48}$$

Furthermore, to ensure numerical stability, the following limit is imposed to λ_θ at all times, as proposed in [5]:

$$-0.1 \leq \lambda_\theta \leq 0.1. \tag{49}$$

This translates to the following limited value of θ_t:

$$\bar{\theta}_t = \min\left(\max(\theta_t, 0), \sqrt{\frac{0.1}{|\lambda_\theta(\theta_t = 1)|}}\right). \tag{50}$$

Furthermore, to ensure stability, as well as positivity, the following variables are replaced by limited variables in the equations above, as proposed in [5]:

$$\bar{\gamma} = \min(\max(\gamma, 0), 1), \tag{51}$$

$$\bar{\mathrm{Re}}_{\theta t} = \max(\tilde{\mathrm{Re}}_{\theta t}, 20), \tag{52}$$

$$\bar{Tu} = \max(Tu, 0.027). \tag{53}$$

3. Flux Reconstruction Method

The present work uses the high-order FE-type method called Flux Reconstruction (FR). FR was originally developed by Huynh in 2007 [16]. This approach provides a unifying framework for several existing high-order schemes, such as Spectral Difference (SD) [17] and Discontinuous Galerkin (DG) [18]. Only limited results exist in the literature of the application of the FR method to the RANS equations. These are limited to the Spalart-Allmaras model and the Wilcox $k-\omega$ model [19; 20; 21]. This section presents an overview of the FR method for tensor elements, equivalent to the method found in [22].

Consider solving a system of N_{eq} advection-diffusion conservation equations:

$$\frac{\partial u_i(\mathbf{x}, t)}{\partial t} = -\nabla \cdot \mathbf{F}_i\left(\mathbf{u}, \nabla\mathbf{u}\right) \text{ for } i = \{1, \ldots, N_{eq}\}. \tag{54}$$

In this equation, u_i is the i-th conservative variable for which the system is solved, and $\mathbf{F}_i$ is the flux vector related to the i-th conservative variable. The exact solution vector $\mathbf{u}$ of the conservation law in 54 is approximated by a polynomial of degree P $\mathbf{u}_n^\delta$ within each element Ω_n. Each element Ω_n together with the approximate solution $\mathbf{u}_n^\delta$ and flux $\mathbf{F}_n^\delta$ inside it, is transformed to a standard reference element Ω_S, which in 3D is given by: $\Omega_S = \{\boldsymbol{\xi} = (\xi, \eta, \zeta) \mid -1 \leq \xi, \eta, \zeta \leq 1\}$. The transformation between Ω_n and Ω_S is carried out by means of a mapping function $\Theta_n(\boldsymbol{\xi})$.

The solution $\mathbf{u}_n^\delta$ within each sub-domain Ω_n can be obtained by solving the transformed conservation equation within the reference element Ω_S:

$$\frac{\partial \hat{u}_i^\delta}{\partial t} = -\nabla_{\boldsymbol{\xi}} \cdot \hat{\mathbf{F}}_i^\delta \quad \text{with} \quad \boldsymbol{\xi} \in \Omega_S, \tag{55}$$

with the transformed physical quantities given by:

$$\hat{u}_i^\delta = J_n u_i^\delta(\Theta_n(\boldsymbol{\xi}), t) \quad \text{and} \quad \hat{\mathbf{F}}_i^\delta = \mathbf{F}_i^\delta(\Theta_n(\boldsymbol{\xi}), t). \tag{56}$$

In equation 56, J_n represents the Jacobian of the mapping $\Theta_n(\boldsymbol{\xi})$. Hats on $\mathbf{u}$ and $\mathbf{F}$ and the superscript δ will

be omitted in the rest of the present paper to benefit readability.

The FR method for solving equation 55 consists of seven subsequent steps. In the first step, a specific form for the approximate solution u_i is defined. To this end, a set of $N_s = (P+1)^{N_{dim}}$ distinct solution points are chosen where N_{dim} is the spatial dimensionality of the problem to be solved. Consequently, the approximate solution u_i is defined as a degree P polynomial of the following form:

$$u_i = \sum_{k=1}^{N_s} {}_k u_i \; l_k(\boldsymbol{\xi}) = \sum_{k=1}^{N_s} {}_k u_i \; l_k^{\xi}(\xi) l_k^{\eta}(\eta) l_k^{\zeta}(\zeta), \tag{57}$$

where ${}_k u_i$ is the value of u_i at the k-th solution point and $l_k^{\xi}(\xi)$ is a Lagrange polynomial in the ξ-direction related to the k-th solution point.

The second step consists of determining a common interface solution u_i^I at the boundaries of the standard element Ω_S. On each face of the element, $(P+1)^{N_{dim}-1}$ flux points are defined. In order to compute the interface value at the f-th flux point ${}_f u_i^I$, equation 57 is evaluated in the f-th solution point. The approximate solution of the current element in f is denoted by ${}_f u_i^c$ and the solution of the neighboring element in f by ${}_f u_i^n$. ${}_f u_i^I$ is then computed as the average of the two solutions in a flux point.

The third step of the FR method consists of calculating a corrected solution gradient ${}_k \mathbf{q}_i$ in each solution point k for each variable i. The previously defined interface solution values are used to obtain a continuous solution polynomial. To this end, correction functions h_f for each flux point f are defined which have the following property for all flux points f and their opposite flux point g:

$$h_f(\boldsymbol{\xi}_f) = 1 \text{ and } h_f(\boldsymbol{\xi}_g) = 0. \tag{58}$$

Due to the tensor basis previously used for the solution points, these correction functions are one-dimensional and are only defined in the direction related to flux point f. Flux point g is on the same spatial direction as f but on the opposite side of the element as shown in figure 1. Furthermore, it can be seen that to each solution point k there will be N_{dim} 1D Lagrange polynomials associated, each defined on a different spatial direction, shown by two dashed lines. The form of the correction polynomials is defined by the VCJH scheme, which can be found in [23].

The corrected solution gradient ${}_k \mathbf{q}_i$ is then computed via the following expression:

$${}_k q_i^d = \sum_{s=1}^{N_s} {}_s u_i \frac{dl_s^d}{d\xi}(\xi_k) + \sum_{f=1}^{N_f} \frac{dh_f}{d\xi^f}(\boldsymbol{\xi}_k) \left({}_f u_i^I - {}_f u_i^c \right) n_f^d, \tag{59}$$

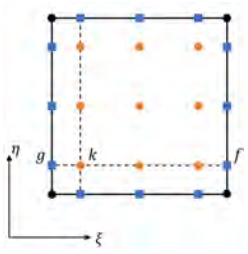

Figure 1: Tensor basis in 2D tensor element

where ${}_k q_i^d$ is the i-variable gradient in solution point k in the d-direction, where d is either ξ, η or ζ, N_f is the total number of flux points in an element, ξ^f the direction related to flux point f and n_f^d the d-component of the normal in flux point f.

The fourth step consists of calculating the approximate discontinuous flux polynomial $\mathbf{F}_i^D(\boldsymbol{\xi})$. To this end, the flux is computed at each solution point $\boldsymbol{\xi}_k$, denoted by ${}_k \mathbf{F}_i$. The approximate discontinuous flux $\mathbf{F}_i^D(\boldsymbol{\xi})$ is constructed as a polynomial of degree P in the same manner as u_i in equation 57:

$$\mathbf{F}_i^D(\boldsymbol{\xi}) = \sum_{k=1}^{N_s} {}_k \mathbf{F}_i({}_k u_i, {}_k \mathbf{q}_i) \; l_k^{\xi}(\xi) l_k^{\eta}(\eta) l_k^{\zeta}(\zeta). \tag{60}$$

The fifth step of the FR framework involves computing the common interface fluxes $\mathbf{F}_i^I$ at the flux points. In order to compute these interface fluxes, it is necessary to first obtain in each flux point f the values of ${}_f u_i$ and ${}_f \mathbf{q}_i$ using equations 57 and 59. For the convective interface flux, an upwind biased approximate Riemann solver is used. The diffusive interface flux is calculated following the BR2 scheme [24].

The flux must be continuous across element boundaries in order to obtain a conservative scheme. Therefore, the sixth stage of the FR framework consists of adding a correction flux function $\mathbf{F}_i^C(\boldsymbol{\xi})$ to the approximate discontinuous flux $\mathbf{F}_i^D(\boldsymbol{\xi})$ resulting in the continuous flux $\mathbf{F}_i(\boldsymbol{\xi})$. The correction flux $\mathbf{F}_i^C$ is a polynomial of degree $P+1$ defined in such a manner that the continuous flux $\mathbf{F}_i$ equals the common interface flux $\mathbf{F}_i^I$ in the flux points, while approximating the discontinuous flux $\mathbf{F}_i^D$ within the standard element. In order to satisfy the aforementioned requirements, $\mathbf{F}_i^C$ is constructed by means of the degree $P+1$ correction functions $h_f(\xi)$ that were previously used to obtain the corrected gradient ${}_k \mathbf{q}_i$.

The continuous flux $\mathbf{F}_i(\boldsymbol{\xi})$ is written as the sum of the approximated discontinuous flux and the correction flux, which takes the following form:

$$\mathbf{F}_i(\boldsymbol{\xi}) = \mathbf{F}_i^D(\boldsymbol{\xi}) + \sum_{f=1}^{N_f} h_f(\boldsymbol{\xi}) \left({}_f \mathbf{F}_i^I - {}_f \mathbf{F}_i^D \right), \tag{61}$$

where ${}_f\mathbf{F}_i^D = \mathbf{F}_i^D(\boldsymbol{\xi}_f)$.

The final step of the FR method consists of computing the divergence of the total flux $\mathbf{F}_i(\boldsymbol{\xi})$ at each solution point k. To this end the divergence of equation 61 is taken, taking into account the expression for the discontinuous flux in equation 60:

$$\nabla\cdot_k\mathbf{F}_i = \sum_{s=1}^{N_s}\sum_{d=1}^{N_{dim}} {}_sF_i^d \frac{dl_s^d}{d\xi^d}(\xi_k^d) + \sum_{f=1}^{N_f} \frac{dh_f}{d\xi^f}(\boldsymbol{\xi}_k)\left({}_f\mathbf{F}_i^I - {}_f\mathbf{F}_i^D\right)\cdot\mathbf{n}_f, \tag{62}$$

where ξ^d is the d-th spatial direction and ${}_sF_i^d$ the ξ^d-component of ${}_s\mathbf{F}_i$.

Finally, a time marching strategy such as the backward Euler method is applied to advance the approximate solution u_i in time.

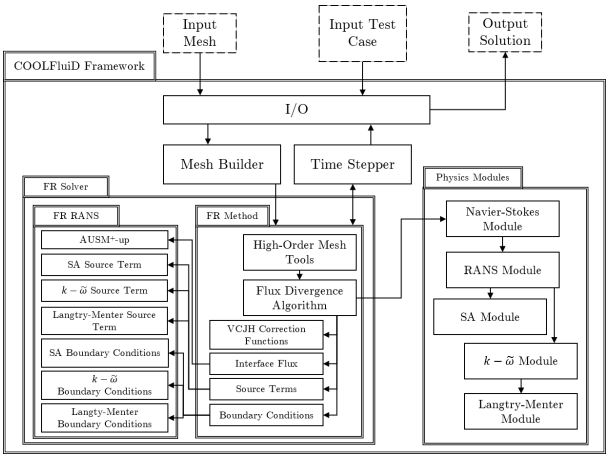

Figure 2: Overview of the major parts of the FR solver

4. Implementation

The present section presents a brief overview of the implementation of the developed FR solver. After giving an overview of the core FR solver structure, focusing on the newly developed parts for RANS cases, the boundary condition treatment for the present cases is outlined in section 4.1.

The present FR solver is implemented in the open-source COOLFluiD platform, which offers a component-based framework for complex multi-physics simulations. More information on the development of this platform can be found in [25; 26]. An in-depth presentation of the structure of the core FR solver can be found in [22].

The core FR solver has been developed to solve advection and advection-diffusion problems in general. In order to solve any specific set of equations, the core solver interacts with physics-dependent modules. On the one hand, these include the FR-independent parts, such as flux evaluation and variable transformations. On the other hand, these include the FR-dependent parts, such as the boundary condition implementations and the source term implementation. Consequently, a physics module was implemented for the RANS equations with the Spalart-Allmaras model, the $k-\tilde{\omega}$ SST model as well as the Langtry-Menter LCTM, and a numerical module was implemented extending the core FR solver to handle all physics-dependent computations, such as boundary condition evaluation and source term computation. Figure 2 presents a schematic overview of these modules and how they interact with the other parts of the COOLFluiD platform.

Reading the mesh and test case file is handled by the COOLFluiD framework. The mesh data, e.g. connectivities, nodal coordinate arrays, solution arrays, etc., is then passed on to the FR solver, where the appropriate high-order mesh data is created. Next, the FR flux divergence algorithm computes the convective and diffusive flux divergences, as well as the residual Jacobian. To this end, the flux divergence algorithm interacts with the VCJH correction functions, interface flux schemes, source term implementations, boundary condition implementations and the physics modules. For the RANS equations, the AUSM$^+$-up interface flux scheme, as found in [27], is used in the present work, but others have been implemented as well, as found in [22]. For both the source terms and boundary conditions, the FR solver interacts with their implementations in the FR RANS module. Furthermore, in order to compute fluxes and other physics-dependent variables, the solver interacts with the Spalart-Allmaras, $k-\tilde{\omega}$ and Langtry-Menter physics modules present in the RANS module.

A semi-analytical method for the flux Jacobian is used, while a fully-analytic and simplified Jacobian is used for the source term Jacobian. The derivation of the semi-analytic Jacobian for the FR method, that was carried out in a previous work, can be found in [28]. Since the source terms in the present set of RANS equations are particularly stiff, careful treatment of their Jacobian is needed in order to obtain stable simulations with favorable convergence characteristics. To this end, the approximate Jacobian approach that is equivalent to the one found in [29], is used for the source term Jacobian.

For high-order FE-type methods, the evaluation of the Jacobian is costly and largely dictates the performance of the implicit method. From an implementation perspective, a numerical approach to compute

the Jacobian is relatively straightforward: the whole FR procedure is repeated for each solution point state variable ${}_l u_j$ that influences the current residual, with a perturbed solution point variable. However, this approach is costly and does not scale well with the order of the FR method: it was shown in previous work in [28] that a (semi-)analytical approach scales much better with the order.

4.1. Boundary Condition Treatment

In the FR framework, boundary conditions are imposed by defining ghost states and gradients in the flux points on the boundary. The inner and ghost states and gradients in a flux point are then used to evaluate the interface flux scheme on the boundary.

The following turbulent values are imposed at a no-slip wall, following the approach in [5; 9; 10; 15]:

$$\tilde{\nu}_{ghost} = 0; \quad k_{ghost} = 0, \quad \tilde{\omega}_{ghost} = \ln\left(\frac{60\mu}{\rho\beta_1 d_1^2}\right); \tag{63}$$

$$\left(\frac{\partial\gamma}{\partial n}\right)_{ghost} = 0, \quad \left(\frac{\partial\tilde{\mathrm{Re}}_{\theta t}}{\partial n}\right)_{ghost} = 0, \tag{64}$$

where d_1 is the wall distance of the closest solution point to the wall in the current element and n designates the normal direction to the wall. It should be noted here that since the boundary condition in the FR method is evaluated on the wall itself, d_1 theoretically should be taken as 0, which would lead to an infinite $\tilde{\omega}_{ghost}$. In order to avoid this, the wall distance of the first DoF near the wall in the current element is taken.

The following turbulent values are imposed at the inlet, following the approach in [5; 9; 10; 15]:

$$\tilde{\nu}_{ghost} = \frac{\mu_{t,\infty}}{\rho_\infty}\frac{\chi_\infty^3 + c_{v1}^3}{\chi_\infty^3}; \quad k_{ghost} = \frac{3}{2}\left(U_\infty \frac{Tu_\infty}{100}\right)^2, \tag{65}$$

$$\tilde{\omega}_{ghost} = \ln\left(\frac{\rho_\infty k_{ghost}}{(\mu_t/\mu)_\infty \mu_\infty}\right); \quad \gamma_{ghost} = 1, \tag{66}$$

$$\tilde{\mathrm{Re}}_{\theta t,ghost} = \begin{cases} 1173.51 - 589.428Tu_\infty + \\ 0.2196Tu_\infty^{-2}, & Tu_\infty \le 1.3, \\ 331.5(Tu_\infty - 0.5658)^{-0.671}, & 1.3 < Tu_\infty, \end{cases} \tag{67}$$

where Tu_∞ is the free stream turbulence intensity in percentage and $(\mu_t/\mu)_\infty$ the ratio of turbulent and laminar viscosity in the free stream.

5. Results

In the present section, the developed FR solver is verified with various test cases for the RANS equations with the Spalart-Allmaras model, the $k-\tilde{\omega}$ SST model and the Langtry-Menter LCTM. First, the fully turbulent flow over a flat plate is presented in section 5.1. Next, a series a flat plate cases with LTT are presented in section 5.2.

In all presented cases, the implicit Newton time marching method is used. Furthermore, the Gauss-Legendre points are used for both the solution and flux points. The VCJH correction functions are used in all cases with c_{SD}.

5.1. Fully Turbulent Flow over a Flat Plate

The present section discusses the flow over a flat plate simulated with the RANS Spalart-Allmaras and $k-\tilde{\omega}$ SST model. The test case was first proposed by Wieghardt in [30; 31]. The Reynolds number based on the flat plate length L is $\mathrm{Re}_L = 1.03 \cdot 10^7$, the free stream turbulence intensity Tu_∞ is 10^{-2} and $(\mu_t/\mu)_\infty$ is 10^{-4}. In order to accelerate convergence, the free stream Mach number was increased from 0.096 to 0.2, as was done in [11; 32].

The present case was run on a mesh consisting of 784 quadrilateral elements (22 elements on the flat plate, 28 normal to the plate and 6 in the upstream direction of the leading edge). For this mesh, $y_1^+ \simeq 10$, where y_1^+ denotes y^+ based on the first element height. It should be noted that the value of y_1^+ at higher orders is significantly larger than the y^+ value based on the first DoF near the wall. As such, even if y_1^+ is much larger than 1, an adequate result of velocity profile and friction coefficient can be obtained at high orders. y^+ is computed as follows:

$$y^+ = \frac{y u_\tau \rho_w}{\mu_w}, \quad u_\tau = \sqrt{\frac{\mu_w}{\rho_w}\left.\frac{\partial u_x}{\partial y}\right|_w}, \tag{68}$$

where subscript w denotes a variable at the wall.

Figure 3 shows the velocity profile evaluated at $\mathrm{Re}_x = 1.02 \cdot 10^7$, for orders P0 to P4 for the Spalart-Allmaras model. The velocity profile consists of u^+ as a function of y^+, where $u^+ = U/u_\tau$. The figure also shows the value of y_1^+ at the slice where the velocity profile is obtained. The solution of the developed FR solver is compared with experimental data from [30; 31]. In figure 4 the P4 solution is further compared with with the Spalding law of the wall found in [33], the analytical solution for the Spalart-Allmaras model found in [14] and a solution obtained with the DG method, found in [32]. It should be noted that the reference DG result uses artificial viscosity for stabilization purposes, while this was not found to be necessary in the present solver. It is clear that at the higher orders, the FR solutions coincide with each other and correspond well with the references from the literature.

Figure 5 presents the velocity profiles for the $k-\tilde{\omega}$ SST model for orders P0 to P4. The solution of the FR solver is compared with the aforementioned experimental data and Spalding law of the wall. Additionally, it is compared with a P2 solution obtained with the DG method and the Wilcox $k-\tilde{\omega}$ model on a 8800-element mesh, found in [11]. At the higher orders, the FR solutions coincide with each other and correspond well with the references from the literature.

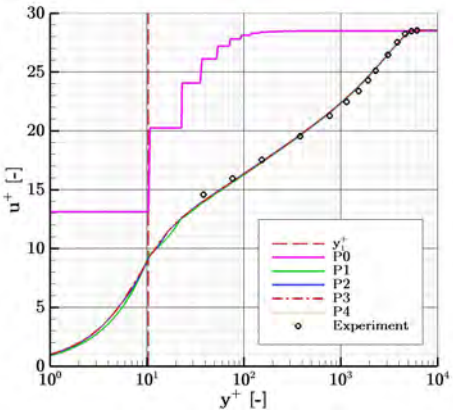

Figure 3: Spalart-Allmaras velocity profile

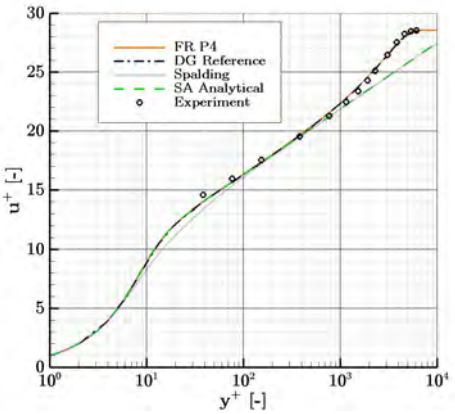

Figure 4: Spalart-Allmaras velocity profile compared to various references

Figures 6 and 7 present the friction coefficient for respectively the Spalart-Allmaras and $k-\tilde{\omega}$ SST models. The FR solutions are compared the aforementioned experimental and DG results. A good agreement is obtained again for both models. Here, the friction coefficient is the adimensionalized wall shear stress τ_w:

$$C_f = \frac{\tau_w}{\frac{1}{2}\rho U^2}. \tag{69}$$

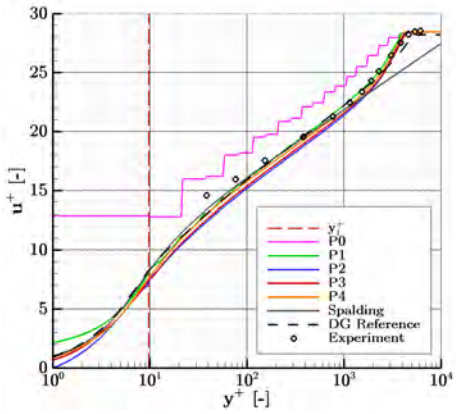

Figure 5: $k-\tilde{\omega}$ SST velocity profile

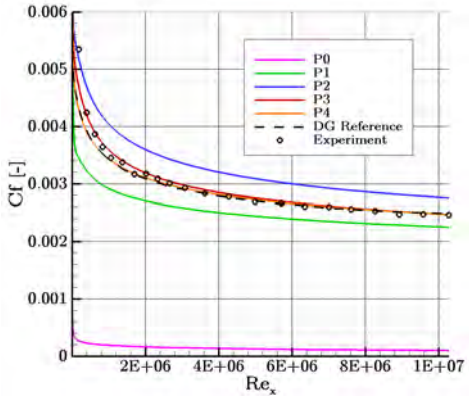

Figure 6: Spalart-Allmaras friction coefficient

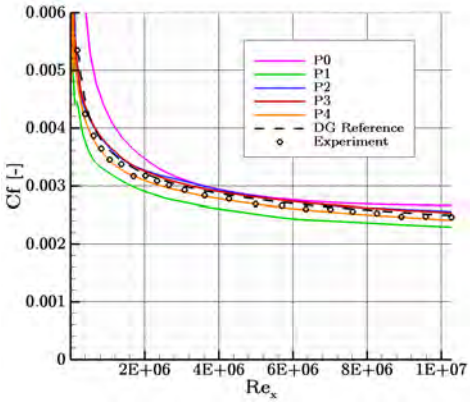

Figure 7: $k-\tilde{\omega}$ SST friction coefficient

5.2. ERCOFTAC Flat Plate Cases

In order to verify the Langtry-Menter model, the ERCOFTAC T3 series of flat plate cases, as found in [34; 35; 36], was considered. These cases are characterized by the by-pass transition regime and have different levels of free stream turbulence intensity. Table 4 presents the free stream conditions.

The present cases are run on a coarse mesh with 143 quadrilateral elements (10 elements on the flat plate,

Table 4: T3 series free stream conditions

Case	U_∞ $[\frac{m}{s}]$	Tu_∞ [%]	$\left(\frac{\mu_t}{\mu}\right)_\infty$ [−]	ρ_∞ $\left[\frac{kg}{m^3}\right]$	μ_∞ $\left[\frac{kg}{ms}\right]$
T3A	5.4	3.5	13.3	1.2	$1.8{\cdot}10^{-5}$
T3B	9.4	6.5	100.0	1.2	$1.8{\cdot}10^{-5}$
T3A-	19.8	0.874	8.72	1.2	$1.8{\cdot}10^{-5}$

11 elements normal to the plate and 3 elements in the upstream direction in front of the leading edge). For the present mesh $y_1^+ \simeq 3$ for the T3A case, $y_1^+ \simeq 7$ for the T3B case and $y_1^+ \simeq 10$ for the T3A- case. The friction coefficient for the T3A case for P0 to P6 is shown in figure 8. Figures 9 and 10 show the friction coefficient for P0 to P5 for the T3B and T3A- cases. A good agreement is found between the P5 solutions and both the reference solutions, obtained with the FV method in [2], and the experimental results from [34; 35; 36]. It can also be noted that on the present very coarse mesh, the low orders do not provide an adequate solution, where in the P0 case no transition is even present, while the higher orders get progressively closer to the experimental results. In the T3A and T3A- case, the FR solution is very close to the reference FV solution, which was obtained with a much finer mesh of around 39,000 elements and a small rounding of the plate leading edge. Furthermore, for all cases the two highest order solutions coincide with each other.

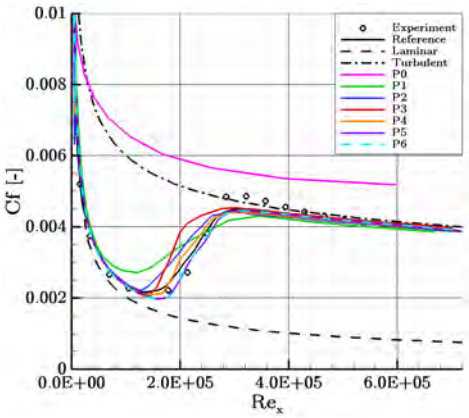

Figure 8: Friction coefficient for the T3A case

6. Conclusion

A novel high-order FR solver was developed for flows governed by the RANS equations with the Spalart-Allmaras, $k-\tilde{\omega}$ SST and Langtry-Menter models. Some modifications were made to the original $k-\omega$ SST model in order to increase robustness.

The present solver was verified with several test cases. The fully turbulent flow over a flat plate was

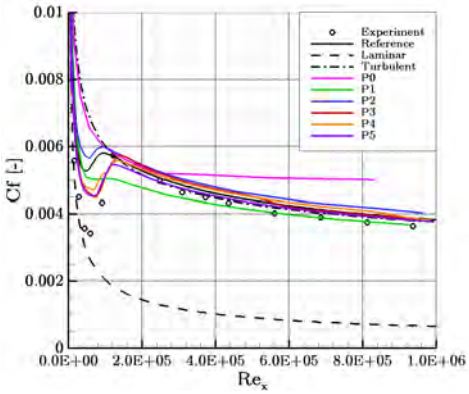

Figure 9: Friction coefficient for the T3B case

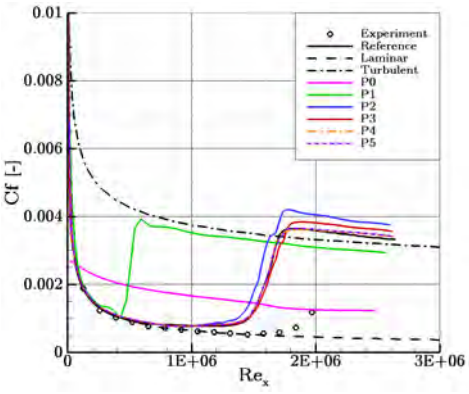

Figure 10: Friction coefficient for the T3A- case

simulated. The solver solution agrees well with results found in the literature and it was shown that for increasing orders, the present solver converges to the same solution. This was shown both for the velocity profile and the friction coefficient.

Furthermore, the T3 series of transitional flows was investigated. At high orders a good agreement with references from the literature was found. It was shown for all developed RANS models that high-order FR obtains good results even with very coarse meshes that have a large y_1^+.

As future work, the solver will be applied to more complex 3D transitional cases. Furthermore, the solver will also be fully ported to Graphical Processing Units (GPUs) in order to further speed up computations. Finally, the $\gamma-\alpha$ LCTM [37] will be investigated, which exhibits more accurate results for high-speed flows. This method will be used together with a robust shock capturing scheme.

Acknowledgments

The research of Ray Vandenhoeck is supported by SB PhD fellowship 1S19918N of the FWO.

References

[1] A. M. O. Smith, Transition, pressure gradient and stability theory, Douglas Aircraft Co., Report ES 26388.

[2] F. Menter, R. Langtry, S. Likki, Y. Suzen, P. Huang, S. Völker, A correlation-based transition model using local variables: Part Imodel formulation, in: Turbo Expo: Power for Land, Sea, and Air, Vol. 41693, 2004, pp. 57–67.

[3] R. Langtry, F. Menter, S. Likki, Y. Suzen, P. Huang, S. Völker, A correlation-based transition model using local variables: Part IItest cases and industrial applications, in: Turbo Expo: Power for Land, Sea, and Air, Vol. 41693, 2004, pp. 69–79.

[4] F. Menter, R. Langtry, S. Völker, Transition modelling for general purpose CFD codes, Flow, turbulence and combustion 77 (1-4) (2006) 277–303.

[5] R. B. Langtry, F. R. Menter, Correlation-based transition modeling for unstructured parallelized computational fluid dynamics codes, AIAA journal 47 (12) (2009) 2894–2906.

[6] A. Lani, N. Villedie, K. Bensassi, L. Koloszar, M. Vymazal, S. M. Yalim, M. Panesi, COOLFluiD: an open computational platform for multi-physics simulation and research, in: 21st AIAA Computational Fluid Dynamics Conference, 2013, p. 2589.

[7] A. Lani, T. Quintino, D. Kimpe, H. Deconinck, S. Vandewalle, S. Poedts, Reusable object-oriented solutions for numerical simulation of PDEs in a high performance environment, Scientific Programming 14 (2) (2006) 111–139.

[8] A. Lani, T. Quintino, D. Kimpe, H. Deconinck, S. Vandewalle, S. Poedts, The COOLFluiD framework: Design solutions for high-performance object oriented scientific computing software, in: V. S. Sunderan, G. D. van Albada, P. M. A. Sloot, J. J. Dongarra (Eds.), Computational Science ICCS 2005, Vol. 1 of LNCS 3514, Emory University, Springer, Atlanta, GA, USA, 2005, pp. 281–286.

[9] F. R. Menter, M. Kuntz, R. Langtry, Ten years of industrial experience with the SST turbulence model, Turbulence, heat and mass transfer 4 (1) (2003) 625–632.

[10] NASA Langley Research Center, turbulence modeling resource, the Menter shear stress transport turbulence model, `turbmodels.larc.nasa.gov/sst.html`, accessed: 19-12-2020.

[11] F. Bassi, A. Crivellini, S. Rebay, M. Savini, Discontinuous Galerkin solution of the Reynolds-averaged Navier–Stokes and k–ω turbulence model equations, Computers & Fluids 34 (4-5) (2005) 507–540.

[12] D. C. Wilcox, et al., Turbulence modeling for CFD, Vol. 2, DCW industries La Canada, CA, 1998.

[13] P. Spalart, S. Allmaras, A one-equation turbulence model for aerodynamic flows, in: 30th aerospace sciences meeting and exhibit, 1992, p. 439.

[14] S. R. Allmaras, F. T. Johnson, Modifications and clarifications for the implementation of the Spalart-Allmaras turbulence model, in: Seventh international conference on computational fluid dynamics (ICCFD7), Big Island, HI, 2012, pp. 1–11.

[15] NASA Langley Research Center, turbulence modeling resource, the Langtry-Menter 4-equation transitional SST model, `turbmodels.larc.nasa.gov/langtrymenter_4eqn.html`, accessed: 19-12-2020.

[16] H. T. Huynh, A flux reconstruction approach to high-order schemes including discontinuous Galerkin methods, AIAA paper 4079 (2007) 2007.

[17] D. A. Kopriva, J. H. Kolias, A conservative staggered-grid Chebyshev multidomain method for compressible flows, Journal of computational physics 125 (1) (1996) 244–261.

[18] W. H. Reed, T. Hill, Triangular mesh methods for the neutron transport equation, Los Alamos Report LA-UR-73-479.

[19] L. Shi, C. Zhou, Z. J. Wang, Adaptive RANS solution with the high-order correction procedure via reconstruction method, in: 54th AIAA Aerospace Sciences Meeting, 2016, p. 1826.

[20] K. Miyaji, R. Nagasawa, Extension of the flux reconstruction method to high-reynolds number RANS simulations around high-lift devices, TRANSACTIONS OF THE JAPAN SOCIETY FOR AERONAUTICAL AND SPACE SCIENCES 60 (1) (2017) 18–26.

[21] H. Zhu, S. Fu, L. Shi, Z. J. Wang, A hybrid RANS-implicit LES approach for the high-order FR/CPR method, in: 54th AIAA Aerospace Sciences Meeting, 2016, p. 1599.

[22] R. Vandenhoeck, A. Lani, Implicit high-order flux reconstruction solver for high-speed compressible flows, Computer Physics Communications 242 (2019) 1–24.

[23] P. E. Vincent, P. Castonguay, A. Jameson, A new class of high-order energy stable flux reconstruction schemes, Journal of Scientific Computing 47 (1) (2011) 50–72.

[24] F. Bassi, S. Rebay, A high-order accurate discontinuous finite element method for the numerical solution of the compressible Navier-Stokes equations, Journal of computational physics 131 (2) (1997) 267–279.

[25] A. Lani, An object oriented and high performance platform for aerothermodynamics simulation, Ph.D. thesis, Université Libre de Bruxelles (2008).

[26] T. Quintino, A component environment for high-performance scientific computing: design and implementation, Ph.D. thesis, Ph. D. Thesis, KU Leuven, von Karman Institute for Fluid Dynamics, Leuven (2008).

[27] M. S. Liou, A sequel to AUSM, part II: AUSM$^+$-up for all speeds, Journal of Computational Physics 214 (2006) 137–170.

[28] R. Vandenhoeck, A. Lani, J. Steelant, Massively parallel and robust high-order methods for transitionalhypersonic flow modelling on unstructured grids, in: 11th Symposium of VKI PhD Research 2020, St.-Genesius-Rode, Belgium, 2020.

[29] B. Merci, J. Steelant, J. Vierendeels, K. Riemslagh, E. Dick, Computational treatment of source terms in two-equation turbulence models, AIAA journal 38 (11) (2000) 2085–2093.

[30] K. Wieghardt, W. Tillmann, On the turbulent friction layer for rising pressure.

[31] S. J. Kline, D. E. Coles, E. Hirst, Computation of Turbulent Boundary Layers–1968 AFOSR-IFP-Stanford Conference: Proceedings, Vol. 1, Thermosciences Division, Stanford University, 1969.

[32] N. Nguyen, P.-O. Persson, J. Peraire, Rans solutions using high order discontinuous galerkin methods, in: 45th AIAA Aerospace Sciences Meeting and Exhibit, 2007, p. 914.

[33] F. White, Viscous fluid flow 2nd edition McGraw-Hill, New York.

[34] J. Coupland, ERCOFTAC special interest group on laminar to turbulent transition and retransition: T3A and T3B test cases, A309514.

[35] A. Savill, Some recent progress in the turbulence modelling of by-pass transition, Near-wall turbulent flows (1993) 829–848.

[36] A. Savill, One-point closures applied to transition, in: Turbulence and transition modelling, Springer, 1996, pp. 233–268.

[37] J. Van den Eynde, J. Steelant, Two-equation transition model based on intermittency and empirical correlations, Proceedings of HiSST.

Simulations of supersonic mixing of alternative fuels for air breathing engines based on data mining techniques

Ali Can Ispir

Aeronautics and Aerospace Department, von Karman Institute for Fluid Dynamics, Belgium, mymail@vki.ac.be

Bayindir H. Saracoglu and Thierry Magin

Research Manager, Turbomachinery and Propulsion Department, von Karman Institute for Fluid Dynamics, Belgium, bayindir.saracoglu@vki.ac.be

Professor, Aeronautics and Aerospace Department, von Karman Institute for Fluid Dynamics, Belgium, magin@vki.ac.be

Axel Coussement

Professor, Aero-Thermo-Mechanics Department, Universit libre de Bruxelles (ULB), axcousse@ulb.ac.be

Abstract

Dual mode ramjet engine is commonly preferred in the design of combined cycle air-breathing propulsion systems of hypersonic aircraft concepts. It basically offers two distinct operation mode which are ramjet (subsonic combustion) and scramjet (supersonic combustion). The mode can be switched depending on the flight regime. The engine is generally comprised of four main parts; inlet, isolator, combustor and nozzle. Even though it does seem as structurally simple, the flow physics is quite complex along the engine duct. One should pay attention in modeling of the physical phenomenon that happen in the duct in order to determine the engine performance and make sure that engine can fulfill the flight trajectory requirements. One of the most significant challenge in its design is to model fuel air mixing process taking place under supersonic flow regime. This phenomenon plays an important role on combustion efficiency and pollutant emission of the engine. In the current dual mode ramjet engine concept of interest, the fuel is injected along the struts into the air stream and self-ignition is expected when the mixture reaches flammability point. There are several parameters highly affecting this process such as fuel struts location, strut geometry, fuel and air stream flow properties. Performing CFD simulations is a remarkable candidate to see the importance of these effects on the mixing process. Nevertheless, running CFD simulations for various scenarios including aforementioned effects means infinite number of simulations and prohibitively expensive computational costs. Therefore, machine learning and data mining techniques are proposed in this doctorate work to be coupled with a number of numerical simulations. They are utilized for making the prediction of the points which are not explored throughout the numeric studies. Thereby, the parameters affecting mixing process will be examined by avoiding high computational price.

Keywords: high speed propulsion, hypersonic aircraft, 1D thermodynamic simulations, supersonic flow, data mining

1. Introduction

The dual mode ramjet (DMR) engine can be considered as one of the most promising air-breathing propulsion system for hypersonic air transportation in the near future. It is a viable solution in terms of that not only there is no need for an on-board oxidizer storage but also it can be operated in both supersonic and hypersonic flight speeds. These characteristics enable the air vehicle to fly in a long flight range with various cruise speed [1]. Basically, in the operation of DMR engine, the air flow is taken into the duct by a supersonic intake, compressed when it passes through the oblique shock waves generated along the intake ramps and isolator. Then, the fuel is injected into

air stream in combustor section. When the mixture reaches flammability point, combustion takes place and exhaust gases are expanded along the diverged nozzle [2]. Even though it has aforementioned advantages and simpler geometry rather than other types of aero-engine, the flow physics along the DMR engine duct is quite complex and one of most significant issues of the engine design is to model fuel - air mixing process [3]. This phenomenon plays an important role not only on non-premixed combustion efficiency but also, overall performance of the engine such as thrust and total pressure loss along the duct [4]. As considering the very short residence time of air stream and difficulties in the penetration of two different streams due to high momentum values, researchers have been attracted to develop several injection strategies in order to have efficient mixing [5]. Among these methods, one technique used commonly in scramjet engine concept is to generate a penetration zone between fuel and air flows along a confined two jet mixing. The fuel flow is injected into the air stream in parallel direction from struts that located at the center of the combustor. Many parameters associated with geometrical properties of the fuel struts and injectors can effect mixing and combustion efficiencies significantly. Sujith et al. performed experimental and numerical studies to investigate the effect of trailing ramp angle on supersonic mixing efficiency with various angles and two configurations [6]. In their findings, the highest total pressure loss was seen in the sample which had best mixing performance. It was noted that vorticity generated by the struts improved the mixing nevertheless caused a remarkable loss in the total pressure. Manna et al. investigated different fuel injection strut arrangements with various combustor inlet flow conditions in order to see their effects on combustion efficiency, thrust, heat release and total pressure loss [7]. The authors concluded that incurred drag losses due to fuel injectors played more significant role on engine performance such as thrust rather than the efficiencies. Choubey and Pandey run CFD simulations on DLR scramjet concept for examining the effect of two strut configuration with different angle of attack values of the fuel injectors on performance parameters [8]. They found that multi strut configurations had a positive impact on performance parameters while the maximum combustion efficiency and smallest ignition time were provided when injector angle of attack was set as zero. The flight conditions have an important effect on the engine performance as well as the strut geometries and configurations. Reddy and Venkatasubbaiah performed numerical studies on the same case with Choubey and Randey, and found also that multi strut injector arrangement provides better performance than single strut [9]. They also conducted their works for different flight conditions and noted that increasing of total pressure and temperature with the flight speed led the combustion efficiency to rise. Huang and Yan investigated ram - scram transition mechanism in a strut-based dual-mode scramjet combustor by performing numerical simulations at cruise speeds of Mach 4, 5, 6 and 7 [10]. They showed that inlet boundary conditions higher freestream Mach number is beneficial for the fuel - air mixing process. However, they also noted that the mixing efficiency did not vary after the freestream Mach number reaches high enough values.

The numerical investigation of supersonic flow field in both reactive and non-reactive cases require high numerical resolution i.e high computational costs. Recently, surrogate assisted evolutionary algorithms and reduced order models have been widely used in reactive flow applications, they are seen as attractive options to explore supersonic flow field by avoiding expensive computational prices without sacrificing accuracy [11; 12; 13].

Even though scramjet based hypersonic engine concept has attracted the researchers and scientist to solve supersonic combustion phenomenon, there are no so many attemps for scramjets having multi-strut injection systems. In the present work, STRATOFLY MR3 that is European hypersonic civil transportation concept was selected for examining the supersonic mixing and combustion phenomena in DMR engine. The aircraft is planned to carry 300 passengers with a gross take-off weight of 400 tons and fly at stratospheric altitudes with the design cruise speed of Mach 8 [14]. The two-dimensional supersonic flow field of DMR combustor was investigated numerically in order to see effects of the strut wedge angle and the fuel struts location on the performance parameters such as total pressure loss, combustion and mixing efficiencies. Kriging surrogate model and principal component analysis (PCA) were used and make numerical prediction of the points which are not explored in the CFD simulations in order to comprehend aforementioned parameters effects better.

2. Physical Model

The propulsion plant of the aircraft under investigation is inherited from LAPCAT II - MR2.4 vehicle [15] and one of the main elements, DMR engine depicted in Fig. 1 enables the aircraft to fly at strato-

spheric conditions with hypersonic cruise speeds. It kicks in after the aircraft reaches low supersonic conditions which is Mach 1.5 in order to contribute thrust level by operating ramjet mode [16]. The engine has dorsal orientation on the aircraft and the combustor lies down between supersonic intake and diverged nozzle sections. The number of 23 fuel struts are located in the shape like "V" at the entrance of combustor. There are totally 1248 injectors on the struts. The diamond shape strut are used and their angle was oriented depending on which side of the middle axis they are located [15].

3. Numerical methodology

In present study, the two-dimensional Reynolds averaged Navier-Stokes (RANS) equations and k - ω SST turbulence model have been coupled to perform numerical studies for multi-strut injection DMR engine combustor. k - ω turbulence model was noted as a very effective predictor to resolve the interaction between shock - expansion waves and mixing layer [11]. Compressible real gas Navier-Stokes/Euler equation set which is recommended for variable density, multi-species flows and flows in which the global Mach number is generally higher than about 0.2 [17]. The multiple species compressible governing equations can be expressed as given in equation 1.

Q is defined as the dependent variable vector; F_n and G_n are given as inviscid and viscous flux vectors, respectively; and S represents the source term vector [18]. The equations are solved by a density based solver with double precision in commercial computational fluid dynamics code Ansys Fluent [19; 20].

Non-premixed combustion of air-hydrogen in supersonic flow regimes is modeled with mixture fraction-β pdf framework. A strained flamelet model is recommended by previous researchers and used in the present work to handle turbulence - chemistry interactions [21; 22]. The flamelet library is generated by using modified Jachimowski detail chemistry mechanism including 19-step and 9 species [23], the Nitrogen reactions were not considered at the moment for the simplicity.

4. Computational modeling

The computational domain seen in Fig. 2 is represented by the top view of the STRATOFLY MR3 vehicle DMR combustor and the investigation is done by dividing it by two and defining the bottom boundary(3) as symmetric for the simplicity. The boundary type and flow conditions are given in Table 1. The computational domain was meshed with structured quadrilateral grid type. First of all, the mesh dependency analysis was done by using a domain including only one strut to find an optimal mesh configuration. The three different grid numbers were determined as 362, 580 and 746 thousands and named as coarse, medium and fine, respectively. The simulations were done for non-reactive case and medium mesh type was found as optimum.

5. Data mining techniques

5.1. Principal component analysis (PCA):

A number of high-fidelity simulations i.e Full Order Model (FOM) that is $y(x) = F(x) \in \Re^N$ have been done throughout CFD simulations. The CFD solver provides physical information in the function of y(j) for one value of input parameter(s) x at every grid point (Eq. 2). Where L is the total number of grid points, r_1 and x_j represent i^{th} spatial location and j_{th} point in the input parameter space, respectively. As stated before, this input space involves the varying strut location and flight conditions. The main purpose of the PCA method is to reduce a large number of interdependent variables in y(j) functions by defining them as smaller number of uncorrelated variables without sacrificing accuracy of original data as much as possible [24; 25]. The reactive supersonic flow field can be represented by the following variables [Y_1, ... ,$Y_{N_{sp}}$, T, p], where Y_i is the mass fraction of ith species, N_{sp} is the number of species, T and p represent temperature and pressure, respectively. In order to represent data-set Y(NxM) mentioned above, including M observations of N original variables, PCA enables to establish linear correlations between the N variables. These linear correlations are comprised of a set of basis functions $\phi = \phi_1, \phi_1, ..., \phi_q$, where q is called as approximation order and a set of coefficients $a(x) = a_1(x), a_2(x), ..., a_q(x)$ called as PCA scores [24].

5.2. Kriging:

Kriging is used to interpolate response function by fitting a regression model created by PCA. The predicted response is modeled with a random function F and objective function response z at each evaluated point [26] (Eq. 3 and 4).

6. Objective functions and performance parameters:

The supersonic fuel-air mixing phenomenon can be comprehended by examining several parameters such as combustion & mixing efficiency and total pressure recovery [11; 19].

1. Combustion efficiency: It is given in eq. 5.
2. Mixing efficiency:
   It is given in eq. 6 and reactive molar concentration of oxygen is given with eq. 7.
3. Total pressure recovery efficiency:
   It is given in eq. 8. p_{t1} and p_{t0} are defined as the mass-averaged total pressure at the exit and the entrance of the combustor, respectively.

7. Results

The numeric simulations were done to create a data-set with varying fuel strut locations and strut wedge angle. 21 cases were firstly created by moving the struts in 290mm interval on the streamwise direction. The default wedge angle of the fuel strut is 160°. 11 cases were secondly determined by increasing and decreasing the wedge angle as 5°.

As it can be seen in Figs. 3 and 4, the cold flow analysis was firstly done to see the solver performance for modeling diffusion and capturing shock-expansion waves along the domain.

8. Figures

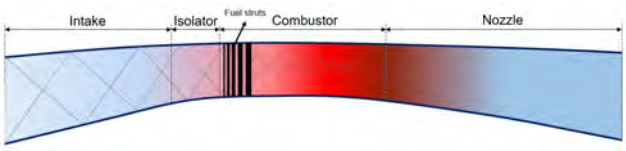

(a) DMR scheme of the STRATOFLY MR3 Aircraft

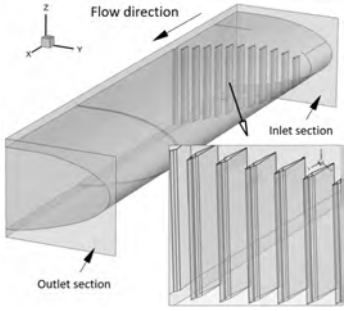

(b) Detailed figure of DMR combustor and settlement of fuel struts

Figure 1: Physical model of the present work



Figure 2: Fined mesh used around the fuel struts

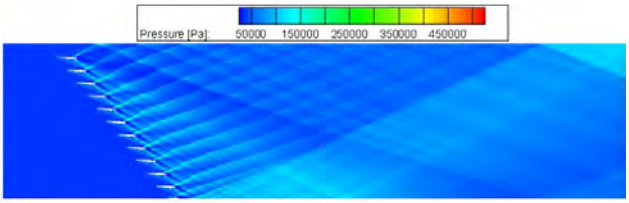

Figure 3: Fined mesh used around the fuel struts

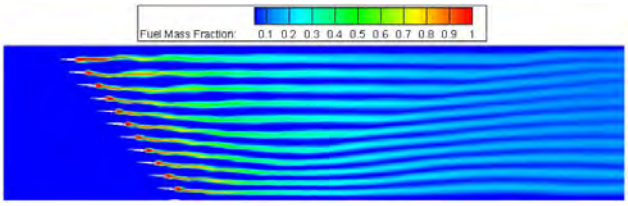

Figure 4: Fined mesh used around the fuel struts

9. Tables

Table 1: Boundary type and flow conditions in CFD studies

Number	Boundary type	Flow conditions
1	Air velocity inlet	0.28bar, 790K, Mach 4
2	Adiabatic wall	-
3	Symmetrical	-
4	Pressure outlet	-
5	Fuel velocity inlet	2.02bar, 282K, Mach 2.35

10. Equations

$$\frac{\partial Q}{\partial t} + \frac{\partial}{\partial x}(F_1 + G_1) + \frac{\partial}{\partial y}(F_2 + G_2) = S \tag{1}$$

$$y(j) = [T(r_1, x_j), ..., T(r_L, x_j), p(r_1, x_j), ..., p(r_L, x_j), Y_{H_2}(r_1, x_j), ..., Y_{H_2}(r_L, x_j), ...]^T \tag{2}$$

$$y = F(\beta, x) + z(x) \tag{3}$$

$$F = \beta_1 a_1(x) + ... + \beta_q a_q(x) \tag{4}$$

$$\eta_{comb}(x) = 1 - \frac{\int_A C_{H_2} d\dot{m}|_x}{\dot{m}_{H_2,injected}} \tag{5}$$

$$\eta_{mix}(x) = 1 - \frac{\int_A C_{O_2,reactive} d\dot{m}|_x}{\dot{m}_{O_2,injected}} \tag{6}$$

$$C_{O_2,reactive} = min(C_{O_2}, \frac{C_{O_2,in} - (C_{O_2,in} - C_{O_2,stoich}).\phi}{C_{H_2,stoich}.\phi}.C_{H_2}) \tag{7}$$

$$\zeta = \frac{p_{t1}}{p_{t0}} \tag{8}$$

11. Conclusion

The present doctorate work carries out the numerical investigation of supersonic fuel - air mixing phenomena for the DMR engine combustor of STRATOFLY MR3 vehicle. In order to understand the effect of fuel strut geometry and multiple strut settlement in the engine duct on the mixing process, numerical simulations were performed in the commercial Ansys Fluent code. A database comprised of full order models have been created by various fuel struts location and strut wedge angle. The objective functions were determined as combustion & mixing efficiency and total pressure recovery factor. PCA which is data compression method was used to create linear correlations between the interdependent variants in this data-set. Kriging surrogate mode was also utilized to make a prediction of the points which were unexplored in the CFD simulations. More results of CFD simulations and data mining study will be added in the final version of the article.

Acknowledgments

This project has received funding from the European Union's Horizon 2020 research and innovation program under grant agreement No 769246.

References

[1] A. Vincent-Randonnier, Y. Moule, M. Ferrier, Combustion of hydrogen in hot air flows within lapcat-ii dual mode ramjet combustor at onera-laerte facility-experimental and numerical investigation, in: 19th AIAA International Space Planes and Hypersonic Systems and Technologies Conference, 2014, p. 2932.

[2] A. C. Ispir, B. H. Saracoglu, Development of a 1d dual mode scramjet model for a hypersonic civil aircraft, in: AIAA Propulsion and Energy 2019 Forum, 2019, p. 3842.

[3] H. Ogawa, Mixing characteristics of inclined fuel injection via various geometries for upstream-fuel-injected scramjets, Journal of Propulsion and Power 31 (6) (2015) 1551–1566.

[4] J.-H. Kim, Y. Yoon, I.-S. Jeung, H. Huh, J.-Y. Choi, Numerical study of mixing enhancement by shock waves in model scramjet engine, AIAA journal 41 (6) (2003) 1074–1080.

[5] Z. Gao, C. Lee, Numerical research on mixing characteristics of different injection schemes for supersonic transverse jet, Science China Technological Sciences 54 (4) (2011) 883–893.

[6] S. Sujith, T. Muruganandam, J. Kurian, Effect of trailing ramp angles in strut-based injection in supersonic flow, Journal of Propulsion and Power 29 (1) (2013) 66–78.

[7] P. Manna, R. Behera, D. Chakraborty, Liquid-fueled strut-based scramjet combustor design: a computational fluid dynamics approach, Journal of Propulsion and Power 24 (2) (2008) 274–281.

[8] G. Choubey, K. Pandey, Effect of variation of angle of attack on the performance of two-strut scramjet combustor, international journal of hydrogen energy 41 (26) (2016) 11455–11470.

[9] P. Nithish Reddy, K. Venkatasubbaiah, Numerical investigations on development of scramjet combustor, Journal of Aerospace Engineering 28 (5) (2015) 04014120.

[10] W. Huang, L. Yan, Numerical investigation on the ram–scram transition mechanism in a strut-based dual-mode scramjet combustor, International Journal of Hydrogen Energy 41 (8) (2016) 4799–4807.

[11] W. Huang, Design exploration of three-dimensional transverse jet in a supersonic crossflow based on data mining and

multi-objective design optimization approaches, international journal of hydrogen energy 39 (8) (2014) 3914–3925.
[12] G. Aversano, J. C. Parra-Alvarez, B. J. Isaac, S. T. Smith, A. Coussement, O. Gicquel, A. Parente, Pca and kriging for the efficient exploration of consistency regions in uncertainty quantification, Proceedings of the Combustion Institute 37 (4) (2019) 4461–4469.
[13] D. S. Gipe, Surrogate modelling of combustion systems for robust optimized scramjet design.
[14] J. Steelant, Sustained hypersonic flight in europe: first technology achievements within lapcat ii, in: 17th AIAA International Space Planes and Hypersonic Systems and Technologies Conference, 2011, p. 2243.
[15] P. Roncioni, P. Natale, M. Marini, T. Langener, J. Steelant, Numerical simulations of the lapcat mr-2 vehicle scramjet engine, in: 21st International Symposium Air Breathing Engines, ISABE-2013-1656, American Institute of Aeronautics and Astronautics, 2013.
[16] V. F. Villacé, Simulation, Design and Analysis of Air-Breathing Combined-Cycle Engines for High Speed Propulsion, Doctoral Thesis. Von Karman Institute for Fluid Dynamics, 2013.
[17] S. Chakravarthy, U. Goldberg, P. Batten, S. Palaniswamy, Peroomian, 0, CFD++ User Manual, Version 96.
[18] A. S. Pudsey, R. R. Boyce, V. Wheatley, Influence of common modeling choices for high-speed transverse jet-interaction simulations, Journal of Propulsion and Power 29 (5) (2013) 1076–1086.
[19] W. Huang, S.-b. Li, L. Yan, Z.-g. Wang, Performance evaluation and parametric analysis on cantilevered ramp injector in supersonic flows, Acta Astronautica 84 (2013) 141–152.
[20] A. Fluent, et al., Ansys fluent theory guide, ANSYS Inc., USA 15317 (2011) 724–746.
[21] S. Aravind, R. Kumar, Supersonic combustion of hydrogen using an improved strut injection scheme, International Journal of Hydrogen Energy 44 (12) (2019) 6257–6270.
[22] W. Luo, Large eddy simulation of turbulent supersonic combustion and characteristics of supersonic flames, Ph.D. thesis, University of Leeds (2014).
[23] P. Gerlinger, H. Möbus, D. Brüggemann, An implicit multigrid method for turbulent combustion, Journal of Computational Physics 167 (2) (2001) 247–276.
[24] G. Aversano, A. Bellemans, Z. Li, A. Coussement, O. Gicquel, A. Parente, Application of reduced-order models based on pca & kriging for the development of digital twins of reacting flow applications, Computers & chemical engineering 121 (2019) 422–441.
[25] A. Coussement, B. J. Isaac, O. Gicquel, A. Parente, Assessment of different chemistry reduction methods based on principal component analysis: Comparison of the mg-pca and score-pca approaches, Combustion and Flame 168 (2016) 83–97.
[26] B. Sparkman, Scramjet fuel injection array optimization utilizing mixed variable pattern search with kriging surrogates.

Multi-Disciplinary modelling of the aerothermodynamically-induced fragmentation of re-entering bodies

Fábio Morgado

Department of Mechanical and Aerospace Engineering, University of Strathclyde, Scotland, fabio.pereira-morgado@strath.ac.uk

Supervisor: Thierry Magin

Professor, Aeronautics and Aerospace Department, von Karman Institute for Fluid Dynamics, Belgium, thierry.magin@vki.ac.be

University Supervisor: Marco Fossati

Associate Professor, Department of Mechanical and Aerospace Engineering, University of Strathclyde, Scotland, marco.fossati@strath.ac.uk

Abstract

The progressive increase of man-made orbiting objects and subsequent higher frequency of atmospheric re-entry carries risks of space and ground collisions that need to be correctly addressed. The object break-up that results from the severe aerothermal loads experienced during reentry greatly affects re-entry predictions. Due to the multi-disciplinary nature of aerothermal induced fragmentation and its inherent complexity, the majority of modelling tools are still based on strong simplifying assumptions, leading to large uncertainties in the prediction of the demise process and deteriorating the capability to perform design for demise. To reduce this uncertainty, a new approach based on a high-fidelity framework to model fragmentation is proposed.

To ensure the accuracy of the computed aerothermal loads in the critical instants before and after fragmentation, the open-source solver SU2-NEMO coupled to the thermochemistry library Mutation++ is used, together with adaptive meshing techniques and mesh regeneration tools, to account the topology change due to fragmentation. The crack propagation and topology change are modelled using a peridynamics formulation with the open-source software Peridigm. A 6 DoF model is used to account for the break-up impact on the fragments dynamics. Due do the demanding computational cost, the high-fidelity models are only used immediately before and after the fragmentation process. The remaining re-entry process is simulated using a low-fidelity approach.

Preliminary results have proven the capability of SU2-NEMO to accurately compute aerothermal loads in the slip flow regime using a Maxwell velocity slip and Smoluchowski temperature jump formulation. Furthermore, the obtained results showcase the ability of the solver to use highly anisotropic meshes that sharply capture the flow directional features, i.e., shock interaction patterns caused by the presence of multi-bodies. Such patterns can lead to severe localized pressure and heat loads, thus initializing cracks on the impinged object.

Keywords: fragmentation, re-entry, design for demise

RAREFIED AND PLASMA FLOWS

The intercardinal Lagrangian-Eulerian scheme: solving kinetic equations with quadrature-based moment methods fast, accurate and realizable

Maxim Van Cappellen

Environmental and Applied Fluid Dynamics Department, von Karman Institute for Fluid Dynamics, Belgium, maxim.van.cappellen@vki.ac.be

Supervisor: Delphine Laboureur

Assistant Professor, Environmental and Applied Fluid Dynamics Department, von Karman Institute for Fluid Dynamics, Belgium, delphine.laboureur@vki.ac.be

University Supervisor: Maria Rosaria Vetrano

Associate Professor, Faculty of Engineering Science, Katholieke Universiteit Leuven, Belgium, rosaria.vetrano@kuleuven.be

Abstract

In this work we propose a new numerical framework for solving kinetic equations using quadrature-based moment methods (QBMM). This framework takes full advantage of the discrete particle velocity distribution (VDF) by offering the possibility to solve the terms appearing in the kinetics equation in an Eulerian and/or Lagrangian way. For the advection term we propose two Lagrangian-Eulerian schemes: one that is shown to be equivalent to the classic first order kinetic-based finite volume scheme and one that exhibits significantly less numerical diffusion by better taking into account the true direction of the flow of particles. This novel advection scheme is shown to always result in realizable moments while having a time step constraint equal to that of the first order kinetic scheme. In this Lagrangian-Eulerian framework we have the liberty to resolve source terms and boundary conditions is an Eulerian or Lagrangian framework. We demonstrate the advantage of this feature by showing how to resolve the source terms for Stokes drag in a accurate and realizable way. The methods and results shown in this work are applied to structured uniform Cartesian grids. In future work extension towards non-uniform and unstructured grids will be investigated.

Keywords: Poly-kinetic, particle-laden flows, particle trajectory crossing, method of moments, QBMM, multivariate quadrature, Lagrangian Eulerian particle kinetics.

1. Introduction

The behavior of a population of inertial particles suspended in a fluid can be described by a velocity-based number density function (VDF) that complies with a kinetic equation [1; 2; 3]. This kinetic equation can be solved by numerous numerical models, generally divided into two classes of solvers: the Lagrangian methods which directly solve the kinetic equation on a mesoscale level and the Eulerian models that apply an averaging procedure to find the transport equations of certain lower order statistics of the VDF (*i.e. macroscale methods*).

Conventionally, the kinetics of particles with high Stokes and Knudsen number are solved using the Lagrangian methods. However, these methods suffer from statistical noise when coupled with the Eulerian physics of the carrier flow. Furthermore, they are expensive for large populations of particles. These disadvantages create a high demand for Eulerian models that can describe the kinetics of particle-laden flows across a wide range of regimes.

In the last decade, a new type of Eulerian solvers has emerged to meet this demand, the so-called quadrature-based moment methods (QBMM) [4; 5; 6; 7; 8; 2; 9; 10]. Here, the higher-order moments required for closure are evaluated by a multi-dimensional quadrature that corresponds to a certain

set of lower-order transported moments. In our previous works we described how to efficiently calculate this multi-dimensional quadrature such that the transport equations of the lower-order moments forms a strictly hyperbolic system [11].

The closed moment system is numerically solved using kinetic based finite volume methods (KBFVMs). The first order KBFVM is computationally efficient but suffers from high numerical diffusion. Higher-order KBFVMs have been proposed to increase spatial accuracy but significantly reduce the maximum allowable time step and are far less efficient [12]. Besides, in the true sense, numerical diffusion is not an artifact of the truncation of the Taylor-series but rather originates from the fact that the differencing scheme fails to account for the true direction of the flow in a multi-dimensional setting [13]. Furthermore, due to the highly coupled moment system, resolving source terms directly on the level of the moments (i.e. the macroscale level) often involves dubious assumptions which can affect numerical accuracy and moment realizability (i.e. the moments no longer correspond to a physically plausible VDF).

In this work we redefine the computational framework for solving the moment transport equations on an Eulerian grid when using QBMMs. Instead of describing the spatial fluxes using higher order moments we make advantage of the discrete description of the velocity-based number density function in order to update the moment equations. This novel framework offers several important advantages:

- The numerical diffusion is decreased significantly without reducing the time step, revealing more accurately small scale spatial features of the particle distribution without compromising numerical efficiency and stability.
- The time step can easily be verified to be realizable, even for complicated source terms.
- The transport equations can now be solved in a decoupled way, reducing non-realizability, specifically in the higher order moments.
- Boundary conditions and source terms can be evaluated in an Eulerian or Lagrangian framework, greatly reducing mathematical/programming complexity.

2. The Lagrangian-Eulerian Framework

The novel numerical framework here presented originates from the simple fact that the evolution of a particle moving through (non-relativistic) space-time can be described equivalently in a Lagrangian and an Eulerian framework. Suppose we have a particle p at location $\bar{x}_p = [x_p, y_p]^T$ with velocity $\bar{u}_p = [u_p, v_p]^T$ at time t. This particle can be described by the one-particle velocity-based number density function $f_p(t, \bar{x}_p, \bar{u}_p)$:

$$f_p(t, \bar{x}, \bar{u}) = \rho(t, \bar{x})\delta(u - u_p(t, \bar{x}))\delta(v - v_p(t, \bar{x})) \quad (1)$$

where ρ represent the number of particles, in this case one. In an Eulerian framework this VDF evolves (*in the absence of external forces*) according to the kinetic equation

$$\partial_t f_p + \partial_{\bar{x}} \cdot \bar{u} f_p = 0. \quad (2)$$

The equivalent Lagrangian dynamics of particle p are

$$\frac{dx_p}{dt} = u_p, \quad \frac{dy_p}{dt} = v_p, \quad \frac{du_p}{dt} = \frac{dv_p}{dt} = 0. \quad (3)$$

In case we want to know the evolution of many particles both the Eulerian and Lagrangian dynamic equations are expensive to solve. A convenient way to reduce the number of degrees of freedom and hence the number of transported variables are the quadrature-based method of moments (QBMMs). Applying the bivariate power moments transformation, defined by

$$M_{k,l}(t, \bar{x}) = \int_{\mathbb{R}} \int_{\mathbb{R}} u^k v^l f(t, \bar{x}, \bar{u})\, du\, dv, \quad (4)$$

results in the (*unclosed*) moment transport equations

$$\partial_t M_{k,l} + \partial_x M_{k+1,l} + \partial_y M_{k,l+1} = 0. \quad (5)$$

The VDF $f(t, \bar{x}, \bar{u})$ appearing in eq. (4) is the sum of all one-particle VDFs at a certain location in space-time. This system of equations can be closed by using the quadrature representation of the moments:

$$M_{k,l} \approx \sum_{\alpha=1}^{N} \rho_\alpha u_\alpha^k v_\alpha^l. \quad (6)$$

Here, ρ_α are called the weights, u_α, v_α the abscissas and N the order of the quadrature. Finding these weights and abscissas from a know set of lower order moments can be done by the optimization-based quadrature inversion algorithm described in our previous work [11].

2.1. The Eulerian numerical scheme

Conventionally the moment transport system in eq. (5) is numerically solved using the kinetic based finite volume method. Let us denote the volume averaged moments on a uniform mesh with spacing $(\Delta x, \Delta y)$ at time t and cell-center (x_i, y_i) (see fig. 1)

$$M_{k,l}|^t_{i,j} = \frac{1}{\Delta x \Delta y} \int_{x_i-\Delta x/2}^{x_i+\Delta x/2} \int_{y_i-\Delta y/2}^{y_i+\Delta y/2} M_{k,l}(t,x,y)\, dx\, dy. \tag{7}$$

Making use of the quadrature representation of the moments in eq. (6), we can write a kinetic based flux splitting finite volume scheme. For a single step forward Euler temporal discretization and a first order upwind flux scheme we get the following numerical scheme:

$$\begin{aligned} M_{k,l}|^{t+\Delta t}_{i,j} &= M_{k,l}|^t_{i,j} \\ &- \frac{\Delta t}{\Delta x}\left(M^{+u}_{k+1,l}|^t_{i,j} - M^{+u}_{k+1,l}|^t_{i-1,j} + M^{-u}_{k+1,l}|^t_{i+1,j} - M^{-u}_{k+1,l}|^t_{i,j}\right) \\ &- \frac{\Delta t}{\Delta y}\left(M^{+v}_{k,l+1}|^t_{i,j} - M^{+v}_{k,l+1}|^t_{i,j-1} + M^{-v}_{k,l+1}|^t_{i,j+1} - M^{-v}_{k,l+1}|^t_{i,j}\right) \end{aligned} \tag{8}$$

with the flux splitted moments defined by

$$\begin{aligned} M^{+u}_{k,l} &= \sum_{\alpha=1}^{N} \rho_\alpha \max(0, u_\alpha)^k\, v^l \\ M^{-u}_{k,l} &= \sum_{\alpha=1}^{N} \rho_\alpha \min(0, u_\alpha)^k\, v^l \\ M^{+v}_{k,l} &= \sum_{\alpha=1}^{N} \rho_\alpha u^k \max(0, v_\alpha)^l \\ M^{-v}_{k,l} &= \sum_{\alpha=1}^{N} \rho_\alpha u^k \min(0, v_\alpha)^l\,. \end{aligned} \tag{9}$$

2.2. The cardinal Lagrangian-Eulerian numerical scheme

As mentioned before, the particle dynamics can also be described by the Lagrangian equations in eq. (3). Since, the quadrature representation assumes that the VDF is equal to

$$f(u,v) = \sum_{\alpha=1}^{N} f_\alpha(u,v) = \sum_{\alpha=1}^{N} \rho_\alpha \delta(u-u_\alpha)\delta(v-v_\alpha), \tag{10}$$

we can evolve the moment transport system by solving the Lagrangian equations for each one-particle VDF $f_\alpha(u,v)$ in this summation. One possible procedure is as followed: assume we have a particle p with velocity $\bar{u}_p = [u_p, v_p]^T = [u_\alpha, v_\alpha]^T$ at location $\bar{x}_p = [x_i, y_i]^T$ at time t. At time $t + \Delta t$ this particle will have moved to

$$x_p(t+\Delta t) = x_p(t) + \Delta t u_p, \quad y_p(t+\Delta t) = y_p(t) + \Delta t v_p. \tag{11}$$

this is indicated in fig. 1. The next step in to re-inject the particle p on the numerical grid. We can observe that if

$$\Delta t \leq \frac{\Delta x}{\max(|u_\alpha|)} + \frac{\Delta y}{\max(|v_\alpha|)} \tag{12}$$

the particle p at $t+\Delta t$ will remain in cell (i,j) and inside the triangle described by cell centers (i,j), (i+1,j) and (i,j+1). We now redistribute the VDF of particle p at time $t + \Delta t$ over these three cell by writing

$$\begin{aligned} f_\alpha(t+\Delta t, x_i, y_j) &= w_{i,j} f_\alpha(x_p(t+\Delta t), y_p(t+\Delta t)) \\ f_\alpha(t+\Delta t, x_{i+1}, y_i) &= w_{i+1,j} f_\alpha(x_p(t+\Delta t), y_p(t+\Delta t)) \\ f_\alpha(t+\Delta t, x_i, y_{j+1}) &= w_{i,j+1} f_\alpha(x_p(t+\Delta t), y_p(t+\Delta t)). \end{aligned} \tag{13}$$

Here the weights w represent how much of the particle mass is attributed to a specific cell. In order for the updated solution on the grid to be realizable and consistent, all weights w should be positive and the center of mass of the Lagrangian particle must be equal to the center of mass of the Eulerian distributed particle. Hence, the weights w can be found by solving the linear system

$$\begin{bmatrix} 1 & 1 & 1 \\ x_{i,j} & x_{i+1,j} & x_{i,j+1} \\ y_{i,j} & y_{i+1,j} & y_{i,j+1} \end{bmatrix} \begin{bmatrix} w_{i,j} \\ w_{i+1,j} \\ w_{i,j+1} \end{bmatrix} = \begin{bmatrix} 1 \\ x_p(t+\Delta t) \\ y_p(t+\Delta t) \end{bmatrix}. \tag{14}$$

Note that this linear system represents the conversion from Cartesian coordinates $(x_p(t+\Delta t), y_p(t+\Delta t))$ to the barycentric coordinates $(w_{i,j}, w_{i+1,j}, w_{i,j+1})$ of a triangle's plane with vertices at $(x_{i,j}, y_{i,j})$, $(x_{i+1,j}, y_{i+1,j})$ and $(x_{i,j+1}, y_{i,j+1})$. If the point $(x_p(t+\Delta t), y_p(t+\Delta t))$ is inside this triangle, all barycentric coordinates will have a value between zero and one. On a structured uniform grid this is always the case if the time-step is chosen according to eq. (12). Now that we know the updated VDF on the computational grid, we can calculate the moments at time $t + \Delta t$ by using the quadrature representation in eq. (6).

With this scheme we (implicitly) transported the moment equations in two cardinal directions (i.e north and east). One can observe that if both u_p and v_p are both non zero, we can always find two cardinal adjacent cells that together with the original cell form a triangle in which the particle will remain after Lagrangian transport.

2.3. Recovering the first order kinetic scheme

In this section we will demonstrate that the proposed cardinal Lagrangian-Eulerian scheme is equivalent to the first order kinetic scheme given in eq. (8). For ease of notation we assume that the neighboring cells do not contain any particles and the cell (i,j) contains one particle p with positive x and y velocity component. Thus, without loss of generality, we can rewrite the Eulerian discrete moment transport equations in cell (i,j) as:

$$M_{k,l}|_{i,j}^{t+\Delta t} = M_{k,l}|_{i,j}^{t} - \frac{\Delta t}{\Delta x}\left(M_{k+1,l}^{+u}|_{i,j}^{t}\right) - \frac{\Delta t}{\Delta y}\left(M_{k,l+1}^{+v}|_{i,j}^{t}\right). \quad (15)$$

The one-particle VDF at cell (i,j) using the cardinal Lagrangian-Eulerian scheme is equal to

$$f_\alpha(t+\Delta t, x_i, y_j) = w_{i,j} f_\alpha(x_p(t+\Delta t), y_p(t+\Delta t)), \quad (16)$$

with the weight $w_{i,j}$ equal to

$$w_{i,j} = 1 - \frac{\Delta t}{\Delta x}u_p - \frac{\Delta t}{\Delta u}v_p. \quad (17)$$

Applying the moment transformation and observing that $f_\alpha(x_p(t+\Delta t), y_p(t+\Delta t)) = f_\alpha(x_p(t), y_p(t))$ in the absence of particle forces, we can see that the cardinal Lagrangian-Eulerian scheme recovers exactly the first order Eulerian scheme in eq. (15). Since this is true for a one-particle VDF this is also the case for a multi-particle VDF.

3. Advantages of the Lagrangian-Eulerian framework

3.1. Reducing two dimensional numerical diffusion

The cardinal Lagrangian-Eulerian scheme presented before is one possible solution. In the example depicted in fig. 1 we can observe that the updated particle location is also inside the green triangle with vertices at cell centers (i,j), (i+1,j) and (i+1,j+1). Thus if we redistribute the Lagrangian-ly updated one-particle VDF over these cells according to the procedure in eq. (14) we will be sure to have a realizable and consistent numerical scheme. By doing so we obtain a scheme that accounts better for the true direction of the flow and hence exhibits far less numerical diffusion (see results). This scheme is hence forward called the intercardinal Lagrangian-Eulerian scheme. We can observe that on a uniform Cartesian grid, if both u_p and v_p are non zero, we can always find one cardinal and one intercardinal

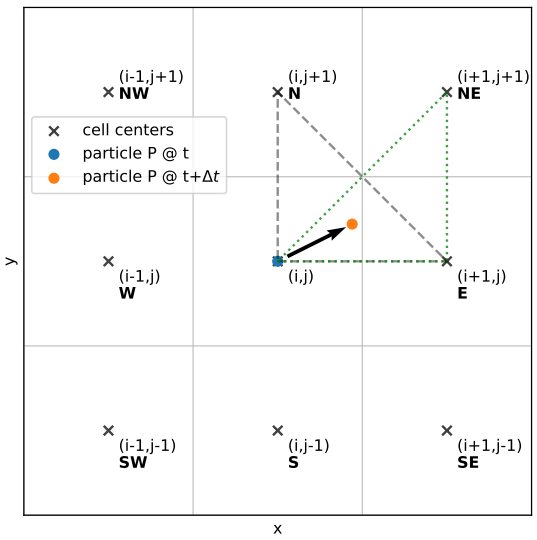

Figure 1: Lagrangian movement of a particle P in a uniform structured cell centered computational grid. The gray triangle connects the cells used in the cardinal L-E scheme, the green triangle show the cells used in the intercardinal L-E scheme.

adjacent cell such that the intercardinal Lagrangian-Eulerian scheme is realizable and consistent. Compared to the quasi-higher order kinetic schemes, with this novel intercardinal-Lagrangian-Eulerian scheme we can decrease numerical diffusion without reducing the time step nor increasing the computational cost nor affecting numerical stability. Furthermore, because we solve the evolution of the moment transport equations by transporting all the one-particle VDFs appearing in the quadrature representation, we effectively decouple the moment transport equations allowing more control over the realizability of the updated moments. Note that the Lagrangian dynamic equations can be coupled, although in far less number of variables.

3.2. Reducing numerical instabilities

In our previous work we showed that, because the quadrature representation always exhibits some numerical error, the definition of the realizable time step using the Eulerian kinetic scheme is in fact not correct and appears to be a source of numerical instabilities related to non-realizability [11]. However, we demonstrated that if we recompute the moments at time t with the quadrature representation before updating towards $t + \Delta t$ we are (more) sure to respect the realiz-

ability constraint and greatly increase stability of the solution. In the Lagrangian-Eulerian scheme we automatically and implicitly ensure that the quadrature representation is exact.

3.3. Solving source terms

The Lagrangian-Eulerian framework gives us the liberty to solve the contribution of source terms using Eulerian and/or Lagrangian dynamics. To illustrate this we take the example of particles suspended in a fluid undergoing Stokes drag. The evolution of the velocity-based number density function now reads:

$$\partial_t f + \partial_{\bar{x}} \cdot \bar{u} f + \partial_{\bar{u}} \cdot F f = 0 \tag{18}$$

with $F = (F_u, F_v)$ and

$$F_u = \frac{u_g - u_p}{\tau}, \quad F_v = \frac{v_g - v_p}{\tau}. \tag{19}$$

Here (u_g, v_g) is the velocity of the fluid surrounding the particle and τ is the relaxation time. Applying the moment transformation results in:

$$\begin{aligned} &\partial_t M_{k,l} + \partial_x M_{k+1,l} + \partial_y M_{k,l+1} \\ &\quad = \frac{1}{\tau}\left[k M_{k-1,l} u_g + l M_{k,l-1} v_g - (k+l) M_{k,l}\right]. \end{aligned} \tag{20}$$

Conventionally this system of equations is solved by operator splitting. Here, the moments are first updated using the Eulerian kinetic scheme in absence of source terms and thereafter updated by adding the contribution of the source term. The contribution of Stokes drag is solved using the semi-analytical solution:

$$\begin{aligned} M_{k,l} = \left(k M_{k-1,l} u_g + l M_{k,l-1} v_g\right) \frac{\left(-1 + \exp\left(\frac{-(k+l)\Delta t}{\tau}\right)\right)}{-(k+l)} \\ + M_{k,l} \exp\left(\frac{-(k+l)\Delta t}{\tau}\right) \end{aligned} \tag{21}$$

where the fluid velocity is assumed constant. Important to note here is that in literature it is often neglected that this semi-analytical solution assumes that the moments $M_{k-1,l}$ and $M_{k,l-1}$ are also constant. Furthermore is there no proof that the updated moment set will be realizable. If one tries to find an (semi-)analytic solution in which these moments are not assumed constant, one will soon realize that the mathematical complexity quickly becomes unmanageable due to the fact that all moment equations are coupled. Here the strength of the Lagrangian-Eulerian framework becomes clear. If we look at the equivalent Lagrangian dynamics:

$$\frac{dx_p}{dt} = u_p, \quad \frac{dy_p}{dt} = v_p, \tag{22}$$

$$\frac{du_p}{dt} = F_u, \quad \frac{dv_p}{dt} = F_v, \tag{23}$$

we can see that we only have two coupled equations and finding the semi-analytical solution, assuming constant fluid velocity, is easy. The semi-analytic solution of this system is:

$$\begin{aligned} x_p(t+\Delta t) &= \tau u_p(t)\left(1 - \exp\left(-\Delta t/\tau\right)\right) \\ &\quad + u_g\left(-\tau\left(1 - \exp\left(-\Delta t/\tau\right)\right) + \Delta t\right) + x_p(t) \end{aligned} \tag{24}$$

$$u_p(t+\Delta t) = u_g\left(1 - \exp\left(-\Delta t/\tau\right)\right) + u_p(t)\exp\left(-\Delta t/\tau\right) \tag{25}$$

and equivalent equations for $y_p(t+\Delta t)$ and $v_p(t+\Delta t)$ can be found. Now if we update each one-particle VDF according to these equations and redistribute the solution on the Eulerian grid, we are sure to have a accurate and realizable solution if the time step is chosen such that the particle remains in its original cell. Furthermore is there no more need for operator splitting.

3.4. Resolving boundary conditions

Same as for the source terms, we can freely chose to resolve boundary conditions in an Eulerian or Lagrangian framework. Resolving zero-gradient, periodic, processor and reflecting wall boundary conditions in an Eulerian framework is relatively straightforward and are hence adopted in the current solver. Exploring the possibility to resolve boundaries in the Lagrangian framework will be investigated in future work.

3.5. The algorithm

In this last subsection we summarize the pseudo-algorithm for solving the moment transport equations using the proposed Lagrangian-Eulerian framework (algorithm 1).

4. Results and discussion

In this section we demonstrate the usefulness of the proposed Lagrangian-Eulerian framework. First, we show the effect of the cardinal and intercardinal L-E schemes on the numerical diffusion. Secondly, we show the solution when a source term, namely Stokes drag, is present.

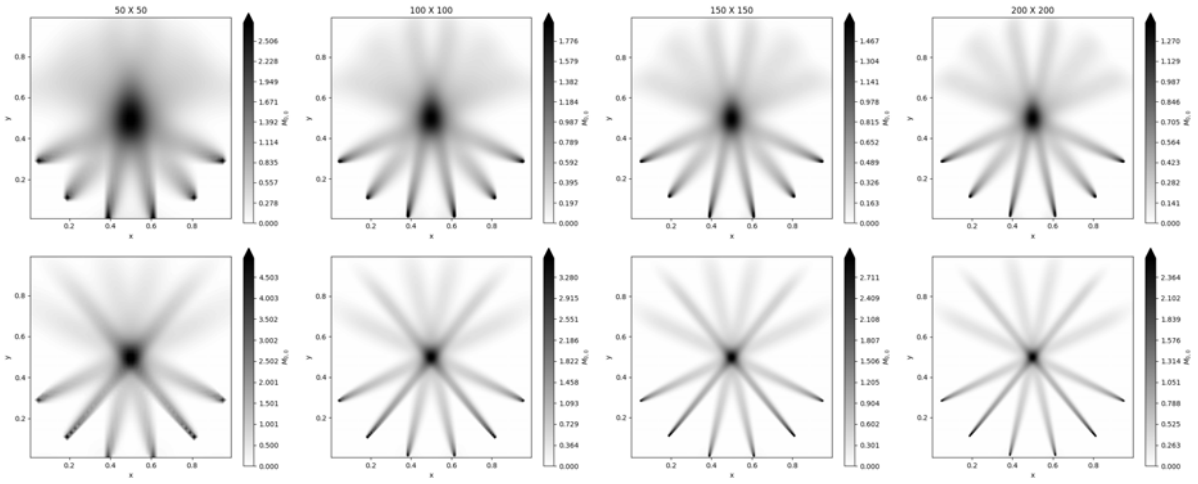

Figure 3: Six jets crossing in a vacuum: density distribution ($M_{0,0}$) at time $t = 1$. The upper row is solved using the cardinal L-E scheme, the lower row with the intercardinal L-E scheme. From left to right the uniform Cartesian computational grids are: 50×50, 100×100, 150×150 and 200×200. The colorbars are linearly scaled between zero and the value of $M_{0,0}$ at the center of the domain.

4.1. Jets in a vacuum

The effect of the cardinal and intercardinal L-E schemes on the numerical diffusion is best shown in the absence of source terms. We do so by simulating 2D crossing jets in a vacuum. In this idealized case, the jets should travel on straight paths without influencing one another. The initial solution is described in fig. 2. The transported moment in this case are the marginal moments: $[M_{0,0}, M_{1,0}, M_{0,1}, \cdots, M_{11,0}, M_{0,11}]$ and the mixed moments $[M_{1,1}, M_{1,2}, M_{2,1}]$, giving a total of 26 moments. The resulting number concentration $M_{0,0}$ at time $t = 1$ is depicted in fig. 3. In the upper row of fig. 3 we solve the moment transport equations in eq. (8) using the cardinal Lagrangian-Eulerian scheme. In the lower row we applied the intercardinal Lagrangian-Eulerian scheme. The number of cells in the uniform Cartesian computational grid is increased from left to right with the number of cells used written above the respective columns. The most noticeable aspect of this figure is the fact that the intercardinal scheme is clearly far less diffusive as the cardinal one. Roughly the same precision is seen between the solution of the cardinal scheme on a 200×200 grid as with the intercardinal scheme on a 50×50 grid. Thus with the intercardinal scheme we need 93.75% less cells to observe roughly the same level of detail of the spatial distribution of the particles compared to the first order kinetic based Eulerian scheme. Quantitatively we analyze the re-

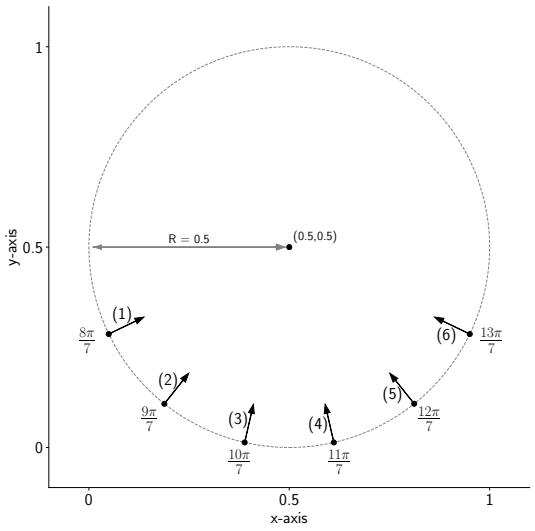

Figure 2: Location of the sources of the jets. The jets are located on a circle around the center of the domain $(x, y = 0.5, 0.5)$ with radius $R = 0.5$. The absolute velocity of all jets is equal to one and oriented towards the center of the domain. The initial number concentration at the source points is set to one.

Algorithm 1: Lagrangian-Eulerian moment transport framework: advancing the solution towards $t + \Delta t$.

for *all cells* **do**
  Solve the multivariate moment inversion problem;
  Correct the quadrature for mass, momentum and energy conservation;
  Save the quadrature in a container of quadratures;
  Update the maximum realizable time step Δt;
end
for *all cells* **do**
  for *all quadrature points* **do**
    Evolve each one-particle VDF to $t + \Delta t$ using the Lagragian dynamics;
    Redistribute the evolved one-particle VDF over the appropriate adjacent cells such that all weights in eq. (14) are ≥ 0 ;
    if *all adjacent cells* $\in$ *computational grid* **then**
      for *all moments* **do**
        Add the contribution of each redistribute evolved one-particle VDF to the updated moment;
      end
      Remove the non-evolved one-particle VDF from the container of quadratures;
    end
  end
end
for *all boundary cells* **do**
  for *all quadrature points* **do**
    for *all moments* **do**
      Add the contribution of each one-particle VDF to the positive and negative flux moments in eq. (9);
    end
  end
end
for *all boundary faces* **do**
  In each adjacent cell update the moments to $t + \Delta t$ using the Eulerian numerical scheme in eqs. (8) and (9);
end

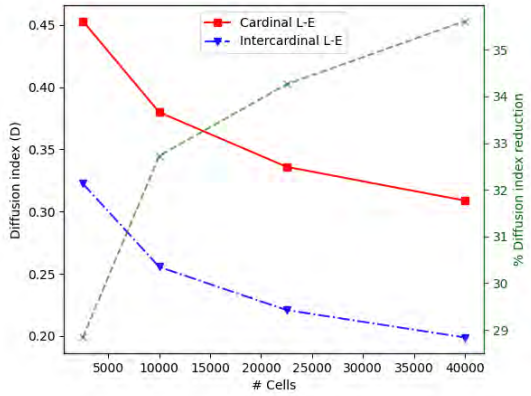

Figure 4: Six jets crossing in a vacuum: Diffusion index at time $t = 1$. The left y-axis gives the value of D while the right y-axis represents the percentage of reduction of D obtained by using the intercardinal scheme compared to the cardinal one.

duction of numerical diffusion by comparing the here proposed diffusion index D

$$D = \frac{1}{S} \quad \text{with} \quad S = \frac{\left\langle M_{0,0}^2 \right\rangle}{\langle M_{0,0} \rangle^2}, \tag{26}$$

where S is called the segregation index. If S = 1 the distribution is spatially uniform. When S increases clusters of particles will be present [7]. Thus the diffusion index D will converge to one for increasing numerical diffusion. Because the particles should in theory all reside on an infinity thin lines, the reference value of D is zero. The diffusion index for all cases presented before are plotted in fig. 4. The left y-axis gives the value of D while the right y-axis represents the percentage of reduction of D obtained by using the intercardinal scheme compared to the cardinal one. As expected the diffusion index is significantly lower for the intercardinal scheme. Furthermore does the diffusion index decrease faster for the intercardinal scheme when the cell size is reduced. If we assume that the diffusion index is proportional to the accuracy of the solution,than again we observe that for this particular test case the intercardinal scheme needs 93.75% less cells to obtain the same accuracy as the solution found by using the first order scheme.

4.2. Taylor-Green vortices

In this test case, the evolution of particles suspended in a TaylorGreen vortex flow, undergoing

Stokes drag (eq. (19)), is presented. The domain consists of a square (1 x 1) box with periodic boundaries. The fluid velocity is given by:

$$\begin{aligned} u_g(x,y) &= \sin(2\pi x)\cos(2\pi y) \\ v_g(x,y) &= -\sin(2\pi y)\cos(2\pi x) \end{aligned} \tag{27}$$

and the relaxation time τ in eq. (19) is set to one. As a reference we use the solution obtained with the OpenFOAM® Lagrangian solver "icoUncoupledKinematicParcelFoam" in which we added the model for Stokes drag. The transported moments in this case are the marginal moments: $[M_{0,0}, M_{1,0}, M_{0,1}, \cdots, M_{6,0}, M_{0,6}]$ and the mixed moments $[M_{1,1}, M_{1,2}, M_{2,1}, M_{3,1}, M_{1,3}, M_{2,2}]$, giving a total of 19 moments. The resulting number concentration $M_{0,0}$ at time $t = 4$ for two different grid sizes is depicted in fig. 5. The moments of the Lagrangian reference solution in the left column are obtained by simply binning the particles on the Eulerian grid (thus an, albeit small, error is made on the true center of gravity of the particles). One million particles where used in order to find a close to grid converged solution. Note that converting Lagrangian particles to an Eulerian field is always scale dependent and the results should be interpreted with caution.

The number concentration $M_{0,0}$ at time $t = 4$ is depicted in fig. 5. From left to right the solution using the Lagragian solver, cardinal L-E scheme and intercardinal L-E scheme are shown for two different grid sizes. As for the jets in a vacuum the intercardinal scheme clearly does a better job of approximating the spatial structure of the particle distribution. This is well demonstrated in the solution with the intercardinal scheme on a 50×50 grid, which shows a similar level of detail as the solution using the cardinal one on a 200×200 grid.

In fig. 6 we evaluate quantitatively the results by plotting the time evolution of four phase-averaged statistics for each simulation. The first is the segregation index (S, eq. (26)), the second the phase-averaged macroscopic kinetic energy (MKE), the third is the phase-averaged internal energy (IKE) and the last is the phase-averaged total kinetic energy (TKE). Respectively, the kinetic energy of the macroscopic motion, the kinetic energy of identical particles as measured in the rest frame (also called granular temperature) and the total kinetic energy transferred from the fluid to the particle phase [3; 10]. Their definitions are given by:

$$\begin{aligned} MKE &= \frac{\left\langle M_{0,0}(R_{1,0}^2 + R_{0,1}^2)\right\rangle}{2\left\langle M_{0,0}\right\rangle}, \\ IKE &= \frac{\left\langle M_{0,0}(C_{2,0} + C_{0,2})\right\rangle}{2\left\langle M_{0,0}\right\rangle} \text{ and} \\ TKE &= \frac{\left\langle M_{2,0} + M_{0,2}\right\rangle}{2\left\langle M_{0,0}\right\rangle} \end{aligned} \tag{28}$$

with

$$\begin{aligned} R_{1,0} = M_{1,0}/M_{0,0},\ \ R_{0,1} = M_{0,1}/M_{0,0}, \\ C_{2,0} = \frac{M_{2,0}}{M_{0,0}} - R_{1,0}^2 \text{ and } C_{0,2} = \frac{M_{0,2}}{M_{0,0}} - R_{0,1}^2. \end{aligned} \tag{29}$$

In general the Eulerian solutions follows quite accurately the trends of the Lagrangian reference solutions for all four statistics. The difference between the cardinal and intercardinal L-E simulations is not as pronounced as for the test case with the jets. The most noticeable effect of the intercardinal scheme is the improved approximation of the macroscopic energy on a coarse grid. Another point to be made from these graphs is that the Lagrangian reference solution is clearly scale dependent, as can be seen in the segregation index. The Lagrangian energy statistics are less dependent on the grid resolution.

5. Conclusion

In this paper we present a novel framework for solving kinetic equations using quadrature-based moments methods on an Eulerian grid. Unlike conventional Eulerian kinetic based finite volume schemes, which define the spatial fluxes from higher order moments, we take advantage from the discrete approximation of the particle velocity distribution in order to evolve the VDF using Lagrangian dynamics. We propose two schemes for redistributing the Lagrangianly evolved VDF on the Eulerian grid in a consistent and realizable way. The first is called the cardinal Lagrangian-Eulerian scheme, which we demonstrate to be equivalent to the first order KBFVM. The second is the intercardinal Lagrangian-Eulerian scheme, which better accounts for the true direction of the flow of particles and consequently exhibits far less numerical diffusion compared to the cardinal scheme. A secondary advantage of the Lagrangian-Eulerian framework is the fact that we are free to chose to resolve source terms and boundary conditions using the Eulerian or Lagrangian dynamics of the particles. We demonstrate for the simple case of Stokes drag that

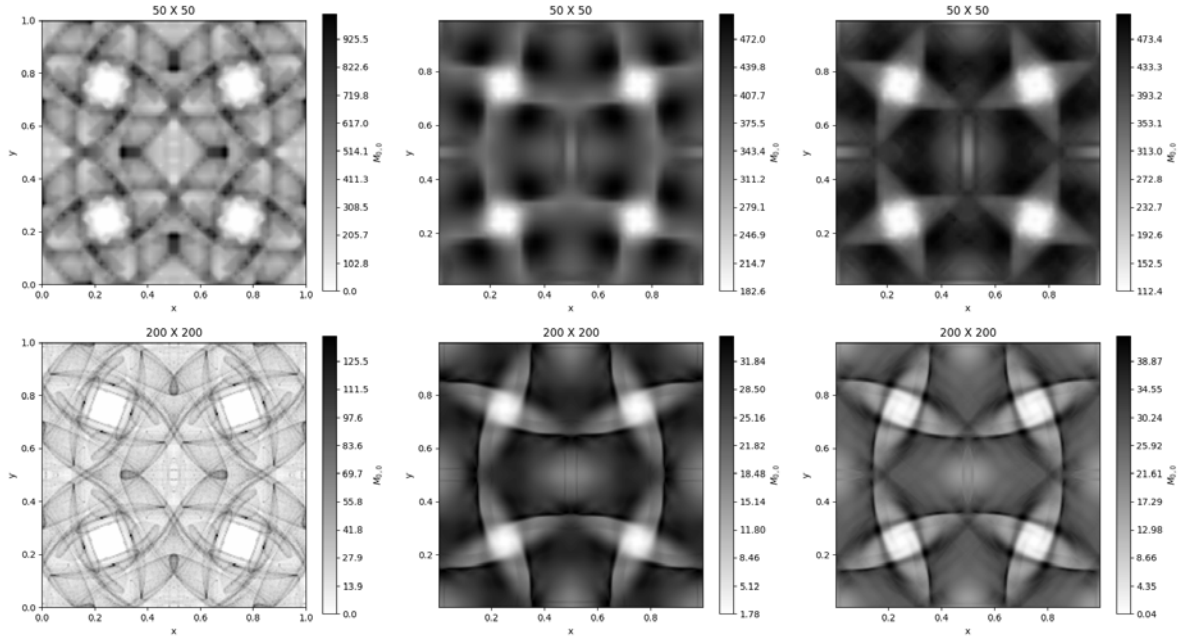

Figure 5: Taylor-Green vortex flow: density distribution ($M_{0,0}$) at time $t = 4$ with $\tau = 1$. The left column is the reference solution found using the Lagrangian solver, the middle using the cardinal Lagrangian-Eulerian scheme and the right column using the intercardinal Lagrangian-Eulerian scheme. From top to bottom the uniform Cartesian computational grids are: 50×50 and 200×200. The colorbars are linearly scaled between zero and the maximum value of $M_{0,0}$ in the domain.

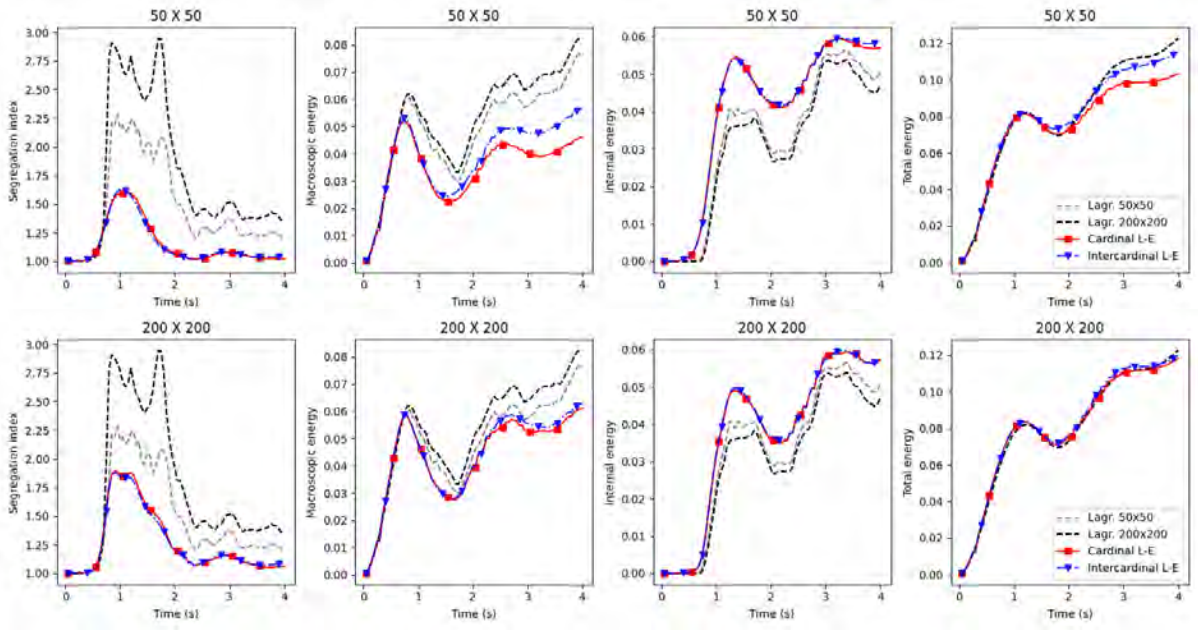

Figure 6: Taylor-Green vortex flow: evolution in time of the phase-average statistics (eqs. (26) and (28)). The segregation index, macroscopic kinetic energy, internal kinetic energy and total kinetic energy are given for two grid sizes: upper row = 50×50, lower row = 200×200.

the Lagrangian dynamics are much easier to handle and its contribution can be calculated with less simplifications and are hence believed to be superiors to the Eulerian approximation suggested in literature.

Acknowledgments

This work is funded by the PhD fellowship Strategic Basic Research of the Research Foundation-Flanders (FWO), as part of the project (1S C61 19N).

References

[1] D. Ramkrishna, Population Balances, Vol. 1, 2000.
[2] D. L. Marchisio, R. O. Fox, Computational Models for Polydisperse Particulate and Multiphase Systems, Cambridge Series in Chemical Engineering, 2013.
[3] H. Struchtrup, Grad's moment method, Springer Berlin Heidelberg, Berlin, Heidelberg, 2005, pp. 87–107. doi:10.1007/3-540-32386-4-6.
[4] R. O. Fox, A quadrature-based third-order moment method for dilute gas-particle flows, Journal of Computational Physics 227 (12) (2008) 6313–6350.
[5] C. Chalons, R. Fox, M. Massot, A multi-gaussian quadrature method of moments for gas-particle flows in a les framework, Studying Turbulence Using Numerical Simulation Databases, Center for Turbulence Research, Summer Program 2010, Stanford University (2010) 347–.
[6] C. Yuan, R. Fox, Conditional quadrature method of moments for kinetic equations, Journal of Computational Physics 230 (22) (2011) 8216–8246.
[7] F. Laurent, A. Vié, C. Chalons, R. O. Fox, M. Massot, A hierarchy of Eulerian models for trajectory crossing in particle-laden turbulent flows over a wide range of Stokes numbers, Proceedings of the Summer Program 2012 - Center for Turbulence Research (2012) 193–204.
[8] C. Chalons, D. Kah, M. Massot, Beyond pressureless gas dynamics: Quadrature-based velocity moment models, Communications in Mathematical Sciences 10 (4) (2012) 1241–1272.
[9] C. Chalons, F. Laurent, M. Massot, A. Vié, Multivariate Gaussian extended quadrature method of moments for turbulent disperse multiphase flow.
[10] R. O. Fox, F. Laurent, A. Vié, Conditional hyperbolic quadrature method of moments for kinetic equations, Journal of Computational Physics 365 (2018) 269–293.
[11] M. Van Cappellen, M. R. Vetrano, D. Laboureur, Higher order hyperbolic quadrature method of moments for solving kinetic equations, Journal of Computational Physics (*submitted*).
[12] V. Vikas, Z. J. Wang, A. Passalacqua, R. O. Fox, Realizable high-order finite-volume schemes for quadrature-based moment methods, Journal of Computational Physics 230 (13) (2011) 5328–5352.
[13] D. P. Karadimou, N.-C. Markatos, Study of the Numerical Diffusion in Computational Calculations, Numerical Simulations in Engineering and Science-doi:10.5772/intechopen.75660.

Development of a high-order fluid solver for multicomponent air plasma sheath

Giuseppe Matteo Gangemi

Aeronautics and Aerospace Department, von Karman Institute for Fluid Dynamics, Belgium, giuseppe.gangemi@vki.ac.be

Supervisor: Thierry Magin

Professor, Aeronautics and Aerospace Department, von Karman Institute for Fluid Dynamics, Belgium, magin@vki.ac.be

University Supervisor: Koen Hillewaert

Associate Professor, Aerospace and Mechanical Engineering, University of Liege, Belgium, koen.hillewaert@uliege.be

University Supervisor: Alejandro Alvarez Laguna

Research Fellow, Laboratory of Plasma Physics, École Polytechnique, France, alejandro.alvarez-laguna@lpp.polytechnique.fr

Abstract

Low temperature plasmas in contact with solid walls tend to form two distinct regions: the bulk region, where quasi-neutrality prevails, and the sheath region near the walls, where positive space charge is built. This phenomenon is due to a higher mobility of electrons, that creates an electric potential structure that accelerates the ions towards the surface and repels electrons. Fluid simulations of the formation of air plasma sheath come with great challenges: the system of equations is particularly stiff due to the disparity of velocity, space and time scales; electrons travel at speeds lower than their sonic velocity, leading to difficulties for classical compressible solvers; finally, a complex air chemistry mechanism needs to be coupled to the flow solver. For this project, we aim to develop a high order fluid solver to simulate the formation of air plasma sheath and tackle all these challenges: the work will address the modeling of the physics and chemistry of the mixture, the development of efficient numerical methods, and the validation of the computational tool using existing experimental data. We plan to implement an innovative multicomponent diffusion model in the high-order platform Argo, focusing on implicit and asymptotic preserving scheme strategies. In turn, the tool developed will allow us to perform highly accurate simulations of plasma-wall interactions, in particular the study of the electron transpiration cooling phenomenon for materials used as heat shield of hypersonic cruise vehicles.

Keywords: air plasma, sheath, asymptotic-preserving scheme, discontinuous galerkin

Development of gas-surface interaction models from continuum to rarefied flow regimes

Pedro Jorge

Aeronautics and Aerospace Department, von Karman Institute for Fluid Dynamics, Belgium, pedro.jorge@vki.ac.be

Supervisor: Thierry E. Magin

Professor, Aeronautics and Aerospace Department, von Karman Institute for Fluid Dynamics, Belgium, magin@vki.ac.be

University Supervisor: Annick Hubin

Professor, Department Materials and Chemistry, Vrije Universiteit Brussel, Belgium, annick.Hubin@vub.be

Abstract

In low Earth orbits (300-150 km), used for new concepts of air-breathing satellites, the interaction between high velocity gases and surface materials enhances corrosion reactions that would be otherwise impossible with low flow velocity and surface temperatures. Moreover, the accommodation of the particles momentum to the surface impacts platform drag and the collector efficiency, which optimization is of paramount importance to maintain orbit with minimal propulsion. At lower altitudes (100-60 km), the thermal behavior of materials and surface chemical reactions play a crucial role in predicting the survivability of reentering objects. Thus, understanding the Gas-Surface Interaction (GSI) of different pairs of chemical species and materials requires studying which reactions occur between the surface and impinging flow, and the mechanisms of momentum and energy transfer to the surface.

This project aims to study GSI with both experimental and numerical investigations. To this end, we propose to use a ground-breaking low-density facility currently being developed at VKI to perform aerodynamic and GSI studies in the rarefied regimes, as well as the Plasmatron facility to study oxidation in the continuum regime. Furthermore, the flow in the newly built low-density facility will be characterized comprehensively through both invasive and non-invasive diagnostics and the facility will be extended to allow for experiments that quantify gas-surface interaction. Relevant space materials will be tested in both rarefied and continuum regimes and their surface degradation will be assessed post-test via material characterization techniques available at the SURF group lab at VUB.

Moreover, the predictions of existing GSI models will be compared to data from experimental campaigns and their validity assessed for the conditions of interest. Possible model refinements for specific gases and surfaces materials pairings will be envisaged based on detailed molecular dynamics simulations. The developed model will be implemented into the SPARTA DSMC code and validated based on VKI's low-density facility experimental campaigns. The final goal is to obtain, through an experimentally validated multiscale approach, a database of GSI coefficients to perform predictive numerical simulations and evaluate candidate space materials regarding their drag, thermal, and chemical behaviour.

Keywords: Gas-Surface-Interaction, Rarefied flow, Oxidation

Modeling and simulation of air plasmas using particle methods applied to Air-Breathing Electric Propulsion

Pietro Parodi

Aeronautics and Aerospace Department, von Karman Institute for Fluid Dynamics, Belgium, pietro.parodi@vki.ac.be

Supervisor: Thierry Magin

Professor, Aeronautics and Aerospace Department, von Karman Institute for Fluid Dynamics, Belgium, magin@vki.ac.be

University Supervisor: Giovanni Lapenta

Professor, Department of Mathematics, KU Leuven, Belgium, giovanni.lapenta@kuleuven.be

Abstract

An emerging concept called Air-Breathing Electric Propulsion (ABEP) could allow to fly spacecraft in the currently unexploited Very Low Earth Orbit using air collected from the atmosphere as propellant for a plasma thruster. A small-scale hypersonic low density facility funded by ESA is going to be commissioned at the von Karman Institute for Fluid Dynamics (VKI) for experimental testing of an ABEP intake-collector system. The stream of fast particles needed in the facility will be accomplished through electrostatic particle acceleration, using a so-called particle flow generator (PFG). These devices are derived from laboratory plasma sources and plasma thrusters for space propulsion. Plasma modeling and simulation is required to design the ground testing facility and the experiments, as well as to extrapolate the results obtained from ground testing to orbital conditions. The hybrid Particle-in-Cell (PIC)/Direct Simulation Monte Carlo (DSMC) method is appropriate to simulate the collisional, nonequilibrium plasma flow involved. The 2D PIC–DSMC code PANTERA is currently being developed at VKI. In this PhD work, we will use this tool and expand its capabilities, taking advantage of the experience accumulated at the Centre for mathematical Plasma Astrophysics (CmPA) of KU Leuven on advanced Particle-in-Cell methods. The interaction between species composing the air mixture is complex, and will require adequate modeling of collisions, internal molecular degrees of freedom, chemical reactions, and plasma-wall interaction. Additionally, since the systems length and time scales are large compared to the typical length and time scales of plasma oscillations, particle methods present a great computational cost. We will develop and implement advanced numerical schemes, such as the energy conserving semi-implicit method, to help overcome these limitations. Appropriate grid discretization methods and efficient parallelization procedures will be investigated. The final objective is to enable the simulation of a complex, coupled, and multi-scale plasma system such as the ABEP system at the kinetic level, and to provide a predictive model of the ABEP intake in ground testing conditions. Results from experiments in the VKI low density facility, together with a procedure for uncertainty quantification of the numerical results, will allow a robust validation of our models and methods.

Keywords: Particle-in-Cell, Direct Simulation Monte Carlo, particle flow generator, low density facility, nonequilibrium, rarefied.

Development of high-order adaptive algorithms for simulating magnetic reconnection processes with uncertainty quantification.

Firas Ben Ameur

Aeronautics and Aerospace Department, von Karman Institute for Fluid Dynamics, Belgium, firas.benameur@vki.ac.be

Supervisor: Andrea Lani

Research Expert, Aeronautics and Aerospace Department, von Karman Institute for Fluid Dynamics, Belgium, lani@vki.ac.be

University Supervisor: Stefaan Poedts

Professor, Centre for mathematical Plasma-Astrophysics, KU Leuven, Belgium – Institute of Physics, University of Maria Curie-Skłodowska, ul. Radziszewskiego 10, PL-20-031 Lublin, Poland stefaan.poedts@kuleuven.be

Abstract

The present paper addresses the development and implementation of the first r-adaptive mesh refinement (r-AMR) algorithm for a high-order Flux Reconstruction solver. The r-refinement consists of nodal re-positioning while keeping their number and connectivity constants. The developed algorithms are based on physics-driven spring-analogies, where the mesh can be seen as a network of fictitious springs. While AMR increases the local mesh density, the high-order Flux Reconstruction method potentially provides more accurate detection of complex flow features over relatively coarser mesh resolution, when compared to low-order methods. In this work, a concise overview of the Flux Reconstruction method and spring-based mesh adaptation techniques will be given, followed by some promising results of r-AMR applied to benchmark high-order supersonic flow simulations.

Keywords: High-Order CFD, Hypersonics, Flux Reconstruction, r-refinement, Curved meshes.

1. Introduction

The vast majority of state-of-the-art Computational Fluid Dynamic (CFD) codes tackling high-speed flows rely upon low-order solvers, including Finite Volume (FV), Finite Difference (FD), and Finite Element (FE) schemes, that are robust and easy to implement. CFD analysts acknowledge the importance of using well-designed grids to obtain accurate flow results, since mesh/shock misalignment leads to shock instability, noisy post-shock regions and poor heat flux predictions [1; 2]. State-of-the-art aerothermodynamics (ATD) simulations require demanding mesh generation processes and grid convergence studies resulting in a high run-time and considerable computational effort. All this makes the numerical analysis more challenging and time-consuming especially for those kinds of applications where high-grid density is needed, around shocks, in order to resolve flow discontinuities and obtain accurate physical results [3; 4; 5]. To overcome those deficiencies, Adaptive Mesh Refinement (AMR) represents, on one hand, a robust procedure for improving the quality of the physical results due to a local increase of the grid resolution and mesh/shock alignment. On the other hand, high-order methods have drawn considerable attention among researchers in the field of CFD due to their increased computational efficiency "per degree of freedom" over their low-order counterparts [6]. In our previous work [7; 8], a robust and efficient r-refinement algorithm (i.e. repositioning of mesh points based on the solution of a pseudo-elastic system of equations) has been developed and applied to multiple Finite Volume test cases. The existing FV-AMR algorithm works on triangles, quadrilateral and tetrahedral cells, is fully parallel, implemented as a standalone module, and totally physics-independent, letting the user decide which monitor physical quantity to use for driving the adaptation according to the application. In addition, in [9; 10; 11], a state-of-the-

art parallel and fully implicit high-order Flux Reconstruction (FR) code has been implemented and used to solve Euler/Navier- Stokes equations, where its structure is extremely modular and can be easily coupled to arbitrary sets of advection-diffusion-reaction partial differential equations. In this work, we propose the development of r-adaptive mesh refinement (r-AMR) algorithms within the FR framework as well and its application to a number of representative test cases featuring high-speed flows. This novel coupling will benefit from:

1. a low initial mesh resolution,
2. an increase of the solution order (i.e. isotropic p-refinement),
3. a shock/mesh alignment to avoid smearing of the flow that leads a non-physical distribution of the entropy between streamlines,
4. and finally, an increase of the grid density around the flow discontinuities in order to overcome the reduced order of accuracy in the shock area (i.e. the shock is contained in a more confined space).

The resulting solver has been implemented within the COOLFluiD platform [12; 13] (a world-class open-source framework for multi-physics modeling and high-performance computing, particularly focused on simulating hypersonic flows [14; 15], radiation [16], laboratory [17] and space plasmas [18; 19; 20; 21; 22]). After giving a review about state-of-the-art FR method, following the work of Vandenhoeck and Lani [10], in Sec.2 and spring-based AMR, following the work of Ben Ameur and Lani [7; 8] in Sec.3, a simple and intuitive method, denominated: ***Vertex springs***, will be presented in Sec.4 as well as the results of the adaptation derived from the latter method. Section 5 will be the center of our novel work: the novel method, denominated ***Sub-cell order-dependent spring analogy***, will show its potential, in Sec.6, for linear and curvilinear meshes compared to some analytical and h-refinement state-of-the-art results.

2. Flux Reconstruction Solver

The FR method was originally developed by Huynh in [23]. It is a compact high-order FE-type method that offers a unifying formulation for various classes of high-order schemes (e.g. nodal Discontinuous Galerkin, Spectral Finite Difference). The formulation of the FR approach proposed by Huynh is applicable to deal with advection-diffusion problems on structured and unstructured grids [24]. This section presents a brief review of the Flux Reconstruction method in one dimension (1D), including the following main algorithmic steps, taken from [9; 10; 11]:

1. Consider solving the one-dimensional advection-diffusion problem within an arbitrary domain Ω, given by:
$$\frac{\partial u}{\partial t} + \frac{\partial f}{\partial x} = 0 \tag{1}$$
In Eq.1, $x \in \Omega = [x_L, x_R]$ is the one dimensional coordinate, t is the time variable, $u(x,t)$ is a conservative variable, and $f = f\left(u, \frac{\partial u}{\partial x}\right)$ is the flux which is a scalar for the 1D case. As the FR method is classified as a FE-type method, the first step of the procedure involves partitioning the spatial domain Ω into a finite number N of non-overlapping, non-empty, open sub-domains Ω'_n such that:
$$\Omega'_n = \{x \mid x_n < x < x_{n+1}\}, \tag{2}$$
with $x_1 = x_L$ and $x_{N+1} = x_R$.
2. The exact solution u of the conservation law (Eq.1) is approximated by a continuous function u_n^δ within each element Ω_n. This function u_n^δ corresponds to a polynomial of degree P within Ω_n and is identically zero on $\Omega \backslash \Omega_n$, while being generally discontinuous across elements. The approximate solution polynomial u^δ within the entire domain Ω is constructed as:
$$u^\delta = \sum_1^N u_n^\delta. \tag{3}$$
In the same manner, the exact flux f is approximated by a polynomial of degree $P+1$ within each sub-domain Ω_n.
3. Each element Ω_n together with the approximate solution u_n^δ and flux f_n^δ inside it, is transformed to a standard reference element $\Omega_S = \{\xi \mid -1 \leq \xi \leq 1\}$, where all computations are performed. The solution u_n^δ within each sub-domain Ω_n can then be obtained by solving the transformed conservation equation (Eq.1) within the reference element Ω_S:
$$\frac{\partial \hat{u}^\delta}{\partial t} + \frac{\partial \hat{f}^\delta}{\partial \xi} = 0, \tag{4}$$
with $\xi \in \Omega_S$, $\hat{u}^\delta = \hat{u}^\delta(\xi,t) = J_n u_n^\delta(\Theta_n(\xi),t)$ and $\hat{f}^\delta = \hat{f}^\delta(\xi,t) = f_n^\delta(\Theta_n(\xi),t)$, where J_n represents the Jacobian of the mapping $\Theta_n(\xi)$.

4. The approximate solution $\hat{u}^{\delta}$ is defined as a degree P polynomial based on a Lagrange polynomial basis related to the set of $P+1$ distinct solution points ξ_i within Ω_S, where the two endpoints of the standard element Ω_S, i.e. $\xi = 1$ and $\xi = -1$, are referred to as the flux points.
5. This step consists of determining a common interface solution $\hat{u}^{\delta I}$ at the boundaries of the standard element Ω_S, i.e. $\xi = \pm 1$, where the flux points of two neighboring elements coincide.

$$u^{\delta I} = \frac{u^{\delta -} + u^{\delta +}}{2}, \tag{5}$$

where $u^{\delta -}$ and $u^{\delta +}$ are respectively the approximate solutions evaluated at the left and right boundaries.
6. A corrected solution gradient $\hat{q}^{\delta}$ is computed. $\hat{q}^{\delta}$ is defined in terms of two correction functions $g_L(\xi)$ and $g_R(\xi)$ of degree $P+1$, which approximate the zero function within the reference element Ω_S, and satisfy the following boundary conditions: [25]

$$g_L(-1) = 1, \qquad g_R(-1) = 0, \tag{6}$$

$$g_L(1) = 0, \qquad g_R(1) = 1. \tag{7}$$

Furthermore, the correction function for the right boundary $g_R(\xi)$ is defined as the reflection of the correction function $g_L(\xi)$ with respect to the vertical axis in order to ensure symmetry of the correction process $g_L(\xi) = g_R(-\xi)$. The corrected solution gradient $\hat{q}^{\delta}$ is then computed via the following expression:

$$\hat{q}^{\delta} = \frac{\partial \hat{u}^{\delta}}{\partial \xi} + (\hat{u}_L^{\delta I} - \hat{u}_L^{\delta})\frac{dg_L}{d\xi} + (\hat{u}_R^{\delta I} - \hat{u}_R^{\delta})\frac{dg_R}{d\xi}, \tag{8}$$

where $\hat{u}_L^{\delta I}$ and $\hat{u}_R^{\delta I}$ are the common interface solutions at the left and right boundaries of Ω_S, and $\hat{u}_R^{\delta} = \hat{u}^{\delta}(1)$ and $\hat{u}_L^{\delta} = \hat{u}^{\delta}(-1)$ are the values of the approximate solution polynomial at the left and right boundaries. The Vincent-Castonguay-Jameson-Huynh (VCJH) scheme is used to define the exact polynomial expression of g_L and g_R, as found in [26].
7. On the reference element Ω_S, the approximate discontinuous flux $\hat{f}^{\delta D}(\xi)$ is calculated. Based on $\hat{u}^{\delta}$ and $\hat{q}^{\delta}$, the approximate discontinuous flux $\hat{f}^{\delta D}$ is constructed as a polynomial of degree P in the same manner as the approximate solution $\hat{u}^{\delta}$.
8. The transformed common interface fluxes $\hat{f}^{\delta I}$ at the flux points of the standard element Ω_S, i.e. $\xi = \pm 1$, is calculated. $\hat{f}_L^{\delta I}$ and $\hat{f}_R^{\delta I}$ are denoted as the common interface flux at the left and right end of the standard element, respectively. In the case of the Navier-Stokes equations, it is computed as the sum of a convective and a diffusive term. More details can be found in [10; 11].
9. The flux must be continuous across element boundaries in order to obtain a conservative scheme. Therefore, a correction flux function $\hat{f}^{\delta C}$ is added to the approximate discontinuous flux $\hat{f}^{\delta D}$ in order to obtain a continuous flux $\hat{f}^{\delta}$. The correction flux $\hat{f}^{\delta C}$ is a polynomial of degree $P+1$ defined as:

$$\hat{f}^{\delta C} = (\hat{f}_L^{\delta I} - \hat{f}_L^{\delta D})h_L(\xi) + (\hat{f}_R^{\delta I} - \hat{f}_R^{\delta D})h_R(\xi), \tag{9}$$

where $\hat{f}_L^{\delta D} = \hat{f}^{\delta D}(-1)$ and $\hat{f}_R^{\delta D} = \hat{f}^{\delta D}(1)$ are the values of the approximate discontinuous flux at the left and right boundaries. The continuous flux $\hat{f}^{\delta}$ within the standard element Ω_S is then written as the sum of the approximated discontinuous flux and the correction flux.
10. The divergence of the total flux $\hat{f}^{\delta}$ at each solution point ξ_i is computed. This step is relatively straightforward as the derivatives of both the Lagrange polynomials and correction functions are exactly known.
11. Finally, a time marching strategy is applied to advance the approximate solution $\hat{u}^{\delta}$ in time using the following expression:

$$\frac{d\hat{u}_i^{\delta}}{dt} = -\frac{\partial \hat{f}^{\delta}}{\partial \xi}(\xi_i). \tag{10}$$

The extension of the 1D philosophy of the FR method to deal with 2D quadrilateral is relatively straightforward. Genuinely, a tensor product basis is defined based on the 1D Lagrange polynomials on the reference element, as shown in [23].
Since the FR method can obtain arbitrary high orders of accuracy simply by increasing the order of the polynomials that represent the approximated solution, the method is inherently compact and does not require a wide stencil at higher orders. This fact goes hand in hand with r-refinement since this latter also requires only compact stencils.

3. Spring-Based Adaptive Mesh Refinement

The numerical investigation of high-speed flow problems may require extremely fine meshes over narrow regions of the physical domain to resolve the

steep gradients occurring in the flow. The high-gradient regions are not known to the analyst a priori. Thus, a-posteriori AMR techniques represent a robust procedure to better capture the relevant flow features, to improve the quality of the physical results, and to ensure, for example, the alignment of the computational grid cells with the flow discontinuities at the price of an increased algorithmic complexity. In [7; 8], the authors have proposed and developed, within a Finite Volume framework, r-AMR based on a user-defined flow field variable, e.g. density or pressure, that relies upon the solution of pseudo-elastic systems associated to the given mesh. This section presents a brief review of the r-refinement method that can be found in [7; 8].

Let $n \in \mathbb{N}$ be the number of the nodes in a mesh $\mathcal{M}$ and let $\mathbf{P}$ the set of the node's positions inside $\mathcal{M}$. The incidence matrix $\mathbf{L}$ is defined as:

$$L_{ij} = \begin{cases} 1, & \text{if nodes } i \text{ and } j \text{ are edge-connected} \\ 0, & \text{otherwise.} \end{cases}$$

We want to equidistribute the mesh nodes according to a positive scalar function $W = W(x)$. For the 1D case, between node positions x_i and x_{i+1} we have,

$$\int_{x_i}^{x_{i+1}} W(x)dx = constant. \tag{11}$$

For the multidimensional case, let $\{\mathbf{P_i},\mathbf{P_j}\}$ be a set of two node's positions such that $L_{ij} = 1$, and let $\mathbf{r}(s)$ be the edge parametrization obeying to the Eq.12

$$\mathbf{r}(s) = \mathbf{P_i} + s(\mathbf{P_j} - \mathbf{P_i}). \tag{12}$$

Then, in order to equidistribute the mesh nodes, the line integral I, expressed in Eq.13, must be constant.

$$I = \int_0^1 W(\mathbf{r}(s)) \cdot r'(s)ds = constant. \tag{13}$$

The Eq.13 is the solution of the Euler-Lagrange equation to the minimization of the energy equation (14).

$$E_{ij} = L_{ij} \int_0^1 W(\mathbf{r}(s))(\mathbf{P_j} - \mathbf{P_i})^2 ds, \tag{14}$$

where, the incidence matrix $\mathbf{L}$ is artificially added ensuring the physical meaning of the energy function E. The weight function W is considered constant between two edge-connected nodes, such that $W = W_{ij}$. Hence, the energy equation can be simplified into Eq.15

$$E_{ij} = L_{ij}W_{ij}(\mathbf{P_j} - \mathbf{P_i})^2 \tag{15}$$

Equation 15 is analogous to the mechanical spring potential energy equation with a stiffness coefficient W and equilibrium spring length set to zero. The optimization process of the nodes mesh positions is formulated through the assembly and solution of a linear system, including the following main algorithmic steps:

1. The analytic Jacobian is defined as:

$$\frac{\partial E_{ij}}{\partial \mathbf{P_i}} = -2L_{ij}W_{ij}(\mathbf{P_j} - \mathbf{P_i}) = 0. \tag{16}$$

2. After simplifying the constant and collecting the contributions of each node, we obtain:

$$\sum_{j=1}^{n} L_{ij}W_{ij}(\mathbf{P_j} - \mathbf{P_i}) = 0. \tag{17}$$

3. The resulting linear system, to be solved, can be expressed as:

$$\mathbf{AP} = \mathbf{b}, \tag{18}$$

where

$$A_{ij} = \begin{cases} -L_{ij}W_{ij}, & if\ i \neq j \\ \sum_{j=1}^{n} L_{ij}W_{ij}, & if\ i = j. \end{cases}$$

and $\mathbf{b}$ contains the non-homogeneous terms of the Dirichlet or the Neumann boundary conditions.

4. Solving the linear system using an iterative solver, i.e. the Generalized Minimal RESidual (GMRES) algorithm complemented by a parallel Additive Schwartz Preconditioner as provided by the PETSc toolkit [27; 28; 29; 30].

As a result, the nodal re-positioning obeys to the following relation:

$$\mathbf{P}^{k+m} = (1 - \omega)\mathbf{P}^k + \omega\mathbf{P}_{new}, \tag{19}$$

where $\mathbf{P}^k$ is the old node position at iteration k, $\mathbf{P}^{k+m}$ is the new *relaxed* node position at iteration $k + m$ and $\mathbf{P}_{new}$ is computed from Eq.18. An under-relaxation factor ω is also added to the nodal re-positioning equation to smooth the nodal displacement and mitigate, for certain cases, mesh tangling. However, ω affects negatively the convergence rate, consequently, a trade-off between the flow solver convergence and the pseudo-elastic convergence rate was sought and found in $\omega = O(10^{-2})$.

Two types of the boundary conditions are defined within our r-AMR algorithms:

1. Dirichlet (i.e. locked node) where the node position is kept constant:

$$P_i^m = P_i^0,$$

2. Neumann (i.e. moving node in boundary) where only the tangential displacement is allowed. Mathematically, this implies:

$$\frac{\partial(\mathbf{P_i} \cdot \mathbf{n_i})}{\partial \mathbf{x}} = 0,$$

where $\mathbf{n_i}$ is the boundary face normal vector.

4. Vertex Spring approach for linear meshes

4.1. Methodology

Figure 1(left) shows the linear spring analogy for 2D quadrilateral meshes, whereas, Eq.20 expresses the linear spring physics-based stiffness coefficient, k_{ij}^L, between two edge-connected nodes i and j with a respective nodal state U_i and U_j. The weight function introduced in the previous section is described as:

$$W_{ij} = k_{ij}^L = |U_j - U_i|. \tag{20}$$

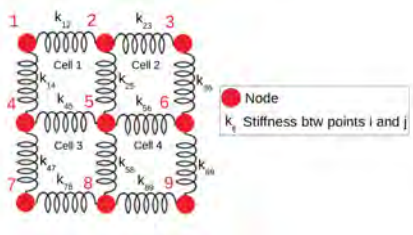

Figure 1: Spring network of 2D quadrilaterals

In order to evaluate the nodal states used to compute the linear spring stiffness in Eq.20, the Pth-order polynomial describing the approximated solution is extrapolated, thanks to the Lagrange polynomials, to the corner nodes as shown in Fig.2. To this end, the nodal state at a node i is evaluated as the average of the contributions of each solution polynomial inside elements attached to the considered node i. Eq.21 corresponds to the latter approach.

$$U_i = \frac{1}{N} \sum_{n=1}^{N} \hat{u}_n^{\delta}(\boldsymbol{x_i}), \tag{21}$$

where $\hat{u}_n^{\delta}$ is the approximated solution polynomial within the elements n, $\boldsymbol{x_i}$ is the coordinates of the node i and N represents the number of elements attached to the node i.

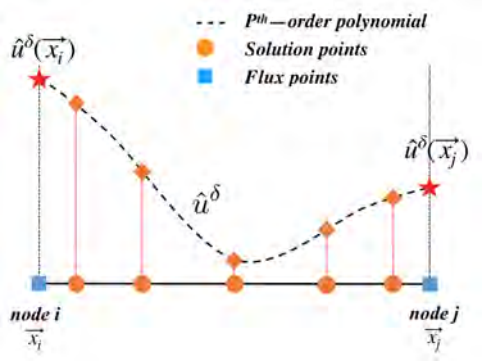

Figure 2: Evaluation of the nodal states

4.2. Results

The results of the vertex spring method are obtained for the steady 2D wedge channel flow. The test case conditions are presented in Tab.1, Tab.2 and Tab.3, while the test case geometry and the corresponding structured mesh are shown in Fig.3.

Table 1: 2D wedge – Flow characteristics

Physical Model	M	ρ [-]	ρu [-]	ρv [-]	ρE [-]
Perfect gas	2	1	2.36643	0	5.3

Table 2: Wedge – Mesh characteristics

Dimensions	Type	# Elements	
2D	Quadrilateral	3710	
BC 1	BC 2	BC 3	BC 4
Inlet	Outlet	Symmetry	no-slip wall

Table 3: Wedge – r-refinement

Spring Network	Monitor Variable	Process Rate
Linear	Density	20
Stop AMR Iteration	minPer	maxPer
7000	0.30	0.55

minPer and maxPer (minimum percentile and maximum percentile, respectively) are user-defined parameters that truncate and bound the linear spring stiffness coefficient through a P^2 algorithms. More details about the P^2 algorithms can be found in [31] and about the choice of the minPer and maxPer in [8]

As shown in Fig.4, in the final adapted solution, the oblique shock, the expansion wave, and their reflections are perfectly resolved for the different orders,

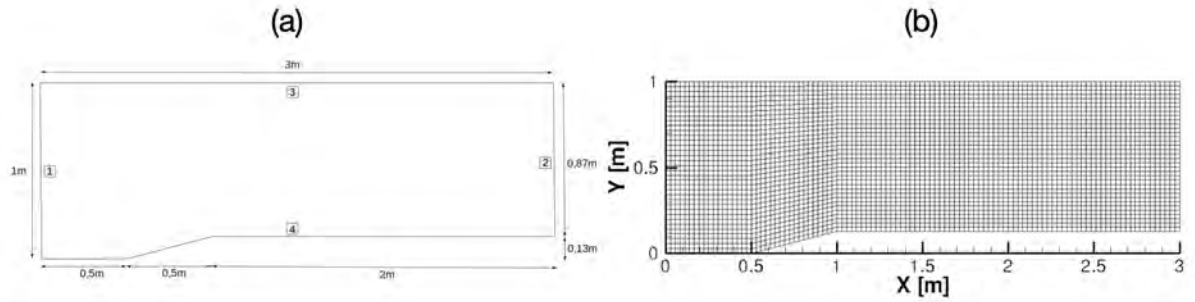

Figure 3: (a) 2D wedge geometry – (b) Initial mesh

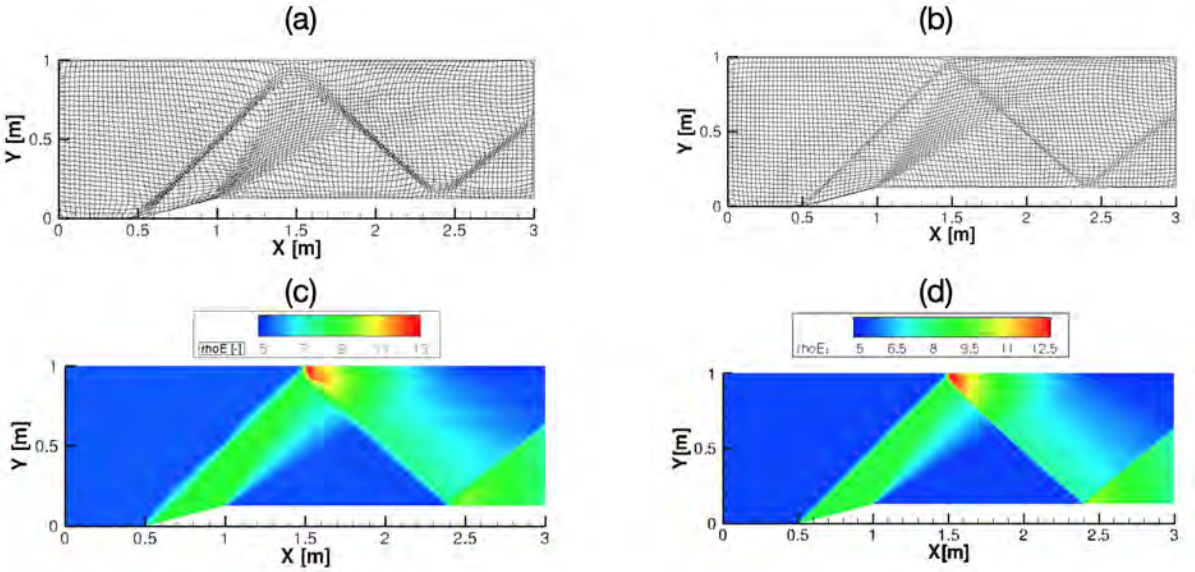

Figure 4: (a) P1 Adapted Mesh – (b) P3 Adapted Mesh – (c) P3 non-adapted energy density field – (d) P3 adapted energy density solution

mainly $P1$ (i.e. second order of accuracy in space) and $P3$ (i.e. fourth-order of accuracy in space). The best accuracy is obtained by combining the AMR algorithms and the FR solver, as demonstrated by the $P3$ adapted wedge test case (Fig.4,d) compared to the $P3$ non-adapted case (i.e. Fig.4,c).

5. Sub-cell Order-dependent spring analogy

5.1. Motivation: Limitation of the vertex spring approach

The FR method is based on the knowledge of the state values in the solution points. These solution points are always interior to the element and are therefore different from the mesh nodes. If we consider the use of a coarse mesh across a shock (which should be possible since we are using a high-order method), the state values obtained at the mesh nodes might be very close to each other. To illustrate this possibility, let us consider a P3 polynomial reconstruction in a 1D reference element as shown in Fig.5. This graph, which was generated with Matlab, displays the variations of a normalized density. Starting with the known state values at the 4 solution points (located at the Gauss-Legendre quadrature points), a polynomial Lagrangian fit was computed and the state values at the boundaries (or flux points) were obtained by extrapolation.

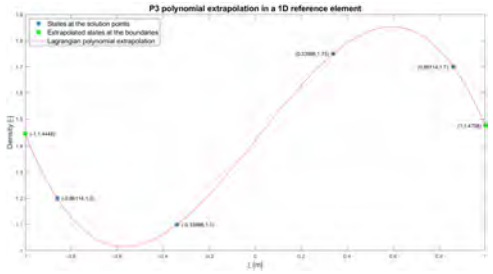

Figure 5: P3 polynomial reconstruction in a 1D reference element with the solution points located at the Gauss-Legendre quadrature points

The normalized density profile seems to indicate the presence of a physical phenomenon causing a high-gradient in a narrow region because of the abrupt density increase between the two centre solution points. However, when looking at the densities extrapolated at the boundaries, the values appear to be very close to each other. The ratio of the maximum density variation inside the cell and of the density variation between the flux points is indeed equal to

$$\frac{1.75 - 1.1}{1.4758 - 1.4448} \approx 23.38$$

. This ratio, which could be infinite if the polynomial fit leads to equal state values at both flux points, shows that basing the r-AMR on the boundary points or on the corner nodes in 2D (a.k.a. vertex spring approach) can result in a huge lack of information. The main consequence is that the mesh is much stiffer than it should as the physical gradients (which are the main driver of the refinement process) are not detected properly. Therefore, the r-AMR tends to be less effective and does not capture all the characteristic complexity of supersonic flow phenomena.
This problem is further illustrated in Fig.6 which represents the loss of information caused by a negligence of the internal behaviour of the polynomial reconstruction. Whereas the sum of the gradients between each flux and solution point (purple lines) is 1.7225, the gradient seen with the flux points only (yellow lines) is 0.031. As these values are equal to the physics-based linear spring constant through Eq.20, the mesh will be much more flexible in the purple case than in the yellow one. In order to reach this flexibility, we adapted the spring analogy and took into account these internal variations by exploiting the order of the polynomial reconstruction.

5.2. Concept

To accomplish this goal, we decided to exploit the properties of the FR method and to build a novel sub-cell order-dependent spring analogy. It is illustrated in Fig.7 for a P2 polynomial extrapolation. This figure depicts the edge linking two nodes and shows where the new springs are placed: between the flux points and the nodes.
Our key idea is based on considering a network of springs located at both sides of a face. Indeed, the polynomial reconstruction does not impose the continuity of the solution across the elements and, therefore, the state values are generally different at each side of the face, i.e. $U_{i,\text{Left}} \neq U_{i,\text{Right}}$. In order to take into account this discontinuity, the stiffnesses of the springs on the left side of the face are computed based on the state values obtained at the left of the face only. This assertion holds for the stiffnesses of the springs located on the right side of the face as they depend on the right state values only. In COOLFluiD, the flux points are not geometric entities and cannot be moved independently as the nodes can. Therefore, they cannot be included in the stiffness matrix $\mathbf{A}$ (see Eq.18). As a result, equivalent spring constants between each pair of edge-connected nodes need to be computed from the stiffnesses illustrated in Fig.7. To do so, we should note that, on each side of the face, the springs are connected end-to-end, i.e. in series. A look at the Hooke's law yields that the equivalent stiffness k_{eq} of springs placed in series with a stiffness k_i should be computed as: $\frac{1}{k_{\text{eq}}} = \sum_i \frac{1}{k_i}$. However, the physics-based linear spring constant of Eq.20 behaves inversely with respect to a mechanical spring. Indeed, when the gradient of the monitored field variable U increases, the linear stiffness increases, tends to make the mesh more flexible, and thus the nodes will move more easily. As a consequence, we compute the equivalent stiffness on the left of a face $k_{\text{eq,L}}$ as $k_{\text{eq,L}} = \sum_i^N k_{i,i+1,\text{L}}$ where N equals the number of springs placed in series ($N = 4$ for a P2 extrapolation) and $k_{i,i+1,\text{L}}$ is the stiffness of the spring placed between point i and $i+1$ on the left side of the face. The same procedure is followed for the right side of the face. The total stiffness between two edge-connected nodes can finally be computed. Although the equivalent spring of stiffness $k_{\text{eq,L}}$ and the equivalent spring of stiffness $k_{\text{eq,R}}$ appear to be parallel to each other, their contributions are summed. Because an inner edge of a quadrilateral element is shared by two elements (left and right), its total stiffness k_{eq} is computed as $k_{\text{eq}} = k_{\text{eq,L}} + k_{\text{eq,R}}$. The main benefits of this method are its sub-cell res-

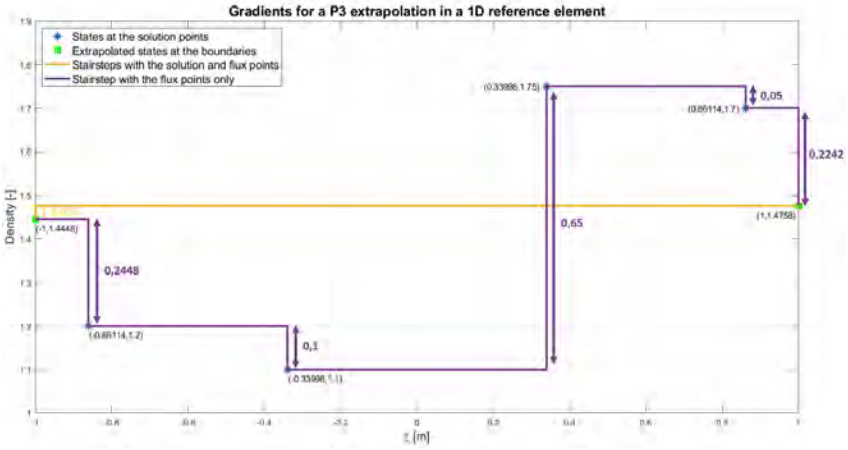

Figure 6: Gradients for a P3 polynomial reconstruction in a 1D reference element

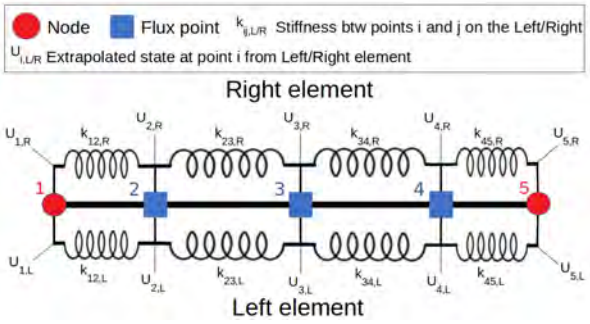

Figure 7: Sub-cell order-dependent spring analogy, face linking node 1 and 2 (red dots) with 3 flux points (blue squares) for a P2 reconstruction

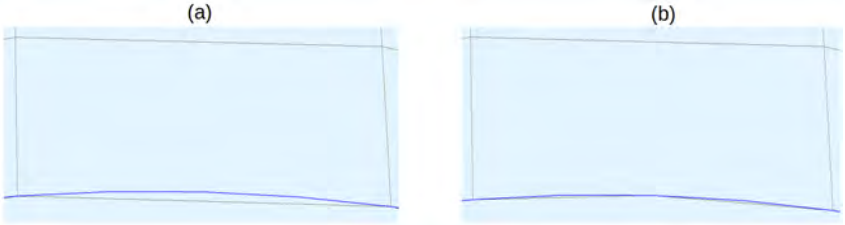

Figure 8: Approximation of the dark blue curved boundary with: (a) Q1, (b) Q2

olution and its order dependency. Indeed, it tends to increase the flexibility of the mesh as the order of the polynomial extrapolation grows (because the number of spring contributions increases with the order). This is very important as we would like to use high-order polynomial reconstructions (to improve the accuracy per DOF) with coarse grids (to decrease the computational cost). Our novel spring analogy allows the use of these coarse grids even in zones of high-gradient thanks to its sub-cell resolution.

5.3. Extension to curved meshes

5.3.1. Motivation

When studying flows over curved bodies (such as cylinders), Q1 meshes produce unsatisfying solutions. This is due to the discrepancy between the physical boundary which is curved and its numerical description which is straight. As illustrated in Fig.8, the Q1 mesh is not capable of fitting the curved boundary properly. As already reported in [32; 33], if the order of the numerical method increases and becomes highly different from the order of the geometrical ap-

proximation of the boundary (P4Q1 for instance), the quality of the physical results decreases significantly.

5.3.2. Connectivity information

While Q1 meshes have 4 nodes per 2D quadrilateral (at the 4 corners of the element), Q2 meshes have 9 nodes per cell: 4 at the corners, 4 at the midpoint of each edge and finally 1 at the center of the cell. The extra-nodes at the midpoint of each face allow for a parabolic description of the edge. However, the flux points (and the solution points) are placed at the same locations as for Q1 meshes, as shown in Fig.9 for a simplified mesh of 4 quadrilateral elements and a P3 reconstruction. In our case, the solution points remain thus at the Gauss-Legendre quadrature points. In this same Fig.9, we introduce the following nomenclature to clarify our subsequent explanations: the 4 nodes that were already present in Q1 meshes are called corner nodes, the 4 grid points which are located at the middle of each edge are called middle nodes, and the node located at the center of the cell is called center node. Let us specify that this classification is only fictitious as of now. Indeed, these nodes are all COOLFluiD geometric entities and possess the same characteristics. Indeed, we would like to identify which nodes are edge-connected to which nodes in order to place our fictitious springs at the correct locations. The added complexity is that we now have a center node that is not located on one edge and we have middle nodes that are edge-connected to two corner nodes. Our idea is the following: we consider that each center node is connected to the 4 middle nodes belonging to the same element. Reciprocally, we assume that each middle node is linked to the two center nodes of the two neighboring cells to which it is connected. Finally, we consider that each middle node is linked to the two corner nodes belonging to the same face. These considerations are illustrated in Fig.10 where the grey segments show the new connectivity between corner and middle nodes.

Now that the connectivity information is established, we can compute the stiffnesses between the edge-connected nodes. The same idea of order-dependent spring concept given is used for the nodes located on faces. However, we should remember that we do not want to place springs between corner nodes (as we did before in Q1) but rather between middle and corner nodes. From the set of the flux points of a face, we have to discriminate the ones that are not located on the part of the face we are dealing with. An illustration of this consideration can be seen in Fig.11: if we wish to place a spring between middle node 4 and corner node 7, we should only take the two flux points located in between (i.e. the right flux points 5 and 6) and not the two flux points located on the same face but between corner node 1 and middle node 4 (i.e. the left flux points 2 and 3). To do so, the FR-AMR algorithm compares the distances between the flux points and the nodes and deduces if the considered flux points are located between the two nodes of interest. Then, for all the flux points which satisfy this latter condition, a sorting algorithm is applied in order to determine how these flux points are oriented with respect to the two edge-connected nodes. For the connection between center and middle nodes, the situation is more complex as the order-dependent spring concept is not applicable. Indeed, no flux points are located inside the cell and the solution points cannot be forced to be on the grey segments shown in Fig.10. Instead, a spring with the usual linear stiffness given by Eq.20 is placed between each corner and middle node. These extra-springs should alleviate the risk that the corner nodes exit the cells to which they belong.

6. Results: Sub-cell Order-dependent spring analogy FR-AMR Simulations

6.1. Wedge channel

6.1.1. First test of the FR-AMR solver

The density fields and final meshes obtained with the FR-AMR solver are given in Fig.12. For all orders, the mesh adapts itself properly to the phenomena encountered in the wedge channel. We can indeed see that the mesh is adequately refined around the shocks, the expansion waves and their reflections. Moreover, we can note that the boundary nodes are also attracted by the zones of high-gradient. The results are depicted for P1, P2 and P3 respectively in Fig.13, Fig.14 and Fig.15. In each of these figures, the results are given with and without the AMR process and are compared with the second-order FV solution. In Fig.16, the results are plotted for P1, P2, and P3 with AMR. The analytical density solution is plotted as a reference for all of these figures.

The results obtained in Fig.13, Fig.14 and Fig.15 show a considerable advantage brought by the AMR procedure: the shock (which is characterized by the density jump) is steeper with the adapted mesh than without and is also much better resolved than with the second-order FV solver, whatever the simulation order. Moreover, the density reached after the shock is closer to the analytical value with the AMR process. This effect is particularly visible in Fig.15, where the

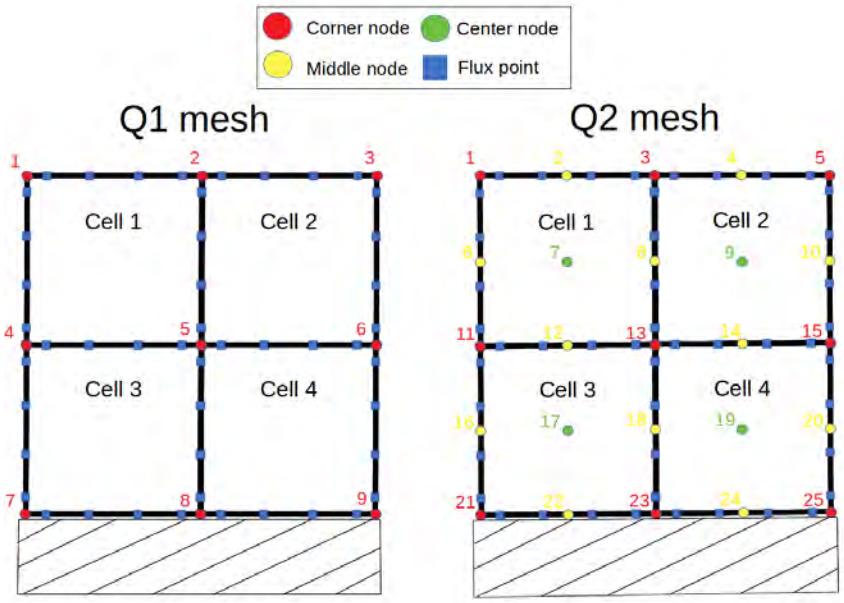

Figure 9: Location of the nodes and of the flux points for P3Q1 and P3Q2

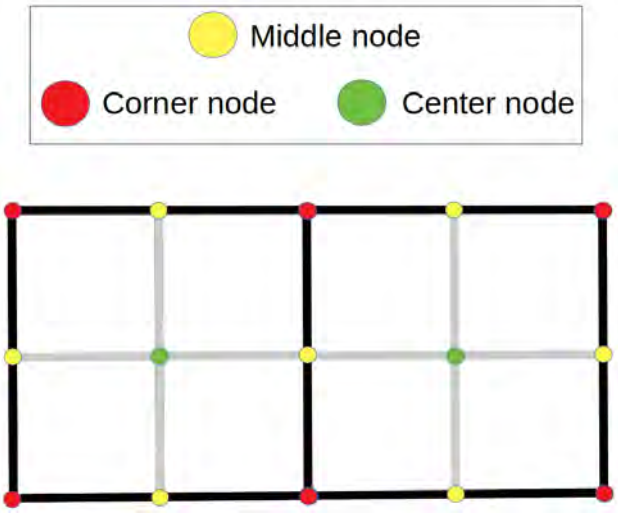

Figure 10: Nodal connectivity for Q2 grids

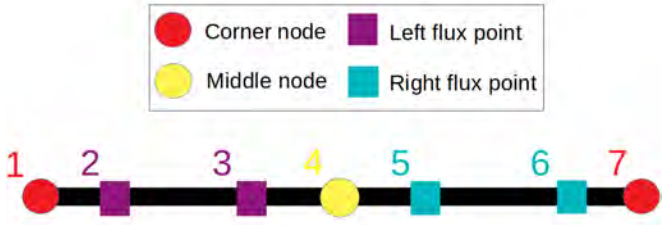

Figure 11: Discrimination of left and right flux points with respect to the middle node

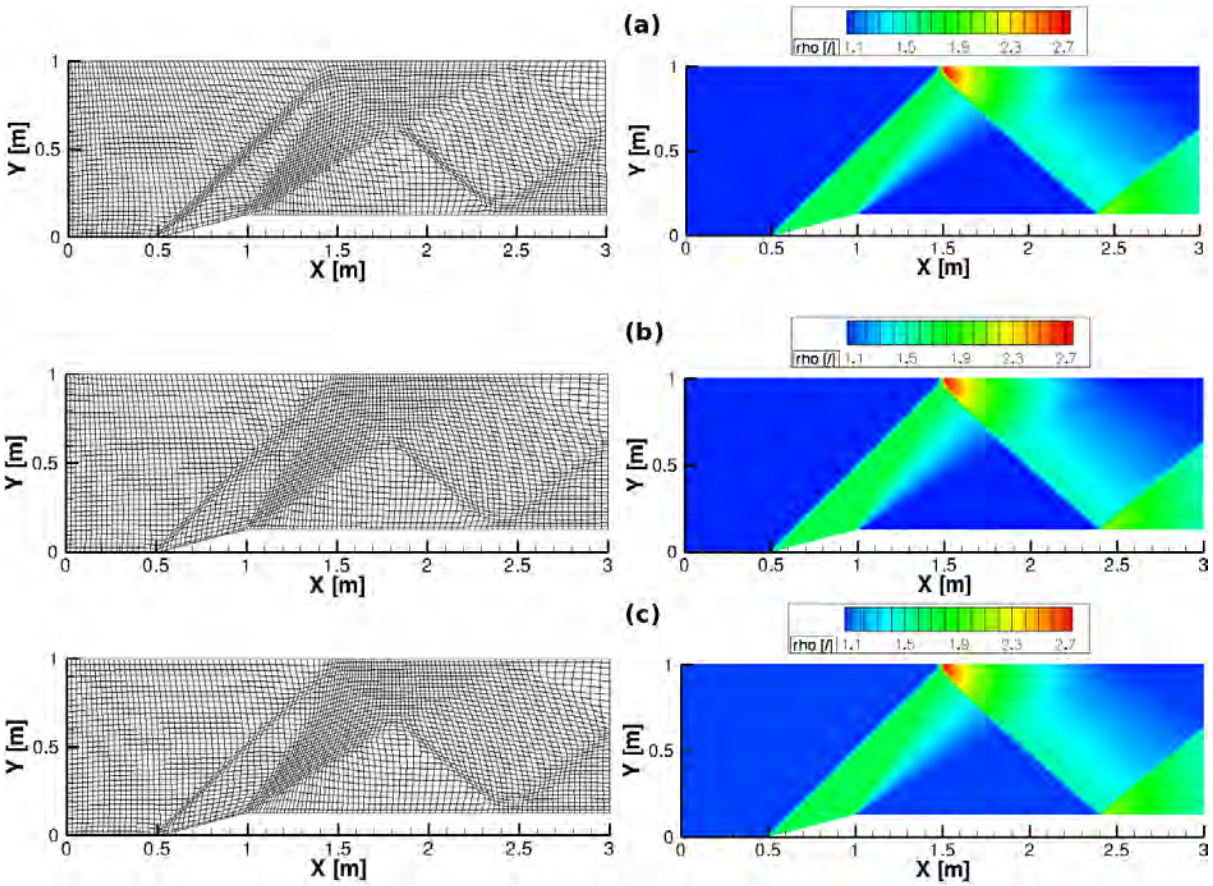

Figure 12: Final meshes and converged density fields: (a) P1, (b) P2, (c) P3

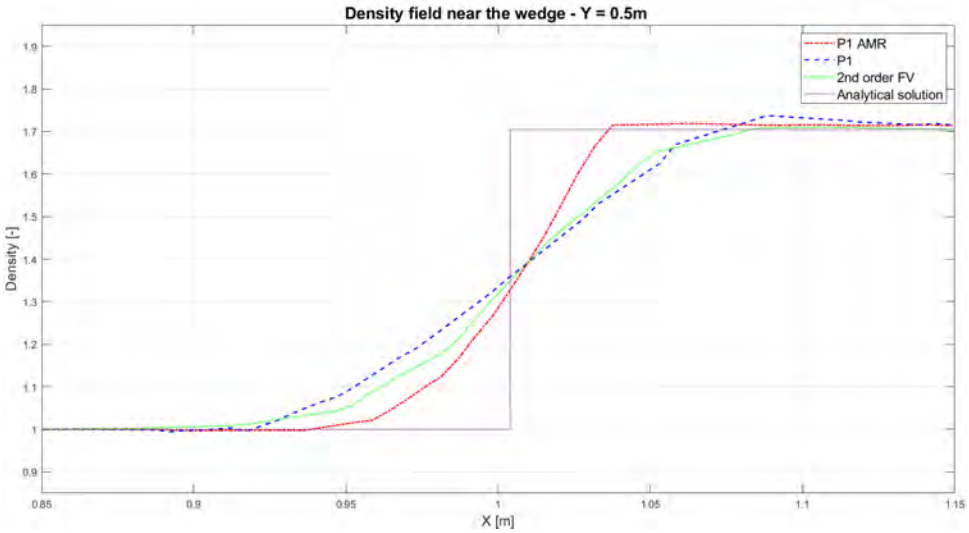

Figure 13: Comparison of the density fields obtained around the oblique shock for P1 with AMR, for P1 without AMR and with the FV solver

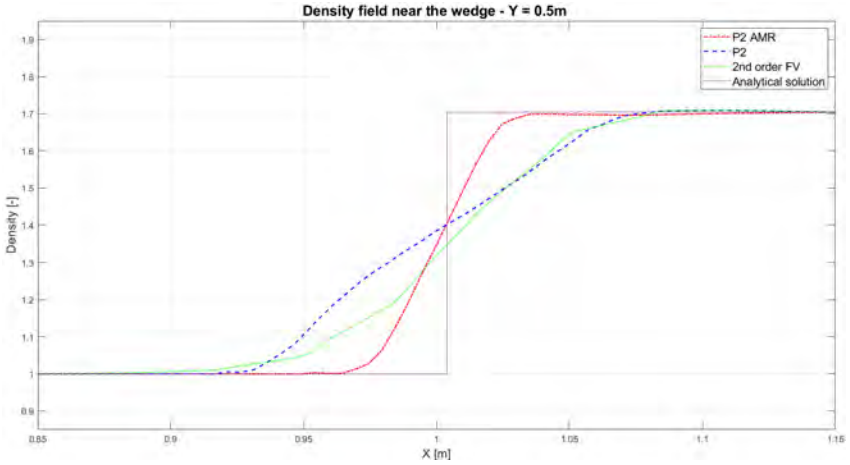

Figure 14: Comparison of the density fields obtained around the oblique shock for P2 with AMR, for P2 without AMR and with the FV solver

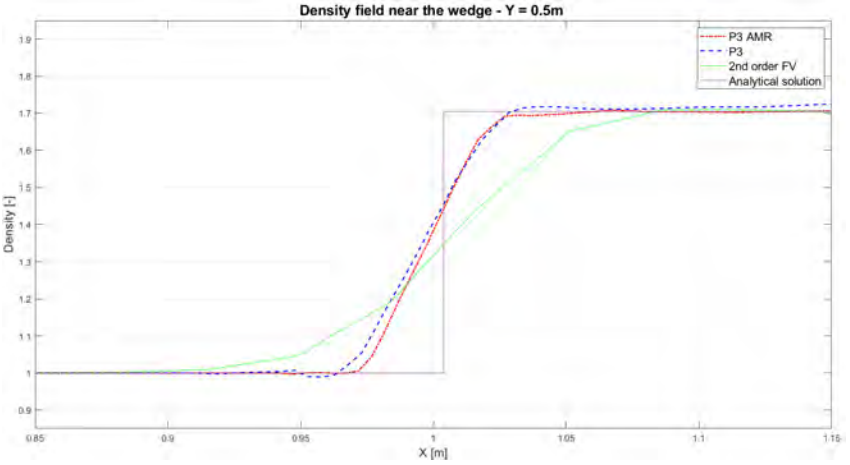

Figure 15: Comparison of the density fields obtained around the oblique shock for P3 with AMR, for P3 without AMR and with the FV solver

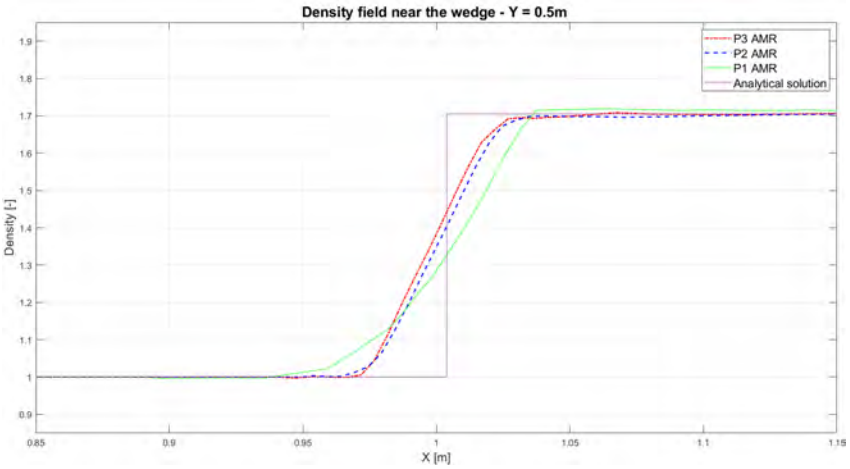

Figure 16: Comparison of the density fields obtained around the oblique shock for P1, P2 and P3, all with AMR

density for P3 AMR stabilizes almost perfectly on the analytical solution whereas the density for P3 without AMR presents a clear overshoot and does not reach the correct post-shock value. Interestingly, in this same Fig.15, the Gibbs oscillations obtained with P3 are smaller with AMR than without. This is again because the shock is better captured, i.e. because there are more cells in the shock region with AMR so that the LLAV procedure is more effective. Fig.16 illustrates that the shock is resolved in a narrower region with an increase in the simulation order: as expected, the accuracy gets better with (isotropic) p-refinement.

6.1.2. Comparison with literature results

In order to assess the reliability of the results obtained with the FR-AMR algorithms, a slightly modified wedge channel is considered. Its length is increased to 5 m and the angle of the wedge is reduced to 10°. However, the inlet and boundary conditions are the same as the ones of the previous subsection. Thanks to these geometry changes, the wedge is now exactly the same as the one studied by Ripley et al. in [34]. Two Q1 meshes coarser than the one reported in the literature are considered to study this new wedge: a mesh of 2040 elements (called M_m) and another mesh of 845 elements (called M_c). Both grids are depicted in Fig.17. Simulations with and without AMR are performed for P1, P2 and P3 on M_m and for P4 on M_c.

The final meshes obtained with the r-refinement procedure for P1, P2 and P3 on M_m and P4 on M_c are given in Fig.18 and are compared to the final mesh of 50837 cells obtained with h-refinement in the reference paper [34]. Although the mesh of the reference paper contains many more elements than the ones used here (almost 25 times the number of elements of M_m and more than 60 times the number of cells of M_c), the final grids obtained by the FR-AMR algorithms target the zones to refine much better. Indeed, whereas the h-refinement process leads to a refinement in regions where there are no physical gradients (such as before the first shock), our r-refinement procedure captures very well the shocks and the expansion waves along with their reflections on the walls. The normalized pressure contours obtained for P1, P2, P3 and P4 with the AMR algorithm are compared in Fig.19 with the solutions obtained without it. In particular, the pressure contours appear to be much smoother for P3 thanks to the AMR process. Similarly, the oblique shock is better captured for P4 with the AMR process than without (for which it is more diffusive). In Fig.20, the isobar lines obtained for P1, P2, P3 and P4 with AMR are compared with the reference ones given in [34]. The isobar plot of P3 AMR on M_m is particularly well in agreement with the reference one although the number of cells used here is much smaller. The isobar lines of P4 AMR on M_c are also very similar to the reference plot.

The Mach numbers computed at each point defined in Fig.20 (e) with our FR-AMR algorithm are compared with the analytical solutions and with the values obtained by [34] in Tab.4. As expected, the Mach number predictions get better when the order increases with the same mesh M_m (cf. the columns of P1, P2 and P3). Another observation is that the results obtained with P4 on M_c are the closest to the analytical solutions. This is particularly interesting if we take into account the number of degrees of freedom (DOF) of each simulation. For FR simulations, the number of degrees of freedom is determined by the number of solution points. In the case of 2D quadrilaterals, it is given by $N_{\text{DOF}} = N_{\text{elements}} \cdot (P+1)^2$ where P is the order of the polynomial reconstruction. For $P3$ on M_m, we have $N_{\text{DOF}} = 32640$ whereas for $P4$ on M_c, we have $N_{\text{DOF}} = 21125$. Hence, although the number of degrees of freedom is smaller for the $P4$ simulation, the results obtained are more accurate. This confirms the advantage of p-refinement over h-refinement and the better accuracy per DOF of higher-order FR over lower-order FR already highlighted in [9].

In order to quantify the improvements brought by each method, we propose two assessment parameters. Firstly, we define the gain in accuracy with respect to the reference results [34]:

$$\text{Gain} = \frac{\text{Ma [-] Sim} - \text{Ma [-] Ref}}{\text{Ma [-] Sim}} \times 100.$$

Secondly, we define the difference with respect to the analytical solution:

$$\text{Diff} = \frac{\text{Ma [-] Analytical} - \text{Ma [-] Sim}}{\text{Ma [-] Analytical}} \times 100.$$

These values are given in Tab.5 for the P4 AMR simulations performed on M_c, where the relative difference with respect to the analytical solution appears to considerably decrease for the state point 4.

Then, we illustrate the convergence history of the different FR-AMR simulations in Fig.21. Every simulation shows a similar pattern: the oscillations in the residual during the AMR phase are followed by a drop within the convergence behavior. This illustrates particularly well the choice that has to be made in the value of the acceleration factor ω. Indeed, it appears that the simulation does not converge while the

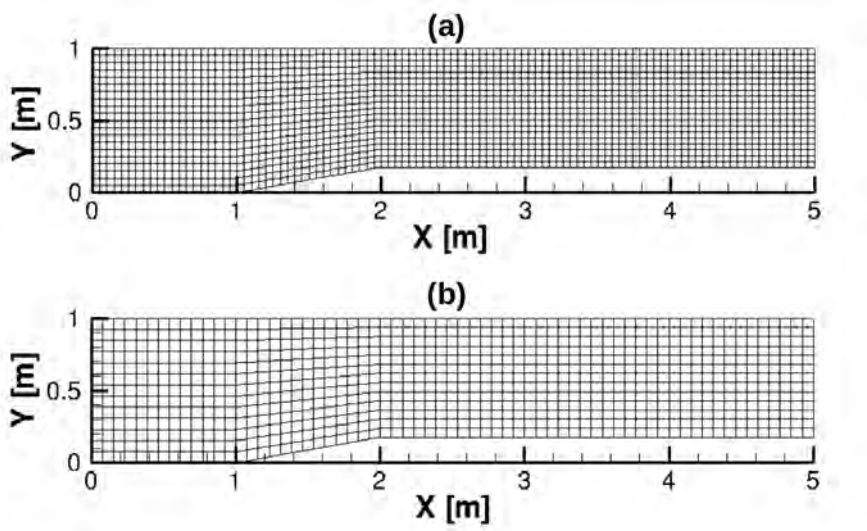

Figure 17: Initial meshes: (a) Middle mesh with 2040 cells M_m, (b) Coarse mesh with 845 cells M_c

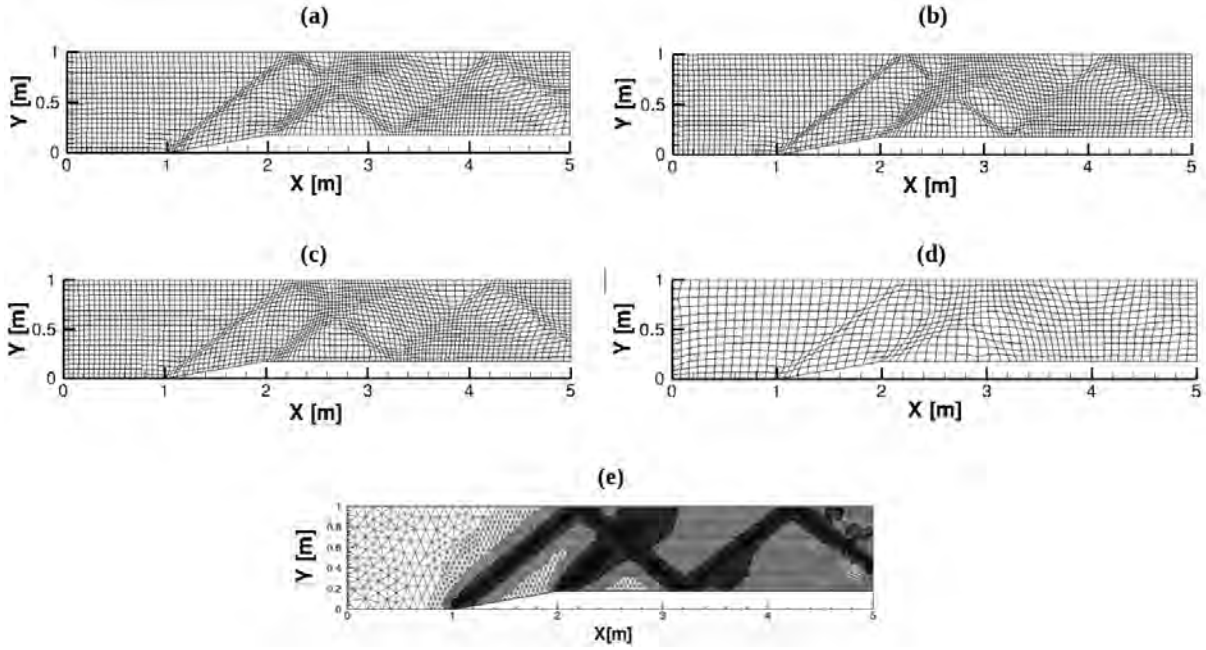

Figure 18: Final meshes: (a) M_m - P1, (b) Final M_m - P2, (c) Final M_m - P3, (d) Final M_c - P4. (e) Last level of h-adaptation - mesh with 50837 cells, taken from [34]

State point	Analytical Mach [-]	Ref. Mach [-]	Ref. % difference	P1 Mach [-] M_m	P2 Mach [-] M_m	P3 Mach [-] M_m	P4 Mach [-] M_c
1	2	2	0	2	2	2	2
2	1.65	1.639	0.7	1.6405	1.6425	1.6442	1.6456
3	1.3	1.287	1.0	1.2875	1.2905	1.2943	1.2955
4	2	1.985	0.8	1.9907	1.9909	1.9910	1.9923

Table 4: Comparison of the Mach numbers of the analytical solution, the reference results [34] and our FR-AMR simulations

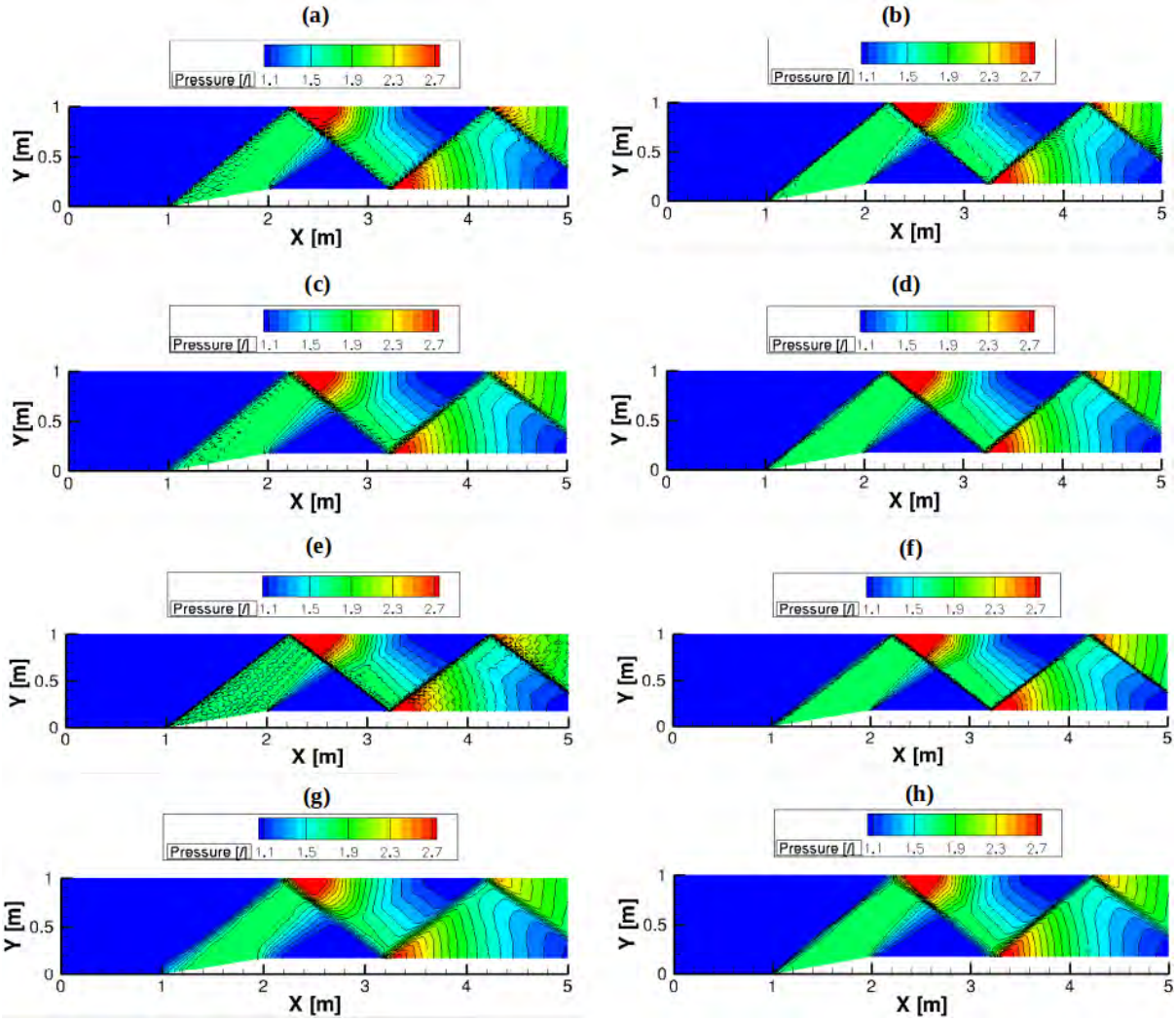

Figure 19: Pressure contours and isobar lines obtained with the FR solver. On M_m: (a) P1 no AMR, (b) P1 AMR, (c) P2 no AMR, (d) P2 AMR, (e) P3 no AMR, (f) P3 AMR. On M_c: (g) P4 no AMR, (h) P4 AMR

State point	Analytical Mach [-]	Ref. Mach [-]	Ref. % difference	P4 Mach [-] M_c	Diff. % with P4	Gain % with P4
1	2	2	0	2	0	0
2	1.65	1.639	0.7	1.6456	0.398	0.269
3	1.3	1.287	1.0	1.2955	0.658	0.344
4	2	1.985	0.8	1.9923	0.366	0.386

Table 5: Improvements obtained with P4 AMR on M_c

AMR process is activated. Hence, a trade-off has to be found: if ω is too low, the number of required AMR iterations has to increase and thus convergence is delayed and, if ω is too high, the number of AMR iterations can decrease but risks of instabilities appear and a crash of the simulation becomes very likely. Thus, as already discussed in sec.3, a value of 0.05 is generally chosen.

Finally, we quantify the penalty in computational cost due to the AMR procedure. To do so, we compute the wall time per iteration by dividing the total time of the simulation by the number of iterations,

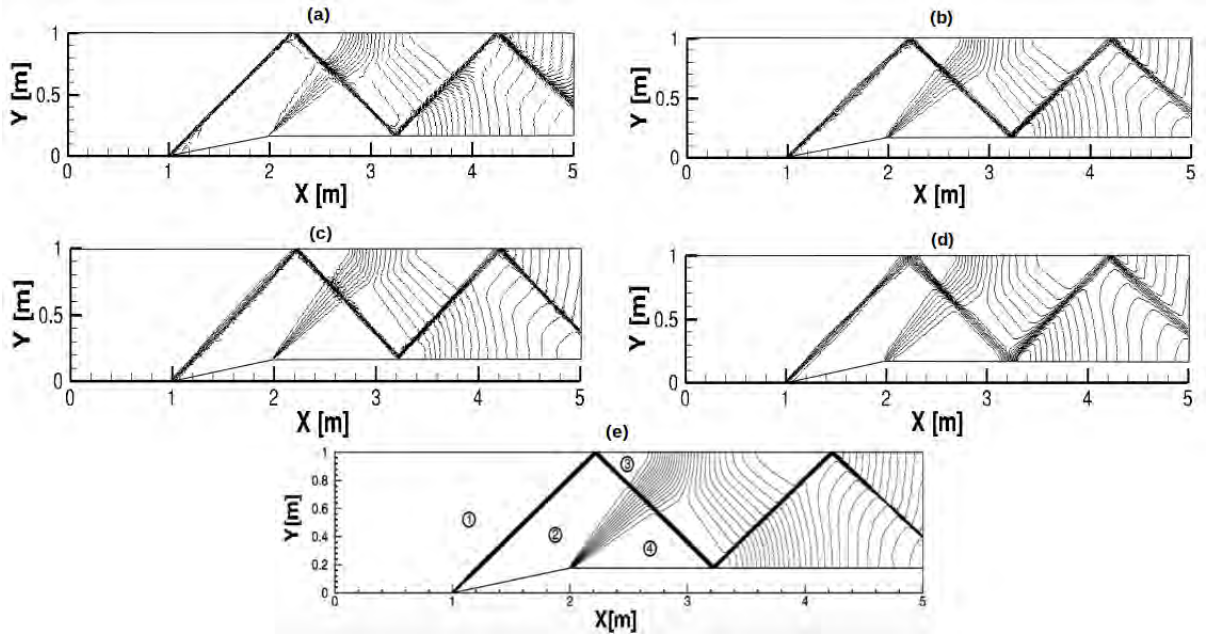

Figure 20: Isobar lines obtained with the FR solver. On M_m: (a) P1 AMR, (b) P2 AMR, (c) P3 AMR. On M_c: (d) P4 AMR. (e) Reference isobar lines - mesh with 50837 cells, taken from [34]

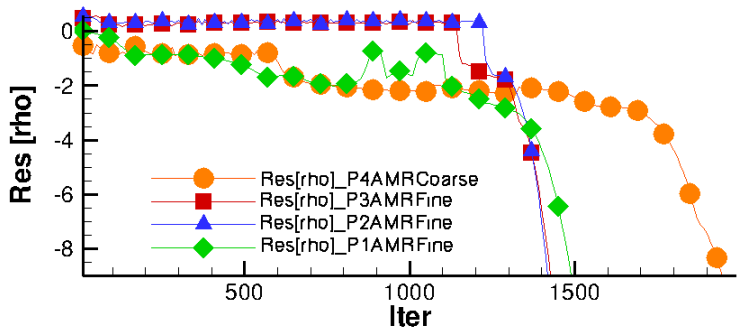

Figure 21: Convergence history for the FR-AMR simulations

both with and without r-refinement. To obtain the extra cost caused by the r-refinement procedure, let us introduce the factor C such that :

$$C = \frac{\text{Wall time per iteration with r-AMR}}{\text{Wall time per iteration without r-AMR}} \quad (22)$$

The values of C for the simulations performed in P1, P2, P3 and P4 on the wedge channel flow are respectively equal to 1.055, 1.069, 1.047 and 1.012. This factor is close to 1 for each simulation, leading to the conclusion that the relative computational cost per iteration of our r-refinement algorithm with respect to the overall time per iteration of the FR simulation is small. Indeed, the maximum computational time penalty is of 6.9% for P2. Let us note that, after P2, the extra cost of our r-AMR-FR algorithm decreases with the order. This can be explained by the fact that the cost for solving the pseudo-elastic system vanishes and becomes negligible as the polynomial order increases with respect to the FR computations on the wedge channel. For more information about the performance and the scalability with the simulation order of the FR solver, we refer the reader to [10]. As the parallelization of the FR-AMR algorithm is handled by the HPC infrastructure of the COOLFluiD platform and has not been modified throughout this work, we encourage the reader to consult [13] for more details

about the implementation.

6.2. Circular bump

The geometry of the 2D inviscid bump is shown in Fig.22. The bump is circular with a thickness equal to 4% of the channel width and is described by a second-order polynomial (Q2 mesh). The bump has been generated by creating a circular arc whose center coordinates are $\{1.5, -3.105\}$ [m] and whose radius is 3.145 m. The imposed flow conditions are given in Tab.6 and correspond to an inlet Mach number $M = 1.4$. The types of boundary conditions are the same as for the wedge channel flow.

M [-]	ρ [-]	ρu [-]	ρv [-]	ρE [-]
1.4	1.0	1.656502339	0.0	3.872

Table 6: 2D bump inlet flow characteristics

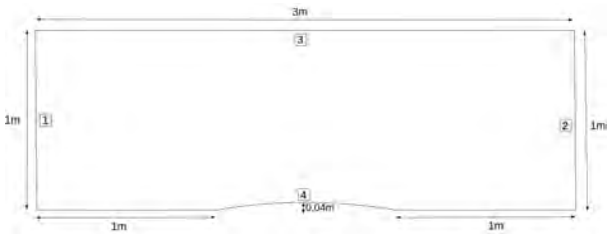

Figure 22: 2D bump geometry

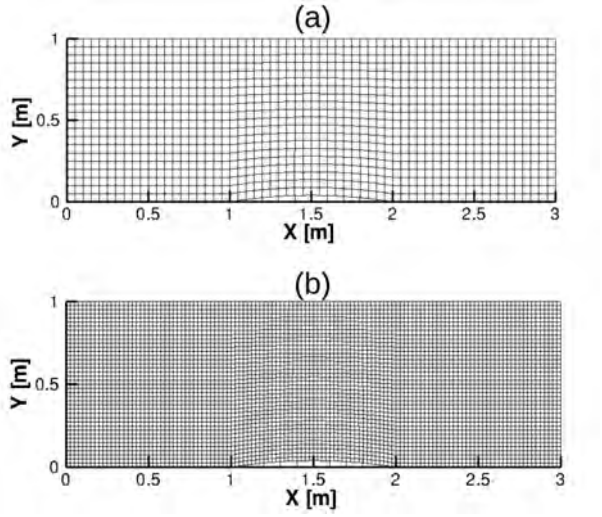

Figure 23: 2D bump initial meshes: (a) Coarse mesh with 1200 cells M_c, (b) Fine mesh with 4800 cells M_f

The two meshes used by Premasuthan et al. in [35] are considered here: a fine mesh of 4800 cells called M_f and a coarse mesh of 1200 cells called M_c, which makes the number of nodes of M_c half the number of nodes of M_f in both the x- and y- directions. While M_f describes the bump surface with 40 cells in the tangential direction, M_c only uses 20 elements for this purpose. These two meshes are depicted in Fig.23. Simulations with P2 AMR and P3 AMR were performed on both meshes. The final meshes and pressure contours are shown for M_c in Fig.24 and for M_f in Fig.25. The obtained pressure fields match the ones already reported in [35]: the oblique shock created at the leading edge of the bump is reflected on both walls whilst the expansion waves are created all over the bump length. Moreover, the final mesh confirms the proper functioning of the novel AMR algorithm for Q2 meshes as the mesh resolution is larger around the zones of high-gradient. The region after the bump, which displays complex interactions between reflections of the oblique shock and expansion waves, is also correctly refined. Fig.26 shows the pressure along the line of equation $Y = 0.4m$ for our simulations (P2 and P3 on M_c and M_f) as well as for the reference solution (Spectral Difference with artificial viscosity taken from [35]). The latter figure shows that our solutions agree with the reference one and the shock are narrowly resolved without noteworthy Gibbs phenomena. One of the main advantages of the FR-AMR is that our method (at least for P3) was able to detect the last pressure jump that lies close to the joining point of the two oblique shocks on the coarse mesh as shown in Fig.27. Fig.28 shows already the improved capabilities of the FR-AMR with the P2 solution over the fine mesh as the pressure jumps are narrower and better resolved. Similar conclusions can be drown out from Fig.29 – 31.

7. Conclusion and Future work

A novel r-AMR algorithm has been developed and, in combination with an existing Flux Reconstruction CFD solver, successfully applied to benchmark test cases. The proposed sub-cell order-dependent spring analogy shows its promising results with respect to the vertex spring method. In addition, the resulting algorithm has been developed as a standalone module which can be coupled to any CFD/plasmas solvers. Finally, our r-AMR-FR solver showed a promising performance when compared to some h-AMR second-order FV codes reported in the literature.

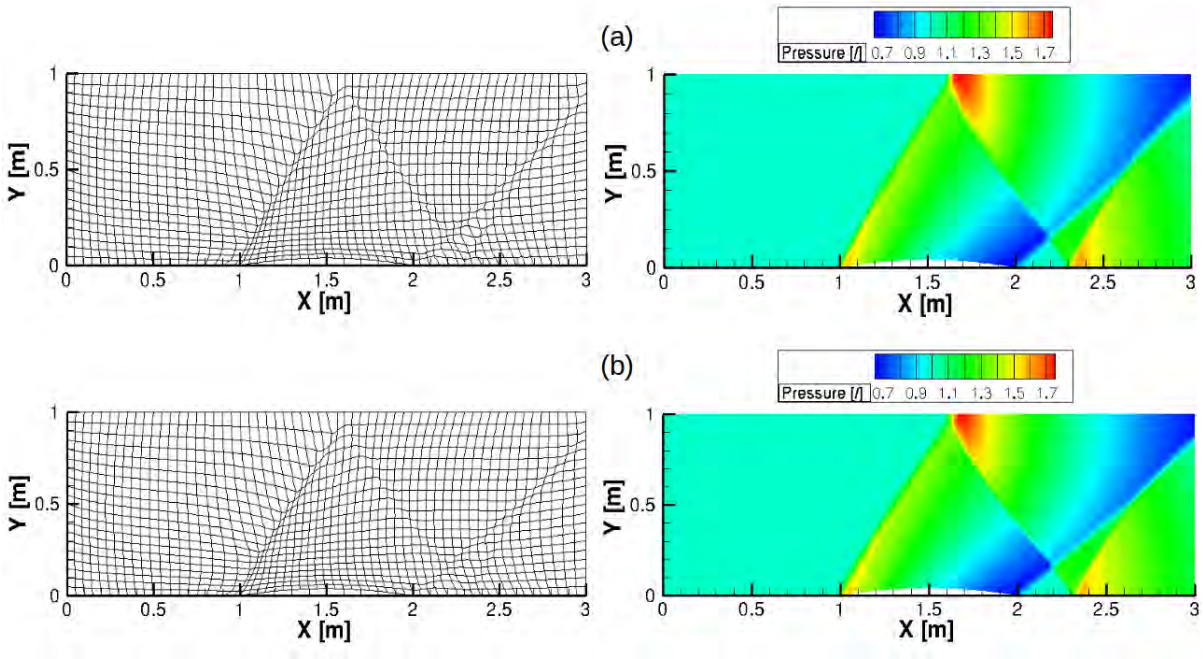

Figure 24: Final meshes and results on the coarse mesh M_c: (a) P2 AMR, (b) P3 AMR

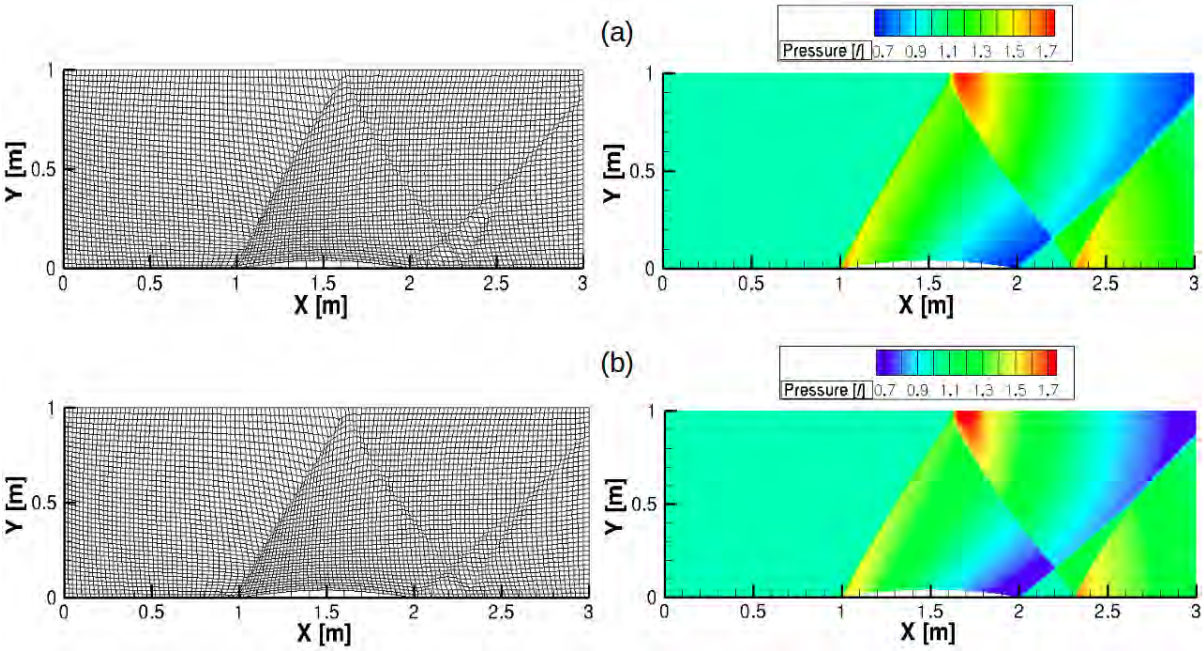

Figure 25: Final meshes and results on the fine mesh M_f: (a) P2 AMR, (b) P3 AMR

Acknowledgement

I would like to thank Joachim Balis and Ray Vandenhoeck for their contributions in this work. In addition, the research of Firas Ben Ameur and Ray Vandenhoeck is supported by SB PhD fellowship 1SC3519N and 1S19918N, respectively, of the FWO.

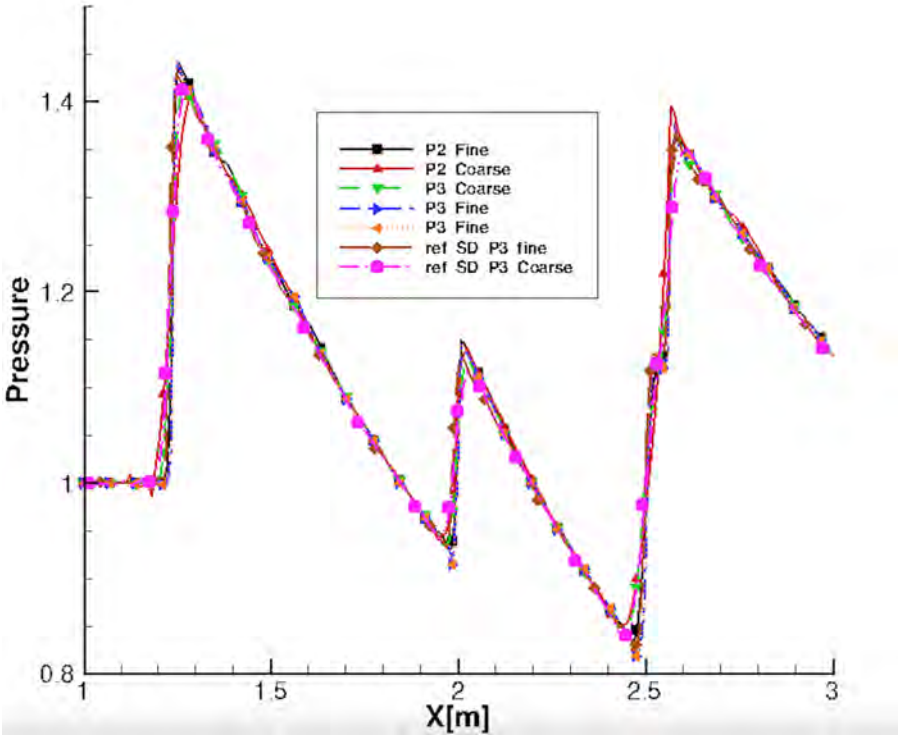

Figure 26: Pressure along the line $Y = 0.4m$ for P2 and P3 on the coarse and the fine mesh as the P3 SD reference solution on the same meshes

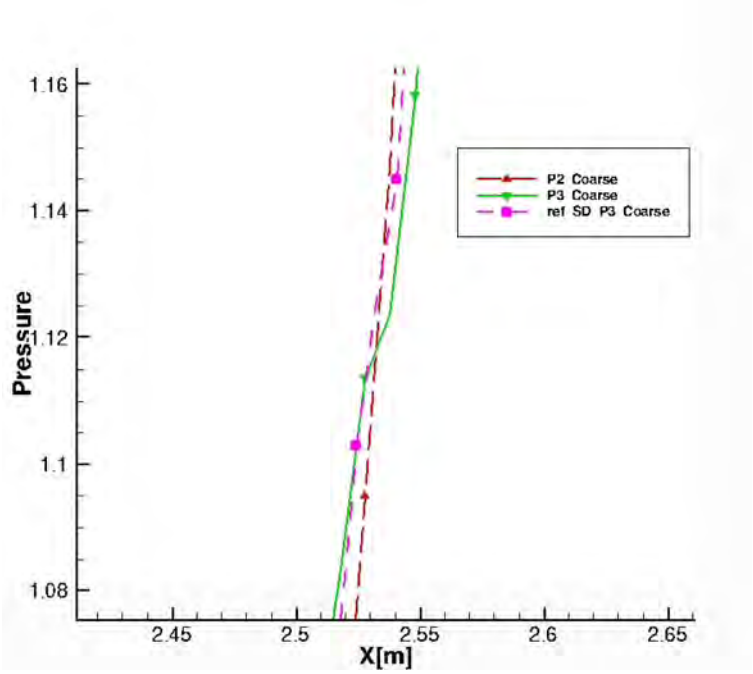

Figure 27: Zoom around the joining point of the two oblique shocks

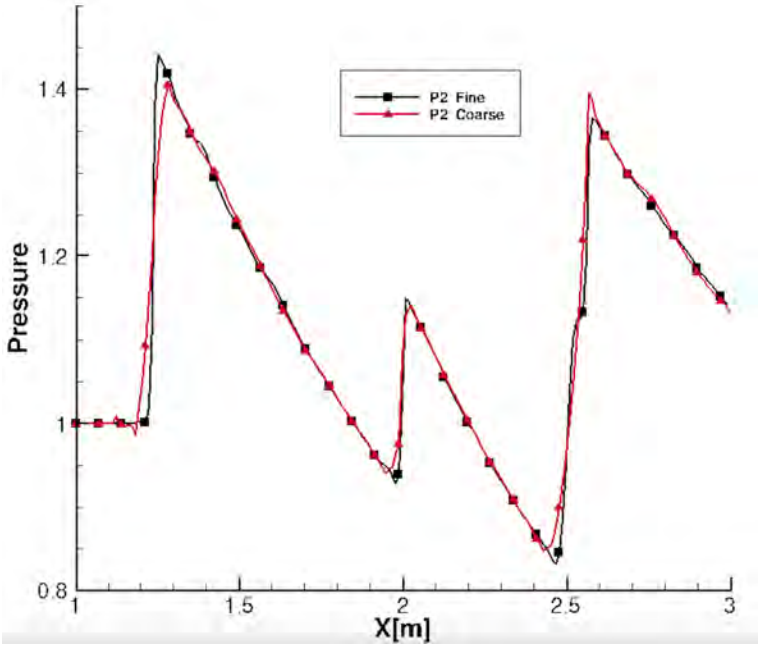

Figure 28: Line pressure for P2 on the coarse and fine meshes

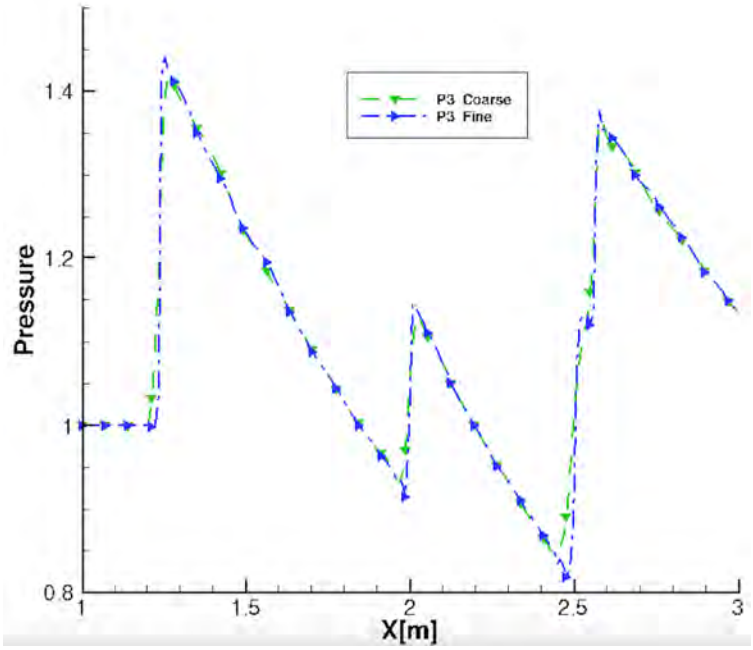

Figure 29: Line pressure for P3 on the coarse and fine meshes

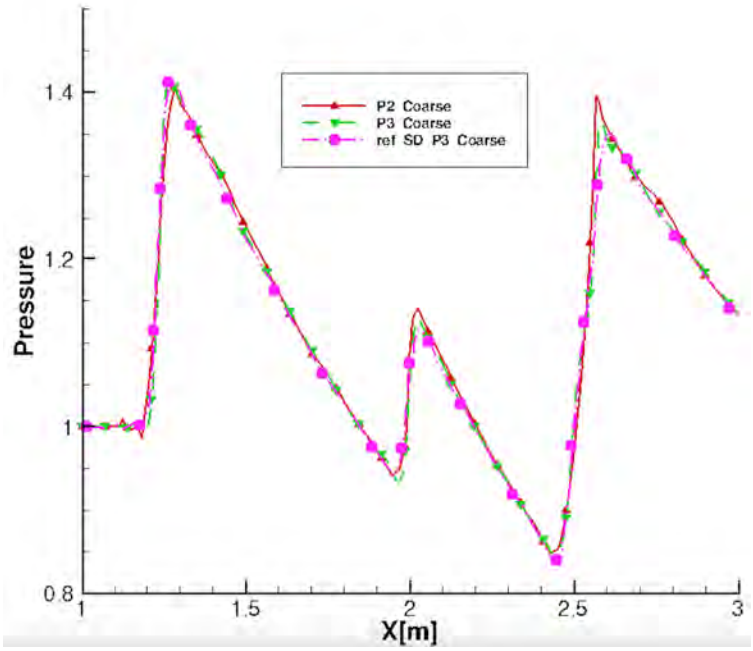

Figure 30: Line pressure for P2, P3 and reference SD P3 on the coarse mesh

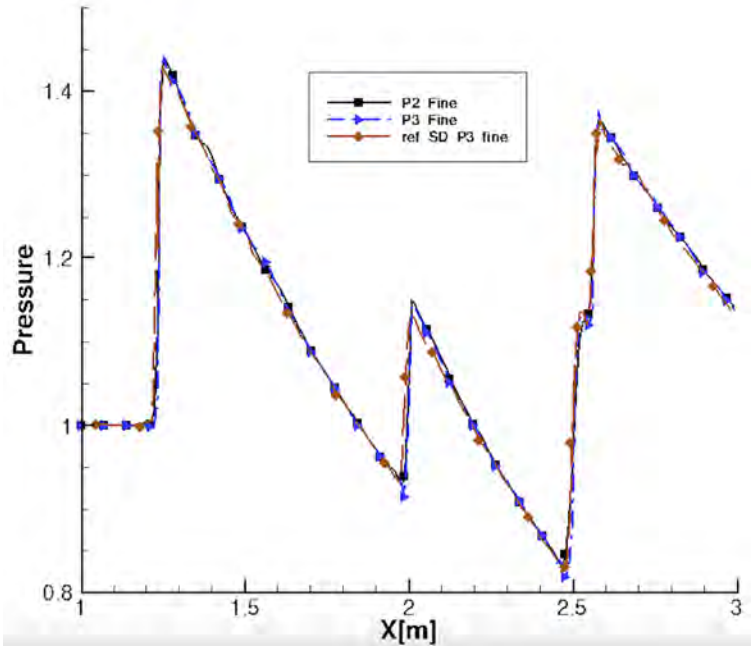

Figure 31: Line pressure for P2, P3 and reference SD P3 on the fine mesh

References

[1] P. Gnoffo, Multi-Dimensional Inviscid Flux Reconstruction for Simulation of Hypersonic Heating on Tetrahedral Grids, in: 47th AIAA Aerospace Sciences Meeting, Aerospace Sciences Meetings, American Institute of Aeronautics and Astronautics, 2009.

[2] P. Gnoffo, J. White, Computational Aerothermodynamic Simulation Issues on Unstructured Grids, in: 37th AIAA Thermophysics Conference, Fluid Dynamics and Co-located Conferences, American Institute of Aeronautics and Astronautics, 2004.

[3] K. H. Kim, C. Kim, O.-H. Rho, Methods for the accurate computations of hypersonic flows: I. ausmpw+scheme, Journal of Computational Physics 174 (1) (2001) 38 – 80.

[4] C.-L. Chang, M. Choudhari, Hypersonic Viscous Flow Over Large Roughness Elements, in: Theoretical and Computational Fluid Dynamics, Vol. 25, 2011, pp. 85–104.

[5] K. H. Kim, C. Kim, O.-H. Rho, Methods for the accurate computations of hypersonic flows: Ii. shock-aligned grid technique, Journal of Computational Physics 174 (1) (2001) 81 – 119.

[6] H. Huynh, Z. J. Wang, P. E. Vincent, High-order methods for computational fluid dynamics: a brief review of compact differential formulations on unstructured grids, Computers & Fluids 98 (2014) 209–220.

[7] F. Ben Ameur, A. Lani, Physics-based mesh fitting algorithms for hypersonic flows simulations, in: AIAA Scitech 2019 Forum, San Diego, California, 2019.

[8] F. Ben Ameur, A. Lani, r-adaptive algorithms for high-speed flows and plasma simulations, Computer Physics Communications (2020) 107700.

[9] R. Vandenhoeck, A. Lani, Implicit high-order flux reconstruction positivity preserving llav scheme for viscous high-speed flows, in: AIAA Scitech 2019 Forum, San Diego, California, 2019.

[10] R. Vandenhoeck, A. Lani, Implicit high-order flux reconstruction solver for high-speed compressible flows, Computer Physics Communications 242 (2019) 1 – 24. doi:https://doi.org/10.1016/j.cpc.2019.04.015.

[11] F. Ben Ameur, R. Vandenhoeck, A. Lani, High-order flux reconstruction scheme for thermo-chemical nonequilibrium high-speed flows, in: AIAA Scitech 2019 Forum, San Diego, California, 2019.

[12] D. Kimpe, A. Lani, T. Quintino, S. Poedts, S. Vandewalle, The coolfluid parallel architecture, in: B. Di Martino, D. Kranzlmüller, J. Dongarra (Eds.), Recent Advances in Parallel Virtual Machine and Message Passing Interface, Springer Berlin Heidelberg, Berlin, Heidelberg, 2005, pp. 520–527.

[13] A. Lani, N. Villedie, K. Bensassi, L. Koloszar, M. Vymazal, S. M. Yalim, M. Panesi, Coolfluid: an open computational platform for multi-physics simulation and research, in: 21st AIAA Computational Fluid Dynamics Conference, 2013, p. 2589.

[14] J. G. Mena, R. Pepe, A. Lani, H. Deconinck, Assessment of heat flux prediction capabilities of residual distribution method: Application to atmospheric entry problems, Communications in Computational Physics 17 (3) (2015) 682–702.

[15] M. Panesi, A. Lani, T. Magin, J. Molnar, O. Chazot, H. Deconinck, Numerical investigation of the non equilibrium shock-layer around the expert vehicle, in: 18th AIAA Computational Fluid Dynamics Conference, 2007, p. 4317.

[16] P. D. Santos, A. Lani, An object-oriented implementation of a parallel monte carlo code for radiation transport, Computer Physics Communications 202 (2016) 233–261.

[17] W. Zhang, A. Lani, M. Panesi, Analysis of non-equilibrium phenomena in inductively coupled plasma generators, Physics of Plasmas 23 (7) (2016) 073512.

[18] A. A. Laguna, N. Ozak, A. Lani, H. Deconinck, S. Poedts, Fully-implicit finite volume method for the ideal two-fluid plasma model, Computer Physics Communications 231 (2018) 31–44.

[19] A. A. Laguna, A. Lani, N. N. Mansour, H. Deconinck, S. Poedts, Effect of radiation on chromospheric magnetic reconnection: reactive and collisional multi-fluid simulations, The Astrophysical Journal 842 (2) (2017) 117.

[20] Y. G. Maneva, A. A. Laguna, A. Lani, S. Poedts, Multi-fluid modeling of magnetosonic wave propagation in the solar chromosphere: effects of impact ionization and radiative recombination, The Astrophysical Journal 836 (2) (2017) 197.

[21] A. A. Laguna, A. Lani, H. Deconinck, N. Mansour, S. Poedts, A fully-implicit finite-volume method for multi-fluid reactive and collisional magnetized plasmas on unstructured meshes, Journal of Computational Physics 318 (2016) 252 – 276. doi:https://doi.org/10.1016/j.jcp.2016.04.058.

[22] A. Lani, M. S. Yalim, S. Poedts, A gpu-enabled finite volume solver for global magnetospheric simulations on unstructured grids, Computer Physics Communications 185 (10) (2014) 2538–2557.

[23] H. Huynh, A flux reconstruction approach to high-order schemes including discontinuous galerkin methods, AIAA paper 4079 (2007) 2007.

[24] H. Huynh, High-order methods including discontinuous galerkin by reconstructions on triangular meshes, AIAA Paper 44 (2011) 2011.

[25] P. Castonguay, D. M. Williams, P. E. Vincent, M. Lopez, A. Jameson, On the development of a high-order, multi-gpu enabled, compressible viscous flow solver for mixed unstructured grids, AIAA paper 3229 (2011) 2011.

[26] P. Castonguay, P. Vincent, A. Jameson, Application of high-order energy stable flux reconstruction schemes to the euler equations, in: 49th AIAA Aerospace Sciences Meeting, Vol. 686, 2011.

[27] S. Abhyankar, J. Brown, E. M. Constantinescu, D. Ghosh, B. F. Smith, H. Zhang, Petsc/ts: A modern scalable ode/dae solver library, arXiv preprint arXiv:1806.01437.

[28] S. Balay, S. Abhyankar, M. F. Adams, J. Brown, P. Brune, K. Buschelman, L. Dalcin, V. Eijkhout, W. D. Gropp, D. Kaushik, M. G. Knepley, D. A. May, L. C. McInnes, R. T. Mills, T. Munson, K. Rupp, P. Sanan, B. F. Smith, S. Zampini, H. Zhang, H. Zhang, PETSc Web page, `http://www.mcs.anl.gov/petsc` (2018).
URL `http://www.mcs.anl.gov/petsc`

[29] S. Balay, S. Abhyankar, M. F. Adams, J. Brown, P. Brune, K. Buschelman, L. Dalcin, V. Eijkhout, W. D. Gropp, D. Kaushik, M. G. Knepley, D. A. May, L. C. McInnes, R. T. Mills, T. Munson, K. Rupp, P. Sanan, B. F. Smith, S. Zampini, H. Zhang, H. Zhang, PETSc users manual, Tech. Rep. ANL-95/11 - Revision 3.9, Argonne National Laboratory (2018).
URL `http://www.mcs.anl.gov/petsc`

[30] S. Balay, W. D. Gropp, L. C. McInnes, B. F. Smith, Efficient management of parallelism in object oriented numerical software libraries, in: E. Arge, A. M. Bruaset, H. P. Langtangen (Eds.), Modern Software Tools in Scientific Computing, Birkhäuser Press, 1997, pp. 163–202.

[31] R. Jain, I. Chlamtac., The P2 Algorithm for Dynamic Calculation of Quantities and Histograms Without Storing Observations, Eastern Research Laboratory, Digital Equipment Corporation, 1985.

[32] L. Krivodonova, M. Berger, High-order accurate implementa-

tion of solid wall boundary conditions in curved geometries, Journal of Computational Physics 211 (2) (2006) 492512. doi:10.1016/j.jcp.2005.05.029.

[33] X. Luo, M. Shephard, J.-F. Remacle, Influence of geometric approximation on the accuracy of higher order methods, 8th International Conference on Numerical Grid Generation in Computational Field Simulations.

[34] R. C. Ripley, F. S. Lien, M. M. Yovanovich, Adaptive mesh refinement of supersonic channel flows on unstructured meshes, International Journal of Computational Fluid Dynamics 18 (2) (2004) 189–198.

[35] S. Premasuthan, C. Liang, A. Jameson, Computation of flows with shocks using spectral difference scheme with artificial viscosity, 48th AIAA Aerospace Sciences Meeting Including the New Horizons Forum and Aerospace Expositiondoi:10.2514/6.2010-1449.

Fluid modeling of low-temperature partially-magnetized plasmas in the presence of sheaths: numerical issues for the simulation of instabilities and comparison with kinetic simulations

Louis Reboul

Centre de Mathémtatiques Appliquées (CMAP), CNRS, École polytechnique, Institut Polytechnique de Paris (IPP), France, louis.reboul@polytechnique.edu

Supervisor: Thierry Magin

Professor, Aeronautics and Aerospace Department, von Karman Institute for Fluid Dynamics, Belgium, magin@vki.ac.be

University Supervisor: Marc Massot

Professor, Centre de Mathématiques Appliquées (CMAP), CNRS, École polytechnique, Institut Polytechnique de Paris (IPP), France, marc.massot@polytechnique.edu

University Supervisor: Anne Bourdon

Doctor, Laboratoire de Physique des Plasmas (LPP), CNRS, École polytechnique, Institut Polytechnique de Paris (IPP), France, anne.bourdon@lpp.polytechnique.fr

University Advisor: Alejandro Alvarez Laguna

Doctor, Laboratoire de Physique des Plasmas (LPP), CNRS, École polytechnique, Institut Polytechnique de Paris (IPP), France, alejandro.alvarez-laguna@lpp.polytechnique.fr

Abstract

Hall-effect thrusters are efficient and reliable devices increasingly used to equip satellite missions. However the physics of such thrusters, involving the modeling of low-temperature magnetized plasmas, is intricate and nonlinear and is still an active field of research. We propose to study a 2D magnetized column configuration as a test-case which is representative of the main challenges encountered in modeling Hall-effect thrusters. We assess the potential of fluid models and corresponding Finite Volume Methods (FVM) for the modeling and simulation of such configurations including sheaths. Our methods are implemented in the massively-parallel collaborative code CanoP and the validation of our approach is conducted via a comparison with Particle-In-Cell (PIC) solutions and demonstrate that the proper dynamics of instabilities can be predicted by fluid models if advanced numerical methods are implemented.

Keywords: Hall-effect thrusters, magnetized plasma columns, low-Mach regime, numerical schemes

1. Introduction

Hall thrusters are very efficient and competitive devices for satellite propulsion. They are currently commercialized by several companies and are used to equip, for instance, telecommunication or government spacecrafts. The operating principle of Hall thrusters is to create a local electric field within a plasma by reducing the electron axial mobility by means of a magnetic field. As a result, the electric field extracts and accelerates the positive ions, thus producing thrust [1]. The plasma within these thrusters is at low temperature and low pressure, out of thermal equilibrium (ions and electrons have different temperatures), and partially magnetized (only electrons are considered to be affected by the magnetic field). It is crucial to have a

good understanding of the onset of instabilities within the thruster [2; 3; 4; 5] as well as an accurate representation of the sheaths, that are the thin boundary layers that forms in the vicinity of the walls of the thrusters [6]. As a matter of fact, the electron confinement that is produced by the magnetic field is fundamental for the creation of an electric field within the plasma. However, the magnetic field triggers instabilities that enhance the transport of electrons across the magnetic field and can hinder the overall performance of the thruster. Regarding sheaths, understanding at which rate and at what velocity ions collide with the wall of the thruster allows for predicting the erosion of the walls and consequently the life-span of the thruster. Another particularity of low-temperature magnetized plasmas is the large disparity of the scales that are present in the problem. Regarding spatial scales, the Debye length λ_D, which can be defined as the characteristic length over which electrostatic interactions are screened, can be several orders of magnitude smaller than the macroscopic scale of the problem. The small mass of electrons compared to the one of ions also means that their characteristic frequency of oscillation ω_{pe} (called the plasma frequency) is high or, conversely, that phenomena involving electrons happen at a much smaller time scale than those linked to ions. Finally, electrons are also at a much higher temperature than ions. Typically, for an Argon RF discharge at 1 Pa [6] the macroscopic scale of the device is of the order of a few centimeters while the Debye length λ_D is 1.5×10^{-4} m. The ratio between the mass of ions and that of electrons is 1.36×10^{-5} resulting in a plasma frequency ω_{pe} of 1.77×10^{-10} s^{-1} whereas the characteristic time for the formations of the sheaths for instance is of the order of a few microseconds. Finally, the temperature of ions and electrons are respectively $T_i = 0.05$ eV and $T_e = 2$ eV.

As a first step to model and simulate Hall-effect thrusters we study a relevant simplified configuration: we considered the case of a 2D magnetized plasma column as represented in Figure 1. The setup is the following: a square domain containing a plasma, with the wall set at electric potential zero and in the presence of a magnetic field perpendicular to the plane of simulation. Although the geometry considered here is much simpler than that of a Hall-effect thruster, this configuration is representative of the challenges faced when modeling a great number of low-temperature plasma applications since:

- We have included the boundary layer close to the wall, namely the sheath.

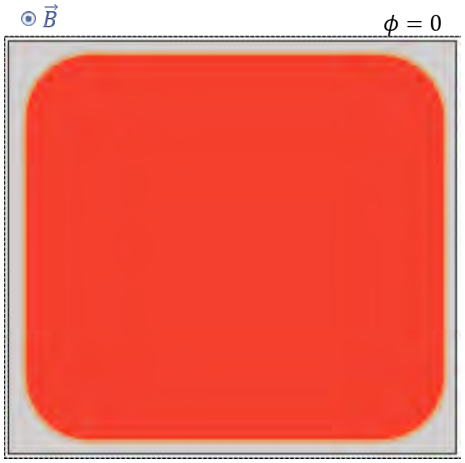

Figure 1: The configuration that we consider consists in a 2D square domain filled with a plasma, with walls set at electric potential $\phi = 0$ and in the presence of a magnetic field **B**.

- The presence of a magnetic field allows for studying its effect on the confinement of electrons as well as on the possible onset of instabilities when the magnetic field increases.

- The configuration is strongly multi-scale and features all the relevant scales of the original problem that can be problematic at a numerical level.

- Although it is not yet a 3D configuration, many non-trivial phenomena are already present in 2D (for instance in steady state the flux can be non-ambipolar) as compared to 1D.

For all these reasons, we believe that this configuration is well suited to assess the adequacy of models and performances of numerical methods in simulating a wide range of low-temperature magnetized plasma applications.

There are several challenges that arise when trying to model and simulate such low-temperature magnetized plasmas. First of all, we have to choose a suitable type of model for the plasma. More specifically, we have to choose between fluid and kinetic models. As the plasmas that we consider are at low pressure, we often are at the very limit of what can be modeled with classical fluid equations. For this reason, some of the phenomena that are observed (including some instabilities and the sheaths) can mainly be explained at a kinetic level. However, kinetic models have a seven dimensional set of variables (one dimension for time and 3 dimensions for position and velocity, respectively) when we consider 3D configurations and,

as a result, are computationally very costly to simulate. One of the corresponding numerical method that is used as a reference in the low-temperature plasma community is the so-called Particle-In-Cell (PIC) method. It consists in discretizing the kinetic equations by considering a certain number of macroparticles. These particles interact with an electrostatic field that is computed on a grid over the domain via the Poisson equation while considering averaged densities in each cell, and the collision between particles are incorporated via a random Monte-Carlo process. The computational cost of this method remains high and, typically, restrains this type of simulation to 2D configurations. More specifically, for the Argon plasma mentionned earlier, it would take 50 years on 10 000 processor to simulate only 20 μs in a domain of 10 cm $\times$ 10 cm $\times$ 10 cm [7] with this method because of the spectrum of scales that are involved. On the other hand, fluid models are generally known to be suitable for 3D configurations, but will need additional work in order to incorporate crucial effects that occur at a kinetic level and to ensure that the empolyed numerical method can tackle specific phenomena that can occur in the context of hyperbolic nonlinear systems such as the onset of shocks. In particular it has been shown recently that we can, for instance, predict the sheaths in a fluid model [8].

Both classical finite volume and PIC methods are also confronted to the large disparity of scales present in the problem. This disparity of scales brings stiffness to the model and will translate into restrictive constraints on the time step and mesh size used in the numerical method. A way to tackle efficiently the limitations induced by these fine scales is to use so-called asymptotic preserving numerical methods, as shown for instance in [9; 10]. It is also possible to use adaptive mesh refinement techniques to dynamically modify the size of the mesh so it resolves the finest scales in areas where it is needed (for instance in the sheaths).

In the recent work of Lucken *et al.* [11; 12], a PIC code called LPPic was used to study the development of instabilities in magnetized columns at different pressure and magnetic field regimes, and to quantify how it enhanced the transport of electrons towards the walls of the domain. In her PhD thesis [13], Sadouni has used a fluid approach with a quasineutral (meaning electrons and ions densities are assumed to be identical, thus excluding the resolution sheaths) code called MAGNIS to conduct a similar study of the developing of instabilities in a magnetized context. To the best of our knowledge, there are not yet simulations associated to fluid models that tackle this magnetized case including the boundary layer close to the walls. Additionally, the growth, nonlinear evolution and saturation of instabilities induced by the magnetic field are not completely understood in fluid models, particularly in the presence of sheath. Moreover, there are only a few works that directly compare the performances of PIC to fluid based numerical method directly for 2D configurations.

The contribution of the present work is to assess the ability of a two-fluid (ions+electrons) low-order moment model that includes the sheaths to accurately capture the physics that leads to instabilities in a magnetized context. We detail the impact of the numerical diffusion, which is intrinsic of Finite Volume Methods (FVM), on the onset of such instabilities. The methods we developed were implemented into *CanoP* [1], a massively-parallel code that allows for implementing finite volume schemes into an Adaptive Mesh Refinement (AMR) framework. We use PIC simulations obtained via the LPPic code developed at the Laboratoire de Physique des Plasmas, École polytechnique, as a reference for our work. We show that a fluid multiscale model with specific numerical methods is able to predict accurately the instabilities of interest in the studied configuration.

This paper is organized as follows: in Section 2, we will expose the model used as well as the basic mechanism behind the development of instabilities in the magnetized plasma column. In section 3, we present the numerical method that was applied to our problem and how to control its potentially excessive numerical diffusion in some specific regime that we encounter in our problem. Finally, our results are presented in section 4.

2. Model

2.1. Set of equations

We use the isothermal Euler equations for two fluids (ions and electrons), coupled with the Poisson equation to obtain the electric field. This model can be derived by taking the first two moments of the kinetic equations for electrons and ions and assuming an isotropic pressure with constant temperature (see

[1] CanoP is a collaborative code developed at Maison de la simulation, École polytechnque and the Institut Franais du Pétrole et des Énergies Nouvelles (IFPEN). For more details on canoP, see [14; 15].

for instance [16]). The dimensional set of equations reads:

$$\partial_t n_e + \boldsymbol{\nabla}.(n_e \mathbf{u}_e) = n_e \nu^{iz}, \quad (1)$$

$$m_e \partial_t (n_e \mathbf{u}_e) + \boldsymbol{\nabla}.(m_e n_e \mathbf{u}_e \otimes \mathbf{u}_e + p_e \mathbf{I}_d) = -n_e e (\mathbf{E} + \mathbf{u}_e \times \mathbf{B}) - m_e n_e \nu_e \mathbf{u}_e, \quad (2)$$

$$\partial_t n_i + \boldsymbol{\nabla}.(n_i \mathbf{u}_i) = n_e \nu^{iz}, \quad (3)$$

$$m_i \partial_t (n_i \mathbf{u}_i) + \boldsymbol{\nabla}.(m_i n_i \mathbf{u}_i \otimes \mathbf{u}_i + p_i \mathbf{I}_d) = n_i e (\mathbf{E} + \mathbf{u}_i \times \mathbf{B}) - m_i n_i \nu_i \mathbf{u}_i, \quad (4)$$

$$\boldsymbol{\nabla}.\mathbf{E} = \frac{n_e - n_i}{\epsilon_0} e, \quad (5)$$

where n_e and n_i are, respectively, electrons and ions number densities, $\mathbf{u}_e$ and $\mathbf{u}_i$ their macroscopic velocities, m_e and m_i their masses, p_e and p_i the pressure of the two gases, ν^{iz} the ionization rate (that can be determined via the Arrhenius law), $\mathbf{E}$ is the electric field and $\mathbf{B}$ the magnetic field, ν_e and ν_i the collision frequencies between the charged particles and neutral particles, e, the electron charge, and finally ϵ_0 is the vacuum permittivity. We also use the following classical notations

$$\boldsymbol{\nabla} = \begin{pmatrix} \partial_x \\ \partial_y \end{pmatrix}, \quad \mathbf{I}_d = \begin{pmatrix} 1 & 0 \\ 0 & 1 \end{pmatrix}.$$

For the pressure terms, the law of perfect gases is used, as follows,

$$p_e = n_e \mathrm{k_B} T_e, \quad (6)$$

$$p_i = n_i \mathrm{k_B} T_i. \quad (7)$$

In this model, we neglected elastic collisions between electrons and ions as well as recombination between ions and electrons. However, what is important here is that we do not neglect electron inertia as it would prevent the development of some instabilities, we do not assume that the plasma is quasi-neutral ($n_e \neq n_i$) as it would prevent the formation of the sheaths, we do not assume that the fluxes are ambipolar ($n_e u_e \neq n_i u_i$) neither, nor do we assume that the plasma is at thermal equilibrium ($T_e \neq T_i$). This degree of generality is needed in order to obtain a configuration that is relevant with regards to the original problem.

We can now normalize these equations both to highlight the disparity of scales as well as to manipulate reasonable numbers on a numerical level. We use the following normalization quantities:

- n_0 the characteristic density of electrons and ions,
- L_0 the reference length of the problem,
- T_e the temperature of the electrons,
- T_i the temperature of the ions.

All the other characteristic parameters can be derived from those:

- Reference velocity u_0 set at the Bohm velocity $u_0 = \sqrt{\frac{\mathrm{k_B} T_e}{m_i}}$, at which the transition between the quasi-neutral plasma and the sheaths occurs.
- Characteristic time scale $t_0 = \frac{L_0}{u_0}$.
- Reference potential is set at $\phi_0 = \frac{\mathrm{k_B} T_e}{e}$, where we introduce the electric potential ϕ such that $-\boldsymbol{\nabla}\phi = \mathbf{E}$.
- Reference magnetic field is set at $B_0 = \frac{m_i}{e t_0}$

The normalized equations hence read

$$\partial_{\bar{t}} \bar{n}_e + \bar{\boldsymbol{\nabla}}.(\bar{n}_e \bar{\mathbf{u}}_e) = \bar{n}_e \bar{\nu}^{iz}, \quad (8)$$

$$\partial_{\bar{t}} \bar{n}_i + \bar{\boldsymbol{\nabla}}.(\bar{n}_i \bar{\mathbf{u}}_i) = \bar{n}_e \bar{\nu}^{iz}, \quad (9)$$

$$\partial_{\bar{t}} (\bar{n}_e \bar{\mathbf{u}}_e) + \bar{\boldsymbol{\nabla}}.\left(\bar{n}_e (\bar{\mathbf{u}}_e \otimes \bar{\mathbf{u}}_e + \varepsilon^{-1} \mathbf{I}_d)\right) = \varepsilon^{-1} \bar{n}_e \left(\bar{\boldsymbol{\nabla}}\bar{\phi} - \bar{\mathbf{u}}_e \times \bar{B}\right) - \bar{n}_e \bar{\nu}_e \bar{\mathbf{u}}_e, \quad (10)$$

$$\partial_{\bar{t}} (\bar{n}_i \bar{\mathbf{u}}_i) + \bar{\boldsymbol{\nabla}}.(\bar{n}_i (\bar{\mathbf{u}}_i \otimes \bar{\mathbf{u}}_i + \kappa \mathbf{I}_d)) = \bar{n}_i \left(-\bar{\boldsymbol{\nabla}}\bar{\phi} + \bar{\mathbf{u}}_i \times \bar{B}\right) - \bar{n}_i \bar{\nu}_i \bar{\mathbf{u}}_i, \quad (11)$$

$$\bar{\Delta}\bar{\phi} = \chi^{-1} (\bar{n}_e - \bar{n}_i), \quad (12)$$

where $\varepsilon = \frac{m_e}{m_i}$ is the mass ratio, $\kappa = \frac{T_i}{T_e}$ the temperature ratio, $\chi = \frac{\mathrm{k_B} T_e \epsilon_0}{e^2 n_0 L_0^2} = \frac{\lambda_D^2}{L_0^2}$ the squared Debye length normalized by the scale of our problem, $\bar{\nu}^{iz} = \nu^{iz} t_0$ and

$$\bar{\nu}_i = \frac{L_0}{\lambda_i} \sqrt{\frac{8\kappa}{\pi} + \frac{\pi^2}{4} u_i^2}, \quad \bar{\nu}_e = \frac{\sigma_{en}}{\sigma_{in}} \frac{L_0}{\lambda_i} \sqrt{\frac{8}{\pi\varepsilon}},$$

by using a scaling of the values used in [8].

It is worth mentioning that, even with such a rather minimal fluid model, we already include all the scales that are going to be challenging on a numerical level. To give some perspective of what we can expect in terms of the order of these scales, we can give their value for a typical Argon low-pressure inductively coupled discharge mentionned in the introduction: $\varepsilon = 1.36 \times 10^{-5}$, $\kappa = 0.025$, $\lambda_D / L_0 = 3.5 \times 10^{-3}$.

Regarding the boundary conditions, we assume that the flux of electrons at the wall is the random flux and

that electrons have Maxwellian distribution function, which yields

$$\bar{n}_e \bar{\mathbf{u}}_e . \mathbf{e}_n = \bar{n}_e \sqrt{\frac{1}{2\pi\varepsilon}} \tag{13}$$

where $\mathbf{e}_n$ is the outgoing normal of the domain boundaries. This relatively simple boundary condition can be used to incorporate the sheaths into our model [8], although it relies on the rather strong assumption that electrons have a Maxwellian distribution and neglects more complex kinetic phenomena such as secondary electron emission.

2.2. Some key concepts to understand this configuration

In this subsection we will briefly present the concept of sheath as well as two instabilities of interest for the comprehension of our test-case.

2.2.1. Sheaths

A detailed description of the sheaths can be found in most classical plasma textbooks (see for instance [6; 17; 18]). Here, we only describe in a nutshell and in a few steps what occurs in the boundary layer close to the wall. First, as the electrons are at higher temperature and have a much lower inertia than ions, they tend to have a greater thermal velocity than the heavy particle. As a result, electrons are absorbed at a more significant rate than ions by the walls of the domain, causing them to charge negatively, thus breaking the usual quasi-neutrality of the plasma in their vicinity. This has two main consequences: on the one hand, an electric field develops that will repel electrons from the walls and accelerate ions from the bulk of the plasma toward the sheath; on the other hand, a pressure gradient will form that will attracts electrons towards the wall as well. When the sheath is in steady state, all those phenomena balance each other. The level of particles is then maintained constant within the domain by ionization process:

$$\begin{aligned} \int_{\bar{\Omega}} \bar{\nabla} . (\bar{n}_e \bar{\mathbf{u}}_e) \, \mathrm{d}\bar{V} &= \int_{\bar{\Omega}} \bar{n}_e \bar{\nu}^{iz} \mathrm{d}\bar{V} \\ \Leftrightarrow \bar{\nu}^{iz} &= \frac{\int_{\partial\bar{\Omega}} \bar{n}_e \mathrm{d}\bar{S}}{\int_{\bar{\Omega}} \bar{n}_e \mathrm{d}\bar{V}} \sqrt{\frac{1}{2\pi\varepsilon}}. \end{aligned} \tag{14}$$

The ionization rate can be seen as an eigenvalue of the problem, as when we solve for our problem we obtain both density and fluxes profiles but also a unique value of the ionization rate, all other conditions being set (size of the domain, density of neutrals...).

2.2.2. Two-stream instability

The two-stream instability is a well-known instability that can appear whenever there is a significant drift between the macroscopic velocities of ions and electrons. A detailed description of the mechanism behind the onset of this instability and of the corresponding dispersion relation and growth rate can be found in [18; 19]. On a heuristic level, we can describe the onset of this instability as follows: we consider a periodic 1D domain where ions are at rest and electrons have an nonzero velocity u_{eq}. The difference between velocities, when it is high enough, can induce a Doppler effect that will somehow synchronize the relative frequencies of oscillations of electrons and ions, allowing for resonance phenomena, and as result instabilities, to appear.

In the context of this work, we will see that in a rather counterintuitive manner a large numerical diffusion specifically on electrons, due to their low-Mach regime, can lead to a significant difference in velocities, in turn generating a spurious two-stream instability whereas one would reasonably expect a scheme that is too diffusive to dampen and not trigger instabilities.

2.2.3. Resistive-drift instabilities

Lastly, we want to briefly mention some mechanisms that are believed to be responsible for the development of instabilities in a magnetized context. It is essential to stress that this type of instabilities is still not fully understood, hence the fact that is still an active field of research. The element of explanation given here simply are mostly heuristic. A more comprehensive description can be found in [11; 12].

First we recall that when sheaths are present we have an electric field $\mathbf{E}$ generating via the Lorentz force a drift of the electrons in the direction $-\mathbf{E}$ (in this case toward the center of the domain). Conversely, the pressure gradient generates a drift in the direction $-\boldsymbol{\nabla} p_e$ (toward the walls). When a magnetic field B is applied over the domain, subsequent drifts appear in the azimuthal direction (both aforementioned drifts being in the radial direction in the absence of magnetic field), that are called the $\mathbf{E}\times\mathbf{B}$ and diamagnetic drifts. At low magnetic field, those drifts cancel each other out (see Figure 2), however as the magnetic field increases the diamagnetic drift becomes greater than the $\mathbf{E}\times\mathbf{B}$ one, leading to an overall augmentation of the azimuthal velocity of the electrons. In the meantime, ions are little or not affected by the magnetic field simply because their mass is several orders of magnitude superior to that of electrons (typically their Larmor

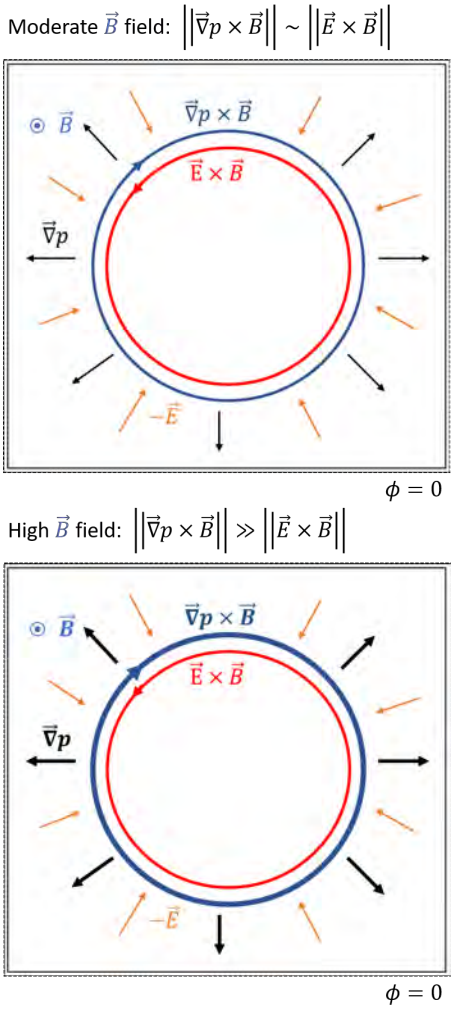

Figure 2: Representation of the drift fluxes in the plasma in the presence of moderate or high magnetic field.

radius is greater than the size of the domain) and, as a consequence, do not have an azimuthal component to their velocity. As a result, the electrons confinement increases and so does the density drop between the center of the domain and the walls (and by extension the density gradient) as the magnetic field increases. As the pressure gradient increases, it creates high fluxes in the azimuthal direction, ultimately leading to the onset of instabilities, so long as the condition $\nu = \nu_e + \nu^{iz} > 0$ is verified [11], which is the case because the ionization and collision rates are always non-negative. These are called resistive drift instabilities.

3. Numerical methods

Before we move on to detailing the numerical method and applying our chosen FVM to our system of equation, we must first write the equations, for both fluids, under the formalism of conservation laws with source term. A presentation of the general framework associated to conservation laws and the corresponding classical numerical methods, finite volume methods (FVM) can be found in [20; 21]. Both fluids obey an equation of the form:

$$\partial_t w + \partial_x f(w) + \partial_y g(w) = S(w)$$

with

$$w = \begin{pmatrix} n \\ nu \\ nv \end{pmatrix}, \quad f(w) = \begin{pmatrix} nu \\ nu^2 + nc^2 \\ nvu \end{pmatrix}, \quad g(w) = \begin{pmatrix} nv \\ nuv \\ nv^2 + nc^2 \end{pmatrix},$$

and

$$S(w) = \begin{pmatrix} n\bar{\nu}^{iz} \\ qn\left(-\partial_{\bar{x}}\bar{\phi} + v\bar{B}\right) - n\bar{\nu}u \\ qn\left(-\partial_{\bar{y}}\bar{\phi} - u\bar{B}\right) - n\bar{\nu}v \end{pmatrix}, \quad \mathbf{u} = \begin{pmatrix} u \\ v \end{pmatrix}$$

where

$c = \varepsilon^{-1/2}, q = -1$ (electrons) or $c = \kappa^{1/2}, q = +1$ (ions)

We can already emphasized that because both ε and κ are small parameters. For this reason, it is expected that electrons are going to be subsonic ($u < c$, in the so-called low-Mach regime) whereas ions are likely to be supersonic ($u > c$) in some areas of the domain.

Using a cell-centered finite volume scheme for cartesian 2D meshes for the hyperbolic right-hand side and a first order implementation of the source term left-hand side we obtain

$$w_{i,j}^{n+1} = w_{i,j}^n - \frac{\Delta t}{\Delta x}\left(F_{i+1/2,j}^n - F_{i-1/2,j}^n\right) - \frac{\Delta t}{\Delta y}\left(G_{i,j+1/2}^n - G_{i,j-1/2}^n\right) + \Delta t S(w_{i,j}^n)$$

3.1. The Lax-Friedrichs scheme

We use a variation of the Lax-Friedrich scheme, as often found in literature, to compute the approximate fluxes at the interface of each cell:

$$\mathcal{F}(w_R, w_L) = \frac{1}{2}\left(f(w_R) + f(w_L)\right) - \frac{\lambda_{max}}{2}\left(w_R - w_L\right)$$
$$\mathcal{G}(w_{up}, w_{dwn}) = \frac{1}{2}\left(g(w_{up}) + g(w_{dwn})\right) - \frac{\lambda_{max}}{2}\left(w_{up} - w_{dwn}\right)$$

with $\lambda_{\max}$ being an upper bound to the highest eigenvalue encountered in our convective problem and defined by the formula:

$$\lambda_{max} = \max\left(|u_R|, |u_L|\right) + c$$

This scheme is only first order. This scheme was chosen because it is considered to be very robust for fluid applications. The Poisson equation is solved via an iterative process. Regarding the stability conditions, the convective part of the equation and the resolution of the Poisson equation impose the main constraints:

$$\frac{\Delta t}{\Delta x} \leq \frac{1}{2\max_{i+1/2,j+1/2}\left(\lambda_{\max}\right)}, \quad \Delta x \leq \sqrt{\chi}, \tag{15}$$

bearing in mind that $\lambda_{\max}$ will scale as $\varepsilon^{-1/2}$ for electrons. The stability conditions linked to the source term are the following: $\Delta t \leq 1/\max\left(\bar{\nu}_e, \bar{\nu}_i, \bar{\nu}^{iz}\right)$, $\Delta t \leq \varepsilon/\bar{\mathbf{B}}$. These stability conditions can be obtained via von Neumann analysis.

Regarding the boundary conditions, we use a classical implementation of Neumann boundary conditions found in [21]. We copy the value of the cell at the boundary of the domain into the ghost cell, except for the component of the flux that is normal to the boundary of the domain, for which we impose:

$$\frac{(n\mathbf{u})_e^{ghst} + (n\mathbf{u})_e^{bndry}}{2} \cdot \mathbf{e}_n = n_e^{bndry}\sqrt{\frac{1}{2\pi\varepsilon}}, \tag{16}$$

where we recall that $\mathbf{e}_n$ is the outgoing normal of the domain. On the boundary, we consequently have $\lambda_{\max} = \left(\frac{1}{\sqrt{2\pi}} + 1\right)\frac{1}{\sqrt{\varepsilon}}$ and this must be included when sheaths are considered in our stability conditions.

Finally, the ionization rate $n\bar{\nu}^{iz}$ is computed dynamically so that it compensates for the loss of ions at the walls in order to maintain the overall quantity of ions in the domain constant:

$$\left(\bar{\nu}^{iz}\right)^n = \frac{\sum_i\sum_j \bar{n}_{i_{i,j}}^{n+1/2}\Delta x^2 - \sum_i\sum_j \bar{n}_{i_{i,j}}^{n}\Delta x^2}{\Delta t\sum_i\sum_j \bar{n}_{e_{i,j}}^{n}\Delta x^2} \tag{17}$$

where the superscript $n + 1/2$ denotes the updated quantities after the application of the convective part only (no source term).

This method was implemented in *CanoP*, however the AMR feature of the code was not used in this preliminary work since its interaction with the development of instabilities is quite complex and would require AP schemes to be fully operational.

3.2. Numerical diffusion and low-Mach correction

Taking a closer look at our fluxes at the cell interface,

$$\mathcal{F}(w_R, w_L) = \frac{1}{2}\left(f(w_R) + f(w_L)\right) - \frac{\lambda_{max}}{2}\left(w_R - w_L\right), \tag{18}$$

we can see that it consists of a first term that is a second order approximation of the flux at the interface plus a term that we will refer to as a term of numerical diffusion. The idea behind the numerical diffusion comes from the theory of modified equations that can be found in many classical textbooks on numerical methods (see for instance [20]). This numerical diffusion plays a central role in ensuring the stability of the numerical scheme. However, it also introduces an error term of order $\lambda_{\max}\Delta x$. For electrons that are in the low Mach regime (i.e. very subsonic), we have $\lambda_{\max} \sim \varepsilon^{-1/2}$. Consequently, instead of being negligible, the numerical diffusion term can actually be of order Δx^0 if we do not have $\Delta x \ll \varepsilon^{1/2}$. In particular, this means that we will observe a significant diffusion in our numerical solution that does not come from the physics of our problem, potentially influencing the onset of instabilities by severely dampening the electron fluxes.

In order to compensate for this effect in the low-Mach regime for electrons, we introduce a so called Low-Mach Correction (LMC) adapted from [22]. We rescale the maximum eigenvalue of the problem in the following way:

$$\lambda_{max} = \max\left(|u_R|, |u_L|\right) + f(\hat{M})c \tag{19}$$

with

$$f(\hat{M}) = \frac{\sqrt{(1-M_0)^2\,\hat{M}^2 + 4M_0}}{1 + M_0^2} \tag{20}$$

and

$$M_0 = \sqrt{\min\left(1, \max\left(\hat{M}^2, M_{co}^2\right)\right)} \tag{21}$$

Where $\bar{M}$ is an adapted Roe average of the Mach number at the interface that we will define shortly. The idea is to modify the velocity of propagation of the

information c. The function f basically behaves as $\min\left(1, |\hat{M}|\right)$ in that is saturates at 1 and scale as $\hat{M}$ provided $\hat{M} \geq M_{co}$. Nevertheless, it differs from the the function in two regards: first it is a smooth function of $\hat{M}$ and secondly it does not go below the cut off value M_{co} when $\hat{M}$ goes to zero. This is very important as it prevents the numerical diffusion from vanishing in areas of the bulk of the plasma where the macroscopic velocity goes to zero, hence ensuring numerical stability. In [22], the average value of the Mach number is defined by

$$\hat{M} = \frac{\sqrt{\bar{n}_L}\bar{u}_L + \sqrt{\bar{n}_R}\bar{u}_R}{\sqrt{\bar{n}_L} + \sqrt{\bar{n}_R}}\varepsilon^{1/2},$$

However the Liou LMC was initially designed for the AUSM schemes that naturally incorporate a first order diffusive term that is a Laplacian of the pressure. Because this term is not present in our scheme, the application of this LMC can lead to the development of so-called checkerboard instabilities [23]. In order to solve this issue, we modify the average value of the Mach number at the interface following [23]:

$$\begin{aligned}\hat{M} &= \frac{|\hat{u}| + |\hat{v}|}{c} \\ &= \left(\left|\frac{\sqrt{\bar{n}_L}\bar{u}_L + \sqrt{\bar{n}_R}\bar{u}_R}{\sqrt{\bar{n}_L} + \sqrt{\bar{n}_R}}\right| + \left|\frac{\sqrt{\bar{n}_L}\bar{v}_L + \sqrt{\bar{n}_R}\bar{v}_R}{\sqrt{\bar{n}_L} + \sqrt{\bar{n}_R}}\right|\right)\varepsilon^{1/2},\end{aligned}$$

taking into account both normal and transverse component of the velocity at the interface. To our knowledge this combination of the two approaches is a new contribution to the subject.

4. Results

4.1. First test-case: non-magnetized configuration

The first case that we considered is a non-magnetized configuration. This can be considered as a first step for the validation of our model, numerical method and implementation. We use the following parameters: $\varepsilon = 1/1836$, $\sqrt{\chi} = \bar{\lambda}_D = 0.2$, $\kappa = 0.025$. This specific mass ratio corresponds to a plasma made of protons, the lighter possible ions that exist. Although actual plasma based on hydrogen are more complex (in particular they might contain molecules of H_2 and negative ions H^-), this seems a suitable choice as it remains reasonable in terms of physics but it is also easily attainable on a numerical level. The reference density and temperature of electrons are respectively set at $n_0 = 2\times10^{-5}\ 2\times10^{15}$ m^{-3} and $T_e = 14$ eV (values found in reference PIC simulations for this configuration [12]). In terms of dimensional parameters, this corresponds to $L_0 = 50\bar{\lambda}_D \approx 3$ cm and a simulation time of $\bar{t}_f = 4$ to $t_f \approx 4$ μs. We used a 256×256 mesh ($\Delta x \approx \bar{\lambda}_D/5$) and a time step $\Delta t = CFL \times \Delta x/\lambda_{\max} \approx 10^{-5}$ (with $CFL = 0.6$ here), resulting in approximately $3 - 5h$ of simulation on 64 CPUs. The result of the simulation are shown in Figure 3.

As can be seen in Figure 3, the simulation has converged in time to a steady state with sheaths. In particular, when taking a 1D horizontal cut at the center of the simulation domain, we can observe the characteristic shape of ions and electrons densities, with the central bulk of plasma being quasi-neutral and charge separation close to the walls (as expected from [6]). This constituted a first validation of our approach as the sheath structure is well-reproduced by in our simulations.

Regarding the fluxes of ions and electrons, we obtain the result depicted in Figure 4.

As expected from PIC simulations the fluxes are not ambipolar. More precisely, we can observe a specific structure where electron fluxes are higher in the corners of the domain whereas ion fluxes are maximum at the center of the faces of the domain.

However, we can observe that close to the center of the faces of the domain (wide blue areas for electron fluxes in Figure 4 (c)), the simulation that we produced seems to differ significantly from the PIC simulation, since the flux of electron is lesser than what it was expected to be from PIC simulations. This limitation of the fluxes, if particularly visible near the center of the walls, actually applies to the whole domain. The consequence of these limitations can be multiple when it comes to the onset of instabilities. One of the obvious consequences is that the fluxes might not be high enough to trigger an instability. Nevertheless, it can also create areas where the fluxes of electrons are artificially much lower than that of ions, potentially resulting in a two-stream like instability if the numerical diffusion is not so high that it dampens any growing oscillation. This problem must be carefully dealt with, as is shown in the next section.

4.2. Application of the low-Mach correction

In figure 5 we compare electrons fluxes with and without the low-Mach correction (for $M_{co} = 0.05$ and $CFL = 0.4$) to the reference PIC simulation. We can observe that not only are the fluxes significantly higher with the low-Mach correction than without, but

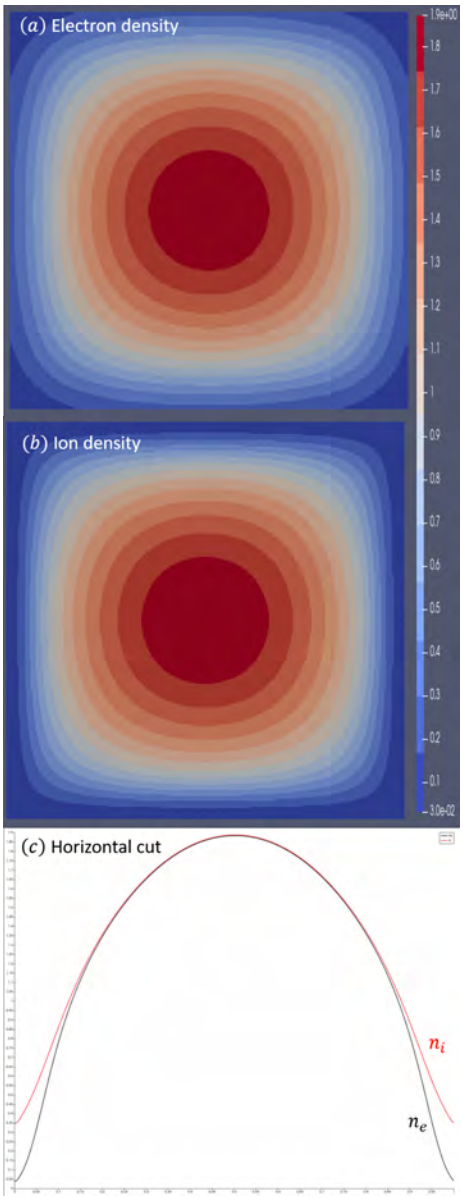

Figure 3: Steady state including sheaths: (a) electron density, (b) ions density, (c) horizontal 1D cut taken at the center of the domain, ion density is the red line and electron density the black one.

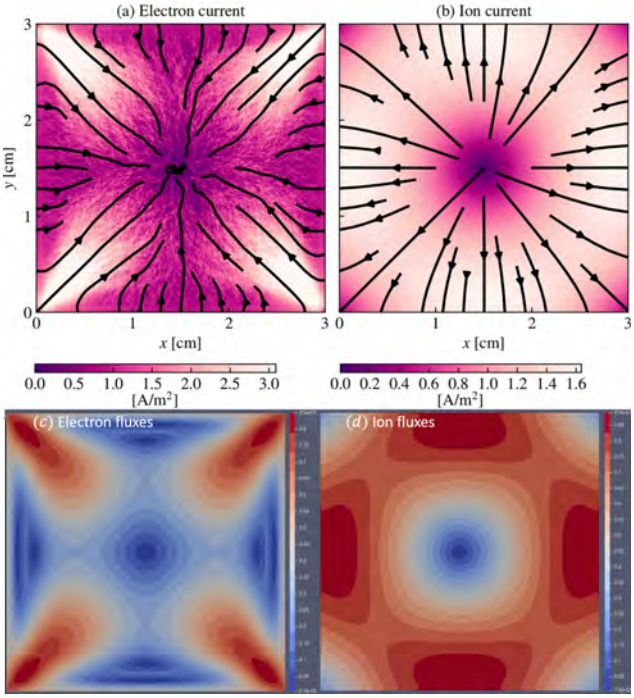

Figure 4: Electrons and ions fluxes. (a), (b) are reprinted from [12], PIC simulation, whereas (c), (d) are obtained with our approach

their structure also seems to be much closer to that of the PIC simulation.

Interestingly enough, for intermediate values of the cut-off parameter M_{co}, for instance $M_{co} = 0.2$ and $CFL = 0.4$, we observed that spurious instabilities develop. The simulation obtained firstly evolved to a quasi-steady state where the difference between ion and electron remained relatively high, but oscillations emerged later on in the simulation, whereas the non-magnetized case is expected to be stable. We believe that in this specific regime the difference between ion and electron fluxes was high and the numerical diffusion was low enough to allow for the onset of this spurious instabilities. When the cut-off M_{co} is chosen to be lower this instabilities in the non-magnetized case disappears.

4.3. Second test-case: high magnetic field

Now that we have proposed a low-Mach correction that allowed to produce accurate fluxes for electrons, we could move on to a magnetized configuration, identical to the first one in terms of parameter, save for the fact that now $\bar{\mathbf{B}} > 0$. In what follows the low-Mach correction is applied with $M_{co} = 0.05$, unless specified otherwise.

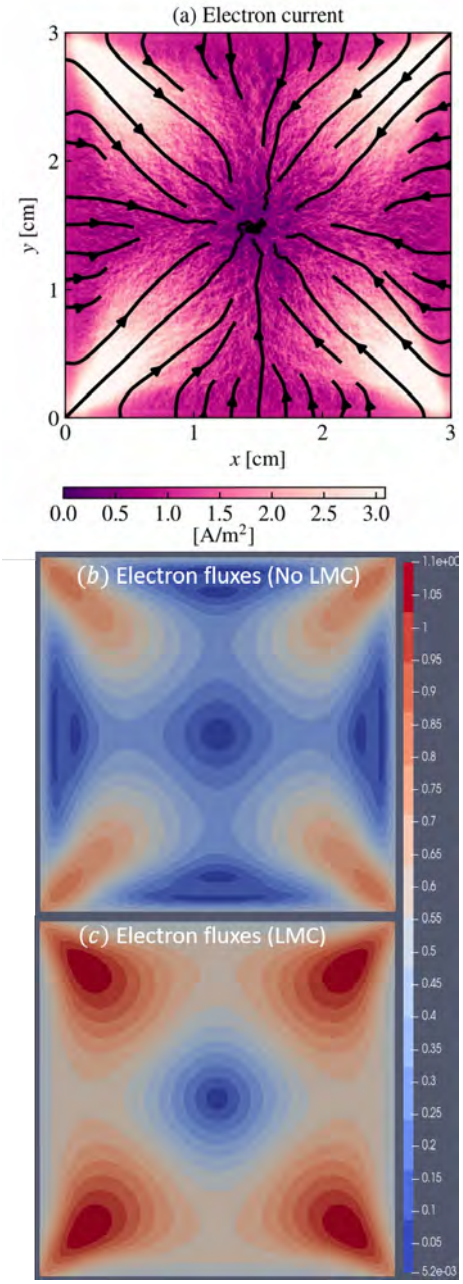

Figure 5: Comparison of the effect of the LMC: (a) reference simulation reprinted from [12], (b) simulation without the LMC, (c) LMC with $M_{co} = 0.05$

For low values of the magnetic field, the simulation converged towards a stable state. For instance, for $\bar{\mathbf{B}} = 0.3$, i.e. $\mathbf{B} \approx 1$ mT, which means that $L_0 \approx \rho_e$ and $\rho_i \approx 10L_0$ (where ρ_e and ρ_i are respectively the ion and electron Larmor radius), the behavior of the ions was similar to that of the non-magnetized case, while electron density also kept a similar structure as compared to the non-magnetized case, except that the density was higher in the center due to the magnetic confinement. Only the electron fluxes show a major evolution and resembles a rotor shape. However, no instability triggers for this reasonably low value of the magnetic field, as was expected from the results with PIC simulations [12; 11].

When we move to a higher value of the magnetic field, $\bar{\mathbf{B}} = 0.5$, corresponding to $\mathbf{B} \approx 6$ mT and $L_0 = 20\rho_e$ and $\rho_i = 2L_0$, an instability that we believe corresponds to the resistive drift instability of [11] develops in the simulated plasma. In Figure 6, we can see one frame in time of the instability, both for electron density and flux. We emphasize that without the low-Mach correction, the electron fluxes remained to low for the instability to develop and we obtain the rotor shape characteristic of lower magnetic field values as can be seen in Figure 6 (c), thus demonstrating the necessity of applying some form of correction to compensate for the excessive numerical diffusion of our finite volume method.

We observe that this instability seems to interact strongly with the sheath region. More precisely, it seems important to include the sheaths in our simulations since the accuracy of using a Bohm-like criteria on a square boundary for ions seems questionable. Neglecting charge separation might lead to significant error in the results.

5. Conclusion and future plans

First, we have shown that a relatively simple low-order moment model, i.e., the two-fluid (ion+electron) isothermal Euler equations, coupled with the Poisson equation, can encompass enough of the relevant physics to observe the onset of instabilities similar to those that were described in [11] and obtained with the PIC approach. Indeed, the model can be considered as a rather minimal model that includes relevant scales of the physics, also exemplifying the challenges that appear on a numerical level due to the stiffness of models attempting to describe low-temperature magnetized plasmas in general. Our simulations also allowed to demonstrate how crucial it was to tackle the issue of numerical diffusion when

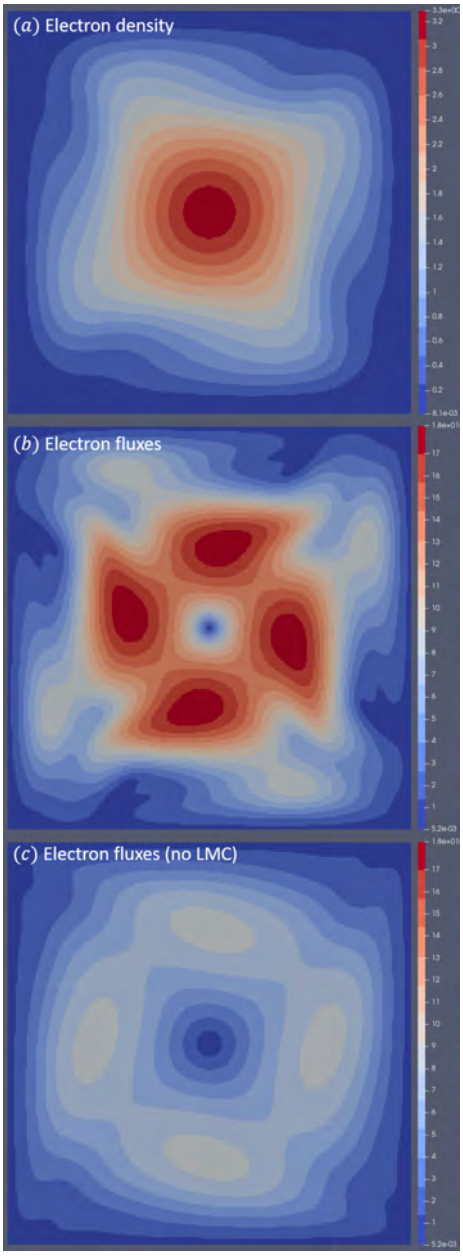

Figure 6: Onset of the magnetic instability: (a) electron density, (b) electron fluxes, (c) electron fluxes without the LMC

using finite volume methods in that context. An excessive value can obviously dampen all instabilities, but more subtle phenomena can also occur for intermediate values of excessive numerical diffusion, with the artificial disparity between ion and electron fluxes leading to the onset of spurious instabilities. We are currently working on writing a comprehensive paper on these results [24]. We are also investigating so called Asymptotic Preserving (AP) methods as a way to deal efficiently with the multiple scales that are present in our problem [25]. Finally, we also consider to exploit the Adaptive Mesh Refinement feature of CanoP, the code into which we implemented our numerical methods. Implementing these various numerical strategies is part of a long-term effort to develop accurate and efficient fluid code for low-temperature magnetized plasmas.

Acknowledgment

This work is funded by a joint PhD grant from the French Ministry of Defence (Direction Générale de l'Armement, DGA) and the Région Île-de-France (DIM Math Innov).

References

[1] J.-P. Boeuf, Tutorial: Physics and modeling of hall thrusters, Journal of Applied Physics 121 (1) (2017) 011101.

[2] T. Lafleur, S. Baalrud, P. Chabert, Theory for the anomalous electron transport in hall effect thrusters. II. kinetic model, Physics of Plasmas 23 (5) (2016) 053503.

[3] S. Barral, E. Ahedo, Low-frequency model of breathing oscillations in hall discharges, Physical Review E 79 (4) (2009) 046401.

[4] T. Lafleur, P. Chabert, The role of instability-enhanced friction on 'anomalous' electron and ion transport in Hall-effect thrusters, Plasma Sources Science and Technology 27 (1) (2017) 015003.

[5] J.-P. Boeuf, L. Garrigues, E×B electron drift instability in hall thrusters: Particle-in-cell simulations vs. theory, Physics of Plasmas 25 (6) (2018) 061204.

[6] P. Chabert, N. Braithwaite, Physics of radio-frequency plasmas, Cambridge University Press, 2011.

[7] T. Charoy, J.-P. Boeuf, A. Bourdon, J. A. Carlsson, P. Chabert, B. Cuenot, D. Eremin, L. Garrigues, K. Hara, I. D. Kaganovich, et al., 2d axial-azimuthal particle-in-cell benchmark for low-temperature partially magnetized plasmas, Plasma Sources Science and Technology 28 (10) (2019) 105010.

[8] A. Alvarez-Laguna, T. Magin, M. Massot, A. Bourdon, P. Chabert, Plasma-sheath transition in multi-fluid models with inertial terms under low pressure conditions: Comparison with the classical and kinetic theory, Plasma Sources Science and Technology 29 (2) (2020) 025003.

[9] A. A. Laguna, T. Pichard, T. Magin, P. Chabert, A. Bourdon, M. Massot, An asymptotic preserving well-balanced scheme for the isothermal fluid equations in low-temperature plasmas

at low-pressure, Journal of Computational Physics 419 (2020) 109634.
[10] P. Crispel, P. Degond, M.-H. Vignal, An asymptotic preserving scheme for the two-fluid euler–poisson model in the quasineutral limit, Journal of Computational Physics 223 (1) (2007) 208–234.
[11] R. Lucken, A. Bourdon, M. Lieberman, P. Chabert, Instability-enhanced transport in low temperature magnetized plasma, Physics of Plasmas 26 (7) (2019) 070702.
[12] R. Lucken, Theory and Simulation of Low Pressure Plasma Transport Phenomena, Application to the PEGASES thruster., Ph.D. thesis, École doctorale n^o572 Ondes et Matire (EDOM), https://tel.archives-ouvertes.fr/tel-02435208 (2019).
[13] S. Sadouni, Fluid modeling of transport and instabilities in magnetized low-temperature plasma sources, Ph.D. thesis, École doctorale GEED, https://tel.archives-ouvertes.fr/tel-02978476 (2020).
[14] F. Drui, Eulerian modeling and simulations of separated and disperse two-phase flows : development of a unified modeling approach and associated numerical methods for highly parallel computations, Ph.D. thesis, École Centrale Paris, https://tel.archives-ouvertes.fr/tel-01618320 (2017).
[15] Q. Wargnier, Mathematical modeling and simulation of non-equilibrium plasmas: application to magnetic reconnection in the sun atmosphere, Ph.D. thesis, École doctorale CentraleSupelec, https://tel.archives-ouvertes.fr/tel-02500745 (2019).
[16] S. Braginskii, Transport processes in a plasma reviews of plasma physics, Ed. Ma Leontovich (New York: Consultants Bureau).
[17] M. A. Lieberman, A. J. Lichtenberg, Principles of plasma discharges and materials processing, John Wiley & Sons, 2005.
[18] F. F. Chen, et al., Introduction to plasma physics and controlled fusion, Vol. 1, Springer, 1984.
[19] A. Soosaleon, B. Jose, et al., Two stream instability as a source of coronal heating, International Journal of Astronomy and Astrophysics 5 (02) (2015) 61.
[20] R. J. LeVeque, et al., Finite volume methods for hyperbolic problems, Vol. 31, Cambridge University Press, 2002.
[21] E. F. Toro, Riemann solvers and numerical methods for fluid dynamics: a practical introduction, Springer Science & Business Media, 2013.
[22] M.-S. Liou, J. Edwards, 30th Computational Fluid Dynamics, Lecture Series 1999-03, von Karman Institute for Fluid Dynamics, 2004.
[23] F. Rieper, A low-Mach number fix for Roes approximate riemann solver, Journal of Computational Physics 230 (13) (2011) 5263–5287.
[24] L. Reboul, A. A. Laguna, T. Magin, P. Chabert, A. Bourdon, M. Massot, Efficacy of multifluid models for the simulation of instability-enhanced transport in low-temperature magnetized plasmas, In preparation (2021).
[25] L. Reboul, A. A. Laguna, T. Pichard, M. Massot, Advanced numerical methods for the simulations of multi-scale fluid models of low-temperature plasmas in the presence of sheath, In preparation (2021).

Modeling strategy for blackout analysis of re-entry phases in space exploration missions

Vincent Fitzgerald Giangaspero

Aeronautics and Aerospace Department, von Karman Institute for Fluid Dynamics, Belgium, vincent.giangaspero@vki.ac.be

Supervisor: Thierry Magin

Professor, Aeronautics and Aerospace Department, von Karman Institute for Fluid Dynamics, Belgium, magin@vki.ac.be

Advisor: Andrea Lani

Research Expert, Aeronautics and Aerospace Department, von Karman Institute for Fluid Dynamics, Belgium, lani@vki.ac.be

University Supervisor: Stefaan Poedts

Professor, Department of Mathematics, KU Leuven, Belgium, stefaan.poedts@kuleuven.be

Abstract

The numerical simulation model that combines plasma flows and ray tracing is applied to evaluate radio frequency blackout for the atmospheric reentry demonstrator of the European Space Agency. Bi-dimensional analysis is performed at four different trajectory points characterized by different ionization levels. The results show how this methodology is suited to analyze blackout for Earth re-entry missions.

Keywords: Plasma flows, atmospheric re-entry, CFD, ray tracing, communicaiton blackout, ionization

1. Introduction

The re-entry phase is one of the most challenging phases of a space mission and it's one of the most critical aspects to be considered for the design of a successful space mission. The severe conditions experienced during hypersonic re-entry flights pose specific spacecraft design constraints and the characterization of the corresponding flows requires advanced theoretical, experimental and numerical investigation, which are all part of ongoing research efforts. Among the open challenges in the aerospace sector, communication blackout is an important issue for space exploration missions and it is extremely important to develop strategies for ensuring the propagation of telemetry during atmospheric re-entry flights.

Communications blackout is a well-known phenomenon since the early days of the space era and it applies to any atmospheric re-entry in which ionization occurs within the flow surrounding the spacecraft. During blackout, vehicles cannot receive guidance or maneuvering information from a control center and can travel for hundreds of miles, possibly endangering the whole mission and deeply affecting crew or payload safety. Clearly a way to minimize or remove this disruption would provide a significant advantage for future missions, allowing the transmission of more data and a safer control of the vehicle during the delicate re-entry phase. In the present paper the developed numerical model to analyze communications blackout is applied to the Earth re-entry of the atmospheric reentry demonstrator (ARD). The proposed methodology, based on research efforts carried on at the von Karman Institute for Fluid Mechanics over the past years, has been applied to the Martian re-entry of the ExoMars Schiaparelli module in [1] and [2]. This work has been the first study in literature of the ExoMars Schiaparelli blackout period (duration and location on trajectory) by the use of a novel blackout analysis methodology which incorporates a decoupled CFD approach in combination with a ray tracing algorithm. In this work we focus on the first attempt to analyze re-entry blackout for an

Earth re-entry. In this work, bi-dimensional, zero angle of attack re-entry flight conditions are simulated. Future work will be focus on the application of the ray tracing technique on tri-dimensional conditions to perform real flight conditions analysis. After giving an overview of the re-entry Blackout from a physical point of view in Section 2, the ARD re-entry mission is summarized in Section 3. The numerical model to analyze blackout is presented in Section 4. Finally, Section 5 presents results at four different re-entry trajectory points, discussing the results in terms of rays behaviour and physical characterization of the flow.

2. The Blackout phenomena

When a spacecraft enters a planetary atmosphere at hypersonic speed, high velocities (typically around or higher than 10 km/s) generate strong shock waves and extreme aerodynamic heating of the vehicle. High post-shock temperatures result in dissociation and ionization of the hot gas, generating an ionized flow, a.k.a. plasma, around the vehicle. Due to the presence of free charge carriers, plasma reacts to electromagnetic fields and interacts with the on-board transmission systems of the spacecraft. Fig. 1 shows a sketch representation of this phenomenon. Plasma attenuates the radio frequency (RF) signal emitted from the spacecraft, and transmission is possible only at RF frequencies greater than the characteristic plasma frequency [3].

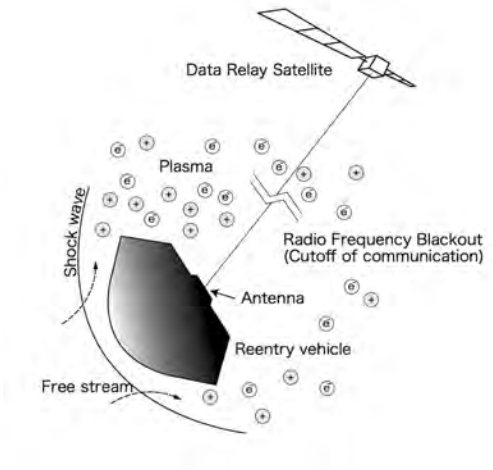

Figure 1: Sketch representation of plasma flow formation during re-entry

The plasma frequency is directly related to the electron number density around the vehicle, which represents the ionization degree of the gas. At different signal transmission frequencies correspond different electron number densities that disrupt the signal propagation. The ionization degree of the flow depends on the vehicles geometry, flight conditions, atmosphere composition and altitude [4]. During re-entry flights, electron production is low in the beginning due to the general low neutral density of the atmosphere. As the capsule flights at high-speed through gradually more dense layers of the atmosphere, electron production increases, reaching a maximum approximately at the time of the aerodynamic heating peak. Afterwards, electron production diminishes due to the low-speed capsule in the landing phases of the re-entry. In order to minimize the risk of blackout, missions such as MSL, Mars Pathfinder, and ExoMars Schiaparelli have placed an antenna in the vicinity of the vehicle aft, where the flow is less ionized. This design solution allows to reduce the overall time of communication disruption, avoiding RF signal to travel through zones at high electron density, but is not enough to guarantee a continuous signal communication during the whole re-entry phase. Communication is restored when the plasma frequencies decrease, which is due primarily to the deceleration of the re-entry vehicle. During the re-entry, depending on the ionization level of the flow, the RF signal from the spacecraft can be either degraded (brownout) or completely attenuated (blackout) by the plasma layer.

3. Atmospheric Re-Entry Demonstrator (ARD)

In this work, the developed blackout prediction model is applied to the atmospheric re-entry of the ARD capsule. The Atmospheric Reentry Demonstrator (ARD), part of the technological activities of the European Space Agency (ESA) in the frame of the Manned Space Transportation Program (MSTP), is the very first guided sub-orbital reentry vehicle built, launched and recovered by Europe. The mission was aimed at demonstrating the ability of the European space industry to design low-cost reentry vehicles and to master most of the critical phases relative to their missions (sub-orbital flight, reentry and recovery). On-board measurements provide the opportunity to gather a lot of information about the physical phenomena involved in these successive phases, and to build an experimental data base to be used in the development of future Reentry Vehicles [5]. ARD aeroshape is an Apollo-70% scaled capsule of 2.8 m diameter weighing 2.8 tons. The ARD was launched by ARIANE 5 V503 on October 21, 1998. After a

fully successful sub-orbital and reentry flight, it was recovered in the Pacific Ocean. An overview of the mission profile is reported in Fig 2.

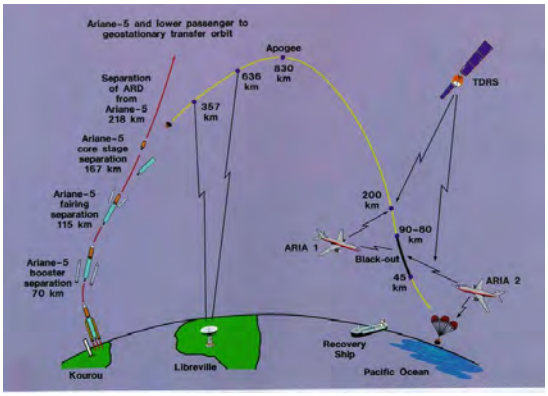

Figure 2: ARD mission profile [5]

The ARD employed eight dedicated skin antennas for a telemetry link and communication with the GPS satellites, TDRS, and airplanes (ARIA 1 and ARIA 2) during its fight. The GPS and TDRS link frequencies were approximately 1.575 and 2.267 GHz, respectively. Measurements were made of the RF blackout and plasma attenuation caused by the plasma around the vehicle generated by the shock wave. The beginning and end of the RF blackout for the GPS link on the trailing edge were at altitudes of 90 km and 40 km, respectively. On the other hand, no RF blackout for the TDRS link was observed, even though a strong plasma attenuation of the link was measured from an altitude of 86 km to an altitude of 44 km [6]. In this work, the TDRS link blackout will be studied by the application of a bi-dimensional ray tracing technique.

4. Blackout Analysis Methodology

The methodology used in this work starts with the numerical simulations of different trajectory points during the atmospheric re-entry flight. The CFD solver needs to be capable to deliver accurate electron density fields, which are needed for the analysis of interaction between electromagnetic waves and plasma. For this purpose the numerical simulations are performed with the COOLFluiD ATD solver [7] coupled to the thermochemical library solver PLATO, developed at the University of Illinois at Urbana-Champaign (UIUC) [8], [9]. The second step is the use of a ray tracing technique, an high-frequency method that approximate a radio wave propagating in a medium as a ray. A ray interacts with objects in the

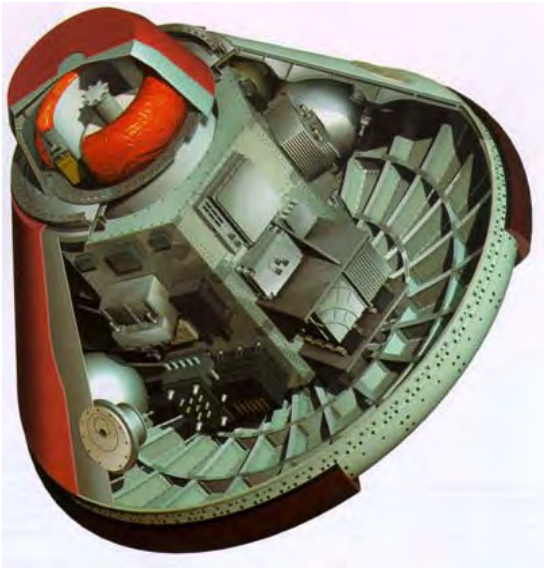

Figure 3: ARD capsule [5]

propagation environment and undergoes refractions, reflections and absorptions depending on the geometrical characteristics of the plasma flow. Ray tracing theory is founded on geometrical optics, and provides a reliable method to estimate the dominant path of energy flow in propagating EM waves. The propagation of electromagnetic waves in a medium is described by the Appleton equation, which Davies presents in various forms in [10]. The propagation is governed by the complex refractive index of the plasma n, consisting of a real part, μ, and an imaginary part, χ. The real part μ represents the real refractive index while the imaginary part χ represents the absorptivity, responsible of attenuation effects on the travelling wave.

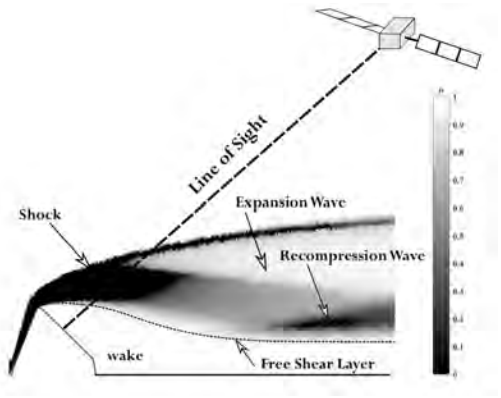

Figure 4: Wake flow structure with refractive index μ

Fig. 4 describes the distinctive flow structure within

the wake flow of the ExoMars Schiaparelli re-entry module and its refractive index field. The front part of the flow is characterized by the presence of an hypersonic thin shock layer, with peaks of aerothermodynamic heating and, thus, electrons production. This zone presents the higher values of electron densities, making communications impossible in this direction, with an overall refractive index equal to 0 in the whole front shock layer. The flow is then turned around the shoulder of the vehicle resulting in an expansion fan, which curves the bow shock, decrease the temperature and accelerates the flow. In this region, due to lower temperature values, recombination occurs, reducing the presence of free electrons, as visible from higher values of the refractive index. The expansion region is followed by a recompression shock, that is created as the flow realigns with the axis due to the axisymmetric boundary condition. The occurrence of different flow features significantly changes the optical properties of the gas, with generally refractive index around unity in the colder regions, approaching zero values where electrons are abundant.

The ray tracing technique employed in this work has been developed and applied for the first time to a mars re-entry in [1]. It is an iterative marching technique that assumes discrete, straight wave propagation over small distances. The rays are emitted at the vehicles aft position, from the antenna location, and the antenna is assumed to be half-omnidirectional, i.e. the signal is equally strong in each direction away from its surface. At each step, the direction of the ray is determined using the laws of geometrical optics. The deviation of a rays path from a straight line is computed by the use of Snells law, as illustrated in Fig. 5:

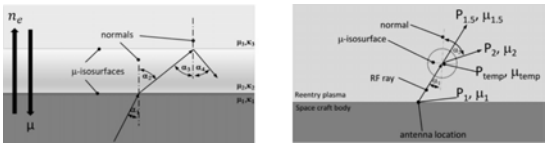

Figure 5: Snells Law application (left) and ray tracing marching technique (right)

$$\mu_1 \sin\alpha_1 = \mu_2 \sin\alpha_2 \tag{1}$$

The ray-tracing algorithm is a marching-in-space method and the signal is modeled as a ray that advances for a chosen finite distance, defined as the marching step. A schematic of the procedure is shown in Fig. 5. A chosen step size in the domain represents a region of constant refractive index, which is called an iso-surface. Snells Law is then applied at the boundaries of the iso-surfaces. The marching technique starts by advancing one step size from P_1 to $P_{1.5}$. The refractive index is determined at $P_{1.5}$ and the algorithm then goes back to P_{temp} by advancing backwards at half the step size. The radius of the iso-surface and its associated normal is found. Snells Law is then applied between P_1 and $P_{1.5}$ to find α_2. The algorithm then advances to P_2 by advancing half the value of the step size from P_{temp} at an angle α_2. The process is repeated until a border of the domain is reached or the attenuation of the signal reaches a threshold. The described methodology is implemented in a Matlab based software called Black-Out-RAy-Tracer (BORAT) of which version 1.2 is used in this work.

5. Results

In this section results from the application of the combined CFD simulations of the flow-field and ray tracing analysis will be presented. The computational domain is shown in figure 6. ANSYS ICEM CFD, Release 18.1, has been used to create a single block grid where the grid is made orthogonal to the body at its surface.

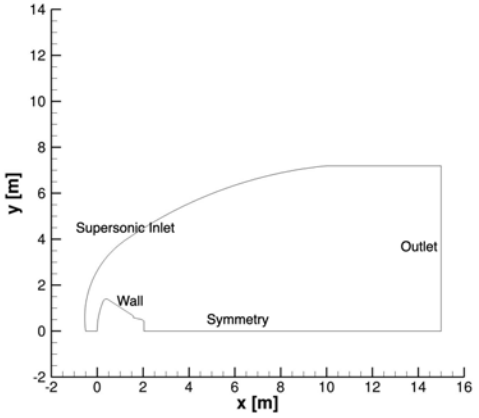

Figure 6: Computational domain

In this study, the following assumptions are made. (1) The flow is laminar, steady, continuum, and axisymmetric. (2) The inflow gas is air. (3) The flowfield is in thermochemical nonequilibrium, and the temperature is separated into translational (T) and vibrational (Tvib). The flowfield is described by the Navier-Stokes equations with a multi-temperature model and

the equation of state. For chemical reactions in high-temperature air, the test gas is assumed to consist of 11 chemical species (N2, O2, NO, N+2, O+2, NO+, N, O, N+, O+, and e-), and 49 reactions are assumed to occur. In the present study, the forward and backward reaction rates of the chemical reaction are given by Park's model [11]. The non-slip condition for the velocity and the non-catalytic condition for the mass concentration are imposed at the wall surfaces. The translational (T) and vibrational (Tvib) temperatures are fixed at the wall and are set to be 800 K. An axisymmetric condition is imposed along the symmetry axis.

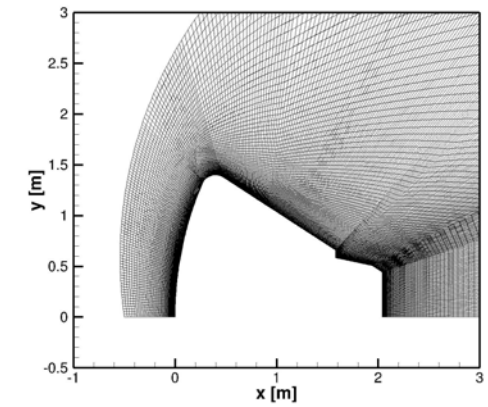

Figure 7: Mesh distribution

The present calculations are performed for 4 cases with altitudes between 85 km and 45 km. Inflow parameters such as the freestream velocity, density, and temperature are set according to the flight conditions in [5] as listed in 1.

Table 1: Computational conditions

Altitude	ρ_∞	V_∞	T_∞	M_∞
km	kg m^{-3}	m s^{-1}	K	-
45	2.25E-3	3323	255.6	10.3
60	3.40E-4	6105	242.0	19.5
75	4.01E-5	7592	201.7	26.6
85	8.22E-6	7577	191.0	27.3

5.1. CFD solutions

In this section the flow-field solution at the four different trajectory points are shown. The first step has been the duplication of the solution respect the symmetry axis in order to set-up a full bi-dimensional analysis of the blackout phenomena. Fig. 11, 10, 9, 8 show the evolution of temperature field during the re-entry tajectory.

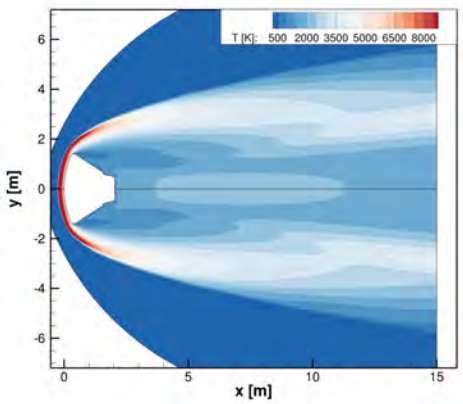

Figure 8: Altitude 85km

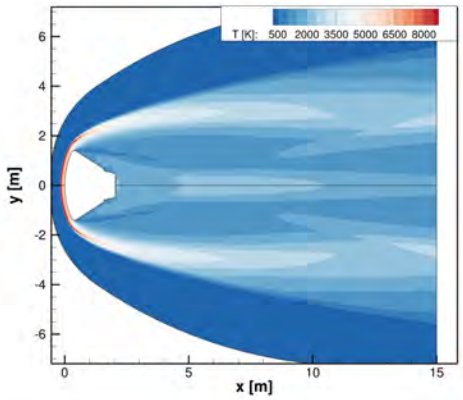

Figure 9: Altitude 75km

The main flow feature that characterize the solutions is the strong shock generated in front of the spacecraft that allows the flow to decelerate and pass over the surface of the body. In this region high temperature peaks arise and the ionization levels of the flow reach their maximum. Subsequently, the flow is cooled down and accelerated over the vehicle shoulder by an expansion fan, that lowers the ionization levels of the flow. Generally, this is the region where spacecrafts mount communications antennas to partially overcome blackout conditions during the re-entry. The wake region is characterized by a recircu-

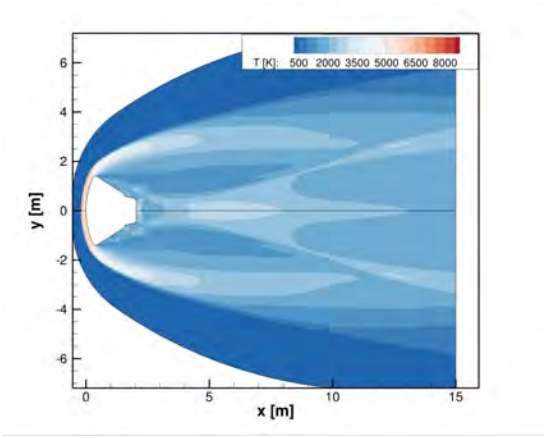

Figure 10: Altitude 60km

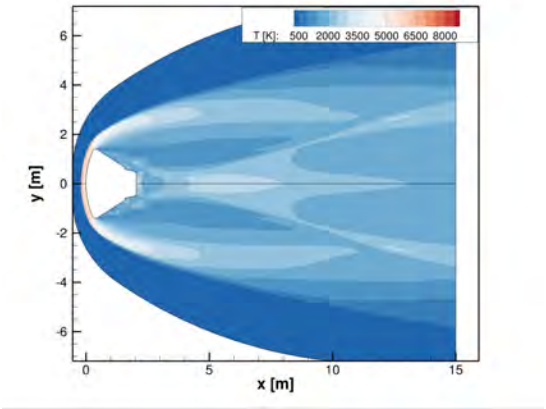

Figure 11: Altitude 45km

lation region and a recompression zone, that highers electron densities in the wake. Despite the low ionization levels in the wake, that in the methodology presented in [1] was neglected in first approximation, the improved capabilities of the CFD solver now allows to extract information from this region, essential for a proper characterization of the RF signal path.

5.2. Ray Tracing

The parameters describing the propagation of an EM wave in plasma introduced in section 4 are then computed and displayed for the selected ARD trajectory points. The ARD on-board antenna transmission frequency is $f = 2.2$Ghz. The refractive index μ is computed over the whole field by the use of the Appleton equation, and it defines the optical properties of the flow, used as computational domain for the ray tracing integration.

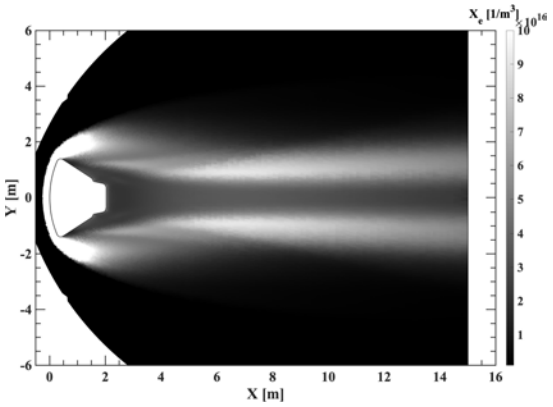

Figure 12: Altitude 85km

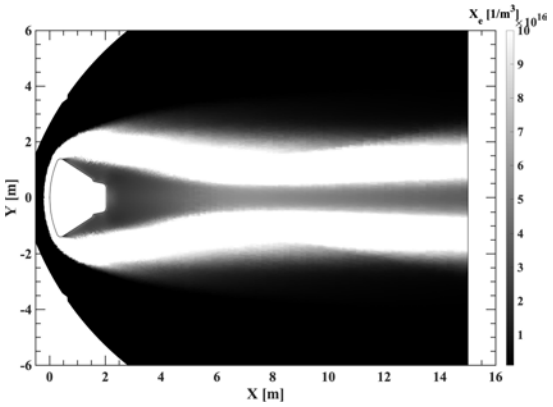

Figure 13: Altitude 75km

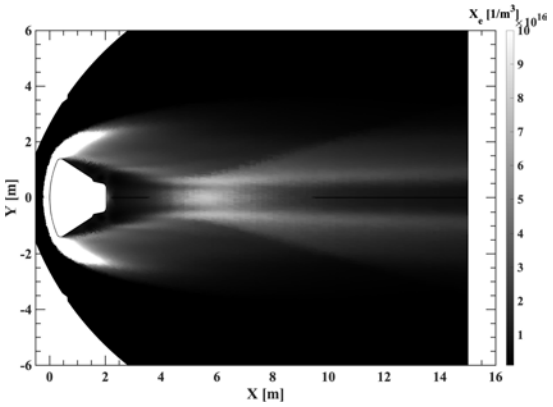

Figure 14: Altitude 60km

6. Conclusion

This work presents the application of a ray tracing method for the blackout analysis of the the Atmospheric Re-entry Demonstrator mission. The present computations were performed for 4 cases with alti-

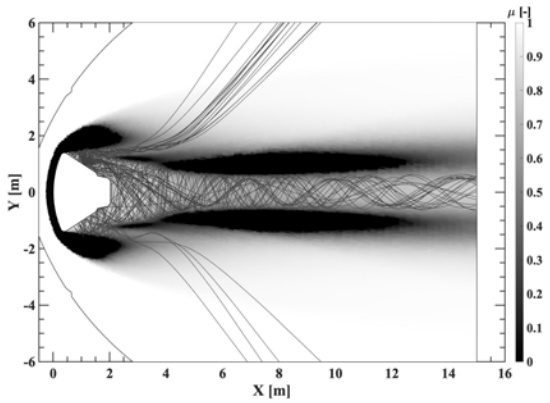

Figure 15: Altitude 85km

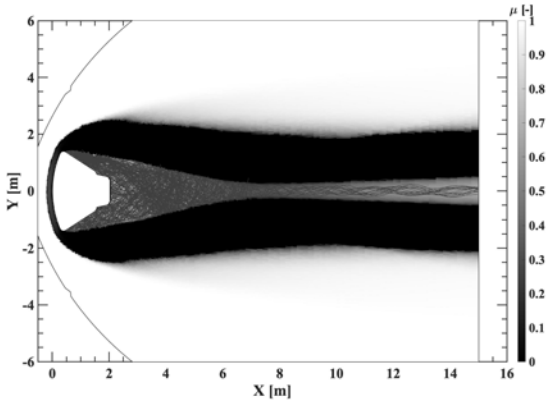

Figure 16: Altitude 75km

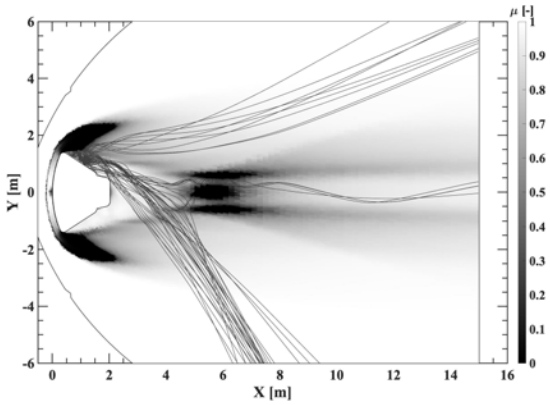

Figure 17: Altitude 60km

tudes between 85 km and 45 km based on the reentry orbit data. This analysis was carried on coupling the CFD solver COOLFLuiD and the thermochemical library PLATO. The newly updated solver showed accurate results, capable of reproducing ionized re-

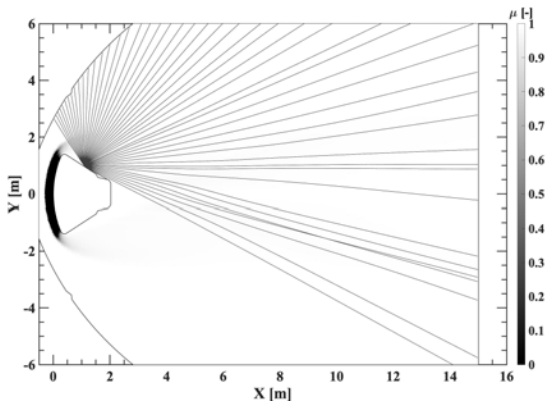

Figure 18: Altitude 45km

entry flows during re-entry trajectory. It was confirmed that the present simulation model can be effectively used to investigate the radio frequency blackout and plasma attenuation of the radio wave communication between a reentry vehicle and a data-relay satellite and for the design and development of reentry vehicles.In the present study, for ensuring simplicity and lower computational cost, an axisymmetric condition was imposed for the flowfield, whereas a three-dimensional model of the flowfield may change the formation of the plasma in the wake region of the vehicle. The possible contributions of these issues may need to be examined to develop the calculation further in a future study. Future work will focus on improving the capabilities of the ray tracing algorithm as in calculating the total attenuation of the signal which will allow one to directly compare between the LOS plasma frequency method and the ray tracing results. The ray tracing results from this study show that the LOS method might yield inaccurate results at the onset and end of the blackout period or when all the EM waves are not fully contained within the plasma layer. Thus, accurate prediction of the communication blackout phases, both in terms of duration and possible mitigation, requires ray tracing in the plasma layer.

Acknowledgments

The research of Vincent Fitzgerald Giangaspero is supported by SB PhD fellowship 1SA8219N of the FWO.

References

[1] S. Ramjatan, A. Lani, S. Boccelli, B. Van Hove, Ö. Karatekin, T. Magin, J. Thoemel, Blackout analysis of mars entry missions, Journal of Fluid Mechanics 904.

[2] V. F. Giangaspero, A. Lani, S. Poedts, J. Thoemel, A. Munafò, Radio communication blackout analysis of exomars re-entry mission using raytracing method, in: AIAA Scitech 2021 Forum, 2021, p. 0154.

[3] R. Hartunian, G. Stewart, S. Fergason, T. Curtiss, R. Seibold, et al., Causes and mitigation of radio frequency (rf) blackout during reentry of reusable launch vehicles, Tech. rep., Aerospace Corporation (2007).

[4] R. Savino, D. Paterna, M. De Stefano Fum, M. DElia, Plasma-radiofrequency interactions around atmospheric re-entry vehicles: modelling and arc-jet simulation, The Open Aerospace Engineering Journal 3 (1).

[5] J. Paulat, P. Boukhobza, Re-entry flight experiments lessons learned-the atmospheric reentry demonstrator ard, Tech. rep., EUROPEAN AERONAUTIC DEFENCE AND SPACE (EADS ST) LES MUREAUX (FRANCE) (2007).

[6] Y. Takahashi, K. Yamada, T. Abe, Prediction performance of blackout and plasma attenuation in atmospheric reentry demonstrator mission, Journal of Spacecraft and Rockets 51 (6) (2014) 1954–1964.

[7] A. Lani, An object oriented and high performance platform for aerothermodynamics simulation, Ph.D. thesis, Université Libre de Bruxelles (2008).

[8] A. Alberti, A. Munafò, M. Koll, M. Nishihara, C. Pantano, J. B. Freund, G. S. Elliott, M. Panesi, Laser-induced non-equilibrium plasma kernel dynamics, Journal of Physics D: Applied Physics 53 (2) (2019) 025201.

[9] A. Munafò, A. Alberti, C. Pantano, J. B. Freund, M. Panesi, A computational model for nanosecond pulse laser-plasma interactions, Journal of Computational Physics 406 (2020) 109190.

[10] K. Davies, Ionospheric radio propagation, Vol. 80, US Department of Commerce, National Bureau of Standards, 1965.

[11] C. Park, Review of Chemical-Kinetic Problems of Future NASA Missions, I: Earth Entries, Journal of Thermophysics and Heat Transfer 7 (3) (1993) 385–398.

AEROACOUSTICS

A wall pressure fluctuations model beneath turbulent boundary layer using Artificial Neural Network

Joachim Dominique

Environmental and applied fluid dynamics Department, von Karman Institute for Fluid Dynamics, Belgium, joachim.dominique@vki.ac.be

Supervisor: Christophe Schram

Professor , Environmental and applied fluid dynamics Department, von Karman Institute for Fluid Dynamics, Belgium, christophe.schram@vki.ac.be

University Supervisor: Wim Desmet

Professor, Mechanical Engineering, KU Leuven, Belgium, wim.desmet@kuleuven.be

Abstract

This paper presents a procedure for computing turbulent boundary layer parameters including the wall shear stress and wake coefficient in strong adverse pressure gradient flow, which has shown to have a significant impact on the von Karman coefficients for the log-law. This procedure is later used to build a database for a neural network model predicting wall pressure fluctuations.

Keywords: Wall pressure spectra, turbulent boundary layer, neural network

1. Introduction

The modelling of the pressure field induced by a turbulent boundary layer is relevant to a broad range of applications in fields including aeronautics, ground transportation or wind energy. The space and time characteristics of the pressure field beneath the boundary layer developing over an aircraft fuselage or train rooftop, and how they match with the structural response of the wall, dictate the importance of the fluid-structural coupling and noise transmission [1]. In the automotive sector, wind noise is considered to be the dominating sound source within the cabin for speeds above 100 km/h [2]. Also, the noise generated by the interaction of the turbulent boundary layer with an airfoil trailing edge is the minimum sound level emitted by a fan or an airfoil subjected to a clean, laminar inflow [3].

The pressure fluctuations beneath a turbulent boundary layer at low Mach number are given by the divergence of the Navier-Stokes equations, reducing to the Poisson equation in the case of incompressible flows:

$$\frac{1}{c^2}\frac{\partial^2 p}{\partial t^2} - \frac{\partial^2 p}{\partial x_i^2} = \frac{\partial^2 \left(\rho v_i v_j - \langle \rho v_i v_j \rangle\right)}{\partial x_i \partial x_j}, \qquad (1)$$

where ρ is the fluid density, c is the speed of sound, v_i is the i-th velocity component and $\langle\cdot\rangle$ denotes an ensemble average. The above equation can be solved through integration [4]. However, such an integral model is complex for three reasons: *i*) the velocity fluctuations in all parts of the boundary layer participate to the wall pressure fluctuations, *ii*) the turbulent velocity fluctuations are advected at different speeds, and *iii*) different scaling approaches can be used to describe the velocity field in the boundary layer [5].

Those issues have motivated sustained research on turbulent wall pressure fluctuations. Following the work of Kraichnan [4], Panton & Linebarger [6] and Blake [7] derived integral models of the Poisson equation in the wavenumber-frequency domain. However, such solutions may present difficulties from the numerical point of view due to the presence of multi-dimensional integrals [8]. Following a different approach, Amiet [9], Chase & Howe [10] proposed em-

pirical models of increasing complexity for engineering applications. The empirical model of Chase-Howe was improved by Goody [11] to account for Reynolds number effects and improve the high frequency behaviour. This model describes accurately boundary layers in the absence of pressure gradient, as demonstrated through an extensive review by Hwang *et al.* [12]. The effect of a pressure gradient requires further modifications, such as proposed by Kamruzzaman [13], Rozenberg [14], Hu [15] or Lee [16].

An important issue remains nevertheless: if each of those models describes fairly well the dataset on which it was based, they rarely provide a satisfactory agreement over the complete range of available data [16]. As it will be shown in Sec. 2, many of the available models are based on the mathematical expression proposed by Goody, designed to yield the desired frequency dependence that is expected from first principle or observed in experiments (e.g. the ω^2 growth at low frequencies resulting from the Kraichnan-Phillips theorem [5], the ω^{-1} decay predicted by Bradshaw [17] for the inertial range, and the ω^{-5} decay at high frequencies predicted by Blake [7]). In this methodology, referred to as the *physics-based* approach in this paper, the only remaining degrees of freedom are the model constants, tuned to best fit the amplitudes and transition frequencies between the low, intermediate and high frequency regimes that are observed in a given experiment.

However, the growing number of available experimental datasets and the recent improvements of data analysis techniques have made possible to consider a new approach, where the underlying mathematical expression is no longer obtained from the Goody model, but directly built from data. Such *data-based* approach will be investigated in this work using a Neural Network (NN).

This paper presents an implementation of NN for regression of wall spectral pressure fluctuations models. We start by reviewing previously existing models and their implementation, in the second part we describe the methodology used to construct the dataset investigated within this approach and finally we discuss the NN implementation and results

2. Existing empirical models

Different empirical models predicting the wall pressure fluctuations beneath a turbulent boundary layer already exist. In this section, we review five recent models proposed by different authors and compare how they represent the effects of pressure gradient.

2.1. Goody in 2004

The empirical wall pressure spectra proposed by Goody was built based on the principle of scaling and self-similarity [11]. The main precept being that the wall pressure spectra is proportional to different set of scales at low and high frequencies. The low frequency scales with outer flow variables and the high frequency scales with inner variables. This is similar to the two-layer scaling of turbulent boundary layer velocity profile [18].

Based on this principle, Goody further extended the model of Chase and Howe [10] to account for this outer-to-inner scaling ratio by including the Reynolds number into the equation:

$$\frac{\Phi_{pp} u_e}{\tau_w^2 \delta} = \frac{C_2(\omega\delta/u_e)^2}{((\omega\delta/u_e)^{0.75} + C_1)^{3.7} + (C_3(\omega\delta/u_e))^7},$$

where $C_1 = 0.5$, $C_2 = 3.0$, and $C_3 = 1.1R_T^{-0.57}$ describes the effect of Reynolds number, with $R_T = (u_\tau^2\delta)/(u_e\nu)$. This model describes accurately boundary layer in the absence of pressure gradients, as demonstrated in the review of Hwang [19].

2.2. Rozenberg in 2012

Rozenberg aimed at improving the Goody model by including the effects of adverse pressure gradient. It was assumed that they could be incorporated into the model using the Clauser parameter $\beta_C = (\theta/\tau_w)(\partial p/\partial x)$ and the boundary layer wake parameter as introduced by Cole Π_c. This assumption originated from an analogy with the scaling of turbulent boundary layer velocity profile, which requires a wake correction.

Rozenberg enforced several changes to the Goody model. The slope of the inertial range and the amplitude of the spectrum was set to vary with the pressure gradient. Finally yet importantly, the reference length used for the scaling of the model was changed to the displacement thickness.

$$\frac{\Phi(\omega) u_e}{\tau_w^2 \delta^*} = \frac{\left[2.82\Delta^2(6.13\Delta^{-0.75} + F_1)^{A_1}\right]\left[4.2\frac{\Pi_c}{\Delta} + 1\right](\omega\delta^*/u_e)^2}{[4.76(\omega\delta^*/u_e)^{0.75} + F_1]^{A_1} + (C3(\omega\delta^*/u_e))^7},$$

where $F_1 = 4.76\left(\frac{1.4}{\Delta}\right)^{0.75}[0.375A_1 - 1]$, $A_1 = 3.7 + 1.5\beta_C$ and $C_3 = 8.8R_T^{-0.57}$. This formulation falls back to the model of Goody in case of zero-pressure gradient (ZPG). However, this model was only calibrated on adverse pressure gradient (APG) data and is

therefore unable to predict favourable pressure gradient flows (FPG).

2.3. Kamruzzaman in 2015

Kamruzzaman followed a similar objective than Rozenberg on a larger database, including both adverse and favourable pressure gradients. Another important difference is in the procedure to evaluate boundary layer parameters used for the modelling. Kamruzzaman used Xfoil and empirical relationships for the Clauser parameter β_C and the wake coefficient Π such as $\Pi_c = 0.8\,(\beta_C + 0.5)^{0.75}$. Consequently, this forces a non-necessarily existing dependency between those variable. This emphasized the need for a robust procedure to compute boundary layer parameters form different sources.

The amplitude of the model predictions were slightly increased for both APG and FPG. The dependency of the Reynolds number suggested by Goody was also changed to best fit their database. As a result, this model does not collapse on Goody for ZPG. In addition, the variations of the slope in the inertial range were not observed in this study.

$$\frac{\Phi(\omega)u_e}{\tau_w^2\delta^*} = \frac{B_2(\omega\delta^*/u_e)^2}{[(\omega\delta^*/u_e)^{1.64} + 0.27]^{2.47} + [B_3(\omega\delta^*/u_e)]^7},$$

where $B_2 = 0.45(1.75(\Pi^2\beta_C^2)^{0.5(H/1.31)^{0.3}} + 15)$ and $B_3 = (1.15R_T)^{-2/7}$. This model tends to reduce the extent of the overlap region considerably.

Due to the empirical relationship between the wake coefficient and the Clauser parameters, both variables act similarly on the model. The shape factor H is also used for the first time as a modelling tool to account for history effects of the boundary layer developments. The use of the shape factor to model history effects in wall pressure spectra was later used in 2018 by Hu [15] to proposed another empirical wall pressure spectral model with no direct influence of the pressure gradient.

2.4. Catlett in 2016

Catlett's approach was much more "data-driven" than his predecessors. Using a single set of experimental data, Catlett relaxed the Goody model to show multiple empirical coefficients. Those coefficients were fitted to empirical equations depending only on the pressure gradient and Reynolds number using different normalizations. This model usually under-predicts the amplitude of the spectrum and does not collapse to the goody model for ZPG.

$$\frac{\Phi(\omega)u_e}{\tau_w^2\delta} = \frac{a(\omega\delta/u_e)^2}{[(\omega\delta/u_e)^c + d]^e + [fR_T^g(\omega\delta/u_e)]^h},$$

$$\ln(a - a_g) = 7.98(\beta_\Delta Re_\theta^{0.35})^{0.31} - 10.7$$

$$c - c_G = 20.9(\beta_\delta Re_\delta^{0.05})^{2.76} + 0.162$$

$$d - d_G = 0.238(\beta_\Delta Re_\Delta^{0.35})^{0.31} - 0.103$$

$$e - e_G = -1.93(\beta_\delta Re_\delta^{0.05})^{0.628} + 0.172$$

$$f - f_G = -2.57(\beta_\delta Re_\delta^{0.05})^{0.224} + 1.09$$

$$g - g_G = 38.1(\beta_\delta H^{-0.5})^{2.11} + 0.0276$$

$$h - h_G = 0.797(\beta_\Delta Re_\Delta^{0.35})^{0.0724} + 0.310$$

2.5. Lee in 2018

Lee performed an extensive comparison between all the models previously discussed and shown that although each of them was performing well on their own dataset their provided mixed performances on different spectra. Therefore, Lee proposed a new model accounting for their respective disparities.

Lee's model was inspired from Rozenberg with three additional corrections: 1) a modification of the onset of the transition from the overlap to the high frequency depending on the pressure gradient 2) a correction of the amplitude of the spectrum at low frequency for zero-pressure gradient flows 3) a sudden increase of the amplitude of the signal for high pressure gradient flow.

$$\frac{\Phi(\omega)u_e}{\tau_w^2\delta^*} = \frac{B_2(\omega\delta^*/ue)^2}{[4.76(\omega\delta^*/u_e)^{0.75} + d^*]^e + [C_3(\omega\delta^*/u_e)]^{h^*}},$$

where $B_2 = max(a, (0.25\beta_C - 0.52)a)$, $a = 2.82\Delta^2(6.13\Delta^{-0.75} + d)^{3.7+1.5\beta_c}$, $d^* = max(1.0, 1.5d)$, $d = 4.76(1.4/\Delta)^{0.75}[0375e - 1]$, $e = 3.7 + 1.5\beta_C$, $C_3 = 8.8R_T^{-0.57}$ and finally $h^* = min(3, 0.139{+}3.1043\beta_C){+}7$.

Lee's model is close to the Goody model for zero-pressure gradient flows with a small disparity in amplitude at low frequency. Despite his complexity, and being non-continuous by using minimum and maximum operations, it is today considered as one of the most accurate empirical models for both favourable and adverse pressure gradient boundary layers. However, even this model still shows inconsistency when used in strong adverse pressure gradient as it will be shown in Sec. 5.

3. Dataset description and influence of pressure gradient

The dataset used in this work was constructed from four separate cases: one set of experimental measurements performed by Salze on a flat plate [20] , and three high fidelity simulations performed respectively by Deuse [21], Hao [22] and Christophe [23] on the control diffusion (CD) airfoil under different inflow conditions.

Zero pressure gradient flat plate boundary layer has been an important field of research both experimentally and numerically for the scaling of velocity profiles and Reynolds stresses. This provides canonical results where the velocity profile fits the classical two-layer scaling and the wall pressure fluctuations should fit the model of Goody for ZPG.

The CD airfoil was initially designed for engine cooling fans for automotive, HVAC systems and turbofans. It has a 4% relative thickness and a leading-edge camber angle of 12°. In typical operating conditions, the airfoil has a laminar boundary layer on the pressure side. On the suction side, the flow reattaches after a short separation bubble at the leading edge, which results in a turbulent boundary layer. This complex configuration is expected to behave differently from the flat plate boundary layer both for the scaling of the velocity profile and for the wall pressure spectra. For each simulation, starting from the trailing edge, 13 points equally spaced along the chord of the airfoil are selected to from the database between $0 \leq x/c \leq 0.65$. The boundary layer parameters and respective wall pressure spectrum were extracted at each point.

3.1. Salze

Salze performed an experimental investigation of the wall pressure spectrum under moderately favourable and adverse pressure gradients in the wind tunnel of the university of Lyon [20]. They used a rotating antenna of pinhole microphones to measure the wall pressure fluctuations and a sloped ceiling to induce pressure gradients. The measurements of boundary layers at zero pressure gradients (ZPG) were found close to the expected Goody model. However, only moderate effects of the pressure gradient were observed. An attenuation of the spectra was seen in FPG and an increase for APG. The pressure gradients also seem be to change the inertial slope in the mid-frequency region as it can be observed in Fig. 1

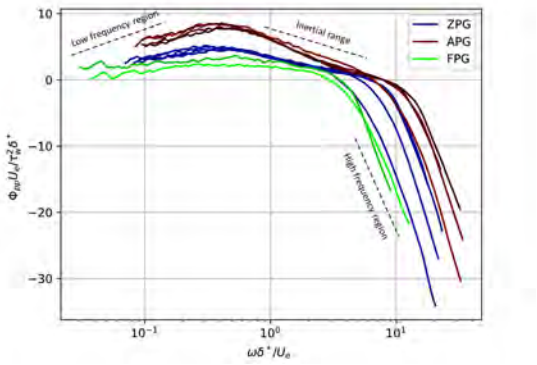

Figure 1: Salze's experimental data - light to dark colouring for increasing pressure gradient

3.2. Deuse

Deuse performed a DNS simulation of the CD airfoil using the finite difference solver named HipSTAR the Reynolds number of the simulation was set at 10^5. The airfoil is embedded in a flow at M=0.2 with an effective angle of attack of attack of $\alpha_e = 8°$ [21]

Such flow is subjected to very strong adverse pressure gradients. The resulting wall pressure fluctuations display a large amplitude of the spectra in Fig. 2, especially when compared with the moderate pressure gradients flows of Salze in Fig. 1. Due to the low Reynolds number, the extent of the inertial range is not observed in this simulation. As a result, eventual effects of the pressure gradient in that region cannot be investigated.

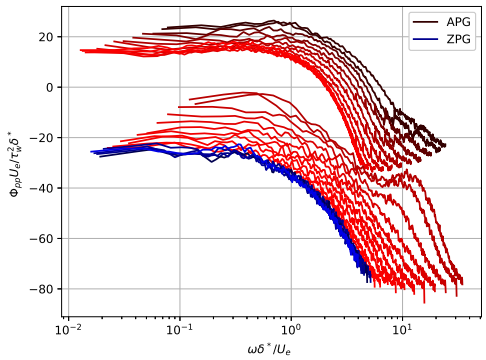

Figure 2: Deuse (top) and Hao (bottom) DNS simulations - light to dark colouring for increasing pressure gradient

3.3. Hao

Hao's also used HipSTAR to perform a similar simulation than Deuse at Mach 0.25 and a Reynolds number of 1.5×10^5. Hao nevertheless included in his simulation the effect of the wind tunnel jet deviation, which changed the effective angle of attack of the airfoil to $\alpha_e = 4°$. This in turn impacted the aerodynamic loading around the airfoil and its wall pressure spectra [22]

It can be seen on Fig. 2 that the amplitude of the wall pressure spectra are far below the one of Deuse despite being investigated on a similar airfoil at a similar flow rate. Another noticeable difference appears from the data of Deuse is the high frequency hump that appears for large pressure gradient close to the trailing edge. The cause of this hump on the wall pressure spectra is still uncertain, but is hypothesized to be caused by the merging of the suction and pressure side after the trailing edge.

3.4. Christophe

Christophe performed a series of six LES simulations on the CD airfoil at Mach 0.05. As in Hao, the LES computations are run on a restricted domain fully embedded in the inviscid jet potential core between the nozzle shear layers. In the present study, the inlet flow profile was changed to test different angle of attacks α_e ranging from 2° to 6° while keeping the geometrical angle of attack constant at 8°. [23]

Initially developed for uncertainty quantification this dataset cover large test cases of different angle of attack. Unfortunately, the numerical scheme used in this work is too disruptive at high frequency and does not capture the correct trends for the high frequency decay. Therefore, it was decided to trim the frequency vector used in this approach and conserved only frequencies below 4kHz.

3.5. Pressure gradient impacts

The experimental data of Salze followed the expected effects of pressure gradient according to existing empirical models: an increase of the amplitude of the spectra at low frequency, a change in the decay of the inertial range and variation of the roll-off at high frequency. Deuse's simulation followed similar trends for the low frequency amplitude, but the impacts on the inertial range could not be observed due to the low Reynolds numbers. In the opposite, Hao's simulation has a smaller amplitude than Salze and Deuse while it was obtained under severe adverse pressure gradients. This suggest that the pressure gradient is not the only factor affecting the amplitude of the spectrum at low frequency.

4. Turbulent Boundary layer parameters

As we are working with different simulations/experiments, we need a consistent way to measure boundary layer parameters. In experimental data, the boundary layer thickness is obtained using 99% of the maximum velocity. However, the same method cannot be applied to the numerical boundary layers because the velocity outside of the boundary layer is not constant. In this case, using the maximum velocity would overestimate the boundary layer thickness. Instead, we use the maximum pseudo-velocity which is defined as the integral of the vorticity $p_s(y) = \int_0^y \omega_z dy$.

The displacement thickness and momentum thickness are defined using the classical definition for incompressible turbulent boundary layer as :

$$\delta^* = \int_0^\delta \left(1 - \frac{u(y)}{u_e}\right) dy, \tag{2}$$

$$\theta = \int_0^\delta \left(\frac{u(y)}{u_e}(1 - \frac{u(y)}{u_e}\right) dy, \tag{3}$$

where u_e is the equilibrium velocity at $y = \delta$. Based on the empirical wall pressure spectra models described in Sec. 2, we can see that additional boundary parameters are necessary for the modelling such as the friction velocity u_τ and the wake parameter Π. Those parameters are going to be obtained using an iterative method that minimizes the difference between the boundary layer points and a parametric boundary layer model showed in Eq. 4

$$u^+(y^+) = \begin{cases} u^+_{inner}(y^+) + \frac{2\Pi}{\kappa} W\left(\frac{y}{\delta}\right), & \text{if } y \leq \delta \\ u_e/u_\tau & \text{otherwise} \end{cases} \tag{4}$$

This parametric boundary layer model so-called composite boundary layer is built from the theoretical law of the wall and law of the wake. It combines u^+_{inner} with the Musker's law of the wall [24] and the Chauhan correction W [25] for the law of the wake. The amplitude of the Chauhan correction given by the parameter Π is chosen to fit $u(\delta) = 0.99 u_e$.

Although relatively simple, this approach assesses well the friction velocity for the different boundary layers and provides a way to determine the amplitude of the wake parameters without relying on empirical relationships.

database	N	$\tilde{\omega}$	Δ	H	M	Π	C_f	R_T	β_C
Salze (2014)	10	0.03 → 33.6	0.09 → 0.16	0.07 → 0.12	0.07 → 0.17	0.03 → 0.75	0.002 → 0.004	7.60 → 22.5	−0.47 → 0.57
Deuse (2020)	13	0.01 → 24.2	0.15 → 0.32	0.11 → 0.15	0.21 → 0.27	0.14 → 2.26	0.001 → 0.004	2.58 → 3.54	0.36 → 15.59
Hao (2020)	16	0.02 → 34.4	0.13 → 0.35	0.09 → 0.16	0.27 → 0.34	0 → 2.2	0.001 → 0.006	1.56 → 2.25	−0.15 → 5.93
Christophe (2011)	78	0.002 → 4.65	0.11 → 0.30	0.86 → 0.16	0.05 → 0.06	0.0 → 1.43	0.002 → 0.006	1.49 → 3.48	−0.05 → 7.94
All	117	0.01 → 34.4	0.09 → 0.35	0.07 → 0.16	0.05 → 0.34	0 → 2.26	0.001 → 0.006	1.49 → 22.5	−0.47 → 15.59

Table 1: Boundary layer parameters range used by the NN model

4.1. Pressure gradient correction

Unfortunately, it was observed that this composite boundary layer model was not fitting well the boundary layers with strong pressure gradient. This happens especially in the logarithmic region where the boundary layers do not seem to follow the classical log-law evolution based on the von Karman coefficient $\kappa = 0.41$ and $B = 5.0$ as shown in Fig. 3.

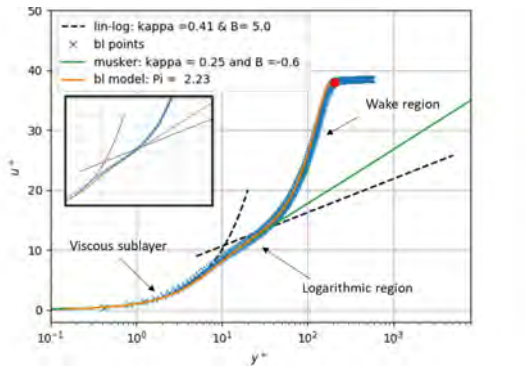

Figure 3: Example of composite boundary layer fitting with pressure gradient

To overcome this issue, a pressure gradient correction was proposed to the boundary layer model in Eq. 4. This correction is based on the work of Nickels [26] assuming that, in a turbulent boundary layer, the viscous sublayer behave as a laminar flow and grows until a critical Reynolds number is reached. From this point, the flow becomes unstable, perturbation grows, and turbulence is generated. Strong pressure gradients can reduce this critical Reynolds number and therefore force the sub-viscous layer to transition sooner, which affects also the velocity scale of the logarithmic layer and its slope.

Nickels starts by expounding the classical law for the viscous sublayer by including higher order terms within the Taylor expansion.

$$u^+ = y^+ + \frac{1}{2}p_x^+(y^+)^2 + H.O.T \tag{5}$$

$$\frac{\tau}{\tau_w} = \frac{1}{u_{\tau^2}}\frac{\nu\partial u}{\partial y} = 1 + p_x^+ y^+ \tag{6}$$

where $p_x^+ = \frac{\nu}{\rho u_\tau^3}\frac{\partial p}{\partial x}$. It is often considered that pressure gradient is an outer flow parameter that cannot influence the inner turbulent boundary layer. However, Eq. 5 shows that this is not the case and strong pressure gradients can have an impact down to the viscous sublayer.

Using the definition of the critical Reynolds number as $Re_c = \frac{U_T y_c}{\nu}$ and the new definition of the wall shear stress. Nickels devices an equation for the point of transition from the viscous sub-layer $y_c^+ = \frac{y_c u_\tau}{\nu}$

$$p_x^+(y_c^+)^3 + (y_c^+)^2 - Re_c^2 = 0 \tag{7}$$

where $Re_c = 12$ is a constant obtained using zero-pressure gradient boundary layer measurements. It can be seen from Eq. 7 that adverse pressure gradients will increase the critical y_c^+ in opposition to favourable pressure gradients that will reduce it.

Because the model defines an inner scale for the thickness of the viscous sub-layer, it also defines a velocity scale U_T. At this point, the flow becomes unstable and the turbulent eddies will grow. The velocity scale of those eddies is determined by the critical velocity scale of the sublayer affecting in turns the slope of the logarithmic layer.

$$\frac{\kappa}{\kappa_0} = \frac{1}{\sqrt{1 + p_x^+ y_c^+}} \tag{8}$$

where $\kappa_0 = 0.41$ is the classical von Karman constant for the slope of the logarithmic layer. From this equation, we can expect a larger slope of the logarithmic layer for adverse and a lower one for favourable pressure gradients. This is consistent with what has been observed in this database and also with the discussion on the non-universality of the von Karman coefficient in the paper of Nagib [27].In this last paper, Nagib introduces the κB empirical relation as :

$$\kappa B = 1.6[\exp(0.1663B) - 1] \tag{9}$$

Using both Eq. 8 and 9, we can now provide the full algorithm for the determination of the friction velocity including pressure gradient correction in Fig. 4 and Tab. 1. The idea is to correct the κ and B values of the

logarithmic layer by changing the coefficient within the Musker's law. The normalization of the pressure gradient depends on the friction velocity, which is the parameter that we are trying to minimize iteratively. Therefore, the normalized value of the pressure gradient p_x^+ must change at each iteration with u_τ.

It should be noted that by only changing the κ and B constants within the Musker profile change the slope of the logarithmic region without changing the points of transition $y_c^+ = 12$.

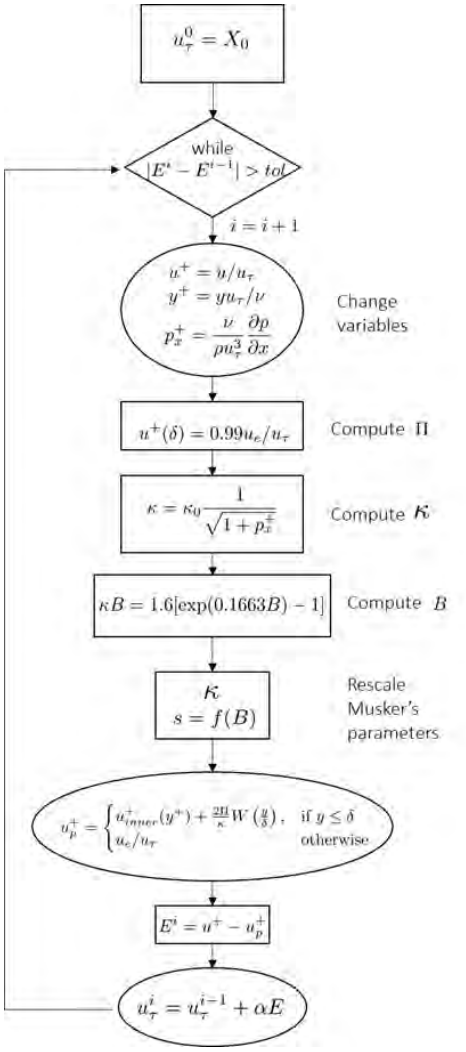

Figure 4: Optimisation loop for boundary layer parameters

5. Neural network model

The neural network used in this work is a typical neural network for regression problems. It is a feed-forward neural network using 8 dimensionless inputs describes in Tab. 1 and has a single dimensionless output $10\log_{10}(\frac{\phi_{pp}u_e}{\tau_w\delta^*})$. The variables used as input and output were chosen using a dimensional analysis and the Buckingham pi theorem.

For each boundary layer, the number of frequency points characterizing the wall pressure spectra has been set to 500 points for a total of 58500 samples. As the number of cases per database is not equal, a weight has been attributed to each boundary layer so that each database is equally represented.

The network is composed of 5 layers. The first is a normalization layer that scales the input variables using their mean and standard variation. The four next layers are fully connected layers with Selu activation function with 16 nodes. The training was performed using the mean-square error as fitness and Nadam optimizer with a learning rate of 10^{-4}. To avoid overfitting, the dataset was partitioned into three subsets. First, six boundary layers and respective wall pressure spectra are set apart not to be used within the neural network. They are instead used within the so-called testing set to compare the prediction of the neural network with unseen data in Fig. 5. For the remaining points, 80% will be used for the training of the model through back-propagation (training set) and the remaining 20% will be used to compute a validation error to avoid overfitting as it can be seen in Fig. 6

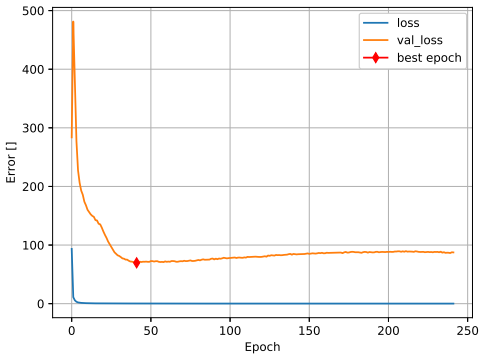

Figure 6: Evolution of training and validation error

We can see the predictions of the neural network for boundary layers of the testing set in Fig. 5. The neural network is predicting the wall pressure spectra much better than already existing empirical models. This is particularly true for the prediction of the CD airfoil, where the models of Goody, Rozenberg, Lee, etc generally miss-evaluate the true amplitude of

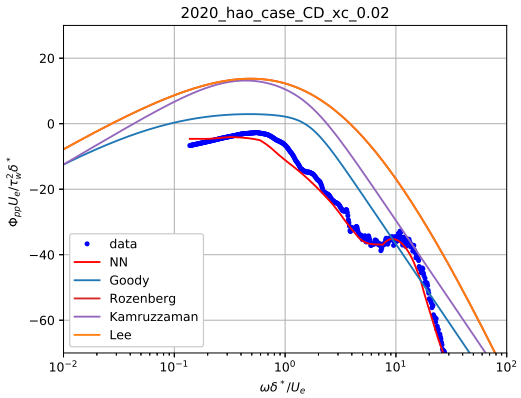

(a) Hao $\alpha_e = 8°$ at $x_c = 0.02$

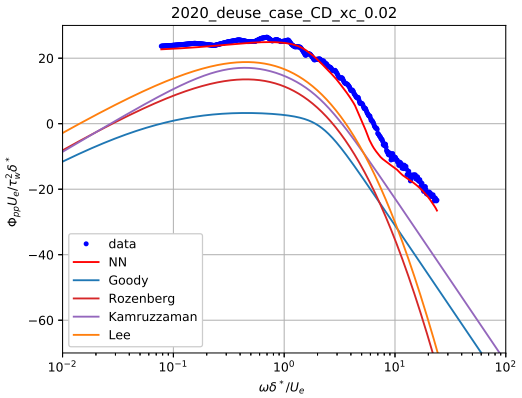

(b) Deuse $\alpha_e = 8°$ at $x_c = 0.02$

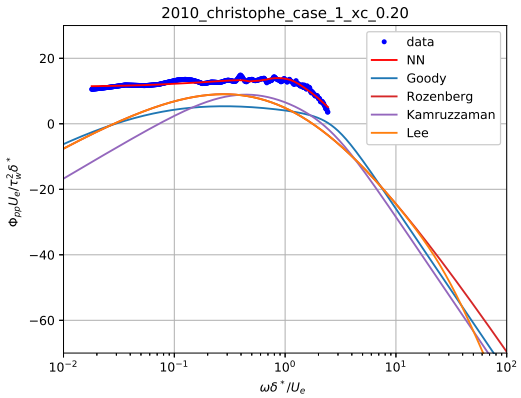

(c) Christophe $\alpha_e = 6°$ at $x_c = 0.05$

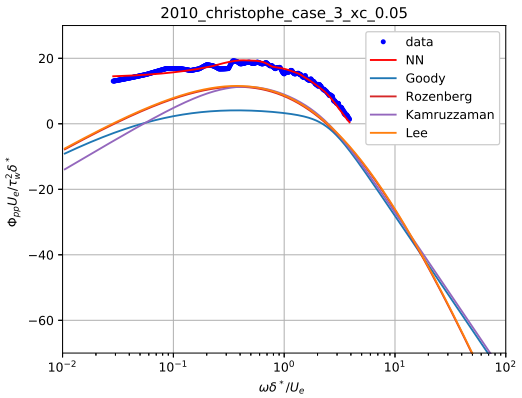

(d) Christophe $\alpha_e = 5.42°$ at $x_c = 0.05$

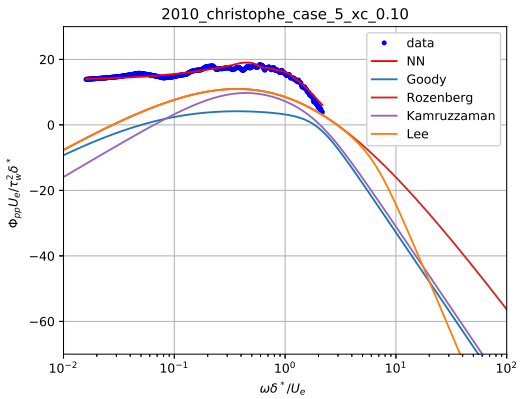

(e) Christophe $\alpha_e = 3.24°$ at $x_c = 0.05$

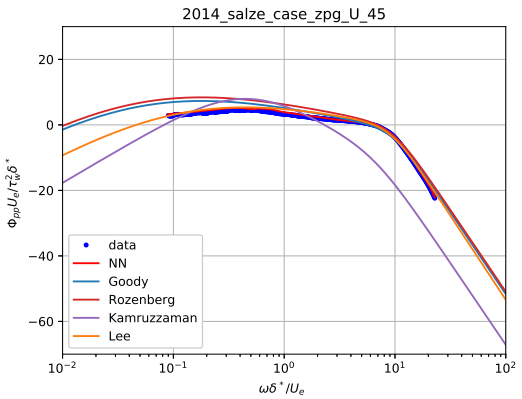

(f) Salze ZPG at $u_e = 45m/s$

Figure 5: Prediction of NN model and comparison with existing semi-empirical models on the testing set

the spectra. However, the neural network has problem approaching the spectrum of Salze on the flat plate where already existing wall pressure spectral models gave good prediction. This could be due to the disparity in the representation of some of the inputs. The present dataset has many spectra under heavy APG, but very few measurements under ZPG and FPG that are almost all within the Salze's database. This disparity could cause the neural network to model very well the strong APG cases at the detriment of FPG and ZPG cases.

6. Conclusion

The existing empirical wall pressure spectral model clearly shows a miss prediction for strong adverse pressure gradient boundary layer such as the ones that are encountered within industrial applications. This is caused by the modelling difficulties of such flow configuration. In that context, data-driven models such as neural network can be attractive alternative solutions.

Such data-driven method heavily relies on the quality of their inputs. Therefore, a methodology for computing boundary layer parameters in strong adverse pressure gradient flow was presented. This method is based on the theoretical developments of Nickles [26] and Nagib [27] on the non-universality of the von Karman coefficient, which is partly reproduced in this paper. This procedure shown that the von Karman coefficients of the log-law are strongly impacted by the pressure gradient. We accounted for these changes while computing the boundary layer parameters.

The database investigated in this work provides a thorough investigation for the CD airfoil under a broad range of inflow parameters. As a result, the neural network constructed in this work was able to provide accurate predictions below $\pm 5 dB/Hz$ accuracy for the different flow cases considered. This is a significant improvement over existing empirical models that provided a prediction with up to $20 dB/Hz$ errors. However, the prediction for traditional flat plate boundary layer without pressure gradient were less accurate than existing models. This discrepancy could be attributed to either a lack of diversity in the databases used or a lack of data to train the model for low favourable and adverse pressure gradient.

In the long term, the authors conjecture that this approach could be extended to a broader range of boundary layer parameters without additional modifications. This would make a great tool to propose models that perform well on larger dataset including different physical assumptions (e.g. pressure gradient, compressibility effects,etc) without requiring additional effort on the methodology front.

Acknowledgments

This research was partly supported by the French global automotive Valeo in the context of a thesis for the investigation of noise induced by HVAC systems. The authors thank Dr. Salze and Pr. Bailly from Ecole Centrale de Lyon, Ing. Deuse and Pr. Sandberg from University of Melbourne, Dr. Hao and Pr. Moreau from Universit de Sherbrooke and Dr. Christophe from von Karman Institute for providing the experimental and numerical data. This work would not have been possible without the help of Ing. Van den Berghe.

References

[1] E. Ciappi, S. De Rosa, F. Franco, J. Guyader, S. Hambric, et al., Flinovia-Flow Induced Noise and Vibration Issues and Aspects, Springer, 2015.

[2] N. Van de Wyer, A. Zapata, D. Nogueira, C. Schram, Development of a test rig for the measurement of turbulent boundary layer wall pressure statistics, 2018 AIAA/CEAS Aeroacoustics Conferencedoi:10.2514/6.2018-3122.

[3] M. Roger, S. Moreau, Back-scattering correction and further extensions of amiets trailing-edge noise model. part 1: theory, Journal of Sound and Vibration (286) (2005) 477, 506. doi:10.1016/j.jsv.2004.10.054.

[4] H. Kraichnan, R, Pressure fluctuations in turbulent flow over a flat plate, The Journal of the Acoustical Society of America 28 (3).

[5] M. Bull, Wall-pressure fluctuations beneath turbulent boundary layers: some reflections on forty years of research, Journal of Sound and vibration 190 (3) (1996) 299–315.

[6] R. L. Panton, J. H. Linebarger, Wall pressure spectra calculations for equilibrium boundary layers.

[7] W. Blake, Mechanics of Flow-Induced Sound and Vibration - Volume 1: General Concepts and Elementary Sources, Vol. 1, Academic Press, 1986.
URL https://ui.adsabs.harvard.edu/abs/1986ApMat..17.....B

[8] G. Grasso, P. Jaiswal, H. Wu, S. Moreau, M. Roger, Analytical models of the wall-pressure spectrum under a turbulent boundary layer with adverse pressure gradient, Journal of Fluid Mechanics 877 (2019) 1007–1062.

[9] K. Amiet, R, Noise due to turbulent flow past a trailing edge, Journal of Sound and Vibration 47 (3) (1976) 387, 393.

[10] M. Howe, Acoustics of Fluid-Structure Interactions, Cambridge University Press, 1998.
URL https://ui.adsabs.harvard.edu/abs/1998afsi.book.....H

[11] M. Goody, Empirical spectral model of surface pressure fluctuations, AIAA journal 42 (9) (2004) 1788–1794.

[12] F. Hwang, Y, K. William, S. Bonness, A. Hambric, Comparison of semi-empirical models for turbulent boundary layer wall pressure spectra, Journal of Sound and Vibration (319) (2007) 199, 217. doi:10.1016/j.jsv.2008.06.002.

[13] M. Kamruzzaman, D. Bekiropoulos, T. Lutz, W. Würz, E. Krämer, A semi-empirical surface pressure spectrum model for airfoil trailing-edge noise prediction, International Journal of Aeroacoustics 14 (5-6) (2015) 833–882.
[14] Y. Rozenberg, G. Robert, S. Moreau, Wall-pressure spectral model including the adverse pressure gradient effects, AIAA journal 50 (10) (2012) 2168–2179.
[15] N. Hu, Empirical model of wall pressure spectra in adverse pressure gradients, AIAA J. 56 (9) (2018) 3491–3506. doi:10.2514/1.J056666.
[16] S. Lee, Empirical wall-pressure spectral modeling for zero and adverse pressure gradient flows, AIAA Journal 56 (5) (2018) 1818–1829.
[17] P. Bradshaw, 'Inactive' motion and pressure fluctuations in turbulent boundary layers, J. of Fluid Mechanics 30 (2) (1958) 241–258. doi:10.1017/S0022112067001417.
[18] F. H. Clauser, The turbulent boundary layer, in: Advances in applied mechanics, Vol. 4, Elsevier, 1956, pp. 1–51.
[19] Y. Hwang, W. K. Bonness, S. A. Hambric, Comparison of semi-empirical models for turbulent boundary layer wall pressure spectra, Journal of Sound and Vibration 319 (1-2) (2009) 199–217.
[20] É. Salze, C. Bailly, O. Marsden, E. Jondeau, D. Juvé, An experimental characterisation of wall pressure wavevector-frequency spectra in the presence of pressure gradients, in: 20th AIAA/CEAS Aeroacoustics Conference, 2014, p. 2909.
[21] M. Deuse, R. D. Sandberg, Parametric study of multiple aerofoil self-noise sources using direct noise computation, in: 25th AIAA/CEAS Aeroacoustics Conference, 2019, p. 2681.
[22] H. Wu, M. Sanjose, S. Moreau, R. D. Sandberg, Direct numerical simulation of the self-noise radiated by the installed controlled-diffusion airfoil at transitional reynolds number, in: 2018 AIAA/CEAS Aeroacoustics Conference, 2018, p. 3797.
[23] J. Christophe, J. Anthoine, S. Moreau, Trailing edge noise of a controlled-diffusion airfoil at moderate and high angle of attack, in: 15th AIAA/CEAS Aeroacoustics Conference (30th AIAA Aeroacoustics Conference), 2009, p. 3196.
[24] A. Musker, Explicit expression for the smooth wall velocity distribution in a turbulent boundary layer, AIAA Journal 17 (6) (1979) 655–657.
[25] K. Chauhan, H. Nagib, P. Monkewitz, On the composite logarithmic profile in zero pressure gradient turbulent boundary layers, in: 45th AIAA Aerospace Sciences Meeting and Exhibit, 2007, p. 532.
[26] T. Nickels, Inner scaling for wall-bounded flows subject to large pressure gradients, Journal of Fluid Mechanics 521 (2004) 217.
[27] H. M. Nagib, K. A. Chauhan, Variations of von kármán coefficient in canonical flows, Physics of fluids 20 (10) (2008) 101518.

Numerical investigation of vertical axis wind turbine noise under uniform flow conditions

Kartik Venkatraman

PhD Student, Environmental and Applied Fluid Dynamics dept., von Karman Institute for Fluid Dynamics, Belgium, kartik.venkatraman@vki.ac.be

Julien Christophe

Senior Research Engineer, Environmental and Applied Fluid Dynamics dept., von Karman Institute for Fluid Dynamics, Belgium

Christophe Schram

Professor, Environmental and Applied Fluid Dynamics dept., von Karman Institute for Fluid Dynamics, Belgium

Abstract

A simulation chain for noise prediction of a model vertical axis wind turbine (VAWT) is developed. A two-dimensional Unsteady Reynolds-Averaged Navier-Stokes (URANS) model is setup using OpenFOAM with the $k-\omega$ SST turbulence model. The flow solution is then coupled to a Ffowcs Williams and Hawkings (FW-H) analogy to predict the sound pressure level at the blade passing frequency harmonics. A validation case from literature with uniform inflow has been simulated. The flow appears as highly chaotic with the formation of a complex vortex system shed by the blades along their trajectory and interacting with them. The sound pressure levels at the blade passing frequencies are compared with published experimental data on the same model turbine. Blade vortex interaction and dynamic stall are meant to play a key role in loading and noise radiation at some azimuthal rotation angles.

Keywords: VAWT, URANS, FW-H

1. Introduction

The need for reducing carbon emissions has put limelight on renewable energy sources for securing future energy supply. An interesting prospect is the installation of wind turbines in urban locations that have high wind potential with significant local accelerations of the flow. They have an advantage of reducing electricity transmission losses as they are located closer to the consumption point. Studies have shown that VAWT are more adapted to the urban environment [1] as they have a better performance in turbulent sites [2] compared to HAWTs. The noise produced by these wind turbines plays an important role in their acceptance, certification and integration into the urban landscape.

2. Baseline VAWT Model

The work presented in Ref. [3] studied the aeroacoustics of a model scale Darrieus wind turbine comprising of 3 blades of NACA0018 cross section with a chord length of 0.05 m as shown in Fig. 1. The diameter and height of the rotor was 0.2 m corresponding to a solidity of 0.75. Microphone measurements were carried in an anechoic chamber at four different azimuthal positions at 1 m distance from the model, at half rotor height. The flow conditions corresponded to a chord based Reynolds number Re_c of 28,000 and a rotational speed of 800 rpm. A numerical study was performed using scale adaptive simulations SAS coupled to a Ffowcs Williams and Hawkings [4] solver and validated with experimental measurements. Velocity and pressure contours, pressure coefficient on blades at four different azimuth positions of the blade are provided for comparison of the

CFD model. Sound pressure level spectra at the microphone position corresponding to the first blade at azimuthal position 0° is provided for validation of the aero-acoustic model.



Figure 1: Model VAWT rotor used in Ref. [3]

3. Aeroacoustic Model

The noise prediction model follows the Ffowcs Williams and Hawkings analogy [4], which has the following integral solution for the acoustic density perturbation in free-field conditions [5]:

$$c_0^2\rho'(\mathbf{x},t) = \frac{1}{4\pi}\frac{\partial^2}{\partial x_i x_j}\int_{V_e}\left[\frac{T_{ij}}{R\,|1-M_r|}\right]\boldsymbol{\eta} - \frac{1}{4\pi}\frac{\partial}{\partial x_i}\int_S\left[\frac{P_i}{R\,|1-M_r|}\right]\boldsymbol{\eta} + \frac{1}{4\pi}\frac{\partial}{\partial t}\int_S\left[\frac{\rho_0 V_n}{R\,|1-M_r|}\right]\boldsymbol{\eta} \tag{1}$$

where c_0 is the speed of sound in the reference propagation medium and the integrals are performed over the external volume V_e bounded by the solid body surface S. The coordinate system $\boldsymbol{\eta}$ is attached to the body moving at the Mach number $\mathbf{M}$, and $\mathbf{x}$ is the listener coordinate in the non-moving reference frame. The bracketed terms in the integrals are to be evaluated at the retarded time τ solution of the equation $t-\tau-R/c_0=0$, where $R=|\mathbf{x}-\mathbf{y}(\boldsymbol{\eta},\tau)|$ is the distance between the listener and source point at the emission time τ. The first integral involves the Lighthill's tensor $T_{ij}=\rho v_i v_i+(p'-c_0^2\rho')_{ij}+\sigma_{ij}$, where $\mathbf{v}$ is the aerodynamic velocity and σ_{ij} is the viscous tensor, and appears to have quadrupolar efficiency. The second integral exhibits a dipolar character and corresponds to the loading noise, with $\mathbf{P}$ the net force vector per unit area, which includes formally the hydrodynamic pressure fluctuations and the acoustic pressure that is scattered by the body surface. The third integral appears as a monopole related to the displacement of the fluid traversed by the moving body, and is often referred to as thickness noise. The three integrals share the same term $R\,|1-M_r|$ as denominator, where M_r is the Mach number of the source relative to the listener, projected in the direction from the source to the listener. It translates the Doppler effect that is responsible for both the amplitude modulation and shift between the emission and reception frequencies. The noise producing region of the blades is assumed to be acoustically compact, the loading noise due to the dipole contribution being dominant. The present work focuses on the tonal noise resulting from the periodic component of the forces, leading to the following solution [6] for the noise emitted by the B equally-spaced blades of the VAWT rotor at the Blade Passing Frequency Harmonics (BPFH):

$$\rho_{sB} = -\frac{Bk_{sB}}{4\pi c_0^2}\frac{^{-k_{sB}x}}{x}\sum_{p=-\infty}^{+\infty}{}^{-(sB-p)(\varphi-\pi/2)}\Big(_{-sB+p}(-k_{sB}r'\sin\theta)\,F_p^{(z)}\cos\theta - \frac{sB-p}{k_{sB}r'}\,{}_{-sB+p}(-k_{sB}r'\sin\theta)\,F_p^{(\varphi)} - {}'_{-sB+p}(-k_{sB}r'\sin\theta)\,\sin\theta\,F_p^{(r)}\Big) \tag{2}$$

where $s=1,2,\ldots$ and $k_{sB}=sB\Omega/c_0$ is the wavenumber of the sth BPFH for a rotation pulsation Ω. Using a coordinate system with origin at the center of the dipole center of rotation as sketched in Figure 2, the listener spherical coordinates are $\mathbf{x}=(|\mathbf{x}|,\theta,\varphi)$ and the point dipole figuring the point force exerted by one reference blade is located at the cylindrical coordinate $(r',\Omega t+\varphi',0)$. The Bessel function ${}_{-sB+pV}$ and its derivative account for the modulation of the frequency shift due to the Doppler effect. $F_p^{(X)}$ is the pth Fourier component of the blade force $F_\xi(\tau)$, with $\xi=(r,\varphi,z)$ denoting the force component in the radial, tangential and axial directions, respectively):

$$\mathrm{F}_\xi(\tau)=\sum_{p=-\infty}^{\infty}F_p^{(\xi)}\,{}^{p\Omega\tau}\,.$$

Given the geometry of the VAWT shown in Figure 3, the axial force F_z can be safely assumed to be negligible compared with the radial and tangential components

4. Computational Fluid Dynamics model

A two-dimensional Unsteady Reynolds-Averaged Navier-Stokes (URANS) model has been implemented in OpenFOAM using the unsteady solver *pimpleFOAM*. This constitutes the first step towards a

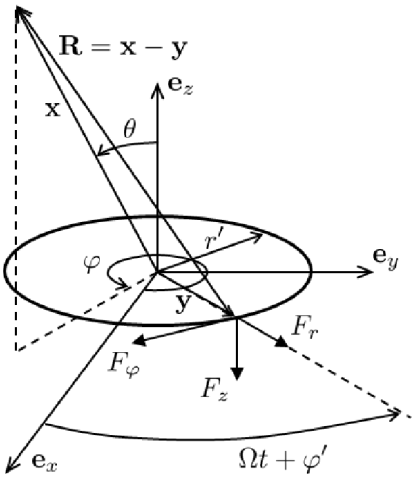

Figure 2: Coordinate system for the rotating point dipole.

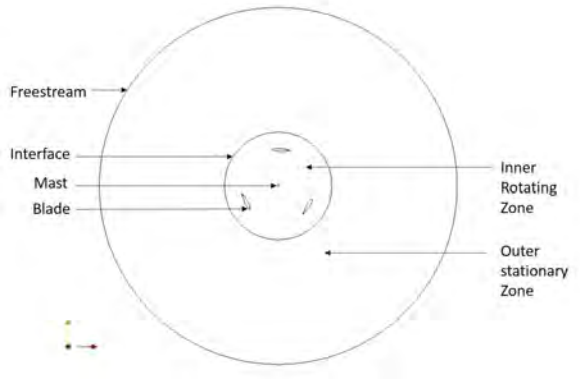

Figure 3: CFD model of the VAWT showing the different regions and boundary conditions.

more realistic three-dimensional scale-resolved simulations, and provides already some insight about the periodic features of the flow. An unstructured mesh is generated using *ANSYS ICEM CFD* from a CAD model of an identical wind turbine model as presented in [3]. Freestream boundary conditions are defined in the farfield as shown in Fig. 3. The domain comprises a stationary outer zone and an inner rotating zone. The diameter of the domain is set to 15 times the rotor diameter. Refinement regions are defined to capture the flow features in the interior and the wake of the turbine. A sufficient number of inflation layers is defined close to the blade surface and the mast to ensure a wall $y^+ < 1$. The interface between the regions is assigned *cyclicAMI* condition and the blades, mast are assigned the *movingWallVelocity* boundary condition. The flow parameters are setup to match the experimental conditions provided in [3]. The $k - \omega$ SST turbulence model is used as it is shown to provide good prediction in strongly separated flows [7]. A second order discretization scheme is used for the flow variables. Simulations are performed with a fixed time step of 10^{-6} s for 20 revolutions required until convergence of the average periodic forces between consecutive rotations and as per VAWT simulation recommendations specified in [8].

5. Results

The flow around the VAWT is highly chaotic with the formation of leading and trailing edge vortices at the blades followed by vortex shedding and interaction between these shed vortices as seen in the velocity and pressure contours shown in Fig. 4 and 5. The mean flow direction is aligned along the positive x-direction (left to right). All results are analysed with respect to the blade located at the top-most position (defined as azimuth 0° position). Following the motion of this blade, it can been seen that at 40° leading edge vortex is formed which convected towards the trailing edge at 80° and at 120° another leading edge vortex begins to form on the opposite side of the blade. Force coefficients are integrated and computed in a blade coordinate system using the inbuilt functions in OpenFOAM. The time history of the forces are shown in Fig. 6 and 7.

Sound pressure level predictions using the FW-H method at the blade passing frequencies harmonics (BPFH) are shown corresponding to an azimuthal position of $\phi = 90°$ in Fig. 8 and compared with experimental data from [3]. A good agreement is found for the first blade passing frequency and harmonic. The Fourier transform is computed over the forces extracted over several rotation periods of this single blade and a phase locked averaging is performed. Without the phase locked average the effect of cycle to cycle force variations is dominant, leading to the spectral energy content being shifted to higher energy content. The blades experience higher loads in the upwind (azimuth of 45° to 135°, convention defined in [9]) corresponding to the presence of leading edge vortex and in the downwind (225° to 315°) due the impulsive loads due to interaction of the blade with the vortices shed from the other blades and mast.

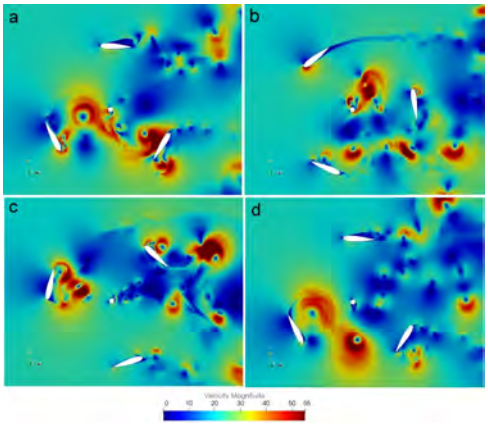

Figure 4: Velocity contours at different azimuthal angles a) 0° b) 40° c) 80° d) 120° rotation.

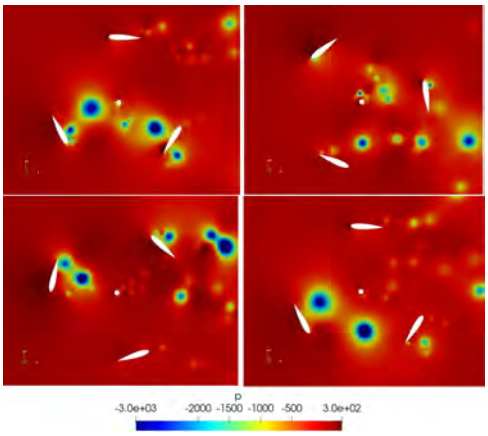

Figure 5: Pressure contours at different azimuthal angles a) 0° b) 40° c) 80° d) 120° rotation.

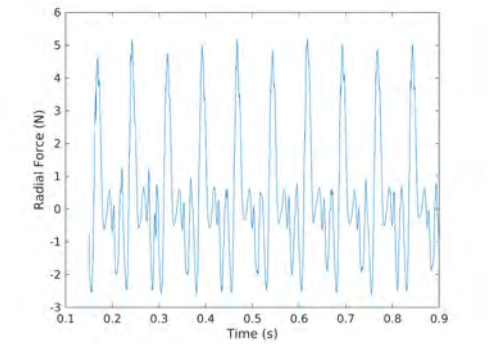

Figure 6: Plot of radial forces over time

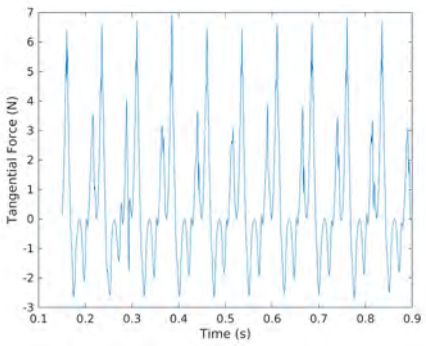

Figure 7: Plot of tangential forces over time

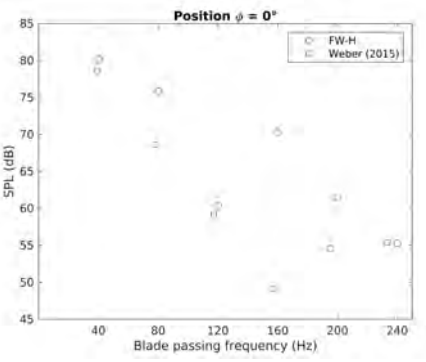

Figure 8: Sound pressure level vs Frequency plot, present results compared with experimental results from [3] at Microphone position corresponding to azimuth 0°

6. Conclusion

A simulation chain has been setup to model the noise generated by vertical axis wind turbines. A CFD model has been developed in OpenFOAM and coupled to an aeroacoustic solver based on the Ffowcs Williams and Hawkings analogy for the prediction of tonal noise. The model has been setup to match experimental conditions from Ref. [3], for which the incoming flow was uniform, in a view to validating the simulation chain. The sound pressure levels are favorably compared with experimental results at the blade passing frequency harmonics.The dynamic stall and blade vortex interaction phenomenon in the upwind and downwind rotation of the blades play a key role in noise radiation. Future work includes performing a grid independence study, simulations with non-uniform flow conditions more representative of an urban environment. Understanding and reducing the noise impact in realistic flow conditions is important for improving certification for small wind turbines and their adoption in urban areas.

Appendix

Acknowledgments

The authors acknowledge the European Commission for its financial support through the project H2020-MSCA-ITN-2019 zEPHYR (Grant Agreement No. 860101).

References

[1] H. Riegler, Hawt versus vawt: Small vawts find a clear niche, Refocus 4 (2003) 44–46.

[2] I. Belmabrouk, A. ELHami, L. Walha, B. Zghal, M. Haddar, Dynamic vibrations in wind energy systems: Application to vertical axis wind turbine, Mechanical Systems and Signal Processing 85.

[3] J. Weber, S. Becker, C. Scheit, J. Grabinger, M. Kaltenbacher, Aeroacoustics of darrieus wind turbine, International Journal of Aeroacoustics 14 (2015) 883–902. doi:10.1260/1475-472X.14.5-6.883.

[4] D. L. Ffowcs Williams, J E; Hawkings, Sound generated by turbulence and surfaces in arbitrary motion, Proceedings of the Royal Society of London. Series A, Mathematical and Physical Sciences 264 (1151) (1969) 321–342.

[5] M. Roger, Aeroacoustics of installed propellers, von Karman Institute for Fluid Dynamics Lecture Series, Rhode-St-Genèse, 2019.

[6] C. Schram, H. Bériot, M. Roger, H. Reese, T. Carolus, On the importance of near-field terms in the assessment of acoustic installation effects for ducted low-Mach number fans, 15th AIAA/CEAS Aeroacoustics Conference (30th AIAA Aeroacoustics Conference) (May) (2009) 11–13. doi:10.2514/6.2009-3334.

[7] A. Sagharichi, M. Zamani, A. Ghasemi, Effect of solidity on the performance of variable-pitch vertical axis wind turbine, Energy 161. doi:10.1016/j.energy.2018.07.160.

[8] A. Rezaeiha, I. Kalkman, B. Blocken, Cfd simulation of a vertical axis wind turbine operating at a moderate tip speed ratio: Guidelines for minimum domain size and azimuthal increment, Renewable Energy 107 (2017) 373–385. doi:10.1016/j.renene.2017.02.006.

[9] A. Rezaeiha, H. Montazeri, B. Blocken, Towards accurate cfd simulations of vertical axis wind turbines at different tip speed ratios and solidities: Guidelines for azimuthal increment, domain size and convergence, Energy Conversion and Management 156 (2017) 301–316. doi:10.1016/j.enconman.2017.11.026.

LIQUID METAL AND INDUSTRIAL FLOWS

Modal analysis of the gas-liquid interaction in jet wiping

David Barreiro-Villaverde

CITIC Research, Spain, david.barreiro1@udc.es

Environmental and Applied Fluid Dynamics, von Karman Institute for Fluid Dynamics, Belgium, david.barreiro@vki.ac.be

Supervisor: Miguel A. Mendez

Associate Professor, Environmental and Applied Fluid Dynamics, von Karman Institute for Fluid Dynamics, Belgium, miguel.alfonso.mendez@vki.ac.be

University Supervisor: Anne Gosset

Professor, Technological Research Center (CIT), University of A Coruña, Spain, anne.gosset@udc.es

Abstract

This work aims at the numerical investigation of the jet wiping process via CFD simulations and modal analysis. In galvanization, two slot gas jets impinge on both sides of the steel band to control the coating thickness. The process is inherently unsteady, which leads to the formation of undulations in the final product. We investigate their link with the behaviour of the gas jet using 3D simulations. The numerical model, based on the Volume of Fluid (VOF) and Large Eddy Simulation (LES), is validated with the experimental work performed by Mendez *et al.*[1] at the von Karman Institute. The Multiscale Proper Orthogonal Decomposition (mPOD) is used to detect the most dominant patterns in the liquid film and to correlate them with specific structures in the gas. This allows for a full description of the gas-liquid interaction that results in the undulations.

Keywords: jet wiping, free-surface flows, liquid metals, modal analysis

1. Introduction

The hot dip galvanization is an industrial process used to protect steel products from corrosion. The coating layer is attached to the ferrous substrate after dipping on a bath with molten zinc due to viscosity. The jet wiping is a crucial part in the process in which the thickness of the coating is reduced by the impigement of planar gas jets on the liquid metal, as sketched in Fig. 1. Consequently, the final film thickness is reduced and the excess of thickness is forced to reverse direction, inducing a *runback flow*. The wiping effect of the gas jet on the film is conducted through the wiping actuators, namely the stream-wise pressure gradient $\partial_x p_g(x)$ and shear stress $\tau_g(x)$ at the interphase. The process is characterized by the nozzle opening (d), its distance to the substrate (Z), stagnation pressure (ΔP_N, which leads to a jet exit velocity U_J) and the substrate speed (U_p). The relevant fluid properties are the gas and the liquid densities (ρ_g, ρ_l) and viscosities (μ_g,μ_l) as well as the gas-liquid surface tension (σ).

It is the most widely used technique in galvanization because of its comparatively low maintenance cost, high productivity and energy efficiency. Nevertheless, two unsteady phenomena restrict the operational windows in industrial lines. The first is known as *splashing* and consists in the violent breakup of the runback flow in droplets, of major concern for safety issues. The second is related to the appearance of non-uniformities, referred to as *undulations*, in the final coating, which dramatically affect the quality of the products.

According to the recent experimental work of Gosset *et al.*[2] and Mendez *et al.*[1], the undulation seems to be the result of a hydrodynamic feedback between the gas and the liquid flows promoted by the unsteady confinement driven by the waves of the runback flow. This mechanism periodically influence the wiping efficiency of the gas jet, propagating the dis-

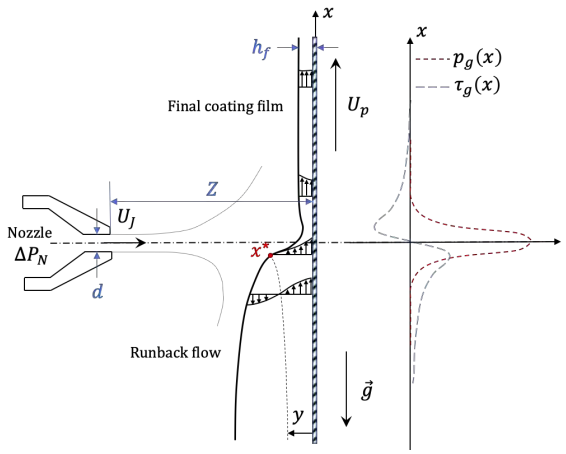

Figure 1: Schematic of the jet wiping process, recalling the main operating parameters. The substrate moves upwards (positive x direction) at a speed U_p. The average final film thickness is denoted h_f, and the wiping point, at which the surface flow reverses direction, x^*. The pressure and shear stress distributions produced by the impinging jet at the film interface are denoted $P_g(x)$ and $\tau_g(x)$, respectively, and their typical shape is represented on the right hand side.

turbances to the final coating.

The process has been previously investigated numerically by Myrillas *et al.*[3; 4] and Pfeiler *et al.*[5] using Volume of Fluid (VOF) and Large Eddy Simulation (LES). They observed a similar interaction between the liquid and the gas, characterized by a low frequency motion of the jet coupled with the formation of waves in the runback flow. Moreover, simplified models based on the long-wave approximation have shown that low frequency perturbations (oscillations and pulsations) of the wiping actuators leads to the formation of undulations similar to the ones observed in the experiments[6; 7].

This work aims at the investigation of the jet wiping process using 3D LES-VOF simulations with twofold objective. First, the validation of the numerical model with extensive experimental data of the liquid and the gas from the work of Mendez *et al.* [1] in order to use the model in the investigation of wiping configurations closer to the industrial lines. Second, the detailed description of the undulation mechanism using the Multiscale Proper Orthogonal Decomposition (mPOD). This is a data-driven decomposition in which the frequency content of the modes is constrained to a certain frequency band. It allows to identify the most dominant travelling wave patterns in the liquid The temporal evolution of the modes in the liquid are used to project the data of the gas in order to identify correlations between the undulations and the gas jet behaviour.

Section 2 presents the investigated test cases, the numerical methodology employed for the LES-VOF simulations and the data processing focused on the fundamentals of mPOD. Section 3 presents and discusses the results, while conclusions and perspectives are reported in section 4.

2. Test Cases and Numerical Methods

This section is organized as follows. First, the configuration of the investigated cases is presented in subsection 2.1. Second, the details of the numerical methodology used in the CFD simulation are described in subsection 2.2. Finally, the fundamentals of the Multiscale Proper Orthogonal Decomposition (mPOD) and its application to the analysis of the gas-liquid interaction is presented in subsection 2.3.

2.1. Test cases

The test cases analyzed in this work are three of the experiments described in previous works[1; 8]. The substrate is assumed to be flat, and withdrawn from a bath of isothermal coating. The working liquid is dipropylene-glycol, with density $\rho_l = 1023$ kg/m^3, dynamic viscosity $\mu_l = 0.075$ Pa·s and surface tension $\sigma = 0.032$ N/m. The gas is air, with density $\rho_g = 1.2$ kg/m^3, dynamic viscosity $\mu_g = 1.776 \times 10^{-5}$ Pa·s. The coating liquid dragged by the substrate is impinged by a slot air jet, with a nozzle opening $d = 1.3$ mm. The internal and external geometry of the nozzle reproduces the one of the experiments. The substrate speed is constant and equal to $U_p = 0.34$ m/s. The selected wiping conditions include two standoff distances ($Z = 25.2$ and 18.5 mm, corresponding to normalized distances $\hat{Z} = Z/d = 14.2$ and 17.2), and two nozzle pressures for $\hat{Z} = 14.2$ ($\Delta P_N = 425$ and 875 Pa). The three configurations are summarized in Table 1 in which the dimensionless wiping number $\Pi_g = \Delta P_N d / \left(\rho_l g Z^2\right)$, known to be representative of the process [2], is indicated.

The domain used for computations is represented in Fig. 2 (left). This includes the coating bath, the moving flat substrate emerging from it, and a portion of the slot nozzle. The domain spans 300 *mm* in the direction of the moving substrate (x), 100 mm in addition to the stand-off distance Z in the jet axis direction (y), and 30 *mm* in the span-wise direction (z).

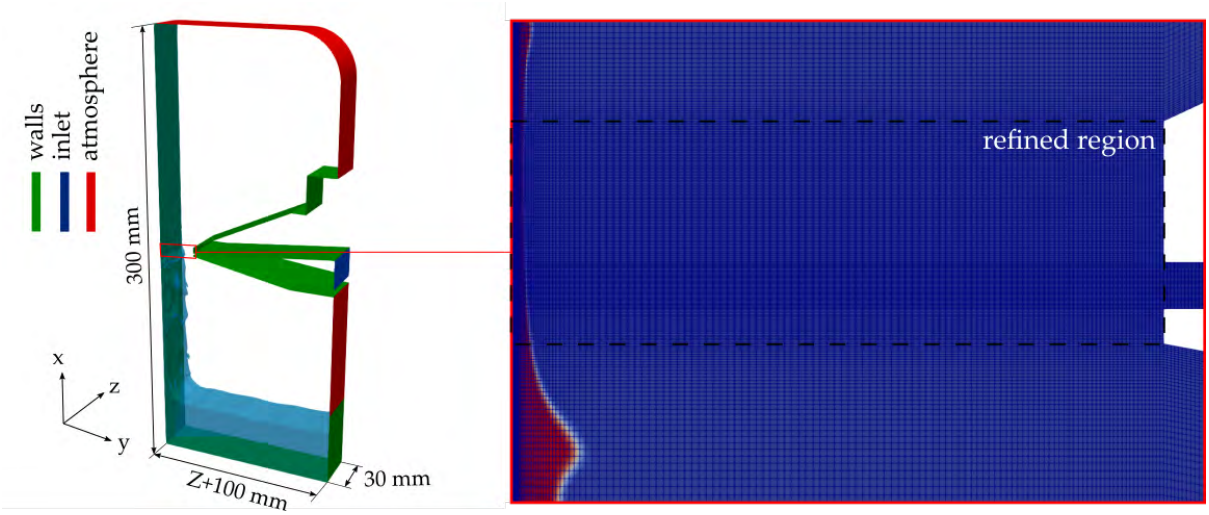

Figure 2: Left: 3D view of the computational domain with the prescribed boundary conditions and relevant units 2D representation of the computational domain, mesh details and boundary conditions. The front and back patches are defined as cyclic and the mesh is extruded 30 mm in the direction perpendicular to the present plane.

Table 1: Conditions of the three analyzed test cases, in terms of dimensionless stand-off distance $\hat{Z} = Z/d$, nozzle pressure ΔP_N and wiping number $\Pi_g = \Delta P_N d/(\rho_l g Z^2)$. The remaining set of parameters is recalled in the text.

Case #	$\hat{Z}$ [-]	ΔP_N [Pa]	Π_g [-]
1	14.2	425	0.16
2	14.2	875	0.33
3	19.4	875	0.18

The computational domain is discretized with a structured mesh built-in *blockMesh*. 10 million cells are used for cases 1 and 2 and 12 milion cells are used for the case 3 at larger Z (cf. Table 1). The cell size in the refined region, shown in Fig. 2 (right) is $\Delta x \approx 50$ μm along the x while Δy ranges from 2 μm close to the substrate to 200 μm at the exit of the nozzle. The cell width around the interface is of the order of 50 μm. The cell size in z is set constant an equal to $\Delta z = 500$ μm.

The boundaries open to atmosphere are modelled as outlet condition in which the reference pressure is set to 0. The solid boundaries are defined as walls, and the gas jet flow is established through an inlet condition in which the stagnation pressure ΔP_N is prescribed.

2.2. *Numerical methodology*

The numerical simulations were carried out using a combination of Large Eddy Simulation (LES) to model turbulence in the gas flow and Volume of Fluid (VOF) to account for the two-phase flow nature of the problem. The VOF method is based on the transport of a color function which represents the liquid volume fraction α in each computational cell. This function is equal to 1 when this is filled with liquid, and 0 when it is filled with gas. The gas-liquid interface is in the cells where $0 < \alpha < 1$. The local fluid properties ϕ are computed as a weighted average of the properties of the liquid (ϕ_l) and the gas (ϕ_g), depending on α:

$$\phi = \phi_l \alpha + \phi_g (1 - \alpha) \tag{1}$$

Starting from the conservation equations for an incompressible, immsicible two-phase flow with single fluid formulation:

$$\nabla \cdot \mathbf{U} = 0 \tag{2a}$$

$$\frac{\partial (\rho \mathbf{U})}{\partial t} + \nabla \cdot (\rho \mathbf{U} \otimes \mathbf{U}) = -\nabla p + \rho \mathbf{g} + \nabla \cdot [2\mu \mathbf{S}] + S_\sigma \tag{2b}$$

where $\mathbf{U} = (U, V, W)$ is the velocity, p the pressure, μ the dynamic viscosity, $\mathbf{S} = (\nabla \mathbf{U} + \nabla^T \mathbf{U})/2$ is the strain rate tensor and S_σ is the term accounting for

the Laplace pressure due to surface tension at the interface, computed using the continuum surface force (CSF) model. These equations are combined with a transport equation for the volume fraction α:

$$\frac{\partial \alpha}{\partial t} + \nabla \cdot (\alpha \mathbf{U}) = 0 \tag{3}$$

The computations in this work were performed using the *interFoam* solver from OpenFoam[9], which implements an algebraic VOF formulation. To limit the numerical diffusion of the interface, an artificial relative velocity term $U_r = U_l - U_g$ is defined in order to compress the gas-liquid boundary, where U_g is the velocity of the gas and U_l the velocity of the liquid in the interface. The major benefit of this method relies on its low computational cost and simple implementation. For the flux corrected transport scheme, the algorithm implemented in *interFoam* is known as the Multidimensional Universal Limiter with Explicit Solution solver (MULES [9]), which adjusts the compression by means of the face fluxes and a user-defined parameter C_α to guarantee boundedness and stability (validation in [10]).

The LES consists in the filtering of the turbulence scales based on the grid scale [11]. The scales smaller than the grid (sub-grid scales) are modeled as they are supposed to have a universal and isotropic behaviour. The larger scales are more case-dependent and crucial in the global mechanism we are interested in, so their accurate resolution is of capital importance. The coupling of LES with multiphase flows modeling, commonly referred to as Large Eddy Interface Simulations (LEIS) is a complex subject and the numerical treatetment is not yet mature; the state of the art and the perspectives of this method are presented in [12]. The Smagorinsky model used for the computations is based on the Boussinesq approximation, in which the turbulent eddy viscosity μ_t reads:

$$\mu_t = \rho (C_s \Delta x_{cell})^2 |\mathbf{S}| \tag{4}$$

where C_s is the Smagorinsky model constant, set to 0.158 (usual values are in the range 0.1-0.2), Δx_{cell} is the cell size and $|\mathbf{S}| = \sqrt{2\mathbf{S} : \mathbf{S}}$ is Frobenious norm of the the strain rate tensor.

2.3. The multiscale analysis of the gas-liquid interaction

The mPOD is a linear technique for dimensionality reduction, combining the advantages of the two most popular alternatives, namely the Proper Orthogonal Decomposition (POD[13; 14]) and the Dynamic Mode Decomposition (DMD[15; 16]).

Every linear decomposition can be seen as a modal expansion in which a dataset $d(\mathbf{x},t)$, sampled over a spatial domain $\mathbf{x} := (x,y)$ and evolving in time $t \in [0,T]$, is written as a summation of modes with variable separated form:

$$d(\mathbf{x},t) = \sum_{r=1}^{R} \sigma_r \phi_r(\mathbf{x}) \psi_r(t)\,, \tag{5}$$

where σ_r is the mode amplitude, $\phi_r(\mathbf{x})$ is the mode's spacial structure and $\psi_r(t)$ is the mode temporal evolution. The structures ϕ_r and ψ_r form, respectively, a basis for spatial distribution and temporal evolution of the data.

The mPOD modes are derived using a combination of energy optimality of the POD and the spectral purity of the DMD. In particular, mPOD modes are optimal within a certain frequency bandwidth. This combination is achieved by combining the POD with classic Multi-resolution Analysis (MRA) which is performed on the temporal correlation matrix. The temporal structure ψ_r is built from the eigenvectors of the filtered correlation matrix. The associated spatial structures are then computed via projection and normalization:

$$\sigma_r \phi_r(\mathbf{x}) = \langle d(\mathbf{x},t), \psi_r(t) \rangle_T = \int_T d(\mathbf{x},t) \psi_r(t) dt\,, \tag{6}$$

with $\sigma_r = ||\langle d(\mathbf{x},t), \psi_r(t) \rangle_T||_2$.

The mPOD decomposition has been performed using the opensource software package MODULO[17].

The detection of the interface is carried out from the α field along z-constant planes. After the interpolation of the volume fraction, an image processing routine based on morphological erosion and dilation was used to detect and filter out droplets produced by the interface splashing and gas bubbles entrained within the liquid film. Then, the interface detection is performed using gradient-based edge detection techniques on the pre-processed contours of α.

These thickness contourmaps are the main focus of the wave pattern analysis via modal decomposition. The decomposition is nevertheless not performed directly on the extracted thickness maps, as the waves in the runback flow have much larger amplitudes than those of the final coating film. This difference biases the decomposition towards the dynamics of the run back flow. To give comparable weight to both final coat and runback flow, a normalization step is performed prior to the modal decomposition. This step, which allows for avoiding the need for weighted inner products, reads

$$\check{h}(\mathbf{x},t) = \frac{h(\mathbf{x},t) - \bar{h}(\mathbf{x})}{\sigma_h(\mathbf{x})}, \tag{7}$$

where $\bar{h}(\mathbf{x})$ is the time average thickness $\sigma_h(\mathbf{x})$ is the distribution of the thickness standard deviation. The normalized thickness fields (7) is decomposed using the mPOD described previously in this subsection.

For the investigation of the liquid film in section 3.2, only the travelling patterns identified in the 30 most dominant modes are considered. Using trigonometric identities, it can be seen that travelling pattern is defined by a pair of standing waves (modes) delayed $pi/4$ in both time and space.

The modal analysis of the gas field is not considered in this work, which focuses on the correlation between the gas jet flow and the relevant patterns in the coating film. Accordingly, given $\psi_{\check{h},r}(t_k)$ the temporal structure of the $r-th$ mPOD mode of $\check{h}(\mathbf{x}_i,t_k)$, the most correlated gas structure is computed using the same projection as in (6):

$$\phi_{g,r}(\mathbf{x}) = \langle d_g(\mathbf{x},t), \psi_r(t) \rangle_T, \tag{8}$$

where the subscript g denotes quantities from the gas jet flow (e.g. velocity, wall pressure or interface pressure). This correlation analysis can be seen as an extended mPOD analysis, similar to the extended POD presented by Borée [18].

3. Results

This section aims at the analysis of the results obtained in the CFD simulation of the three cases of study. An overview of them in presented in Fig. 3 with one snapshot of the 3D liquid film interface and a contourmap of the velocity magnitude in the gas flow in the middle plane $z = 15mm$.

The three cases produce very different undulation patterns. Case 1 ($\hat{Z} = 14.2$, $\Pi_g = 0.16$), is characterized by nearly bidimensional waves on the final coating film. Waves remains bidimensional also in the runback flow for a distance of about 25 mm from the averaged impingement point. At larger distances, the steeping of the wave front is combined with the growth of 3D instabilities that eventually leads to the break-up of the liquid interface. Case 2, with the same stand-off distance but larger nozzle pressure ($\Pi_g = 0.33$) produces a 3D wave pattern on both the final coating and the runback flow regions. This configuration features splashing: the breaking of the run back flow occurs much closer to the wiping region, promoted by the high shear of the gas flow released from the impact. The momentum exchange between the two phases leads to the ejection of liquid droplets.

Case 3 has a wiping number comparable to Case 1 but operates at a much larger stand-off distance. This case generates wave patterns that are similar to those of Case 2, but with more pronounced three-dimensionality and reduced splashing. The significant difference in the waves is thus mostly due to the different stand off distance and hence the gas flow field, analyzed in details in the following subsection.

In subsection 3.1, we present the validation of the numerical model through the comparison with experimental work of Mendez *et al.*[1]. The multiscale analysis of the film and the link between the undulations and the gas jet behaviour is discussed in subsection 3.2.

3.1. Validation

The most relevant features of the liquid film and gas jet dynamics are compared with the data obtained in the experiments. The mean flow is analyzed in terms of the spatio-temporal average film thickness computed as in Eq. 9. The comparison for the three test cases is shown in Table 2. The numerical model satisfactory predict the mean final thickness h_f. The final thickness scales well with the wiping number Π_g as observed in Gosset *et al.*[2] and the trends with the wiping parameters are correct: at a constant standoff distance Z, an increase of the stagnation pressure ΔP_N leads to lower film thickness h_f; while the opposite happens when the stagnation pressure ΔP_N is kept and standoff distance Z is increased.

$$\bar{h}_f = \frac{1}{x_2 - x_1} \frac{1}{T} \int_{x_1}^{x_2} \int_{t_1}^{t_2} h(x',t') dt' dx' \tag{9}$$

taking $[x_1, x_2] = [120, 150]$mm and $[t_1, t_2] = [0, 1]$s. Here, the time $t = 0$ is the one from which the data processing begins, i.e. after two flow-through that allows the jet wiping process to be fully established.

It is worth noticing that the CFD model systematically predicts lower film thickness, in accordance with the work of Myrillas[3] for a very similar numerical configuration. This may be explained by the differences with the experimental setup in the Ondule laboratory at the von Karman Institute, where the moving substrate is a rotatory cylinder and the thickness is measured much downstream where gravity acts perpendicular to the liquid, not parallel as in the numerical setup.

In order to validate the dynamics of the gas-liquid interaction we analyze the frequency spectra of the

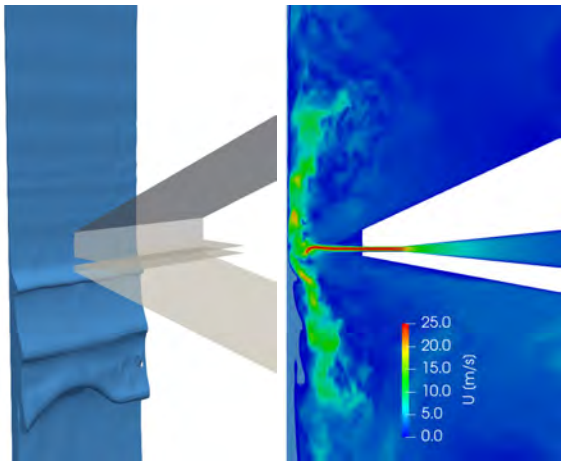

(a) Case 1: $\hat{Z} = 14.2 \mid \Pi = 0.16$

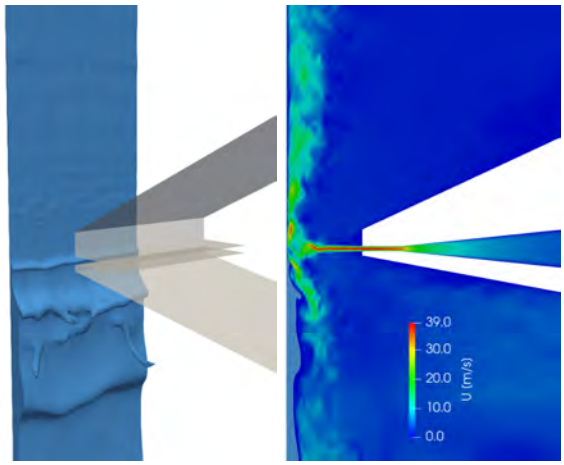

(b) Case 2: $\hat{Z} = 14.2 \mid \Pi = 0.33$

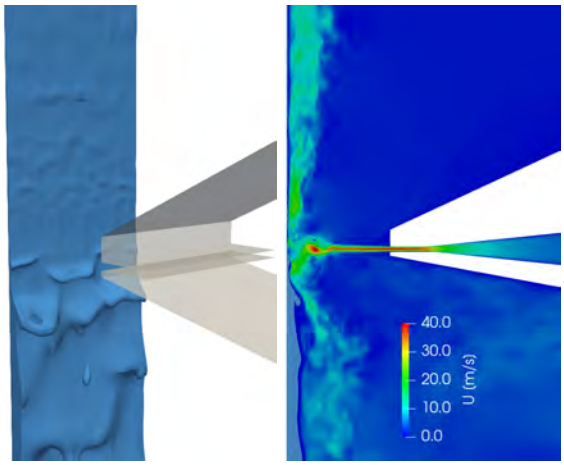

(c) Case 3: $\hat{Z} = 19.4 \mid \Pi = 0.18$

Figure 3: Exemplary of the 3D reconstruction of the liquid film (left) and 2D velocity field (right) before data processing for the three investigated cases.

Table 2: Comparison of the spatio-temporal average of the final film thickness $\bar{h}_f$ (in microns) in the CFD calculations and experimental conditions[1].

Case #	Numerical [μ m]	Experimental [μ m]
1	435	$449 \pm 5\%$
2	263	$311 \pm 5\%$
3	335	$399 \pm 5\%$

spatio-temporal thickness of the film and the velocity field in the gas flow for a midplane at $z = 15$ mm. In the comparison of Fig. 4 only the leading modes of the mPOD analysis are considered.

The three test cases show a remarkable agreement between experimental and numerical data. While in all the cases the runback flow is characterized by a single dominant frequency, with fairly good agreement between experimental and numerical data, the same comparison for the cases 2 and 3 is of more difficult interpretation. As illustrated in Fig. 3, these cases are characterized by three dimensional waves and are probably more influenced by the differences between the experimental and the numerical configurations. Interestingly, the dominant frequency in the final film, in case 2, is lower than the one observed in the runback flow. This is observed in both numerical and experimental data although the position of the frequency peaks is different.

The agreement between numerical and experimental data is satisfactory and shows that the leading mechanisms driving the jet flow is a nearly harmonic behavior at the frequency of the run back flow. Although with different intensities, we systematically detect a dominant frequency present in the final film, runback flow *and* gas jet. As described in previous works[2; 1; 8], this is the footprint of the hydrodynamic feedback responsible for the undulation.

The details of the coupling are further investigated in the following subsection.

3.2. The main mechanism of undulation

The multiscale analysis of the gas-liquid interaction is only shown for case 1. The film dynamics are investigated with the mPOD decomposition of the normalized thickness $\check{h}$, computed as in Eq. 7. A single pair of modes linked to traveling waves is identified (modes 2 and 3). The associated spatial structure is shown in Figure 5 (ϕ_2, in the middle), together with its frequency spectra ($|\widehat{\psi}_{2,3}|$, on the right) and a snapshot

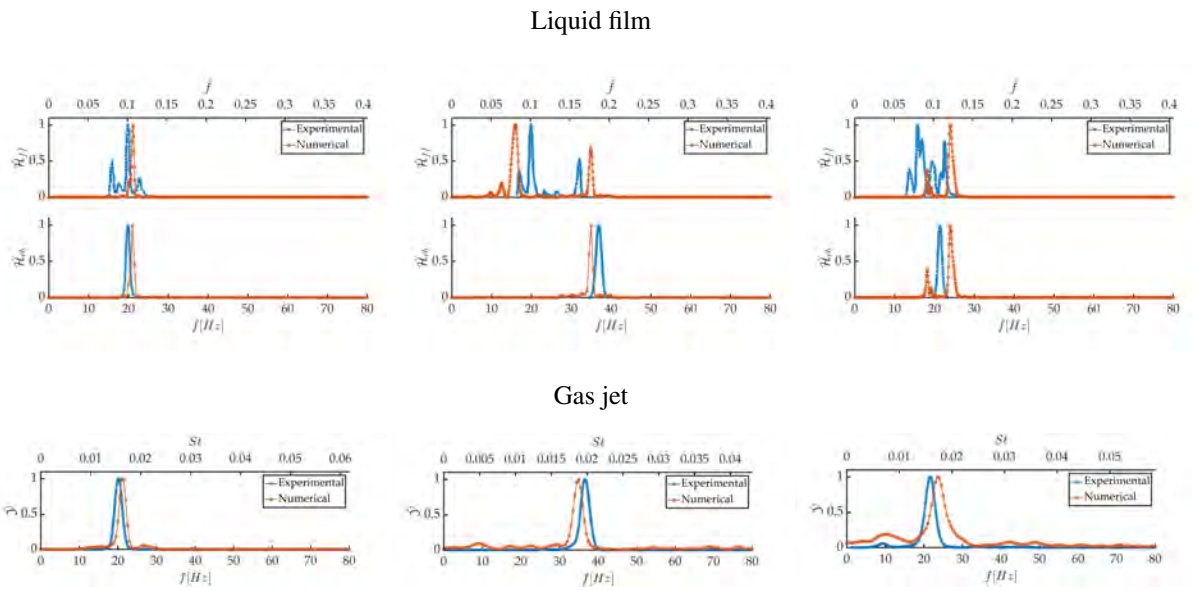

(a) Case 1: $\hat{Z} = 14.2 \mid \Pi = 0.16$ (b) Case 2: $\hat{Z} = 14.2 \mid \Pi = 0.33$ (c) Case 3: $\hat{Z} = 19.4 \mid \Pi = 0.18$

Figure 4: Original normalized thickness (left) Spatial structure (center) and frequency content of the temporal structure (right) of the most dominant/representative modes of the test cases.

of the scaled thickness map ($\check{h}$, on the left). Comparing the snapshot with the detected structures gives a qualitative indication of their relative importance and hence how well these modes approximate the data.

For this test case, featuring almost bi-dimensional waves, the identified traveling pattern accounts for a significant portion of the undulation amplitude. It is worth noticing that the liquid film and the gas jet are locked at the same frequency (see Fig. 4) and the detected pattern is present in the *entire domain*, i.e. both the final film and the run back flow. In these regions, waves have significantly different shapes, travel in opposite direction with different speed, and evolve over a film with largely different thickness. It is thus remarkable that, despite these differences, waves in both regions are produced at the same frequency, which is also observed in the jet flow. This component is hereinafter referred to as *2D coupled undulation*.

An extended mPOD analysis is now performed to correlate, using (8), this pattern in the film with specific flow structures in the gas jet. Since the waves are two-dimensional, we limit our analysis to a midplane taken at $z = 15$mm. The reconstruction of the velocity field using the pair of modes correlated with the 2D coupled undulation is shown in Fig. 6. Every column represents one snapshot of a single period of the undulation mechanism. The formation of the waves in the runback flow is completely correlated with the deflection of the side jet attached to the film. This suggests that, in fact, the unsteady confinement of the jet flow in close interaction with the runback flow is the main source of instability of the flow.

In order to link this motion with the formation of the undulations, in Fig. 3.2 we investigate the impact of the film dynamics (left column) in the wiping actuators (right column). The first three time steps of Fig. 6 are displayed in rows in descending order. At the interphase, some key points are highlighted: $x^P = x(P_{max})$ is the impact point, $x^* = x(\partial_x P_{max})$ is the wiping point , $x^\tau = x(\tau_{max})$ the shearing point and $x^0 = x(u = 0)$ are x-velocity stagnation points. The coupling mechanism is explained as follows.

In the first snapshot, the nearest runback wave is far from the impact point x^P and the film is gently sloped. The relative confinement of the jet is low, so that the pressure gradient is mostly symmetric. On the other hand, the shear stress is consistently higher in the runback flow because it is naturally linked to the relative velocity between phases. At this point, the wiping work is very localized in the vicinity of the impact point x^P, since the wiping point x^* and is very close. Because a new wave is emergind at this position, the local thickness is increasing; what is remarkable is that at x^* all the flow is actually going upwards, as if the wiping actuators were not sufficient to induce a runback flow. The confinement is raised with the in-

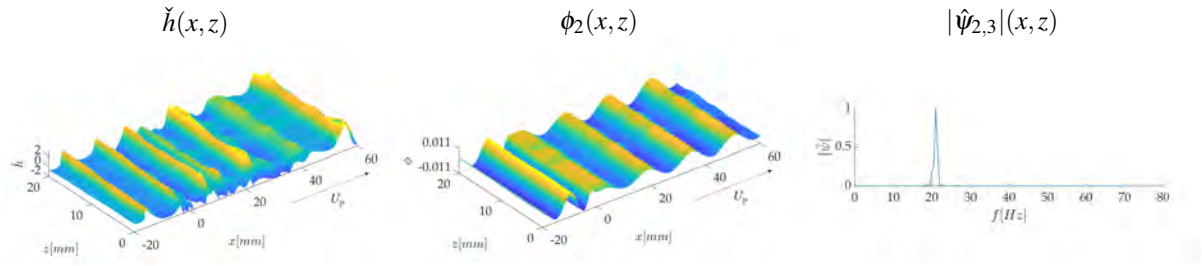

Figure 5: Detected traveling wave pattern in test case 1. A snapshot of the normalized thickness $\check{h}$ is shown on the left. The figure in the middle shows the most representative traveling wave structure. The associated frequency spectra is shown on the right.

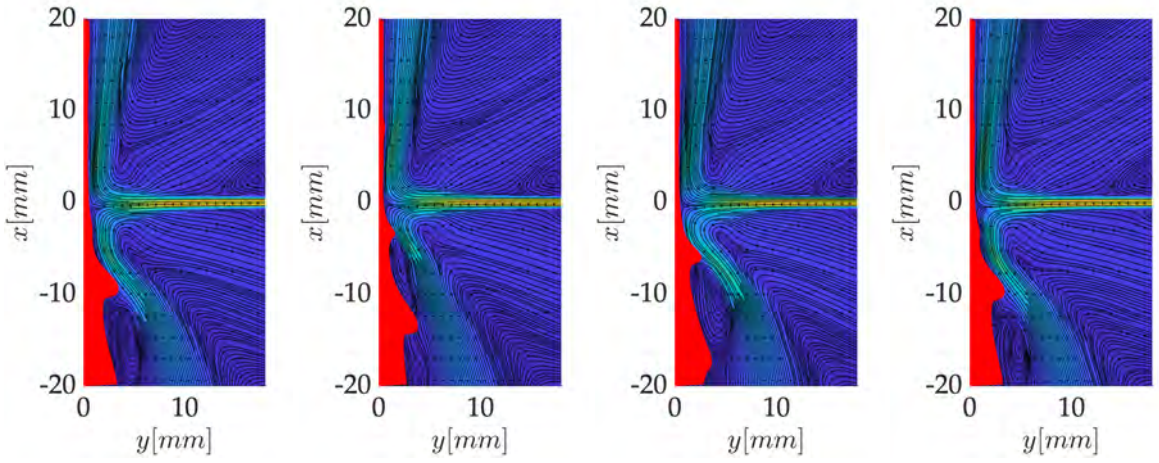

Figure 6: Velocity field reconstructed from the pair of modes correlated with the 2D coupled undulation. The time-dependent liquid film profile is coloured in red and each column corresponds to one snapshot during the formation of a wave.

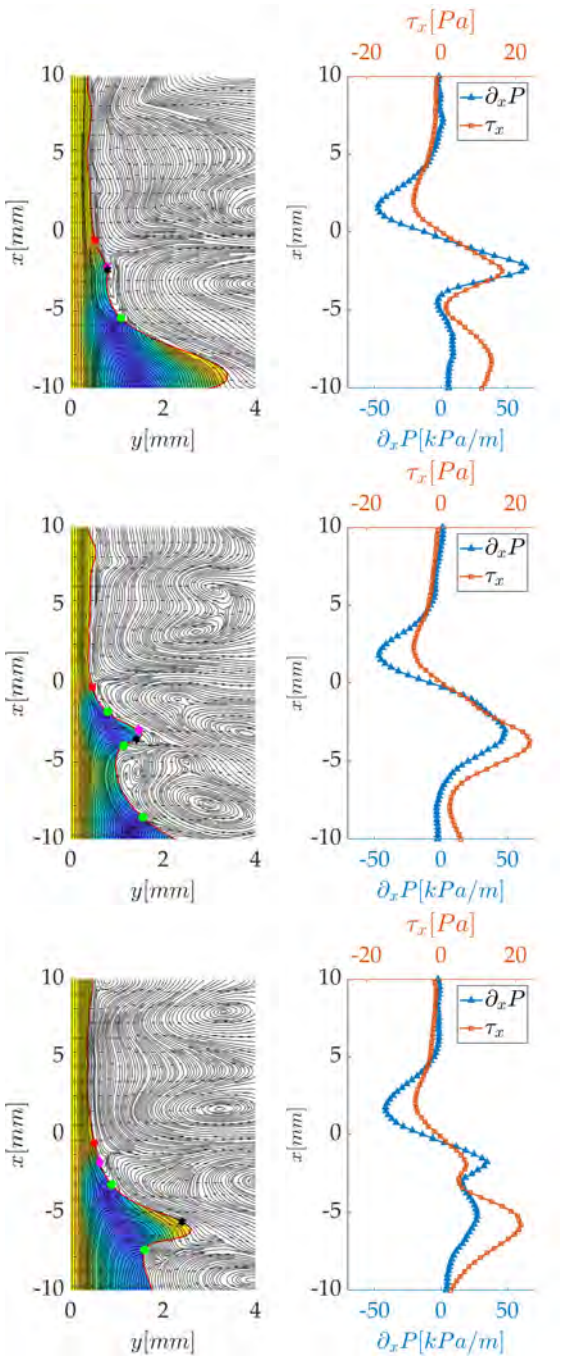

Figure 7: Representation of the original velocity field (left) and mPOD filtered wiping actuators (right) for several snapshots in a given undulation period. Some key points are highlighted at the interphase: $x^P = x(P_{max})$ is the impact point, $x^* = x(\partial_x P_{max})$ is the wiping point , $x^\tau = x(\tau_{max})$ the shearing point and $x^0 = x(u = 0)$ are x-velocity stagnation points.

creasing film thickness below the wiping, boosting the maximum pressure gradient, and therefore enhancing the wiping capabilities of the jet.

Eventually, the film becomes too thick that the shear stress and gravity dominate over viscosity, developing a runback flow as seen in the second snapshot. The pressure gradient evolve into a more asymmetric shape and the maximum value starts to decrease as the wave leaves the area of maximum interaction. Finally, the wiping point x^* goes back to the symmetric position and the shear stress still helps to push the wave until the pressure gradient is sufficient to restart the cycle.

For this configuration, the wiping work is essentially performed by the pressure gradient; however, we observe how the shear stress is contributing to "push" and deform the runback wave once it is formed. The role of the pressure gradient is therefore to control the flow allowed to reach the final film, and the shear stress governs the force balance that drives the waves back to the coating bath. The frequency of the aforementioned process obviously depends on the wiping strength, but also on the force balance in the falling wave.

In essence, the mechanism is captured by a pair of modes mostly active on the side of the runback flow. They describe a similar behaviour as the one observed in the previous experimental works[1; 19], referred to as *hydrodynamic feedback*. The mechanism is driven and self-sustained by the unsteady confinement produced by the waves of the runback flow. In contrast with what was observed in the experiments, the jet stays "rigid" and there is no such downward deflection of the impinging jet.

In terms of wiping actuators, the main source of instability is the pulsation of the maximum pressure gradient associated to the runback flow, which is also in complete agreement with the numerical investigation of the liquid film patterns performed via integral modelling [7] since in the scenario of a pulsation predicts relative wave amplitudes that are substantially larger in the runback flow than in the final film, as it is observed in the CFD simulations.

4. Conclusion

The dynamics of the gas-liquid interaction in the jet wiping process has been analyzed via CFD simulations and modal analysis. The numerical model has been validated with experimental data. There is a remarkable agreement in terms of the most characteristic features of the dynamics of the gas-liquid interac-

tion: mean thickness and frequency spectra. In this sense, these results pave the way for the investigation of wiping configurations closer to the industrial lines, as well as to validate the integral model formulation of Mendez (ref).

The multiscale Proper Ortogonal Decomposition (mPOD) allowed to detect several travelling wave patterns dominant in the liquid; which are mostly two-dimensional and originated at the same point slightly bellow the jet axis: the 2D coupled undulations. They constitute the footprint of the coupling between the liquid and the gas, because the frequency content is almost identical to the one of the leading modes in the gas flow.

The extended analysis of the gas allowed to reveal the main mechanism of undulation. The formation of waves in the runback flow periodically affects the confinement of the lower part of the gas jet, and hence modulating the wiping efficiency of the gas jet. These perturbations are propagated through the entire domain due to advection. This further confirmed the hydrodynamic feedback between the gas jet and the runback waves [1; 19] as the principal mechanism of undulation. Nevertheless, no significant deflection of the jet has been identified in the CFD simulations. The main source of instability in the wiping actuators is a pulsation of the pressure gradient, self-sustained by the formation of waves in the runback flow.

Acknowledgments

D.Barreiro-Villaverde is financially supported by Xunta de Galicia with the pre-doctoral grant "Programa de axudas á etapa predoutoral" and the research project is founded by Arcelor-Mittal. The authors also wish to thank the “Red Española de Supercomputación” for the attribution of special computational resources at FinisTerrae II (CESGA) and Tirant (UV) (FI-2018-3-0040, FI-2019-1-0044).

References

[1] M. A. Mendez, A. Gosset, J. M. Buchlin, Experimental analysis of the stability of the jet wiping process, part II: Multiscale modal analysis of the gas jet-liquid film interaction, Experimental Thermal and Fluid Science 106 (2019) 48–67. doi:10.1016/j.expthermflusci.2019.03.004.

[2] A. Gosset, M. A. Mendez, J. M. Buchlin, An experimental analysis of the stability of the jet wiping process: Part I – Characterization of the coating uniformity, Experimental Thermal and Fluid Science 103 (2019) 51–65. doi:10.1016/j.expthermflusci.2018.12.029.

[3] K. Myrillas, Experimental and Numerical Investigation of Gas Jet and Liquid Film Interaction, Ph.D. thesis, Université Libre de Bruxelles (2011).

[4] K. Myrillas, P. Rambaud, J. M. Mataigne, P. Gardin, S. Vincent, J. M. Buchlin, Numerical modeling of gas-jet wiping process, Chemical Engineering and Processing: Process Intensification 68 (2013) 26–31. doi:10.1016/j.cep.2012.10.004.

[5] W. Eßl, C. Pfeiler, G. Reiss, W. Ecker, C. K. Riener, G. Angeli, LES-VOF Simulation and POD Analysis of the Gas-Jet Wiping Process in Continuous Galvanizing Lines, steel research international 89 (2) (2018) 1700362. doi:10.1002/srin.201700362.

[6] A. D. Johnstone, B. Kosasih, L. Q. Phan, A. Dixon, W. Renshaw, Coating Film Profiles Generated by Fluctuating Location of the Wiping Pressure and Shear Stress, ISIJ International 59 (2) (2019) 319–325. doi:10.2355/isijinternational.ISIJINT-2018-413.

[7] M. A. Mendez, A. Gosset, B. Scheid, M. Balabane, J. M. Buchlin, Dynamics of the Jet Wiping Process via Integral ModelsarXiv:2004.13400.

[8] M. A. Mendez, Dynamics of Gas Jet Impinging on Falling Liquid Films, Ph.D. thesis, Université Libre de Bruxelles (2018).

[9] S. Márquez Damián, An Extended Mixture Model for the Simultaneous Treatment of Short and Long Scale Interfaces, Tech. rep., Universidad Nacional del Litoral (nov 2013).

[10] S. S. Deshpande, L. Anumolu, M. F. Trujillo, Evaluating the performance of the two-phase flow solver interFoam, Computational Science & Discovery 5 (1) (2012) 014016. doi:10.1088/1749-4699/5/1/014016.

[11] P. Sagaut, Large Eddy Simulation for Incompressible Flows: An Introduction (2006).

[12] D. Lakehal, Status and future developments of Large-Eddy Simulation of turbulent multi-fluid flows (LEIS and LESS) (jul 2018). doi:10.1016/j.ijmultiphaseflow.2018.02.018.

[13] L. Sirovich, Analysis of turbulent flows by means of the empirical eigenfunctions, Fluid Dyn. Res. 8 (1991) 85–100. doi:https://doi.org/10.1016/0169-5983(91)90033-F.

[14] P. Holmes, J. L. Lumley, G. Berkooz, Turbulence, Coherent Structures, Dynamical Systems and Symmetry, Cambridge University Press, 1996. doi:10.1017/cbo9780511622700.

[15] P. J. Schmid, Dynamic mode decomposition of numerical and experimental data, Journal of Fluid Mechanics 656 (2010) 5–28. doi:10.1017/S0022112010001217.

[16] C. Rowley, I. Mezić, S. Bagheri, P. Schlatter, D. Henningson, Spectral analysis of nonlinear flows, J. Fluid Mech. 641 (2009) 115. doi:10.1017/s0022112009992059.

[17] D. Ninni, M. A. Mendez, MODULO: A software for Multiscale Proper Orthogonal Decomposition of data, SoftwareX 12 (2020) 100622. doi:https://doi.org/10.1016/j.softx.2020.100622.

[18] J. Borée, Extended proper orthogonal decomposition: A tool to analyse correlated events in turbulent flows, Experiments in Fluids 35 (2) (2003) 188–192. doi:10.1007/s00348-003-0656-3.

[19] M. A. Mendez, M. T. Scelzo, J. M. Buchlin, Multiscale modal analysis of an oscillating impinging gas jet, Experimental Thermal and Fluid Science 91 (2018) 256–276. doi:10.1016/j.expthermflusci.2017.10.032.

Prospects in machine learning-based flow control for liquid metal coating

Fabio Pino

Environmental and Applied Fluid Dynamics Department, von Karman Institute for Fluid Dynamics, Belgium, fabio.pino@vki.ac.be

Supervisor: Miguel Alfonso Mendez

Assistant Professor, Environmental and Applied Fluid Dynamics Department, von Karman Institute for Fluid Dynamics, Belgium, miguel.alfonso.mendez@vki.ac.be

University Supervisor: Benoit Scheid

Professor, Transfers, Interfaces and Processes (TIPs) laboratory, Universit libre de Bruxelles, Belgium, benoit.scheid@ulb.ac.be

Abstract

The accurate control of liquid film thickness is critical in the hot-dip galvanizing coating process. This is achieved by impinging gas jets, in a technique called jet wiping. Albeit its reliability, under certain conditions a detrimental undulation pattern appears. This work presents the black box control of this instability on a representative test case along with the modeling of electromagnetic actuators.

Keywords: liquid film, flow control, metal coating, modeling, machine learning, reinforcement learning

1. Introduction

Flow control aims at manipulating a fluid system with the intent of improving its engineering benefits[1]. This research discipline lies at the intersection between fluid dynamics, control theory and dynamical systems. Due to its complexity, it has been an open and active research area for decades. However, new sizable room for improvement has been unveiled, owing to the birth of new data driven techniques in the past few years.

The peculiar aspect of this field, customarily known as machine learning, relies on the lack of a proper mathematical formulation of the control problem. For the most part, classic control methods demands for a precise and cumbersome mathematical formalization.

This tedious part is replaced in machine learning by a self-taught algorithm. An algorithm capable of learning by himself, resorting on the black-box input/output relations provided by the system at hand. The machine by interactions with an environment, tests its action selection capabilities, and based on some error measure, improves its performance.

Although this has been an object of academic curiosity since the 60s, not until the 2010s has machine learning gained clear academic and industrial prominence. The cause of this new machine learning summer has to be found in the amount of data nowadays available and in improved computing capacities. Recent machine learning success in classification, regression and control have attracted the attention of the fluid dynamic and flow control communities [2]. Among different machine learning tools which can be used for control, the branch entirely devoted to decision making process is called Reinforcement Learning (RL). This collection of algorithms has already given proof of being very promising solution for complex control problem [3], [4] ranging from drag reduction [5] to improved swimming abilities [6]. In the domain of liquid film, a first proof of concept on a 2D model of falling liquid film has been presented in [7].

This work intent is to extend the analysis to a 3D configuration in the framework of the hot-dip galvanization. This is one of the most extensively used method for coating iron and steel. It aims at preventing the corrosion of the underneath metal covering it with a thin layer of zinc. As shown in Fig.1, this consists in dipping a metal plate into a bath of molten zinc, withdrawing it and controlling the excess of zinc by wiping the free surface with some im-

pinging gas jets, also know as jet-wiping. Although the jet-wiping is a very simple, cost effective and easily operated technique, due to the existence of zero dimensional engineering models, in certain operating condition some instabilities occur [8]. The liquid film triggers jet oscillations, these combined with inertia engenders the formation of undulation patterns in the final zinc coating, limiting the range of operating conditions.

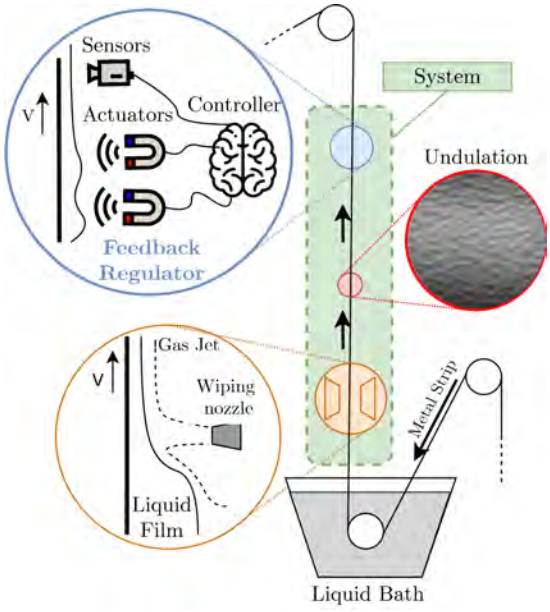

Figure 1: Representation of the hot-dip galvanizing process via jet wiping, the undulation instability resulting in wavy patters in the final coating, and position of the envisaged feedback regulation to cope with this issue

The goal of this research project is to develop a feedback regulator capable of damping these undulations in the liquid film. This tool will be composed of three main parts: **sensors** observing the free surface, **actuators** interacting with the system and a **control logic** managing the two. The main focus of this research project is on the development of an effective control strategy capable of handling the control action in a close-loop manner, using observations to modify its action. Three different approaches can be followed in the design of a controller, depending on the amount on insight about the system dynamics: white box, gray box and black box.

- **White Box** A complete knowledge about the governing equations is available, the controller can be designed based on the stability analysis of the system.
- **Gray Box** A limited knowledge of the system is available and this is generally used to derive an empirical model. In this case, the controller can be designed based on a linearisation of the system equations or on a surrogate model using system identification methods. This would allow to use simple control design techniques as linear control.
- **Black Box** The controller design is based solely on data, assuming no knowledge about the dynamics. The system is seen as a black box and only input/output relations are available. This is the case of many complex systems where a proper mathematical formulation might represent a burden. In this area resides the machine learning based control. As mentioned above, the branch of ML concerned with decision making problems is called Reinforcement Learning. Here, the control action is defined by means of a learning process based on interaction with the environment and a trial and error paradigm.

This first year of research was focused on two main tasks, the steady and unsteady modeling of magnetic actuators and the testing of black-box based control methods on representative test cases.

Section 2 presents the steady and unsteady magnetic modeling based on an already existing integral model of the process [8]. Several alternatives to jet wiping have been proposed [9]. Among these, the use of magnetic wiping has been considered as viable solution to assist or eventually replace the gas jet actuation. Thus, it was thought that this could be instrumental for the control purpose too. In magnetic wiping, the actuation is due to the steady magnetic field generated by a permanent magnet [10], [11], modeled as a Gaussian function along stream-wise direction. Section 3 focuses on the optimal control and on the description of the machine learning-based techniques. The reason behind this choice was due to the underlying capability of black-box control to cope with uncertainty and noise. Given the complexity of the physical phenomenon, the integral model developed at the institute, is capable of featuring accurately only the most relevant aspects. So, it is highly likely that in the real application the controller will face more complex unpredictable conditions. The control performance have been tested on different toy problems in 4. The one most representative of the actual undulation was the propagation of a perturbation in the viscous Burgers equation in 4.3.

2. Electromagnetic actuators modeling

In this first attempt of modeling electromagnetic actuators, the actuation was considered as part of a hybrid magnetic/jets wiping system. As shown in Fig.2 the permanent magnet and the jets are working one next to the other to ensure a better wiping performance. This is an illustrative representation; in real industrial application, the magnet is positioned upstream the jet in a much closer location.

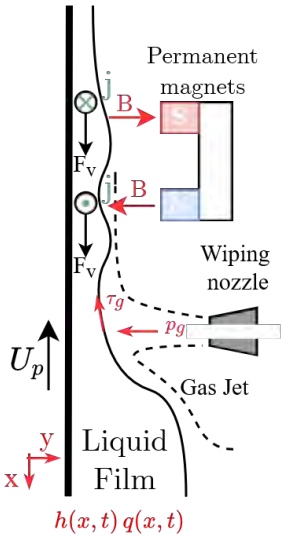

Figure 2: Illustrative figure of the joint magnetic and jet action in the wiping process.

Both the forces induced by the magnetic flux and the jets are accounted for the derivation of the models. In line with [11], it is assumed a transverse magnetic flux vector generated by a permanent magnet. Starting from the Maxwell-Faraday law it is possible to derive an expression for the induced current inside the liquid film j_y,

$$j_y = -\sigma_M \frac{\partial \phi}{\partial y} + \sigma_M u B \approx \sigma_M u B, \tag{1}$$

where u is the streamwise velocity, σ_M is the electrical conductivity of the medium, B is the magnetic flux and ϕ represents the electric scalar potential. In this first attempt, due to its not significant contribution, this quantity is neglected. The current density generated inside the liquid film interacts with the magnetic flux generating a Lorentz force directed downwards:

$$F = \vec{j} \times \vec{B} = j_y \cdot B = \sigma_M u B^2. \tag{2}$$

A stationary model of the process was developed first. This was subsequently extended to an unsteady integral formulation of the liquid film following the footsteps in [8].

2.1. Steady State Model

Simplified engineering models for the jet wiping process consider the flow unidimensional along the streamwise direction ($v \sim 0$) and steady ($\partial_t \sim 0$), so that the Navier-Stokes equations reduce to

$$\partial_x u = 0 \tag{3a}$$

$$0 = -\frac{1}{\rho}\partial_x p_l + \frac{\mu_l}{\rho_l}(\partial_{yy} u) + g - \sigma_M B^2 u \tag{3b}$$

$$0 = -\partial_y p_l, \tag{3c}$$

where last term in 3(b) is the Lorentz force previously introduced. p_l is the pressure inside the liquid film, g is the gravitational acceleration, μ_l and ρ_l are the dynamic viscosity and the density of the liquid zinc respectively. The boundary conditions (BCs) are the non-slip condition on the plate:

$$u(0) = -U_p \quad \text{for} \quad y = 0, \tag{4}$$

and dynamic and kinematic conditions at the interface ($y = h$), which at the leading order are respectively:

$$p_l = p_g(x) - \sigma \partial_{xx} h \quad \text{and} \quad \partial_y u = \frac{1}{\mu}\tau_g(x), \tag{5}$$

where $\partial_{xx} h$ is the interface curvature, $p_g(x)$ is pressure and $\tau_g(x)$ the shear stress induced by the jet at the free surface. By replacing p_l from the dynamic BC into Eq. 3(b) two new terms appear, the jet pressure gradient $\partial_x p_g(x)$ and the surface tension $\partial_{xxx} h(x)$. The equations and the BCs were then put into non-dimensional forms using the scaling quantities in [8]. The reference quantity for the magnetic flux was given by its maximum value, $[B] = \max(B)$. A general solution for both the homogeneous and particular equations is:

$$\hat{u}(\hat{y}) = k_1 e^{(H_{a_0}\hat{B}\hat{y})} + k_2 e^{(-H_{a_0}\hat{B}\hat{y})} + \frac{A_1 + 1}{H_a^2 \hat{B}^2}, \tag{6}$$

where A_1 is given by $A_1 = -\partial_{\hat{x}}\hat{p}_g + \frac{\epsilon^3}{Ca}\partial_{\hat{x}\hat{x}\hat{x}}\hat{h}$, where $Ca = \mu U_p/\gamma$ is the capillary number and $\epsilon = [h]/[x]$ is the film parameter given by the ratio of the reference quantities in the y direction ($[h]$) and x direction ($[x]$). $\hat{B} = B/[B]$ is the non-dimensional magnetic flux. H_a is a dimensionless number called Hartmann number, given by $H_a = \sqrt{\frac{\sigma [B]^2 U_p}{\rho g}}$, U_p is the velocity of the ascending strip. By using the boundary conditions to

define the integration constants, k_1 and k_2, it is possible to find the particular solution of the problem in terms of non-dimensional velocity profiles, this reads:

$$\hat{u}(\hat{y}) = \left\{ \frac{\hat{\tau}_g/(H_a\hat{B}) + \sinh(\hat{h}H_a\hat{B})\left(1 + \frac{A_1+1}{H_a^2\hat{B}^2}\right)}{\cosh(\hat{h}H_a\hat{B})} \right\} \sinh(\hat{y}H_a\hat{B}) + \\ - \cosh(\hat{y}H_a\hat{B})\left(1 + \frac{A_1+1}{H_a^2\hat{B}^2}\right) + \frac{A_1+1}{H_a^2\hat{B}^2}. \tag{7}$$

H_a quantity represents the ratio between magnetic forces to gravitational forces and it accounts for the intensity of the magnetic wiping. Introducing the definition of flow rate per unit width, $\hat{q} = \int_0^{\hat{h}} \hat{u}\, d\hat{y}$, it is possible to derive a relation between the flow rate and the liquid film thickness $\hat{h}$:

$$\hat{q} = \frac{\hat{\tau}_g}{H_a^2\hat{B}^2} + \frac{A_1+1}{H_a^2\hat{B}^2}\hat{h} + \\ - \left\{ \frac{\hat{\tau}_g/(H_a\hat{B}) + \sinh(\hat{h}H_a\hat{B})\left(1 + \frac{A_1+1}{H_a^2\hat{B}^2}\right)}{\cosh(\hat{h}H_a\hat{B})} \right\} \frac{1}{H_a\hat{B}} \tag{8}$$

2.2. The Unsteady Model

The unsteady formulation was based on the one derived for the non-magnetic jet-wiping in [8]. The dimensionless boundary layer equations are integrated along the liquid film thickness resulting in a set of two nonlinear hyperbolic partial differential equations in $\hat{q}$ and $\hat{h}$:

$$\boxed{\begin{aligned} \partial_{\hat{t}}\hat{h} &= -\partial_{\hat{x}}\hat{q} \\ \partial_{\hat{t}}\hat{q} &= -\partial_{\hat{x}}\mathcal{F}(\hat{q},\hat{x}) - \hat{h}\partial_{\hat{x}}\hat{p}_g + \hat{h} + \frac{\epsilon}{Ca}\partial_{\hat{x}\hat{x}\hat{x}}\hat{h} + \\ &\quad + \hat{\tau}_g + \hat{\tau}_w(\hat{q},\hat{h}) - H_{a_0}^2\hat{B}^2(\hat{x})\hat{q} \end{aligned}} \tag{9}$$

To be well posed, this problem needs for two closure relations for the non-linear advection term ($\mathcal{F}$) and the shear stress at the wall ($\hat{\tau}_w$).

$$\mathcal{F}(\hat{q},\hat{h}) = \int_0^{\hat{h}} \hat{u}^2\, d\hat{y} \quad \text{and} \quad \hat{\tau}_w(\hat{q},\hat{h}) = -\partial_{\hat{y}}\hat{u}|_{\hat{y}=0}. \tag{10}$$

This passes through the definition of a velocity profile form. To this end, it was necessary to rely on the self-similarity hypothesis. This states that the equilibrium between gravitational, magnetic and viscous forces is not considerably affected by the other terms (surface tension and inertia). In other terms, the velocity profile can be considered of the same shape as the one found in the steady state solution, Eq (6):

$$\hat{u}(\hat{y}) = k_1 e^{H_{a_0}\hat{B}\hat{y}} + k_2 e^{-H_{a_0}\hat{B}\hat{y}} + k_3\frac{A_1+1}{H_{a_0}^2\hat{H}^2}, \tag{11}$$

The three constants in this case (k_1, k_2, k_3) are function of the system states, allowing for the velocity profile to accommodate the variations of $\hat{h}$ and $\hat{q}$ throughout the dynamics. These relations are found by solving a linear system formed with the boundary conditions and the definition of the flow rate:

$$\hat{u}(0) = -1 \quad \partial_{\hat{y}}\hat{u}(\hat{h}) = \hat{\tau}_h \tag{12a}$$

$$\hat{q} = \int_0^{\hat{h}} \hat{u}\, d\hat{y}. \tag{12b}$$

The model is implemented in the framework of the already existing finite volume software for 2D jet-wiping called BLEW [12].

3. Optimal control problem

An optimal control problem is a constrained optimization problem with a dynamical system as constraint. In the general framework, given a dynamical system represented by some kind of differential equation [13]:

$$\dot{\mathbf{u}}(t) = f(\mathbf{u}(t), \mathbf{c}(t), t), \quad t \in [0, T], \quad \mathbf{u}(0) = \mathbf{u}_0 \tag{13}$$

where $u(t) \in \mathbb{R}^n$ is the *state* vector, $c(t) \in \mathcal{S} \subset \mathbb{R}^m$ is the *control action* and t is the independent variable. Considering a cost functional $J : \mathbb{R}^n \times \mathbb{R}^m \to \mathbb{R}$:

$$J(\mathbf{c}) = \underbrace{\mathcal{M}(\mathbf{u}(T))}_{\textit{Mayer term}} + \int_0^T \underbrace{\mathcal{L}(\mathbf{u}, \mathbf{c}, t)}_{\textit{Lagrange term}}\, dt. \tag{14}$$

This is composed by two terms, the Mayer terms accounts for the final state condition and the Lagrange terms considers the evolution of the states and the control action in the temporal domain. The final objective of this problem is to find the function $\mathbf{c}(t)$ which minimizes the cost functional while respecting the dynamics equations.

There exist two main approaches to this problem. The first, tries to address the problem directly finding the optimal function $\mathbf{c}(t)$. This is usually called open-loop solution. The second, where the control action is defined as a function of the state vector, $\mathbf{c} = \mathbf{c}(\mathbf{u}(t))$, is called closed-loop solution. It was decided to resort

on the second method in our problem, since it is best suited for global optimization and low-dimensional problems. The next critical process after the mathematical formalization of the problem is called transcription. The basic idea is that it is possible to transform the original optimal control problem in a constrained parameter optimization problem. The continuous problem is brought to finite dimension through discretisation. In this way, the optimal solution is given by a set of real number with some algebraic constraints, instead of an optimal control function and differential equation as constraint.

Two machine learning tools are compared to solve this problem: Reinforcement Learning (RL) and Bayesian Optimization (BO). In the case of the RL, the relation between the observed states of the system and the action is given by a neural network. The selection of the action and the learning process will be detailed in the following section. Concerning the use of Bayesian Optimization instead, for simplicity the relation between action and observation is given by a linear combination of states. The control action at each time step is defined by a linear combination of the system observation ($\overline{u}_{tj}$) multiplied by some weights (w_j):

$$c_t = \sum_{j=1}^{N} w_j \overline{u}_{tj}. \tag{15}$$

The optimal weights are the result of an optimization process.

3.1. Numerical Methods for Optimal Control

3.1.1. Reinforcement Learning

Reinforcement Learning (RL) represents one of the three main paradigms of machine learning, together with Supervised Learning (SL) and Unsupervised Learning (UL). The peculiar feature of RL is its ability to cope with decision making problems by using a self-taught intelligent agent [14]. In Fig.3 the general framework of any RL problem is presented, this is composed by two main blocks: an environment and an agent. The agent embeds a policy which based on the actual state of the system (s_t) interacts with the environment through some actions (a_t). As a result, the environments evolves to a new state (s_{t+1}) providing at the same time a reward (r_{t+1}). The final objective is to find the decision policy that maximizes the sum of rewards.

Going deeper in the definition of these objects, the **policy** is a mapping between elements of the state space to elements of the actions space. Depending on the problem, this could be deterministic or probabilistic. The stochastic one outputs the parameters of a probability density function from which the action will be drawn.

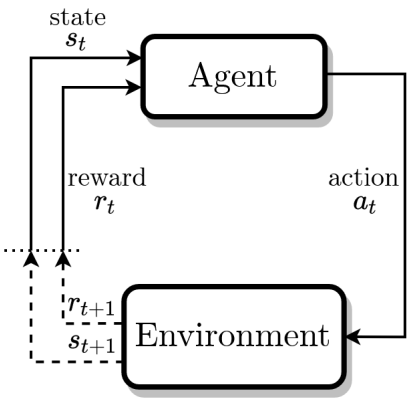

Figure 3: The two main RL blocks, the agent and the environment and their connections through the action a_t, the consequent environment new state s_{t+1} and reward r_{t+1}

$$\begin{gathered} s \in \mathcal{S}, a \in \mathcal{A} \\ \pi : \mathcal{S} \rightarrow \mathcal{A} \; \textit{deterministic} \\ \pi : \mathcal{S} \times \mathcal{A} \rightarrow [0,1] \; \textit{stochastic} \end{gathered} \tag{16}$$

The **reward** plays a key role in the agent training. By carefully shaping the reward function, it is possible to lead the control of the system towards the desired state. The RL algorithm based on the evolution of the system and on the value of the reward will modify its actions. The data acquisition process from the environment is the result of trial and error process, structured in two phases: exploration and exploitation. During the exploration, the policy selects random actions to explore the action space. Thereby, a series of state-action-reward-new state is created. These are customarily called **trajectories** ($\tau = (s_0, a_0, r_1, s_1, \ldots, r_T, s_T)$). The collection of trajectories comprise the dataset upon which the policy is updated. Once a relevant amount of knowledge has been gained, the agent will gradually exploit the existing trajectories reinforcing the actions which led to higher rewards.

The **environment** represents the governing equations of the system at stake. The great majority of reinforcement learning problems can be formulated as a Markov Decision Process (MDP). A MDP is an environment in which all states are Markov. Meaning that the transition to a next state is predictable without any need for information from the past states but only

the present state. From a mathematical perspective, the state transition probability functions is exclusively conditioned by the present state:

$$\mathcal{P}[S_{t+1}|S_t] = \mathcal{P}[S_{t+1}|S_1, \ldots, S_t] \tag{17}$$

An MDP is often defined as tuple $(S, A, \mathcal{D}, R, \gamma)$, where S is the state space, A is a finite set of actions, R is the reward function, γ the discount factor and $\mathcal{D}$ is the probability of moving to a certain state s' having taken action a in the previous state s:

$$\mathcal{D}^a_{ss'} = \mathbb{P}[S_{t+1} = s'|S_t = s, A_t = a] \tag{18}$$

After the general description of the main blocks, it is now important to highlight the relevant objects common to any RL algorithm. First of all the **Discounted Future Reward** is defined as the sum of all the future reward the agent will collect starting from the present time step. The reward are weighted by a discount factor ($\gamma \in [0, 1]$). In this way, the near future rewards will have a greater importance compared to those in the medium and long term.

$$R = \sum_{t=0}^{\infty} \gamma^t r_t, \qquad \gamma \in [0, 1), \qquad t \in \mathbb{N}^+ \tag{19}$$

where r_t is the reward at time step t and γ is the discount factor. Mathematically speaking, having a decimal discount factor ensure the convergence of the geometric series of the discounted reward. Each state is featured by a **Value Function** $V_\pi(s)$, this is defined as the expected return starting with state s, and successively following policy π. It represents how good is a state for an agent to be in.

$$V : \mathcal{S} \times \pi \to \mathbb{R} \qquad V^\pi(s) = \mathbb{E}[R|s, \pi] \tag{20}$$

A similar function is defined for state-actions pairs (s_t, a_t) which is called **Action-Value Function or Q function**. It is the expected return starting from state s, taking action a and from then on following policy π.

$$Q : \mathcal{S} \times \mathcal{A} \to \mathbb{R} \quad Q^\pi(s, a) = \mathbb{E}_\pi[R|S_t = s, A_t = a] \tag{21}$$

The relationship between Q^π and V^π (the value of that state) is given by:

$$Q^\pi(s_t, a_t) = r(s_t, a_t) + \gamma V^\pi(s_{t+1}) \tag{22}$$

Additionally it is possible to define another function called **Advantage Function** which specifies the potential benefit of taking a specific action 'a' compared to the other actions, at the given state 's' and following a policy π afterwards.

$$A(s_t, a_t) = Q^\pi(s_t, a_t) - V^\pi(s_t) \tag{23}$$

Among the great variety of tools and algorithms developed over the past decade by the RL community, actor critic plays definitely a privileged role in pursuit of performance. Thanks to its innovative approach at the intersection between policy-based and value-based paradigms it gathers the advantages of both methods. It features an agent and a critic playing different yet complementary roles. This family of algorithms contains the most efficient and cutting edged model developed so far (e.g; TRPO, A2C and PPO).

This algorithm is composed of three main parts: an actor, a critic and an environment. The policy is represented by the actor. As previously stated, this part is concerned with the action selection process given some environment observations. Instead, the critic aims at estimating the value function, it receives as input the observations and it outputs the estimated discounted future reward associated to that state. As the name suggests, this structure criticizes the action selected by the policy. The critic takes the form of a Temporal Difference (TD). This scalar signal is the sole output of the critic and drives learning in both actor and critic. After each action selection, the critic evaluates the new state to determine whether things have gone better or worse than expected. That evaluation is the TD error:

$$\delta_t = r_t + \gamma V^\pi(s_{t+1}) - V(s_t) \tag{24}$$

The TD error is the advantage function previously defined. It is used to assess the action (a_t) just selected in the state (s_t). Depending on this value, the tendency of selecting a certain action in a certain state can be reinforced (positive) or weakened (negative).

3.1.2. Bayesian Optimization

Many optimization problems of relevant engineering interest presents a series of intrinsic difficulties. The objective function structure could be non-convex, the evaluation of a solution could be computationally expensive and the outcomes might be affected by uncertainty or stochastic noise. Bayesian optimization (BO) has emerged as an ideal solution for these complex optimization problems. BO is comprised by a statistical surrogate function for modeling the objective function and by an acquisition function to decide where to take the next samples. As the name suggests,

BO is based on the Bayes Theorem:

$$P(H|D) = \frac{P(D|H)P(H)}{P(D)}. \quad (25)$$

where $P(A \mid B)$ is the conditional probability, the probability of one event (A) given the occurrence of another event (B). This theorem states that the conditional probability of H given D, the *posterior*; is given by the probability of H, *prior*, multiplied by the conditional probability of D given H, the *likelihood*. This theorem is employed in the framework of a Bayesian inference method. These methods consists in updating the probability for a statistical hypothesis as more evidence or information becomes available. In the case of BO the hypothesis is represented by the approximation of the objective function by the surrogate model. The information about the objective function embedded in the surrogate are used by an acquisition function to gauge where would best to place the next samples.

Algorithm 1 Pseudo-code for BO (credit:[15])

Place a Gaussian process prior on f
while $n \leq N$ **do**
  Update the posterior probability distribution using all available data
  Let x_n be a maximize of the acquisition function over x, where the acquisition function is computed using the current posterior distribution.
  Observe y_n=f(x_n)
  $n \leftarrow n + 1$
end while
Return a solution: either the point evaluated with the largest f(x), or the point with the largest posterior mean.

Table 1 reports the pseudo code followed by the BO algorithm. First of all, a surrogate function is placed as posterior on the objective function to optimize f. This statistical model is usually a Gaussian process. Each time a new set of samples is collected, the posterior is updated in accordance with the Bayes Theorem. In other terms, the surrogate approximation of the function is progressively refined. Based on the surrogate, an acquisition function extracts relevant information on where to sample next the objective function. There exist many different types of probabilistic acquisition functions that can be used, each with different trade-off for between exploitation and exploration. The three most commonly used are Probability of Improvement, Expected Improvement, and Lower Confidence Bound. Once the new data are sampled the posterior is updated again. This process goes on until either the maximum number iteration or the global optimum of the objective function is reached. Even though an in-house implementation of the algorithms has been carried out, a software called OPTUNA was used for our computations [16] due to better performance.

3.2. Test Case - Viscous burgers equation

The Burgers equation is undoubtedly the simplest of a family of canonical equations describing different aspects of nonlinear wave motion. Burgers proposed this equation as a toy model to illustrate the major traits of turbulence creation [17]. The model mimics the Navier-Stokes equations through its nonlinear advection and diffusion terms.

$$\frac{\partial u}{\partial t} + u\frac{\partial u}{\partial x} = \nu\frac{\partial^2 u}{\partial x^2} + f(x,t) + c(x,t) \quad (26)$$

Two forcing terms are introduced in the RHS, a disturbance term ($f(x,t)$) and a control term ($c(x,t)$). The disturbance is modeled as an harmonic in time and a Gaussian in space, $f(x,t) = A\sin(\omega t)\cdot\mathcal{N}(x - x_0; 0, 2)$. Whereas the control action is given by a Gaussian in space and a certain action in time defined by the controller in time, $c(x,t) = b(t)\cdot\mathcal{N}(x - x_1; 0, 2)$. A set of observations of the environment is provided at 12 different spatial locations and at 3 different time steps, for a total of 36 observations. Given that the perturbations propagate both rightwards and leftwards, the observations point were pinpointed around the control action Gaussian. The last ingredient to be defined for the control problem to be well posed is the reward function. This is defined as -L^2 norm of the displacement in a portion of the domain right after the control action. In the RL case the reward is calculated at each iteration and fed back to the agent. For the BO optimization this is given by the sum of the displacement along the simulation:

$$J(\theta) = \sum_{t=0}^{T} \|u(x_{min}, x_{max}\|_2^2. \quad (27)$$

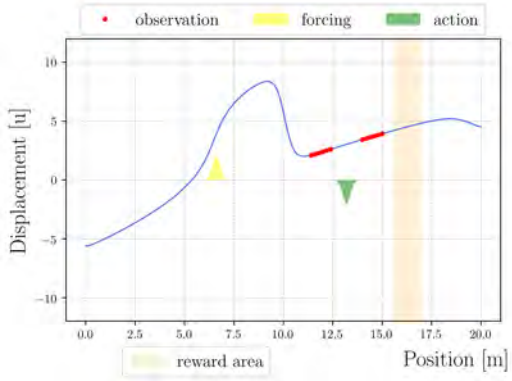

Figure 4: Optimal control environment for the 1D viscous Burgers equation showing the forcing action (yellow Gaussian) the control action(green Gaussian), the observation location (red dots) and the reward area (light orange shadowed area)

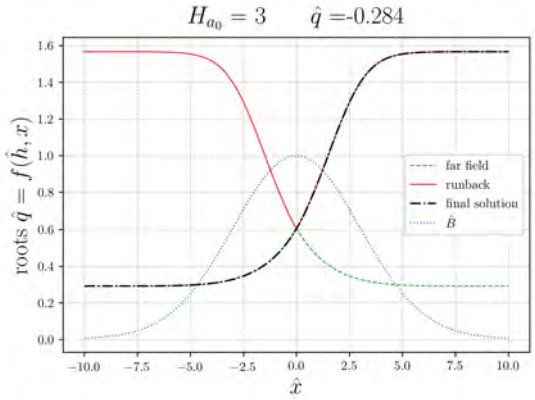

Figure 5: Solution of the steady wiping problem. Final liquid film(black curve), the two physical roots of Eq.8 (green and red curve) and the magnetic flux distribution (blue curve)

Fig.4 is representative of the test case, showing the *forcing*, yellow Gaussian, the *control action*, green Gaussian, the *observation locations*, red dots and the region where the reward is computed, light orange area.

4. Results

4.1. Magnetic actuator modeling - Steady Case

Taking Eq. 8 and assuming $\hat{q}$ as a parameter, this equation reduces to an algebraic equation in $\hat{h}$ at different liquid film location $\hat{x}$. At each location, this equation admits two physical roots. One describe the behavior of the liquid film in a region close to the molten bath called ran-back flow and the other the behavior in the far field in the other direction. To find a physical solution to the wiping problem, it is necessary that the equation presents a double root in the wiping region. This allows to have a smooth joining of the two branches of the solution. This is achieved solving repeatedly Eq. 8 by playing with the flow rate until a suitable solution is found. For simplicity, in this simulation the contribution of the jet wiping and the surface tension were not considered. The model has been validated by assessing its asymptotic behavior both analytically and numerically. For very small values of the Hartmann number ($Ha \rightarrow 0$) the model retrieves asymptotically the one without magnetic effects. For values of the Hartmann number (Ha) above a certain threshold a particular phenomenon has been observed. In the run-back part of the profile, a 'hump' appears in the proximity of the wiping region.

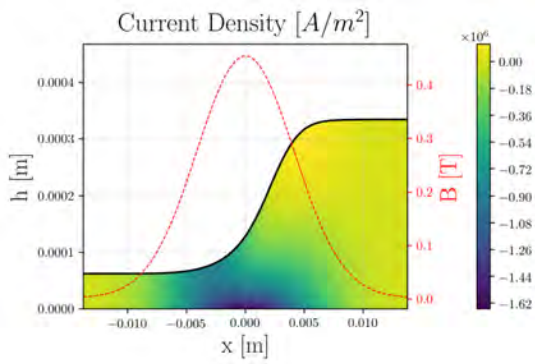

Figure 6: Liquid film solution of steady state model along with current density distribution inside the liquid film for low intensity magnetic flux

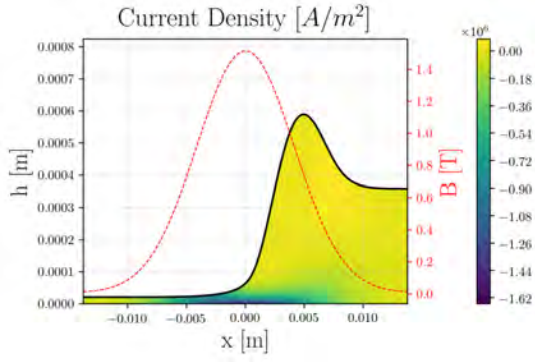

Figure 7: Liquid film solution of steady state model along with current density distribution inside the liquid film for high intensity magnetic flux

Fig. 6 and 7 show the liquid film for different intensities of the magnetic flux. It is interesting to remark

that the position of the hump peak does not coincides with the maximum of the magnetic flux but with an intermediate value. From a physical standpoint, this configuration might be caused by unbalance between the Lorentz force and viscous effects. Both terms are

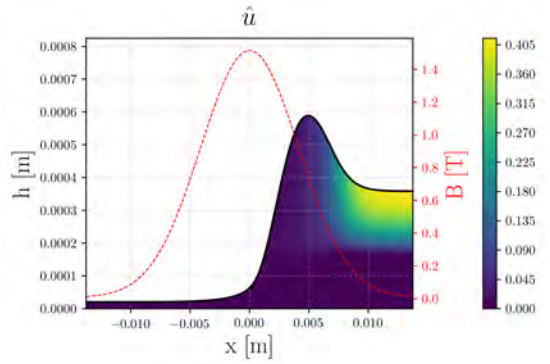

Figure 8: Stream-wise velocity distribution in the liquid film, $\hat{u}(x, y)$ steady state model for high intensity magnetic flux

functions of the velocity profile $\hat{u}(\hat{y})$. In the upper part of the run-back region, the streamwise velocity experiences an inversion of its profile with the streamwise velocity becoming negative. This affects the direction of the Lorentz force which does not push downwards anymore but upwards. To compensate this increment, the viscous term needs to extend the liquid film profile and increase the curvature of the velocity profile to find an equilibrium. Fig.8 shows the positive values of the streamwise velocity distribution inside the liquid film. Around the hump the velocity profile is mostly positive. Even if the highest values are not close to the wiping region, the high curvature of the profile with the decreasing effect of the magnetic flux allow to have a flat equilibrium.

Fig. 6 and 7 present even other sources of interest owing to the current density distribution inside the medium. The charges concentrate around the magnetic flux peak near the strip, where the magnitude of the velocity vector is higher. However, around this location, the current presents a not even distribution, resulting form the variation of the velocity profile combined with the magnetic flux. An important aspect that is worth investigating is the respect of the current continuity equation:

$$\nabla \cdot j = 0. \tag{28}$$

Given that in the model construction no assumptions have been done in that respect. This condition is important because it ensures the total amount of charge is conserved into a control volume. All these aspect related to the formation, the maximum position and the stability of the hump along with the current density distribution will be further investigated in a paper for the European coating symposium of this year called Modeling of magnetic wiping via integral models.

4.2. Magnetic actuator modeling - Unsteady Case

The unsteady simulation was run using the solution of the steady case as initial condition for both the flow rate ($\hat{q}$) and the thickness ($\hat{h}$). A time marching algorithm based on a finite volume formulation was used. Fig.9 shows the final steady solution of the unsteady simulation. As in the steady case a hump is present in the run-back region. Although, this appears for much smaller values of H_a. The fact that the flow rate does not attain a flat configuration is due to the very poor mesh refinement. This was necessary to guarantee the convergence of the simulation. Indeed, for very small values of the numerical viscosity, the peak tends to become a Dirac indefinitely growing. The artificial diffusion is necessary to limit this growth even if it is damaging for the quality of the results. This is an issue that have been under the spotlight for a while now. We are still digging to find the root case of this behavior and to validate our self-similarity assumption is valid in this case.

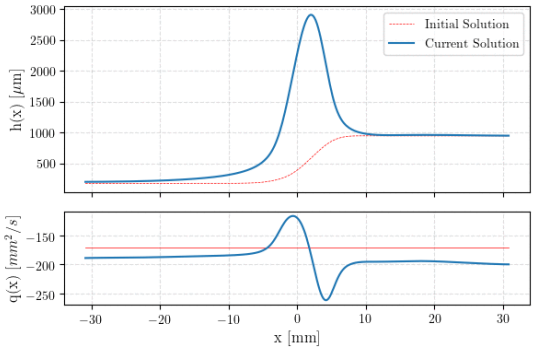

Figure 9: Numerical solution of the unsteady model in terms of $\hat{h}$ and $\hat{q}$ with solution of the steady model as initial condition. Hump formation in the proximity of the wiping region.

4.3. Control of viscous Burgers equation

Fig.10 shows the evolution of the viscous Burgers displacement controlled with RL and BO. Both methods were capable of finding optimal solutions to the control problem. However, the solution found by the RL have to be considered as a local optimum, since the undulation is not completely put to rest but it is damped to a point where the viscous effects break it down completely. The solution found via BO instead is a global optimum. The control action damps utterly

the perturbation. BO outperforms RL also in terms on learning time. For the RL to reach this solution it was necessary countless hours of training and an intense hyperparameter optimization campaign. BO instead took few hours to find the optimum.

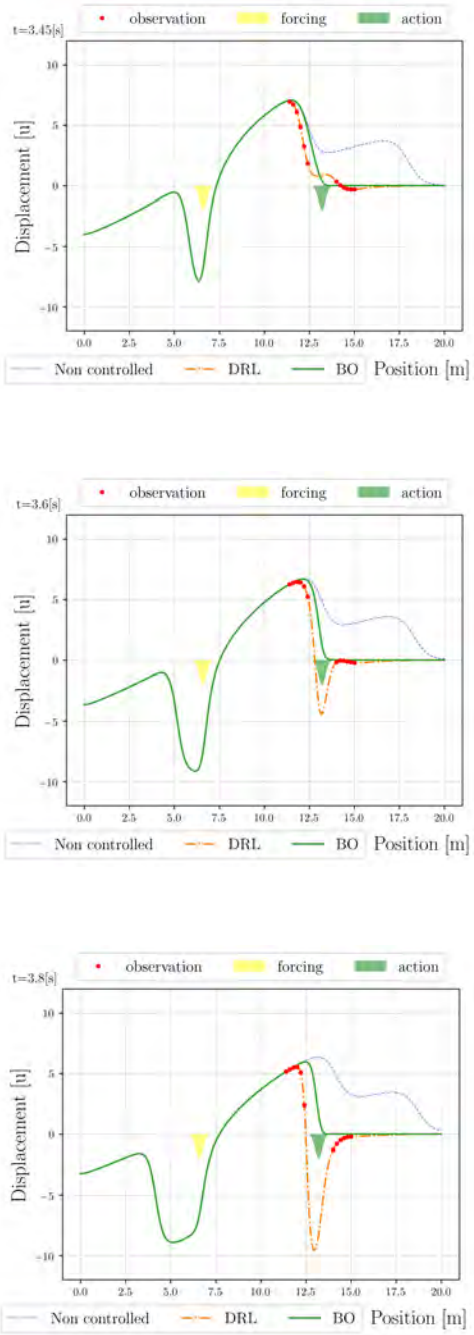

Figure 10: 1D controlled viscous Burgers equation displacement evolution at different time steps. Uncontrolled solution (blue curve), controlled with Deep RL (orange curve) and BO (green curve). Observation points (red dots).

Fig.11 show the forcing (orange) and the two control actions b_t of the BO (red) and the Deep RL (blue) as a function of the simulation time steps. It is worth drawing attention to the shape of the close-loop policy of the BO. This is constantly negative and as expected it presents a sort of periodic trend. It is not completely periodic because the control action introduced in the system propagates in the two directions, so affecting the subsequent observations. This is synonym of good robustness margins of the linear control solution. RL actions instead, although having some periodic patterns, are very variable. What stands out this analysis are the difficulties of the RL in finding a relatively simple solution. The concern raised about the degree of complexity demanded by the RL, which leads to useless computational efforts, has attracted our attention. In this respect, a collaboration with two prominent actors of this field has been established, Jean Rabault and Alexander Kuhnle. A paper titled "Comparative analysis of machine learning methods for flow control" is envisaged to be published by the end of this year. The intent of this work is to compare the capabilities of RL in solving some representative flow control test case to other machine learning-based techniques.

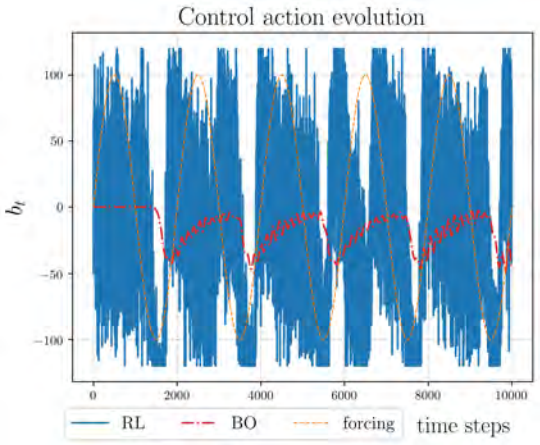

Figure 11: Forcing (orange dashed curve) and control action evolution, Deep RL(blue curve) and BO (red dash-dotted curve) as a function of simulation time steps

5. Conclusion

The control problem of an instability called undulation has been approached using a simplified model. The 1D viscous Burgers equation, although being one of the simplest of nonlinear wave motion family, it

inherits all the relevant features of our objective problem. Due to their inherent ease of application, their capability of dealing with uncertainty and noise, two machine learning techniques have been compared in a close-loop control framework. The limits of the RL in solving simple problems have been highlighted. The outstanding performance of BO in finding parametric control action were presented.

At the same time, a first modeling attempt of the electromagnetic actuator has been presented. This was modeled as a steady transverse magnetic flux generated by a permanent magnet. The steady and unsteady model presented in [8] has been extended to account for the Lorentz force induced by the magnetic flux in the moving medium. Despite the validation of the steady case, many issues remains open in the assessment of the unsteady formulation. Moreover, the steady model has open several prospects for a more insightful investigation of the phenomenon.

In the short term, we foresee to investigate more thoroughly the reasons behind the hump formation both in the steady and unsteady case. At the same time, we are planning to test the black box techniques directly to control the undulation in the liquid film environment. An extension of the model to a 3D configuration is expected to be accomplished in the next months too.

Acknowledgments

I would like to express my deepest appreciation to my supervisor Prof. Miguel Alfonso Mendez whose valuable assistance and support were crucial to obtain these achievements. I would like to extend my gratitude to Prof. Benoit Scheid and Jean Rabauld too, for several helpful discussions. I also wish to thank Lorenzo Schena for his assistance in solving tedious numerical problems.

References

[1] M. Gad-el Hak, Introduction to flow control, in: Flow Control, Springer, 1998, pp. 1–107.

[2] S. L. Brunton, B. R. Noack, P. Koumoutsakos, Machine learning for fluid mechanics, Annual Review of Fluid Mechanics 52 (2020) 477–508.

[3] T. Duriez, S. L. Brunton, B. R. Noack, Machine learning control-taming nonlinear dynamics and turbulence, Vol. 116, Springer, 2017.

[4] M. A. Bucci, O. Semeraro, A. Allauzen, G. Wisniewski, L. Cordier, L. Mathelin, Control of chaotic systems by deep reinforcement learning, Proceedings of the Royal Society A 475 (2231) (2019) 20190351.

[5] H. Tang, J. Rabault, A. Kuhnle, Y. Wang, T. Wang, Robust active flow control over a range of Reynolds numbers using an artificial neural network trained through deep reinforcement learning, Physics of Fluids 32 (5) (2020) 053605. arXiv:2004.12417, doi:10.1063/5.0006492.

[6] S. Verma, G. Novati, P. Koumoutsakos, Efficient collective swimming by harnessing vortices through deep reinforcement learning, Proceedings of the National Academy of Sciences 115 (23) (2018) 5849–5854.

[7] V. Belus, J. Rabault, J. Viquerat, Z. Che, E. Hachem, U. Reglade, Exploiting locality and physical invariants to design effective deep reinforcement learning control of the unstable falling liquid film, arXiv preprint arXiv:1910.07788.

[8] M. Mendez, A. Gosset, B. Scheid, M. Balabane, J.-M. Buchlin, Dynamics of the jet wiping process via integral models, Journal of Fluid Mechanics 911.

[9] J. . G. P. . Bregand, O ; Crahay, New wiping techniques to efficiently produce suitable coating layers at high speed in the hot dip galvanising process.

[10] C. Lloyd-Jones, H. Barker, V. Worner, Investigation into magnetic wiping techniques as alternative to gas wiping on hot dip galvanising lines, Ironmaking & steelmaking 25 (2) (1998) 117.

[11] F. Dughiero, E. Baake, M. Forzan, M. Dumont, R. Ernst, Y. Fautrelle, B. Grenier, J. Hardy, M. Anderhuber, New dc electromagnetic wiping system for hot-dip coating, COMPEL-The international journal for computation and mathematics in electrical and electronic engineering.

[12] D. Ninni, Development of a software package for the integral modelling of the jet wiping process, May 2019. URL https://library.vki.ac.be/articles/sr2019/sr201922.pdf

[13] D. E. Kirk, Optimal control theory: an introduction, Courier Corporation, 2004.

[14] R. S. Sutton, A. G. Barto, Reinforcement learning: An introduction, MIT press, 2018.

[15] P. I. Frazier, A tutorial on bayesian optimization, arXiv preprint arXiv:1807.02811.

[16] T. Akiba, S. Sano, T. Yanase, T. Ohta, M. Koyama, Optuna: A next-generation hyperparameter optimization framework, in: Proceedings of the 25th ACM SIGKDD international conference on knowledge discovery & data mining, 2019, pp. 2623–2631.

[17] J. M. Burgers, The nonlinear diffusion equation: asymptotic solutions and statistical problems, Springer Science & Business Media, 2013.

Thermal turbulence modelling of liquid metal flows via data analysis and machine learning

Matilde Fiore

Environmental and Applied Fluid Dynamics Department, von Karman Institute for Fluid Dynamics, Belgium, matilde.fiore@vki.ac.be

Supervisor: Lilla Koloszar

Research Engineer, Environmental and Applied Fluid Dynamics Department, von Karman Institute for Fluid Dynamics, Belgium, lilla.koloszar@vki.ac.be

Supervisor: Miguel Alfonso Mendez

Assistant Professor, Environmental and Applied Fluid Dynamics Department, von Karman Institute for Fluid Dynamics, Belgium, miguel.alfonso.mendez@vki.ac.be

Supervisor: Jeroen van Beeck

Dean of Faculty, Environmental and Applied Fluid Dynamics Department, von Karman Institute for Fluid Dynamics, Belgium, vanbeeck@vki.ac.be

University Supervisor: Yann Bartosiewicz

Professor, Mechanical Engineering Department, Universite catholique de Louvain UCL, Belgium, yann.bartosiewicz@uclouvain.be

Abstract

Thermal turbulence modelling of liquid metal flows is challenged by the low Prandtl number of these fluids, for which the assumption of similairity between thermal and momentum fields looses its theoretical justification. Current research is then committed to develop advanced thermal models based on high-fidelity data, which can be efficiently analysed and exploited with Machine Learning techniques.
This paper provides a data-driven approach for the modelling of the turbulent heat flux. The methodology is based on the use of an Artificial Neural Network constructed to satisfy realizability and invariance properties. The resulting algebraic anisotropic model provides a complete vectorial representation of the turbulent heat flux and the predictions fit the reference data in a wide range of Prandtl numbers. The comparison with the Manservisi model shows that the methodology is very promising.

Keywords: Prandtl number, heat flux, turbulence modelling, ANN

1. Introduction

Liquid metal heat transfer governs many phenomena and engineering applications, including high performance cooling systems in new generation nuclear reactors. For such systems, the thermal hydraulics conditions establishing during normal operation and transients must be carefully analyzed for economic and safety reasons.
Due to the opacity of liquid metals and consequent limitations of experimental approach, numerical investigations play a dominant role during design and testing. Numerical approaches are required to provide accurate descriptions of the thermal-hydraulics conditions with reasonable computational costs. These strict requirements often collide with the limited availability of RANS thermal models in commercial codes: the Reynolds analogy [1] is usually provided to model the turbulent heat flux. This simple model is based on a simple gradient hypothesis, and on the definition of

a constant turbulent Prandtl number[1]. The approach is widely accepted in presence of forced convection of common fluids, as water or air, having near unity or higher than unity Prandtl numbers. However, at the low Prandtl numbers characterizing liquid metals, the similarity hypothesis is less justified, since the thermal boundary layer becomes much thicker than the velocity one at low Prandtl numbers. Low Prandtl number fluids then require a more sophisticated modelling that should go beyond the assumptions of similarity and isotropy.

Researchers developed a variety of thermal turbulence models for low Prandtl numbers [2; 3; 4; 5]. Despite the huge modelling efforts, the models seem to lack of generality and only cover the range of Prandtl numbers employed for the validation. In addition, none of the models is able to give a complete vectorial representation of the turbulent heat flux: the components normal to the mean temperature gradient are often misrepresented.

Clearly, the increasing amount of DNS data for many Prandtl numbers and flow configurations represents a valuable source of information that should be efficiently used to construct more accurate models. The information should be extracted from data, summarized and translated in a mathematical form. Machine learning is able to draw knowledge from big data following structured methods and its use is emerging in the context of turbulence modelling.

Data-driven methods were firstly proposed for the modelling of the Reynolds stress tensor to improve common representations. Algebraic turbulence models for the Reynolds stress or the Reynolds stress discrepancy were developed using symbolic regression [6; 7], random forests [8] or artificial neural networks [9; 10; 11]. The capability of such methodologies to improve the representation of momentum turbulence was widely proved in these works. An open issue remains the definition of the applicability limits for the data-driven closures, which often show a certain overfitting of the training data [10] and can easily trigger instabilities of the governing equations in arbitrary flow conditions. Duraysamy [12] proposed a completely different approach that partially mitigate these problems, based on the use of Bayesian inference and artificial neural networks to recalibrate source terms of existing one or two equation models. Although this approach seems more robust, its perspectives are limited to the improvement of already existing mathematical formulations.

Some of the above techniques were recently applied also for the thermal turbulence modelling to provide a more accurate representation of the turbulent heat flux. Sotgiu et al. [13], developed an artificial neural network to derive the functional form of the coefficients of an algebraic scalar flux model at $Pr = 0.71$. The model was trained and validated for turbulent channel flows at four different Reynolds numbers. A different approach was proposed by Milani et al.[14] who used a regression forest to improve the modelling of the turbulent Prandtl number in case of film cooling flows. In both studies, the amount of training and validation data were too limited to expect that the resulting model formulation could be generalized to different kind of flows. In addition, restrictive hypothesis are introduced into the mathematical structure of the model and its parametric space. These a priori assumptions considerably narrow the potentialities of machine learning in this field.

This work employs deep learning to construct a general thermal model for the turbulent heat flux to be valid in a wide range of Prandtl numbers and for different flow configurations. The regression problem was properly constrained with mathematical/physical principles to promote the realizability and the robustness of the resulting model. The preliminary validation test cases presented in section 4 show that the methodology is promising. Moreover, the data data-driven approach is able to provide interesting information about the significance of the given turbulence parameters. This would give fundamental insight about the generation of turbulent heat flux, especially at low Prandtl numbers, and aid future data-driven or analytical modelling deveolopments.

2. The Machine learning approach

The data-driven approach is based on the development of a general mathematical structure that is presented in section 2.1. The closure coefficients a_i of the algebraic expression are then modelled with an artificial neural network, whose structure is defined in section 2.2. The regression problem consists then in finding the network parameters that lead the model fitting the available DNS data presented in section 3. The optimization of the weights and biases $\mathbf{W}$ of the network is guided by an appropriate objective function that is given in section 2.3.

[1] Recommended values for the turbulent Prandtl numbers are 0.85 for near unity Prandtl numbers and 2.0 for low Prandtl number fluids.

2.1. Mathematical formulation

The algebraic model for the turbulent heat flux $\overline{\mathbf{u}\theta}$ was derived starting from a general functional relationship involving tensors, vectors and scalars of interest:

$$\overline{\mathbf{u}\theta} = f\left(\mathbf{b}, \mathbf{S}, \mathbf{\Omega}, \nabla T, \mathbf{g}, k, \epsilon, k_\theta, \epsilon_\theta, \alpha, \nu\right) \tag{1}$$

where k, ϵ, k_θ, ϵ_θ and $\mathbf{g}$ denote the turbulent kinetic energy, the dissipation rate, the thermal variance, the thermal dissipation rate and the gravity vector, respectively. α and ν are the molecular diffusivity and viscosity, while tensors $\mathbf{b}$, $\mathbf{S}$ and $\mathbf{\Omega}$ are defined as:

$$b_{ij} = \frac{\overline{u_i u_j}}{k} - \frac{2}{3}\delta_{ij} \tag{2}$$

$$S_{ij} = \frac{1}{2}\left(\frac{\partial U_i}{\partial x_j} + \frac{\partial U_j}{\partial x_i}\right) \tag{3}$$

$$\Omega_{ij} = \frac{1}{2}\left(\frac{\partial U_i}{\partial x_j} - \frac{\partial U_j}{\partial x_i}\right) \tag{4}$$

The ansatz (1) implicitly assumes locality, as the turbulent flux is expressed as a function of local quantities. From a numerical point of view, this assumption is convenient, as it avoids the expense of a second order closure model for the heat flux. On the other hand, if transport equations are solved for k_θ and ϵ_θ, historical and non-local effects can be still represented, though at an isotropic level. Equilibrium turbulence is also assumed, since the gradients of the turbulent statistics (k, k_θ and b_{ij}) are not involved in the parametrization. This requires that thermal turbulence production, destruction and redistribution mechanisms are more significant than transport terms, as it is assumed in many other works [15; 16; 17; 18] on this topic. In addition, if the analysis is limited to forced convection flows, the dependence on the gravity vector can be eliminated.
Since the model is supposed to be algebraic and explicit, it could be also written as a product of a dispersion tensor $\mathbf{D}$ with the temperature gradient:

$$\overline{\mathbf{u}\theta} = -\mathbf{D}\nabla T \tag{5}$$

where

$$\mathbf{D} = f\left(\mathbf{b}, \mathbf{S}, \mathbf{\Omega}, \nabla T, k, \epsilon, k_\theta, \epsilon_\theta, \alpha, \nu\right) \tag{6}$$

For the sake of simplicity, we can assume that the anisotropy of the dispersion tensor $\mathbf{D}$ depends on the flow, not on the temperature distribution. Then, the functional relationship simplifies to:

$$\mathbf{D} = f\left(\mathbf{b}, \mathbf{S}, \mathbf{\Omega}, \|\nabla T\|, k, \epsilon, k_\theta, \epsilon_\theta, \alpha, \nu\right) \tag{7}$$

The mathematical modelling is aided by the introduction of physical and mathematical constraints. In particular, we seek to construct a thermal turbulence model which satisfies the following properties:

- Galileian and geometrical invariance
- Invariance under rotation
- Consistency with the second law of thermodynamics

In particular, the Galileian and geometrical invariance are naturally ensured by the parametric set defined by eq. (1), which does not contain any information about reference lengths and reference velocities.
The second property can be analytically expressed as

$$\mathbf{Q}\mathbf{D}\mathbf{Q}^T = f\Big(\mathbf{Q}\mathbf{b}\mathbf{Q}^T, \mathbf{Q}\mathbf{S}\mathbf{Q}^T, \mathbf{Q}\mathbf{\Omega}\mathbf{Q}^T, \|\nabla T\|, k, \epsilon, k_\theta, \epsilon_\theta, \alpha, \nu\Big) \tag{8}$$

where $\mathbf{Q}$ is any rotation matrix. Hence, the compliance with the invariance property requires to constraint the functional form introduced by eq. (7).
Let us consider a general tensor $\mathbf{T}^i$ that can be formed through products of $\mathbf{b}$, $\mathbf{S}$ and $\mathbf{\Omega}$. A linear mapping of the $\mathbf{T}^i$ would satisfy the rotational invariance:

$$\mathbf{Q}\mathbf{K}\mathbf{Q}^T = \sum_{i=1}^{n} a_i \mathbf{Q}\mathbf{T}^i\mathbf{Q}^T \tag{9}$$

if the coefficients $a_1, ..., a_n$ are isotropic functions, i.e. functions of the invariants of the tensorial set described by eq.(7). Clearly, infinitely many tensor products can be formed from tensors $\mathbf{b}$, $\mathbf{S}$ and $\mathbf{\Omega}$, thus leading to an infinite series expansion and, accordingly, an infinite number of tensorial invariants. However, the tensor representation theory shows [19] that, for a finite tensorial set, exists a finite integrity basis of independent invariants under the proper orthogonal group. Given the minimum tensor basis of a certain degree, higher order tensor products can be expressed as polynomials of the basis tensors, whose coefficients depending on the invariant basis. This property bounds the parameter space and make the regression problem more tractable.
The complete derivation of the tensor basis and the corresponding invariants under the assumption of 2-D flow is out of the scope of this brief introduction

and will be given in an extended version of this paper which is currently under preparation. In particular, it can be shown that the minimal basis of tensors consists of the following set:

$$\mathbf{I}, \mathbf{b}, \mathbf{S}, \mathbf{\Omega}, \mathbf{bS}, \mathbf{S\Omega}, \mathbf{b\Omega}, \mathbf{\Omega SW}$$

and the corresponding minimal basis of invariants is given by

$$\{\mathbf{b_2}\}, \{\mathbf{b}^2\}, \{\mathbf{S}^2\}, \{\mathbf{\Omega}^2\}, \{\mathbf{bS}\}, \{\mathbf{bS\Omega}\}$$

where the notation $\{\dot{}\}$ indicates the tensor trace and $\mathbf{b}_2$ denotes the projection of $\mathbf{b}$ on the plane of the flow:

$$\mathbf{b}_2 = \begin{pmatrix} b_{11} & b_{12} & 0 \\ b_{12} & b_{22} & 0 \\ 0 & 0 & 0 \end{pmatrix} \tag{10}$$

The coefficients a_i will be then functions of the following isotropic quantities:

$$a_i = f_i\Big(\{\mathbf{b_2}\}, \{\mathbf{b}^2\}, \{\mathbf{S}^2\}, \{\mathbf{\Omega}^2\}, \{\mathbf{bS}\}, \{\mathbf{bS\Omega}\}, \\ \|\nabla T\|, k, \epsilon, k_\theta, \epsilon_\theta, \alpha, \nu\Big) \tag{11}$$

The number of parameters involved in eq.(11) was further reduced by appylying the Buckingham Theorem to the group of physical quantities. The approach led to the definition of 9 independent dimensionless groups, which are indicated in the first column of Table 1:

$$a_i = f_i(\pi_i, Re_t, Pr) \tag{12}$$

The consistency with the second law of thermodynamics had to be guaranteed by imposing that the real part of the eigenvalues of $\mathbf{D}$ are positive. This property is particularly important to prevent counter gradient heat fluxes in forced convection regimes, and consequent problems of realizability and numerical instability. A sufficient condition to satisfy this requirement is the positive definitess of tensor $\mathbf{D}$. To this end, tensor $\mathbf{D}$ is enforced to admit a Cholesky decomposition:

$$\mathbf{D} = \mathbf{K}^T\mathbf{K} \tag{13}$$

where $\mathbf{K}$ is the result of the series expansion:

$$\mathbf{K} = \sum_{i=1}^{n} a_i \mathbf{T}^i \tag{14}$$

According to eq.(13) and (14), the tensors constituting the basis were multiplied by powers of k and ϵ to retrieve a dimensionally consistent turbulent heat flux. The resulting definition of the tensors $\mathbf{T}^i$ is given in the second column of Table 1.

2.2. Structure of the artificial neural network and training

The coefficients a_i of the expansion series introduced by eq.(14) are modelled by an artificial neural network developed in Pytorch. The structure of the ANN is depicted in Figure 1: the network consists of two input layers for the invariant basis and the molecular Prandtl number, respectively. Six hidden layers of 50 neurons are set for the first branch of the network, which has rectified linear unit activation functions. It can be noted that the invariants π_i undergo a logarithmic transformation in the input layer, and an exponential activation function is set in the last hidden layer. This choice ensures the reconstruction of polynomials of π_i, which is judged particularly important since the Buckingham Theorem does not lead to an unique choice for the basis of independent invariants. Indeed, an arbitrary number invariant basis can be formed by constructing monomials with the invariants indicated in Table 1. The second branch of the network consists of two hidden layers of 20 units each with rectified linear unit and hyperbolic tangent activation functions. The two branches of the network merge through a multiplication of the outputs performed in the final layer. Then, the turbulent heat flux is calculated following eq. (14) and (13).
The network is trained using the Adaptive Moment Estimation (Adam) optimizer, which is a classic mini-batch gradient descend with momentum estimates and a constant learning rate, that here is set to 0.001. In this work, the batches are constructed by sampling partitions of the flows belonging to different test cases. Sampling of partitions is preferred over sampling of points to allow the numerical spatial differentiation of the output. Indeed, numerical differentiation is required for the calculation of the proposed loss function, as explained in the next section.

2.3. Objective function and regularization

The objective function is defined accordingly with the physical meaning of the turbulent heat flux and the form where it appears in the averaged energy equation:

$$\frac{\partial T}{\partial t} + U_j\frac{\partial T}{\partial x_j} = \alpha\frac{\partial^2 T}{\partial x_j \partial x_j} - \frac{\partial \overline{u_j\theta}}{\partial x_j} \tag{15}$$

Eq.(15) shows the divergence of the turbulent heat flux on the right hand side. This suggests to fit the derivatives of the turbulent heat flux, rather than the turbulent heat flux itself, to obtain an accurate thermal field. On the other hand, the smoothness of the predicted

Table 1: Basis tensors and invariants.

Invariant Basis	Tensor Basis
$\pi_1 = \frac{k^2}{\epsilon^2}\{\mathbf{S}^2\}$, $\pi_2 = \frac{k^2}{\epsilon^2}\{\mathbf{\Omega}^2\}$, $\pi_3 = \frac{1}{\{\mathbf{b}\}}$, $\pi_4 = \frac{k}{\epsilon}\{\mathbf{bS}\}$, $\pi_5 = \{\mathbf{b}_2\}$, $\pi_6 = \{\mathbf{bS\Omega}\}$, $\pi_7 = \frac{\|\nabla T\|}{\sqrt{k_\theta}}\frac{k^{3/2}}{\epsilon}$, $\pi_8 = \frac{k_\theta \epsilon}{k \epsilon_\theta}$, $Re_t = \frac{k^2}{\epsilon\nu}$	$\mathbf{T_1} = \frac{k}{\epsilon^{1/2}}\nabla T$, $\mathbf{T_2} = \frac{k}{\epsilon^{1/2}}\mathbf{b}\nabla T$, $\mathbf{T_3} = \frac{k^2}{\epsilon^{3/2}}\mathbf{S}\nabla T$, $\mathbf{T_4} = \frac{k^2}{\epsilon^{3/2}}\mathbf{\Omega}\nabla T$, $\mathbf{T_5} = \frac{k^2}{\epsilon^{3/2}}\mathbf{bS}\nabla T$, $\mathbf{T_6} = \frac{k^2}{\epsilon^{3/2}}\mathbf{b\Omega}\nabla T$, $\mathbf{T_7} = \frac{k^3}{\epsilon^{5/2}}\mathbf{S\Omega}\nabla T$, $\mathbf{T_8} = \frac{k^3}{\epsilon^{5/2}}\mathbf{bS\Omega}\nabla T$

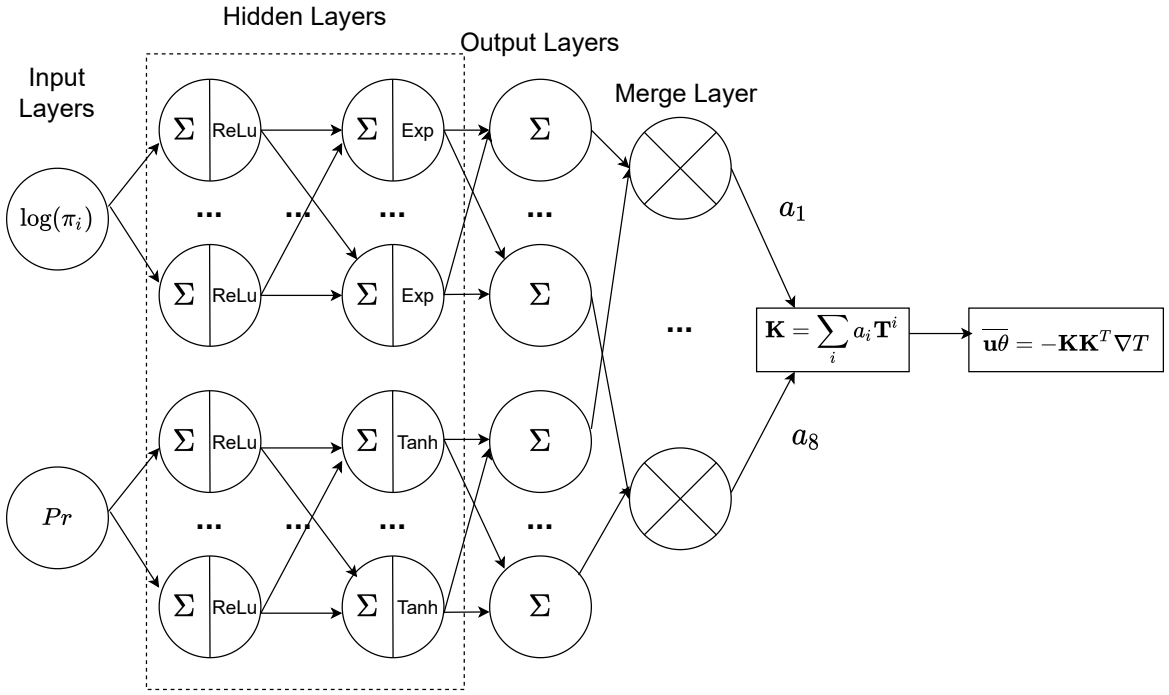

Figure 1: Structure of the artificial neural network used to predict the turbulent heat flux as a function of the molecular Prandtl number and the basis of invariants indicated in Table 1.

fields is an important requirement to guarantee their numerical integration.
Based on such considerations, the following loss function was employed for the training:

$$\mathcal{L}(\mathbf{W}) = \frac{1}{N}\left(\sum_{i=1}^{N}\sum_{j=1}^{3}\left(\hat{q}_j^i - q_j^i\right)^2\right) + \lambda\left(\sum_{i=1}^{N}\sum_{j,k=1}^{3}\left|\frac{\partial \hat{q}_j^i}{\partial x_k} - \frac{\partial q_j^i}{\partial x_k}\right|\Delta x_k\right) \tag{16}$$

where $\hat{q}_j$ indicates the prediction of the ANN and q_j the effective value provided by DNS data (both values are normalized with respect to the maximum DNS value achieved in each flow configuration). The partial derivatives appearing on the right hand side are numerically approximated with finite differences. N indicates the number of points contained in each mini-batch, while λ is an hyperparameter that was empirically set[2] to 10.0.
As shown in section 4, this particular choice of the loss function has positive effects in terms smoothness of the predictions and generalization capabilities of the resulting model. Indeed, the second term on the right hand side od eq. 16 introduces a penalty that tends to preserve the degree of smoothness of the reference input data. Hence, this term acts as a regularizer during the training: the increase of the weight values is mitigated to avoid the generation of unphysical wiggles that would corrupt the level of smoothness of the training data. This promotes the development of a simpler functional form.

[2]Actually, the choice of λ should be related to the smoothness requirements for the heat flux, that could be locally different depending on the resolution adopted for the CFD simulations.

2.4. Uncertainty quantification

The Gaussian Stochastic Weight Averaging (SWAG) algorithm [20] was implemented and used during the training to quantify the epistemic uncertainty of the data driven model. The method relies on the assumption that the model uncertainty is highly correlated to the trajectory followed by the optimizer in the weight space. Hence, an approximate gaussian posterior distribution for the network weights W is constructed during the training by collecting first and second moments of the updated parameters:

$$\mathbf{W} \sim \mathcal{N}(\mu, \Sigma) \tag{17}$$

where the covariance matrix Σ is herein assumed to be diagonal to simplify the implementation of the SWAG. After the training, model averaging is performed by sampling the parameters from the resulting gaussian distribution:

$$\mathbf{W} = \mu + \frac{1}{\sqrt{2}}\Sigma^{1/2} z_1 \text{ where } z_1 \sim \mathcal{N}(0, I_d) \tag{18}$$

The averaging provides the mean prediction and the standard deviation of the network output, which can be used to construct confidence intervals for the predicted components of the turbulent heat flux. This information could give important indications about the effectiveness of the learning process and its convergence, as well as the nature of the prediction error observed during testing. It could also highlight possible under-fitting and/or over-fitting problems, thus suggesting improvements for the model structure and the training methodology. Further details about the SWAG approach for uncertainty quantification can be found in [20].

3. Description of the database

The database used to train the artificial neural network consists of DNS datasets related to different forced convection flows at various Re and Pr numbers. The details of the datasets are summarized in Table 2. In particular, the databases of Kawamura et al. [21] and Tiselji et al. [22] consist of DNS simulations of non-isothermal turbulent channel flow at Reynolds number ranging from Re_τ = 180 to 640 and Prandtl number from 0.01 to 0.71. Li et al. [23] provided the DNS data of a turbulent boundary layer flow simulation at Re_θ=800, and Prandtl numbers of 0.71 and 0.2. The last database indicated in Table 2 refers to a backward facing step flow [24] at Re_b = 3200 and simulated at Prandtl numbers of 0.1 and 0.005.

4. Results

4.1. Results of the training

The network was trained with mini-batches taken from the whole database (Table 2) at each training iteration. The validation dataset was properly selected to avoid extrapolation during the test phase, and it consisted of 20% of the available data.

Figure 2 shows the decay of the loss function during the training over the training and validation sets. The validation loss does not degrade during the training, showing that the network does not tend to over-fit the training data. This seems a consequence of the choice of the loss function: the penalty introduced in eq. (16) operates a strong regularization that increases the generality of the developed functional form.

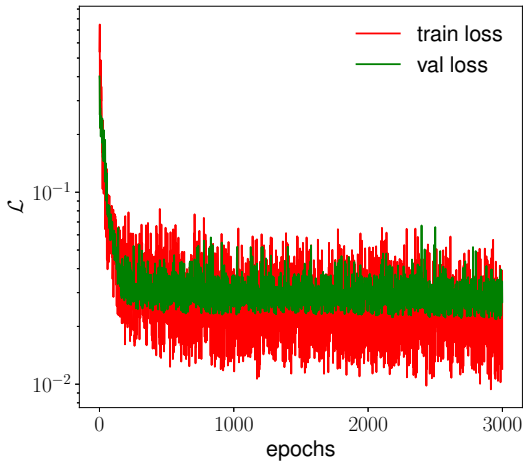

Figure 2: Evolution of the loss function during the training.

Figure 3 and 4 show the results of the training obtained for different flow configurations. It can be seen that the same level of accuracy is reached for data in the training range and in the validation range. The data-driven model seems to generalize quite well and efficiently interpolate for various Reynolds and Prandtl numbers. In addition, both the components of the turbulent heat flux are reconstructed with a satisfactory accuracy. Minor discrepancies can be seen for the stream-wise component of the heat flux (figures 3b and 3d) close to the symmetry line of the channel, where the DNS data tend to an asymptotic, non-zero value. However, this behaviour cannot be reconstructed by an algebraic model, as ∇T is zero on the centerline. Small inaccuracies can be also appreciated in figure 4b, where the neural network predic-

Table 2: Available DNS databases for forced convection at different Re and Pr numbers

Author and Ref.	Flow Configuration	Reynolds number*	Prandtl number
Kawamura et al.[21]	Channel flow	$Re_\tau = u_\tau\delta/\nu$=180-640	0.025-0.71
Li et al. [23]	Turbulent Boundary Layer Flow	$Re_\theta = u_\tau\theta/\nu$=830	0.2, 0.71
Tiselj et al. [22]	Channel flow	Re_τ=180-590	0.01
Oder et al. [24]	Backward-Facing Step Flow	$Re_b = \dot{m}h/A\nu$=3200	0.1,0.005

* The complete definition of the Reynolds number for each flow configuration can be found in the related references.

tions tend to overestimate the extension of the thermal separation zone.
Figure 3 highlights also the epistemic uncertainty of the model resulting from the SWAG algorithm. The estimated uncertainty seems very limited[3] and lower than 5.5% for both training and test data, which confirms the good convergence of the training process and the generalization properties of the model.

4.2. Simulation of non-isothermal turbulent channel flows

The a posteriori validation of the data driven model was carried out in OpenFoam 6.0. The structure of the artificial neural network and its trained parameters were implemented into an existing library for thermal turbulence models. The implementation method is based on the conversion of the model from Pytorch to Tensorflow, passing through an Onnx version, and the coupling of the Tensorflow C API library with the OpenFoam library. A similar procedure is described in detail in the recent work of Maulik et al. [25].
According to Table 1, the neural network takes as input the anisotropic part of the Reynolds stress tensor **b**, which is also included in the basis of independent tensor products. Hence, the developed model is subjected to the use of an advanced, wall-resolved representation of the Reynolds stresses. The Elliptic Blending Reynolds stress model [26] was implemented in OpenFoam for such purpose. The model is of second order, and it solves an elliptic differential equation for the blending parameter α which accounts for the blockage effects due to the distribution of the walls. Figure 5 compares the predicted Reynolds stress components with the DNS data for a turbulent channel flow at Re_τ = 395.
Also, the ANN takes as input the thermal variance

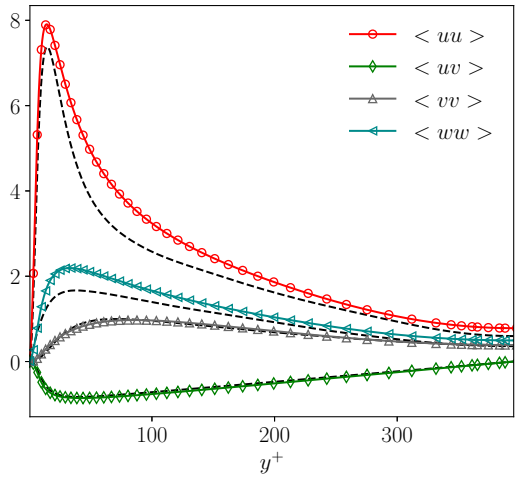

Figure 5: Distribution of the Reynolds stresses obtained by applying the Elliptic Blending model [26] in case of a turbulent channel flow at Re_τ = 395.

[3] A more complete estimation of the epistemic uncertainty will be provided by implementing the calculation of the non-diagonal part of the covariance matrix Σ.

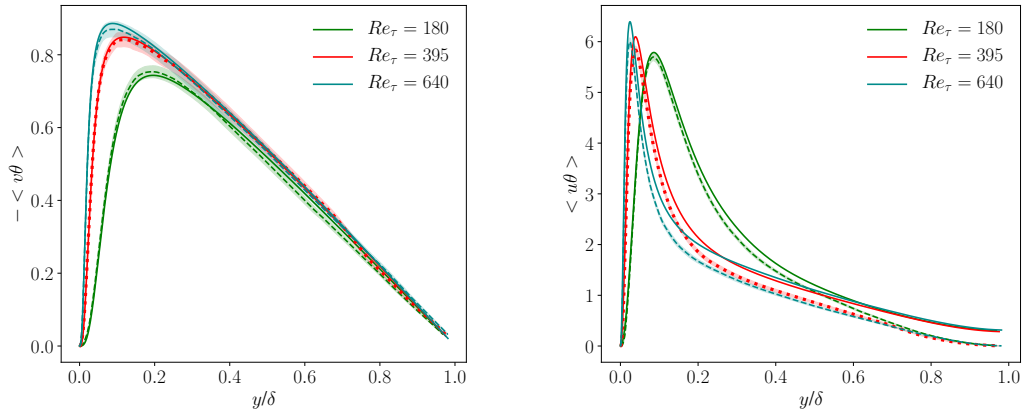

(a) Wall-normal, $Pr = 0.71$

(b) Stream-wise, $Pr = 0.71$

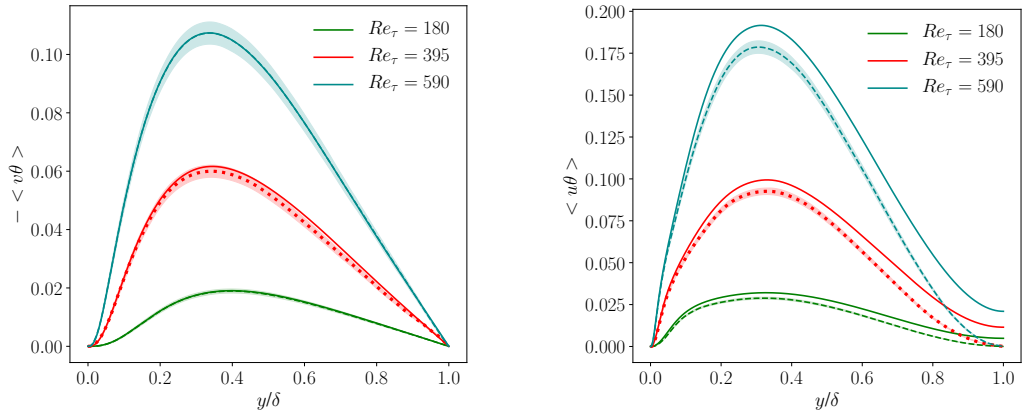

(c) Wall-normal, $Pr = 0.01$

(d) Stream-wise, $Pr = 0.01$

Figure 3: Stream-wise and wall-normal components of the turbulent heat flux predicted by the ANN after the training. Predictions in the training range and validation range are depicted with dashed and dotted lines, respectively. DNS data [21] are represented with solid lines.

k_θ (see Table 1) that has to be properly modelled in a full RANS simulation. Hence, k_θ is herein computed by solving the differential equations for k_θ and ϵ_θ proposed by Manservisi et al.[2] for liquid metal flow simulations:

$$\frac{\partial k_\theta}{\partial t} + U_i \frac{\partial k_\theta}{\partial x_i} = \frac{\partial}{\partial x_i}\left[\left(\alpha + \frac{\alpha_t}{\sigma_{k\theta}}\right)\frac{\partial k_\theta}{\partial x_i}\right] + P_\theta - \epsilon_\theta \quad (19)$$

$$\frac{\partial \epsilon_\theta}{\partial t} + U_i \frac{\partial \epsilon_\theta}{\partial x_i} = \frac{\partial}{\partial x_i}\left[\left(\alpha + \frac{\alpha_t}{\sigma_{\epsilon\theta}}\right)\frac{\partial \epsilon_\theta}{\partial x_i}\right] + \frac{\epsilon_\theta}{k_\theta}\left(C_{p1}P_\theta - C_{p2}\epsilon_\theta\right) + \frac{\epsilon_\theta}{k}\left(C_{p2}P_k - C_{d2}\epsilon\right) \quad (20)$$

The exhaustive definition of the parameters appearing in eq. (19) and (20) can be found in the work of Manservisi and Meneghini [2].

The test case selected for the a posteriori validation is a non-isothermal turbulent channel flow at $Re_\tau = 395$ and $Pr = 0.025$ and 0.01. The reference data for these flow conditions were not used during the training to ensure a meaningful validation. At the walls, a constant heat flux boundary condition is imposed for the temperature, k_θ is set to zero and ϵ_θ is calculated as

$$\epsilon_\theta = \alpha \frac{2k_\theta}{\delta^2} \quad (21)$$

where δ is the distance from the closest wall.
The predictions obtained with the data-driven model have been directly compared with the results of the Manservisi model which relies on a simple gradient

diffusion hypothesis:

$$\overline{\mathbf{u}\theta} = -\alpha_t \frac{\partial T}{\partial x_i} \tag{22}$$

The results of the simulations are shown in figure 6. For both the Prandtl numbers, the data-driven model gives very accurate predictions, despite the imprecision introduced by the other turbulence models involved in the simulations, i.e. the Elliptic Blending model for the momentum field and equations (19) and (20) for the calculation of k_θ. Compared to the Manservisi model, the developed model shows a better agreement with DNS data in terms of all the thermal turbulence statistics. In addition, Figure 6c clearly shows that one of the advantages of the data-driven model is its ability to approximate the streamwise component of the turbulent heat flux, thanks to its anisotropic formulation.

4.3. Feature Importance

The data-driven model represents a source of information that should be properly interpreted to gain insight about the problem and propose new modelling developments. One of the most important information to extract is the feature importance, i.e. the sensitivity of the network outputs to the change of the input parameters. These quantities can be calculated with the method of the Integrated Gradients [27]. The approach foresees the calculation of the integral of the output gradients with respect to the inputs along a path from a baseline to a target solution:

$$I_{ij} = (\pi_i - \pi_i') \int_{\alpha=0}^{1} \frac{\partial a_j(\mathbf{\Pi}' + \alpha((\mathbf{\Pi} - \mathbf{\Pi}'))}{\partial \pi_i} d\alpha \tag{23}$$

where $\mathbf{\Pi}$ and $\mathbf{\Pi}'$ denote the target and baseline vectors of the input features, respectively. Herein, the integrals were computed over the whole input space to obtain mean sensitivities.

Table 3 presents the relative feature importance of the ANN inputs for the expansion coefficients a_1,..., a_8. Based on the values reported, the parameters π_7, π_4, Pr and Re_t seem the most significant. Indeed, the influence on π_7 and Pr is not surprisingly, as they are the only thermal-based features involved in the parametrization. Re_t represents instead the dimensionless turbulent viscosity, which is the key parameter of existing thermal models based on similarity assumptions. On the other hand, other parameters as π_3 and π_6 seem to have a limited influence on the values predicted by the model and could be possibly eliminated from the parameter space to generate a simpler model with minimal loss of accuracy.

This is a simple example of the considerations that could be made by interpreting the machine learning model. Further analysis could be carried out along these lines if critical choices are made for the baseline and the target solutions. This approach would allow to understand, for example, which terms of the expansion drive the change of the heat flux when passing to near unity to low Prandtl numbers, or govern its evolution in case of spatially evolving flows.

5. Conclusion

A data driven model for the turbulent heat flux was developed based on the available DNS databases for forced convection flows at near unity and low Prandtl numbers. The approach is based on the construction of a deep neural network consistent with a highly constrained mathematical structure ensuring invariance properties and realizability. A specific objective function was chosen for the training to promote the smoothness of the predictions and their integrability. An uncertainty quantification method (SWAG) was implemented and used to evaluate the likelihood of the predictions. Preliminary results showed that the methodology is promising, as it is able to give a general anisotropic formulation which satisfactorily adapt to the different Prandtl numbers and flow configurations.

Several future developments can be identified based on this work. First of all, a full parametric study based on the network structure and its hyperparameters should be carried out to optimize the training process and provide a slim network, if possible. The training and validation databases will be then enriched with other flow configurations to further increase the generality of the approach. A wider testing phase will bring out the effective performance and limitations of the current mathematical structure and clarify its advantages compared to other existing models for the turbulent heat flux.

Beside dealing with issues of practical applicability, the project will continue to focus on the understanding of thermal turbulence with special attention to low Prandtl number fluids. As already shown in section 4.3, the predicted dispersion tensor and its sensitivity to the input parameters represent a valuable source of information that could be exploited to get insight about the properties of turbulent heat tranfer and the mechanisms of generation/destructions of thermal turbulence acting at different Prandtl numbers and flow conditions. From a modelling point of view, this is the

Table 3: Relative importance of the input features with respect to the model coefficients.

Features	a_1	a_2	a_3	a_4	a_5	a_6	a_7	a_8
π_1	-0.600	-0.719	-3.074	10.849	-2.670	4.568	9.099	-1.031
π_2	0.478	0.733	1.454	-8.213	2.017	-3.951	-7.33	0.953
π_3	-0.731	-0.745	-1.489	2.502	-0.564	0.839	3.093	-0.667
π_4	**-0.979**	**-1.186**	**-9.705**	**40.209**	**-11.911**	**20.577**	**36.377**	**-1.967**
π_5	-0.610	-0.955	-4.658	20.652	-5.438	9.518	16.860	-1.271
π_6	-0.047	-0.054	-1.305	7.098	-2.315	4.190	7.206	0.266
π_7	**-2.790**	**-2.829**	**-21.358**	**87.543**	**-25.594**	**43.679**	**75.706**	**-3.79**
Re_t	**0.944**	**0.876**	**17.416**	**-21.095**	**11.264**	**-10.193**	**-27.420**	**1.067**
Pr	**0.970**	**1.329**	**3.293**	**-33.503**	**-1.891**	**1.019**	**-26.350**	**-11.01**

most interesting machine learning perspective, which views the knowledge continuously passing from the modeller to the machine and vice versa.

Acknowledgments

M. Fiore is supported by a F.R.S.-FNRS FRIA grant and gratefully acknowledges Prof. Iztok Tiselj and Dr. Jure Oder for providing their datasets, as well as Dr. Clyde Fare from IBM for his valuable suggestions during the course of this work.

References

[1] C. J. Geankoplis, Transport processes and separation process principles:(includes unit operations), Prentice Hall Professional Technical Reference, 2003.

[2] S. Manservisi, F. Menghini, A cfd four parameter heat transfer turbulence model for engineering applications in heavy liquid metals, International Journal of Heat and Mass Transfer 69 (2014) 312–326.

[3] A. Shams, A. De Santis, F. Roelofs, An overview of the ahfm-nrg formulations for the accurate prediction of turbulent flow and heat transfer in low-prandtl number flows, Nuclear Engineering and Design 355 (2019) 110342.

[4] K. Suga, K. Abe, Nonlinear eddy viscosity modelling for turbulence and heat transfer near wall and shear-free boundaries, International journal of heat and fluid flow 21 (1) (2000) 37–48.

[5] L. Carteciano, D. Weinberg, U. Müller, Development and analysis of a turbulence model for buoyant flows, in: 4th World Conference of Exp. Heat Transfer, Fluid Mechanics and Thermodynamics, Bruxelles, Vol. 3, 1997, pp. 1339–1347.

[6] J. Weatheritt, R. Sandberg, A novel evolutionary algorithm applied to algebraic modifications of the rans stress–strain relationship, Journal of Computational Physics 325 (2016) 22–37.

[7] M. Schmelzer, R. P. Dwight, P. Cinnella, Discovery of algebraic reynolds-stress models using sparse symbolic regression, Flow, Turbulence and Combustion 104 (2) (2020) 579–603.

[8] J.-X. Wang, J.-L. Wu, H. Xiao, Physics-informed machine learning approach for reconstructing reynolds stress modeling discrepancies based on dns data, Physical Review Fluids 2 (3) (2017) 034603.

[9] J. Ling, A. Kurzawski, J. Templeton, Reynolds averaged turbulence modelling using deep neural networks with embedded invariance, Journal of Fluid Mechanics 807 (2016) 155–166.

[10] C. Jiang, J. Mi, S. Laima, H. Li, A novel algebraic stress model with machine-learning-assisted parameterization, Energies 13 (1) (2020) 258.

[11] C. Sotgiu, B. Weigand, K. Semmler, P. Wellinger, Towards a general data-driven explicit algebraic reynolds stress prediction framework, International Journal of Heat and Fluid Flow 79 (2019) 108454.

[12] Z. J. Zhang, K. Duraisamy, Machine learning methods for data-driven turbulence modeling, in: 22nd AIAA Computational Fluid Dynamics Conference, 2015, p. 2460.

[13] C. Sotgiu, B. Weigand, K. Semmler, A turbulent heat flux prediction framework based on tensor representation theory and machine learning, International Communications in Heat and Mass Transfer 95 (2018) 74–79.

[14] P. M. Milani, J. Ling, G. Saez-Mischlich, J. Bodart, J. K. Eaton, A machine learning approach for determining the turbulent diffusivity in film cooling flows, Journal of Turbomachinery 140 (2).

[15] R. So, L. Jin, T. Gatski, An explicit algebraic reynolds stress and heat flux model for incompressible turbulence: Part i non-isothermal flow, Theoretical and Computational Fluid Dynamics 17 (5-6) (2004) 351–376.

[16] R. So, T. Sommer, An explicit algebraic heat-flux model for the temperature field, International journal of heat and mass transfer 39 (3) (1996) 455–465.

[17] P. Wikström, S. Wallin, A. V. Johansson, Derivation and investigation of a new explicit algebraic model for the passive scalar flux, Physics of fluids 12 (3) (2000) 688–702.

[18] W. Lazeroms, G. Brethouwer, S. Wallin, A. Johansson, An explicit algebraic reynolds-stress and scalar-flux model for stably stratified flows, Journal of Fluid Mechanics 723 (2013) 91–125.

[19] A. Spencer, R. Rivlin, The theory of matrix polynomials and its application to the mechanics of isotropic continua, in: Collected Papers of RS Rivlin, Springer, 1997, pp. 1071–1098.

[20] W. Maddox, T. Garipov, P. Izmailov, D. Vetrov, A. G. Wilson, A simple baseline for bayesian uncertainty in deep learning, arXiv preprint arXiv:1902.02476.

[21] H. Kawamura, H. Abe, K. Shingai, Dns of turbulence and heat transport in a channel flow with different reynolds and prandtl numbers and boundary conditions, Turbulence, Heat and Mass Transfer 3 (2000) 15–32.
[22] I. Tiselj, R. Bergant, B. Mavko, I. Bajsic, G. Hetsroni, Dns of turbulent heat transfer in channel flow with heat conduction in the solid wall, J. Heat Transfer 123 (5) (2001) 849–857.
[23] Q. Li, P. Schlatter, L. Brandt, D. S. Henningson, Dns of a spatially developing turbulent boundary layer with passive scalar transport, International Journal of Heat and Fluid Flow 30 (5) (2009) 916–929.
[24] J. Oder, A. Shams, L. Cizelj, I. Tiselj, Direct numerical simulation of low-prandtl fluid flow over a confined backward facing step, International Journal of Heat and Mass Transfer 142 (2019) 118436.
[25] R. Maulik, H. Sharma, S. Patel, B. Lusch, E. Jennings, Deploying deep learning in openfoam with tensorflow, in: AIAA Scitech 2021 Forum, 2021, p. 1485.
[26] R. Manceau, Recent progress in the development of the elliptic blending reynolds-stress model, International Journal of Heat and Fluid Flow 51 (2015) 195–220.
[27] M. Sundararajan, A. Taly, Q. Yan, Axiomatic attribution for deep networks, arXiv preprint arXiv:1703.01365.

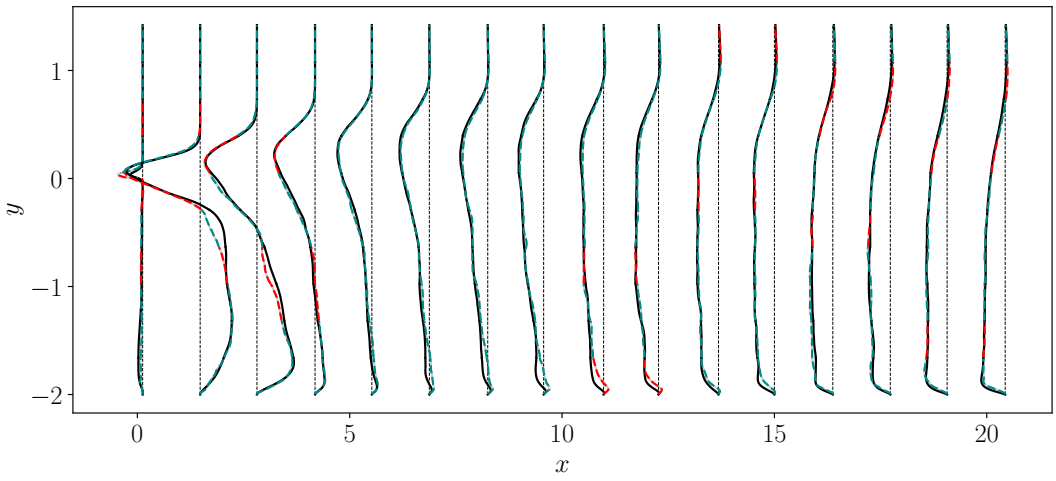

(a) Wall-normal heat flux

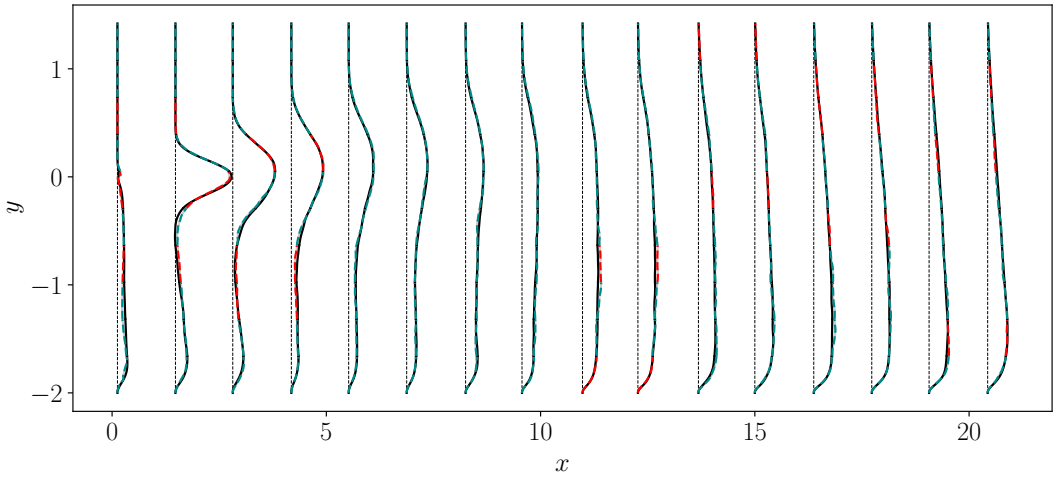

(b) Stream-wise heat flux

Figure 4: Stream-wise and wall-normal components of the turbulent heat flux predicted by the ANN after the training for a non-isothermal, backward-facing step flow at $Pr = 0.1$. Predictions of training and validation data are depicted with blue and red dashed lines, respectively. DNS data [24] are represented with solid lines.

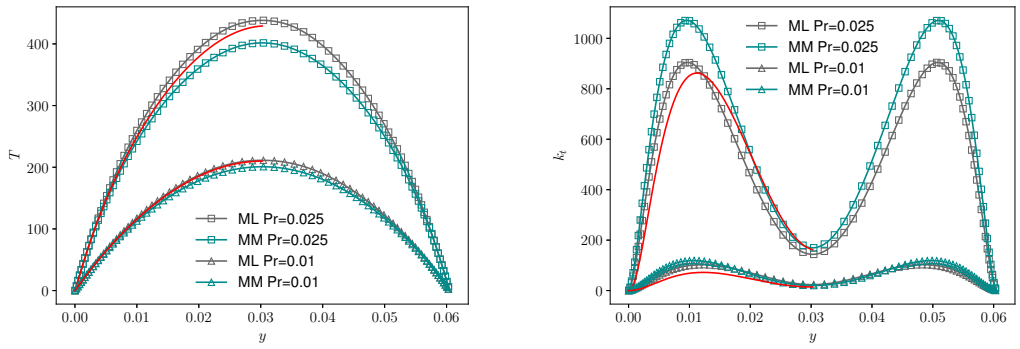

(a) T (b) k_θ

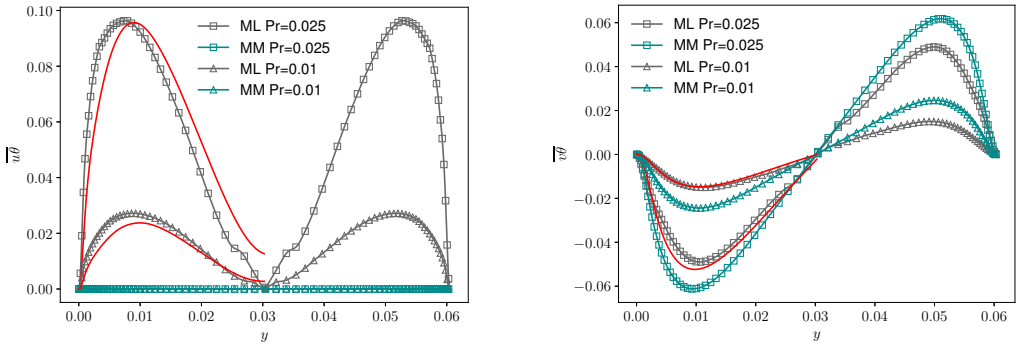

(c) $\overline{u\theta}$ (d) $\overline{v\theta}$

Figure 6: Comparison of the results obtained with the data-driven model (ML) and the Manservisi model (MM) with the DNS data provided by Kawamura et al. [21] and Tiselji et al. [22].

Experimental characterization of evaporation heat exchangers using low Global Warming Potential fluids

Aude Lecardonnel

Environmental and Applied Fluid Dynamics Department, von Karman Institute for Fluid Dynamics, Belgium, aude.lecardonnel@vki.ac.be

Supervisor: Delphine Laboureur

Associate Professor, Environmental and Applied Fluid Dynamics Department, von Karman Institute for Fluid Dynamics, Belgium, delphine.laboureur@vki.ac.be

University Supervisor: Piero Colonna

Full Professor, Chair of Propulsion and Power, Delft University of Technology, The Netherlands, P.Colonna@tudelft.nl

Abstract

The new low global warming potential (GWP) refrigerants such as R1234ze(E) and R1234yf have a rising number of studies about their use in air conditioning cycles. Like any other refrigerant, when entering the evaporator, they can be subject to flow misdistribution between the different channels. This phenomenon is amplified when the fluid is in a two-phase state. The purpose of the present research is to propose a design of an adiabatic test bench that will simulate the flow misdistribution study of a refrigerant in an evaporator, by mean of a air-water mixture flow at representative conditions. Several parameters, whether it influences the inlet flow patterns or geometrical features, can impact the flow distribution of refrigerant over the different channels. Some solutions that lead to improvement have been found in the literature and will be implemented in the test bench. In an attempt of experimental results prediction, a wide number of correlations in channels about pressure losses, heat transfer coefficients and void fraction calculations exists in literature for different types of fluids or geometrical configurations. To reproduce the expected refrigerant mass-flows, similarity parameters are introduced to find the corresponding air-water mixture conditions to be tested. Based on examples of good flow distribution results found in literature, the geometrical parameters of the test bench were sized accordingly. to properly monitor the main properties of interest and characterize the flow distribution, the measurement methods were carefully chosen and combined. Since the flow misdistribution will be investigated at different mass-flows and inlet vapor qualities to explore a wide range of inlet flow patterns, the prediction of the later ahead of the measurements is important. A scheme is developed based on several transitions criteria found in the literature that are compared.

Keywords: Fluid dynamics, heat transfer, low GWP refrigerants, evaporators, aircraft air conditioning

1. Introduction

Vapor cycle systems are closed loop that can be used for equipment cooling and environmental control purposes such as air conditioning. They are composed of several key components (compressor, condenser, expansion valve,...), among which evaporators are continuously subjects of research to improve their efficiency by reducing their volume and increasing their overall aerothermal performances. One straightforward way to improve the heat exchange is to improve the flow distribution among the different channels of the evaporator. Indeed, flow misditribution of the inlet two-phase fluid can cause up to 30% of thermal losses [1].Commonly, high Global Warming Potential (GWP) refrigerants like R134a are used as fluids [2] [3] [4], meaning that their behavior, when it comes to flow distribution in the header and channels, is well characterized and rather predictable. However, their use is already strictly regulated for domestic use or other industrial applications. Eventhough it does not yet apply for the aeronautical field, research is cur-

rently undergoing in this industry to explore the low GWP refrigerants in order the reduce the environmental impact of aircrafts. The present work is part of the exPerimental And Numerical mulTiscale mulTiphasic Heat ExchangeR (PANTTHER) Clean Sky 2 project, which will aim at studying and characterizing the behavior of the low GWP refrigerants like R1234ze for which research works focused mainly so far on simpler geometries [5] [6], as well as improving the flow distribution in the header of the evaporator. The Von Karman Institute is in charge of the experimental approach. To do so, two experimental test benches will be constructed: one transparent adiabatic to develop and validate the methods and the measurement techniques chosen, and a full-scale diabatic one. One fundamental objective of this work will also be the better understanding and prediction of the flow patterns transitions in two-phase flows. This paper deals with the first adiabatic test facility. Firstly the bibliographic review on flow misditribution in evaporators and the different parameters impacting it will be presented as well as good flow distribution examples. Secondly the process to size the test section of the adiabatic facility is developed. Finally, the most relevant two-phase flow measurement techniques and instruments are discussed.

2. Bibliographic review on flow misdistribution

Vapor-liquid two-phase flows are complex phenomena that are hard to fully characterize. These flows are involved in evaporators and are found in several processes in the industry such as power plants, automotive vehicles and air conditioning systems [7]. Non-homogeneous flow distribution in parallel channels heat exchanger headers has been studied for decades in literature, as it may lead to uneven flow in the different channels, and thus decrease the efficiency of the heat transfer [1]. It is even in of greater importance in the case when the flow is in a two-phase state in the header. Indeed, the equal separation of the phases in each channel is particularly difficult to achieve since it is influenced by many parameters [8]. An homogeneous distribution of the liquid phase is especially important to ensure, as underfed channels may lead to the total vaporization of the liquid after leaving the header, and thus leading to a dry out phenomenon which drastically decreases the heat transfer at the wall. Unsurprisingly, this subject has been extensively studied in literature.

Originally, several methods were developed to study the optimization of the two-phase flow distribution. The first idea was to optimize a design for a single-phase flow and then improve it for a two-phase flow. However, the flow structure and the forces acting in a two-phase flow are much more complex than a single-phase flow, even if they share a common basis. The second idea was to study two-phase flow separation in T-junctions then to multiple T-junctions [9], and to generalize it to header which could be seen as parallel T-junctions systems [10]. However, this technique was found not so conclusive as well, since flows in header are more complex than a series of T-junctions. This is why in the most recent studies, the flow in the header has been studied in its full scale, whether with refrigerants or other mixtures [11] [10] [2] [12].

The flow distribution inside the header is affected by numerous parameters from the fluid properties to the tube protrusion and the feeding tube position (see Figure 1. These parameters impact the several forces acting on the flow. Indeed, besides the usual forces that can be found in single phase flows (inertial, gravitational and viscous forces), two phase flows present specific surface tension forces at the liquid-vapor interfaces due to the interaction between the two phases.

of influence.PNG

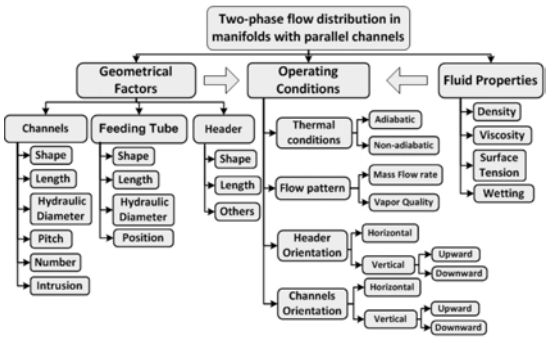

Figure 1: Parameter impacting the flow distribution inside the header with multiple parallel channels of a two-phase fluid [8]

However, only some of these parameters have a strong influence on the distribution. These parameters of paramount importance will be developed in the following sections. Beforehand, several essential two-phase flow characteristics will be introduced to ease the understanding of the formulas and maps explained later in this article.

2.1. Two-phase flow reference parameters

In a two-phase flow, some physical quantities can be defined for the liquid and gaseous phases sepa-

rately or for the overall flow [13]. These physical quantities or dimensionless numbers can also be general to all kinds of flows or specific to fluid in a two-phase state. The first main characteristic quantity that can be introduced is the titer or also called the quality x, and which is defined for an adiabatic flow:

$$x = \frac{m_v}{m_v + m_l} \tag{1}$$

Where m_v and m_l are the vapor and liquid mass flow rates respectively in kg.s^{-1}, and $m = m_v + m_l$. It gives an indication of the amount of the vapor proportion in the flow. The mass velocities G are another two-phase internal flow that can be determined through the mass flow rates but which also takes into account the influence of the cross-section area A and is expressed in kg.(s^{-1}m^{-2}):

$$G = \frac{m}{A} \tag{2}$$

The mass velocity is very often used in flow pattern maps that aim at representing graphically all the flow structures that can present both phases. The void fraction α is usually expressed as the cross-section area occupied by the vapor phase in the pipe over the total area. Thus, it is a very useful dimensionless parameter to partly characterize the flow pattern, but also to estimate the pressure-drops:

$$\alpha = \frac{A_v}{A_v + A_l} \tag{3}$$

Its complementary definition is called the liquid hold-up. The actual velocities of each phase u_l and u_v are of great importance to characterize the flow. However, their calculations depend on both evaluations of the void fraction and the quality:

$$u_l = \frac{G(1-x)}{\rho_l(1-\alpha)} \tag{4}$$

$$u_v = \frac{Gx}{\rho_v \alpha} \tag{5}$$

Where ρ_l and ρ_v represent the liquid and vapor phase densities respectively. However, in practice, the void fraction is a parameter rather challenging to obtain. Instead, superficial velocities j_l and j_v are often used to characterize the flow pattern transitions:

$$j_l = \frac{G(1-x)}{\rho_l} \tag{6}$$

$$j_v = \frac{Gx}{\rho_v} \tag{7}$$

2.2. Geometrical factors

The geometrical factors are the subjects of only few studies when it comes to flow distribution, and especially the influence of some parameters such as the channels geometry and number, or the header geometry is rather nonexistent.

The main parameters among the geometrical factors that present a strong impact are the channels intrusion inside the header that have been mostly studied by Jun Kyoung Lee and al. [11] [14], but also the feeding tube hydraulic diameter and length [2] [15] and finally its position on the header. However, varying the dimensions of the feeding tube is equivalent to varying the inlet flow patterns, and the influence of the inlet flow regimes on the distribution will be developed in the following section 2.2.1. In two distinct experiments, Jun Kyoung Lee first studied different intrusions depths of 0, $\frac{1}{8}$, $\frac{1}{4}$ and $\frac{1}{2}$ of the square shape header width of 24mm [11], in a vertical upward header having a feeding tube of the same dimensions as the header. The flow distributions of the air/water mixture were studied for each intrusion at mass flux of 54-134 kg/m^2 and inlet quality of 0.2-0.5. In [14], intrusion depth of 0, $\frac{1}{8}$ and $\frac{1}{4}$ in a 16mm square shape header. The mass flux and inlet quality of the air/water mixture were 40-150 kg/m^2 and inlet quality of 0.1-0.4. Two configurations were experimented: an upward vertical header and a horizontal header with horizontal channels.

Two conclusions could be drawn from these experiments. The first one is that the tube intrusion in a horizontal header with horizontal channels seems to worsen the distribution as it amplifies the mistribution problem associated with this configuration. Indeed, the tube intrusion seems to decrease the liquid feeding in the first channels and to increase it in the last. In a horizontal header, since the first tubes are already underfed and the last ones overfed, the liquid mistribution is amplified, while the vapor distribution is nearly not altered and rather homogeneous in all cases.

For the upward vertical header, it is the opposite. The first channels are originally overfed in the case of no intrusion while in the last region where recirculation occurs, not enough liquid is distributed. The vapor phase exhibits the inverse trend. Thus, the tube intrusion tends to improve both the liquid and vapor distributions.

However, it appears from both [11] and [14], that in an upward vertical header, an optimal tube intrusion exists which seems to be around $\frac{1}{8}$ of the header width in both studies. When this tube intrusion is exceeded

or is 0, the liquid and vapor distribution is worsen. Finally in [11], a very homogeneous liquid distribution is achieved at several inlet qualities which will be developed later in 2.4.

Those two studies allow an investigation of the impact of the number of channels on the flow distribution as well as the header size. Indeed, in both [11] and [14], the operating conditions are very similar, but the number of tubes differs from being 6 in [11] to 15 in [14], and the square shape header size from 24mm to 16mm. The results in term of liquid distribution show the same global trend from overfeeding of the first tube to underfeeding of the last ones. However, in the case of the 6 tubes study in [11], the tendency is very pronounced and the plateau found in the central part of the curve in the case of 15 tubes is not present at all. Thus, it means that the overall misditrubution tendency is not affected by the amount of channels, but is flattened when the number of tubes is increased, as long as liquid still reaches the last tubes.

2.2.1. Operating Conditions

First, it should be highlighted that most of the studies on flow distribution are achieved in adiabatic conditions. However, [15] performed a diabatic study of R134a in vertical upward and downward flow configurations. The head load of the second flow was varied from 40°C, 50°C to 60°C in a 16mm manifold and then in a 8mm manifold. Apart from the case at 40°C in the 8mm header that exhibits a vapor distribution slightly improved, no effect at all of the heat load could be detected. It means that the conclusions drawn from flow distribution studies achieved in adiabatic conditions can be extrapolated to diabatic conditions.

The header and channels can be combined into 5 configurations that are shown in the Figure 2. Depending on the orientation, the flow distributions present very different behaviors because of the impact of the forces acting on the fluid. A general study is given by Jun Kyoung Lee in [16] that covers all the configuration except the vertical downward header with horizontal channels. In the case of vertical upward header, vapor distribution is rather homogeneous even if the last channel receive slightly more vapor. However, concerning the liquid distribution, due to the gravity force acting in the opposite direction of the flow, the first channels tend to be overfed while the last ones do not receive any liquid. As the mass-flow rate increases, this trend remains unchanged, but liquid reaches and feeds the last channels. At even higher mass-flow rates, a recirculation zone at the end plate

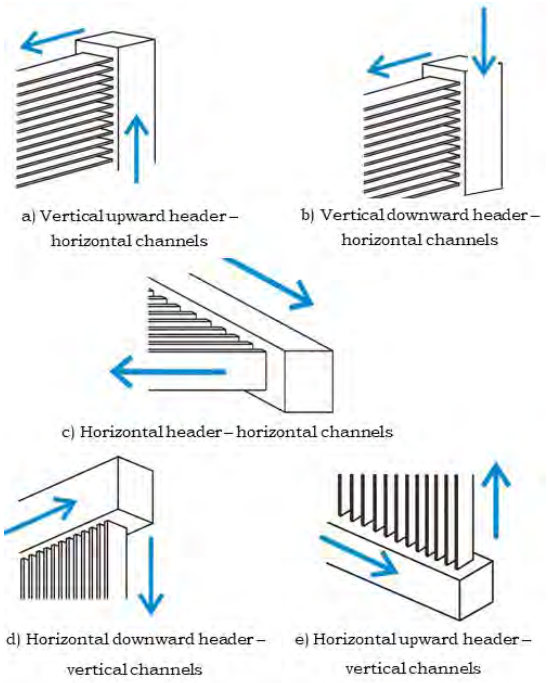

Figure 2: All header and channels configurations [16]

of the header starts to appear, and the overfeeding of the last channels becomes as high as the first ones. For a vertical downward header with horizontal channels, the distribution show a similar but opposite trend [17] [18]. Indeed, in that case the gravity acts with and not against the flow, and thus pushes the liquid phase to accumulate at the bottom part of the header. Thus, the last channels present a high liquid overfeeding along with the couple of first channels, and this phenomenon is amplified as the mass-flow rate increases. The vapor phase shows a more homogeneous distribution, even if the feeding of the tubes tends to slightly but continuously increase in the axial direction of the header. As shown in [14] and [11], the distribution in the vertical upward header with horizontal channels can be improved by tube intrusion. However, for a vertical downward header with horizontal channels, no example of distribution improvement has been found in literature. The horizontal headers have been the most widely studied configurations. Concerning the upward flow in vertical channels,the work of Vist and Peterson [15], [19] and [16] report the same results concerning the liquid and vapor phase distributions. They both exhibit step-like shapes, but in an opposite trend. Indeed, the liquid phase overfeeds the last channels, which accumulates at the rear part of the header, due to the difficulty of the fluid to flow against

the gravity force, while the first ones receive almost no liquid mass flow rate. For the vapor phase, it is exactly the opposite. The first channels receive almost only vapor, while the last ones, due to the liquid accumulation that creates a blockage, are highly underfed. When the channels are oriented horizontally as well as the header, the flow does not have to overcome the gravity force and thus more liquid is distributed in the first channels, even if the division remains strongly non homogeneous as reported by Jun Kyoung Lee [16]. Due to the diminution of the liquid blockage effect in the rear part of the header, more vapor is received by the last channels, allowing a quite homogeneous distribution of the vapor phase among the tubes. The last configuration concerns horizontal headers connected to vertical downward channels. As reported by [16] and [4], the vapor phase is almost equally distributed between all the channels as it can flow in the entire header since no liquid is accumulated anywhere due to the gravity forcing the liquid to flow down in the channels. However, the situation is different for the liquid phase. Indeed, almost all the liquid flow is distributed in the first channels while from the channels located in the middle of the header until the last ones, no liquid is received. When the mass-flow rate is increased and due to the annular flow pattern, some liquid reaches the rear part of the header and thus feeds the last tubes. The distribution improvement has been widely studied by the work of Fei and Hrnjak [2], and Ahmad [20] [21]. Firstly, Fei and Hrnjak decreased the feeding tube length to generate a jet to allow the distribution of liquid to further down the channels. They also noticed that by generating a mist flow pattern inside the feeding tube, a good liquid distribution could be obtained. Ahmad used a splashing grid at the end of the feeding tube to create droplet jets, reproducing the effect created by a mist flow pattern. Thanks to this device, good vapor and liquid distributions could be obtainedl. Examples of good flow distribution that were encountered in literature are presented later in section 2.4.

2.3. Fluid properties

The flow distribution in headers in literature is generally achieved by studying and improving the misdistribution for one specific fluid. Thus, this raises the question of the validity of this improvement when using other fluids. This subject has been dealt with only few studies, but their conclusions are however consistent. Indeed, as mentioned in [8], it has been showed by [22] that when testing on the same facility, for almost equal ranges of mass flux G and inlet quality x, R134a and then a water/air mixture, different flow distributions were obtained. They explained these results by the difference in fluid properties. Indeed, R134a and air/water mixture present very different liquid and vapor phase densities, as well as different liquid to vapor phase density and viscosity ratios $\frac{\rho_l}{\rho_v}$ and $\frac{\mu_l}{\mu_v}$. This directly impacts the predominance of the forces acting of the flow, and thus the flow patterns. Indeed, for the same G and x in [22], R134a present mostly stratified and also annular structures, while air/water mainly exhibits annular flow regime (Figure 3). Thereby, depending on the flow pattern in the feeding tube, the distribution in the same header will be strongly influenced. This is confirmed by the studies of [4] and [3]. In [4] experiments obtained for R134a and air/water mixture at the same mass flux G and inlet quality x were compared, and while the vapor phase distribution is quite homogeneous in both cases, the liquid distribution is very different, as well as the inlet flow patterns. In [3], the distribution of R245fa, R134a, R410a and R32 were compared at the same operating conditions and in the same facility. It appears also in that case that the distribution varies from being quite different to totally different.

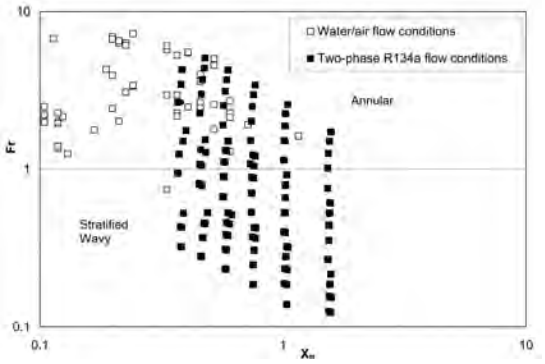

Figure 3: Flow pattern map comparing R134a and water/air [22]

All these works highlight the need of a similarity study between the adiabatic and diabatic facilities, since different fluids will be used but the dimensions of the two test benches will be equivalent. In particular, attention has been paid to studying similar flow patterns when choosing the similarity parameters.

2.4. Examples of good distribution

Three main examples of good flow distribution inside headers have been found through literature. The first one concerns the work of Fei and Hrnjak [2], on a horizontal header with vertical downward channels. As explained in 2.2.1, a mist flow in the feeding tube

was generated which led to a highly homogeneous flow distribution as can be seen in Figure 4

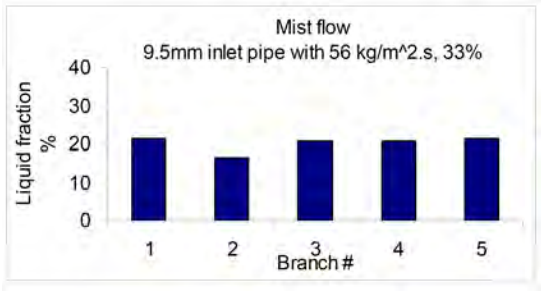

Figure 4: Liquid distribution for mist flow inlet flow regime [2]

The second one is found in the work from Lee and Lee [11] that studied the impact of the intrusion depth inside the vertical upward header, and that found an homogeneous distribution for an intrusion of $\frac{1}{8}$ of the header width and for an annular flow regime as can be seen in Figure 5

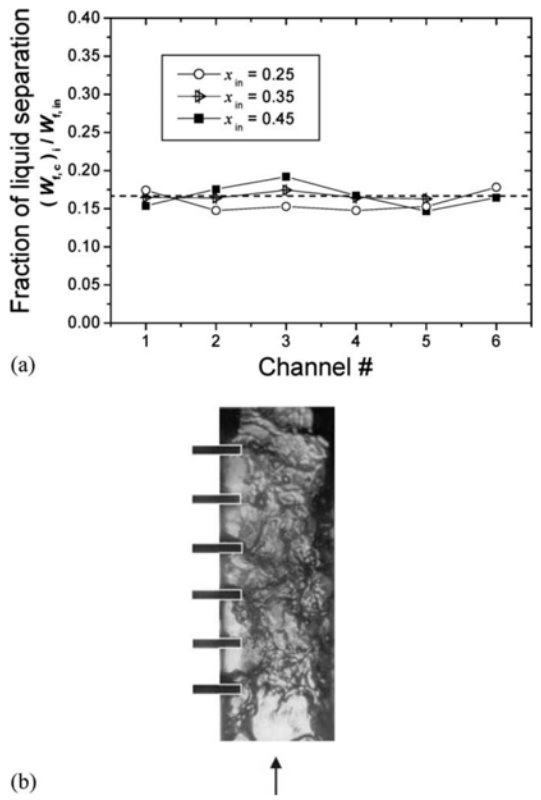

Figure 5: Flow distribution obtained with an intrusion depth of 3mm at $G_{in} = 70kg/m^2$.(*a*) Liquid fraction in each channel. (*b*) Visualization at inlet quality of 0.35 [11]

Finally the last good example of flow distribution is obtained by Ahmad et al. [20] by mean of a splashing grid (Figure 6) that disperses the inlet stratified flow in a horizontal header. The vapor and liquid distributions present a rather homogeneous profile inside the vertical downward channels at two mass-flow rates and at an inlet quality of 5%, which strongly improves when the inlet quality is increased to 20% (Figure 7).

grid combo.png

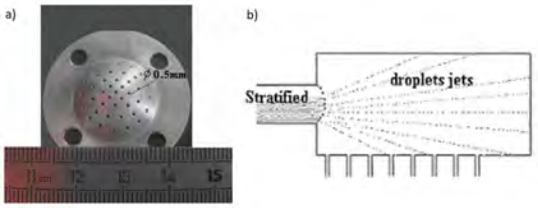

Figure 6: Splashing grid device. (*a*) Dimensions and design. (*b*) Splashing grid effect on flow distribution [20]

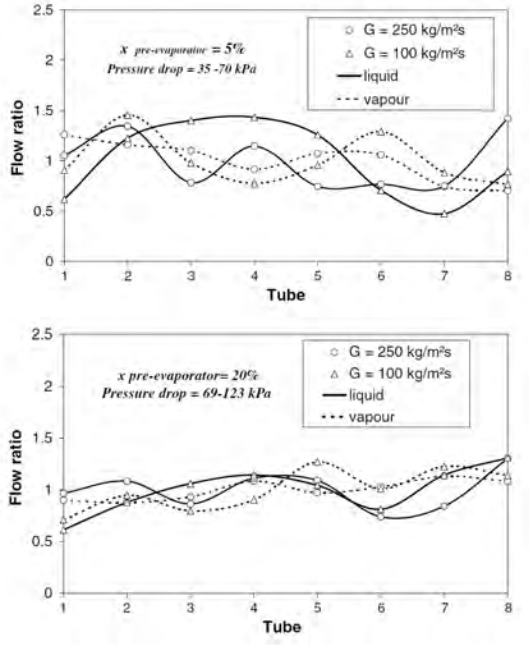

Figure 7: Flow distribution inside channels after the splashing grid [20]

3. Design of adiabatic facility

3.1. Flow patterns: representation and prediction

In vapor-liquid flows in a pipe, depending on the liquid mass-flow rate, the quality and the orientation,

the two phases can present different structures, which are referred as flow patterns or flow regimes. These flow patterns can still be modified if the flow velocity is too high, as it may trigger a vaporization of some liquid mass. Indeed, those two phenomena both lead to a change of the quality x and thus might change the flow pattern. The exhaustive list of flow patterns that can be found in horizontal or vertical pipes are presented in Figure 8, for increasing liquid but also vapor mass-flow rates.

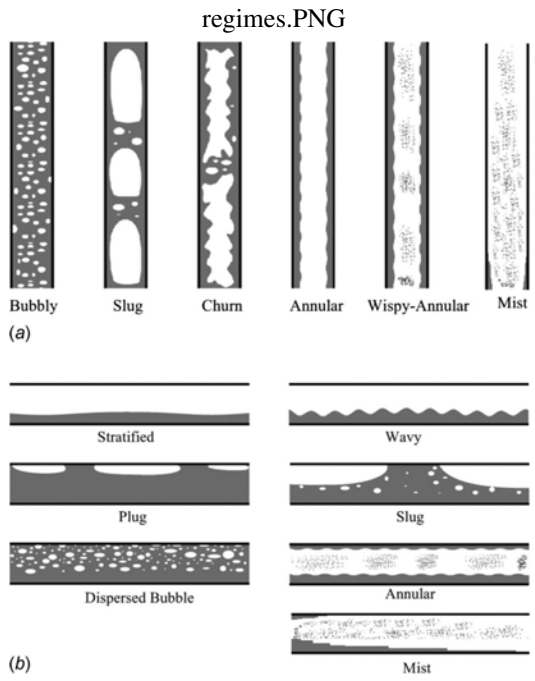

Figure 8: Flow regimes for horizontal and vertical pipes [23]

Since the flow pressure drops, the heat transfer coefficient along the walls and the flow distribution in the header (see section 2) depend on the flow regime [24] as well as the calibration of some instruments [25] [26], its estimation beforehand is of paramount importance. To do so, clear transitions between all the flow regimes have to be established. The work of Taitel and Duckler [27] represents a strong baseline concerning the modelling of the transitions between the flow regimes in an horizontal pipe. His work has served as basis since then by several authors to improve and modify the flow transitions criteria to accurately predict the flow regimes for different fluids [28], for different orientations, for adiabatic or diabatic flows, and to implement the dry-out flow regime [29] [30]. The works of Wojtan et al. [31] [32] and Cheng et al. [23] presents extensive reviews on studies and evolution of flow pattern maps representation and transition criteria through literature over the last decades. Oliemans and Pots [33] developed a predictive algorithm based on the transitions criteria developed by the work of Taitel and Duckler [27] and their different further co-workers that has been implemented in the present study to predict accurately the flow patterns expected given the inlet water and air mass-flow rates. This algorithm will be further improved by implementing the flow transitions criteria between the plug, slug and annular flow regimes that are characteristic of R1234ze and that are provided by the work of Yang et al. [34]. Originally the classification between the flow regimes was achieved through visualization of the flow in experimental facilities, which has the substantial disadvantage to be rather subjective since it is depending on the appreciation of an operator. In the last decade, authors tended to develop criteria that rely on data clustering of signals from capacitance probes [35] or pressure fluctuations [36], and thus intended to find objective transitions between the flow regimes.

3.2. Test section sizing

As highlighted in 2.3, since the use of different fluids for the same set-up and operating conditions lead to different distribution results, there is the need to carry a similarity study between the refrigerant R1234ze and the air-water mixture. In the work of Webb [12] that achieved a similarity between R-404A and air-water mixture, three main parameters are selected, assuming that the geometrical features of the facility are equal. The first one to be kept constant between the two cases is the density ratio since it seems to impact greatly the distribution (see section 2.3). However, to reach this goal, given the fluid properties of R1234ze (Table 1), the compressed air needs to be kept at 8 bar absolute pressure to obtain the desirable density (Table 2).

Table 1: R1234ze properties at 273K (add ref)

μ_l Pa.s^{-1}	μ_v Pa.s^{-1}	ρ_l kg.m^{-3}	ρ_v kg.m^{-3}
2.69 10^{-4}	1.12 10^{-5}	1240.6	11.65

The second parameter defined by Webb [12] is the Martinelli parameter χ_{tt} which is a kind of liquid fraction in case of both phases in turbulent regime and is

defined as follows:

$$\chi_{tt} = \left(\left(\frac{\rho_v}{\rho_l}\right)^{0.5}\left(\frac{\mu_l}{\mu_v}\right)^{0.125}\left(\frac{1-x}{x}\right)\right) \quad (8)$$

Finally, the third parameter is the densimetric Froude number F_{TD} that compares the inertial and the gravity forces acting on the fluid:

$$F_{TD} = \left(\frac{\rho_v j_v^2}{(\rho_l - \rho_v)Dg}\right)^{0.5} \quad (9)$$

The purpose of fixing the Martinelli and densimetric Froude is to ensure as much as possible that equivalent flow patterns will be studied between the test benches, since flow regimes influence in the feeding tube influence strongly the distribution of the two phases (see section 2.3). Based on these three parameters, on the required operating conditions (30g/s < $m_{refrigerant}$ < 350g/s and 0 < $x_{refrigerant}$ < 0.8) and on the properties of the fluids, the similarity study results in the following equivalent air-water mixture mass-flow rates and qualities presented in Table 2.

Table 2: Similarity study

Parameter	Refrigerant		Air/water	
x	0	0.8	0	0.82
Min flow rate				
$m_v\ (g/s)$	0	24	0	19.5
$m_l\ (g/s)$	30	6	21.8	4.4
Max flow rate				
$m_v\ (g/s)$	0	280	0	227
$m_l\ (g/s)$	350	70	254	51
$\frac{\rho_l}{\rho_v}$	107	107	105	105

Concerning the geometrical dimensions, the design was based on first the maximum sizing allowed in the project, then on the header and channels sizes of good distribution examples found in literature and presented in section 2.4, and the flow patterns targeted in this study. Covering all flow patterns from stratified to mist is impossible with only one feeding tube. Thus, two feeding tube diameters will be considered: 20mm and 50mm. The objective in the pipe of larger diameter is to be able to cover all the stratified inlet flow regimes, while in the smaller pipe, the objective is to cover the remaining flow patterns: slug, intermittent, annular, dry out and mist.

3.3. Test section design

Based on the similarity calculations presented in section 3.2 and the typical facility design that can be found in literature (see section 2.4), the test section was designed accordingly and is shown in Figure 9. It is composed of a feeding tube connected to a visualization piece made of plexiglass, followed by a removable splashing grid that can be inserted before the inlet of the header. Five different inlet positions can be tested on the square shaped header of dimensions 85mm x 85mm. The front and back faces of the header are made transparent to enable flow visualization inside the header. Eight tubes of 10mm diameter made in stainless steel are connected to the manifold. Their extremities are threaded so that extensions of these tubes can be screwed on it, to study easily several intrusion depths.

up design.png

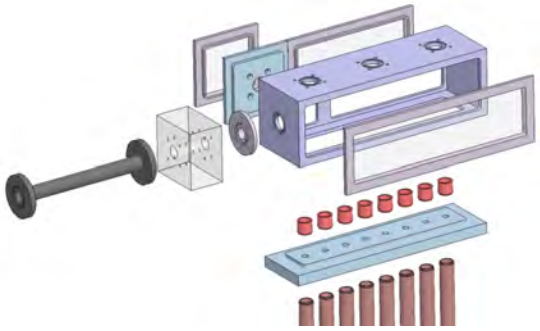

Figure 9: Test section design

3.4. Experimental facility

The overall experimental apparatus is shown on Figure 10.

Air/water mixture is used as a fluid. Water is pumped from a reservoir and its mass flow rate is measured and then mixed to a mass flow rate of compressed air at 8 bar coming from a pressurized line, that is adjusted and measured by mean of valve and flow meter, to control the air inlet quality. The test section is connected to the rest of the facility by mean of flexible hoses, since it will be tested in several of the orientations presented in section 2.2.1, and thus there is the need to have easily adjustable connections. As explained in section 3.2 the flow regimes at the inlet of the test section need to be characterized, as well as the void fraction. The pressure will be monitored at different locations before, inside and after the test section to calculate the aeraulic performances of the adiabatic heat exchanger. The total mass-flow and the void fraction in each channel will be measured to verify the homogeneity of the distribution. Several combinations of instruments are possible [7] for two-phase flows,

apparatus.png

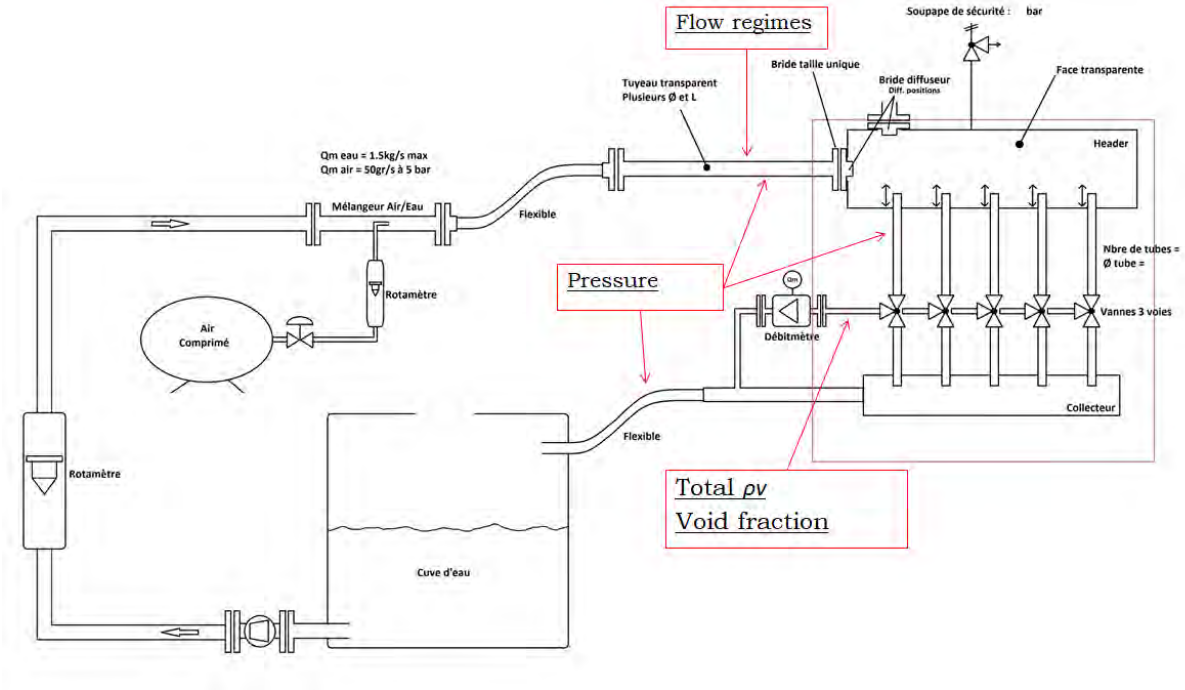

Figure 10: Experimental apparatus of the adiabatic set-up

but the separation of the phases wants to be avoided in the present work because of its cumbersomeness. Thereby, to measure the two-phase mass-flow rates, Venturi are selected and are calibrated by mean of a Coriolis flowmeter. The pressure will be measured by acquiring the voltage of pressure-sensing diaphragms. The void fraction will be obtained from conductance probes [25] as well as dual optical probes for comparison purpose. Finally, the flow regimes will be visualized at the inlet, and compared to flow patterns guessed from the data clustering of the conductance probe signal [26] and the fluctuations of the pressure signal [25] [37].

4. Conclusion

Misdistribution can decrease the thermal performances of the evaporator up to 30 % [1] and thereby is to be avoided. This paper presents some aspects of the bibliographic review that have been achieved on the two-phase flow distribution inside header with multiple parallel channels, showing the parameters impacting the most this distribution like the header and channel orientation, tube intrusion or inlet flow patterns.

Three examples of homogeneous flow distribution have been found through literature [2] [11] [20] and their geometrical features and dimensions are considered as a baseline for the design of the test section of the present work, as well as the maximum sizing available from the project requirement and the flow patterns that will be covered.

The similarity study between the R1234ze refrigerant that will be used in the final set-up, and the air/water mixture that will be used in the adiabatic experimental facility is based on constant phase density ratios $\frac{\rho_l}{\rho_v}$, Martellini parameter χ_{tt} and densimetric Froude number F_{TD}.

In the experimental set-up, the total mass-flow in each channel will be measured by mean of a Venturi calibrated through a Coriolis flow-meter. Conductance and dual optical probes will be used to measure the void fraction inside each tube. The data clustering of the the conductance probe probe and pressure signals will allow the flow pattern prediction.

Acknowledgments

This project has received funding from the Clean Sky2 Joint Undertaking (JU) under grant agreement No 886698. The JU receives support from the Eu-

ropean Unions Horizon 2020 research and innovation programme and the Clean Sky 2 JU members other than the Union. This paper reflects only the author's view and that the JU is not responsible for any use that may be made of the information it contains. The author wishes to thank Pr. Delphine Laboureur from von Karman Institute and Pr. Piero Colonna for their supervision and guidance.

References

[1] J. M. Choi and W. V. Payne and P. A. Domanski, Effects of non-uniform refrigerant and air flow distributions on finned-tube evaporator performance, International Congress of Refrigeration, Washington, DC (2003) 1–8.

[2] P. Fei and P. Hrnjak, Adiabatic Developing Two-Phase Refrigerant Flow in Manifolds of Heat Exchangers, Air Condtioning and Refrigeration Center TR-225.

[3] Y. Zou and P. S. Hrnjak, Effects of fluid properties on two-phase flow and refrigerant distribution in the vertical header of a reversible microchannels heat exchanger, Applied Thermal Engineering 70 (2014) 966–976.

[4] N. -H. Kim and D. -Y. Kim and H. -W. Byun, Effect of inlet configuration on the refrigerant distribution in a parallel flow minichannel heat exchanger, International Journal of Refrigerant 34 (2011) 1209–1221.

[5] A. Diani and S. Mancin and L. Rossetto, R1234ze(E) flow boiling inside a 3.4 mm ID microfin tube, International Journal of Refrigeration 47 (2014) 105–119.

[6] M. A. Kedzierski and K.-J. Park, Horizontal Convective Boiling of R134a, R1234yf/R134a, and R1234ze(E) within a Micro-Fin Tube with Extensive Measurement and Analysis Details, NIST Technical Note 1807.

[7] G. Falcone, G. F. Hewitt, C. Alimonti, Multiphase Flow Metering - Pinciple and Applications, Elsevier, 2010.

[8] E. R. Dario and L. Tadrist and J. C. Passos, Review on two-phase flow distribution in parallel channels with macro and micro hydraulic diameters: Main results, analyses, trends, Applied Thermal Engineering 59 (2013) 316–335.

[9] B. J. Azzopardi , Phase separation at T junctions, Multiphase Science and Technology 11 (2000) 223–329.

[10] S. Vist, Two-phase Flow Distribution in Heat Exchanger Manifolds, Ph.D. thesis, NTNU - Norwegian University of Science and Technology, Faculty of Engineering Science and Technology, Department of Energy and Process Engineering (2003).

[11] J. K. Lee and S. Y. Lee, Distribution of two-phase annular flow at header-channel junctions, Experimental Thermal and Fluid Science 28 (2004) 217–222.

[12] R. L. Webb and K. Chung, Two-Phase Flow Distribution to Tubes of Parallel Flow Air-Cooled Heat Exchangers, Heat Transfer Engineering 26 (4) (2005) 003–018.

[13] C. E. Brennen, Fundamentals of Multiphase Flows, Cambridge University Press, 2005.

[14] J. K. Lee, Study on Effect of Channel Intrusion Depth on the Two-Phase Flow Distribution at Header-Channel Junction, Korean Journal of Air-Conditioning and Refrigeration Engineering 28 (11) (2016) 444–449.

[15] S. Vist and J. Pettersen, Two-phase flow distribution in compact heat exchanger manifolds, Experimental Thermal and Fluid Science 28 (2004) 209–215.

[16] J. K. Lee, The Effect of Header and Channel Angle Variation on Two-Phase Flow Distribution at Multiple Junctions, Korean Journal of Air-Conditioning and Refrigeration Engineering 27 (11) (2015) 559–566.

[17] F. Poggi, Etude de la distribution d'coulements mono- et diphasiques dans un changeur mini-canaux. Pertes de pression rgulires et singulires, Ph.D. thesis, Universit Joseph Fourier, Grenoble, France (2008).

[18] T. Yoo, P. Hrnjak, T. Newell, An Experimental Investigation of Two-phase Flow Distribution in Microchannel Manifolds, Tech. Rep. TR-207, Air Conditioning and Refrigeration Center, University of Illinois at Urbana-Champaign (2002).

[19] Y. Hwang and D.-H. Jin and R. Radermacher, Refrigerant Distribution in Minichannel Evaporator Manifolds, HVAC&R Research 13 (4) (2007) 543–555.

[20] M. Ahmad and G. Berthoud and P. Mercier, General characteristics of two-phase flow disitrbution in a compact heat exchanger, International Journal of Heat and Mass Transfer 52 (2009) 442–450.

[21] M. Ahmad, Etude exprimentale et numrique d'coulements diphasiques l'entre des vaporateurs de cycles thermodynamiques, Ph.D. thesis, Institut National Polytechnique de Grenoble (2007).

[22] Q. Zhang and P. Hrnjak and T. Newell, An experimental Investigation of R134a Flow Distribution in Horizontal Microchannel Manifolds, Air Conditioning and Refrigeration Center TR-223.

[23] L. Cheng and G. Ribatski and J. R. Thome, Two-Phase Flow Patterns and Flow-Pattern Maps: Fundamentals and Applications, Applied Mechanics Reviews 61.

[24] U. Soupremanien, Ecoulements diphasiques aux petites chelles - Application au refroidissement d'une Pile Combustible (PEMFC), Ph.D. thesis, Mcanique des fluides [physics.class-ph]. Grenoble INP, France (2010).

[25] Y.-R. Deng and N.-D. Jin and Q.-Y. Yang and D.-Y. Wang, A differential pressure sensor coupled with conductance sensors to evaluate pressure drop prediction models of gas-water two-phase flow in a vertical small pipe, Sensors 19 (2723).

[26] A. Shafquet and I. Ismail, Measurement of void fraction by using electrical capacitance sensor and differential pressure in air-water bubble flow, no. 4th International Conference on Intelligent and Advanced Systems, Kuala Lumpur, Malaysia, 2012.

[27] Y. Taitel and A. E. Duckler, A model for predicting flow regime transitions in horizontal and near horizontal gas-liquid flow, AIChE J. 22 (2) (1976) 43–55.

[28] D. Steiner, Heat transfer to boiling saturated liquids, VDI-Warmeatlas (VDI Heat Atlas), Verein Deutscher Ingenieure, VDI-Gessellschaft Verfahrenstechnik und Chemie- ingenieurwesen (GCV), Dsseldorf.

[29] N. Kattan and J. R. Thome and D. Fravat, Flow boiling in horizontal tubes. Part I: Develoment of a diabatic two-phase flow pattern map, Journal of Heat Transfer 120 (1) (1998) 140–147.

[30] N. Kattan and J. R. Thome and D. Fravat, Flow boiling in horizontal tubes. Part 3: Development of a new heat transfer model based on flow patterns, Journal of Heat Transfer 120 (1) (1998) 156–165.

[31] L. Wojtan and A. T. Ursenbacher and J. R. Thome, Investigation of flow boiling in horizontal tubes: Part IA new diabatic two-phase flow pattern map, International Journal of Heat and Mass Transfer 48 (2005) 2955–2969.

[32] L. Wojtan and A. T. Ursenbacher and J. R. Thome, Investigation of flow boiling in horizontal tubes: Part IIDevelopment of a new heat transfer model for stratified-wavy, dryout and mist flow regimes, International Journal of Heat and Mass Transfer 48 (2) (2005) 2970–2985.

[33] R. V. A. Oliemans, B. F. M. Pots, Chapter 2, Multiphase Flow Handbook, Taylor & Francis Group, LLC, Edited by C. T. Crowe, 2006.

[34] Z.-Q. Yang and G.-F. Cheng and X.-R. Zhuang and Q.-L. Song and Z. Deng and J. Shen and M.-Q. Gong, A new flow pattern map for flow boiling of R1234ze(E) in a horizontal tube, International Journal of Multiphase Flow.

[35] W. H. Ahmed, Capacitance Sensors for Void-Fraction Measurements and Flow-Pattern Identification in AirOil Two-Phase Flow, IEEE SENSORS JOURNAL 6 (5) (2006) 1153–1163.

[36] S. Lin, PRESSURE FLUCTUATION AND FLOW REGIMES OF AIR-WATER FLOW IN A SMALL TUBE, Experimental Heat Transfer 14 (2001) 135–144.

[37] J. Jia and A. Babatunde and A. Wang, Void fraction measurement of gas-liquid two-phase flow from differential pressure, Flow Measurement and Instrumentation 41 (2015) 75–80.

Development of an advanced experimental technique for the measurement of the turbulent heat flux in liquid metals

Tommaso Carlesi

Environmental and Applied Fluid Dynamics Department, von Karman Institute for Fluid Dynamics, Belgium, tommaso.carlesi@vki.ac.be

Supervisor: Delphine Laboureur

Associate Professor, Environmental and Applied Fluid Dynamics Department, von Karman Institute for Fluid Dynamics, Belgium, delphine.laboureur@vki.ac.be

University Supervisor: Patrice Mégret

Professor, Electromagnetism and Telecommunication Department, University of Mons, Belgium, patrice.megret@umons.ac.be

Mentor: Katrien Van Tichelen

Unit head LBE-components and experiments, SCK-CEN, Belgium, katrien.van.tichelen@sckcen.be

Abstract

Turbulent heat fluxes are an important factor in the determination of primary coolant temperatures in a nuclear reactor. Measurement of these fluxes is challenging as it requires simultaneous measurement of velocity and temperature fluctuations in a particular environment. This Ph.D. thesis aims at developing high-fidelity instruments to acquire simultaneous measurement of velocity and temperature in liquid metals. MYRRHA (Multi-purpose hYbrid Research Reactor for High-tech Applications) is a flexible fast-spectrum research reactor under design at SCK CEN, the Belgian Nuclear Research Centre. MYRRHA is a pool-type reactor with Lead Bismuth Eutectic (LBE) as the primary coolant. For the design and safety evaluation of MYRRHA, the temperature of the primary coolant must be assessed for nominal operation as well as in accidental conditions. The instruments developed in this Ph.D. will provide unique information on the turbulent heat flux and will quantify the turbulent thermal diffusivity, which is a fundamental term in the modeling of turbulent heat transfer in natural and forced convection. Nowadays, techniques for the measurement of temperatures and velocities in opaque fluids like LBE allow to acquire data with good accuracy but with a limited spatial and/or temporal resolution. Moreover, no technique is currently available for the simultaneous measurement of these two quantities and for application in a liquid metal environment (high temperatures, chemical corrosion...). State-of-the-art techniques such as hot-wire anemometry and Ultrasonic Doppler Velocimetry for velocity and optical fiber temperature sensors will be developed for application in a low melting point liquid metal at the Von Karman Institute for Fluid Dynamics during the first two years of the project. Innovative techniques based on local measurements using the electromagnetic properties of the metal like Lorentz Force Velocimetry (LFV) and Contactless Inductive Flow Tomography (CIFT) will be also taken into account. During the last two years, the selected technique will be applied for turbulent heat flux measurements in an LBE facility at SCK CEN with the final purpose of supporting the design of the MYRRHA reactor.

Keywords: Measurement techniques, velocity measurement, temperature measurement, MYRRHA, Lead Bismuth Eutectic (LBE), Galinstan, natural convection, turbulent heat flux, liquid metals

Modelization of heat and mass transfer in multiphase heat exchangers core

Yohanna Henrotel

TEMISTh Marignane, France, yohanna.henrotel@temisth.com

Supervisor: Damien Serret

Head of R&D, TEMISTh Marignane, France, damien.serret@temisth.com

University Supervisor: Olivier Le Metayer

Professor, Mechanical Engineering & Energy, Aix-Marseille University - IUSTI / UMR CNRS 7343, France, olivier.le metayer@univ-amu.fr

Abstract

A proper heat exchanger sizing can increase the efficiency of any system and the recent advances in electronics (miniaturization) makes thermal management more challenging than ever. Development of new kinds of heat exchangers are ever in progress, to reduce the volume and enhance the performances in terms of pressure drop or heat transfer efficiency, and it generally comes with a high computational cost. To this end, the aim of this work was to develop a CFD tool based on the NTU method to co-simulate 3D headers and 0D core in a micro-channel heat exchanger using the StarCCM+ software.

Keywords: Heat exchanger, Heat transfer, thermal engineering, single-phase flow, StarCCM+, co-simualtion, micro-channel, NTU-method

1. Introduction

Micro-channel heat exchangers (MCHX) are characterized by reduced tubes with hydraulic diameters within an average range of a few 100 micrometers to a few 100 millimeters. They are widely used thank to their small dimensions, high compactness and a great overall performance. Yet, in regards of the high number of tubes patterns in those HX, the cost and time of global computation via CFD models can quickly increase. To overcome this problem, an alternative solution can be investigated, one of these options is a 0D model based on NTU-ε method and pressure drop correlations coupled to a full simulation of the headers and a small part of the tube where the outlet pressure and Temperature are implemented in a step interface into the model.

2. Interface method

2.1. Pressure drop

The Yang correlation [1] for an adiabatic horizontal flow was used to calculate the friction factor:

$$4 * f = 0.203 * Re^{-0.22} \tag{1}$$

Giving the pressure drop in a channel:

$$\frac{\Delta P}{L} = \frac{2\rho f u^2}{D} \tag{2}$$

From there pressure drop should be plotted for different velocities to fit with the Darcy-Forchheimer law as found in the porous interface in StarCCM+:

$$\Delta P = -\rho(P_i|u| + P_v)|u| \tag{3}$$

by plotting the results the following expression cand be found with X_1 and X_2 depending on the geometry and velocity range:

$$\frac{\Delta P}{L} = X_1 u^2 + X_2 u \tag{4}$$

Therefor the inertial resistance and viscous resistance parameters are respectively:

$$P_i = -\frac{X_1 * L}{\rho} \tag{5}$$

$$P_v = -\frac{X_2 * L}{\rho} \tag{6}$$

2.2. Outlet temperature

The pourous baffle offers a heat source condition as a way to enable a temperature step at the interface, the NTU-ε method is used to calculate outlet temperature and total power exchanged in a tube. First step is to find the heat transfer coefficient inside the tubes, Mills correlation [2] gives:

$$Nu = \frac{hD}{k} = 3.66 + \frac{0.065 RePr\frac{D}{L}}{1 + 0.04(RePr\frac{D}{L})^{2/3}} \quad (7)$$

For a cross flow exchanger:

$$\eta = \left(\frac{1}{1 - e^{-NTU}} + \frac{Z}{1 - e^{-NTU*Z}} - \frac{1}{NTU} \right)^{-1} \quad (8)$$

$$NTU = \frac{h_{tot} * S}{m.Cp_{min}} \quad (9)$$

$$\eta = \frac{T_{1i} - T_{1o}}{T_{1i} - T_{1i}} \quad (10)$$

Then the heat exchanged in the channel is:

$$Q = mCp(T_{1i} - T_{1o}) \quad (11)$$

3. Validation

3.1. Simulation case

Relation (1) to (11) are applied it to the case of a Cross-flow heat exchanger with the following inlet conditions

Air conditions (outside tubes):

- T_i = 15 degC
- h=175 W/m^2.K

Water conditions (inside tubes):

- T_i = 35 degC
- P_i = 1.10^5 Pa
- u = 0.2 m/s

Tube geometry:

- D = 1 mm
- L_{sim} = 2 cm (length simulated in StarCCM+, 1cm on each side of the interface)
- L = 1 m (real tube length)

3.2. results comparaison

To validate our method, a comparison is evaluated between the results found for this case with a full CFD simulation of the tube :

	full simulation	interface method	error
	-	-	%
ΔP (Pa)	364	349	4.1
$Toutlet$ (K)	17.65	17.91	1.47

Table 1: Results comparing the interface methode to CFD simulation

4. Conclusion

As shown by the results comparison, the NTU-method works well in a single-phase heat exchanger case, it allows significant gain of computational power as in the example case here only 2% of the tube are actually modelized in the CFD simulation. Such method can be extended to multiphase as done in [3].

Acknowledgments

I thank my supervisors Olivier Le Metayer and Damien Serret as well as the R&D team of TEMISTh. This project has received funding from the Clean Sky2 Joint Undertaking (JU) under grant agreement No 886698. The JU receives support from the European Unions Horizon 2020 research and innovation programme and the Clean Sky 2 JU members other than the Union. This paper reflects only the author's view and that the JU is not responsible for any use that may be made of the information it contains.

References

[1] D. Joseph and B. Yang, Friction factor correlations for laminar, transition and turbulent flow in smooth pipes, Physica D: Nonlinear Phenomena 239 (14) (2010) 1318–1328.

[2] A. Mills, Heat Transfer Second Edition, prentice-Hall, 1999.

[3] Huang Long and Aute Vikrant and Radermacher Reinhard.

Topology optimization of a multiphase heat exchanger manifold

Wassim Abdel Nour

Aeronautics and Aerospace Department, von Karman Institute for Fluid Dynamics, Belgium, wassim.abdel.nour@temisth.com

Industrial Supervisors: Damien Serret, Joseph Jabbour

Research Engineer, Temisth Company, damien.serret@temisth.com

University Supervisors: Aurelien Larche, Phillipe Milega, Elie Hachem

Professor, Numerical Mathematics HPC and Data , Ecole National Suprieure des Mines de Paris, France

Abstract

Heat exchangers are devices that transfer thermal energy from one medium to another. They nd applications in a wide variety of problems such as refrigeration, cooling, heat recuperation, chemical processing, and they are vital parts of many industries. Although the main principle of all heat exchangers is the same, the objective, conguration and size varies greatly. For example, in cooling application, as ours, the objective is to keep a constant temperature with the lowest possible energy loss. 80% of energy utilization is involved in heat transfer. This highlights the major importance of heat exchangers, their involvement in nearly every energy system, and their crucial role. Whether in domestic or industrial applications, they make signicant changes in the performance of the system that they integrate. The optimization of industrial processes for maximum use of their available energy is a very active topic of scientic research in the last years. This applies in particular to heat exchangers. To improve the thermal and dynamic performances of heat exchangers, topology optimization methods has been for some time the center of interest of researchers in this field. Topology optimization was rst proposed by Bendsoe and Kikuchi in 1988, and its basic concept is to replace the optimization problem with a material distribution problem. In this method, every mesh in the design domain is a design parameter. This increases signicantly the number of variables, and thus, the problem complexity. On the other hand, it allows modications in the connectivity. In fact, this method has the ability to add or remove materials, what makes it most of the times independent from the initial design and leads to non-intuitive results. The application of topology optimization to the design of thermo-uid systems has become so appealing for its capacity to reach innovative and complex congurations based strictly on the dened objectives and constraints. In our project, we will develop a new topology optimization method, based on the level-set method, for multiphase flow. This new developed technique will be used to design the inlet and outlet of a plate and ns heat exchangers.

Keywords: Topology Optimization, Heat Exchangers, Multiphase flow.

Acknowledgments

This project has received funding from the Clean Sky2 Joint Undertaking (JU) under grant agreement No 886698. The JU receives support from the European Unions Horizon 2020 research and innovation programme and the Clean Sky 2 JU members other than the Union. This paper reflects only the author's view and that the JU is not responsible for any use that may be made of the information it contains.

ENVIRONMENTAL FLOWS AND SAFETY

Elaboration of Numerical and Experimental Models for Airflow in a Subway Station

Loreline Faugier

Environmental and Applied Fluid Dynamics Department, von Karman Institute for Fluid Dynamics, Belgium, loreline.faugier@vki.ac.be

Supervisor: Delphine Laboureur

Associate Professor, Environmental and Applied Fluid Dynamics Department, von Karman Institute for Fluid Dynamics, Belgium, delphine.laboureur@vki.ac.be

University Supervisor: Walter Bosschaerts & Benoît G. Marinus

Professor, Department of Mechanical Engineering, Royal Military Academy, Belgium, walter.bosschaerts@rma.ac.be

Professor, Department of Mechanical Engineering, Royal Military Academy, Belgium, benoit.marinus@rma.ac.be

University Supervisor: Karim Limam

Professor, Laboratoire des Sciences de l'Ingénieur pour l'Environnement, Université de La Rochelle, France, klimam01@univ-lr.fr

Abstract

This study intends to predict numerically the ventilation and dispersion of an airborne contaminant into a subway station, and to validate these numerical predictions with an experimental database of both field tests and laboratory tests on a scaled station. The toxicity assessment will allow the public transport companies and the medical services to adapt their detection infrastructure and emergency procedures.

One subway station is used as a test case to perform CFD simulations, where the ventilation is only realized by the piston effect caused by the train movement, that is simulated numerically. A simplified geometry of the station is used to implement a scenario of a train passing through the station, with dynamic meshing techniques.

Experimental measurements in the station, with a hot wire for the air velocity and a LiDAR laser for the metro distance, intend to validate the results of the CFD simulations. Elements of the literature mention various sources influencing air flow in the station; the piston wind is one of them, but the weather conditions, the presence of people on the platform, the general air circulation through the tunnel network are also likely to have an influence. The similarity issues of building a small scale model of the station, allowing to perform repeatable PIV measurements in a controlled environment and with a running train within it, are discussed. The experiments will allow the verification of simplifying assumptions for our model, so a validated model could finally be used to calculate different scenarios and feature contaminant dispersion.

Keywords: subway climatology, train, piston effect, CFD, dynamic mesh, PIV, scale model

1. Introduction

1.1. Context

The air quality inside underground public transportation infrastructures faces a growing interest, to maintain a safe and healthy environment. In particular, recent events have demonstrated the vulnerability of these indoor environments to potential terrorist attacks in the form of toxic chemicals release [1]. Valuable instruments to anticipate the consequences of such attacks are the identification and analysis of representative scenarios, allowing a better preparation of the health and emergency services as well as the adaption of our infrastructures.

To tackle these issues, a comprehensive understanding of the airflow in subway stations is necessary. Subway station environment is peculiar in terms of

climate, as part of the built environment open to overground climate and the underground network formed by the tunnels and the stations. This duality, coupled with the high computational resources required to simulate numerically a moving object through a large domain, makes the elaboration of models a complex topic.

In addition, confidence in such models can only be achieved through coupling with experimental validation. The global objective of the present research is therefore to obtain a validated numerical model for contaminant dispersion scenarios in a subway station. Airflow, mainly related to trains passing through the station, is first considered and simulated using Computational Fluid Dynamics (CFD) techniques, and the results are compared to the ones obtained through measurements in a real station. A small scale replica of the same station is designed, in order to use Particle Image Velocimetry (PIV) to observe and compare the flow fields to the ones given by the numerical simulations.

1.2. Previous works

1.2.1. Contaminant dispersion in indoor environment and subway climatology

Following the malicious release of a contaminant in a public space, the rapidity of the emergency response is critical [2]. In the past three decades, various studies have investigated the question of airborne contaminants dispersion and their temporal development in a subway station, in order to better anticipate their consequences. A thorough literature survey about the mechanisms of indoor contaminants was carried out by Gant *et al.* [3]. They listed thermal effects, wind and infiltration, movement (breathing, movement of people and doors), humidity and turbulence as some of the most important factors controlling the indoor distribution of gases and aerosols. Endregard *et al.* [4] simulated the emptying of a sarin bottle in the ventilation shaft of a large convention center, a highly toxic nerve agent that was used in the infamous Tokyo 1995 attack that caused mass casualties [1]. They provided results in the form of sarin concentration fields and number of potential victims up to 50 minutes after the release, and addressed the emergency management challenges: alarm and response time, detection and identification of the toxic agent, rescue operations and decontamination of victims.

With the same issues in mind and aiming to differentiate between safe and unsafe emergency routes regarding a rescue, Pflitsch *et al.* [5] undertook tracer gas measurements in two complex subway stations to better understand the temporal and spatial aspects of dispersal. While some escape routes became insecure shortly after the release, at least one safe exit in each case remained uncontaminated over a period of time making self-rescue possible. As well using tracer gas measurements, Brüne *et al.* [6] noted that staircases in subway stations are sucking air from the lower parts of the structure. In a Berlin station, coupled with pedestrian simulations, Charlton & Brune [7] have highlighted that the most intuitive ("go up and take the nearest exit") escape routes may not be the safest ones. They recommend that an optimal evacuation system would be a dynamic one, adapting to the location of the contaminant and the subway climatology at the time.

In another work from Pflitsch *et al.* [8] measurements were performed in a Newcastle upon Tyne complex station at night, to assess the different contribution to airflow independently of train operation. With all fans of and doors closed, an airflow velocity of 0.5 m/s to 1.5 m/s was observed on the platforms. This phenomenon is called background airflow, in opposition to the train-induced flow which is observable for only one or two minutes after the passage of a train. Air behaviour in the station is also affected by several factors that differ with the station architecture: presence and operation of escalators, activation of mechanical ventilation, position of the station gates... Fortain [9] has also pointed out source discrimination as a limit to the measurement and modeling of particles in a Parisian subway station at night, including when a train is running. She was able to study independently the activation of the ventilation, the presence of people in the station and the passage of train, but obtaining reproducible signals is a challenge.

Waymel [10] simulated the mass flow rates through different surfaces of a Parisian subway station after 5 passages of train in two directions to evaluate thermal comfort of the passengers and found a periodicity related to the train passage frequency appearing in the results. A substantial work of particulate and gas concentration measurements in 10 stations in Barcelona was led by Moreno *et al.* [11], and evidenced the influence of train length, speed, tunnel length and station design on train-induced wind. Monitoring underground particulate concentration in a Parisian station during a week, Walther *et al.* [12] identified piston effect and ventilation as key phenomena affecting the dilution mechanism of particles.

1.2.2. Piston effect and its numerical models

Most of the studies including train operation indeed agree on the fact that a major contribution to ventilation in subway stations is performed by the piston wind. This phenomenon appears when a train travels through a narrow tunnel, and the air pushed by the train cannot completely flow to the rear end of the train; a positive pressure volume is formed at the front, while a negative pressure and highly turbulent region appears behind the train [13]. Those changing pressures on top of ambient wind cause flows with varying directions and intensities. The resulting flow velocities, monitored at the entrance and the exit of a scaled tunnel by Kim & Kim [14], are visible in Figure 1.

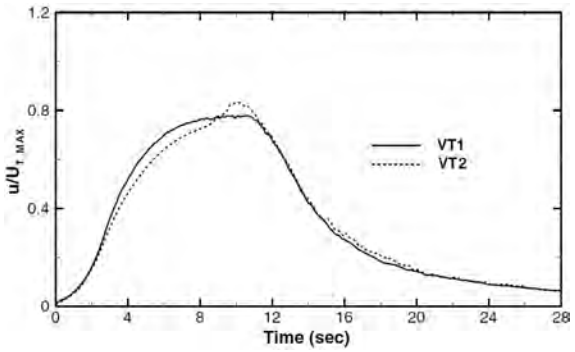

Figure 1: Variations of non-dimensional axial velocity with time at the tunnel entrance (VT1) and exit (VT2), from [14]

Through momentum balance equations, W. G. Brown [15] gave a developed expression for air velocity in tunnels of different lengths, and calculated that the air velocity in the tunnel can reach about 3 m/s for a train running at 15 m/s speed in a double-track tunnel. Xue *et al.* [16] and Cross *et al.* [17], [13] have used dynamic meshing techniques in CFD models to simulate the flow velocities induced by train passing through a station and in a tunnel, respectively. Cross *et al.* validated their results using different versions of the small scale model designed by Kim & Kim [14], and Xue compared the numerical models with flow velocities measurements near the exits – a staircase away from the platform – of a subway station in Shenyang and obtained maximal velocities of 0.8 to 1.4 m/s for a train entering the station at 20.68 m/s. Both obtained a very good agreement between the model and the experiments, but it is hard to draw a link between the studies, as they consider very different architectures.

Velocity can be made comparable using a velocity coefficient $u/u*$, where $u*$ is a reference velocity, in this case the maximum train velocity, *i.e.* the cruise speed of the train in the tunnel before it brakes while arriving in the station. Out of the different parameters influencing the magnitude and the temporal evolution of the piston wind, the blockage ratio β can be used to compare tunnel and station design in a non-dimensional form. It is defined as the ratio of the train and tunnel cross-sectional areas:

$$\beta = \frac{A_{train}}{A_{tunnel}} \tag{1}$$

Cross *et al.* [17] for instance studied the influence of blockage ratio on tunnel outlet velocities. They observed that during acceleration and deceleration phases, higher blockage ratios translates into steeper and earlier variations in the velocities, and that the maximum attained velocity is higher. During the constant velocity phase, increasing blockage ratio from 0.65 to 0.85 results in an increase of 36% in the outlet velocity.

1.2.3. Production of experimental data

For some studies and depending on the factors of interest, several adaptations of normal operation and schedule of the subway station were made possible for on-site measurements: measurements at night ([6], [5], [7], [9], [8]) with presence of a group of people or of a train executing predefined scenarios ([9]), tracer gas release in the station ([6], [7], [8]) and in the train ([6]), activation or deactivation of mechanical ventilation ([8], [11]), opening or closing the relief shafts ([16]) or the station's gates ([8])... However, the cost of these measures in terms of coordination with public services, staff involved, compliance to procedures, etc, is generally high, and the site is usually available only for a very limited time period. Depending on the case, a limited number of parameters can be controlled, or not, affecting the reproducibility of the results obtained. Since the measurements are always taking place in an already built infrastructure, Pflitsch *et al.* [8] underlined that additional and extensive measurements are needed to obtain a comprehensive understanding of airflow in subway underground networks.

In his review of tools used to predict ventilation performance in buildings, Chen [18] argues that small scale experimental models are generally less expensive than the full-scale experimental model. For this reason, small scale models are still often used, despite difficulties in modeling simultaneously inertial and buoyancy forces. In addition, they can allow more control on the experimental conditions, and can

also provide excellent flow visualization by using PIV techniques.

In their highly-cited study to validate a numerical simulation of piston effect, Kim & Kim [14] have used pressure probes and a model of a train in a tunnel at scale 1/20, featuring a 33 m long tunnel that allowed to keep the Reynolds number based on the hydraulic diameter of the tunnel close to the full-scale case. Their findings were subsequently used by various authors ([17], [16]) to compare numerical simulation results. Gouriet [19] designed a scale-model test facility for a train at scale 1/87 in a circular section tunnel. Even though the study was focused on high-speed trains (100 to 250 km/h), he made the choice to conserve the blockage ratio of 0.14 from the full-scale case to the small scale.

Going at smaller scales makes it difficult to obtain the same Reynolds and Grashof numbers, which are necessary to achieve flow similarity between a small scale experimental model and a complex actual subway station [18]. Thus, in situ measurement data and scale-models must complement each other to validate the numerical models.

2. Methodology

For this study, one metro station in a Belgian major city is taken as a test case. In this parallelepipedic station, there are no corridors, just straight staircases to the outside, and the ventilation is only realized by the piston effect caused by the train movements and temperature-gradient induced wind. The architecture of the station including a part of the tunnel on both sides – 150 m upstream and 100 m downstream – is implemented in a numerical model (see Figure 4). Transient two-dimensional (2D) and three-dimensional (3D) computational fluid dynamics simulations with Reynolds-averaged Navier-Stokes (RANS) equations were used to model the airflow in the station related to a train arriving, stopping and departing. Validation of the numerical results is sought through experimental measurements of air velocity in the actual metro station and with a small scale model.

2.1. Test case

The station is 95 m long and symmetrical with respect to the double-track rails, including one platform on each direction of the metro line, forming a cross-shaped cross section detailed in Figure 2. Six exits, three on each side, are separated from the outdoor pressure by a straight staircase. In the vicinity of the station, the tunnels are 4.1 m high and 6.17 m wide on both sides. The train is 90 m long and has a rectangular cross-section of 3.5 m in height and 2.7 m in width. These dimensions give a blockage ratio of 0.37 and 0.21 for the train in the tunnel and in station, respectively. The train speed in the tunnel and at the arrival in the station is 10 m/s, and the corresponding Reynolds number based on the hydraulic diameter of the train in the tunnel is in the order of 10^7.

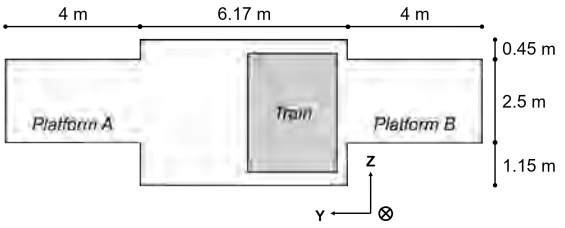

Figure 2: Cross-section of the station geometry

The base scenario taken for the study is the one of a subway train, arriving at a constant speed of 10 m/s through the tunnel. The deceleration is a second order polynomial fitted through the average on-site laser distance measurement (see Section 4.1), as well as the stop duration in the station that lasts 30 seconds. The train is then accelerated at 1.0253 m/s^2 for 10 seconds, computed from the observed departure time of the train, to reach its cruising speed of 10 m/s when exiting the station.

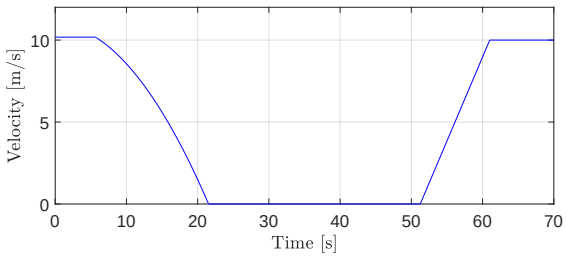

Figure 3: Schedule of train run through the station

The train is initially positioned in the tunnel, with the front of the train 58 m from the station entrance, i.e the tunnel exit portal. The final position of the train is with the rear of the train 10 m from the station entrance, i.e the tunnel entrance portal. The total travel time and distance are 66 s and 253 m, respectively.

2.2. Modeling assumptions

Sections 1.2.2 and 1.2.3 have underlined that on a timescale in the order of a minute, piston wind is the

primary force of the airflow from the tunnel, and the turbulence induced on the platform is transient and complex [16]. Therefore, some simplifying assumptions must be made for quantitative analysis:

- For the numerical and small scale models, we only evaluate a case where a train is running in one direction of the double-track tunnel and station, and there is no train arriving or departing in the other direction.
- The train movement is considered to be the only factor affecting the flow field of the station. In most studies indeed, the influences of mechanical ventilation [16], pedestrian behavior or the effect of heating due to people [4] are not considered. The impact of these effects are deemed of lower magnitude than the train-induced airflow, and it is expected that taking a sufficient number of measurements will make these short-term, temporary and irregular phenomena fade in the average.
- A simplified geometry is adopted for the numerical model and for the small scale model. Structures and objects are removed for similar reasons as those given in the previous point, allowing not only to decrease the computational power required and to simplify the manufacture of the model, but also to make the results more easily comparable to literature and to other station architectures.

Interesting quantities to monitor are the air velocity at given points in the station, at which the experimental measurements are performed.

3. Numerical simulations

The station architecture described in Section 2.1 is reproduced numerically using a Computer Aided Design (CAD) software. The geometry includes 150 m of upstream tunnel and 100 m of downstream tunnel. The internal domain of the station is meshed using the integrated mesher of ANSYS Workbench (2020 R2) and the computational model was solved using the commercial CFD software ANSYS Fluent (2020 R2), with mass conservation and RANS equations for incompressible, transient flow. The six exits and the tunnel extremities are set to atmospheric pressure inlets/outlets.

The dynamic mesh approach used in this model is similar to Cross' [17], [13] and Xue's [16] ones. The

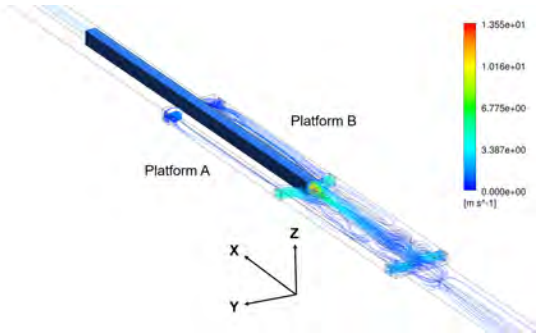

Figure 4: 3D CFD model and streamlines originating and terminating in the outlets (train leaving the station)

train movement through the station, including deceleration, stop, and acceleration as detailed in Section 2.1 and shown in Figure 3 is controlled by an User-Defined Function (UDF). As the train moves, the fluid calculation area delimited by the station walls and the train car boundaries changes. The mesh is hence updated by Fluent at each time step of the train motion. In order to permit a correct remeshing process, the displacement of the train between consecutive time steps should not exceed the mesh cell dimensions. A time step of 0.001 seconds is found to be sufficient while the train is moving; it can be increased to 0.1 seconds when the train is stopped in order to speed up the calculations.

In this study, the k-ε turbulence model is chosen as it was previously used for the simulation of train-induced airflows where it performed well [14], [16]. The continuity, momentum, k and ε residual equations are monitored. Additionally, the velocity at various points on the platform is recorded, for later comparison with the experimental measurement points.

3.1. 2D model

The 2D domain, representing a horizontal cut section located 1 m above platform level, is meshed with a tetrahedral unstructured grid, with a cell size in the station set to be 0.1 m. An enclosure of 30 cm thickness with a cell size 0.03 m is formed around the train walls, so that smaller cells were concentrated around the train to provide sufficient resolution in these regions and larger cells far from the train in order to improve computational efficiency [17]. The meshed domain contains a total of 805 000 elements, and its structure is visible in Figure 5. The results of the 2D simulation, for the velocity at three points along the platform, are available in Figure 6.

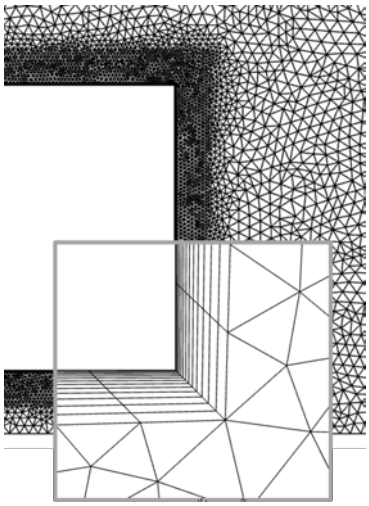

Figure 5: 2D mesh around the front of train and in station with detail of the bottom right corner of the train

3.2. 3D model

The 3D model is similar to the 2D one, with the difference that the mesh does not include the enclosure around the train, as the cells have more degrees of freedom to deform themselves and keep an acceptable skewness; however the remeshing conditions are made stricter to prevent excessive deformation of the cells. The 3D model contains 2 millions cells of target size 0.3 m. A mesh sensitivity analysis performed with a 0.15m grid size has provided the same results. The results of the 3D simulation, for the pointwise velocity at the same locations as in the 2D simulation, are available in Figure 7. The velocity contours and vectors in a horizontal plane around the train body are visible in Figure 8. Streamlines originating and terminating in the outlets are also displayed in Figure 4.

3.3. Discussion of the CFD results

All measurement locations are showing one first peak appearing in the velocity as the front of the train passes the measurement point (t = 6 s for the entrance of the station for instance), followed by a second, smaller peak after the rear of the train passes (t = 19 s). Similarly, two peaks are observed when the train is leaving. In the 3D results (Figure 7), for the station entrance the highest velocity is observed when the train is entering the station, whereas for the station exit the highest velocity comes when the train is leaving the station, which is logical given the expected pressures induced by the train movement described in Section 1.2.2. It is also visible within the velocity contours (Figure 8) that the velocity of the air surrounding the

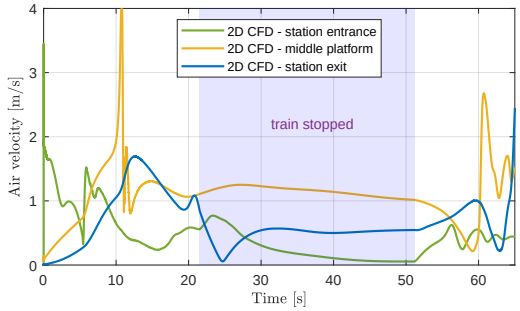

Figure 6: Airflow velocity at three locations on the platform (2D simulation)

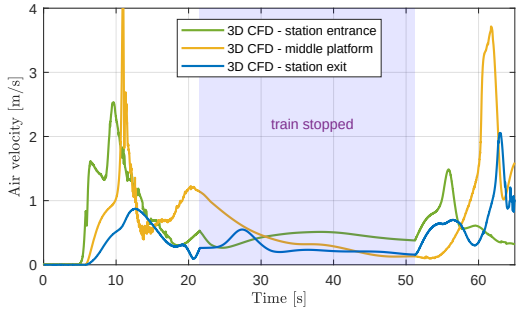

Figure 7: Airflow velocity at three locations on the platform (3D simulation)

train body closely changes in function of the train velocity. During the stop time of the train, it is the inertia of the air previously set in motion that maintains the air movements all across the station [10]. However, it is hard to conclude whether the behaviour regarding air velocity described by Kim & Kim [14] is observable here, as the presence of the station heavily influences the results of the performed simulations, since air has the possibility to leave the station in the used model through the access doors.

Overall, the velocity magnitudes monitored are higher in the 2D simulation that in the 3D simulation. This could be explained by the fact that in the 3D model, the air pushed and carried by the train has more ways to discharge (above and below the train) than in the flat model. However, the differences between the 2D and 3D go beyond just the magnitude of the velocity, as temporal differences are also to be noted, and seem to indicate that the 2D will not predict accurately the flow state in the station, despite having shorter computational time.

The air inside of the station next to the train can be divided into three zones, as it can be observed from

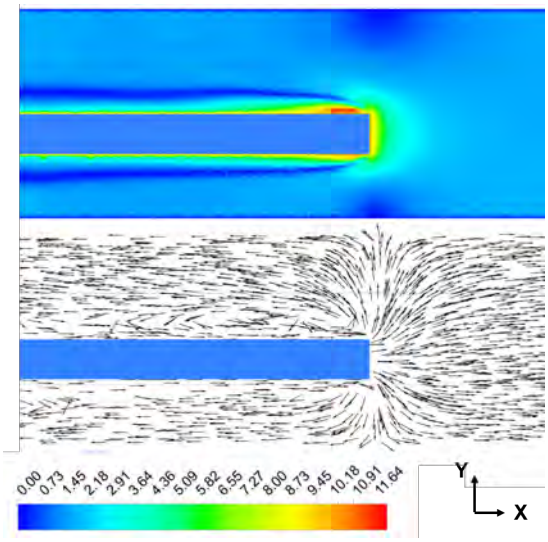

Figure 8: Velocity contours and vectors around the front of the train (3D simulation)

Figure 8. The first layer, closest to the train, flows in the same direction as the train; a second region has very low velocity magnitude; and lastly a region flows in the opposite direction of the train's motion close to the walls of the subway station. If confirmed by experiments, this behaviour could be interesting in terms of most dangerous or safest zones with a contaminant dispersing in the station.

The very beginning of the point velocities exhibit strong variations; and in the same way, it is unclear during the departure of the train whether the velocity is realistic or is coming from the train reaching a boundary of the domain. In fact in the CFD model, as the train starts at its beginning position, all of the air surrounding it is stationary while in reality the air flow around the body would be completely developed as the train has been travelling long enough through the tunnel. The numerical domain far-field limits in our case, the upstream tunnel length – necessary to obtain a boundary independent solution should be studied and determined. These results will be furthermore discussed when compared to the experimental data for the station entrance and exit locations in Section 4.2.

4. On-site velocity measurements

4.1. First measurement campaign (December 2019)

Air velocity measurements have been conducted in the station at several locations along the platform for one direction, including points close to the tunnel exit (entrance in the train of the station) and entrance (exit of the train from the station), using a hot wire anemometer, coupled with a LiDAR laser measuring the distance between the front of the train from the exit side of the station. As measurements were taking place during the daytime, a condition for the whole setup was that it should absolutely not disturb the train operation, and minimize the impact on passenger's experience. The measurements probes should hence be kept of a reasonable size and away from the train doors when stopped in the station; cables on the platform should be avoided when possible. The side on which platform the measures were taken and the opposite side are arbitrarily named B and A, respectively (see Figure 2).

The time at which the train enters and exits the station is observed and written down; these values should however be treated carefully as their uncertainty can be of a couple of seconds. The results are ensemble averaged based on the distance from the LiDAR for all trains passage recorded on the measurement side, regardless of a train potentially arriving, stopped or leaving on the other side. This deviating scenarios from what was aimed for the models in Section 2.2 is also not ideal and could bring major errors to the results. The main objective of this preliminary campaign was to gain experience with the set-up and mitigate the risks for a full-scale campaign.

4.2. Comparison of experimental and CFD results

The results of on-site velocity measurements, 2D and 3D recorded velocity, and distance measurement by the LiDAR are displayed below, for two measurement locations on the platform: one next to the tunnel at the entrance of the train station in Figure 9, and one next to the tunnel at the exit of the train in the station in Figure 10. It is also to be noted that experimental data started to be recorded when the train was at an earlier position (further away in the tunnel before the station entrance) than the initial position of the train in the numerical model to observe how early the flow in the station gets affected by the train. In the following plots, the CFD simulation starts at t=25 s and the train enters the station at time t=30.75 s.

The influence of the CFD initial flow state discussed in Section 3.3 is less prominent around the exit of the station, and the peaks in velocity mentioned in Section 3.3 that seems to result from the air pushed in front of the train and sucked in the rear are aligned in the CFD and in the measurements. At both locations, a strong increase in the velocity is also measured already before the train enters the station, indicating that

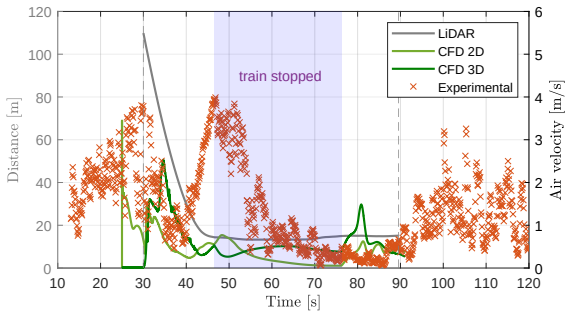

Figure 9: Experimental and numerical air velocities at the station entrance

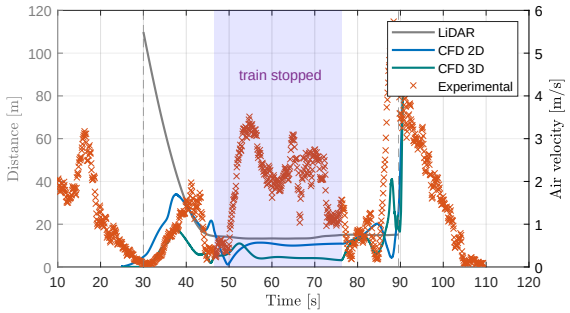

Figure 10: Experimental and numerical air velocities at the station exit

both CFD and data acquisition should start when the train is still travelling in the upstream tunnel.

For both locations, the stop time of the train exhibits a poor correlation, as the velocity is almost constant or slowly decreasing in the CFD, while there are a lot of variations in the experimental data, especially at the exit location on Figure 10 where an additional peak is visible while the train is stopped. This challenges the hypothesis made in Section 2.2 that the piston is the main cause of air flow in the station, but major a source of uncertainty comes from the fact that only 3 to 5 datasets were available for the average. Trains arriving on the A side, or strong variation of external weather conditions such as wind, especially as both measurement points are located near station exits, could explain this behaviour. Measurements should be performed at a location far from the exits to eliminate the influence of outside wind, and data should be also recorded in between trains passages, to evaluate the ambient velocity in the station.

The experimental-to-CFD comparison seems promising, but as the numerical model remain imperfect and the on-site experimental results are bounded to high variability, it is difficult to identify where the pressure waves causing air velocity changes originate from.

4.3. Second measurement campaign (ongoing)

To correct some of the problems that arose in the first measurement campaign, a second measurement campaign is undertaken. Extensive measurements during 9 days, with one different measuring location per day, are conducted. The experimental setup contains the same features as in the first measurement campaign, but it includes additionally an automated detection of the trains presence in the station, and upstream detection of the train in the tunnel.

The measurement locations include five positions evenly spaced along the X direction. For two of these positions that are as far as possible from the exits, two more measurement locations are added on transverse lines (in the Y direction on the platform). Emphasis was also put on making the experimental conditions as close as possible to what we can simulate with the CFD model. Scenarios are defined with trains passing either on the A side, the B side, or both, and only datasets with trains fulfilling one the scenarios are recorded and saved.

The chosen scenarios are clearly distinct and likely to be observed approximately 30 times for each location during the on-site measurements. This new experimental protocol, assisted by setup features, is expected to improve significantly the repeatability of the events, as well as the statistical accuracy.

5. Small scale model of the station

To fully control the environment in which the experiment is performed and obtain a visualization of the complete flow field in the station, a small scale model of the station in plexiglas including a train moving through it is built. The design and the operation of such a model implies that we have to deal with scaling and similarity issues.

The model must be kept small enough to perform PIV measurements; the longer dimension of the area of interest - here, the length of the station - should then not exceed one meter, and the total length of the model including a representative portion of the tunnels should fit in the lab and not exceed 4 meters. The target scaling hence lies around a 1/100 ratio. At this scale, a complete matching of the dynamic similitude parameters is not possible and would lead to unrealistic flow features around the train; for example, the conservation of Reynolds number would require a supersonic speed for the model train. Emphasis is rather

given on the Mach number and the blockage ratio that control the piston effect and to temporal similitude by reproducing the time spent by the train in the station.

For simplicity of operation and fidelity to design, a commercial model train is used as the small scale train. Because an exact replica of the real subway train type was not available, the dimensions of the small scale station are computed in order to keep the blockage ratio similar to the full-scale case. The resulting scaling factors are of 1/100, 1/77 and 1/73 in the X, Y and Z directions respectively. One meter of tunnel is added on each side of the station.

The sampling of the flow necessary to have the right statistical quantities to perform TR-PIV depends on the geometrical and optical parameters of the model as well as on the flow characteristics. A schematic view of the PIV setup is visible in Figure 11.

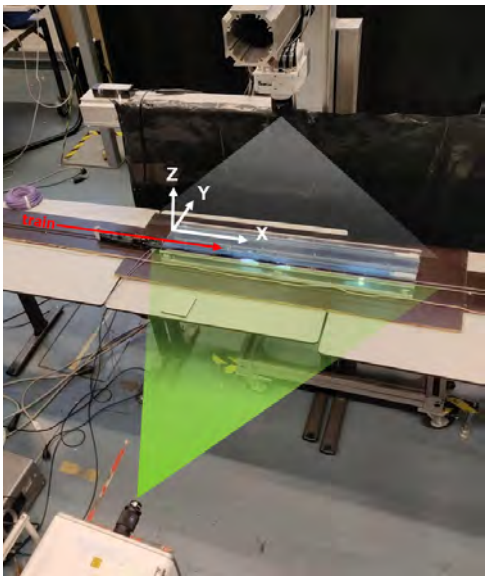

Figure 11: PIV setup: small scale model of the station, laser sheet (green), camera field of view (white) and direction of train (red)

The control of the train speed, through the voltage supply of the rails, to achieve repeatability while running the same experiments several times, must still be perfected, especially as distance sensors considered in a first approach (LiDAR laser) cannot function through the seeding. Image treatment will allow to detect the position of the train to perform ensemble averaging on the flow fields acquired.

6. Conclusion

6.1. Discussion of the results

Finding indicators to observe the complex flow field induced by the passage of a subway train into a station is challenging, especially as results can differ widely from one case to another. In this study, on-site measurement of air velocity in this station were made possible, but they only allow a pointwise measurement and are influenced by many factors, such as the weather conditions or the fact that not all subway trains have the exact same speed since they are operated by humans. In order to get measurement data satisfying the criteria for reproducibility and repeatability, a small scale model of the same station is built and this ensures that we fully control the environment of the experiments and that we can repeat the same scenario multiple times. Improved and extended on-site measurements will also be conducted.

Strong differences between the CFD results and the experiments make it hard to conclude on a successful modeling of the passage of a subway train in the station. From the observation of the first results, it is possible to draw guidelines for improvement of the numerical model: extension of the domain far-field limits and analysis of the sensitivity to those boundaries, parametric study to assess the influence of external conditions and of the geometry, and simulations with the tunnel only to provide data comparable with the literature. Simulations of a train running at constant speed in the tunnel show that at least 30 meters are necessary to obtain a stable flow around the train, meaning that the first 30 meters traveled will only represent the numerical effects, and not the reality. To account for the flow disturbance in the station as the train is still in the tunnel, that additional tunnel length should be considered. The new implementation of these findings will be used to compute the scenarios listed in Section 4.3 and observed in the second measurement campaign, to allow a more accurate comparison with the experimental measurements, and to gain confidence in the accuracy of the numerical model.

6.2. Further work considerations

Once a satisfying match between the models and the real station is reached for the airflow, it will be possible to incorporate a source of contaminant and to investigate other characteristics of the spreading. In the work presented here, air velocity at given locations was taken as the main indicator, as it can provide comparison material with the experimental data. Air velocity distribution along the waiting line on the

platform, mass flow rates reaching a certain location on the platform and leaving the station, and airflow volumes displaced are also proven to be relevant in case of contaminant dispersion [17].

As recalled in Section 1.2.1, the simulation of background airflow is not necessary for the considered time period in our models; however, this contribution could be of great importance in the case of contaminant release scenario, where the train would be stopped in the station following an emergency procedure. Pflitsch also noted in a later study [5] that orography, meaning the altitude differences within the tunnels-stations systems, is the main influencing factor on these background currents. The direction of these currents can be predicted based on background weather conditions information.

This last consideration highlights again the complexity of conducting accurate computation in large underground networks. Dynamic meshing techniques were chosen as a first approach for its simplicity of implementation, but Waymel [10] suggested that sliding mesh or overset mesh techniques could reduce significantly the calculation time, avoiding the regeneration of the whole mesh at each timestep. Coupled 1D-3D models, such as the one developed by Prince [20], could be relevant to simulate larger domains while keeping the computational power required reasonable. This could help getting more reliable models for subway stations become, supported by strong empirical data, that will support the decision-making to develop response procedures and staff training, and lead to the minimization of casualties.

Acknowledgments

The authors would like to acknowledge STIB-MIVB and their employees for their collaboration, as well as Isabeau Sabbe and Joren Vanlaere, master students from the Vrije Universiteit Brussel, Belgium, Fabio Verhulst, master student from the Royal Military Academy, Belgium, and Abderrahmane El Hanafi, intern from the Institut National Polytechnique de Toulouse, France.

References

[1] A. T. Tu, Chemical Terrorism: Horrors in Tokyo Subway and in Matsumoto City, Alaken, Inc., 2002.

[2] A. J. Policastro and L. R. Coke, The use of technology in preparing subway systems for chemical/biological terrorism, in: Proceedings of the 1999 commuter rail/rapid transit conference, Washington, DC, 1999, pp. 226–234.

[3] S. Gant, A. Kelsey, N. Gobeau, Factors influencing the indoor transport of contaminants and modelling implications, PR HSL/2006/29, Health & Safety Laboratory, Buxton (2006).

[4] M. Endregard, B. A. P. Reif, T. Vik and O. Busmundrud, Consequence assessment of indoor dispersion of sarin – A hypothetical scenario, Journal of Hazardous Materials 176 (2010) 381–388.

[5] A. Pflitsch , M. Brüne , M. Killing-Heinze , J. Ringeis , B. Agnew and B. Steiling, Natural Ventilation as a Factor Controlling the Dispersal of Airborne Toxins in Subway Systems in a Disaster Situation, Journal of Transportation Safety & Security 5 (1) (2013) 78–92.

[6] M. Brüne, J. Spiegel, K. Potje-Kamloth, C. Stein and A. Pflitsch, Tracer gas experiments in subways using an integrated measuring and analysis system for sulfur hexafluoride, Journal of Sensors and Sensor Systems 5 (2016) 381–388.

[7] J. Charlton and M. Brune, Towards a dynamic evacuation system: developing methodologies to simulate the evacuation capabilities of subway stations in response to a terrorist attack with CBRNE weapons, in: Proceedings of the 32nd eCAADe Conference, Newcastle upon Tyne, 2009, pp. 109–118.

[8] A. Pflitsch , M. Brüne , B. Steiling, M. Killing-Heinze , B. Agnew, M. Irving and J. Lockhart, Air flow measurements in the underground section of a UK light rail system, Applied Thermal Engineering 32 (2012) 22–30.

[9] A. Fortain, Caractérisation des particules en gares souterraines, Ph.D. thesis, Université de La Rochelle (2010).

[10] F. Waymel, Modélisation des effets thermiques et aérauliques dans les stations de métro, Ph.D. thesis, Université de Valenciennes et du Hainaut Cambrésis (2002).

[11] T. Moreno, N. Pérez, C. Reche, V. Martins, E. de Miguel, M. Capdevila, S. Centelles, M.C. Minguillón, F. Amato, A. Alastuey, X. Querol and W. Gibbons, Subway platform air quality: Assessing the influences of tunnel ventilation, train piston effect and station design, Atmospheric Environment 92 (2014) 461–468.

[12] E. Walther and M. Bogdan, A novel approach for the modelling of air quality dynamics in underground railway stations, Transportation Research Part D: Transport and Environment 56 (2017) 33–42.

[13] D. Cross, B. Hughes, D. Ingham and L. Ma, Enhancing the piston effect in underground railway tunnels, Tunnelling and Underground Space Technology 61 (2017) 71–81.

[14] J. Y. Kim and K. Y. Kim, Experimental and numerical analyses of train-induced unsteady tunnel flow in subway, Tunneling and Underground Space Technology 22 (2) (2007) 166–172.

[15] W. G. Brown, Basic theory of rapid transit-tunnel ventilation, in: IEEE Railroad Conference Proceedings, Pittsburgh, 1965.

[16] P. Xue, S. You, J. Chao and T. Ye, Numerical investigation of unsteady airflow in subway influenced by piston effect based on dynamic mesh, Tunnelling and Underground Space Technology 40 (2014) 195–206.

[17] D. Cross, B. Hughes, D. Ingham and L. Ma, A validated numerical investigation of the effects of high blockage ratio and train and tunnel length upon underground railway aerodynamics, Journal of Wind Engineering and Industrial Aerodynamics 146 (2015) 195–206.

[18] Q. Chen, Ventilation performance prediction for buildings: A method overview and recent applications, Building and Environment 44 (2009) 848–858.

[19] J.-B. Gouriet, Aerodynamics of trains, PR 1999-16, von Karman Institute for Fluid Dynamics (1999).

[20] J. Prince, Coupled 1D-3D simulation of flow in subway transit networks, Ph.D. thesis, Imperial College London (2015).

Application of improved CFD modeling for prediction and mitigation of traffic-related air pollution hotspots in a realistic urban street

Tom Lauriks

Environmental and Applied Fluid Dynamics Department, University of Antwerp, Belgium, tom.lauriks@uantwerpen.be

Supervisor: Jeroen van Beeck

Dean of the Faculty, Head of the Department and Professor, Environmental and Applied Fluid Dynamics Department, von Karman Institute for Fluid Dynamics, Belgium, vanbeeck@vki.ac.be

University Supervisor: Siegfried Denys

Professor, Bioscience Engineering Department, University of Antwerp, Belgium, siegfried.denys@uantwerpen.be

Abstract

Urban air pollution severely affects human health. NO_2 and PM_{10} traffic emissions were studied in an Antwerp street, through CFD, using an ABL simulation RANS approach and variable turbulent Schmidt number. Validation was performed using field data. Pollution hotspots occurred, where high buildings restrict natural ventilation. Two remediation measures, wind catchers and electrostatic precipitation, substantially reduced concentration at the hotspots.

Keywords: urban air pollution, computational fluid dynamics (CFD), mitigation, natural ventilation

1. Introduction

Both in recent and historical times, pollutant dispersion within the urban canopy has severely affected public health and led to other relevant environmental issues [28]. For example, NO, NO_2, particulate matter with an aerodynamic diameter smaller than 2.5 μm ($PM_{2.5}$), and particulate matter with an aerodynamic diameter smaller than 10 μm (PM_{10}) have all been associated to adverse health effects [5, 7, 36, 89]. In fact, NO and NO_2 are frequently combined into the term NO_x [49] and PM_{10} and $PM_{2.5}$ are relevant subdivisions of particulate matter (PM) [90]. According to the latest numbers of the EEA [23], road transport causes 39 % of the European NO_x emissions and 15.8 % and 14.4 % – respectively – of the primary $PM_{2.5}$ and PM_{10} emissions [21]. As a consequence, studying traffic emissions in urban environments both for NO_x and PM remains a meaningful task.
In this regard, data suggests that the concentration of PM as air pollutant in human settlements was approximately stable on a global scale in the period 2010-2016, but that it was decreasing in the Americas and Europe. However, for solid conclusions, more detailed analyses are necessary [91]. Considering NO_x, decreases are also observed in the last decades [22, 61]. Nevertheless, sixteen countries of the European Union (EU) still registered NO_2 concentrations exceeding the annual prefixed limit value [23]. In addition, the number of measurement stations upon which the European Environment Agency (EEA) statistics are based is limited [24]. As a consequence, more detailed measurements are needed, both for NO_x and PM.
For example, in Flanders (Belgium), yearly average NO_2 concentrations exceeded the European limit value in 2017 at only one measurement station [82]. These considerations are however based on just 51 measurement stations, and the actual situation could be more alarming. Fig. 1 (a) demonstrates the scarcity of these measurement stations in the center of Antwerp, in Flanders. Modeling results (e.g. Fig. 1 (a) of VMM [83]) and local measurement campaigns (e.g. Fig. 1 (b) of Meysman and De Craemer [57]) indicate that at many other locations with heavy traffic, the annual average European limit value

for NO_2 of 40 g/m^3 was exceeded [82]. This further emphasizes the need to investigate air pollution more in detail on district scales.

In this study, the main focus was on the evaluation of the pollution level on a very detailed spatial scale in a portion of the Turnhoutsebaan street of Antwerp. Its location is shown in Figs. 1 (a) and (b). Figs. 1 (a) and (b) also display previously established NO_2 concentrations in the Turnhoutsebaan [57, 83], however, on a less detailed spatial scale with respect to the one used in this study [1, 83]. Fig. 1 (b) suggests that the Turnhoutsebaan is clearly problematic regarding NO_2 concentration and that a more detailed analysis is necessary. Such a detailed analysis is also justified, considering the previous evidence of the strong heterogeneity of pollutant distributions within the urban framework [9] delivered by observations and measurement campaigns with a high spatial resolution performed in other cities [4, 10, 48, 55, 86].

Since strong concentration gradients occur in urban areas, applying local mitigation measures at concentration hotspots could substantially contribute to healthier cities. A number of possible local remedial strategies were listed [79], which consist mostly of some form of emission reduction. However, the majority of the proposed measures resulted in a limited benefit, or involved structural changes such as reducing the need for motorized trips. These structural changes will most likely not be a fast process [27, 69] and additional measures might be interesting. Possibilities include removal by vegetation, removal by photocatalysis, electrostatic precipitation, and adapting building geometries to enhance natural ventilation and dilution.

The controversial effect of vegetation on air pollution has already been extensively studied (e.g. [2, 12, 41, 73]). Vegetation can remove both gaseous [3] and particulate pollutants [40]. However, it also affects the velocity field which, in turn, can reduce the dilution process, negatively impacting the concentration level [85].

Photocatalysis, which involves the use of light and a solid catalyst, is capable of completely mineralizing many air contaminants [62], thereby converting them to products that are less harmful for human health and environmentally more acceptable [17]. It can decompose constituents of PM [17, 58], and remove NO_x from the air [59]. High removal percentages are typically obtained under laboratory conditions, e.g. [63, 77, 78, 87]. However, realistic atmospheric conditions can greatly reduce on-site photocatalytic

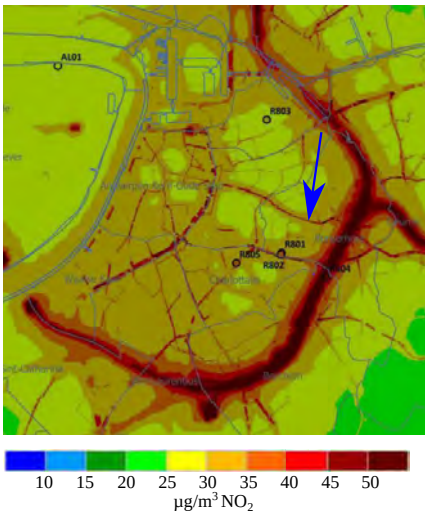

(a) Modeling results for yearly mean NO_2 concentrations in 2018 in Antwerp. The circles represent measurement stations. Adapted from VMM [83].

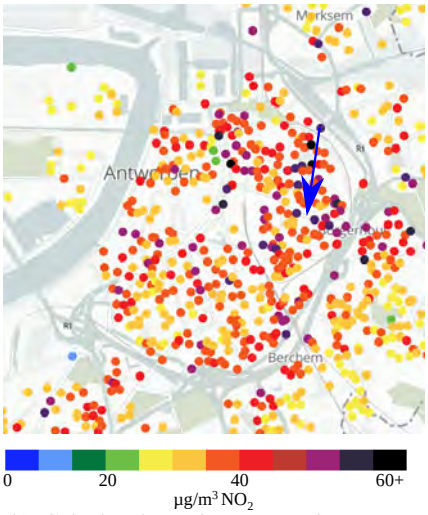

(b) Calculated yearly mean NO_2 concentrations from a one month measurement campaign. Adapted from Meysman and De Craemer [57].

Figure 1: Location of the Turnhoutsebaan (blue arrow) and air pollution indications in Antwerp (Belgium).

degradation [11, 31], which can be caused by fouling of the photocatalytic surface, and sub-optimal air flow rates and air humidities [54, 74, 92]. In addition, in an experimental scale artificial street canyon, an upper limit of 2 % NO_x removal was observed [32], which was attributed to limitations of transport of the pollutants to the photocatalytic surfaces. Besides, applying photocatalysis to purify air pollutants

can result in the formation of harmful by-products [32, 54, 74]. This should certainly be investigated more thoroughly before implementing large scale photocatalytic air purification in public spaces.
As for the local urban geometry/configuration, its significant role in influencing the wind flow [15, 71] and the pollutant concentration at lower heights [37, 43, 88] has already been demonstrated. Since the increase of wind speed is normally associated with a higher dilution process [39], a targeted design and modification of the urban geometry can be acknowledged as an interesting air pollution mitigation measure. A number of potentially beneficial building geometry adaptions have already been suggested [84] (e.g. an increase of street canyon permeability). However, only few studies investigated realistic urban configurations [75]. For example, only a couple of studies modeled the implementation of geometric changes for air pollution remediation in realistic urban cases [30, 42, 60]. Moreover, these measures were mostly suitable for incorporation into future planning, e.g. different shapes and orientations of entire building blocks [45]. Consequently, the application of realistically attainable geometric changes to an existing urban case has not yet been thoroughly investigated.
Finally, electrostatic precipitation (ESP) is a technology that efficiently removes small particles from a carrier gas [14]. Blocken et al. [9] modeled the removal of PM from semi-enclosed parking garages through ESP and the consequent effect on the surrounding urban neighborhood. The results indicated that PM concentrations could be lowered 10-50 % in the vicinity of the parking garages. Vervoort et al. [80] modeled the removal of $PM_{2.5}$ with ESP from the naturally ventilated courtyard of the American embassy school in Delhi. Up to 34.1% overall volume-averaged concentration reduction was obtained as model result. This technology is promising and interesting, especially in case emission reduction by other means is not possible and its effect in a realistic urban canyon was not yet investigated.

Using computational fluid dynamics (CFD) modeling, an extended area around a part of a connecting road (the Turnhoutsebaan) with a high traffic intensity in Antwerp was explicitly depicted and the dispersion phenomena related to vehicular traffic were studied in detail. Two main traffic-related pollutants were analyzed: NO_2 and PM_{10}. Due to the well known problems related to atmospheric boundary layer (ABL) simulations, a Reynolds-averaged Navier-Stokes (RANS) approach specifically for ABL simulations coupled to dispersion modeling using a variable turbulent Schmidt number Sc_t is employed. The model methodology was validated using both velocity and concentration data from a field campaign. Very localized pollution hotspots were identified. To lower the concentration at these hotspots, two local remediation measures were simulated. The first measure is a number of wind catchers located on the roofs of selected buildings, with the aim of redirecting the wind flow to dilute the pollutants. The second measure is the employment of ESP devices, which actively capture the pollutant, close to the hotspots. The main targets of this case study are:

1. to search for relevant traffic-related air pollutant concentration patterns of NO_2 and PM_{10} on detailed spatial scales in an urban street;
2. to employ different realistic and feasible mitigation measures that can be applied locally at pollution hotspots and to analyze their effect.

2. Methodology

2.1. Improved turbulence and dispersion modeling

CFD is considered as a powerful instrument for urban pollutant dispersion research [13, 52, 66]. Nevertheless, commercial CFD codes do not provide specific RANS turbulence models for ABL simulation [68]. However, a proper set of realistic inlet conditions and wall functions consistent with the turbulence model is required [67]. In fact, the lack of this consistency in ABL simulations is a well known problem [6]. This typically results in the rise of horizontal inhomogeneities in the velocity and turbulence profiles, as they travel from the inlet to the outlet of the domain [50, 64, 68], which can drastically affect the outcomes of the simulation.
In addition, when dealing with CFD dispersion simulations, the turbulent Schmidt number, Sc_t, which expresses the ratio of turbulent viscosity to turbulent mass diffusivity, has a relevant influence on the concentration field [19, 34, 52]. When dealing with atmospheric flows, typical values of Sc_t range between 0.2 and 1.3 [76]. The literature tends to prescribe this parameter as a constant quantity, without reporting a precise and definitive guideline for its specification [47, 52]. However, the variable nature of Sc_t has been repeatedly demonstrated [18, 20, 34, 35, 52, 70].

In regard of the mentioned ABL modeling issues, a $k-\epsilon$ turbulence closure specifically for ABL simulations was recently developed [50, 64]. This so called "comprehensive approach" is suitable for undisturbed flow fields and is based on a consistent deployment of realistic inlet conditions for the turbulent kinetic energy, k, the turbulence dissipation rate, ε, and the longitudinal mean velocity, U. Consequently, the turbulence model parameter C_μ is not kept constant but it is varying with height to locally match the turbulence level [65]. Finally, for the sake of consistency, a source term, S_ϵ, was introduced in the turbulence dissipation transport equation (Table 1). Following Parente et al. [65], it is possible to determine coefficients C_1 and C_2, which results in:

$$k(z) = 4.35u_*^2 - 9.1 \cdot 10^{-4} z \tag{1}$$

As for the wall treatment, a wall formulation based on aerodynamic roughness is employed [6, 52, 64]. The latter is able to automatically switch between a smooth and a rough treatment.

Table 1: Set of inlet conditions and turbulence variables for the "comprehensive approach" [50, 52]. u_*: friction velocity, κ: von Kármán constant, z_0: roughness length, ρ: air density, μ_t: dynamic turbulent viscosity and σ_ϵ, $C_{\epsilon 1}$, and $C_{\epsilon 2}$: $k-\epsilon$ model constants. See text for the other symbols.

Inlet conditions	Turbulence model
$U = \frac{u_*}{\kappa} ln\left(\frac{z+z_0}{z_0}\right)$	$\mu_t = C_\mu \rho \frac{k^2}{\epsilon}$
$k(z) = C_1 ln(z+z_0) + C_2$	$S_\epsilon(z) = \frac{\rho u_*^4}{(z+z_0)^2} \times \left(\frac{(C_{\epsilon 2} - C_{\epsilon 1})\sqrt{C_\mu}}{\kappa^2} - \frac{1}{\sigma_\epsilon}\right)$
$\epsilon(z) = \frac{u_*^3}{\kappa(z+z_0)}$	$C_\mu = \frac{u_*^4}{k^2}$

The presence of obstacles (buildings, trees or hills) is taken into account by the building infuence area (BIA) concept [44, 50]. The latter permits to automatically detect the obstacle through a deviation parameter δ, estimating the relative error between homogeneous ABL conditions and the local values of relevant turbulence parameters, and switch to a second turbulence model [50]. In this study, the turbulence model used inside the BIA is the non-linear eddy-viscosity (NLEV) closure proposed by Ehrhard and Moussiopoulos [25], more suitable for disturbed flow conditions [50], in which C_μ is not kept constant. In NLEV closures, the Boussinesq hypothesis of the stress-strain relation is normally extended to higher order terms [16, 25]. However, when simulating flows characterized by reduced swirl and vorticity, the higher order terms can be neglected [50, 56], which was applied to lower the computation time.

Concerning the problem of the variable nature of Sc_t, a general equation for the transport of a passive scalar is adopted, both for the dispersion simulation of NO_2 and PM_{10}, which reads:

$$\frac{\partial}{\partial X}\left(\bar{U}\bar{C} - (D_m + D_t)\frac{\partial \bar{C}}{\partial X}\right) = \bar{\dot{C}}_0, \tag{2}$$

where $\bar{C}$ is the solute concentration, D_m the molecular diffusion coefficient, and $D_t = \nu_t / Sc_t$ the turbulent diffusion coefficient. The deployment of this approach also for the dispersion of particle matter is an acceptable assumption [38]. Besides, air quality regulations are currently based on particle mass concentrations [9]. Finally, Sc_t, a relevant dispersion parameter usually expressed as a constant property [51], is defined as locally variable, according to the formulation proposed by Longo et al. [53].

2.2. Turnhoutsebaan: site location, data and measurements

The Turnhoutsebaan is a main artery street in the city of Antwerp (Belgium, Fig. 1). It was selected as a case study, due to its problematic air pollution levels (Figs. 1 (a) and (b)). The situation was analyzed via CFD modeling.

Measurement data of the wind from Antwerp for the entire year 2017 was obtained from a weather station of the Flanders Environment Agency (VMM), in order to specify the boundary conditions at the inflow. The meteorological conditions selected for the simulation session consist of a wind direction of 202.5°, with a reference wind speed of 3.55 m/s as measured by the VMM station, and a neutrally stratified atmosphere. This specific wind condition was chosen considering its relatively high frequency. Note that a wind direction of 0° corresponds to north wind, 90° to east, 180° to south, and 270° to west.

Regarding traffic data and pollutant emissions, NO_2 and PM_{10} were selected from NO, NO_2, $PM_{2.5}$, and PM_{10} as pollutants to be modeled, to keep the results and discussion section of this paper concise. To quantify traffic emissions of NO_2 and PM_{10}, traffic

count data from the modeled section of the Turnhoutsebaan (Fig. 2) was obtained from the municipality of Antwerp. Hourly observations, spanning approx. 1 month of 2014, are available for traffic lane A and B (Fig. 2 (b)). Using the method of Blocken et al. [9] and the emission factors of the Dutch government of 2017 [72], the vehicle numbers were converted into median substance emissions for time $\in$ [17 h, 18 h[. This resulted in 42.97 g NO_2 h^{-1} and 14.16 g PM_{10} h^{-1} for lane A and 27.23 g NO_2 h^{-1} and 8.88 g PM_{10} h^{-1} for lane B.

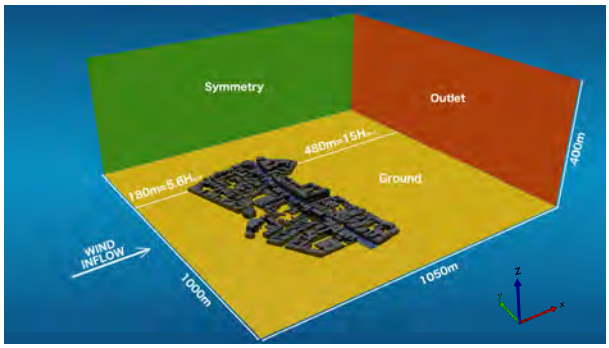

(a) Computational domain extent and adopted boundary conditions. H_{max} = 32 m is the height of the tallest building.

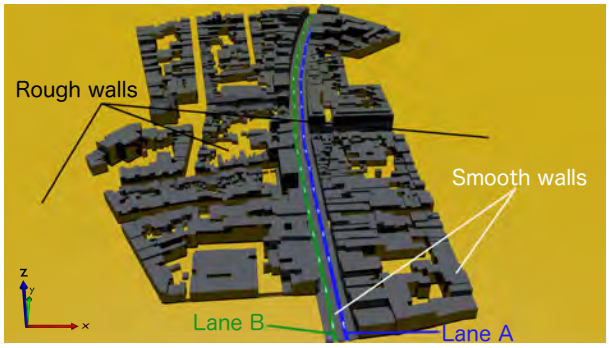

(b) View of the considered Antwerp district around the Turnhoutsebaan, with lane A displayed in blue and lane B displayed in green. The Turnhoutsebaan street and the surrounding buildings are treated as smooth walls. The surrounding ground and the areas enclosed by the building blocks are modeled as rough walls.

Figure 2: Zone of interest, domain extent and CAD model of the Turnhoutsebaan.

Concerning the estimation of the urban pollutant background concentration at the Turnhoutsebaan, concentration data of VMM stations R801 and R802 (Fig. 1 (a)) of 2017 was used. The concentration flowing into the Turnhoutsebaan with the wind is the definition of background concentration used in this work. In order to obtain the needed values, data was selected during appropriate wind conditions and other suitable variable ranges. These selections were averaged, which resulted in an NO_2 concentration of 35.54 µg/m^3 (standard deviation: 11.82 µg/m^3) and a PM_{10} concentration of 26.04 µg/m^3 (standard deviation: 18.38 µg/m^3). These concentration levels were imposed at the inflow of the computational domain (Fig. 2 (a)) of the Turnhoutsebaan model (Section 2.3).

In regard to the wind measurements, Fig. 3 displays the locations within the Turnhoutsebaan where the wind xy velocity magnitude, with $U_{xy} = \sqrt{u_x^2 + u_y^2}$, and direction were measured during the day (9am-18pm), from 27 January to 31 January 2020. Measurements were performed with the KWS1 cup anemometer and the PCE-WL 1 data logger of PCE instruments. The accuracy of the wind speed measurements was ± 0.5 m/s or 5 % of value (largest value applies), while the accuracy of the direction was ± 5°. The starting threshold value for valid measurements is 0.8 m/s.
Measurements were performed similar to the method of Tominaga et al. [76]. One anemometer was set as base instrument, at approx. 1.5 m above the roof of the tallest building in the modeled part of the Turnhoutsebaan, to determine the undisturbed wind conditions. The other anemometer was then displaced in strategic locations inside the urban canyon, recording data at a height of approx. 1.43 m, when the base anemometer was detecting the aimed wind direction, i.e. corresponding as much as possible to the used inflow conditions in the Turnhoutsebaan model. Correspondence of the roof data to the used inflow direction (202.5°) during the measurements used to calculate the average street wind directions was good. Per measured location, the average and the standard error of the mean were calculated. The velocity magnitude at the roof during the measurement campaign was too high and also very variable, which is an aspect that should be improved in future work.

Concerning PM_{10} measurements in the zone of interest and data processing, PM_{10} was measured with a DustTrak II, model number 8530 (aerosol concentration range 0.001 to 400 mg/m^3), using a PM_{10} impactor. Five key locations were considered within the urban canyon (Fig. 3). Due to the fact that the measured time series of the concentration showed sudden drops and increases, averages and standard errors of the mean of the PM_{10} concentration were calculated

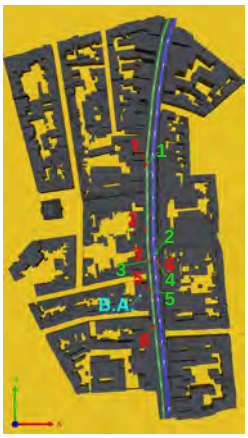

	Velocity			Concentration			
No.	x(m)	y(m)	z(m)	No.	x(m)	y(m)	z(m)
1	-6.60	62.07	1.43	1	-6.60	62.07	1.43
2	-8.03	-45.82	1.43	2	10.60	-85.26	1.43
3	-3.43	-96.63	1.43	3	-3.43	-96.63	1.43
4	11.56	-98.54	1.43	4	11.56	-98.54	1.43
5	-0.07	-146	1.43	5	-0.07	-146	1.43
6	6.15	-206.48	1.43				

Figure 3: Location and numbering of wind and PM_{10} concentration measurements in the Turnhoutsebaan. The base anemometer (B.A.) is indicated in light blue, at coordinates ($x = -17$ m, $y = -151$ m, $z = 32.5$ m).

over time spans, where the average concentration was approximately constant.

Recalling the definition of background concentration used in this work, it is clear that – due to the observed sudden changes in the concentration times series – the background concentration and the street locations should be measured at the same time. However, only 1 DustTrak was available. Hence, the background had to be estimated. This is something that needs to be improved in future work. The estimation was performed based on 2 different sources: 1) from short measurements in an upwind side street, before and/or after a location was measured, and 2) from VMM measurement stations R801, R802, and R803 (Fig. 1 (a)). Besides, the observed values used to estimate the background concentration were variable and never equal to the used background concentration in the model. Therefore, in the comparison of the modeled and measured concentrations, the difference between the concentration and the background concentration is used. The errors for these values were computed through error propagation.

2.3. *Turnhoutsebaan model: computational domain, settings, and grid*

Fig. 2 displays the geometry, boundary conditions, and the extent of the computational domain. The geometry drawing stemmed from a 2 dimensional (2D) plan of the land lots in Antwerp. The third dimension was carefully estimated and drawn, based on information of a website of the Flemish government [81], Google Earth, and Google Maps.

As shown in Fig. 2 (a), the guidelines on the extent of the domain and the minimum distances from the boundaries were respected [29, 76]. The inlet profiles from Table 1 were employed for the turbulence quantities and the velocity, where z_0, the roughness length, was estimated as 0.65 m and u_*, the friction velocity, calculated as 0.3777 m/s. The outlet was modeled with a pressure outlet condition. Both lateral sides were modeled imposing a symmetry condition. The top boundary was set as inlet velocity too, with an x-direction velocity equal to value at the inflow. The ground was treated as a rough wall with z_0 estimated as 0.65 m, while the buildings and the main street were modeled as smooth walls. In the Turnhoutsebaan 1 traffic lane in each direction was modeled. The two lanes were treated as emitting surfaces, with the following estimated pollutant mass flow rates: 42.97 g NO_2 h^{-1} and 14.16 g PM_{10} h^{-1} for lane A; 27.23 g NO_2 h^{-1} and 8.88 g PM_{10} h^{-1} for lane B. Finally, 35.54 $\mu g/m^3$ NO_2 and 26.04 $\mu g/m^3$ PM_{10} were imposed as background concentrations at the inlet.

As for the computational grid, it consists of approximately 35 million hexahedral elements. The grid is finer in the area of interest and towards the ground boundary. In the main urban canyon, an average wall dimensionless distance $y^+ = 290$ is reached. A grid sensitivity analysis was carried out. No substantial error reduction was observed on the refined grid.

The simulations were run in ANSYS Fluent 2019 R3. Second-order schemes were set for the momentum, turbulence quantities and the solute concentration, with a coupled scheme for pressure and velocity. Convergence was assumed when the scaled residuals leveled down to a minimum of 10^{-9} for species concentration and velocity components, 10^{-7} for k, and 10^{-6} for ε.

2.4. *Conceived and simulated local mitigation measures*

In this study, localized pollution hotspots in the modeled street canyon were identified (Fig. 9 (a)). Therefore, the effect of applying local mitigation measures to lower pollution levels at the identified localized hotspots was assessed. In Section 1, available local mitigation measures were discussed. Two interesting possibilities, designing and modifying the local urban geometry and removal by ESP, were identified. Regarding the street geometry modifications, an additional goal in employing the measures, was to find solutions that can be applied realistically in an existing urban area. Upon careful analysis of the Turnhoutsebaan orography and the modeling results, one geo-

metric modification – from a list of possibilities (e.g. [84]) – seemed useful and attainable.

2.4.1. Employment of wind catchers

The first investigated mitigation measure stems from the idea of modifying the local flow field in the street canyon, with the aim of enhancing the dilution process. This, hence, affects both the NO_2 and PM_{10} concentration. It consists of wind catchers, i.e. slanted panels, employed on top of tall building, adjacent to the pollution hotspots. Location, visualization, and dimensions of the wind catchers are shown in Fig. 4. Zhang et al. [93] already reported that this can improve the dilution process, but these authors only studied a simplified 2D urban configuration. Thus, information on the application of this measure in a realistic 3 dimensional (3D) urban fabric is still lacking.

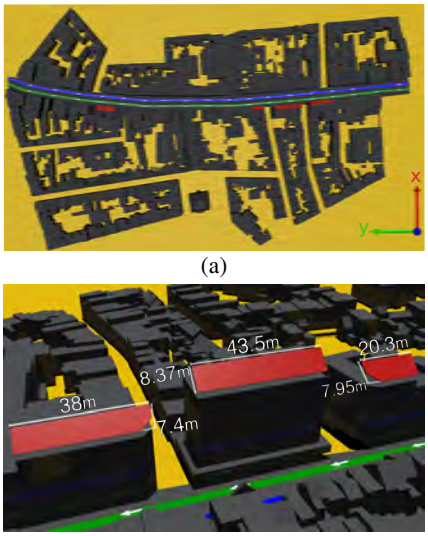

(a)

(b)

Figure 4: (a) Location, (b) visualization, and dimensions of the wind catchers, i.e. slanted panels (highlighted in red), inside the Turnhoutsebaan.

2.4.2. Employment of ESP

The second mitigation measure, only applicable for reducing the PM_{10} concentration, consisted in the employment of 5 commercially available ESP units. They were placed close to the pollution hotspots (at $z = 1$ m). Their location is shown in Fig. 5 (a) and (b). The ESP units (Fig. 5 (c)), type Aufero [26], are commercially available systems with dimensions $L \times W \times H = (2.8 \times 0.72 \times 1.28)$ m^3. For each unit, a flow rate of 7500 m^3/h (or 2.552 kg/s) was assumed, with a constant PM_{10} removal efficiency of 70 %, analogously to Blocken et al. [9]. This mitigation measure was implemented in the CFD model by explicitly depicting the 5 units (Fig. 5 (a) and (b)), and setting the PM_{10} removal and the air flow rate equal to the aforementioned specifications via a user-defined function.

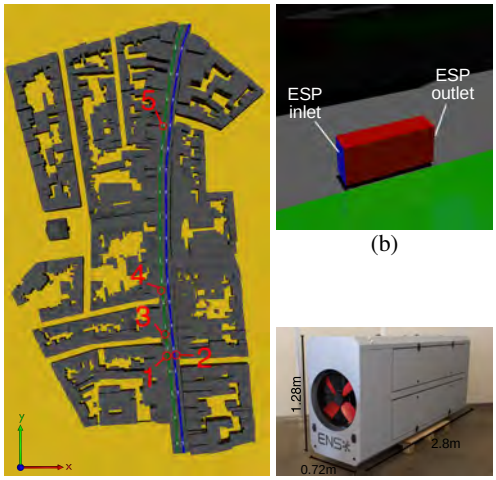

(a) (b) (c)

Figure 5: (a) Locations of the 5 electrostatic precipitation (ESP) units inside the domain, (b) zoom and orientation of the 5th unit, and (c) view of the ESP unit [26].

3. Results and discussion

Fig. 6 shows the comparison of experimental data and numerical prediction of wind directions and *xy* velocity magnitudes inside the urban canyon. The velocity directions were narrowly represented by the applied ABL model, at all the considered locations. Two reasons are likely contributing to the achieved accuracy. Firstly, it was already shown that RANS is sufficiently accurate for near-field pollutant dispersion simulation in urban areas with a high building plan density, resulting in dispersion mainly governed by channeling flow [8]. Fig. 2 (b) demonstrates that the plan density in the very proximity of the Turnhoutsebaan is indeed quite dense. Secondly, it was shown that uncertainty in the determination of the inflowing wind profile, can have a large impact on the accuracy of the prediction of the wind velocity magnitude and direction [33]. However, the inflowing wind was measured very close to the Turnhoutsebaan (base anemometer in Fig. 3), which very likely reduced the uncertainty related to the determination of the inflowing wind. Overall, an accurate prediction was also reached for the *xy* velocity magnitude. However, the

velocity magnitude measurements in the street were performed during less favorable conditions than the wind directions (Section 2.2). Hence, conclusions regarding the velocity magnitude are less certain. In the future, the measurement campaign needs to be improved regarding this aspect.

Fig. 7 shows the comparison of experimental and numerical PM_{10} concentration results. In general, the used modeling methodology showed an accurate performance. In addition to the variable Sc_t, the ABL method was also coupled to dispersion modeling with $Sc_t = 0.3$ and $Sc_t = 0.7$, which are values well inside the range of typical Sc_t values in the literature (0.2 and 1.3) [76]. From the figure, it is clear that the variable Sc_t results are very close to or in between the fixed value Sc_t results, without the need to specify an Sc_t value, which is a very desirable result. Conclusions regarding the performance of the applied model concerning concentration predictions are again less certain, since it was impossible to accurately measure the background concentration (Section 2.2). This comparison, however, clearly indicates that the model at least delivered reasonably accurate concentration results. In addition, the ABL modeling approach coupled to the proposed variable Sc_t formulation was also validated over a scaled and idealized street canyon wind tunnel test case [46], where it showed a good performance regarding the concentration results.

Fig. 8 shows a contour plot of the velocity magnitude in the horizontal plane at $z = 1.43$ m, which reveals that the velocity field is strongly heterogeneous inside the urban canyon. More precisely, areas showing stagnation phenomena can be identified. It is interesting to compare the concentration results of NO_2 (Fig. 9 (a)) to the velocity results. This figure reveals very localized pollution hotspots. It is clear that the high concentration areas correspond narrowly to the low velocity areas. The latter occur mainly at places where high buildings are placed at the upwind side of the Turnhoutsebaan (Figs. 2 (b) and 4 (a) and (b)). Hence, the negative effect of the upwind high buildings on the ventilation capacity can be identified as the main cause of the pollution hotspots.

Considering this conclusion, local mitigation measures were applied. The result of the first measure, the wind catchers, on the NO_2 concentration, can be inspected in Fig. 9 (b). They resulted in a substantial

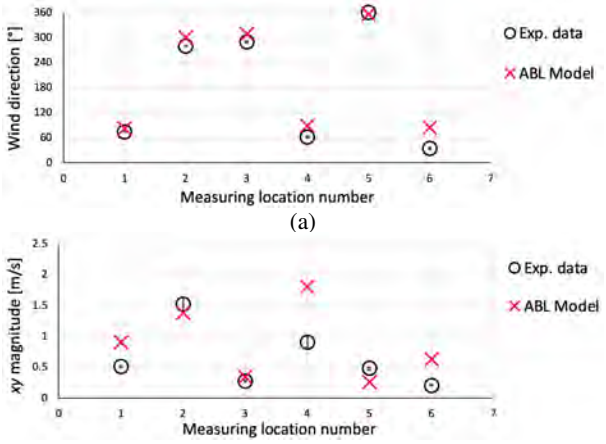

Figure 6: Comparison of experimental data and numerical prediction (a) of wind direction and (b) *xy* velocity magnitude, at the locations shown in Fig. 3.

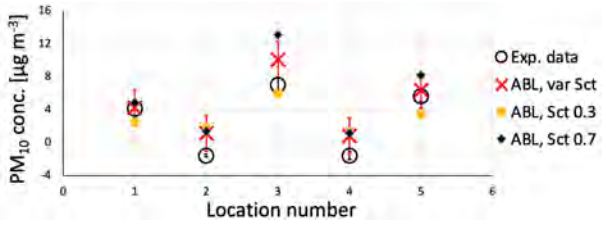

Figure 7: Comparison of experimental data and numerical predictions of PM_{10} concentration, in terms of difference between total concentration and background concentration.

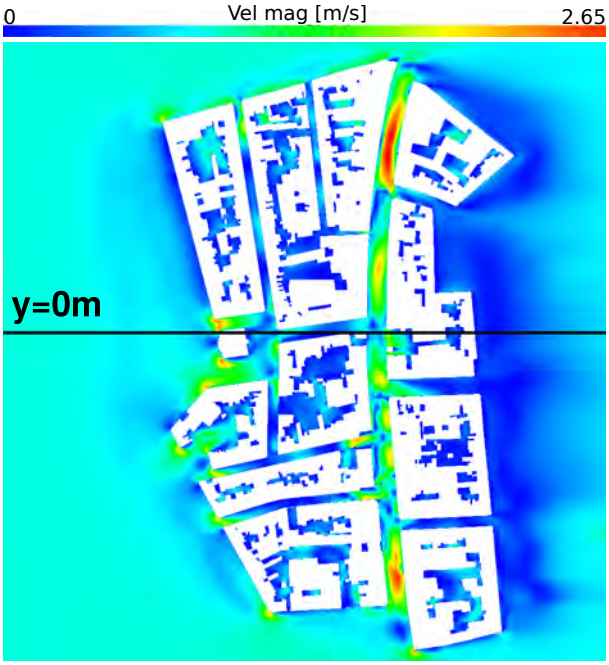

Figure 8: Contour plot of velocity magnitude at the horizontal $z = 1.43$ m plane.

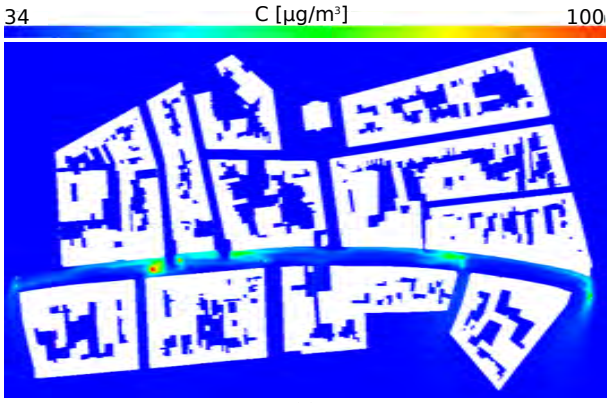

(a)

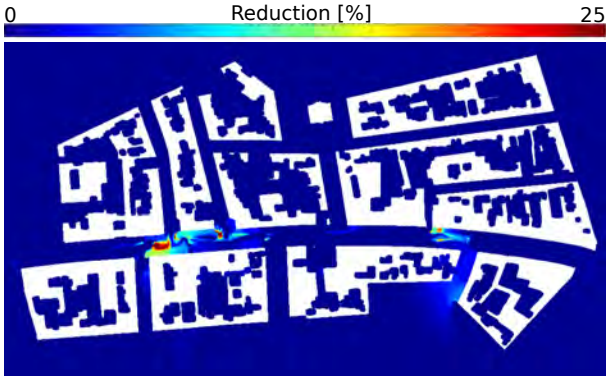

(b)

Figure 9: a) Horizontal contour plot of the NO_2 concentration at z = 2 m for the scenario without mitigation measures. (b) Reduction in percentage of NO_2 concentration due to the application of wind catchers (at z = 2 m). The values are clipped between 0 and 25.

concentration reduction at the pedestrian level, lowering the local peaks of concentration, in the areas targeted by the application. Reduction levels up to 37 % were attained. The PM_{10} concentration reduction as a result of the second measure, the ESP units, is shown in Fig. 10. Again, the measure is able to substantially reduce the concentration level at the targeted locations; and even affects a larger area than the wind catchers. This can be explained by the fact that this strategy removes the pollutant, as opposed to only enhancing the local dilution process. In addition, the ESP units, using ventilators, actively suck in the pollutants. Again, the peaks of PM_{10} concentration are strongly damped. Up to 40 % reduction is attained.

4. Conclusion

The Turnhoutsebaan, a street in Antwerp, has a high traffic intensity and high pollution levels. A CFD model of part of it was developed, using a RANS model specifically for ABL simulations, coupled to a variable Sc_t formulation. Two main traffic-related pollutants were analyzed: NO_2 and PM_{10}. It was found that the pollutant concentration levels inside the street are strongly heterogeneous. Several – very localized – pollution hotspots were identified in the street, at locations where high buildings are restricting the natural ventilation.

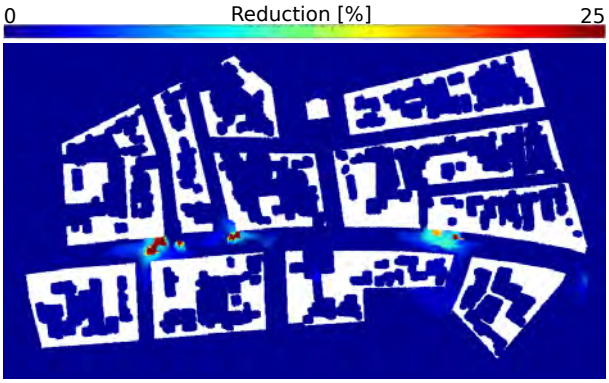

Figure 10: Reduction in percentage of PM_{10} concentration due to the application of ESP units (at z = 2 m). The values are clipped between 0 and 25.

To improve the situation at these hotspots, two mitigation measures were studied: the employment of wind catchers and pollutant removal by ESP devices, implemented only at the affected areas. Substantial pollutant reductions were obtained, up to 40 % by the ESP and up to 37 % by the wind catchers. The area affected by the ESP, was slightly larger than that of the wind catchers.

Model validation was performed, with velocity and PM_{10} concentration field data. The applied modeling method accurately simulated the velocity direction, at the measurement locations. The model also showed a good performance regarding the velocity magnitude and concentration, but the measurement campaign needs to be improved in the future regarding the latter aspects.

Acknowledgments

This work was supported by internal funding of the University of Antwerp and Université libre de Bruxelles. Special thanks go to Riccardo Longo, the developer of the used RANS method and variable Sc_t formulation, for a fantastic cooperation, leading to the publication of the work [46] summarized above.

References

[1] Aarhus University. Description of the OSPM model, 2020. URL https://envs.au.dk/en/research-areas/air-pollution-emissions-and-effects/the-monitoring-program/air-pollution-models/ospm/description-of-the-ospm-model/.

[2] K. V. Abhijith and S. Gokhale. Passive control potentials of trees and on-street parked cars in reduction of air pollution exposure in urban street canyons. *Environmental Pollution*, 204:99–108, 2015. doi: 10.1016/j.envpol.2015.04.013.

[3] K. V. Abhijith, P. Kumar, J. Gallagher, A. McNabola, R. Baldauf, F. Pilla, B. Broderick, S. Di Sabatino, and B. Pulvirenti. Air pollution abatement performances of green infrastructure in open road and built-up street canyon environments - A review. *Atmospheric Environment*, 162:71–86, 2017. doi: 10.1016/j.atmosenv.2017.05.014.

[4] J. S. Apte, K. P. Messier, S. Gani, M. Brauer, T. W. Kirchstetter, M. M. Lunden, J. D. Marshall, J. Portier, R. C. H. Vermeulen, and S. P. Hamburg. High-Resolution Air Pollution Mapping with Google Street View Cars: Exploiting Big Data. *Environmental Science & Technology*, 51(12):6999–7008, 2017. doi: 10.1021/acs.est.7b00891.

[5] R. W. Atkinson, I. M. Carey, A. J. Kent, T. P. van Staa, H. R. Anderson, and D. G. Cook. Long-Term Exposure to Outdoor Air Pollution and Incidence of Cardiovascular Diseases. *Epidemiology*, 24(1):44–53, 2013. doi: 10.1097/EDE.0b013e318276ccb8.

[6] M. Balogh, A. Parente, and C. Benocci. Rans simulation of abl flow over complex terrains applying an enhanced k-ε model and wall function formulation: Implementation and comparison for fluent and openfoam. *Journal of wind engineering and industrial aerodynamics*, 104:360–368, 2012. doi: 10.1016/j.jweia.2012.02.023.

[7] J. Bazyar, N. Pourvakhshoori, H. Khankeh, M. Farrokhi, V. Delshad, and E. Rajabi. A comprehensive evaluation of the association between ambient air pollution and adverse health outcomes of major organ systems: a systematic review with a worldwide approach. *Environmental Science and Pollution Research*, 26(13):12648–12661, 2019. doi: 10.1007/s11356-019-04874-z.

[8] B. Blocken. LES over RANS in building simulation for outdoor and indoor applications: A foregone conclusion? *Building Simulation*, 2018. doi: 10.1007/s12273-018-0459-3.

[9] B. Blocken, R. Vervoort, and T. van Hooff. Reduction of outdoor particulate matter concentrations by local removal in semi-enclosed parking garages: A preliminary case study for eindhoven city center. *Journal of Wind Engineering and Industrial Aerodynamics*, 159:80–98, 2016. doi: 10.1016/j.jweia.2016.10.008.

[10] B. Bonn, E. von Schneidemesser, D. Andrich, J. Quedenau, H. Gerwig, A. Lüdecke, J. Kura, A. Pietsch, C. Ehlers, D. Klemp, C. Kofahl, R. Nothard, A. Kerschbaumer, W. Junkermann, R. Grote, T. Pohl, K. Weber, B. Lode, P. Schönberger, G. Churkina, T. M. Butler, and M. G. Lawrence. BAERLIN2014 – the influence of land surface types on and the horizontal heterogeneity of air pollutant levels in berlin. *Atmospheric Chemistry and Physics*, 16(12):7785–7811, 2016. doi: 10.5194/acp-16-7785-2016.

[11] E. Boonen and A. Beeldens. Recent Photocatalytic Applications for Air Purification in Belgium . *Coatings*, 4(3):553–573, 2014. doi: 10.3390/coatings4030553.

[12] R. Buccolieri, S. Mohamed Salim, L. Sandra Leo, S. Di Sabatino, A. Chan, P. Ielpo, G. de Gennaro, and C. Gromke. Analysis of local scale tree–atmosphere interaction on pollutant concentration in idealized street canyons and application to a real urban junction. *Atmospheric Environment*, 45(9):1702–1713, 2011. doi: 10.1016/j.atmosenv.2010.12.058.

[13] V. Busini and R. Rota. Influence of the shape of mitigation barriers on heavy gas dispersion. *Journal of Loss Prevention in the Process Industries*, 29(13-21):13–21, 2014. doi: 10.1016/j.jlp.2014.01.001.

[14] J. G. Calvert. GLOSSARY OF ATMOSPHERIC CHEMISTRY TERMS - (RECOMMENDATIONS 1990). *Pure and Applied Chemistry*, 62(11):2167–2219, 1990. p. 2186.

[15] L. W. Chew and L. K. Norford. Pedestrian-level wind speed enhancement with void decks in three-dimensional urban street canyons. *Building and Environment*, 155:399–407, 2019. doi: 10.1016/j.buildenv.2019.03.058.

[16] T. J. Craft, B. E. Launder, and K. Suga. Development and application of a cubic eddy-viscosity model of turbulence. *International Journal of Heat and Fluid Flow*, 17(2):108–115, 1996. doi: 10.1016/0142-727X(95)00079-6.

[17] R. de Richter and S. Caillol. Fighting global warming: The potential of photocatalysis against CO2, CH4, N2O, CFCs, tropospheric O3, BC and other major contributors to climate change. *Journal of Photochemistry and Photobiology C: Photochemistry Reviews*, 12(1):1–19, 2011. doi: 10.1016/j.jphotochemrev.2011.05.002.

[18] A. Di Bernardino, P. Monti, G. Leuzzi, and G. Querzoli. Turbulent schmidt number measurements over three- 3 dimensional cubic arrays. *Boundary-Layer Meteorology*, 174(2):231–250, 2019. doi: 10.1007/s10546-019-00482-z.

[19] S. Di Sabatino, R. Buccolieri, B. Pulvirenti, and R. Britter. Simulations of pollutant dispersion within idealised urban-type geometries with cfd and integral models. *Atmospheric environment*, 41(37):8316–8329, 2004. doi: 10.1016/j.atmosenv.2007.06.052.

[20] D. A. Donzis, K. Aditya, K. R. Sreenivasan, and P. K. Yeung. The turbulent schmidt number. *Journal of Fluids Engineering*, 136(6), 2014. doi: 10.1115/1.4026619.

[21] EEA. Emissions of primary PM2.5 and PM10 particulate matter , 2018. URL https://www.eea.europa.eu/data-and-maps/indicators/emissions-of-primary-particles-and-5/assessment-2. European Environment Agency. Accessed on 26 November 2019.

[22] EEA. Air pollutant emissions data viewer (Gothenburg Protocol, LRTAP Convention) 1990-2017 , 2019. URL https://www.eea.europa.eu/data-and-maps/dashboards/air-pollutant-emissions-data-viewer-2. European Environment Agency. Accessed on 25 November 2019.

[23] EEA. Air quality in Europe - 2019 report, 2019. URL https://www.eea.europa.eu/publications/air-quality-in-europe-2019/air-quality-in-europe-2019/viewfile#pdfjs.action=download. European Environment Agency.

[24] EEA. Air quality statistics, 2019. URL https://www.eea.europa.eu/data-and-maps/dashboards/air-quality-statistics. European Environment Agcency. Accessed on 25 November 2019.

[25] J. Ehrhard and N. Moussiopoulos. On a new nonlinear turbulence model for simulating flows around building-shaped structures. *Journal of Wind Engineering and Industrial Aerodynamics*, 88(1):91–99, 2000. doi: 10.1016/S0167-6105(00)00026-X.

[26] ENS Clean Air Solutions. Aufero. Innovative air purification system, 2018. URL https://enstechnology.nl/wp-content/uploads/2018/03/ENS-Clean-Air-Leaflet-Aufero-2018-Q1.1-EN.pdf. Accessed on 21

July 2020.

[27] European Commission. Reclaiming city streets for people. Chaos or quality of life?, 2004. URL https://ec.europa.eu/environment/pubs/pdf/streets_people.pdf. accessed on 23 July 2020.

[28] D. Fowler, P. Brimblecombe, J. Burrows, M. R. Heal, P. Grennfelt, D. S. Stevenson, A. Jowett, E. Nemitz, M. Coyle, X. J. Lui, Y. H. Chang, G. W. Fuller, M. A. Sutton, Z. Klimont, M. H. Unsworth, and M. Vieno. A chronology of global air quality. *Philosophical Transactions of the Royal Society A-Mathematical Physical and Engineering Sciences*, 378(2183), 2020. doi: 10.1098/rsta.2019.0314.

[29] J. Franke, A. Hellsten, H. Schlnzen, and B. Carissimo. Best practice guideline for the CFD simulation of flows in the urban environments. Technical report, 2007. COST Action 732.

[30] X. Fu, J. Liu, G. A. Ban-Weiss, J. Zhang, X. Huang, B. Ouyang, O. Popoola, and S. Tao. Effects of canyon geometry on the distribution of traffic-related air pollution in a large urban area: Implications of a multi-canyon air pollution dispersion model. *Atmospheric Environment*, 165:111–121, 2017. doi: 10.1016/j.atmosenv.2017.06.031.

[31] M. Gallus, V. Akylas, F. Barmpas, A. Beeldens, E. Boonen, A. Boreave, M. Cazaunau, H. Chen, V. Daele, J. F. Doussin, Y. Dupart, C. Gaimoz, C. George, B. Grosselin, H. Herrmann, S. Ifang, R. Kurtenbach, M. Maille, A. Mellouki, K. Miet, F. Mothes, N. Moussiopoulos, L. Poulain, R. Rabe, P. Zapf, and J. Kleffmann. Photocatalytic de-pollution in the Leopold II tunnel in Brussels: NOx abatement results. *Building and Environment*, 84:125–133, 2015. doi: 10.1016/j.buildenv.2014.10.032.

[32] M. Gallus, R. Ciuraru, F. Mothes, V. Akylas, F. Barmpas, A. Beeldens, F. Bernard, E. Boonen, A. Boréave, M. Cazaunau, N. Charbonnel, H. Chen, V. Dale, Y. Dupart, C. Gaimoz, B. Grosselin, H. Herrmann, S. Ifang, R. Kurtenbach, M. Maille, I. Marjanovic, V. Michoud, A. Mellouki, K. Miet, N. Moussiopoulos, L. Poulain, P. Zapf, C. George, J. F. Doussin, and J. Kleffmann. Photocatalytic abatement results from a model street canyon. *Environmental Science and Pollution Research*, 22(22):18185–18196, 2015. doi: 10.1007/s11356-015-4926-4.

[33] C. García-Sánchez, J. van Beeck, and C. Gorlé. Predictive large eddy simulations for urban flows: Challenges andopportunities. *Building and Environment*, 139:146–156, 2018. doi: 10.1016/j.buildenv.2018.05.007.

[34] C. Gorlé, J. van Beeck, and P. Rambaud. Dispersion in the wake of a rectangular building: validation of two reynolds-averaged navier–stokes modelling approaches. *Boundary-layer meteorology*, 137(1):115–133, 2010. doi: 10.1007/s10546-010-9521-0.

[35] C. Gualtieri, A. Angeloudis, F. Bombardelli, S. Jha, and T. Stoesser. On the values for the turbulent schmidt number in environmental flows. 2(2), 2017. doi: 10.3390/fluids2020017.

[36] M. Guarnieri and J. R. Balmes. Outdoor air pollution and asthma. *Lancet*, 383(9928):1581–1592, 2014. doi: 10.1016/S0140-6736(14)60617-6.

[37] J. Hang, Yu. Li, M. Sandberg, R. Buccolieri, and S. Di Sabatino. The influence of building height variability on pollutant dispersion and pedestrian ventilation in idealized high-rise urban areas. *Building and Environment*, 56:346–360, 2012. doi: 10.1016/j.buildenv.2012.03.023.

[38] N. S. Holmes and L. Morawska. A review of dispersion modelling and its application to the dispersion of particles: an overview of different dispersion models available. *Atmospheric Environment*, 40(30):6902–5928, 2006. doi: 10.1016/j.atmosenv.2006.06.003.

[39] H. Huang, Y. Akutsu, M. Arai, and M. Tamura. A two-dimensional air quality model in an urban street canyon: evaluation and sensitivity analysis. *Atmospheric Environment*, 34:689–698, 2000. doi: 10.1016/S1352-2310(99)00333-7.

[40] S. Janhäll. Review on urban vegetation and particle air pollution - Deposition and dispersion. *Atmospheric Environment*, 105:130–137, 2015. doi: 10.1016/j.atmosenv.2015.01.052.

[41] A. P. R. Jeanjean, J. Gallagher, P. S. Monks, and R. J. Leigh. Ranking current and prospective NO2 pollution mitigation strategies: An environmental and economic modelling investigation in oxford street, london. *Environmental Pollution*, 225:587–597, 2017. doi: 10.1016/j.envpol.2017.03.027.

[42] Y.-H. Juan, A.-S. Yang, C.-Y. Wen, Y.-T. Lee, and P.-C. Wang. Optimization procedures for enhancement of city breathability using arcade design in a realistic high-rise urban area. *Building and Environment*, 121:247–261, 2017. doi: 10.1016/j.buildenv.2017.05.035.

[43] P. Kastner-Klein, E. Plate, and E. Fedorovich. Gaseous pollulant dispersion around urban-canopy elements: wind tunnel case studies. *International Journal of Environment and Pollution*, 8(3-6):727–737, 1997. 4th Workshop on Harmonization with Atmospheric Dispersion Modelling for Regulatory Purposes, 1996.

[44] E. Keshavarzian, R. Jin, K. Dong, K. C.S. Kwok, Y. Zhang, and M. Zhao. Effect of pollutant source location on air pollutant dispersion around a high-rise building. *Applied Mathematical Modelling*, 81, 2020. doi: 10.1016/j.apm.2020.01.019.

[45] M. Kurppa, A. Hellsten, M. Auvinen, S. Raasch, T. Vesala, and L. Jarvi. Ventilation and Air Quality in City Blocks Using Large-Eddy SimulationUrban Planning Perspective. *Atmosphere*, 9(2), 2018. doi: 10.3390/atmos9020065.

[46] T. Lauriks, R. Longo, D. Baetens, M. Derudi, A. Parente, A. Bellemans, J. van Beeck, and S. Denys. Application of Improved CFD Modeling for Prediction and Mitigation of Traffic-Related Air Pollution Hotspots in a Realistic Urban Street. *Atmospheric Environment*, 246, 2021. doi: 10.1016/j.atmosenv.2020.118127.

[47] F. Li, J. Liu, J. Ren, and X. Cao. Predicting contaminant dispersion using modified turbulent schmidt numbers from different vortex structures. *Building and Environment*, 130:120–127, 2018. doi: 10.1016/j.buildenv.2017.12.023.

[48] Z. Li, J. C. H. Fung, and A. K. H. Lau. High spatiotemporal characterization of on-road PM2.5 concentrations in high-density urban areas using mobile monitoring. *Building and Environment*, 143:196–205, 2018. doi: 10.1016/j.buildenv.2018.07.014.

[49] J. A. Logan. Nitrogen oxides in the troposphere: Global and regional budgets. *Journal of Geophysical Research*, 88(c15):10785–10807, 1983. doi: 10.1029/JC088iC15p10785.

[50] R. Longo, M. Ferrarotti, C. García Sánchez, M. Derudi, and A. Parente. Advanced turbulence models and boundary conditions for flows around different configurations of ground-mounted buildings. *Journal of wind engineering and industrial aerodynamics*, 167:160–182, 2017. doi: 10.1016/j.jweia.2017.04.015.

[51] R. Longo, A. Bellemans, M. Ferrarotti, M. Derudi, and A. Parente. A new turbulent schmidt number formulation based on the local turbulence level. In *ETMM12 - 12th International ERCOFTAC Symposium on Engineering Turbulence Modelling and Measurements*, Montpellier, France, 2018.

[52] R. Longo, M. Frst, A. Bellemans, M. Ferrarotti, M. Derudi, and A. Parente. Cfd dispersion study based on a variable schmidt formulation for flows around different configurations of ground-mounted buildings. *Building and Environment*,

154:336–347, 2019. doi: 10.1016/j.buildenv.2019.02.041.

[53] R. Longo, A. Bellemans, M. Derudi, and A. Parente. A multi-fidelity framework for the estimation of the turbulent schmidt number in the simulation of atmospheric dispersion. *Building and Environment*, 185, 2020. doi: 10.1016/j.buildenv.2020.107066.

[54] A. H. Mamaghani, F. Haghighat, and C. S. Lee. Photocatalytic oxidation technology for indoor environment air purification: The state-of-the-art . *Applied Catalysis B-Environmental*, 203:247–269, 2017. doi: 10.1016/j.apcatb.2016.10.037.

[55] H. Merbitz, F. Detalle, G. Ketzler, C. Schneider, and F. Lenartz. Small scale particulate matter measurements and dispersion modelling in the inner city of Liege, Belgium . *International Journal of Environment and Pollution*, 50(1-4):234–249, 2012. doi: 10.1504/IJEP.2012.051196.

[56] B. Merci, C. De Langhe, K. Lodefier, and E. Dick. Axisymmetric impingement heat transfer with a nonlinear k-ϵ model. *Journal of Thermophysics and Heat Transfer*, 18(1):100–107, 2004. doi: 10.2514/1.1378.

[57] F. J. R. Meysman and S. De Craemer. CurieuzeNeuzen Vlaanderen: Het cijferrapport, 2018. Data retrieved from `https://curieuzeneuzen.be/in-english/` (website with some English explanation, accessed on 4 November 2019).

[58] K. Misawa, Y. Sekine, Y. Kusukubo, and K. Sohara. Photocatalytic degradation of atmospheric fine particulate matter (PM2.5) collected on TiO(2)supporting quartz fibre filter. *Environmental Technology*, 41(10):1266–1274, 2020. doi: 10.1080/09593330.2018.1530696.

[59] V. H. Nguyen, B. S. Nguyen, C. W. Huang, T. T. Le, C. C. Nguyen, T. T. N. Le, D. Heo, Q. V. Ly, Q. T. Trinh, M. Shokouhimehr, C. L. Xia, S. S. Lam, D. V. N. Vo, S. Y. Kim, and Q. V. Le. Photocatalytic NOx abatement: Recent advances and emerging trends in the development of photocatalysts. *Journal of Cleaner Production*, 270, 2020. doi: 10.1016/j.jclepro.2020.121912.

[60] H. Niu, B. Wang, B. Liu, Y. Liu, J. Liu, and Z. Wang. Numerical simulations of the effect of building configurations and wind direction on fine particulate matters dispersion in a street canyon. *Environmental Fluid Mechanics*, 18(4):829–847, 2018. doi: 10.1007/s10652-017-9563-7.

[61] OECD. Air and GHG emissions, 2019. URL `https://data.oecd.org/air/air-and-ghg-emissions.htm#indicator-chart`. Doi: 10.1787/93d10cf7-en. Accessed on 25 November 2019.

[62] D. F. Ollis. Photocatalytic purification and remediation of contaminated air and water. In *Comptes Rendus de l'Acadmie des Sciences - Series IIC - Chemistry*, 2000. doi: 10.1016/S1387-1609(00)01169-5.

[63] I. Papailias, T. Giannakopoulou, N. Todorova, D. Demotikali, T. Vaimakis, and C. Trapalis. Effect of processing temperature on structure and photocatalytic properties of g-C3N4. *Applied Surface Science*, 358:278–286, 2015. doi: 10.1016/j.apsusc.2015.08.097.

[64] A. Parente, C. Gorlé, J. van Beeck, and C. Benocci. A comprehensive modelling approach for the neutral atmospheric boundary layer: Consistent inflow conditions, wall function and turbulence model. *Boundary-Layer Meteorology*, 140(3):140–411, 2011. doi: 10.1007/s10546-011-9621-5.

[65] A. Parente, C. Gorlé, J. van Beeck, and C. Benocci. Improved k-epsilon model and wall function formulation for the rans simulation of abl flows. *Journal of wind engineering and industrial aerodynamics*, 99(4):267–278, 2011. doi: 10.1016/j.jweia.2010.12.017.

[66] A. Parente, R. Longo, and M. Ferrarotti. *CFD boundary conditions, turbulence models and dispersion study for flows around obstacles*. VKI LS 2017-01, 2017. doi: 10.35294/ls201701.parente.

[67] A. Parente, R. Longo, and M. Ferrarotti. *Turbulence model formulation and dispersion modelling for the CFD simulation of flows around obstacles and on complex terrains*. VKI LS 2019-03, 2019. doi: 10.35294/ls201903.parente.

[68] M. Pontiggia, M. Derudi, M. Alba, M. Scaioni, and R. Rota. Hazardous gas releases in urban areas: Assessment of consequences through cfd modelling. *Journal of Hazardous Materials*, 176(1-3):589–596, 2010. doi: 10.1016/j.jhazmat.2009.11.070.

[69] S. Quarmby, G. Santos, and M. Mathias. Air quality strategies and technologies: A rapid review of the international evidence. *Sustainability*, 11(10), 2019. doi: 10.3390/su11102757.

[70] A. J. Reynolds. The prediction of turbulent prandtl and schmidt numbers. *International Journal of Heat and Mass Transfer*, 18:1055–1069, 1975.

[71] F. Ricciardelli and S. Polimeno. Some characteristics of the wind flow in the lower Urban Boundary Layer . *Journal of Wind Engineering and Industrial Aerodynamics*, 94(11):815–832, 2006. doi: 10.1016/j.jweia.2006.06.003.

[72] Rijksoverheid. Emissiefactoren voor snelwegen en niet-snelwegen, 2018. URL `https://www.rijksoverheid.nl/documenten/publicaties/2018/03/15/emissiefactoren-voor-snelwegen-en-niet-snelwegen-2018`. Accessed in 2018.

[73] J. A. Salmond, D. E. Williams, G. Laing, S. Kingham, K. Dirks, I. Longley, and G. S. Henshaw. The influence of vegetation on the horizontal and vertical distribution of pollutants in a street canyon . *Science of The Total Environment*, 443:287–298, 2013. doi: 10.1016/j.scitotenv.2012.10.101.

[74] Z. Shayegan, C. S. Lee, and F. Haghighat. TiO2 photocatalyst for removal of volatile organic compounds in gas phase - A review. *Chemical Engineering Journal*, 334:2408–2439, 2018. doi: 10.1016/j.cej.2017.09.153.

[75] J. Shen, Z. Gao, W. Ding, and Y. Yu. An investigation on the effect of street morphology to ambient air quality using six real-world cases. *Atmospheric Environment*, 164:85–101, 2017. doi: 10.1016/j.atmosenv.2017.05.047.

[76] Y. Tominaga, A. Mochida, R. Yoshie, H. Kataoka, T. Nozu, M. Yoshikawa, and T. Shirasawa. Aij guidelines for practical applications of cfd to pedestrian wind environment around buildings. *Journal of Wind Engineering and Industrial Aerodynamics*, 96(10-11):1749–1761, 2008. doi: 10.1016/j.jweia.2008.02.058.

[77] J. van Walsem, J Roegiers, B. Modde, S. Lenaerts, and S Denys. Integration of a photocatalytic multi-tube reactor for indoor air purification in HVAC systems: a feasibility study. *Environmental Science and Pollution Research*, 25(18):18015–18026, 2018. doi: 10.1007/s11356-018-2017-z.

[78] J. van Walsem, J. Roegiers, B. Modde, S. Lenaerts, and S. Denys. Proof of concept of an upscaled photocatalytic multi-tube reactor: A combined modelling and experimental study. *Chemical Engineering Journal*, 378:18015–18026, 2019. doi: 10.1016/j.cej.2019.122038.

[79] S. Vardoulakis, R. Kettle, P. Cosford, P. Lincoln, S. Holgate, J. Grigg, F. Kelly, and D. Pencheon. Local action on outdoor air pollution to improve public health. *International Journal of Public Health*, 63(5):557–565, 2018. doi: 10.1007/s00038-018-1104-8.

[80] R. Vervoort, B. Blocken, and T. van Hooff. Reduction of particulate matter concentrations by local removal in a building courtyard: Case study for the delhi american embassy school.

Science of The Total Environment, 686:657–680, 2019. doi: 10.1016/j.scitotenv.2019.05.154.

[81] Vlaamse overheid. Geopunt-kaart, 2019. URL `http://www.geopunt.be/`. Accessed on 20 December 2019.

[82] VMM. ANNUAL AIR REPORT FLANDERS (BELGIUM). Emissions 2000-2016 and air quality in Flanders in 2017, 2018. Flanders Environment Agency.

[83] VMM. Luchtkwaliteit in de antwerpse agglomeratie - jaarrapport 2018, 2019.

[84] D. Voordeckers, T. Lauriks, S. Denys, P. Billen, T. Tytgat, and M. Van Acker. Guidelines for passive control of traffic-related air pollution in street canyons: an overview for urban planning. *Landscape and Urban Planning*, 207, 2021. doi: 10.1016/j.landurbplan.2020.103980.

[85] P. E. J. Vos, B. Maiheu, J. Vankerkom, and S. Janssen. Improving local air quality in cities: To tree or not to tree? *Environmental Pollution*, 183:113–122, 2013. doi: 10.1016/j.envpol.2012.10.021.

[86] I. Wadlow, C. Paton-Walsh, H. Forehead, P. Perez, M. Amirghasemi, É.-A. Guérette, O. Gendek, and P. Kumar. Understanding spatial variability of air quality in sydney: Part 2—a roadside case study. *Atmosphere*, 10(4):217, 2019. doi: 10.3390/atmos10040217.

[87] Z. Wang, X. Xie, X. Wang, A. Mahmood, H. Qiu, and J. Sun. Difference of photodegradation characteristics between single and mixed VOC pollutants under simulated sunlight irradiation. *Journal of Photochemistry and Photobiology A: Chemistry*, 384:112029, 2019. doi: 10.1016/j.jphotochem.2019.112029.

[88] J. B. Wedding, D. J. Lombardi, and J. E. Cermak. A Wind Tunnel Study of Gaseous Pollutants in City Street Canyons. *Journal of the Air Pollution Control Association*, 27(6):557–566, 1977. doi: 10.1080/00022470.1977.10470456.

[89] A. J. White, P. T. Bradshaw, and G. B. Hamra. Air Pollution and Breast Cancer: a Review. *Current Epidemiology Reports*, 5:92–100, 2018. doi: 10.1007/s40471-018-0143-2.

[90] WHO. Ambient (outdoor) air pollution. URL `https://www.who.int/news-room/fact-sheets/detail/ambient-(outdoor)-air-quality-and-health`. Accessed on 11 November 2020.

[91] WHO. WHO ambient (outdoor) air quality database Summary results, update 2018, 2018. URL `https://www.who.int/airpollution/data/AAP\_database\_summary\_results\_2018\_final2.pdf?ua=1`.

[92] G. X. Zhang, Y. Y. Liu, Z. Hashisho, Z. M. Sun, S. L. Zheng, and L. X. Zhong. Adsorption and photocatalytic degradation performances of TiO2/diatomite composite for volatile organic compounds: Effects of key parameters. *Applied Surface Science*, 525, 2020. doi: 10.1016/j.apsusc.2020.146633.

[93] K. Zhang, G. Chen, X. Wang, S. Liu, C. M. Mak, Y. Fan, and J. Hang. Numerical evaluations of urban design technique to reduce vehicular personal intake fraction in deep street canyons. *Science of the Total Environment*, 653:968–994, 2019. doi: 10.1016/j.scitotenv.2018.10.333.

On the Application of Background Oriented Schlieren Technique on Ballistics Field

Abdelhafidh MOUMEN

Environmental and Applied Fluid Dynamics Department, Von Karman Institute for Fluid Dynamics, Belgium, abdelhafidh.moumen@gmail.com

Supervisor: Delphine LABOUREUR

Assistant Professor , Environmental and Applied Fluid Dynamics Department , Von Karman Institute for Fluid Dynamics, Belgium, delphine.laboureur@vki.ac.be

Promotor: Johan GALLANT

Professor, Dept of Weapon Systems and Ballistics, Royal Military Academy, Belgium, johan.gallant@dymasec.be

Promotor: Patrick HENDRICK

Professor, Laboratory of Aero-Thermo-Mechanics, Université Libre de Bruxelles, Belgium, patrick.hendrick@ulb.ac.be

Abstract

The ballistics field is known by the presence of several complex phenomena such as muzzle and flying projectiles flow fields. Consequently, numerical simulations are commonly used to model these complicated flows. However, the validation process of these codes has proven to be problematic due to the lack of experimental quantitative data. In this context, the present paper describes the application of the Background Oriented Schlieren technique (BOS) as a quantitative investigation tool in the ballistics field. We illustrate that BOS can accurately capture the main characteristics of the studied configurations: Firstly, we discuss the visualization and the density field reconstruction around a sniper projectile flying at supersonic and transonic velocities. We demonstrate that these fields are in satisfactory agreement with numerical simulation. Then, the findings of the BOS visualization of the precursors and the propellant flow fields are presented. To this end, the salient features accurately captured by the BOS technique such as vortex rings, shock bottles, Mach disk, and blast wave are described both qualitatively and in terms of density profiles. Two improved approaches that are essential to the aforementioned analysis are proposed: the first is related to density field reconstruction based on Abel inversion and the second approach is a phase separation procedure.

Keywords: Ballistics, Background Oriented Schlieren, flow visualization , supersonic, transonic, muzzle flow fields, underexpanded jet.

1. Introduction

Ballistics is defined as the science that studies the projectile's life cycle all the way from the moment it is fired until it impacts (or intended action) the target [1]. According to this definition, we can subdivide this discipline into four sub-domains. First, the internal ballistics, which covers the ignition and the combustion of propellant powders and the acceleration of the projectile inside the barrel. The projectile launch marks the end of this first stage and the beginning of the second phase called external ballistics (EB). This phase studies the projectile's flight dynamics and interaction with its environment. The third phase is terminal ballistics (TB), which covers the projectile's effects on its target. A fourth phase, generally not considered as a distinct field in the literature, is the intermediate ballistics (IB) where the projectile passes between the first and the second phase.

Although the various sub-domains of ballistics seem to have been known for a long time, they are unfortunately not mastered. This mainly concerns the muzzle flow fields that occur during the IB and the flows around the projectile during the EB. Good knowledge of muzzle flow fields is essential for the design and development of muzzle devices (used for various purposes, such as recoil, flash, and noise reduction), crew and equipment safety, and the flow-projectile interaction. Besides, the study of the flow around the projectile is necessary to optimize its design and for trajectory computation. These topics are currently attracting renewed interest in ballistic research given the evolution of the type of threat, such as urban combat, and the need to engage the target at greater distances (the precision projectile will perform part of its flight in the transonic range) [2; 3].

The muzzle flows consist of two distinct features [2]: Firstly, the precursor flow, essentially composed of air, drove outwards of the barrel by a piston effect. Indeed, the in-bore acceleration of the projectile induces compression waves that merge into a normal shock wave. Once it reaches the exit plane, this shock wave discharges into the open air creating an underexpanded jet and a spherical blast wave known as the precursor blast wave. The second flow phase consists of the propellant flow expansion into the already disturbed surrounding environment after the projectile launch. This flow is created by the same mechanism as the precursor flow, resulting in the creation of the main shock wave and the main underexpanded jet.
The complexity of these flows, added to its multiphase and transient characters, stems essentially from their high Spatio-temporal evolution. They occur in the vicinity of the muzzle within a radius of 100 calibers in a time of about $10\,ms$. Due to these complexities, the determination of the quantitative properties of these flows remains a challenge.

An extensive comprehensive literature in the IB field exists [4–13]. However, they all present the main drawback consisting of their qualitative nature or the complexity and limitations of their experimental setups. Essentially, these experiments were based on optical flow visualization techniques such as schlieren, shadowgraphy, and interferometry. The bulk of these has been conducted by Klingenberg [4], who has provided a detailed understanding of the formation and development of the muzzle flows and their dependence on caliber, type, and weight of propellant powder. Several other studies have been conducted by Schmidt and Shear [9], Schmidt [10], and Fansler [13], whom all have used the same qualitative visualization techniques to study the properties of these flows. Despite their added value, they have all concluded that quantitative experimental methods are limited, given the short duration and spatio-temporal evolution of these flows. Consequently, validated numerical simulations of these flows are limited [10]. Moreover, although numerical modeling has succeeded in predicting the pressure and the velocity, they simultaneously present significantly modified temperatures and densities [14].

Numerical simulations are frequently conducted to study these flows, however, the validation of these codes has encountered considerable difficulties. For instance, the few numerical simulations of muzzle flows reported in the literature are validated either by simple qualitative comparisons with classical shadowgraphs or schlieren images [15; 16], or by comparisons with previously published simulation results [17], which have themselves been validated by a comparison of interferometer images from experiments different than the simulated ones [18; 19]. Furthermore, the results of the different simulations have led to contradictory conclusions, notably concerning the aerodynamic forces and acceleration of the projectile in the IB [15; 17; 20].

In addition to the impact of the IB on the projectile stability, its aerodynamic behavior during the flight in a transonic domain plays an important role in terms of precision and therefore reproducibility of the shots [3]. Despite the technical progress in aero-ballistics and computational fluid dynamics (CFD) and the numerous studies in this field [21–23], the transonic domain still retains many ambiguities such as the determination of the aerodynamic coefficients of the projectiles. In this context, the use of CFD is a real opportunity. Nevertheless, as numerical simulations have a limited value without a solid experimental basis, they should ideally be coupled with a parallel experimental effort.

The general purposes of the current study is to enrich the quantitative data set in the ballistics field for a more comprehensive analysis and modeling of muzzle and projectile flow fields. Therefore, we present and explore the potential of the Background Oriented Schlieren (BOS), a relatively new optical measurement technique [24], as a new investigative technique in the field of ballistics. This density-based technique was chosen for several reasons: BOS is a non-intrusive and a whole-field quantitative measurement technique. Also, the modesty and cost-effectiveness of its experimental setup have made it an attractive experimental alternative. Furthermore, it offers a large

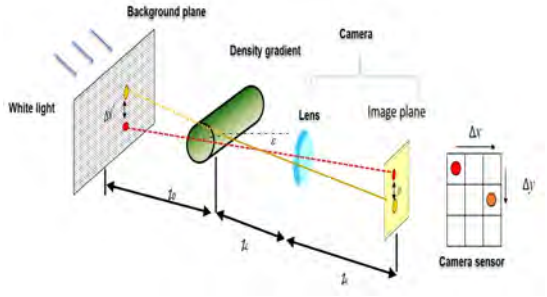

Figure 1: Simplified optical path in the x-y-z plane in a BOS setup. Solid line: the path of a light ray without the density gradient object. Dotted line: the path of a light ray with the density gradient object in between the camera and the light source field, adapted from [25].

field of view (FOV), unlike the classical Schlieren technique, where the size of the FOV depends on the employed optical instrument. This last advantage is a decisive aspect when dealing with large caliber weapons.

2. Background oriented schlieren technique

During this section, we will detail the BOS technique principle, the aspects, the constraints on the dimensioning of the experimental layout (referred to it hereafter as the experiment design), and the proposed methods of density field reconstruction and phase separation.

2.1. BOS Principle and experiment design

From an optical viewpoint, the principle of BOS is similar to the classical schlieren one; both of them exploit the light ray bending due to the variation of the spatial gradient of refraction index (n) in-between the camera and a distant object [26], Fig. 1. From a practical viewpoint, their detection of the refraction index gradient is different. In BOS, the latter is detected by digital comparison between two images [27]. First, a tare or a reference image is recorded while the camera is on sharp focus on the background without the presence of the schlieren object. Then, a second image or a succession of images are taken under the same experimental conditions with the presence of the flow. Due to the dependence of the light path on the n variation, the light ray will be refracted and will impact the camera sensor in a different position than that on the tare one. Thus, the second image will be artificially refracted; the background elements (i.e. dots) will receive an artificial shift in both directions in the image plane. These displacements are computed through an optical flow algorithm such as cross-correlation algorithms, adopted from the Particle Imagery Velocimetry (PIV) community. Here, the information is contained in the displacement fields in x and y directions which are relative to the path integrated refraction index gradient. Assuming small light ray deviations and that the paraxial assumption holds, it can be shown that the angular deflection ϵ is composed of two components, in two orthogonal planes, namely ϵ_x and ϵ_y [28]. Using trigonometric relations, ϵ_x and ϵ_y can be related to both displacement fields in the sensor plane, Δx and Δy. Based on the layout on Fig. 1, the angular deflection in the y plane may be expressed as [27]:

$$\epsilon_y = \frac{\Delta y'}{Z_D} = M \cdot \frac{\Delta y}{Z_D} = \frac{Z_D + Z_C - f}{f \cdot Z_D} \cdot \Delta y \qquad (1)$$

with Z_D and Z_C are the flow mid-plane distance to the background and the camera, respectively, $\Delta y'$ is the displacement in the background plan which is linked to the one in the image plan, Δy, via the magnification factor M, and f is the camera lenses focal length. On the other hand, the integration of Eikonal equation along the light path yields the connection between the angular deflections ϵ_x and ϵ_y and the gradient of the integrated refraction index n integrated along the line of sight [28]:

$$\epsilon_y = \frac{1}{n_0} \cdot \int_{\Delta Z_D} \frac{\partial n}{\partial y} dz \qquad (2)$$

where n_0 is the refractive index of the ambient gas.

From the experiment design viewpoint, several aspects and constraints need to be taken into account. Some constraints are general while others are specific to the considered configurations herein.
The general aspects are all related to the requirement to have the camera focused on the background and thus the dimensioning of the experimental setup. This geometrical dimensioning defines the spatial resolution (A) and the sensitivity (S) of the BOS experiment. For reliable BOS measurement, the signal-to-noise (S/N) should be increased. As the signal is nothing more than the displacements Δx and Δy, the improvement of the S/N consists essentially of increasing these detected displacements in the image plane under the same disturbance (same angular deviation). Thus, the S/N increase is equivalent to enhancing the detected displacement to ϵ ratio, which is referred to

as the BOS system sensitivity and expressed as [29]:

$$S = \frac{\Delta y}{\epsilon} = M \cdot Z_D = \frac{f}{Z_D + Z_C - f}.Z_D \tag{3}$$

Compared to what it is advisable to meet in a PIV experiment, the pixel displacements in BOS experiments are relatively small, of the order of three pixels. Also, to be detected by the camera, the displacement of the background element must be larger than the pixel physical size of the sensor. We can conclude that the improvement of the BOS system sensitivity could be achieved in two ways: Regarding the choice of the camera, it is recommended to choose a camera with small pixel size and equipped with long focal length lenses. On the other hand, the distance Z_D should be as large as possible. However, this last guideline is limited by three factors: First, the need to capture at least one point where the refractive index is known (usually an undisturbed area, used as Dirichlet boundary condition for the Poisson's equation, if applicable). Second, as the camera is on sharp focus on the background patterns, a Z_D greater than the camera's depth of field will result in a blurring of the flow. Thirdly, the relative positioning of the flow between the camera and the background has a contradictory effect between the sensitivity and the spatial resolution. Indeed, by placing the background further away from the flow (the preferred direction for sensitivity), the cone of light emanating from a background element is widened before passing through the flow. Since this cone of light cannot contain independent information and covers a larger area in the flow, this results in a loss of spatial resolution. Based on a simplified optical model [29] has proposed a good approximation of the spatial resolution A:

$$A = \frac{Z_D}{Z_D + Z_c} \cdot \frac{f}{f\#} \tag{4}$$

According to Eq. 4, it is obvious that A is opposite to S (note that $A \approx S/f\#$), which means that there is a trade-off between the two variables. Nevertheless, the aperture $f\#$ constitutes a degree of freedom in this compromise, its increase leads to an improvement of the spatial resolution without affecting the sensitivity. Moreover, it is recommended to operate with the largest possible $f\#$ not only to improve the spatial resolution but also to increase the depth of field of the camera to bring the flow back into focus. The increase of $f\#$ is however limited by the amount of light available. This constraint is particularly relevant in our case where a short exposure time is required due to the transient nature of the flows.

2.2. Reconstruction method of axisymmetric 3D refractive index fields

The accuracy of the BOS refractive index/density field measurement is very sensitive to the gradient field reconstruction procedure. Since the measured flow fields in this work are axisymmetric, we propose a new reconstruction technique for this flow-type. For convenience, we briefly describe this method, details of the mathematical development as well as its analytic and experimental validation are the subject of a separate paper [30]. Consider an axisymmetric flow with the x-axis as the axis of symmetry, and the z-axis as the optical axis. Thanks to its axisymmetry, it can be observed that the dimensions of the problem now depend only on $r = \sqrt{y^2 + z^2}$ and x. The components of the measured deflection angle, ϵ_x and ϵ_y, calculated using Eq. 2, can be reformulated into cylindrical coordinates such as:

$$\epsilon_x(x, y) = \frac{2}{n_0} \int_{r=y}^{R} \frac{\partial n}{\partial x} \frac{rdr}{\sqrt{r^2 - y^2}} \tag{5}$$

$$\epsilon_y(x, y) = \frac{2y}{n_0} \int_{r=y}^{R} \frac{\partial n}{\partial r} \frac{dr}{\sqrt{r^2 - y^2}} \tag{6}$$

To the author's best knowledge, the BOS bi-sensitivity criterion has only been exploited in $2D$ flows. In fact, the local field of the refractive index of axisymmetric flow fields is classically reconstructed from a single angle of view by applying Abel inversion on only radial displacements [31–33]. In this work, we take advantage of this bi-sensitivity property by exploiting the two angular deviations, the radial and the axial, to reconstruct the local field of the refractive index.
The integrals of equations Eq. 5 and Eq. 6 are both of Abel form, but of a different nature. Their inverses will also be computed differently to obtain $\frac{\partial n}{\partial x}$ and $\frac{\partial n}{\partial r}$, respectively. Next, we can calculate the refractive index field n by solving the Poisson's equation in cylindrical coordinates:

$$\Delta n = \frac{\partial^2 n}{\partial r^2} + \frac{1}{r}\frac{\partial n}{\partial r} + \frac{\partial^2 n}{\partial x^2} \tag{7}$$

Compared to the simple Abel inversion, this method offers several advantages:

- More precision, especially along the axis of symmetry.
- More robust against the inevitable experimental noise, which is the main disadvantage of the old technique. This point is particularly relevant in the field of ballistics. Indeed, the simple Abel

inversion requires the improvement of the symmetry as well as the reduction of the noise which are usually performed by temporal and spatial averaging. Thus, it is required to average up to several dozens of images before applying Abel inversion to achieve optimal results. Due to the ballistic dispersion and the limited frame rate of the camera, we only rely on spatial averaging causing significant levels of noise, when applying simple Abel inversion. Indeed, a large number of parameters such as the combustion process, the initial temperature of the gun and propellant powder, as well as the tolerance of the weight of the projectile make each shot different. It is, therefore, practically impossible to capture the same phenomenon with comparable intensity at the same position, rendering it impossible to compute a temporal average.

- The use of the Poisson equation allows boundary conditions to be imposed in known locations, thereby improving the results.

Then thanks to Gladstone-Dale relation the flow density ρ may be calculated by [28]:

$$n - 1 = G(\lambda)\rho \tag{8}$$

where G is the Gladstone-Dale constant, and it is weakly dependent on the light wavelength λ which was taken as constant at 550 nm throughout the study and is defined as:

$$G(\lambda) = 2.2244x10^{-4}(1 + (\frac{6.7132x10^{-8}}{\lambda})^2) \tag{9}$$

2.3. Phase separation

The muzzle's main propellant flow is naturally loaded with unburned propellant particles. Their presence in the flow contaminates the correlation field and prevents the computation of pixel displacements on the BOS raw images. Therefore, these raw images must be pre-processed by masking the particles prior to the cross-correlation. Due to the arbitrary and transient dispersion of these particles, their masking cannot be performed manually, but an inherent phase (pixel) discrimination must be used.

Existing algorithms for phase separation in the PIV community were not used, because they failed to perform a correct separation in our case. For example, the application of Khalitov and Longmire algorithm [34] in BOS suffers from two drawbacks. First, object detection based on a local minimum intensity yields discrete objects and does not detect the powder agglomeration either the projectile. In view of its concept, it seems that this technique is better suited to detect dispersed phases. Secondly, both the particle size map and the brightness map did not show any significant differences between the reference image and the one with the particle's presence, making it complex to decide on the discrimination criteria of the detected objects. The technique proposed by Kiger and Pan [35] has not produced better results, because it also relies on size discrimination based on the assumption that tracer images are smaller in size than particle images. The procedure used for pre-processing two-phase BOS images in this work is based on pixel intensity and can be summarized in four steps:

- First, a sliding average filter is applied to the distorted image. This type of spatial filtering smoothens the image by reducing the strong intensity fluctuation due to unburned powder obstruction and experimental noise. This operation is well known in image processing and is implemented under different algorithms, such as the median or moving average filters. These two types of filters yield comparable results, with a preference for a filter implementation that does not round the outputs to integer values, thereby giving more flexibility in the choice of threshold (see step 3).

- Then, the result of the first step is divided by the reference image. This produces an image whose minimum value corresponds to total obscuration by the unburned powder, while its maximum value corresponds to zero obscuration.

- Thirdly, this image is binarized so that each pixel intensity value below a user-defined threshold is set to zero and all other values to ones.

- Finally, the output of the third step is stored in a separate file that will serve as a mask for cross-correlation as well as a set of images that describe the dispersion of the powder.

The parameters of the proposed method, such as the size of the filter kernel (k) and the binarization threshold (bt), must be adapted to each situation. For instance, $k = 9$ and $bt = 0.45$ worked well in our case. The adequacy of the selected values could be verified by checking that the undisturbed areas are not affected, also by the quality of the cross-correlation pic as well as by the value of the calculated displacement which is generally relatively low.

We adopted this strategy in main propellant flow analysis reported in Sec. 4.2.

3. Experimental setup

A schematic diagram of the implemented experimental setup is shown in Fig. 2. The setup is composed of a high-speed camera type Photron FASTCAM SA5 which focuses on a backlighted background, on the muzzle view, and another time on the projectile view to visualize their respective flow fields. For each series of tests, an optimized random speckle pattern was generated. This optimization can be summarized as follows: the physical size of the elements was determined in such a way that they will be perceived by the camera with a size of three pixels. Also, the number of dots was chosen in such a way that during the cross-correlation the interrogation window (IW) will contain a minimum of seven dots for a good S/N [36]. This speckle was then printed on a transparency film and taped to Plexiglas. The latter was in turn fixed on a rigid metal frame to minimize vibrations during the shooting. The parallelism of this set to the shooting axis as well as its orthogonality to the optical axis were meticulously checked and corrected during the tests. A 575 watt HMI metal halogen lamp was placed behind the background. The camera was equipped with Nikon lenses with variable focal length $f = 27 - 300\,mm$. The image sensor of the camera is a 1-megapixel CMOS type with a pixel size of 20 microns. The exposure time was maintained the same for all tests and is equal to $5\,\mu s$. The remaining camera parameters as well as the setup geometrical dimensions are summarized in Table 1.

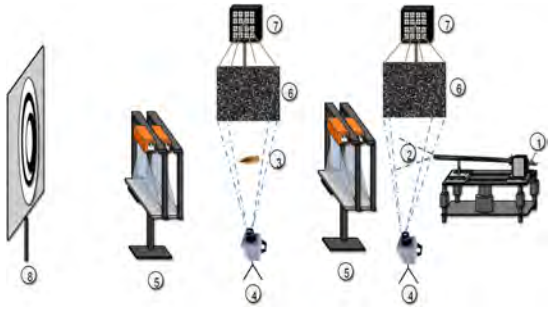

Figure 2: Schematic representation of the built BOS setup 1: weapon system, 2: muzzle flow field, 3: projectile in flight, 4: high-speed camera, 5: velocity light gates, 6: background, 7: backlight, 8: target.

The visualized muzzle flows are issued from the launch of a .300 Blackout caliber projectile launched by a Prototypa laboratory weapon model STZA $16M2$. The propellant powder was Vihtavuori's $N120$ rifle powder [37]. Each cartridge contained a weight $w = 1.1\,g$ of propellant powder, giving an average muzzle velocity of $v_p = 540\,m/s$. In order to visualize the near-field formation as well as the mid-field development and mutual interactions of the different flows, we implemented two different setups (Table 1). Furthermore, to ensure the reproducibility of the reported phenomena, we have fired nine shots under each configuration.
The second part of the experimental campaign was designed to visualize the flow around $HPBT$ (Hollow Point Boat Tail) projectiles with a caliber of 0.338-inches flying freely in the air, Fig. 3. This ammunition is employed in precision weapons and has a nominal Mach number $M = 2.7$. For lower velocities, the amount of propellant powder placed in the casing has been reduced, according to the desired speed. The projectiles velocity were measured using two light velocity gates.

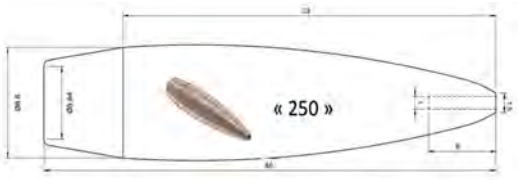

Figure 3: .338 inch caliber projectile, $HPBT$ bullet with the typical dimensions of a 250 grains model, all dimensions are in mm.

We processed all image pairs using PIVLab [38] with an iterative multi-pass window deformation algorithm with 32, 16, and 8-pixel IW with a 50% overlap factor. Due to the presence of discontinuities in the shock waves, we did not use smoothing or outliner detection. The interpolation of the sub-pixels was performed by a 2x3 point Gaussian interpolation method. To minimize the effect of vibrations caused by the firing, we took as a reference image the last frame recorded immediately before the appearance of the flow in the FOV. Also, the displacements detected in both directions in regions that are not expected to present any density variation were treated as an indication of vibration (camera, background, light source). These displacements were averaged and removed from their respective fields.

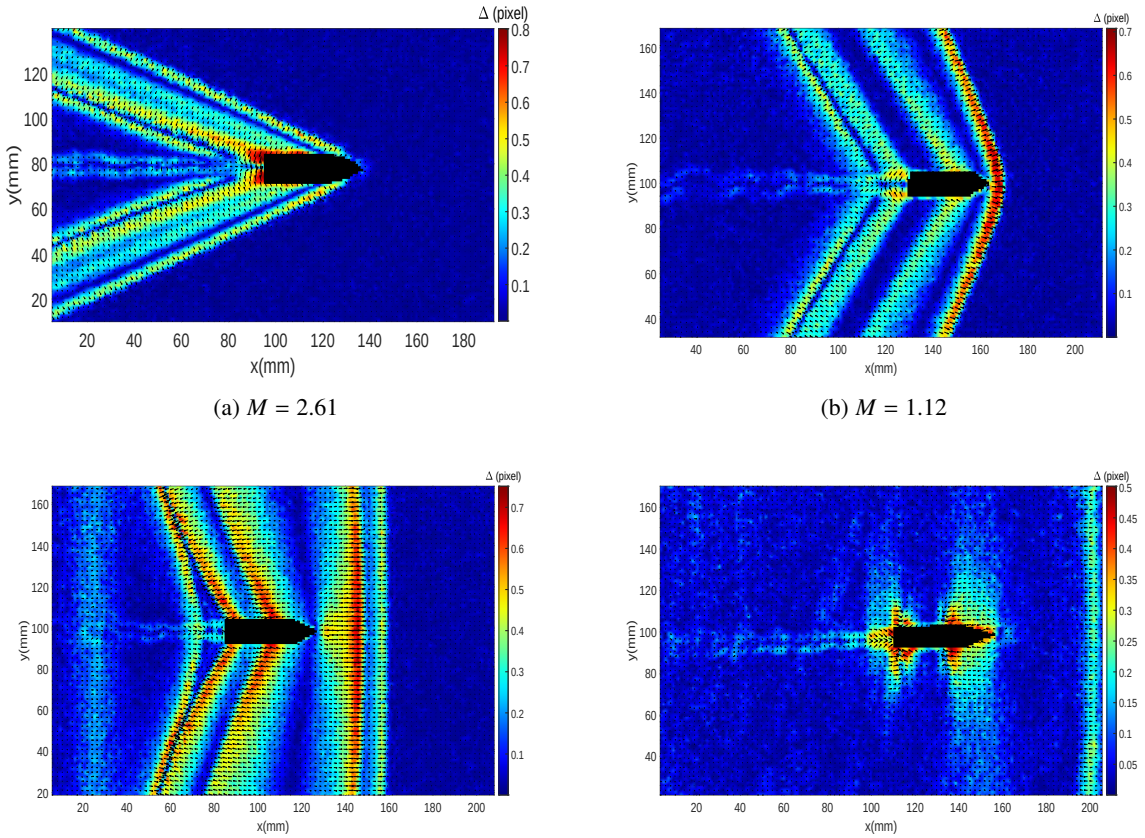

(a) $M = 2.61$ (b) $M = 1.12$

(c) $M = 1.06$ (d) $M = 0.97$

Figure 4: BOS visualization of the flow field around a 0,338 inch *HPBT* projectile (magnitude of displacements).

Table 1: Experimental setup1 parameters

Setup	Z_D mm	Z_C mm	f mm	$f\#$	Frame rate fps
1	828	2000	180	11	20000
2	828	2159	50	8	20000
HPBT	977	1878	130	8	15000

4. Results and discussion

4.1. BOS visualization of flow fields around HPBT projectiles

The substantial changes occurring in the flow pattern surrounding the *HPBT* projectile at various (decreasing) velocities are presented in Fig. 4. BOS results, unless otherwise specified, are presented in terms of displacement magnitude, Δ, relative to the path integrated density gradient ($|\nabla\rho|$), the vectors are pointing to the direction of the lower density and colors show their magnitude in pixel with red being the highest, and all the image axes are in mm.

At supersonic velocity, $M = 2.61$, Fig. 4a, the oblique bow shock, attached and strongly deflected, can be seen on the tip of the projectile. After reaching the projectile shoulder level, the body's curvature changes and becomes almost flat. As a result, the supersonic airflow is deflected by itself and an expansion wave is formed [39]. This flow condition is terminated by recompression waves and the wake at the base level.

As the velocity was reduced, the narrow shock wave near the projectile tip was opening and moving away. This is first seen in Fig. 4b displaying the flow field around the projectile at $M = 1.12$. The expansion and the compression wave angles also increase in aperture and continue to occur at the same level but with a lower intensity.
For $M = 1.06$, Fig. 4c, the air upstream is supersonic,

resulting in the formation of a flat and detached shock wave in front of the projectile. Then, on immediate contact with the tip of the projectile, the air velocity drops. However, it remains supersonic around the projectile and its expansion at the shoulder is clearly visible. This flow structure ends with a characteristic triangular shock pattern at the trailing edge of the projectile.
Fig. 4d illustrates the flow field situation at $M = 0.9$, this is the so-called lower transonic domain [39]. Indeed, in such a case, we can distinguish the typical behavior of a transonic flight featuring a mixture of supersonic and subsonic behavior. The flow in front of the projectile is subsonic but it is accelerated owing to the curvature of the projectile's body front part. When the air speed reaches a critical Mach number, it forms a normal shock wave, typically at the highest curvatures, allowing the air to decelerate abruptly and return to the subsonic condition. this phenomenon reproduces itself at the slope of the projectile's base.
Such observations confirm BOS's capability for capturing very high-speed phenomena occurring in the presence of shock waves.

The density fields of the different configurations have been calculated according to the procedure described in Sect. 2.2. However, due to the presence of projectiles in the integration domain, we applied the inverse gradient method instead of Poisson's equation [40].The experimentally determined density cross-sectional profiles at axial distance $y = 20\,mm$ are compared with the CFD results of De Briey et al [3], Fig. 5. From these graphs, it can be seen that all profiles exhibit the so-called N waveform: the density increases rapidly across the shock wave, then it decreases by a comparable amplitude to a low value before returning to the ambient level behind the projectile. For the transonic projectile, the N waveform shows a local maximum (a twist) during the decreasing fraction, captured accurately by both methods. In addition, these density plots show a strong agreement between the BOS and CFD results. The matches at the peak locations and the density levels for both velocities indicate that the different waves were captured at almost the same locations with the same intensities.

4.2. Muzzle flow fields visualization

In this section, we describe the structures and the interactions between the different muzzle flows. Their similarities and differences are examined qualitatively and quantitatively, based on BOS images and density profiles. The projectile uncorking from the barrel is considered as the time scale origin ($t = 0\,s$).

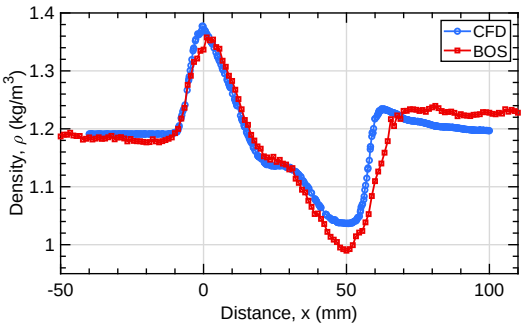

(a) $M = 2.7$, $y = 20mm$

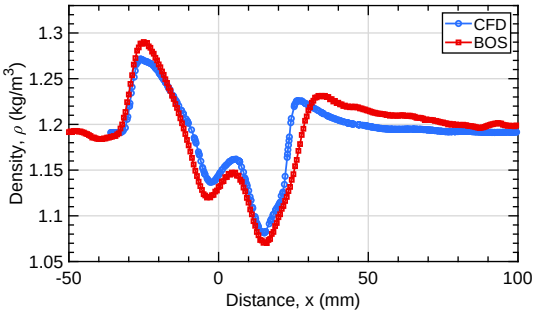

(b) $M = 1.2$, $y = 20mm$

Figure 5: Comparison of cross-sectional density profiles obtained through BOS (experiment) and CFD [3] for a supersonic ($M = 2.7$) and transonic ($M = 1.2$) projectiles at $y = 20\,mm$ (the x-axis being oriented along the projectile symmetry axis with the origin located at the center of its base.

The sequential evolution of the muzzle precursor flow issued from the launch of a supersonic projectile, $v_p = 540\,m/s$, is shown in Fig. 6a-d. At $t = -396.3\,\mu s$, Fig. 6a, the first precursor flow appeared. This appearance comes in the form of a potential jet core encapsulated by an outer spherical blast wave. This jet is dominated by a unique cell, namely the shock bottle, referred to it hereafter as the extremely underexpanded jet. Typically, this supersonic structure occurs for pressure ratio $\eta = p_e/p_0$ larger than $3 - 4$ (where p_e is the pressure at the exit plane and p_0 is the ambient pressure) [41]. The various features of this structure are better visualized under the horizontal displacement Δy proportional to $\partial\rho/\partial y$. Fig. 6e exhibits, in particular, the presence of a PrandtlMeyer expansion fan (marker 1) in the barrel exit plan (marker 0), the intercepting shock (marker 2), the Mach disk (marker 3), the vortex rings (marker 4), the contact surface (marker 5), and the blast wave

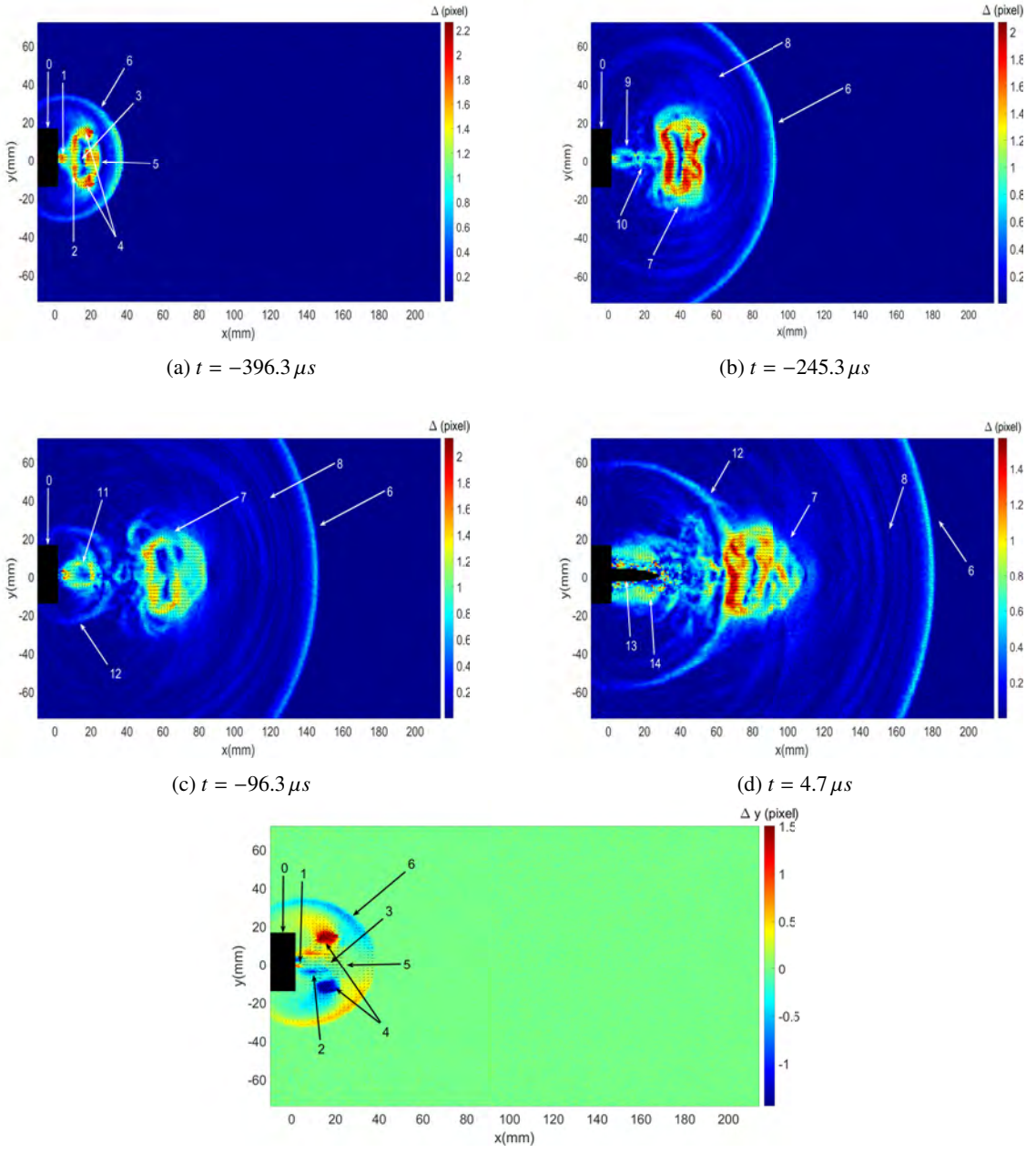

(a) $t = -396.3\,\mu s$

(b) $t = -245.3\,\mu s$

(c) $t = -96.3\,\mu s$

(d) $t = 4.7\,\mu s$

(e) $t = -396.3\,\mu s$

Figure 6: Sequential development of the two precursor flows,
0: the barrel, 1: PrandtlMeyer expansion fan, 2: the intercepting shock, 3: the Mach disk, 4: the vortex ring, 5: the contact surface, 6: the first precursor blast wave, 7: the turbulent gas ball, 8: the pressure waves, 9: the shock bottle of the highly underexpanded jet, 10: the oblique shock structure, 11: the shock bottle of the second precursor flow, 12: the second precursor blast wave, 13: the projectile, 14: combustion gases.

(marker 6).

Subsequently, the pressure at the muzzle decreases, and the blast wave and the turbulent gas ball (marker 7) are separated and travel downstream with the appearance of pressure waves (marker 8) behind the blast wave. At $t = -245.3\,\mu s$, Fig. 6b, following this drop in the exhausted gas pressure, the shape of the first precursor flow shifts from an extremely underexpanded jet with a single body to a highly underexpanded jet with the main body (marker 9) followed by an oblique shock structure (marker 10). This new form occurs at a pressure ratio of $2 < \eta < 4$ [41]. Here, the shock bottle is characterized by a tiny Mach disc followed by one or several shock cells.

Later, the second precursor flow developed at $t = -96.3\,\mu s$. The appearance of this flow is not a general characteristic of all weapon systems. It only appears if the combination of the couple in-bore acceleration of the projectile and the length of the barrel permits the creation and the cohesion of pressure waves in front of the projectile [2]. In the current combination, a second well-differentiated precursor flow, similar to its predecessor, appeared. Indeed, it can be seen in Fig. 6c, the presence of a shock bottle (marker 11) with a second blast wave (marker 12) propagating inside the first flow. This second flow continues to develop until the projectile launch (marker 13) which will interact with it soon after its formation. Getting a deeper knowledge of this interaction is very challenging in the ballistic field due to its high spatio-temporal development [15; 17; 20]. In particular, when the front part of the projectile is immersed in a low-pressure zone (the shock bottle) while its base is still subject to the high pressures of the combustion gases, the launch velocity of the projectile as well as its dynamic stability may be affected.

Thanks to the quantitative nature of BOS, the development of the first precursor flow is now analyzed in terms of density. The density profiles have been reconstructed according to the framework that we outlined in Sect. 2.2. This analysis will be carried out in two parts: Firstly, for the sake of comparison, we performed two other experiments using the same weapon system but with lower propellant powder weights (w) to achieve transonic ($w = 0.8\,g$, $v_p = 374\,m/s$) and subsonic ($w = 0.6\,g$, $v_p = 293\,m/s$) projectile velocities. Secondly, the initial transition stages of the first precursor flow of the main scenario are compared with each other.

The spatial evolution of the centerline density of the extremely underexpanded jets of the three configurations is represented in Fig. 7a. These profiles

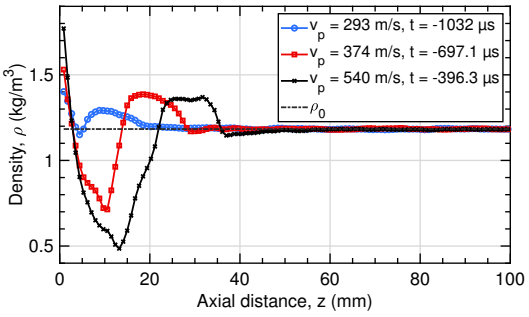

(a)

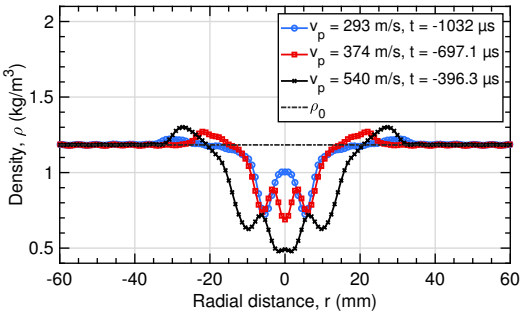

(b)

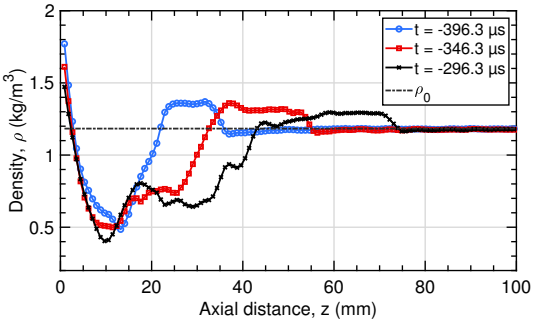

(c)

Figure 7: Comparison between the density profiles in the unexpanded jet of the first precursor flows obtained by BOS. (a) Comparison between centerline density profiles obtained from three different configurations, (b) comparison between radial density profiles obtained from three different configurations, (c) comparison between centerline density profiles obtained from three successive situations of the main configuration.

show the classical shape of an extremely underexpanded jet [42], presenting nevertheless some differences related to the different configurations. It can be seen that the initial density, at $z = 0$, increases from $1.382\,kg/m^3$ for the subsonic case to $1.771\,kg/m^3$ for the supersonic one. This confirms that the higher the velocity of the projectile in the bore, the more the air in front of it is compressed. Then, the density decreases sharply from the high value of the muzzle, thanks to the Prandtl-Meyer expansion fan and the underexpanded shape of the jet. Also, the expansion is stronger during the main case where the density reaches $0.485\,kg/m^3$ compared to $1.163\,kg/m^3$ and $0.6892\,kg/m^3$ for the subsonic and transonic cases, respectively. Then, across the Mach disk, the density is abruptly restored to a value close to the ambient density (ρ_0) but, due to the presence of blast waves, it shows a local peak followed by a local minimum before stabilizing towards ρ_0.

The associated radial density profiles, Fig. 7b, were taken at $z_1 = 8.8\,mm$, $z_2 = 9.6\,mm$, and $z_3 = 12.3\,mm$, the longitudinal location of the minimum density inside the vortex rings, for the subsonic, transonic and supersonic configuration, respectively. These symmetrical graphs display the same pattern and confirm that the flow characteristics of the main case have the largest jet size and the strongest density gradients. They start with a constant density equal to ρ_0 before undergoing a jump at the blast wave level. These are centred at the radial distances around the muzzle $r_1 = 30.8\,mm$, $r_2 = 22.0\,mm$, and $r_3 = 28.1\,mm$ for the three cases considered. Furthermore, it is observed that this jump intensity increases with the propelled projectile velocity. Subsequently, the density profiles drop and present a U-shape as we penetrate the vortex rings with a minimum at its center. It is observed that the vortex ring in the new cases are comparable in size and density while those of the main case presents a greater size and a lower minimum density. Finally, the density drops again within the shock bottle for the last two cases but remains sub-ambient and constant within the shock cell for the subsonic configuration.

The density field sequential development of the first precursor flow, previously described in a qualitative perspective, is represented quantitatively for three successive phases in Fig. 7c. At $t = -345.3\,\mu s$, the centerline density profile shows the shifting of the flow structure from an extremely to a highly underexpanded jet. It consists of a strong decrease in density directly downstream of the muzzle, like that of the extremely underexpanded jet with a lower initial density. However, during the abrupt recovery, the profile undergoes a decrease in density before recovering relatively gradually. This behavior corresponds to the shrinkage of the Mach disk towards the formation of a conical-shaped core of the highly underexpanded jet. $50\,\mu s$ later, the density profile shows that the shock bottle has maintained approximately the same size with a multiplication of the successive shock cells noticeable from the density oscillation before experiencing the density jump at the shock wave level.

Right after the barrel uncorking, the combustion gases discharge near the muzzle through the precursor flows. In general, the main propellant flow develops in the same way as the first precursor flows, with few exceptions. This expansion occurs in an environment that has already been disturbed, with lower pressure and density, which may affect its axisymmetric evolution. Moreover, this development is also influenced by the presence of unburned particles and projectile.

The consecutive development of the main propellant flow is shown in Fig. 8. At $t = 104.7\,\mu s$, the main components of an extremely underexpanded jet such as the barrel shocks (marker 15), the vortex rings (marker 16), and the Mach disk (marker 17), are distinguished. In this case, the formation of the shock bottle is hindered by the presence of the projectile. Indeed, the gas velocities in the shock bottle are supersonic in comparison with the velocity of the projectile which is still moving inside the underexpanded jet. Thus, a shock (marker18) is formed at the base of the projectile, which is located at $x = 54\,mm$, Fig. 8a. This nearly vertical shock is considered as a trap that blocks the unburnt powder (marker 19) particles detected here thanks to the proposed phase separation method. Furthermore, the jet structure is encapsulated by a spherical blast wave (marker 20) which is domed in the downstream direction (marker 21) at the level of the axis of symmetry. This bulge occurrence is the first effect of the interaction of the precursors-propellant flow. Downstream of this front, the turbulent plume of the precursor flow remains present (marker 22).

At $t = 204.7\,\mu s$, Fig. 8b, the particles in the first position has disappeared; this is most likely due to local after-burning. At this stage, the projectile has already overtaken the main blast wave and entered the pocket where the second unburned particle agglomeration is still present. The size of the FOV of the first setup does not allow to visualize the location where the powder has been entirely consumed. However, this can be achieved thanks to the larger FOV of the second setup showing that the unburned powder has been consumed between $t = 304.3\,\mu s$ and $t = 354.3\,\mu s$,

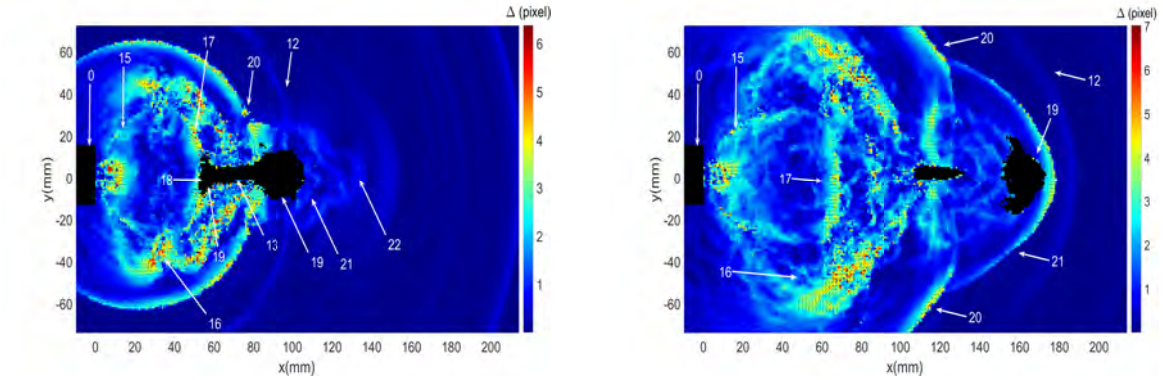

(a) $t = 104.7\,\mu s$

(b) $t = 204.7\,\mu s$

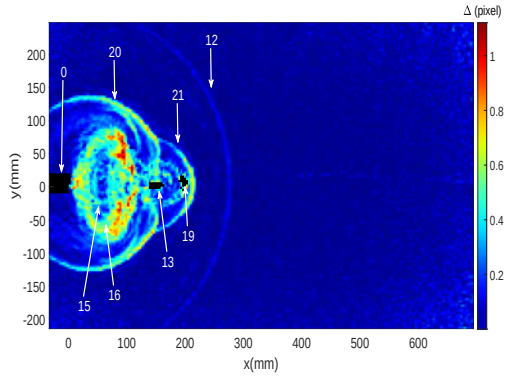

(c) $t = 254.3\,\mu s$

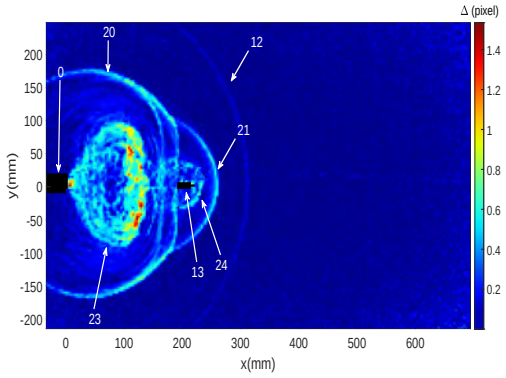

(d) $t = 354.3\,\mu s$

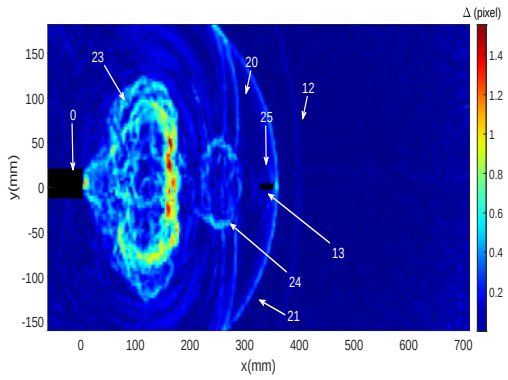

(e) $t = 604.7\,\mu s$

Figure 8: Sequential development of the two precursor flow for the first configuration,
15: the barrel shock, 16:the vortex ring, 17: the Mach disk, 18: normal shock, 19: unburnt powder, 20: the main blast wave, 21: the dome, 22: the turbulent plume, 23: the ball of the combustion gas, 24: the circular zone, 25: The signature of a supersonic projectile.

Fig. 8c and 8d. At this time, it is also seen that the decelerated combustion gas formed a distinctive ball (marker 23) and remained in the vicinity of the muzzle. It should be pointed out that despite the transient dynamic behavior of this flow, all the described phenomena were reproducible.

Moreover, this large FOV allowed us to visualize another reproducible phenomenon, namely the presence of a zone of different density delimited by a circular perimeter (marker 24) centered at $x = 207\,mm$ in Fig. 8e. This zone constitutes the residue of the turbulence ball of the first precursor flow. It is characterized by its low density and high temperature. Furthermore, so far, the projectile is always perceived as locally subsonic. As soon as the projectile crosses this zone and enters the undisturbed environment, it develops an attached shock wave as well as expansion waves characteristic of a supersonic flight projectile (mark 25), Fig. 8e.

5. Conclusion

In this study, we have used the density-based, non-intrusive BOS technique to analyze various flows in ballistics fields. The choice of this technique has been motivated by the simplicity of its implementation, the whole-field nature of its quantitative measurements as well as its unlimited FOV. The results of three typical tests have proven the relevance of this visualization technique as an experimental tool in the field of ballistics.

We have proposed two new contributions to the implementation of BOS. Both are necessary for the implementation of BOS in the ballistic field. Firstly, a new reconstruction technique for the axisymmetric refractive index/density field takes advantage of the two angular deviations. This method is more accurate and more robust against experimental noise than the simple Abel inversion, something important in the ballistic field where the temporal averaging of the visualized field is problematic. Also, since the propellant flow is loaded by unburnt particles, its BOS visualization is not accurate without a phase separation preprocessing of the raw images. Therefore, we have presented a simple approach for the automatic masking of these particles.

We have demonstrated that BOS has succeeded in capturing the main characteristics of the subsequent development of the flow fields around a 0.338-inch projectile launched at supersonic and transonic velocities. Indeed, the discussed results have shown the opening, detachment, and shifting away of the shock waves at the projectile tip as it decelerates and enters the transonic domain. Likewise, the characteristic triangle of expansion waves at the tail of the projectile was visualized. Moreover, the reconstructed density profiles have shown a satisfactory comparison with the CFD results of supersonic and transonic projectiles.

The most challenging case in the foregoing study was the visualization of the evolution and decay of the near and middle muzzle flow fields. The BOS has been able to observe the behavior of these supersonic and transient flow fields and their interactions. Furthermore, we have described the structure and the development of the underexpanded free jets resulting from the launch of a supersonic projectile. Also, their axial and radial density distributions have been measured and we have studied their development under various scenarios. The early development of the precursor flow in the different configurations presents the profile of an extremely underexpanded jet and that it evolves towards another structure according to the launch velocity of the projectile. The relevant findings reported will allow a more in-depth experimental and numerical analysis of these flows in the future.

Acknowledgments

The authors would like to acknowledge the team of the Accredited Ballistic Applications Laboratory at the Royal Military Academy for their efforts during the establishment of the experimental setups.

References

[1] D. E. Carlucci, S. S. Jacobson, Ballistics: Theory and Design of Guns and Ammunition, Third Edition, CRC Press, 2018.

[2] A. Moumen, J. Grossen, I. Ndindabahizi, J. Gallant, P. Hendrick, Visualization and analysis of muzzle flow fields using the Background-Oriented Schlieren technique, J Vis (2020) 1–15doi:10.1007/s12650-020-00639-w.

[3] V. D. Briey, A. Moumen, B. G. Marinus, M. Pirlot, Influence of Crossing the Transonic Domain for Precision Ammunition, 31st International Symposium on Ballistics 0 (0). doi:10.12783/ballistics2019/33109.

[4] G. Klingenberg, J. Heimerl, Gun Muzzle Blast and Flash, Progress in Astronautics and Aeronautics, American Institute of Aeronautics and Astronautics, 1992.

[5] G. Klingenberg, H. Mach, Experimental study of non-steady phenomena associated with the combustion of solid gun propellants, Symposium (International) on Combustion 16 (1) (1977) 1193–1200. doi:10.1016/S0082-0784(77)80407-4.

[6] G. Klingenberg, H. Mach, G. Smeets, Flow Field Measurements of an Unsteady Reacting Muzzle Exhaust Flow, Journal of Heat Transfer 105 (4) (1983) 884–888. doi:10.1115/1.3245677.

[7] G. Klingenberg, Gun Muzzle Blast and Flash, Propellants Explos. Pyrotech. 14 (2) (1989) 57–68. doi:10.1002/prep.19890140204.

[8] E. M. Schmidt, D. D. Shear, THE FLOW FIELD ABOUT THE MUZZLE OF AN H-16 RIFLE, Tech. Rep. AD916646, USA Ballistic Research Laboratory, ABERDEEN PROVING GROUND, MARYLAND (Jan. 1974).

[9] E. Schmidt, D. Shear, The formation and decay of impulsive, supersonic jets, in: 7th Fluid and PlasmaDynamics Conference, American Institute of Aeronautics and Astronautics, Palo Alto,CA,U.S.A., 1974. doi:10.2514/6.1974-531.

[10] E. M. Schmidt, Muzzle Blast Pressure Loadings upon Aircraft Surfaces:, Tech. rep., Defense Technical Information Center, Fort Belvoir, VA (Feb. 1984). doi:10.21236/ADA139132.

[11] E. M. Schmidt, D. Shear, Optical Measurements of Muzzle Blast, AIAA Journal 13 (8) (1975) 1086–1091. doi:10.2514/3.60506.

[12] A. Merlen, A. Dyment, Similarity and asymptotic analysis for gun-firing aerodynamics, J. Fluid Mech. 225 (1991) 497–528. doi:10.1017/S0022112091002148.

[13] K. S. Fansler, Description of Gun Muzzle Blast by Modified Ideal Scaling Models:, Tech. rep., Defense Technical Information Center, Fort Belvoir, VA (Sep. 1997). doi:10.21236/ADA330051.

[14] A. Celmins, Theoretical accuaracy of acoustic gas temperature measurements in guns, Tech. Rep. ARBRL-TR-02134, USA Ballistic Research Laboratory, ABERDEEN PROVING GROUND, MARYLAND (Jan. 1979).

[15] R. Gopalapillai, H.-D. Kim, T. Setoguchi, S. Matsuo, On the near-field aerodynamics of a projectile launched from a ballistic range, Journal of Mechanical Science and Technology 21 (7) (2007) 1129–1138. doi:10.1007/BF03027663.

[16] D. Cler, CFD Application to Gun Muzzle Blast - A Validation Case Study, in: 41st Aerospace Sciences Meeting and Exhibit, American Institute of Aeronautics and Astronautics, Reno, Nevada, 2003. doi:10.2514/6.2003-1142.

[17] C. K. Muthukumaran, G. Rajesh, H. D. Kim, The Launch Dynamics of Supersonic Projectiles, Journal of Spacecraft and Rockets 50 (6) (2012) 27. doi:10.2514/1.A32466.

[18] H. Zhang, Z. Chen, X. Jiang, H. Li, Investigations on the exterior flow field and the efficiency of the muzzle brake, Journal of Mechanical Science and Technology 27 (1) (2013) 95–101. doi:10.1007/s12206-012-1223-8.

[19] Z. Jiang, K. Takayama, B. W. Skews, Numerical simulations of two blasts by a supersonic projectile discharged from a tube, in: C.-H. Bruneau (Ed.), Sixteenth International Conference on Numerical Methods in Fluid Dynamics, Vol. 515, Springer Berlin Heidelberg, 1998, pp. 61–66. doi:10.1007/BFb0106562.

[20] R. Watanabe, K. Fujii, F. Higashino, Numerical simulation of the flow around a projectile passing through a shock wave, in: 13th Applied Aerodynamics Conference, American Institute of Aeronautics and Astronautics, San Diego,CA,U.S.A., 1995. doi:10.2514/6.1995-1790.

[21] J. Sahu, Numerical computations of transonic critical aerodynamic behavior, AIAA Journal 28 (5) (1990) 807–816. doi:10.2514/3.25123.

[22] S. I. Silton, Navier-Stokes Computations for a Spinning Projectile from Subsonic to Supersonic Speeds, Journal of Spacecraft and Rockets 42 (2) (2005) 223–231. doi:10.2514/1.4175. URL https://arc.aiaa.org/doi/10.2514/1.4175

[23] J. Sahu, Transonic Navier-Stokes Computations for a Spinning Body of Revolution, Tech. Rep. AD-A241 015, Ballistic Research Laboratory (BRL) Aberdeen Proving Ground, Maryland (1991).

[24] G. E. A. Meier, New optical tools for fluid mechanics, Sadhana 23 (5-6) (1998) 557–567. doi:10.1007/BF02744579.

[25] L. Venkatakrishnan, Density Measurements in an Axisymmetric Underexpanded Jet by Background-Oriented Schlieren Technique, AIAA Journal 43 (7) (2005) 1574–1579. doi:10.2514/1.12647.

[26] G. S. Settles, Schlieren and Shadowgraph Techniques: Visualizing Phenomena in Transparent Media, softcover reprint of the hardcover 1st edition 2001 Edition, Experimental Fluid Mechanics, Springer, Berlin Heidelberg, 2001.

[27] M. Raffel, Background-oriented schlieren (BOS) techniques, Experiments in Fluids 56 (3) (2015) 60. doi:10.1007/s00348-015-1927-5.

[28] N. A. Fomin, Speckle Photography for Fluid Mechanics Measurements, Springer Berlin Heidelberg, Berlin, Heidelberg, 1998. doi:10.1007/978-3-662-03707-2.

[29] A. B. Gojani, B. Kamishi, S. Obayashi, Measurement sensitivity and resolution for background oriented schlieren during image recording, Journal of Visualization 16 (3) (2013) 201–207. doi:10.1007/s12650-013-0170-5.

[30] A. Moumen, The Quantitative Visualization of Flow Fields around Transonic and Supersonic Projectiles Using Background Oriented Schlieren Technique, Not submitted 14.

[31] D. J. Tan, D. Edgington-Mitchell, D. Honnery, Measurement of density in axisymmetric jets using a novel background-oriented schlieren (BOS) technique, Experiments in Fluids 56 (11). doi:10.1007/s00348-015-2076-6.

[32] J. Dubois, tude exprimentale de jets libres, compressibles ou en prsence dun obstacle, Ph.D. thesis, Aix-Marseille Universit (2010).

[33] F. Klinge, T. Kirmse, J. Kompenhans, Application of Quantitative Background Oriented Schlieren (BOS): Investigation of a Wing Tip Vortex in a Transonic Wind Tunnel, in: Proceedings of PSFVIP-4, 2003, p. 12.

[34] D. A. Khalitov, E. K. Longmire, Simultaneous two-phase PIV by two-parameter phase discrimination, Experiments in Fluids 32 (2) (2002) 252–268. doi:10.1007/s003480100356.

[35] K. T. Kiger, C. Pan, PIV Technique for the Simultaneous Measurement of Dilute Two-Phase Flows, Journal of Fluids Engineering 122 (4) (2000) 811–818. doi:10.1115/1.1314864.

[36] M. Raffel, C. E. Willert, F. Scarano, C. J. Kähler, S. T. Wereley, J. Kompenhans, Particle Image Velocimetry: A Practical Guide, third edition Edition, Springer, Cham, 2018.

[37] N120 rifle powder - Vihtavuori. URL www.vihtavuori.com/powder/n120-rifle-powder/

[38] W. Thielicke, E. Stamhuis, PIVlab – Towards User-friendly, Affordable and Accurate Digital Particle Image Velocimetry in MATLAB, Journal of Open Research Software 2(1):e30doi:http://dx.doi.org/10.5334/jors.bl.

[39] J. D. A. Jr, Modern Compressible Flow: With Historical Perspective, third edition Edition, Elizubrth A. Jones, 2003.

[40] J. D'Errico, Inverse (integrated) gradient, https://nl.mathworks.com/matlabcentral/fileexchange/9734 (2013).

[41] E. Franquet, V. Perrier, S. Gibout, P. Bruel, Free underexpanded jets in a quiescent medium: A review, Progress in Aerospace Sciences 77 (2015) 25–53. doi:10.1016/j.paerosci.2015.06.006.

[42] J. Panda, R. G. Seasholtz, Measurement of shock structure and shock–vortex interaction in underexpanded jets using Rayleigh scattering, Physics of Fluids 11 (12) (1999) 3761–3777. doi:10.1063/1.870247.

Implementation of A Generalized Actuator Disk Model into the Weather Research and Forecasting (WRF) Model for High-fidelity Simulations of Wind Turbine Wakes

Baris Kale

Environmental and Applied Fluid Dynamics Department, von Karman Institute for Fluid Dynamics, Belgium, baris.kale@vki.ac.be

Advisor: Sophia Buckingham

Senior Research Engineer, Environmental and Applied Fluid Dynamics Department, von Karman Institute for Fluid Dynamics, Belgium, sophia.buckingham@vki.ac.be

Supervisor: Jeroen van Beeck

Professor, Environmental and Applied Fluid Dynamics Department, von Karman Institute for Fluid Dynamics, Belgium, vanbeeck@vki.ac.be

University Supervisor: Alvaro Cuerva Tejero

Professor, Aerospace Engineering, Universidad Politécnica de Madrid, Spain, alvaro.cuerva@upm.es

Abstract

A generalized actuator disk model (GAD) is implemented into an open-source numerical weather prediction code (i.e., the Weather Research and Forecasting (WRF) model) in order to perform high spatial resolution microscale simulations of atmospheric flows. Large-eddy simulation (LES) is performed to resolve energy-containing eddies of turbulent motions and the GAD model is used to calculate turbine-induced forces distributed over the rotor disk (psi., thrust, lift and drag) via blade-element momentum theory (BEMT). NREL's publicly available 5 MW wind turbine model is chosen for evaluation of the idealized WRF-LES results. This turbine is a reference wind turbine, and therefore, no comparison studies have been done in the current work. Instead, methodology and the results of an ideal WRF-LES simulation including generalized actuator disk parameterization are given. The nonlinear backscatter and anisotropy (NBA) subfilter-scale turbulence closure was chosen for the idealized simulations of the GAD. The surface boundary conditions were specified using the Monin-Obukhov similarity theory and periodic lateral boundary conditions were prescribed for the outer domain. Coarser LES domain was run 15h to spin-up turbulence consistent with the geostrophic wind of $U_{geo} = 14.5\ m/s$, oriented from $\lambda = 292.5°$ (22.5° N of W) and surface kinematic heat flux of $H_s = 20\ W/m^2$. The inner LES domain with the actuator disk was turned on at the beginning of $15h$ and was run for $50m$.

Keywords: Weather Research and Forecasting model, actuator disk model, blade-element momentum theory, large-eddy simulation

1. Introduction

The most important part of the troposphere is its closest part to the Earths ground named as the Atmospheric Boundary Layer (ABL) where many atmospheric events such as rising thermals, plumes or roll vortices that carry most of the turbulent fluxes of momentum [1], turbulent transport of moisture and pollutants [2], electric fields and electromagnetic radiation take place. These physical phenomenons resulted in formation of complex turbulent structures through the ABL, must be taken into account when simulating the atmospheric flows to solve engineering problems, especially in wind energy applications (psi., wind turbine siting) [3]. The impacts of atmospheric turbulence on wind turbine performance

need to be well represented when simulating turbulence over the diurnal cycle as well as under different meteorological conditions. Accurate modeling of ABL flows and their interactions with an isolated wind turbine or clustered wind turbines within a wind farm depends on the proper representation of atmospheric conditions and the correct parameterization of wind turbine dynamics. Most engineering computational fluid dynamics (CFD) tools used to investigate flow-turbine interaction lack in representing realistic weather effects, and therefore numerical weather prediction (NWP) models, psi., the Weather Research and Forecasting (WRF) [4], are generally preferred to simulate the turbulence field and wake formation under variable weather conditions. Mesoscale weather prediction models which are based on the eddy diffusivity concept and are used to simulate large turbulent structures occurring in atmospheric events are not capable enough to capture turbine-induced wakes in a utility-scale wind farm, due to their limited spatial and temporal resolutions. Unlike wind farm parameterizations utilized in mesoscale applications, microscale modeling combined with an adequate wind turbine model can provide both, a more precise prediction of the turbulent flow, and therefore, a more accurate estimation of the characteristics of wind turbine wake. Moreover, incorporating the mesoscale input into smaller scales, i.e., providing the realistic initial and boundary conditions to microscale models, improves the quality of simulation of resolved atmospheric turbulence and flow-turbine interaction [5]. The WRF model uses grid nesting strategy to couple mesoscale and microscale simulations by forcing lateral boundary conditions into the nested domain(s) to support resolving the energetic scales of atmospheric turbulence obtained from the outer domain(s). Incorporating atmospheric drivers (psi., atmospheric radiation, surface physics, and cloud formation) into the inner-most nested domain allows a promising study of wind turbine aerodynamics and wake formation in real world conditions. Recent studies on wind energy applications have demonstrated the advantages of large-eddy simulation (LES) that permits the accurate reproduction of temporal and spatial turbulence scales in the ABL when performing microscale simulations [5; 6; 7; 8]. The accuracy of LES in atmospheric flow simulations of wind energy applications depends on the parameterization of subfilter-scale (SFS) turbulent fluxes as well as turbine-induced forces [9; 10; 11]. Practically, performing simulations for fully-resolved flow field around a wind turbine, including the shed vortices in the wake, can be computationally very expensive since such simulations require too many computational grid points. Use of computational methods are mostly preferable to the experiments as they are cheaper and comparably easier, also they allow to conduct various parametric studies by only changing a single flow parameter in a numerical simulation. Due to the fact that LES of a fully-resolved turbine model is computationally expensive, the concept of wind turbine parameterization based on blade-element momentum (BEM) theory of Glauert [12] is generally preferred by researchers [13; 14; 15; 16; 17].

There are many methods for predicting wind turbine performance, aerodynamic forces, and the exerted energy due to wind turbine rotor, however, the only approach commonly used today uses the BEM theory. Wind turbine parameterizations such as the generalized actuator disk (GAD) or line (GAL) models have been widely used in high-fidelity numerical simulations. Both models are based on BEM theory to calculate turbine-induced forces, however, the GAL model is superior to the GAD because of its capability to capture small-scale vorticity produced from the blade's tips and roots [5]. Therefore, the GAL model requires higher spatial resolution in order to represent such small turbulent structures (psi., hub and tip vortices) while the GAD model is often used as a permeable drag disk with relatively coarser grid spacing that a few grid points in each direction are enclosed by the rotor swept area. In the GAD parameterization, turbine-induced forces (thrust and torque) are averaged over a two-dimensional disk containing the rotating turbine and added to the filtered momentum equations in LES at the turbine location [8]. Thrust or drag force is the main component of downstream wake formation whereas torque force plays a key role in kinetic energy transport [6]. In addition to that, the fidelity of modeled flow-turbine interactions depends on the effectiveness of the sub-filter turbulence parameterization in LES, and the geometry of the turbine blade and its specifications.

Researchers have been performing atmospheric LES for wind energy applications for decades, for instance, Mikkelsen [15] also applied actuator disk method to wind turbines and examined the flow characteristics as well as yawed inflow effects on the rotor. Sørensen *et al.* [18] investigated actuator disk performance through a constant loading on the full-field wake and demonstrated that the turbulent wake behind the rotor is unstable and varies in spatio-temporal scales. Mirocha *et al.* [6] implemented actuator disk model to a compressible ABL flow solver, WRF, and did simulations using LES and they generated in-

flow conditions for LES by introducing small perturbations on the potential temperature. Aitken *et al.* [7] extended the work of Mirocha *et al.*. [6] by reformulating the aerodynamic forces on the blade and added turbine tilt as well as nacelle and tower drag. They compared their results to nacelle-based scanning lidar measurements taken in stable atmospheric conditions during a field campaign test in the western United States. Mirocha *et al.* [19] studied near wake flow using actuator disk parameterization scheme implemented in WRF, and investigated wind turbine impacts on the reduced downstream flow. Most recently, Arthur *et al.* [8] performed simulations in WRF-LES by coupling mesoscale and microscale and they used a generalized actuator disk concept in the finer scale LES domain to asses the performance of a wind farm during a frontal passage. They also computed the total power production of the wind farm in real-case simulations, i.e., forcing mesoscale inflow and boundary conditions to the microscale child nests, and developed a new algorithm in order to take into account the change in wind direction within the diurnal evolution of the atmospheric boundary layer.

In this paper, the methodology of implementation of the GAD model into WRF-LES is presented. As in contemporary actuator models, this wind turbine parameterization uses BEM theory of two-dimensional stream tube dynamics and airfoil look-up tables enabling the investigation of tilted rotor dynamics, nacelle and tower effects on the wake behind wind turbine(s). It also includes pitch and yaw capability based on an implicit running average algorithm at a designated upstream grid location [8]. The performance of the GAD model is investigated by performing idealized microscale LES simulations. These results are investigated in terms of temporal evolution of the wind speed in the vicinity of wind turbine.

2. Methodology

2.1. GAD formulation and implementation into WRF

The most common approach used nowadays by means of loading and performance prediction of wind turbines uses the BEM theory. The GAD model combines stream tube dynamics with airfoil aerodynamics using look-up tables. Lift and drag forces are computed based on the blade geometry and inflow properties at an upstream location. Induction factors required by BEM theory are then employed to resemble modifications to the flow field near the blades due to the interactions between blade and surrounding air. A brief background of BEM theory is given below. More details can be found in references [12], [18], and [20].

2.1.1. Stream tube dynamics

A rotor acts as a permeable disk and the kinetic energy of the upcoming wind is reduced by wind turbine and converted into the mechanical energy [20]. It adds drag, caused by the pressure drop, into the flow and slows down the far upstream velocity, V_0, hence new reduced-velocities, V_1 at the rotor and V_2 at the wake, form and streamlines get the following structure depicted in Fig. 1.

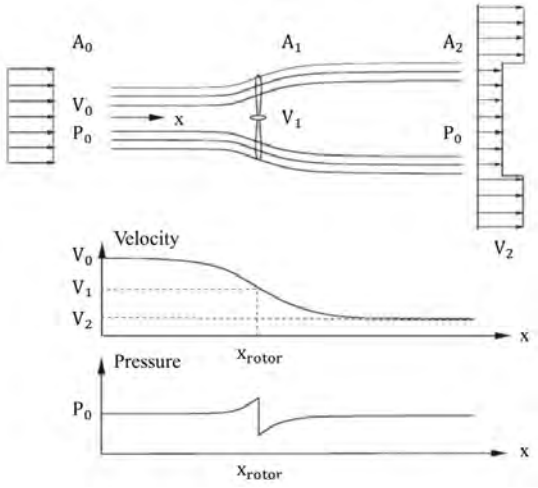

Figure 1: Sketch of streamlines (top), the change of axial velocity (middle), and pressure (bottom) over wind turbine rotor [20].

The sudden pressure drop at the rotor is due to discontinuity of the flow over the rotor, and recovered to the atmospheric pressure level after effect of the rotor blades vanish. Due to the fact that the Mach number of the wind flow is small and thus flow is assumed to be incompressible ($\rho_{air} \approx constant$), the streamwise velocity gradually reduces in the horizontal direction. Due to law of conservation of mass, mass flow rate, $\dot{m}$ should be constant in each cross-section, meaning that

$$\dot{m} = \int \rho V dA = \rho V_0 A_0 = \rho V_1 A_1 = \rho V_2 A_2 \quad (1)$$

where A_0 and A_1 are the fictitious cross-sections (control surfaces) of the upwind and downwind flow, respectively. Following Eq. 1, wind turbine thrust can be formulated as follows:

$$T = \dot{m}(V_0 - V_1) = \rho V_1 A_1 (V_0 - V_1) \quad (2)$$

$$E = 0.5m(V_0^2 - V_1^2) \tag{3}$$

E in Eq. 3 denotes the energy extracted from the upwind air flow. Introducing an *axial induction factor*, a, the flow velocity at the rotor, u, can be re-formulated as $V_1 = (1-a)V_0$, and the downstream velocity is obtained as $V_2 = (1-2a)V_0$. The thrust generated by the rotor, T, and torque, M, are given as

$$\begin{aligned} dT &= 4\pi r\rho V_0^2 a(1-a)dr \\ dM &= 4\pi r^3 \rho V_0 \omega a'(1-a)dr \end{aligned} \tag{4}$$

The left-hand sides, dT and dM in Eq. 4 are found from the local flow around the blade. The stream tube is discretized into N annular elements and each annular element has length, dr, and arising forces are calculated at these actuation points.

2.1.2. Blade aerodynamics

The advantage of using BEM theory is due to the fact that it is computationally easy to implement and cheap, also it accurately represents the wind turbine aerodynamics, however, empirical input data are not always available for some specific airfoils. It uses two-dimensional airfoil data for individual sections of the blade. The formulations of velocity components at each radial section along the blade are based on the upcoming wind speed, induction factors, and the rotational speed of the rotor, and are used to calculate the angle of attack. After the local angle of attack is calculated, the lift and drag coefficients are obtained locally using tabulated input airfoil data, and by doing that, the loading along the blade can be fully calculated. The axial loading and torque of the rotor can be expressed as

$$\begin{aligned} \frac{dT}{dr} &= N_b F_n = 0.5\rho c B V_{rel}^2 C_n \\ \frac{dM}{dr} &= N_b r F_t = 0.5\rho c B V_{rel}^2 C_t \end{aligned} \tag{5}$$

where c is the chord length, B is the total number of blades, V_{rel} is the relative velocity, F_n and F_t are the axial and tangential blade forces, respectively. C_n and C_t denote the two-dimensional force coefficients and are given as:

$$C_n = \frac{2F_n}{\rho c V_{rel}^2}, \quad C_t = \frac{2F_t}{\rho c V_{rel}^2} \tag{6}$$

The axial and tangential velocities can be represented in terms of induction factors: $V_n = V_0(1-a)$ and $V_t = \omega r(1+a')$. Moreover, θ is the local pitch of the blade (i.e., the local angle between the blade chord and plane of rotation) and it is the summation of the blade pitch (control), θ_C, and the geometric (structural) twist, θ_G, ($\theta(r) = \theta_C + \theta_G(r)$). Lastly, ϕ is the flow angle between rotor plane and relative velocity, V_{rel}. The angle of attack, α, is then calculated as the function of radial distance, r,

$$\alpha(r) = \phi(r) - \theta(r) \tag{7}$$

The force coefficients can also be represented through geometrical aspect of the cross-sectional view of an airfoil element (Fig. 2).

$$\begin{aligned} C_n &= C_l cos(\phi(r)) + C_d sin(\phi(r)) \\ C_t &= C_l sin(\phi(r)) - C_d cos(\phi(r)) \end{aligned} \tag{8}$$

If the flow is coming through the identical blade elements at the same angle of attack in a two-dimensional manner, the aerodynamic lift and drag forces acting on these elements are the same [20]. This is the basic assumption of BEM theory, however, in current GAD implementation, non-identical blade cross-sections are used so that each section has unique lift and drag forces per length, $L(r)$ and $D(r)$. These varying forces over the blade span can be written as

$$\begin{aligned} L(r) &= 0.5\rho V_{rel}^2 c(r) C_l \\ D(r) &= 0.5\rho V_{rel}^2 c(r) C_d \end{aligned} \tag{9}$$

Therefore, axial and tangential blade forces, $F_n(r)$ and $F_t(r)$ given in Eq. 8, (also shown in Fig. 2) can be formulated as follows:

$$\begin{aligned} F_n(r) &= L(r)cos(\phi(r)) + D(r)sin(\phi(r)) \\ F_t(r) &= L(r)sin(\phi(r)) - D(r)cos(\phi(r)) \end{aligned} \tag{10}$$

A ratio which is the fraction of the annular area in the control volume, $\sigma(r)$, and named as solidity, is defined as

$$\sigma(r) = \frac{c(r)B}{2\pi r} \tag{11}$$

where $c(r)$ is the local chord length. Using formulations derived above, the incremental thrust and torque of the rotor can be re-formulated incorporating Prandtl's correction factor to the aerodynamic loads, F, as follows:

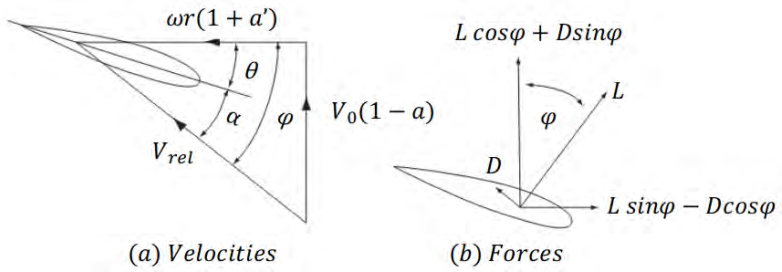

Figure 2: Blade-element (a) velocities and (b) forces on a two-dimensional airfoil geometry.

$$\begin{aligned} dT &= 4\pi r\rho V_0^2 a(1-a)Fdr \\ dM &= 4\pi r^3 \rho V_0 \omega a'(1-a)Fdr \end{aligned} \tag{12}$$

By re-arranging Eqs. 11 and 12, the axial and tangential induction factors, a and a' can be found as:

$$\begin{aligned} a(r) &= \frac{1}{\frac{4F\sin^2(\phi(r))}{\sigma(r)C_n} + 1} \\ a'(r) &= \frac{1}{\frac{4F\sin(\phi(r))\cos(\phi(r))}{\sigma(r)C_t} - 1} \end{aligned} \tag{13}$$

The term F in Eq. 13 accounts for the Prandtl's hub and tip corrections for vorticity generation given as $F = F_{tip}F_{hub}$ where $F_{tip} = \frac{2}{\pi}\cos^{-1}(e^{-f_{tip}})$ and $F_{hub} = \frac{2}{\pi}\cos^{-1}(e^{-f_{hub}})$ with $f_{tip} = B(r_{tip} - r)/2r\sin(\phi(r))$, and $f_{hub} = B(r - r_{hub})/2r\sin(\phi(r))$. r_{tip} and r_{hub} denote the radii of the blade and hub.

2.1.3. Solution procedure

The required equations for the BEM calculation are derived above. Due to the fact that each blade cross-section is individually treated, each solution can be completed before going to the next radial position. To do so, a convergence criteria has to be defined. Thus, the following algorithm is applied for BEM calculations:

1. Initialize axial and tangential induction factors, (i.e., $a = 0$ and $a' = 0$).
2. Compute the flow angle, ϕ using the ratio between axial and tangential velocities.
3. Obtain V_1 at the GAD location.
4. Calculate the rotational speed, Ω, and the local blade pitch angle, θ, as a function of V_0.
5. Compute the local angle of attack, α, using Eq. 7.
6. Read lift and drag coefficients, C_l and C_d from the tabulated data, interpolate if necessary.
7. Compute axial and tangential forces, $F_n(r)$ and $F_t(r)$, as well as their coefficients, C_n and C_t.
8. Calculate axial and tangential induction factors, a and a', using Eq. 13.
9. If a and a' are less than threshold, finish BEM calculation. Else, go to (2) and iterate until a and a' reach to specified convergence criteria.
10. Compute the local loads on each blade cross-section.

In BEM calculations, the rotor blade should be divided into N elements, and typically it is suggested by Sørensen [21] to use $20 - 30$ elements to accurately represent a blade geometry. The BEM calculation converges within $5 - 20$ iterations per each cross-section over the blade.

2.1.4. Force distribution and projection onto WRF's coordinates

The computed lift and drag forces in Eq. 9 are projected onto the normal and tangential directions using Eq. 11. However, these forces cannot be added into WRF's momentum equations directly and must be projected onto WRF's x, y, z directions at first. Considering the effects of yaw and rotor tilt, these forces can be defined as

$$\begin{aligned} F_x &= F_n\cos\delta\cos\Phi + F_t\sin\Phi\sin \\ &\quad - F_t\cos\Phi\cos\ \sin\delta \\ F_y &= F_n\cos\delta\sin\Phi - F_t\cos\Phi\sin \\ &\quad - F_t\sin\delta\cos\ \sin\Phi \\ F_z &= -F_n\sin\delta - F_t\cos\delta\cos\psi \end{aligned} \tag{14}$$

where Φ and ψ show the orientation of an actuation point on the disk, and δ is the rotor tilt angle. It is important to emphasize that the components of turbine forces in Eq. 15 are based on the diagram in Fig. 3 and any directional changes in the wind should

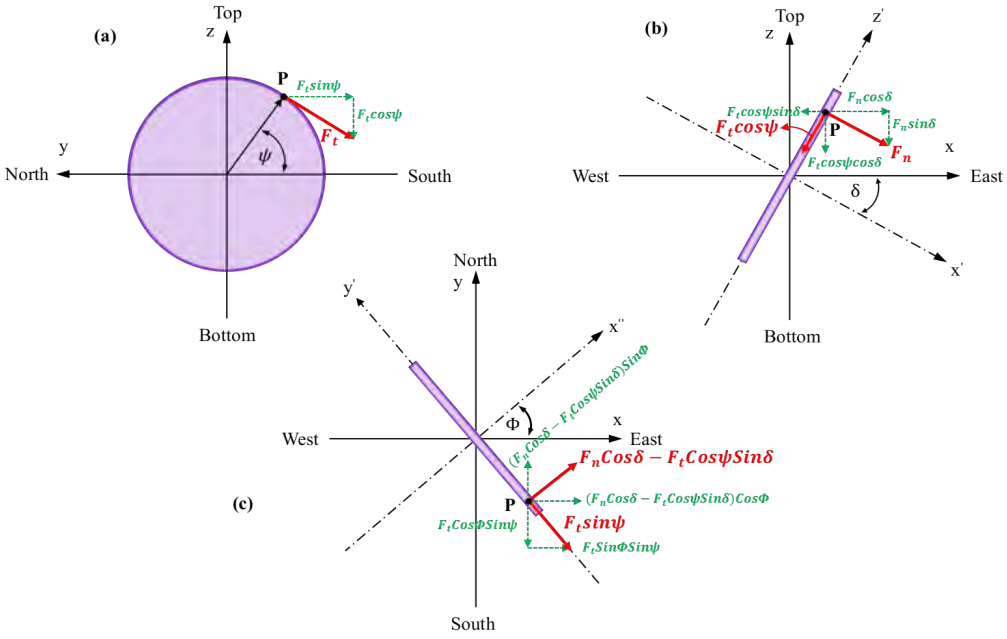

Figure 3: Coordinate system convention and forces acting on the rotor disk. Forces are shown in solid red, force components in dashed green, disk in magenta, axes and angles are in solid black. (a) A front view upwind of the disk normal to the rotor plane, (b) a side view of the rotor along the transverse axis, and (c) a top view looking down at the rotor.

be taken into account by re-formulating Eq. 14 according to wind direction conventions. The freestream wind speed to be used in BEM computations is given as follows:

$$V_0 = u\cos\delta\cos\Phi + v\cos\delta\sin\Phi - w\sin\delta \qquad (15)$$

where u, v, w are the instantaneous velocity components of wind in three directions. V_0 is calculated at an upstream point using running averages of the instantaneous velocity components while lift and drag forces obtained at the actuation points are functions of the instantaneous wind speed at that location. It is worth noting that these computed axial and tangential forces at the actuator disk location must be distributed smoothly over several computational grid points in all directions in order to avoid numerical instabilities at the isolated grid points. After adding F_x, F_y and F_z forces into WRF's filtered momentum equations, the equations in vector notation take the following form

$$\frac{\partial\overrightarrow{U}}{\partial t} = -\frac{G(d)\overrightarrow{F}}{2\pi r\rho}BA_e \qquad (16)$$

The left-hand-side in Eq. 16 is the time derivative of the velocity in x, y, and z directions, $G(d)$ is the three-dimensional Gaussian smoothing term or in other words the regularization kernel used in conventional CFD approach, $\overrightarrow{F}$ is the force vector in all directions, and ρ is the air density. The factor of $2\pi r$ is used to average the forces over the disk. Three-dimensional Gaussian smoothing term, $G(d)$, is given by Eq. 17:

$$G(d) = \frac{1}{\epsilon^3\pi^{3/2}}exp\left[-\left(\frac{d}{\epsilon}\right)^2\right] \qquad (17)$$

Here $d = \sqrt{(x-x_0)^2+(y-y_0)^2+(z-z_0)^2}$ is the distance between cell centered grid points (x, y, z) and actuation points (x_0, y_0, z_0) on each actuator line within the disk and ϵ is a parameter that serves as the width control mechanism and is related to the grid size [14; 16]. A_e is the frontal area of the actuation element on a cylindrical mesh system.

In addition, the impacts of the nacelle and tower on the flow are added to the GAD formulation and can be turned on/off by the user. The nacelle is modeled as a permeable disk as done for the rotor and the area of the nacelle is $A_{nac} = \pi R_{nac}^2$ where R_{nac} is its radius. The drag force exerted by the nacelle is parameterized as $F_{nac} = 0.5C_{D,nac}\rho A_{nac}V_{nac}^2$ where $C_{D,nac} = 1.0$ is the drag coefficient of the nacelle, ρ is the air density and V_{nac} is the instantaneous wind velocity normal to the nacelle face. Similarly, the tower is parameterized as cylindrical-shaped block with radius R_{tow} and area

Table 1: Physical and computational dimensions of ideal WRF-LES simulation. N_x, N_y, and Nz denote the computational grid points in x, y, and z directions while L_x, L_y, and L_z are the physical dimensions of the domains. Δx, Δy and Δz are the horizontal and vertical grid spacings. Δt is the timestep interval in seconds, SFS model is the subfilter scale parameterization used in LES, U_g and V_g are the components of specified geostrophic wind speed.

Domain	$\Delta x = \Delta y$	Δz	$N_x \times N_y \times N_z$	L_x	L_y	L_z	Δt	SFS Model	U_g	V_g
[−]	[m]	[m]	[−]	[m]	[m]	[m]	[s]	[−]	[m/s]	[m/s]
d01	30	~ 10	$201 \times 101 \times 64$	2010	1010	1700	1/4	NBA	13.40	-5.55
d02	10	~ 10	$301 \times 151 \times 64$	3010	1510	1700	1/12	NBA	13.40	-5.55

$A_{tow} = 2R_{tow}H$, where H is the height of the tower. Herein, the drag coefficient of the tower, $C_{D,tow}$ is set to 1.2, such that $F_{tow} = 0.5\rho A_{tow}V_{tow}^2$, where V_{tow} is the incident wind speed at the tower location. These nacelle and tower drag forces are then smoothed over several grid points in a three-dimensional Gaussian manner as done for the rotor forces. Although it is important to mention that the effects of the nacelle and tower on the drag are relatively small compared to the rotor because the total cross-sectional area of them is smaller than that of the disk [7], however, including these effects is significant for the completeness of the wind turbine simulation.

2.1.5. Turbine yaw mechanism

Turbine yaw mechanism implemented in the current GAD model is based on the work of Arthur *et al.* [8] and uses a running average of oncoming wind direction at a designated inflow point. Here, one rotor diameter upstream of the turbine hub normal to the rotor plane, and approximately at the same hub height is chosen as the inflow point. A yaw error is accumulated at each time step until the accumulated error exceeds a certain threshold value, herein it is set to $10,000\ (^\circ)^2 s$ and a yaw rate of $\gamma = 2^\circ s^{-1}$ is used. These parameters are user-defined and are found in the turbine configuration file.

$$E_{yaw}^n = E_{yaw}^{n-1} + sign(\Delta\phi^n)(\Delta\phi^n)^2\Delta t \qquad (18)$$

In above equation, n denotes the time step, $\Delta\phi$ ($\Delta\phi^n = \phi_{wind,ave}^N - \phi_{turb}^n$) is the difference between the incoming wind direction and the rotor plane face normal where ($\phi_{turb}^n = \phi_{turb}^{stored} \pm \gamma\Delta t$), and Δt is the time step interval. ϕ_{turb}^{stored} is the stored turbine direction at the beginning of the actual simulation or restart simulation. E_{yaw} is initially set to zero and is also reset to zero after the turbine is aligned with the oncoming wind (i.e., $\Delta\phi \approx 0$). Turbine yaw orientation is determined by the sign of the *signum* function in Eq. 18. While wind turbine yaws at a user-defined rate, no yaw error is stored. A running average algorithm is chosen to model the yaw mechanism realistically because the incident wind velocity at the inflow point may change instantaneously, and the turbine can not adapt to these sudden changes in wind direction.

$$\phi_{wind,ave}^N = \frac{1}{N}\sum_{n=1}^{N=100}\phi_{wind}^n \qquad (19)$$

where ϕ_{wind}^n is the instantaneous wind direction at the inflow point and at each time step. Basically, the horizontal velocity components of the oncoming wind at the chosen point are averaged over the previous hundred time steps and stored in the model. In the hundredth iteration, the averages of the total wind speed in all directions and the horizontal wind direction to be used for the dynamic yaw mechanism are calculated. In addition, this running average method is used to compute the turbine forces in BEM calculation. An algorithm has also been added to the GAD model to stop calling it when the incoming wind speed is not high enough to move the blades or exceeds the maximum allowed speed (i.e., when the wind speed is outside of the cut-in/cut-out range). In such cases, the model does not calculate any turbine forces or yaw error.

3. Idealized WRF-LES simulations with GAD

In this section, preliminary results of idealized WRF-LES simulations with GAD are presented. These simulations are performed by using WRF model version 4.2.2 [4]. The model forcing is conducted by imposing a surface sensible heat flux value of $H_s = 20\ W/m^2$ in order to examine the sensitivity of the model under weakly convective ABL conditions. There are two domains used in LES, with a fine-scale (d02) LES nested one-way within a coarser outer domain (d01). The horizontal spatial resolution is kept constant on the outer and nested domains, and the computational grid is stretched in the z direction

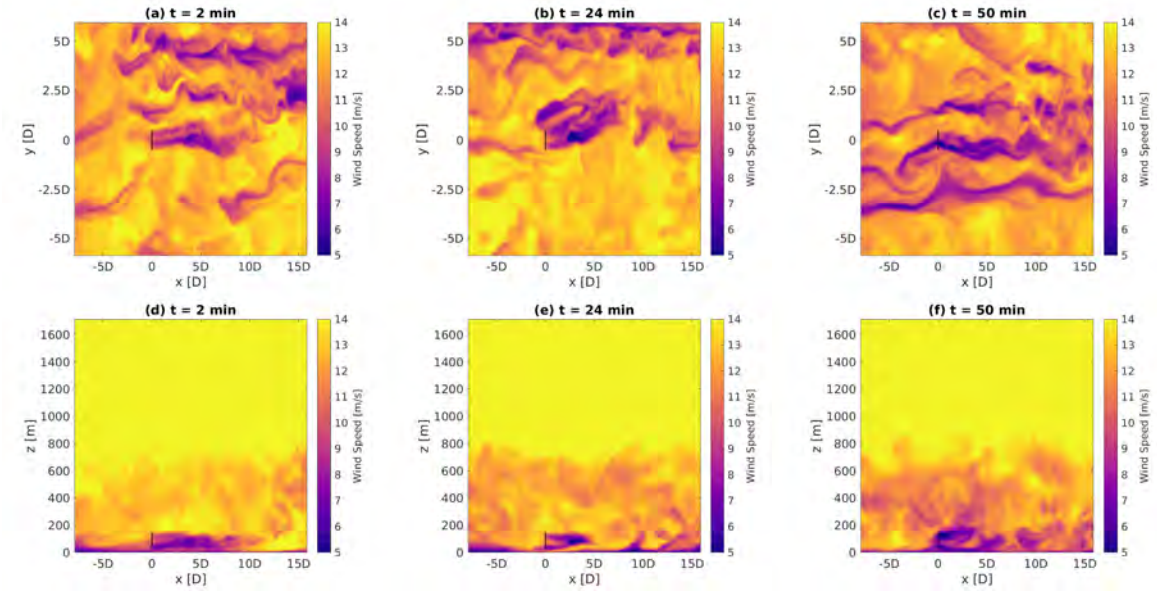

Figure 4: Snapshots of instantaneous horizontal velocity contours after 15h spin-up, (a-c) x-y, and (d-f) x-z domains. The black solid line marks the location of the GAD at $x = y = 0$.

in order to have similar Δz distribution as applied in the horizontal direction (see Table 1 for simulation details). Δz is almost constant up to height of 270 m and Δz is stretched above and is clustered near the model top.

WRF uses a pressure-based vertical coordinate system given by $\eta = (p - p_t)/(p_s - p_t)$, where p_t and p_s are the pressure values at the model top and surface. WRF's default fifth-order horizontal and third-order vertical advection schemes are used. The turbine hub is located at grid locations of $i = 100$ and $j = 75$ within the inner-most domain. The nonlinear backscatter and anisotropy (NBA) sub-filter scale turbulence closure [22]; [23] was chosen to study wake behind the turbine. The idealized simulation was initialized dry, and no radiation, cloud, or land surface models were used. The surface boundary conditions were specified using the Monin-Obukhov similarity theory [24].

Fifty-minutes of 2-min instantaneous velocity fields are generated using a surface heat flux value of $H_s = 20\ W/m^2$. No spin-up simulation is run and the GAD model is introduced at the beginning of the simulation without any wall effects at the bottom of the domain. Also, nacelle and tower effects are ignored. NREL's 5 MW and 126 m rotor diameter wind turbine [25] is chosen for the numerical simulations. Although the GAD model has turbine yaw capability, this feature is not tested in the current study because there is no change in the predominant inflow direction at the hub height parallel to the $x-$axis.

As noted before, the idealized LES is performed for the weakly convective atmospheric stratification with a 15h spin-up run and the contour plots of instantaneous snapshots of horizontal wind speed are depicted in Fig. 4. The first row of the incident velocity fields at $t = 2$ min, $t = 24$ min, and $t = 50$ min are in $x - y$ domain, at the hub height ($z_h \approx 90$ m), while the second row is in $x - z$ plane. GAD model, represented with solid black line, is placed at $x = y = 0$. A geostrophic wind with components of $U_g = 13.40\ m/s$ and $V_g = -5.55\ m/s$, oriented from $\lambda = 292.5°$ is specified for the LES. Periodic lateral boundary conditions were specified for the outer domain, and was run for $15h$ to spin-up turbulence consistent with the geostrophic wind and surface forcing. Due to the fact that turbulence field is uniform at $t = 2$ min, wind turbine wake is symmetric up to 10D, however, this symmetric behavior is lost due to increase in turbulence mixing and larger eddy sizes at $t = 24$ and $t = 50$ minutes. It is noteworthy to note that although the wakes emanating from the GAD are visible in incident contour plots of wind speed in the streamwise direction, they tend to be shorter and less consonant with the weakly convective conditions because of the enhanced turbulent mixing. The wake is relatively co-

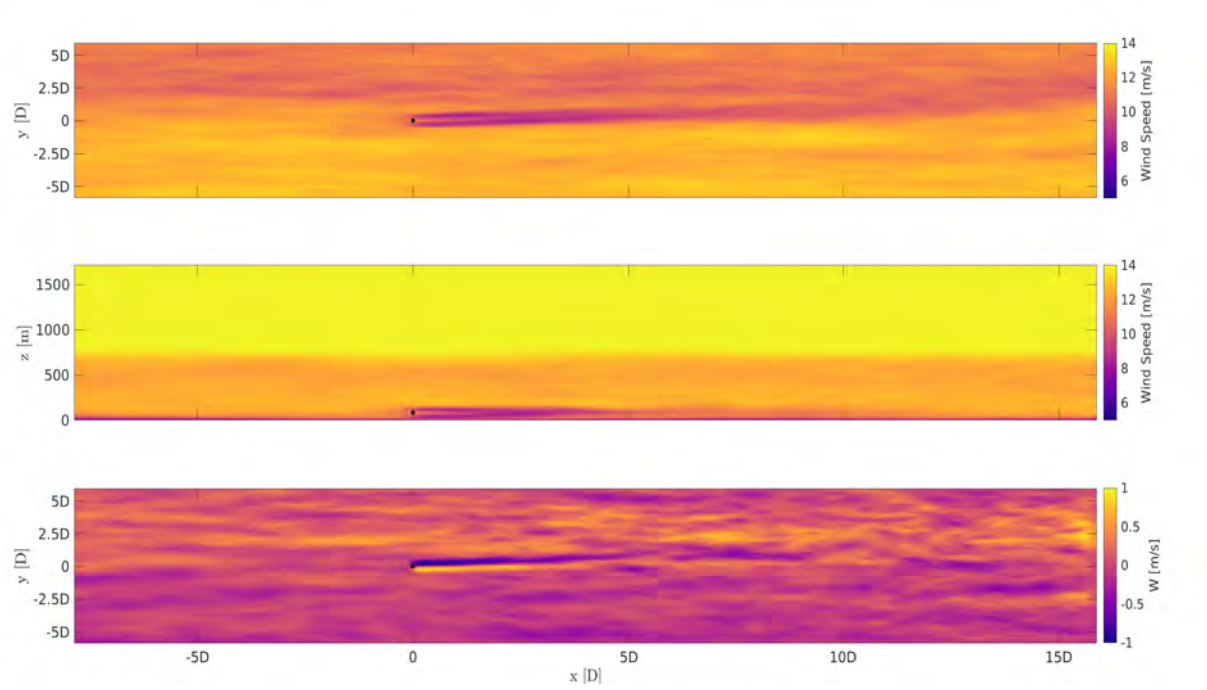

Figure 5: Snapshots of 50m-averaged velocity contours after 15h spin-up, wind speed in (top) x-y, (middle) x-z, and (bottom) vertical velocity in x-y domains. The black dot line marks the location of the GAD.

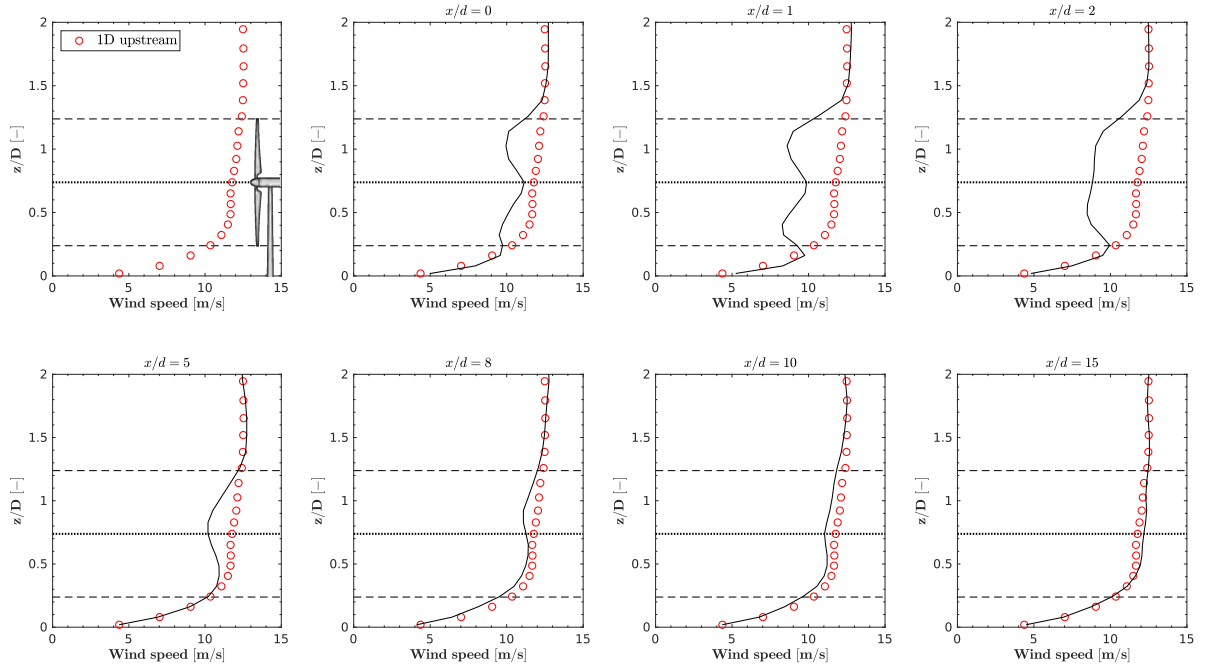

Figure 6: Representation of vertical profiles of the 50m-averaged horizontal velocity in idealized WRF- LES/GAD simulation: $1D$ upstream of the wind turbine (open red circles), different downstream locations (black solid lines). The upper and lower horizontal dashed lines indicate vertical levels cut by the turbine blades and the dotted line shows the hub height. D = 126 m is rotor diameter.

herent when close to the turbine itself. Furthermore, meandering is discernible in the far wake region in both $x-y$ and $x-z$ domains of Fig. 4 at $t = 24$ and $t = 50$ minutes, due to the supremacy of ambient turbulence over predominant wind direction.

The influence of the GAD can be better determined via time averaging of the flow field removing turbulent fluctuations round the mean flow. In Fig. 5, 50m-averaged horizontal wind speed contour plots are shown in $x-y$ (top) and $x-z$ (middle) and vertical velocity (bottom) in $x-y$ domains where the black dot at $x = y = 0$ represents the turbine location. The wakes appear nearly symmetric about the center as in Fig. 4 at $t = 2$ min. In Fig. 5, the bottom contour plot reveals that the lower momentum air moves upward for those vertical velocities $y > 0$, whereas high momentum air is transported from above hub height to downward due to the rotating wake. On the other hand, the comparison of time-averaged vertical wind profiles at several distances downstream from the turbine location can be helpful to understand wind turbine wake evolution in the GAD parameterization. The averaged horizontal wind speed profiles are given in Fig. 6 at distances of -1D, 0, 1D, 2D, 5D, 8D, 10D, and 15D in the longitudinal direction from the turbine revealing that wake attenuation after $x/d = 3$.

4. Conclusion

A generalized actuator disk (GAD) wind turbine parameterization was implemented into the Weather Research and Forecasting (WRF) model to provide more reliable simulation capability when studying flow-turbine interactions and wake formation in large-eddy simulations (LES) of atmospheric flows. The impacts of the actuator model under moderately convective atmospheric conditions were examined. Although the GAD model introduced herein has not been validated yet, however, shows qualitatively reliable and physically consistent results compared to the expected wake behaviors found in the literature [6; 7]. Detailed investigations will be performed to evaluate the accuracy and reliability of simulated wake characteristics under different atmospheric stability conditions (psi., pre-cursor simulation to speed-up turbulence mixing at the beginning of LES, wall effects, impacts of nacelle and tower at high-enough spatial resolutions, etc). It must be noted that the verification of the actuator disk model in WRF-LES is not straightforward and depends on the aerodynamic properties of the turbine blades and the stability conditions evaluated against corresponding measurement data. Note that this implementation is still under development and several improvements to the GAD model such as wind turbine power calculation will be performed in the future.

Acknowledgments

This research has been performed using computational resources of the von Karman Institute For Fluid Dynamics and has received funding from the European Unions Horizon 2020 research and innovation programme under the Marie Skłodowska-Curie grant agreement No 860101.

References

[1] J. R. Garratt, The Atmospheric Boundary Layer, Cambridge University Press, 1992.

[2] C. H. Moeng, Lecture Notes On The Planetary Boundary Layer (jun 2006).

[3] O. Temel and J. van Beeck, Coupling Mesoscale (WRF) to Microscale Simulations, in: CFD For Atmospheric Flows and Wind Engineering, von Karman Institute for Fluid Dynamics, Belgium, 2017.

[4] W. C. Skamarock and J. B. Klemp, A Time-split Nonhydrostatic Atmospheric Model for Weather Research and Forecasting Applications, Journal of Computational Physics 227 (7) (2008) 3465–3485.

[5] N. Marjanovic, J. D. Mirocha, B. Kosovic, J. K. Lundquist, and F. K. Chow, Implementation of A Generalized Actuator Line Model For Wind Turbine Parameterization In The Weather Research and Forecasting Model, Journal of Renewable and Sustainable Energy 9 (6) (2017) 063308.

[6] J. D. Mirocha, B. Kosovic, M. L. Aitken, and J. K. Lundquist, Implementation of A Generalized Actuator Disk Wind Turbine Model Into the Weather Research and Forecasting Model For Large-eddy Simulation Applications, Journal of Renewable and Sustainable Energy 6 (1) (2014) 013104.

[7] M. L. Aitken, B. Kosović, J. D. Mirocha, and J. K. Lundquist, Large Eddy Simulation of Wind Turbine Wake Dynamics in the Stable Boundary Layer Using the Weather Research and Forecasting Model, Journal of Renewable and Sustainable Energy 6 (3) (2014) 033137.

[8] R. S. Arthur, J. D. Mirocha, N. Marjanovic, B. D. Hirth, J. L. Schroeder, S. Wharton, and F. K. Chow, Multi-Scale Simulation of Wind Farm Performance During a Frontal Passage, Atmosphere 11 (3) (2020) 245.

[9] F. Porte-Agel, Y.-T. Wu, H. Lu, and R. J. Conzemius, R, Large-eddy Simulation of Atmospheric Boundary Layer Flow Through Wind Turbines and Wind Farms, J. Wind Eng. Ind. Aerodyn. 99 (4) (2011) 154–168.

[10] Y.-T. Wu and F. Port-Agel, Large-Eddy Simulation of Wind-Turbine Wakes: Evaluation of Turbine Parameterisations, Boundary-Layer Meteorol. 138 (3) (2011) 345–366.

[11] Y.-T. Wu and F. Port-Agel, Modeling Turbine Wakes and Power Losses Within A Wind Farm Using LES: An Application to the Horns Rev Offshore Wind Farm, Renewable Energy 75 (2014) 945–955.

[12] H. Glauert, Airplane Propellers, in: Aerodynamic Theory, Springer, 1935, pp. 169–360.

[13] H. A. Madsen, A CFD Analysis of the Actuator Disc Flow Compared With Momentum Theory Results, Proceedings of the 10th IEA Symposium on the Aerodynamics of Wind Turbines, 1997, pp. 190–124.
[14] J. N. Sørensen and W. Z. Shen, Numerical Modeling of Wind Turbine Wakes, J. Fluids Eng. 124 (2) (2002) 393–399.
[15] R. Mikkelsen, Actuator Disc Methods Applied to Wind Turbines, Ph.D. thesis, Technical University of Denmark (2003).
[16] N. Troldborg, Actuator Line Modeling of Wind Turbine Wakes, Ph.D. thesis, Technical University of Denmark (2009).
[17] J. M. Churchfield, S. Lee, J. Michalakes, and P. J. Moriarty, A numerical Study of The Effects of Atmospheric and Wake Turbulence on Wind Turbine Dynamics, Journal of Turbulence (13) (2012) N14.
[18] J. N. Sørensen, W. Z. Shen, and X. Munduate, Analysis of Wake States by A Full-field Actuator Disc Model, Wind Energy: An International Journal for Progress and Applications in Wind Power Conversion Technology 1 (2) (1998) 73–88.
[19] J. D. Mirocha, D. A. Rajewski, N. Marjanovic, J. K. Lundquist, B. Kosović, C. Draxl, and M. J. Churchfield, Investigating Wind Turbine Impacts on Near-wake Flow Using Profiling Lidar Data and Large-eddy Simulations With An Actuator Disk Model, Journal of Renewable and Sustainable Energy 7 (4) (2015) 043143.
[20] M. O. L. Hansen, Aerodynamics of Wind Turbines, Routledge, 2015.
[21] J. N. Sørensen, General Momentum Theory for Horizontal Axis Wind Turbines, Vol. 4, Springer, 2016.
[22] Kosović, Branko, Subgrid-scale Modelling for the Large-eddy Simulation of High-Reynolds-number Boundary Layers, Journal of Fluid Mechanics 336 (1997) 151–182.
[23] Mirocha, JD and Lundquist, JK and Kosović, B, Implementation of A Nonlinear Subfilter Turbulence Stress Model for Large-eddy Simulation in the Advanced Research WRF model, Monthly Weather Review 138 (11) (2010) 4212–4228.
[24] Monin, Andreı Sergeevich and Obukhov, Aleksandr Mikhaılovich, Basic Laws of Turbulent Mixing in the Surface Layer of the Atmosphere, Contrib. Geophys. Inst. Acad. Sci. USSR 151 (163) (1954) e187.
[25] J. Jonkman, S. Butterfield, W. Musial, and G. Scott, Definition of A 5-MW Reference Wind Turbine For Offshore System Development, Tech. rep., National Renewable Energy Lab.(NREL), Golden, CO (United States) (2009).

Multi-fidelity modeling of offshore wind energy systems including mesoscale variability at wind turbine scale: an application to wind farm control for grid balancing

Benoit Foloppe

Environmental and Applied Fluid Dynamics Department, von Karman Institute for Fluid Dynamics, Belgium, benoit.foloppe@vki.ac.be

Supervisor: Jeroen van Beeck

Dean of the Faculty and Head of the Department and Professor, Environmental and Applied Fluid Dynamics Department, von Karman Institute for Fluid Dynamics, Belgium, vanbeeck@vki.ac.be

University Supervisor: Lieven Vandevelde

Professor, Electromechanical and Systems and Metal Engineering Department, Ghent University, Belgium, lieven.vandevelde@ugent.be

Abstract

The project intends to combine the advantages of multiscale weather predictions and control-oriented modeling of wind farms, in view of facilitating the integration of offshore wind energy into the overall electricity system. The mesoscale variability will be tackled by the Weather Research and Forecasting model (WRF). Thus, the WRF framework has been studied and used during the first months of the project. Eventually, the elaboration of a multi-fidelity modeling approach will require a coupling between WRF and a low computational cost dynamical wind farm model. As one of the main criteria is to have a wind farm model that is dynamic (including time variation of wind speed), current focus is on extending wake modeling capabilities to heterogeneous background velocity fields, before the inclusion of wind farm blockage effects.

For the wind farm model, two different approaches exist: reduced-order Navier-Stokes based models and empirical semi-analytical wake models. An example of the first approach is WFSim, solving 2D Navier-Stokes equations and an example of the second approach is FLORIS, solving the static field based on physics-based analytical wake models. Both are using an Actuator Disk Model. However, WFSim is only 2 dimensional (2D) where FLORIS is 3D. This is an important feature because it is intended to couple the wind farm model with WRF which is 3D. Also, FLORIS is found to be around 10 times faster than WFSim.

The future work is to extend the FLORIS model, which is currently a steady state model, such that it includes wake propagation delays and unsteadiness of the background flow field. This will be done using a Lagrangian approach following particles, generated at the rotor plane, convected by the wind turbine wake. The next step will be on the coupling of high resolution (< 1km) weather predictions using WRF-LES and control-oriented dynamic wake models. Finally, the last step will be to include and improve a new 3D-Planetary Boundary Layer scheme developed at the Von Karman Institute. The application of the project will focus on wind farm control for grid balancing.

Keywords: Multi-fidelity modeling, mesoscale variability, wind farm control, grid balancing

Wind turbine wakes impact on the dynamics of high-voltage cables for fatigue assessment and optimization

Emmanuel Gillyns

Environmental and Applied Fluid Dynamics, von Karman Institute for Fluid Dynamics, Belgium, emmanuel.gillyns@vki.ac.be

Supervisor: Jeroen van Beeck

Professor, Environmental and Applied Fluid Dynamics, von Karman Institute for Fluid Dynamics, Belgium, vanbeeck@vki.ac.be

University Supervisor: Grgoire Winckelmans

Professor, Institute of Mechanics, Materials and Civil Engineering, UCLouvain, Belgium, gregoire.winckelmans@uclouvain.be

Abstract

The present PhD research project is devoted to the study of wind turbine wakes, and their impact on fatigue of high-voltage cables. Wake-induced oscillations in the cables cause vibrations, creating a dynamic load on the cables, which leads to fatigue of the material and ultimately breakage.

The wind turbine wake and its impact on the cable will be studied under various Atmospheric Boundary Layer (ABL) conditions, which has a strong influence on the wake produced. The acting phenomena being fully transient, this dynamic behaviour is explored numerically using Large Eddy Simulation (LES) to provide a highly accurate solution of the turbulent wake, using an actuator line model (ALM). Those computations are performed using the open source, spectral element and high order code Nek5000, for its high accuracy and scalability. Current progress implementing the ALM innovates with forces being well represented along the radial direction, the ability to refine the tip hence to capture the correct local gradient, and a power output corrected for the numerical dispersion of the tip (if not mesh refined).

Moreover, and in complement to the numerical results, experiments will be performed in the wind tunnel L1-B of the von Karman Institute, capable of performing controlled scaled-down experiments of an ABL. A new scale-model wind turbine will be designed to improve upon previous research, aiming for a better scale similarity relative to full scale turbine wakes.

With conclusive results between the numerical model and experiments, the effects of the wake on the cables will be computed numerically using a one-way coupling between the LES and cable dynamics, as those displacement will vary in time with the wind turbine wake. This coupling allows the computation of large displacement of the cables in the wake, giving a better representation of the acting phenomena compared to a spectral analysis. The use of passive control devices such as dampers will be explored to reduce the effect of fatigue on the cables. Fatigue computations will be validated experimentally in UCLouvain's fatigue laboratory with tests on high voltage cables.

Along with the tools that will be developed during this thesis, the main objectives are to provide an improved methodology for designing cables, act on existing ones using passive control devices, and improve the general understanding of the effect of wind turbine wakes.

Near- Field Pollutant Dispersion due to Explosions

Pierrette Atikpo

Researcher, Department of Mechanical Engineering, Royal Military Academy, Belgium,

Prof. Maj Bart Janssens

Associate Professor, Department of Mechanical Engineering, Royal Military Academy, Belgium,

Prof. Maj David Lecompte

Associate Professor, Head of Military and Protective Engineering, Royal Military Academy, Belgium,

Prof. Delphine Laboureur

Associate Professor, Environmental and Applied Fluid Dynamics Department, von Karman Institute for Fluid Dynamics, Belgium,

Prof. Karim Limam

Professor, Engineering Department, University La Rochelle, France,

Abstract

Detonation of explosives is a frequent activity carried out by the military when disposing of conventional munitions. These detonations lead to the dispersal in the atmosphere of gases and pollutant particles that affect the quality of the air, the environment and the health of the people around the detonation sites.

Thus, the purpose of this research is to study the effect of explosions, atmospheric and soil conditions on the initial particle and gas dispersion. In the first phase, an extensive measurements campaign will be carried out in Poelkapelle, West Flanders in Belgium where DOVO (Belgian Defence Unit in charge of Toxic Liquid, Toxic Solid and Explosive Ordnance Disposal and Destruction) disposes of world war I and II explosives. During this experimental phase, we will collect data such as explosive characteristics, atmospheric conditions, soil conditions, particle concentration, particle size, particle velocity, blast wave and plume shape. These data will be collected using a portable weather station, moisture meter, particle counters, pressure sensors and high speed cameras.

The data collected will be exploited to validate a numerical model that will be developed in the second phase. In this numerical model both the Eulerian Eulerian and Eulerian Lagrangian frameworks will be investigated. This model will implement blast propagation algorithm taking into account the effect of initial blast by applying the Variational Multiscale Finite Elements Method to the compressible Navier-Stokes equations.

The outcomes of this research will provide significant added values to both the scientific community and the military. Regarding the scientific community, this study will provide to the scientific literature, full-scale measurements under a range of atmospheric and soil conditions. It will also provide a more accurate blast propagation numerical model. To the Military, it will provide answers regarding the effects of detonations on environment and health, accurate prediction of the consequences of attacks involving CBRN (Chemical, Biological, Radiological, and Nuclear) agents, the assessment of dirty bombs and explosion effects on buildings. This research will also supply the Belgian Royal Military Academy, support for academic courses.

Keywords: Particle Dispersion, Blast Wave, Near Field, Explosions, Earth Covered Pits, Blast Propagation, Variational Multiscale, Finite Element Method, Arbitrary Lagrangian Eulerian.

Weather predictions for offshore wind energy: Case of extreme events

Adithya Vemuri

Environmental and applied fluid dynamics department, von Karman Institute for Fluid Dynamics, Belgium, adithya.vemuri@vki.ac.be

Supervisor: Jeroen van Beeck, Sophia Buckingham, Wim Munters

Professor, Environmental and applied fluid dynamics department, von Karman Institute for Fluid Dynamics, Belgium, vanbeeck@vki.ac.be

University Supervisor: Jan Helsen

Professor, Mechanical Engineering, Vrije Universiteit Brussel, Belgium, jan.helsen@vub.be

Abstract

Extreme weather phenomena such as Low-Level Jets, sudden wind direction changes, extreme wind shear [1], wind ramps[2], storms [3][4] , amongst others, are capable of causing severe dynamic loading on wind farms. These Extreme Weather Events (EWE) play a significant role in the lifetime and power production levels of a wind farm. EWE are critical for determining representative ultimate and fatigue loading conditions. Moreover, such events may cause changes in power production and should be accurately predicted to support a well-balanced grid.

The occurrence of Storm Ciara over the offshore wind farm(s) on the 10th of February 2020 has been selected here as case study. The selection of this event is motivated by the occurrence of fast changes in wind directions at several moments in the storm.

A Mesoscale modelling framework is utilized to study Storm Ciara as experienced by offshore wind farms located in the Belgian offshore concession zone. The Weather Research and Forecasting model (WRF) [5] is used to simulate the local weather using a nested domain configuration down to 1km horizontal resolution. A sensitivity analysis to identify the optimal WRF-physics set-up and temporal resolution of re-analysis dataset is conducted. Two different temporal resolutions (1-hourly and 3-hourly) of the re-analysis dataset ERA5 are considered. The MYNN2.5 PBL [6] scheme and scale-aware Shin Hong PBL scheme [7] are selected for this sensitivity study. WRF predictions are validated against RADAR data on precipitation and wind velocity provided by the Royal Meteorological Institute (RMI) of Belgium. The results show a definite improvement when driven by hourly reanalysis data, in particular in the context of EWE. A scale-aware PBL scheme enables to better reproduce turbulent mixing already at kilometer-scale, by adding local flow details that are otherwise neglected. Based on RADAR images and WRF simulations a frontal passage from the North-West direction and a suspected micro-burst phenomenon over the Belgian offshore concession zone during the early periods of Storm Ciara are observed.

Work by the author(s) was supported by Agentschap Innoveren and Ondernemen (VLAIO) through the Strategisch Basisonderzoek voor Clusters (cSBO) project SeaFD.

Keywords: Mesoscale modelling, Storm Ciara, Extreme weather phenomena, Wind energy, Belgian offshore wind

References

[1] P. C. Kalverla, G.-J. Steeneveld, R. J. Ronda, A. A. Holtslag, An observational climatology of anomalous wind events at offshore meteomast ijmuiden (north sea), Journal of Wind Engineering and Industrial Aerodynamics 165 (2017) 86–99.

[2] C. Gallego-Castillo, A. Cuerva-Tejero, O. Lopez-Garcia, A review on the recent history of wind power ramp forecasting, Renewable and Sustainable Energy Reviews 52 (2015) 1148–1157.

[3] G. Solari, Thunderstorm downbursts and wind loading of structures: Progress and prospect. front, Built Environ 6 (2020) 63.

[4] G. Solari, M. Burlando, P. De Gaetano, M. P. Repetto, Charac-

teristics of thunderstorms relevant to the wind loading of structures, Wind Struct 20 (6) (2015) 763–791.
[5] W. C. Skamarock, J. Klemp, J. Dudhia, D. Gill, D. Barker, M. Duda, X. Huang, W. Wang, J. Powers, A description of the advanced research (wrf) model, version 3, Natl. Ctr. Atmos. Res., Boulder, CO 7.
[6] M. Nakanishi, H. Niino, An improved mellor–yamada level-3 model: Its numerical stability and application to a regional prediction of advection fog, Boundary-Layer Meteorology 119 (2) (2006) 397–407.
[7] H. H. Shin, S.-Y. Hong, Representation of the subgrid-scale turbulent transport in convective boundary layers at gray-zone resolutions, Monthly Weather Review 143 (1) (2015) 250–271.

Assessment and optimization of LiDAR Doppler velocimetry for complex atmospheric flows

Gertjan Glabeke

Environmental and Applied Fluid Dynamics Department, von Karman Institute for Fluid Dynamics, Belgium, gertjan.glabeke@ugent.be

Supervisor: Jeroen van Beeck

Professor, Environmental and Applied Fluid Dynamics Department, von Karman Institute for Fluid Dynamics, Belgium, vanbeeck@vki.ac.be

University Supervisor: Tom De Mulder

Professor, Faculty of Engineering and Architecture - Department of Civil engineering, UGent, Belgium, TomFO.DeMulder@UGent.be

Abstract

LiDAR (Light Detection And Ranging) is an active range-resolving optical measurement technique for almost any property of the atmosphere, such as temperature, pressure, wind, as well as for sensing trace gases, aerosols, and cloud ceiling. In general, a lidar consists of a transmitter (a laser with beam expander), a receiver to collect the photons backscattered from the atmosphere, and an optical analyzing system. Five basic lidar techniques can be distinguished, classified according to a specific interaction process of the emitted radiation with the atmospheric constituents: Elastic-backscatter lidar, Differential-absorption lidar (DIAL), Raman lidar, Resonance fluorescence lidar, and Doppler lidar.

During my Ph.D. I will mainly focus on the Doppler lidar technique. Based on this principle, an in-house miniature Continuous Wave Doppler lidar [1] will be built to first obtain the raw Doppler signal and to get a better understanding of the technique. Since the current commercial Doppler lidars are quite large, heavy, and expensive, and are only focused on the determination of wind profiles, optimization will be made of both the hardware and the software, such as but not limited to detection techniques, scanning techniques, simultaneous wind-temperature profiling. Moreover, a smaller device will allow it to be used more easily, e.g. in large atmospheric wind tunnels [2]. Also, the possibility of installing the lidar under a drone can be considered [3], to have an airborne system. In this way, simulations of offshore weather now- and forecasts can be validated at a lower cost and with greater positional flexibility compared to current systems installed onshore, on a platform, or on a buoy.

The Doppler lidar technique is based on the doppler shift, which expresses a shift in the wavelength and frequency of a wave due to the motion of either the source or the receiver of the waves. In a lidar, this frequency shift occurs when a small fraction of laser light emitted into the atmosphere is received after being scattered by moving molecules and aerosol particles entrained in the atmosphere. The speed of this motion (= wind) along the line-of-sight is directly proportional to the magnitude of the doppler shift $\pm\Delta f_D = 2V_{LOS}/\lambda$. Furthermore, to obtain the three-dimensional wind vector, a scanning scheme consisting of at least three measurements (vertical, tilted east, and tilted north line-of-sight velocities), and assuming horizontal wind field homogeneity, must be performed.

Acknowledgments

This research is part of the SeaFD-project (Realistic CFD wind load computations for offshore wind turbines) and is funded by VLAIO & SIM-spearhead cluster under the MaDurOS research program.

References

[1] C. Werner, Doppler wind lidar, in: Lidar, Springer series in Optical sciences, Wessling, Germany, 2005, pp. 325–354.

[2] P. Hulsman, et al., Wake deflection measurement in a wind tunnel with a lidar windscanner, in: Wind Energy Science Conference, Cork, 2019.

[3] N. Vasiljevi, et al., Wind measurements with drone-based wind lidars, in: Wind Energy Science Conference, Cork, 2019.

Prediction of Potential Future Bearing Failures

Konstantinos Vratsinis

Environmental and Applied Fluid Dynamics Department, von Karman Institute for Fluid Dynamics, Belgium, konstantinos.vratsinis@vki.ac.be

Supervisor: Jeroen van Beeck

Dean of the Faculty, Professor and Head of Department, Enviromental and Applied Fluid Dynamics Department, von Karman Institute for Fluid Dynamics, Belgium, vanbeeck@vki.ac.be

University Supervisor: Jan Helsen

Professor, Department of Applied Mechanics, Vrije Universiteit Brussel, Belgium, jan.helsen@vub.be

Abstract

Offshore wind energy hold promise in the renewable energy sector, particularly due to technological progress that has driven down prices towards a range of 50-70 /MWh much earlier than previously estimated. Novel offshore wind farms now have the potential to run subsidy-free, and even negative-subsidy by generating revenue for the government over their lifetime. As such, they will be fully exposed to merchant risk, where the market price of electricity is the only revenue for the farm. In this unfamiliar territory, the prevention of failures and their early detection have significant importance. Knowing the health condition of critical components at any moment is key to an effective maintenance plan that will ensure efficient wind farm operation. The goal of this research is to develop data-driven models that are capable of predicting rotor loads that lead to premature bearing degradation. Knowing the rotor loads at any moment will facilitate the detection of bearing degradation at an early stage. To accomplish this, a nacelle-based LIDAR will be deployed to collect data. This data will help to identify the aerodynamic events which cause unfavorable loading. Identifying and understanding these aerodynamic events is of major importance. This will allow planning actions to mitigate their damaging effect (for instance, shutting down a wind turbine can be proven helpful). Ultimately, the input for these surrogates will be SCADA data sampled at a 1 Hz rate. This type of data is commonly available in all-new farms and will allow the deployment of such methods in any wind farm. This research aims to improve our understanding of the links between aerodynamic loadings and the premature bearing degradation of wind turbines.

Keywords: wind energy, wind turbines, aerodynamic loading, main bearing

LIQUID AND SOLID PROPULSION

Dynamic contact angle analysis using inverse methods

Domenico Fiorini

Environmental and Applied Fluid Dynamics Department, von Karman Institute for Fluid Dynamics, Belgium, domenico.fiorini@vki.ac.be

Supervisor: Miguel Alfonzo Mendez

Assistant Professor, Environmental and Applied Fluid Dynamics Department, von Karman Institute for Fluid Dynamics, Belgium, miguel.alfonso.mendez@vki.ac.be

University Supervisor: David Seveno

Associate Professor, Department of Materials Engineering, KU Leuven, Belgium, david.seveno@kuleuven.be

University Co-Supervisor: Johan Steelant

Professor, Department of Mechanical Engineering, KU Leuven, Belgium

ESTEC-ESA, Keplerlaan 1, 2200AG Noordwijk, The Netherlands, Johan.Steelant@esa.int

Abstract

The motion of a gas-liquid interface along a solid wall depends on the capillary forces along the contact line, where the interface forms a contact angle. The contact angle is often modelled via empirical correlations which have been derived upon steady state ambient conditions. However, the new technological challenges increased the interest towards studying the contact angle dynamics in a wider set of conditions. In this work we investigate the case of unsteady contact lines. The accurate measurement of contact angles is challenging, and the many correlations available reflect the difficulties in generalizing results from various experiments. This work proposes to use inverse methods to measure dynamic contact angles and derive empirical correlations from oscillatory flows in a quasi-capillary tube. The flow is produced in a transparent U-shaped tube, where the liquid is released after setting the two sides of the tube at different heights. The dynamics of the interface is visualized via high-speed camera and retrieved via image processing. The results are fitted to the analytic solution of the interface force balance in quasi-static condition. Besides increasing the measurement robustness, this allows for assessing the range of velocity and acceleration within which the quasi-static assumption holds. Finally, an inverse method is used to fit and test various correlations linking the contact angle dynamics to velocity and accelerations. The need for differential models accounting for the history of the contact angle is discussed.

Keywords: Wettability, Unsteady contact angles, Inverse problems

1. Introduction

A gas-liquid interface in contact with a wall forms a contact angle at the contact line. In static conditions, the contact angle depends on the combination of gas, liquid and solid; in dynamic conditions, the contact angle also depends on the contact line dynamics. The contact angle strongly influences the capillary forces and thus the motion of the interface. Still, it cannot be predicted in the continuous fluid mechanics framework, for which it represents an essential boundary condition.

Many applications rely on the correct prediction of the dynamic contact angle. Among these, we mention the classic inkjet printing [1], the production and deposition of photographic films [2], slot die coating [3], as well as novel applications such as drop uptake in porous materials [4] and drop manipulations in microfluidic systems [5]. Several theoretical [6; 7; 8; 9; 10; 11] and empirical [12; 13; 14; 15; 16] correlations have been developed to relate the contact angle to the dynamics of the contact line. Most of

these works focus on a "quasi-static" condition, usually linking the contact angle to the contact line velocity via the capillary number. Several authors (see [17; 18; 19; 20; 21] and references cited therein) have shown that these approaches fail in the presence of inertia, which demands correlation able to account for the time history of the contact line (see [17; 18]). Such correlations can be written in the form of ordinary differential equations, which can be tuned, via an inverse method, on experimental data that comprises all the relevant quantities entering in the equations: the time evolution of contact angle and contact angle velocity and acceleration.

Measuring these quantities, however, is particularly challenging. Dynamic contact angles are often referred to as "inaccessible" [22; 23] due to the difficulty of observing the exact position of the contact line near a solid surface, where light reflection and diffraction, combined with the limited resolution of most high-speed optical devices, introduce high uncertainties.

This work presents a first attempt to tackle both problems of the accurate interface and dynamic contact angle measurement, as well as automatic data-driven identification and regression of the best contact angle correlation. The analyzed test case is a quasi-capillary U-shaped tube, where the liquid is suddenly released from an un-balanced configuration. The interface dynamic is monitored via high-speed visualization and detected via image processing techniques. The experimental configuration and procedure are described in section 2.1, while the image processing is briefly described in section 2.2. The image processing results are used to fit a parametric representation of the interface, which is defined as the solution of a quasi-static force balance. This significantly increases the robustness of the contact angle measurements and allows for evaluating the limits of the quasi-static assumption over the full range of velocity and accelerations observed in an experimental run. The interface parametrization is described in 2.3. The regression of both the interface shape and the contact angle correlations was carried out using the optimization strategies described in 2.6, while the set of correlations considered is recalled in 2.7. The results are presented in section 3, conclusions and outlooks are reported in section 4.

2. Materials and methods

2.1. Experimental setup

The experimental setup is a U-shaped quartz tube of 8mm diameter and about 164 mm of axial length (figure 1, on the left). The setup is divided into two sides ("A" and "B" in the figure) connected in a closed-loop by flexible pipes. A fast response valve controls the connection between these sections. Two differential piezo-resistive measuring cells (AMS 5812) are placed at the two entrances of the tube. Side A is connected to an input pressure line, while side B is connected to a discharge pressure line.

The two sides are isolated by partially filling the U-tube with the test liquid. The U-tube is vertically positioned, and the two liquid columns have the same height. The initial conditions of the experiment are defined by setting the initial level difference between the two interfaces and zero velocity of the interface. This is done by closing the fast-response valve while setting the liquid levels by imposing different pressures on the two sides.

The preparatory phase ends by sealing the experiment from the external environment. The experiment starts by opening the fast-response valve, and the two liquid interfaces start oscillating around the equilibrium position. The motion of one of the two interfaces is recorded with a high-speed camera SP-12000-CXP4, acquiring grey-scale images at 300 fps. The interface shape is visualized by a diffused light source on the opposite side of the tube. The active region of the camera is restricted to the central region of size 4096x512 pixels in order to achieve the highest acquisition frequency allowed by the camera. The camera mounts a 105mm lens and is positioned to acquire the full motion of the interface while spanning the full tube width, as shown in Figure 2 on the left.

The liquid tested is HFE7200, which is a synthetic liquid characterized by small equilibrium contact angles. This liquid is often used at ambient conditions to simulate typical properties of cryogenic space fluids [24]. The relevant properties for this work are the density $\rho = 1420.7\,\mathrm{kg/m^3}$, dynamic viscosity $\mu = 0.64\,\mathrm{mPa \cdot s}$ and surface tension $\sigma = 13\mathrm{mN/m}$.

2.2. Image Analysis

The image processing for the interface detection consists of four main steps, recalled in Figure 3. In the first step, the original image (image a) is filtered

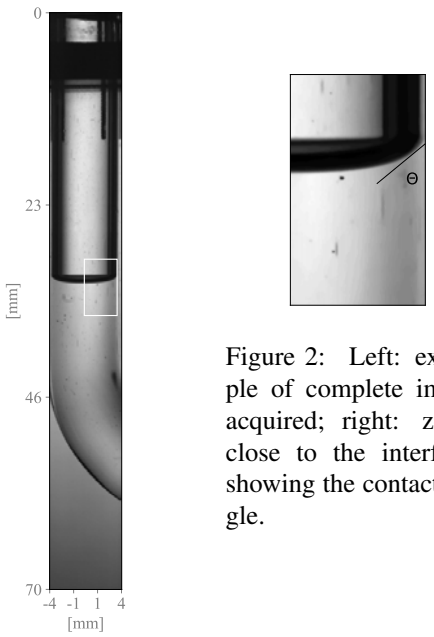

Figure 2: Left: example of complete image acquired; right: zoom close to the interface, showing the contact angle.

denly release the pressure difference at the beginning of the experiment.

via global noise removal based on n-local means denoising algorithm [25], followed by a first image re-contrasting (image b). The second and third step process each column of the image separately. The gray scale profiles are first filtered using a SavitzkyGolay filter [26] and the resulting image re-contrasted using directional gray-scale averaging [27]. This allows for increasing the gray level intensity in the region of the liquid interface close to the tube walls, which appear darker and slightly blurred compared with the center of the channel.

Preliminary gradient based detection is performed to localize the section of interest of the image (near the interface, see image c) and classic Canny-edge algorithm [28] is used to accurately determine the shape of the interface at the location of interest (image d). The interface is preliminary located with one pixel width and outliers are eliminated based on their distance from the expected interface through successive regression with curve proposed in the next section (image e). Approximately 90% of the possible interface data points are determined in 1.5 second per image (Intel(R) Core(TM) i7-4790 CPU @4GHz processor, 32GB of Ram); the remaining pixels do not play a role in the definition of the interface. The final result is shown in figure 8f.

The image of a meniscus in a circular tube appears distorted in the radial direction due to the circular shape of both the tube's internal and external shape. Therefore, the meniscus generally appears larger than its actual size and the meniscus contact point seemingly lies in the region between the inner and outer side of the tube. The non-linear distortion is maximum at the contact point of the meniscus and disappears at the center. The distortion can be corrected using analytical relations [29] knowing the distance of the camera from the center of the tube and the index of refraction of the materials involved.

2.3. Interface Parametrization

The interface shape is modeled by considering the steady-state force balance at the interface (see also [23]). Within the quasi-static assumption, we consider the same balance also in dynamic conditions. This balance includes the Laplace pressure and the gravitational force. Referring to figure 4, this yields to the following boundary value problem:

$$\begin{cases} l_c^2 \, \nabla \cdot \mathbf{n} + h = 0 \\ h_r(R,t) = -\mathrm{ctg}(\theta(t)) \\ h_r(0,t) = 0 \end{cases}, \tag{1}$$

where $l_c = \sqrt{\sigma/(\rho g)}$ is the capillary length of the liquid, $\mathbf{n}$ is the interface normal, $h(r,t)$ is the interface height, herein assumed to be axisymmetric, $\nabla \cdot \mathbf{n}$ is the interface curvature, with ∇ the nabla operator. The

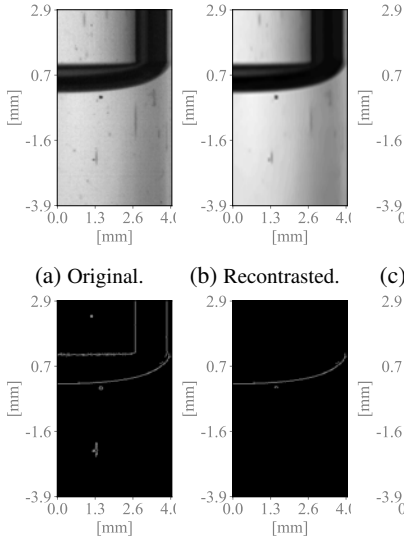

(a) Original. (b) Recontrasted. (c)

(d) Edges. (e) Interface. (

Figure 3: Sequence of image processing steps implemented to identify the liquid interface

subscripts denote partial differentiation. Referring to Figure 4, the axis are located at the center of the interface, i.e. such that $h(0,t) = 0$ for all times, and R is the tube radius. Because $R/l_c \approx 4$, the configuration can be considered as 'quasi-capillary'. The first boundary condition involves the (unknown) contact angle, with ctg the cotangent. Under the axysimmetric assumption, the interface normal and the interface curvature can be written as:

$$\mathbf{n} = \frac{\mathbf{z} - h_r \mathbf{r}}{1 + h_r^2} \qquad \nabla \cdot \mathbf{n} = \frac{-r h_r + r^2 h_{rr}}{r^2 (1 + h_r^2)^{3/2}}, \tag{2}$$

where $\mathbf{z} = (0, z)$ and $\mathbf{r} = (r, 0)$ are the vectors along the reference axes. In the first simplification proposed in this work, it is assumed that h_r/r is everywhere small, hence the interface curvature is approximated as $\nabla \cdot \mathbf{n} \approx h_{rr}$. Then, equation (1) admits analytical solution of the form :

$$h(r, \theta(t)) = \frac{-\mathrm{ctg}(\theta(t))}{2\sinh(R)} \cosh\left(\frac{r}{l_c}\right), \tag{3}$$

with sinh and cosh the hyperbolic sines and cosine. For a given time, the interface is solely function of the contact angle $\theta(t)$, which can was determined via regression analysis.

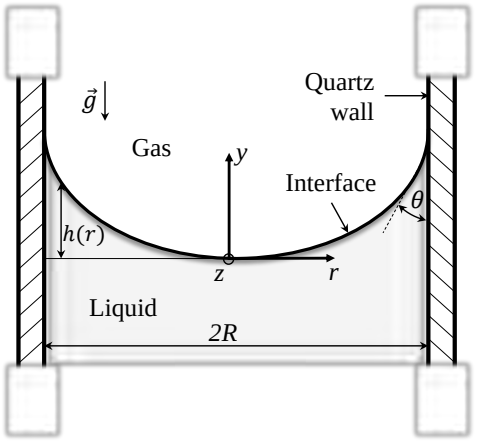

Figure 4: Schematic of the interface model. The origin is located at the interface, in the center of the channel, and moves with it (i.e. $h(0,t) = 0$ for all times)

2.4. Experiment modeling

The motion of the liquid interface in a U-shaped quasi-capillary tube is modeled by a 1D-ODE obtained by the momentum balance of the forces acting on the liquid column.
We define the average height of the interface:

$$\bar{h}(t) = \frac{1}{\pi R^2} \int_0^R 2\pi h(r,t) r dr \tag{4}$$

Hence, assuming a steady and laminar flow, the balance reads as following:

$$\ddot{\bar{h}} = -8\frac{\mu}{\rho R^2}\dot{\bar{h}} - C_f \dot{\bar{h}}|\dot{\bar{h}}| + \frac{2g}{L}\bar{h} + \frac{2\sigma}{\rho R^2 L}(K_A - K_B) \qquad with \;\; K_{A|B} = \int_0^R (\nabla \cdot \mathbf{n}) r dr \tag{5}$$

The term C_f represent a concentrated source of dissipation introduced by the 180° bend at the bottom of tube and $K_{A|B}$ represent the integral of the curvature of the free liquid surfaces in the two sides of the U-tube.

As shown by equation 5, the motion of the fluid column is governed by the balance of inertia with viscous, gravitational and capillary terms. Two of these terms need to be modeled.

- Viscous stress term. The formulation of equation 5 holds assuming that the integral value of the viscous stresses along channel corresponds to a Poiseuille flow velocity profile. However, the oscillating flow in short quasi capillary U-tubes is unsteady and experiments in similar

geometries [30] show velocity profiles significantly different from the parabolic shape. The actual velocity profile could be represented analitically by means of series of Bessel functions [31], which allow to flatten the velocity profile as the frequency of the oscillation increases. The magnitude of this term is therefore verified by performing a "capillary-weak" U-tube experiment which is described in section 3.2

- Capillary term. the term $K_{A|B}$ depends on the shape of the free surface. This term is modeled in capillary rise models [19; 32] assuming that the interface is represented by an arc of a sphere, in this case the curvature of the interface is constant and its integral becomes $R\cos\theta$. This approximation is acceptable for tubes where $(R/l_c < 1)$ and the effects of inertia are negligible. In the more general case the curvature of the liquid interface in a circular tube needs to be computed by using equation 2.

Eq. 5 can be written in dimensionless form by using the capillary length and the gravitational acceleration as characteristic length and acceleration.

$$\ddot{\bar{h}}^* = -8\frac{Oh_{cb}}{R^{*2}}\dot{\bar{h}}^* - C_f\dot{\bar{h}}^*|\dot{\bar{h}}^*| + \frac{2}{L^*}\bar{h}^* + \frac{2}{R^{*2}L^*}(K_A^* - K_B^*)$$
$$with \;\; K_{A|B}^* = \frac{1}{l_c}\int_0^{\bar{R}}(\nabla\cdot\vec{n})rdr \tag{6}$$

R^*, L^* correspond respectively to the dimensionless radius of the tube R/l_c and liquid length L/l_c . $Oh_{cb} = \mu/\sqrt{\rho\sigma l_c}$ is a capillary based Ohnesorge number, which is number depending only on the fluid properties and quantifies the relative weight of viscous and capillary effects.

2.5. Experiment design

Equation 5 has been used to study the experimental configuration, which has been optimized to maximize the effect of the $K_A - K_A$ term on the motion of liquid interfaces. This term is closely linked to the sensitivity of the contact angle to the interface dynamics: if the contact angle holds a static value, K_A and K_B are equal and cancel each other. On the other hand, when the difference between K_A and K_B is maximum, the dynamic contact angle has the biggest impact on the flow motion. Therefore, the optimal U-tube

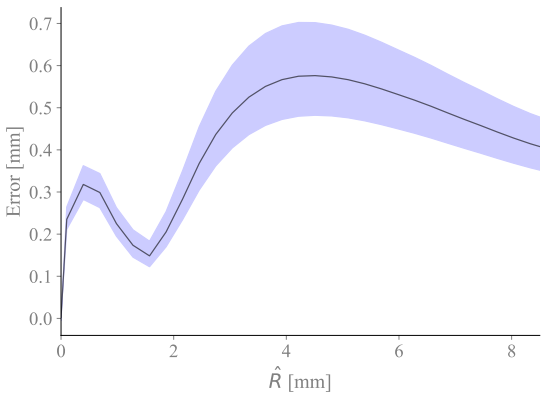

Figure 5: Least square error of the difference in the U-tube interface prediction between the cases accounting for dynamic and static contact angle. The difference is maximum for radius in the range 4 to 5 mm. Uncertainty bounds are obtained by the experimental deviation on C_f coefficient.

for this application holds the maximum difference between the case of static and dynamic contact angle prediction. This means finding the best combination of the main geometrical parameters of the experiment $\mathbf{w} := R, L$.

$$\underset{\mathbf{w}}{\text{argmax}}\, J(\mathbf{w}) = \sum_{j=1}^{n_p}\Big(\bar{h}_j(t_j,\theta,\mathbf{w}) - \bar{h}_j(t_j,\theta_S,\mathbf{w})\Big)^2 \tag{7}$$

Genetic optimization has been used to study the effect of the design parameters $\mathbf{w} := R, L$ [33]. The capillary term has the biggest impact when L assumes the smallest value allowed by the setup, e.g $L > \pi\hat{R} + 2\bar{h}(0)$. The radius of curvature of the tube has been set to $\hat{R} = 3R$ using the smallest value observed in similar experiments [34]. Figure 5 shows that for the smallest L, R has an optimal value located at $R/l_c \approx 4$. A second maximum of lower magnitude is visible in the region were $R/l_c \approx 1$. Indeed, the dynamic contact angle has a significant impact on the motion of the interface on a capillary channel, however due to the reduced size and increased viscous effects, the duration of the experiment would be sensibly lower with fewer observation points.

A second U-tube is needed to perform the "capillary-weak" experiment. In this case the influence of the term $K_A - K_B$ is minimized, which corresponds to a U-tube with large values of L and R/l_c, while keeping the laminar regime and the ratio $\hat{R}/R =$

3. In this case $R = 7.5$ mm was set for this viscous stress validation experiment and liquid volumes comprised between 40 and 50 ml.

2.6. Inverse Method and related Optimization

An optimization is used to solve two inverse problems: a curve fitting and a system identification. The first aims at fitting (3) to the interface detection; the second is that of identifying a correlation for θ as a function of the interface motion. Both inverse problems can be written as nonlinear least square problems, where a function $f(x|\mathbf{w})$, parametrized by the weight vector $\mathbf{w}$, must be fitted to dataset a $\{(x_i, y_i)\}$ with $j \in [1, n_p]$. The weights are thus computed from the minimization of the l_2 norm of the difference between data and model prediction:

$$\underset{\mathbf{w}}{\operatorname{argmin}} J(\mathbf{w}) = \sum_{j=1}^{n_p} \Big(y_j - f(x_j, \mathbf{w})\Big)^2 \tag{8}$$

In this work, the optimization was carried out using the Trust Region Reflective algorithm (TRF) [35], implemented in Python library scipy.optimize [36]. Uncertainties are computed from the covariance matrix, estimated from the Jacobian $\nabla_w J(\mathbf{w})$, which can easily be computed analytically from (8) for the curve fitting problem. In the system identification problem, the Jacobian was evaluated numerically using finite differences and a Tikhonov regularization was added to promote a parsimonious choice of the model weights.

In the interface curve fitting problem, $\mathbf{w} := \theta$, $(x_i, y_i) := (r_i, h_i)$, and $f(x_i|\mathbf{w}) := h(r_i, \theta)$, from (3), for every image. In the identification of contact angle correlations from the contact line dynamics, the definition of functions and weights depends on the correlation analyzed. These are recalled in the next section. In both problems, it is worth stressing the importance of normalizing all the model weights within the range $[0, 1]$.

2.7. Investigated Correlations

As discussed in [2], many of the correlations available for the dynamic contact angle do not have predictive power. These are rather proposals for the functional relation linking θ to the contact line dynamics, but require the tuning of empirical coefficients. We consider two approaches. The first follows the traditional framework while the second accounts for the contact angle history.

- Approach 1. This approach is one of the most popular in the literature and is known as the Hoffman-Tanner law [12; 13]. This correlation has been proved theoretically [7; 8] in quasi static conditions and has only one unknown parameter, denoted as a:

$$\theta^3 - \theta_S^3 = a\,Ca \tag{9}$$

where $Ca = \mu U/\sigma$ is the capillary number, with U the velocity of the contact line, and θ_S is the contact angle in static conditions. In the framework of (8), in this case one has $\mathbf{w} = a$, $(x_i, y_i) = (Ca_i, \theta_i)$ and:

$$f(x_i|\mathbf{w}) := \theta_p(t_i) := f(Ca_i|a) := \left(aCa_i + \theta_S^3\right)^{1/3}, \tag{10}$$

with the subscript p denoting model prediction.

The coefficient a is usually of the order of $\sim 10^2$. For the HFE used in this work, $\theta_S = 0.65\,rad$ ($\approx 37.5^o$). It is important to highlight that this is the *apparent* contact angle, i.e. what can be observed at a macroscopic scale. Finally, it is worth noticing that the contact line velocity was measured from the interface detection via time differentiation, denoted as $U = \dot{h}(R, t)$. The differentiation is carried out after smoothing the time series using a SavitzkyGolay filter to keep frequencies below approximately $50Hz$.

- Approach 2. This approach is inspired by Bian and Perling (2003) [18], who propose a correlation in the form of an Ordinary Differential Equation (ODE) that also accounts for the acceleration of the contact line, here denoted as $A(t)$ and computed by differentiating in time $U(t)$. The proposed ODE is a first order, linear ODE of the form:

$$\alpha\dot{\theta}' + \theta' = a\,Ca(t) + bA^*(t) \text{ with } \theta' = \theta^3 - \theta_S^3 \tag{11}$$

where $A^* = A/g$ is a dimensionless acceleration and the initial condition is $\theta'(0) = 0$. The ODE is designed to recover (9) at the limit $\dot{\theta}' \to 0$. Three parameters need to be fitted, i.e. $\mathbf{w} := (\alpha, a, b)$ and the function evaluation requires the solution of the ODE. Using integrating factors, it is easy to show that (11) admits analytical solution, which is assigned to the parametric function $f(x_i|\mathbf{w})$ for this problem:

$$f(x_i|\mathbf{w}) := \theta_p(t_i) = f(\{Ca, A^*\}|\mathbf{w})$$
$$f(\{Ca, A^*\}|\mathbf{w}) =$$
$$\frac{1}{\alpha}e^{-t_i/\alpha}\Big(a\int_0^{t_i} Ca(t')e^{t'/\alpha}dt' + b\int_0^{t_i} A^*(t')e^{t'/\alpha}dt'\Big) \tag{12}$$

This correlation needs the full history of capillary number and dimensionless acceleration, denoted as $\{Ca, A^*\}$. Interestingly, the parameter α plays the role of the time constant of this (first order) system, and hence accounts for the 'contact angle' memory. The integration of (12) was carried out via trapezoidal integration.

3. Results

3.1. Interface Dynamics

The time evolution of the interface height during a typical experiment is shown in Figure 6. The initial condition was set to $\Delta H_0 = 9.4\,\text{mm}$. The associated contact line velocities and accelerations are shown in Figure 7 in their dimensionless form, namely in terms of capillary number Ca and acceleration number A^*. The orbit is far from a circular spiral, displaying the system's nonlinear behaviour. All orbits vanish at the origin because of the dissipative effects of viscosity and surface tension. As expected, the system experience the largest accelerations during the first phase, when $Ca < 0$.

The extended version of this work analyzes whether it is possible to infer the contact angle evolution from these curves, by-passing the need for interface detection and thus significantly simplifying the experimental procedure. In this work, the focus is given to the interface dynamics and, in particular, to the validity of eq (3).

Figure 8 shows, on the left, the evolution of the l_2 norm of the error resulting from fitting (3) on the retrieved interface. On the right, the detected interface is compared to the resulting fit for three snapshots. As expected, these figures show that the quasi-static force balance in (1) holds at large times, at the limit of vanishing velocity and acceleration, but fails in the initial part of the experiment, where inertia dominates. Inertia tends to decrease the size of the meniscus and flatten the interface in the center of the channel.

The role of velocity and acceleration in the failure of the simplified quasi-static force balance is, on the other hand, less evident. Figure 9 shows the regression's l_2 error as a function of Ca and A^*: the largest discrepancies are observed in regions of comparatively high Ca. This result further highlights the difficulties in linking the interface's shape to the instantaneous conditions and underlines the need for including the contact line history effects in contact angle correlations.

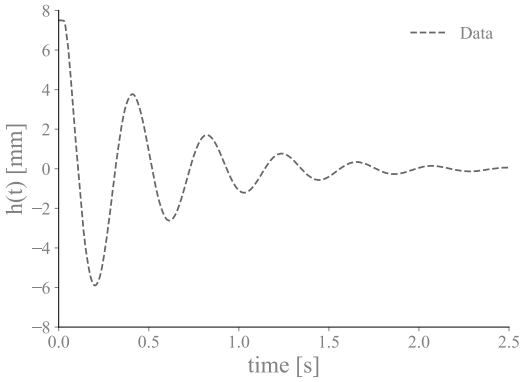

Figure 6: Measured interface height in the visualized channel as a function of time.

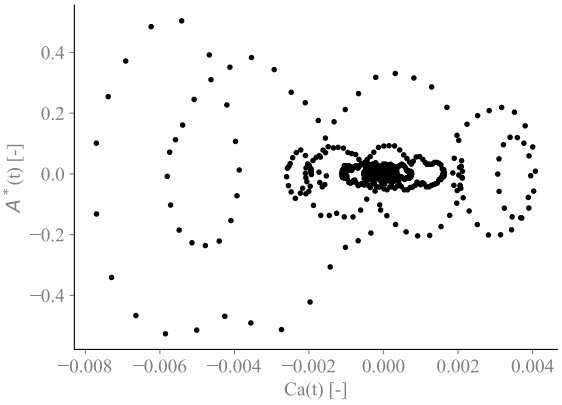

Figure 7: Phase plane of the interface velocity (in terms of Ca) and acceleration (in terms of A^*).

3.2. Viscous stress validation

Equation 5 assumes that the integral of the viscous stress of a quasi-steady flow velocity profile in channel of this size is equivalent to the case of a parabolic flow profile. This hypothesis has been challenged by conducting a second U-tube experiment in a a configuration where the capillary effects are negligible, designed as described in 2.5. In this case equation 5 may

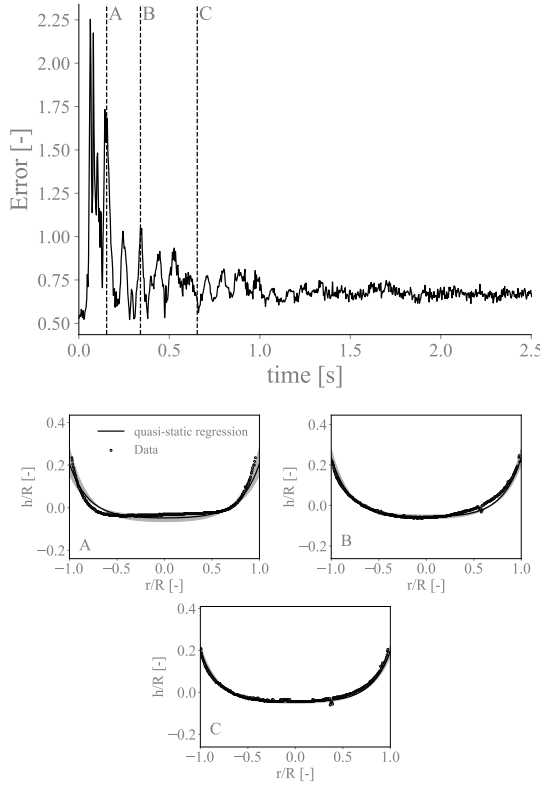

Figure 8: On the top: l_2 error of the interface regression as a function of time. The largest discrepancies are observed within the first 0.2s, where high velocities and accelerations are produced. Three snapshots labeled as (A)-(B)-(C) on the bottom figure. These corresponds to regions of high (A), moderate (B) and small (C) errors. The profiles reveal that most of the discrepancy is due to the flattening of the interface, which cannot be modeled in the quasi-static framework of eq (3).

be simplified as following:

$$\ddot{\bar{h}} = -8\frac{\mu}{\rho R^2}\dot{\bar{h}} - C_f\dot{\bar{h}}|\dot{\bar{h}}| + \frac{2g}{L}\bar{h} \qquad (13)$$

Liquid volumes of 40 and 50 ml have been tested for different starting conditions. Each experiment showed that accounting for an unsteady velocity profile has a very small impact on the flow motion with no visible differences. Figure 10 shows that the increased computational effort needed to account the unsteady velocity profile is not paid off by additional accuracy in the interface motion.

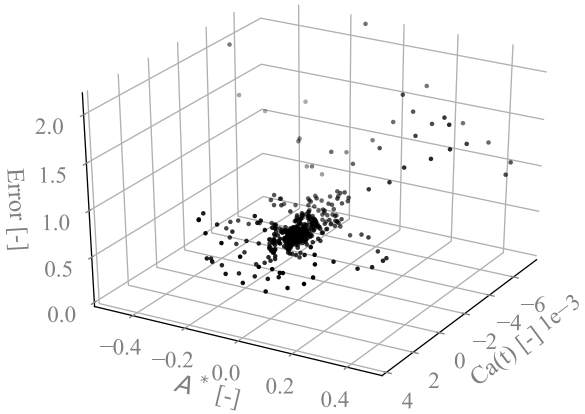

Figure 9: l_2 error in the quasi-static interface regression as a function of Ca and A^*. The major discrepancies are likely linked to the interface history rather than the local values.

3.3. Contact Angle Dynamics

Figure 11 shows the time evolution of the contact angle, measured from the interface tracking and regression, as a function of time. As expected, the highest uncertainties are produced within the first 0.2s and are mostly due to systematic contribution of the the large l_2 error in the regression. This is linked to the failure of the quasi-static formulation previously discussed.

The descending-rising period of the liquid column is initially about $\approx 0.4s$ and tend to increase to 0.5s towards the end of the experiment. During the first rise and the first descend, the contact angle displays a clear oscillation characterized by frequencies of the order of $20Hz$. The same oscillations are not observed in the l_2 error from Figure 8. This confirms that these oscillations are not due to a curve fitting problem but are most likely linked to the large velocities and accelerations experienced by the contact line at the beginning of the experiment.

To highlight the limits of any correlation solely based on the instantaneous contact capillary number, Figure 12 plots the evolution of the dynamic contact angle as a function of Ca. The results from both eq (9) and (11) are also illustrated. In this plot, only the measurements for $t > 0.5s$ are included, hence focusing on the conditions within which the effects of inertia are not strong enough to disturb the quasi-static formulation in (1). Nevertheless, the history effects are visible and their modeling is clearly out of the reach of eq (9). Eq.(11) is on the other hand much closer to the

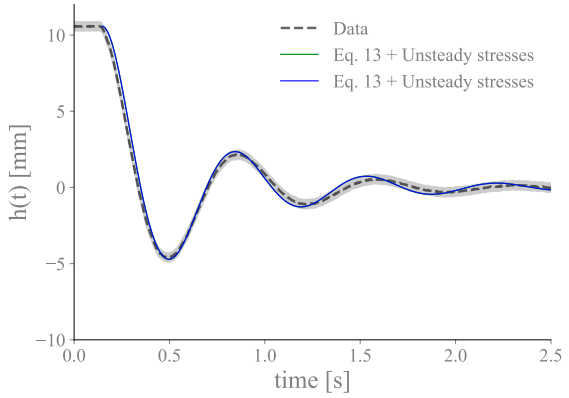

Figure 10: Comparison of interface experimental profile in 15 mm radius U-tube with prediction by integral model of the interface. No visible difference appear between the case of a simulation comprehending an unsteady velocity profile and one considering Poiseuille velocity profile

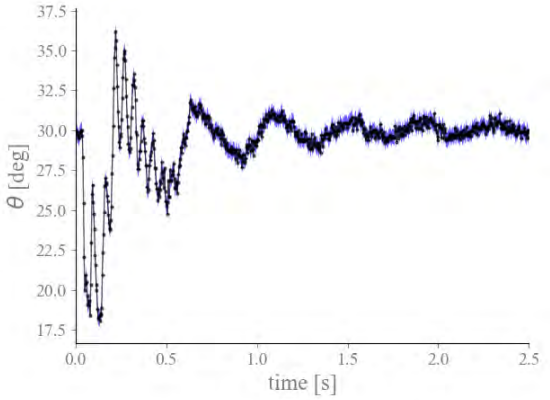

Figure 11: Time evolution of the measured contact angle. Uncertainties are computed from the covariance matrix estimated via Jacobian ∇J_w, which in the case of interface regression has a simple analytical form.

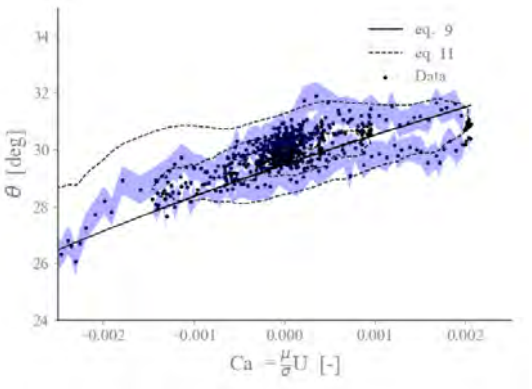

Figure 12: Dynamic contact angle as a function of the capillary number. Comparison between experimental data and the predictions from correlations (9) and (11). The contact angle uncertainties are shown.

experimental data and within the measurement uncertainty for a fairly large portion of the observation time. The prediction of both correlations are shown also in Figure 13 as a function of time. The distribution of the optimal coefficients for eq. 11 against different initial guesses is shown on the non-dimensional search plane in figure 14. A well defined minimum is reached for all the parameters.

Finally, the comparison between experimental data and the prediction of both correlations is shown in Figure 15, here considering the full time interval. Most of the discrepancy occur at the lowest contact angles and are in most cases over-predictions.

3.4. Impact on the interface motion

The optimized form of the dynamic contact angle correlation 9 and 11 have been used in combination with model 6 to predict the motion of the interface for the corresponding test case.

Figure 16 shows similar levels of agreement of the simulations using different optimized contact angle correlations. However greater degree of mismatch is visible comparing to the experiment in "capillary-weak" conditions of figure 10. These differences are addressed to capillary phenomena which are not accounted by the integral formulation of equation 6. Indeed, it has been observed in [30] that vortexes appear in the "wake" of the meniscus and change the direction of rotation when the interface reverts his motion, the effect of these vortexes is not explicitly accounted in the solution of 6 and this could explain the increased damping observed within the experiments.

4. Conclusions and perspectives

This work investigated, experimentally, the dynamics of a moving contact line within a quasi-capillary U-Tube (with $R/l_c \approx 4$). The focus was given to the shape of the gas-liquid interface and the dynamic of the contact angle as a function of contact line velocity

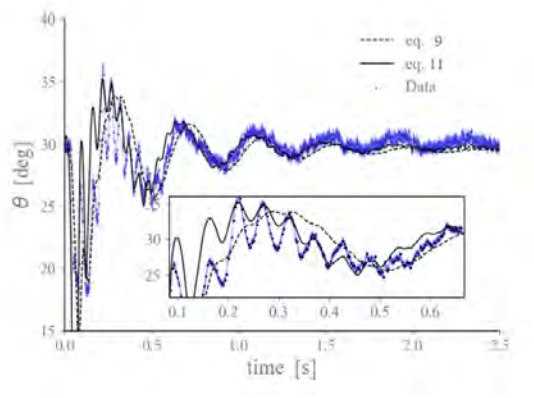

pp

Figure 13: Same comparison as in Figure 12, but as a function of time. Most of the discrepancies occurs within the region in which inertia dominates.

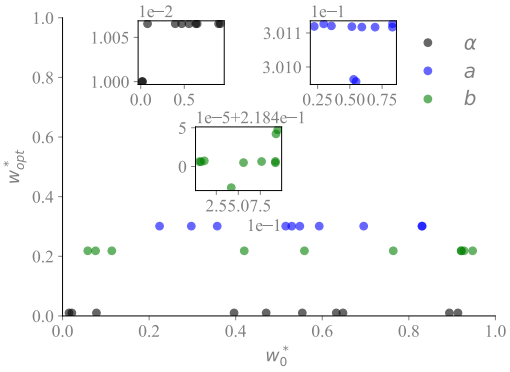

Figure 14: Optimal values of the coefficients for equation 11 for different initial values $\mathbf{w}^*_0 = \alpha^*_0, a^*_0, b^*_0$ in the normalized search space. The coefficients converge to a well defined minimum.

and acceleration.

The experimental set up allowed for visualizing the gas-liquid interface during its motion, while image processing techniques allowed for accurate interface detection. Two inverse problems were solved: 1) the regression of the measured interface with an analytical expression obtained from the quasi-static force balance and 2) the system identification problem of tuning from the data an empirical correlation for the contact angle as a function of capillary and acceleration number. The investigated correlation include both Hoffman-Tanner's and Bian and Perling's correlations.

The behaviour of these correlations has been furthermore tested using the integral model for the interface displacement and comparing with the experimental observation.

The prediction of the interface displacement showed a weak dependence by the chosen dynamic contact angle model, even if visible differences were showed comparing different correlations to the measured contact angles, for these reasons, application of inverse method on the data of the interface motion are currently affected by low sensitivity.

The interface regression results allowed for identifying the regions of validity for the quasi-static assumption within the $Ca - A^*$ plane. Indeed the experiment could be divided in two sections, the first where the combination of high capillary number and

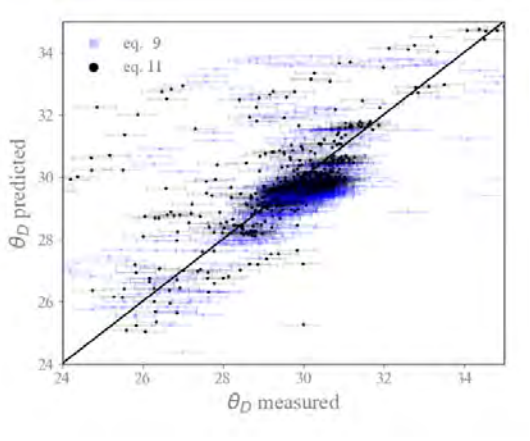

Figure 15: Comparison between experimental data (in the abscissa) and predictions from the two correlations (in the ordinates).

dimensionless acceleration lead to a low quality of the interface model. In the second phase, at low capillary numbers, the quasi-static hypothesis proved valid, however the dynamics of the contact angle proved to be function of the history of its motion. This requires contact angle correlations in the form of ordinary differential, as proposed by Bian and Perling. Future work will explore new correlations and provide a more comprehensive description of the correlation derivation's sensitivity and uncertainty. New data will be extracted from the same experiments by improving the formulation of the force balance at the interface of eq. 1. The quasi-static assumption can be dropped by

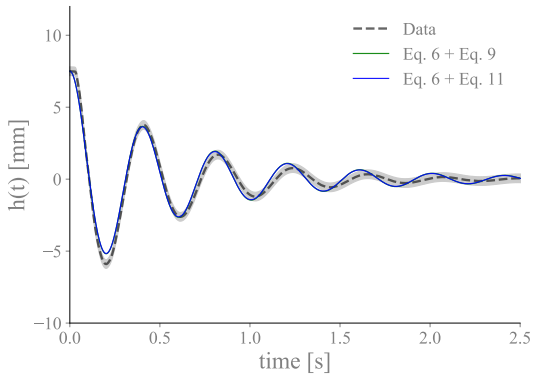

Figure 16: Comparison between experimental data on the interface motion and predictions using the two dynamic contact angle correlations. No significant difference is observed.

introducing models for the visco-inertial forces acting on the interface.

Acknowledgments

D. Fiorini is supported by Fonds Wetenschappelijk Onderzoek (FWO), Project number 1S96120N. This work was supported by the ESA Contract No. 4000129315/19/NL/MG and by ArcelorMittal's 'Minerva Contract'. Both partners are gratefully acknowledged. Finally, the authors thanks Mathieu Delsipee for its support and contribution in the preparation of the experimental set up.

References

[1] H. Eral, J. Oh, et al., Contact angle hysteresis: a review of fundamentals and applications, Colloid and polymer science 291 (2) (2013) 247–260.

[2] T. D. Blake, The physics of moving wetting lines, Journal of colloid and interface science 299 (1) (2006) 1–13.

[3] S. F. Kistler, P. M. Schweizer (Eds.), Liquid Film Coating, Springer Netherlands, 1997. doi:10.1007/978-94-011-5342-3.

[4] G. R. Willmott, C. Neto, S. C. Hendy, Uptake of water droplets by non-wetting capillaries, Soft Matter 7 (6) (2011) 2357–2363.

[5] G. R. Willmott, C. Neto, S. C. Hendy, An experimental study of interactions between droplets and a nonwetting microfluidic capillary, Faraday discussions 146 (2010) 233–245.

[6] T. Blake, J. Haynes, Kinetics of liquidliquid displacement, Journal of colloid and interface science 30 (3) (1969) 421–423.

[7] O. Voinov, Hydrodynamics of wetting, Fluid dynamics 11 (5) (1976) 714–721.

[8] R. Cox, The dynamics of the spreading of liquids on a solid surface. part 1. viscous flow, Journal of Fluid Mechanics 168 (1986) 169–194.

[9] P. Petrov, I. Petrov, A combined molecular-hydrodynamic approach to wetting kinetics, Langmuir 8 (7) (1992) 1762–1767.

[10] Y. D. Shikhmurzaev, The moving contact line on a smooth solid surface, International Journal of Multiphase Flow 19 (4) (1993) 589–610.

[11] P. De Gennes, X. Hua, P. Levinson, Dynamics of wetting: local contact angles, Journal of fluid mechanics 212 (1990) 55–63.

[12] R. L. Hoffman, A study of the advancing interface. i. interface shape in liquidgas systems, Journal of colloid and interface science 50 (2) (1975) 228–241.

[13] L. Tanner, The spreading of silicone oil drops on horizontal surfaces, Journal of Physics D: Applied Physics 12 (9) (1979) 1473.

[14] T.-S. Jiang, O. Soo-Gun, J. C. Slattery, Correlation for dynamic contact angle, Journal of Colloid and Interface Science 69 (1) (1979) 74–77.

[15] M. Bracke, F. De Voeght, P. Joos, The kinetics of wetting: the dynamic contact angle, in: Trends in Colloid and Interface Science III, Springer, 1989, pp. 142–149.

[16] S. F. Kistler, Hydrodynamics of wetting, Wettability 6 (1993) 311–430.

[17] C.-L. Ting, M. Perlin, Boundary conditions in the vicinity of the contact line at a vertically oscillating upright plate: an experimental investigation, Journal of Fluid Mechanics 295 (1995) 263300. doi:10.1017/S0022112095001960.

[18] X. Bian, W. W. Schultz, M. Perlin, Liquid slug motion and contact lines in an oscillatory capillary tube, Journal of Fluid Dynamics (under revision), http://wwwpersonal. umich. edu/schultz/Manuscripts/BianSchultzPerlin. pdf 146 (2003) 151.

[19] D. Quéré, Inertial capillarity, EPL (Europhysics Letters) 39 (5) (1997) 533.

[20] O. Shardt, P. R. Waghmare, J. Derksen, S. K. Mitra, Inertial rise in short capillary tubes, Rsc Advances 4 (28) (2014) 14781–14785.

[21] G. R. Willmott, A. Briole, F. Szczepaniak, Inertial capillary uptake of drops, Physical Review E 101 (4) (2020) 043109.

[22] E. Ramé, S. Garoff, et al., On identifying the appropriate boundary conditions at a moving contact line: an experimental investigation, Journal of Fluid Mechanics 230 (1991) 97–116.

[23] J. G. Petrov, R. V. Sedev, Quasi-static shape of the steady moving meniscuscomparison of the apparent and extrapolated dynamic contact angles, Colloids and Surfaces A: Physicochemical and Engineering Aspects 74 (2-3) (1993) 233–241.

[24] M. H. Rausch, L. Kretschmer, S. Will, A. Leipertz, A. P. Froba, Density, surface tension, and kinematic viscosity of hydrofluoroethers hfe-7000, hfe-7100, hfe-7200, hfe-7300, and hfe-7500, Journal of chemical & engineering data 60 (12) (2015) 3759–3765.

[25] A. Buades, B. Coll, J.-M. Morel, Non-local means denoising, Image Processing On Line 1 (2011) 208–212.

[26] A. Savitzky, M. J. Golay, Smoothing and differentiation of data by simplified least squares procedures., Analytical chemistry 36 (8) (1964) 1627–1639.

[27] M. Mendez, L. Németh, J.-M. Buchlin, Measurement of liquid film thickness via light absorption and laser tomography, in: EPJ Web of Conferences, Vol. 114, EDP Sciences, 2016, p. 02072.

[28] J. Canny, A computational approach to edge detection, IEEE Transactions on pattern analysis and machine intelligence (6)

(1986) 679–698.
[29] M. Darzi, C. Park, Optical distortion correction of a liquid-gas interface and contact angle in cylindrical tubes, Physics of Fluids 29 (5) (2017) 052004.
[30] M. Ratz, Experimental analysis of contact techniques and inverse line dynamics using optical methods (2021).
[31] W. Zielke, Frequency-dependent friction in transient pipe flow.
[32] X. Zhong, B. Sun, S. Liao, Analytic solutions of the rise dynamics of liquid in a vertical cylindrical capillary, European Journal of Mechanics-B/Fluids 78 (2019) 1–10.
[33] D. S. J. S. D. Fiorini, M.A.Mendez, Gas-liquid interface dynamics in non-isothermal sloshing: experimentalanalysis and simplified modeling, vki phd symposium.
[34] M. M. Weislogel, Steady capillary driven flow, NASA Technical Memorandum 107146.
[35] M. A. Branch, T. F. Coleman, Y. Li, A subspace, interior, and conjugate gradient method for large-scale bound-constrained minimization problems, SIAM Journal on Scientific Computing 21 (1) (1999) 1–23.
[36] P. Virtanen, R. Gommers, T. E. Oliphant, M. Haberland, T. Reddy, D. Cournapeau, E. Burovski, P. Peterson, W. Weckesser, J. Bright, S. J. van der Walt, M. Brett, J. Wilson, K. J. Millman, N. Mayorov, A. R. J. Nelson, E. Jones, R. Kern, E. Larson, C. J. Carey, İ. Polat, Y. Feng, E. W. Moore, J. VanderPlas, D. Laxalde, J. Perktold, R. Cimrman, I. Henriksen, E. A. Quintero, C. R. Harris, A. M. Archibald, A. H. Ribeiro, F. Pedregosa, P. van Mulbregt, SciPy 1.0 Contributors, SciPy 1.0: Fundamental Algorithms for Scientific Computing in Python, Nature Methods 17 (2020) 261–272. doi:10.1038/s41592-019-0686-2.

Advanced Numerical Schemes for High-Speed Deflagration and Detonation

Aysu Ozden

Aeronautics and Aerospace Department, von Karman Institute for Fluid Dynamics, Belgium, aysu.ozden@vki.ac.be

Bayindir H. Saracoglu

Research Manager, Turbomachinery and Propulsion Department, von Karman Institute for Fluid Dynamics, Belgium, saracog@vki.ac.be

Georg May

Associate Professor, Aeronautics and Aerospace Department, von Karman Institute for Fluid Dynamics, Belgium, georg.may@vki.ac.be

Abstract

Detonation mode of combustion offers higher thermal efficiency in more compact engine architectures for propulsion or energy conversion, thanks to simultaneous pressure augmentation during heat addition. Consequently, detonation technology proposes superior performance for next generation heat engines. Although Yakov Zeldovich layed the main principles of detonation during the early years of the past century, design and modeling of systems using detonation is quite complex. Detonative combustion is based on producing a strong shock wave that rapidly compresses the reactants to initiate combustion, and a thin flame front through which the heat addition occurs. Zeldovich-Von Neumann-Doring (ZND) cycle in which chemical reactions occur at a finite speed with introducing the reaction kinetics is the best approach approximates the thermodynamic cycle for detonation applications.

In recent years, there has been progressive efforts to develop unsteady reactive flow solvers to model detonation phenomena with high-fidelity. As a result of the efforts, zndFoam solves has been developed on open source OpenFoam platform. The tool solves the three dimensional Navier Stokes equations with URANS approach. While convective terms are integrated through HLLC scheme, time interpolation is performed with a second order Crank-Nicholson scheme. Combustion modeling is achieved with a Partially Stirred Reactor model (PaSR), which uses finite-rate chemistry to model ignition and mixed-controlled combustion which requires high computational time.

The aim of the project is to develop advanced numerical scheme to enable modeling of detonation of Hydrogen, complex fuels with high Carbon number and green fuels like sustainable aviation fuels (SAF) to be implemented on zndFoam through novel numerical schemes and Adaptive Mesh Refinement (AMR) techniques. Consequently, modeling of complex combustion physics occurring in detonation engines using environmentally sustainable fuels with low emission (CO_2, NO_x, SO_x, etc.) can be enabled with affordable computational resources. As seen in the literature, using a MUSCL coupled AUSM scheme or WENO schemes may improve the shock capturing capability and increase its accuracy. Also, including LES turbulence modeling will enlarge the insight of turbulence-chemistry interactions which is important for detonation. Finally, applying AMR technique will allow having a finer mesh around the detonation front while a relatively coarser mesh for the rest of the domain where lower resolution suffice.

Design and Analysis of a Novel High-Supersonic Aircraft Concept

Bora O. Cakir

Turbomachinery and Propulsion Department, von Karman Institute for Fluid Dynamics, Belgium, bora.orcun.cakir@vki.ac.be

Bayindir H. Saracoglu

Research Manager, Turbomachinery and Propulsion Department, von Karman Institute for Fluid Dynamics, Belgium, bayindir.saracoglu@vki.ac.be

Sergio Lavagnoli

Associate Professor, Turbomachinery and Propulsion Department, von Karman Institute for Fluid Dynamics, Belgium, lavagnoli@vki.ac.be

Abstract

Realization of supersonic civil aviation with the prospect of improved performance and environmental sustainability urges for a holistic framework for supersonic aircraft design and assessment. In this regard, the EU-funded MORE&LESS project takes on the task of investigating the global scale impact of civilian supersonic aviation through multi-disciplinary optimization platforms based on high-fidelity simulations and experimental test campaigns. Accordingly, the current project focuses on the design and development of a Mach 5 high supersonic aircraft concept, development of a combined cycle propulsion plant exploiting the concept of Air-Turbo Rocket/Ramjet (ATR) engine setup utilizing alternative fuels for reduced emission levels and extensive investigations of the developed vehicle concepts through computational simulations and experimental campaigns.

The external aerodynamic contours of the vehicle is to be designed employing the waverider approach [1], providing an integrated supersonic or hypersonic vehicle with an attached shock along its leading edge which leads to significant advantages such as a low drag configuration with a blended form, augmented lift of the whole body, precompression of the inlet flow by the forebody shape [2]. Nevertheless, the practical application of the waverider concepts are challenged by downgraded performance especially at off-design conditions [3]. In order to overcome these challenges, an in-house multi-disciplinary optimization code, CADO, is to be used coupled with a numerical solver based on the Taylor-Maccoll equations. Moreover, as the individual utilization of airbreathing engine configurations narrows down the range of Mach numbers for high efficiency thrust production, the propulsion system is to be designed with an ATR concept for increasing propulsive efficiency and reducing emission levels throughout the flight envelope [4].

The experimental test campaigns for the supersonic vehicle concepts are to be conducted at the VKI H3 hypersonic wind tunnel during which a wide range of measurement techniques will be employed. The quantification capabilities of non-intrusive flow visualization approaches such as Schlieren imaging are to be extended towards their utilization in supersonic flows by means of various post-processing algorithms and quantitative measurement methods such as infrared thermography. Furthermore, flight performance information regarding the vehicles will be extracted employing surface pressure sensors, temperature sensitive paints and multiple degree of freedom force balance measurements.

References

[1] D. Küchemann, The Aerodynamic Design of Aircraft, AIAA education series, American Institute of Aeronautics & Astronautics, 2012.

[2] I. M. Blankson, Air-breathing hypersonic cruise - Prospects for Mach 4-7 waverider aircraft, 37th International Gas Turbine and Aeroengine Congress and Exposition.

[3] D. Sziroczak, H. Smith, A review of design issues specific to hypersonic flight vehicles, Progress in Aerospace Sciences 84 (2016) 1–28.

[4] N. Tanatsugu, Y. Naruo, I. Rokutanda, Test results of the air turbo ramjet for a future space plane, Acta Astronautica 32 (12) (1994) 785–796.

SHAPE OPTIMIZATION

Aero-elastic tailoring of composite turbomachinery blades through gradient-based optimisation: harmonic solvers

Tom De Bruyn

Turbomachinery and Propulsion Department, von Karman Institute for Fluid Dynamics, Belgium, tom.de.bruyn@vki.ac.be

Supervisor: Tom Verstraete[1] and Fabrizio Fontaneto[2]

[1]*Professor, Turbomachinery and Propulsion Department, von Karman Institute for Fluid Dynamics, Belgium, tom.verstraete@vki.ac.be*

[2]*Associate Professor, Turbomachinery and Propulsion Department, von Karman Institute for Fluid Dynamics, Belgium, fabrizio.fontaneto@vki.ac.be*

University Supervisor: Joris Degroote

Professor, Department of Electromechanical, Systems and Metal Engineering, Ghent University, Belgium, joris.degroote@ugent.be

Abstract

As optimisation methods for turbomachinery components become increasingly important to enable further design improvements, such methods should incorporate the interaction between fluid and structure (e.g. flutter) to incorporate mechanical stability of the design during the optimisation. In order to do so however, fluid-domain solvers must consider unsteadiness. Harmonic solvers, describing the unsteadiness as set of harmonic perturbations of the mean flow, achieve this at moderate computational cost.

Keywords: CFD, non-linear harmonics, harmonic balance, optimisation

1. Introduction

Several decades after their introduction, Steady Reynolds-averaged Navier-Stokes (RANS) methods remain the dominant approach to turbomachinery CFD, permitting rapid and relatively inexpensive computation. This is especially true in the context of now prevalent optimisation workflows (as considered in the VKI's in-house turbomachinery optimisation framework *CADO*[1], where up to several hundreds of design evaluations may be required. In such cases, higher fidelity methods become prohibitively expensive. RANS methods however insufficiently capture all physical aspects of interest during the optimisation process. Notably vibrational effects (e.g. flutter, vibrations induced by blade row interaction, ...) are by nature unsteady. These effects are of great importance in turbomachinery component development and directly influenced by typical design variables of the optimisation process, hence they must be included directly.

In order to incorporate unsteadiness without suffering the computational penalty of an unsteady RANS (URANS) computation, an harmonic or frequency-domain method is used to capture most of the unsteadiness at reasonable expense. In order to do so, the solution of the URANS equations for a periodic flow is decomposed into it's temporal Fourier components:

$$U(t, \mathbf{x}) = Re\left[\sum_{k=0}^{\inf} \hat{U}_k(\mathbf{x}) e^{\mathbf{i}k\omega t}\right], \tag{1}$$

where $\omega = 2\pi f$ is the base frequency and U the vector of conservative variables:

$$U = \begin{pmatrix} \rho \\ \rho v_x \\ \rho v_y \\ \rho v_z \\ \rho e \end{pmatrix}. \tag{2}$$

Starting from the unsteady form of the Navier-

Stokes equations:

$$\frac{dU}{dT} + R(U) = 0, \tag{3}$$

where $R(U) = F_c(U) - F_v(U) + Q(U)$ is the steady residual comprising of the convective flux, viscous flux and source term respectively, substitution of (1) leads to:

$$\mathbf{i}k\omega \, Im\left[\sum_{k=0}^{\inf} \hat{U}_k(\mathbf{x}) e^{\mathbf{i}k\omega t}\right] + R(U) = 0. \tag{4}$$

the steady residual R in equation (4) can similarly be decomposed in it's Fourier components:

$$R(U) = Re\left[\sum_{k=0}^{\inf} \hat{R}_k(U) e^{\mathbf{i}k\omega t}\right], \tag{5}$$

Combining equations (4) and (5) and grouping terms by frequency, the unsteady equations can be formulated in the frequency domain:

$$\mathbf{i}k\omega \hat{U}_k(\mathbf{x}) + \hat{R}_k(U) = 0. \tag{6}$$

with $\hat{R}_k$ the k-th harmonic of the steady Navier-stokes Residual R, which depend on all harmonics of the solution U. Writing (6) for all k, one obtains a set of balance equations, leading to the name 'harmonic balance' technique[2].

1.1. Finite harmonics

In practice, a finite number of frequencies is used. As the computational effort inevitably increases with an increased number of included harmonics, the number is a trade-off between performance and the improved accuracy representing relevant unsteadiness as more frequencies are included. When the number of harmonics is truncated, (6) is no longer exact. Indeed the non-linearity of the steady RANS residual $R(U)$ means the solution and residual cannot be represented using the same (finite) set of harmonics.

This can be easily understood from the product of two different harmonic components. The multiplication of two variables $f(t)$ and $g(t)$, described using the same number of harmonics can be written out in full:

$$\begin{aligned} f(t)\, g(t) =& \frac{1}{2}\sum_{k=0}^{K}\left[\hat{F}_k e^{\mathbf{i}k\omega t} + \hat{F}_{-k} e^{-\mathbf{i}k\omega t}\right] * \\ & \frac{1}{2}\sum_{l=0}^{L}\left[\hat{G}_l e^{\mathbf{i}l\omega t} + \hat{G}_{-l} e^{-\mathbf{i}l\omega t}\right] \\ =& \frac{1}{4}\sum_{k=0}^{K}\sum_{l=0}^{L}\Big[\hat{F}_k\hat{G}_l e^{\mathbf{i}(k+l)\omega t} \\ & \hat{F}_k\hat{G}_{-l} e^{\mathbf{i}(k-l)\omega t} \\ & \hat{F}_{-k}\hat{G}_l e^{\mathbf{i}(l-k)\omega t} \\ & \hat{F}_{-k}\hat{G}_{-l} e^{-\mathbf{i}(k+l)\omega t}\Big], \end{aligned} \tag{7}$$

where $\hat{F}_{-k}$ and $\hat{G}_{-l}$ are the complex conjugates of $\hat{F}_k$ and $\hat{G}_l$ respectively. It is clear from (7) that if each of the terms has s up to K harmonic, the product contains harmonics up to the $2K$'th harmonic of the base frequency as well as that a particular harmonic of the solution contribute to the residual for several (other) harmonics.

The non-linearity of the RANS residual thus introduces a coupling between the different harmonics, which - depending on the applied methodology - can be neglected, selectively computed or need to be taken into account to prevent aliasing. Regardless of the methodology, a 'harmonic balance' like (6) always neglects harmonics of the residual of higher order than the choice for the decomposition of the solution. However, as the number of harmonics in the solution is increased the approximation error decreases (as generally higher harmonics have a smaller amplitude in the considered cases).

2. Methodology

Writing the residual term in equation (6) first as a Taylor series around the steady solution $\hat{U}_0$ and applying the Fourier transform afterwards leads to the following expressions for the harmonics of the Residual, with K total harmonics considered:

$$\begin{aligned} \hat{R}_0 &= R(\hat{U}_0) + D_0(\hat{U}_0, ...\hat{U}_K) \\ \hat{R}_k &= R(\hat{U}_0) + \left.\frac{\partial R}{\partial U}\right|_{\hat{U}_0} \hat{U}_K + D_k(\hat{U}_0, ...\hat{U}_K) \quad k \neq 0. \end{aligned} \tag{8}$$

The coupling terms D_k are called the deterministic stresses and contain the interaction between the higher harmonics. As the Taylor series expansion introduces

polynomials of degree higher than one, these terms are non-linear, maintaining the coupling between the harmonics considered above. Linear harmonic (also called time-linearised) methods neglect all deterministic stress terms in (8), retaining only the first, linear term for the higher harmonics [3].

Non-linear harmonic methods [4; 5] include at least the D_0 term modelling the influence of the unsteadiness on the mean flow field. This term is computed from the higher order harmonics and given by (split in a convective and viscous contribution)[6]:

$$D_0(U) = D_{C0} - D_{V0} = \begin{pmatrix} 0 \\ \overline{(\rho \mathbf{v})' v_x'} \\ \overline{(\rho \mathbf{v})' v_y'} \\ \overline{(\rho \mathbf{v})' v_z'} \\ \overline{(\rho H)' \mathbf{v}'} \end{pmatrix} - \begin{pmatrix} 0 \\ 0 \\ 0 \\ 0 \\ \tau' \mathbf{v}' \end{pmatrix}, \qquad (9)$$

where the prime indicates $\rho' = \rho - \hat{\rho}_0$ the unsteady part of the solution. Computation of this term then requires a sum over all harmonics e.g.:

$$\overline{(\rho \mathbf{v})' v_x'} = \frac{1}{4} \sum_{k=1}^{K} \left[\rho \hat{V}_{x_k} \hat{\mathbf{V}}_{-k} + \rho \hat{V}_{x_{-k}} \hat{\mathbf{V}}_k \right]. \qquad (10)$$

the evolution of the higher order harmonics is typically modelled by a transport equation using the time-averaged velocity components, neglecting mutual influence of the harmonics on one another, besides through their effect on the mean flow [4; 6]. Including the coupling is however possible as well, though tedious [7].

As such, this method is formulated exclusively in the frequency domain, avoiding the need for Fourier transformations. This does however render the implementation of boundary conditions, classically formulated in the time domain, somewhat more involved. The major drawback is however the neglecting of the coupling terms for the higher harmonics, reducing the overall accuracy of the method in cases where the unsteadiness is more significant.

2.1. time-spectral method

An attractive alternative approach is not to model the deterministic stresses directly, but rather implicitly incorporate these terms by using the discrete Fourier Transform of the non-linear residual. To do so, the solution U is sampled at at least $2K + 1$ sample points (K the index of the highest considered harmonic), for which the Residual is evaluated, resulting in a set of equations:

$$\mathbf{i} k \omega \hat{U}_k(\mathbf{x}) + \mathscr{F}_k(R(\mathscr{F}^{-1}(\hat{U}))) = 0, \qquad (11)$$

where $\mathscr{F}_k$ is the k-th component of the discrete Fourier transform and $\hat{U}$ is (1) truncated at K, the approximate reconstruction of the flow field [8; 9]. Particular care is needed for these methods to avoid aliasing in the forward and inverse transforms. As discussed in section 1.1, the residual $R(U)$ contains higher harmonics than U itself, which during the forward Fourier transform may produce spurious contributions to the lower harmonics. In order to reduce the effect, Orszag [10] has suggested to sample at $N \geq 3K + 1$ time instances (50% higher than the lower bound of the Shannon-Nyquist theorem), which is sufficient to eliminate aliasing for quadratic functions. As the residual computation is generally rational, it contains infinitely many harmonics, however these contributions are third order in the perturbation amplitude, and hence drop of quickly. It must be noted that (over)sampling comes at a non-negligible cost, as at every time instance a residual evaluation is performed.

The time-spectral method holds several important advantages over the 'classic' linear harmonic approach:

- Coupling between harmonics is implicitly included.
- As the RANS residual is evaluated in the time domain, flux evaluation routines developed for steady computations can be applied without modification. This is particularly advantageous for codes with both a steady and harmonic solver, as a single set of routines can be used.
- The joint use of the time and frequency domain, while necessitating the extra cost of the Fourier transforms, means boundary conditions can be formulated in either.

In some cases (11) is cast into the time-domain, corresponding to a pseudo-spectral discretisation of the time-dependent term in the URANS equations[8]. While this removes the need for the forward Fourier transform, the approximation of the time derivative becomes increasingly inaccurate when few (< 16) sampling points are used. Furthermore, it introduces a further coupling between different harmonics, whereas (6) and (as a result) (11) allow one to solve for every wave number independently.

3. treatment of turbulence

For all aforementioned methods, a common assumption is that turbulence models for RANS can be applied for unsteady flow as well, as with a limited number of harmonics, the time scale of the variation of the mean flow (including the harmonic components, but not turbulence), is still orders of magnitude greater than the time scale of the turbulence. Hence existing methods for RANS turbulence modelling such as the (negative) Spalart-Allmaras model[11] can be used. A common simplification is to assume the effect of the harmonic unsteadiness on the turbulence to be negligible. Under that assumption, the computation of turbulent values (e.g. the Spalart-Allmaras transport quantity) is identical to the treatment for steady flow. The resulting eddy viscosity is used in the computation of all harmonics.

The time-spectral methods offer another approach without the need to express the transport equations in the frequency domain. The same approach used to obtain equation (11) can be applied directly. For the Spalart-Allmaras model used in *CADO* this means expressing the transport quantity as:

$$\rho\tilde{\nu}(t,\mathbf{x}) = Re\left[\sum_{k=0}^{K}\hat{\rho\tilde{\nu}}_k(\mathbf{x})e^{\mathbf{i}k\omega t}\right], \tag{12}$$

leading to an evolution equation:

$$\mathbf{i}k\omega\hat{\rho\tilde{\nu}}_k(\mathbf{x}) + \mathscr{F}_k(R^{TUR}(\mathscr{F}^{-1}(\hat{U},\hat{\rho\tilde{\nu}}))) = 0, \tag{13}$$

where to evaluate the turbulence residual both meanflow and turbulence values are brought to the time domain. Hence the solution strategies used for the mean/harmonic flow can straightforwardly be applied to the turbulence model as well.

4. solution strategy

To solve the system of equations (8) or (11) a pseudo-time marching method is used. Hereto, the pseudo-timestep is added to the left-hand side of (6):

$$\frac{d\hat{U}_k}{dt'} + \mathbf{i}k\omega\hat{U}_k(\mathbf{x}) + \hat{R}_k(U) = \frac{d\hat{U}_k}{dt'} + \hat{R}_k^H(U) = 0. \tag{14}$$

Using m to indicate the pseudo-time step, and using

$$\Delta\hat{U}_k^{(m)} = \hat{U}_k^{(m+1)} - \hat{U}_k^{(m)} \tag{15}$$

a theoretical implicit formulation for the numerical update strategy becomes (linearising the residual around the steady component):

$$\left(\frac{1}{\Delta t'} + \mathbf{i}k\omega + \frac{\partial R_k}{\partial U}\right)\Delta\hat{U}_k^{(m)} = -\hat{R}_k(U). \tag{16}$$

In equation (16) different harmonics are generally coupled through the computation of the right-hand side, but also by the jacobian of the linear system. The latter is somewhat problematic, as by using this formulation all harmonics are solved for simultaneously in a linear system of $2K + 1$ equations. As a result the memory requirements increase with the number of harmonics, and quickly become prohibitive for a larger number of harmonics.

Therefore typically the jacobian in the left hand site of (16) is approximated for higher harmonics by the one for the steady computation (e.g. [12]:

$$\left(\frac{1}{\Delta t'} + \mathbf{i}k\omega + \left.\frac{\partial R_0}{\partial U}\right|_{\hat{U}_0^{(m)}}\right)\Delta\hat{U}_k^{(m)} = -\hat{R}_k(U), \tag{17}$$

allowing for the updates of the different harmonics to be solved for sequentially (or in fact in parallel, though in that case read access to the stored system matrix may still be serialised, reducing parallelisation effectiveness). As a result, the system matrix must only be computed once for the update of all harmonics. Alternative strategies with a more accurate left-hand side of the linear system may be beneficial for faster convergence, and especially to accelerate gradient computations using the adjoint method implemented in the *CADO* optimisation framework. To discuss them, the adjoint method is first briefly introduced.

4.1. formulation of the adjoint

In its most general form, the considered optimisation problem may be formulated as:

$$\min_{\mathbf{X}} J(\mathbf{U},\mathbf{X}) \quad \textit{subject to } \mathbf{R}(\mathbf{U},\mathbf{X}) = 0, \tag{18}$$

With $\mathbf{U}$ the solution vector, $\mathbf{R}$ the residual of the CFD[1] computation, $\mathbf{X}$ the vector of grid points making up the mesh and J an objective function.

Writing the Lagrangian function for this optimisation problem:

[1]For the considered harmonic problem, $\mathbf{R}$ is the vector of all Harmonic residuals $\hat{R}_k^H$.

$$\mathscr{L}(\mathbf{U}, \mathbf{X}, \phi) = J(\mathbf{U}, \mathbf{X}) - \psi^T \mathbf{R}(\mathbf{U}, \mathbf{X}), \quad (19)$$

and taking the derivative with respect to ψ, $\mathbf{U}$ and $\mathbf{X}$ respectively leads to KKT (Karush-Kuhn-Tucker) conditions, that must all hold in the optimum:

$$\frac{\partial \mathscr{L}}{\partial \mathbf{\Psi}} = \mathbf{R}(\mathbf{U}, \mathbf{X}) = 0, \quad (20)$$

$$\frac{\partial \mathscr{L}}{\partial \mathbf{U}} = \frac{\partial J}{\partial \mathbf{U}} - \psi^T \frac{\partial \mathbf{R}}{\partial \mathbf{U}} = 0, \textit{ and} \quad (21)$$

$$\frac{\partial \mathscr{L}}{\partial \mathbf{X}} = \frac{\partial J}{\partial \mathbf{X}} - \psi^T \frac{\partial \mathbf{R}}{\partial \mathbf{X}} = 0. \quad (22)$$

Equation (20) simply recovers the forward CFD problem. Taking the transpose of (21) leads to the linear system of adjoint equations:

$$\frac{\partial \mathbf{R}}{\partial \mathbf{U}}^T \psi = \frac{\partial J}{\partial \mathbf{U}}^T. \quad (23)$$

A solution to the KKT conditions is usually found by iterating over equations (20), (23) and (22) until the compuational grid $\mathbf{X}$ no longer changes.

4.2. alternative numerical strategies

5. Conclusion

This paper surmises the most commonly used 'harmonic' methods for solving the Reynolds-averaged Navier Stokes (RANS) equations, used when the unsteadiness of the meanflow is periodic and can be accurately represented by small amount of harmonic pertubations. Situated between steady and unsteady RANS solvers, they offer an interesting solution to capture unsteadiness without the - in the context of an optimisation process - prohibitive cost of full annulus URANS. Time-spectral methods are particularly enticing as they can potentially share subroutines with a steady RANS solver, reducing the overal development effort.

Acknowledgments

This PhD research is supported by a fellowship of the Flanders Scientific Research Fund (FWO)

References

[1] L. Mueller, T. Verstraete, Cad integrated multipoint adjoint-based optimization of a turbocharger radial turbine, International Journal of Turbomachinery, Propulsion and Power 2 (3).

[2] C. Frey, G. Ashcroft, H.-P. Kersken, C. Voigt, A harmonic balance technique for multistage turbomachinery applications, 2014. doi:10.1115/GT2014-25230.

[3] G. Dufour, F. Sicot, G. Puigt, C. Liauzun, A. Dugeai, Contrasting the harmonic balance and linearized methods for oscillating-flap simulations, Aiaa Journal - AIAA J 48 (2010) 788–797. doi:10.2514/1.43401.

[4] S. Vilmin, E. Lorrain, C. Hirsch, M. Swoboda, Unsteady flow modeling across the rotor/stator interface using the nonlinear harmonic method, Vol. 6, 2006. doi:10.1115/GT2006-90210.

[5] L. He, W. Ning, Efficient approach for analysis of unsteady viscous flows in turbomachines, Aiaa Journal - AIAA J 36 (1998) 2005–2012. doi:10.2514/2.328.

[6] S. G. Horcas, F. Debrabandere, B. Tartinville, C. Hirsch, G. Coussement, Extension of the non-linear harmonic method for the study of the dynamic aeroelasticity of horizontal axis wind turbines, Journal of Fluids and Structures 73 (2017) 100–124. doi:https://doi.org/10.1016/j.jfluidstructs.2017.06.008.
URL https://www.sciencedirect.com/science/article/pii/S0889974616306302

[7] P. Vasanthakumar, Three dimensional frequency-domain solution method for unsteady turbomachinery flows, Ph.D. thesis, Durham University (2003).
URL http://etheses.dur.ac.uk/3089/

[8] K. C. Hall, J.P. Thomas and W. Clark, Computation of Unsteady Nonlinear flows in Cascades Using a Harmonic Balance Technique, AIAA Journal 40 (5) (2002) 879–886.

[9] McMullen, Matthew Scott and Jameson, Anthony and Alonso, Juan J., The Application of Non-Linear Frequency Domain Methods to the Euler and Navier-Stokes Equations, Ph.D. thesis, Stanford University, Stanford, CA (3 2003).

[10] S. A. Orszag, On the Elimination of Aliasing in Finite-Difference Schemes by Filtering High-Wavenumber Components., Journal of Atmospheric Sciences 28 (6) (1971) 1074–1074. doi:10.1175/1520-0469(1971)028¡1074:OTEOAI¿2.0.CO;2.

[11] S. R. Allmaras, F. T. Johnson, P. R. Spalart, Modifications and clarifications for the implementation of the spalart-allmaras turbulence model, 2011.

[12] G. Ashcroft, C. Frey, H.-P. Kersken, On the development of a harmonic balance method for aeroelastic analysis, in: E. Onate, X. Oliver, A. Huerta (Eds.), 6th. European Conference on Computational Fluid Dynamics - ECFD VI, 2014, pp. 5885–5896.
URL https://elib.dlr.de/90474/

Elliptic Mesh generation for Industrial Shape Optimization

Luca Zampini

Turbomachinery Department, von Karman Institute for Fluid Dynamics, Belgium, luca.zampini@vki.ac.be

Supervisor: Tom Verstraete

Associate professor, Turbomachinery Department, von Karman Institute for Fluid Dynamics, Belgium, tom.verstraete@vki.ac.be

University Supervisor: Grgory Coussement

Head of Fluid-Machines Department and Professor, Fluid-Machines Department, University of Mons, Belgium, Gregory.COUSSEMENT@umons.ac.be

Abstract

In the current paper a general, versatile and accurate procedure for the structured mesh generation of industrially-relevant geometries is presented. The procedure is mainly made of two steps: initial mesh generation via Transfinite Interpolation and mesh smoothing in order to increase the quality. The mesh smoothing is also enhanced with a in-house regularizing procedure, which guarantees the maximum mesh quality in the proximity of the block boundaries. Finally, a multi-block, high-quality mesh is presented in order to show the capabilities and the versatility of the developped mesh generation procedure.

Keywords: Multi-block structured mesh generation, singular-point treatment, transfinite interpolation, elliptic smoothing

1. Introduction

The design of several high-end products is nowadays performed in a virtual environment. In a virtual environment is indeed possible to model the product, simulate its performance and most importantly to optimize it [1]. This constitutes a great advantage for high-capital industries, such as the aeronautical sector, where the evaluation of the performances of a single design choice requires a high monetary investment. On the one hand, the simulation of a particular design choice allows to reduce the cost of a physically testing it. On the other hand, an automatic tool is able to guide the design choices by narrowing the possibilities in the design space and this becomes crucial when the various design parameters have a mutual and complex interaction. Therefore, nowadays it is particularly of interest the development of platforms for the virtual design with optimization capabilities.
Recent advances in manufacturing techniques, like rapid prototyping and additive manufacturing, have additionally offered the possibility to explore bold and innovative designs. These design choices were once unreachable with conventional manufacturing techniques and therefore existed only on paper. Nowadays, however, they are finally accessible. Therefore, current designers have the possibility to explore a much wider design space with respect to the past. The capability to tackle very complex geometries must be translated also in the aforementioned virtual environment to fully exploit its potential. For this reason, it particularly important for virtual design and optimization platforms to be able to tackle very complex and bold geometries.

1.1. Industrial shape Optimization

An Industrial Shape Optimization platform is a program that allows to simulate and optimize the performances of a particular industrial component. For example, it is very complex in turbomachinery applications to forecast the interaction between the shape of a blade and the aerodynamical performances. Therefore, automatic tools have been developed in order to simulate and optimize the performances of a given blade shape. These tools are called Shape Optimiza-

tion platforms. In particular, in the current paper the platform of interest is the gradient-based platform CADO (Computer Aided Design Optimization) [2], [3] developed at the Von Karman Institute.

1.2. Complex, structured mesh generation

The development of additive manufacturing techniques, as mentioned before, calls for the capability to model very complex geometries. Therefore, it is necessary to provide the Industrial Shape Optimization platform of interest the capability to mesh very complex, 3D geometries. Additionally, a discrete-gradient-based Shape Optimization platform such as CADO is very sensitive of the smoothness of the discretized objective function. If a technique such as unstructured meshing is used, for example, the smoothness of the discretized objective function and hence the quality of the discretized gradient is compromised. In particular, if a different mesh is produced at every iteration, the objective function does not vary with continuity and this creates big problems in the estimation of the discretized gradient. Therefore, in view of the framework of CADO, the approach of the structured meshing is preferred for its better integration in the optimization platform.

2. Mesh generation procedure

The generation of a structured mesh is typically performed in two subsequent steps. First of all, it is necessary to generate the initial distribution of the mesh in the domain of interest. This is typically achieved by identifying a series of reference points in the domain and then using a suitably-defined interpolation procedure to generate the structured blocks starting. This step is typically performed by transfinite interpolation, as it will be explained in the followings.
The resulting mesh after transfinite interpolation is usually not satisfactory in terms of quality. Additionally, it is well-known that the technique does not prevent the grid lines from folding, resulting eventually in negative cell volumes. Therefore, as a second step, it is customary to increase the mesh quality and resolve the grid line folding by means of a suitably-defined smoothing procedure. The smoother aim is to increase the mesh quality, by reducing the skewness, expansion ratio and eventual folding of the cells.
In the following sections will be discussed the two aforementioned steps, which are required to achieve a high-quality, multi-block structured mesh.

3. Transfinite interpolation

Transfinite interpolation (TFI) was first described by William Gordon in [4]. TFI has the advantage of providing complete conformity to boundaries in the physical domain. In the early 1980s, Lars Eriksson described TFI for application to grid generation for computational fluid dynamics [5]. TransFinite Interpolation is in syntheses a multivariate interpolation procedure. In practice, the TFI procedure aims at mapping the Cartesian 3D cube into a three-dimensional space at will, as represented by figure 1. The procedure follows the principle of generating a mesh in successive steps, from the previously available information in a recursive way. For example: edges are constructed by interpolating the position of the vertices. Then, faces are constructed by interpolating the points on edges and vertices. Finally, blocks are constructed by interpolating points on the faces, edges and vertices. A graphical representation of the working principle is provided in figure 4. The point in the upper face uses the data of the edges and vertices, in order to interpulate the position of the point. The The technique of linear TFI is used in the present paper in order to generate the initial grid distribution in the space.

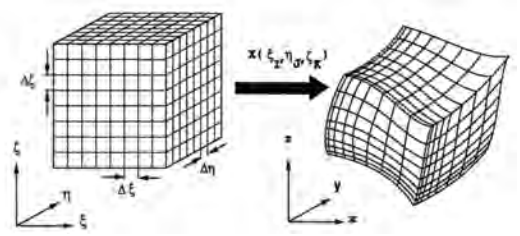

Figure 1: Transfinite Interpolation mapping of the cube

4. Elliptic smoothing

As presented in section 3, the technique of TFI does not prevent from grid folding and in many applications is incapable of providing a high-quality grid point distribution in space. Therefore, a smoothing technique is added in order to increase the quality of the 3D, multiblock structured mesh.
Different types of smoother have been developed in time, such as the hyperbolic and elliptic ones. In general, they are all based on the solution of suitably-defined Partial Differential Equations and the main

difference between each other is the way they interact with the boundaries of the domain. In particular, hyperbolic smoothers start from one side of the domain as an initial condition and then construct the grid through a time marching procedure until the other side of the domain. The elliptic smoothers, on the other hand, take home advantage of the nature of the elliptic nature of the PDE they solve. They are able to consider the domain as a unique entity where the position of every grid point interacts of all the other grid points. Given the advantage that elliptic smoothers offer, they are nowadays the most successful and widespread mesh generators in commerce.

4.1. Elliptic equations

The problem of creating a structured mesh in a given 3D domain can be seen as the identification of iso-surfaces in the 3D space. Every cell is then identified as the volume identified by the intersection between 3 families of iso-surfaces: one for each face of the cubic cell. Every iso-surfaces is a surface where a suitably-defined potential function is constant; since 3 families of iso-surfaces are needed to generate a 3D grid, 3 potential functions have to be defined. The requirement of smoothness of the 3D grid can be translated into a requirement for the 3 scalar, potential functions: they must obey to the Poisson equation in order to generate a smooth grid. The equations at the basis of the 3D grid generation are reported in equation 3. U,V and W represent the potential functions, whereas P, Q and R are the so-called control functions [6]. The problem presented in equation 3 is usually referred to as the direct problem.

$$\nabla^2 U = P \tag{1}$$

$$\nabla^2 V = Q \tag{2}$$

$$\nabla^2 W = R \tag{3}$$

The problem of the grid smoothing is typically not resolved as presented in equation 3. A series of problems indeed arise in the direct solution of the direct problem. For example, the grid domains may show a high degree of non-orthogonality, which hinders the stability of the solution. Instead of solving the direct problem, therefore, the inverse problem is solved in place of it. Instead of solving for 3 scalar functions in the Cartesian domain (x,y,z), indeed, the cartesian position (x,y,z) is solved in the solution space (u,v,w). In order to determine the inverse problem, it is necessary to modify the differential operators through the chain rule and the result of this transformation is reported in equation 4 5 and 6. It is interesting to notice that the equations become non-linear and therefore particular care has to be taken during the discretization phase.

$$\begin{aligned} &G_{11}\frac{\partial^2 x}{\partial u^2} + G_{22}\frac{\partial^2 x}{\partial v^2} + G_{11}\frac{\partial^2 x}{\partial w^2} + \\ &+2G_{12}\frac{\partial^2 x}{\partial u \partial v} + 2G_{13}\frac{\partial^2 x}{\partial u \partial w} + 2G_{23}\frac{\partial^2 x}{\partial v \partial w} = \\ &-g\left(P\frac{\partial x}{\partial u} + Q\frac{\partial x}{\partial v} + R\frac{\partial x}{\partial w}\right) \end{aligned} \tag{4}$$

$$\begin{aligned} &G_{11}\frac{\partial^2 y}{\partial u^2} + G_{22}\frac{\partial^2 y}{\partial v^2} + G_{11}\frac{\partial^2 y}{\partial w^2} + \\ &+2G_{12}\frac{\partial^2 y}{\partial u \partial v} + 2G_{13}\frac{\partial^2 y}{\partial u \partial w} + 2G_{23}\frac{\partial^2 y}{\partial v \partial w} = \\ &-g\left(P\frac{\partial y}{\partial u} + Q\frac{\partial y}{\partial v} + R\frac{\partial y}{\partial w}\right) \end{aligned} \tag{5}$$

$$\begin{aligned} &G_{11}\frac{\partial^2 z}{\partial u^2} + G_{22}\frac{\partial^2 z}{\partial v^2} + G_{11}\frac{\partial^2 z}{\partial w^2} + \\ &+2G_{12}\frac{\partial^2 z}{\partial u \partial v} + 2G_{13}\frac{\partial^2 z}{\partial u \partial w} + 2G_{23}\frac{\partial^2 z}{\partial v \partial w} = \\ &-g\left(P\frac{\partial z}{\partial u} + Q\frac{\partial z}{\partial v} + R\frac{\partial z}{\partial w}\right) \end{aligned} \tag{6}$$

4.2. Source term for boundary layer refinement

In equation 4 - 6 the inverse problem is reported in its more general form. In particular, the presence of 3 control functions P,Q,R appears in the formulation of the inverse problem. These control functions are employed in order to offer direct control over the shape of the grid lines. Particularly interesting is, for example, the control of orthogonality and first cell thickness in the domain for wall-resolved calculations. The mesh generator object of this paper is equipped with a wall-refinement procedure, according to [7]. The advantage of the presented procedure is the generality of the proposed methodology.

5. Numerical discretization

The numerical discretization used in the current paper is the second-order, central finite-difference method. This technique is particularly suited for the solution of the inverse problem. The solution space, contrarily to the Cartesian domain space, is always orthogonal and equidistant. Therefore, the order of

accuracy is always second-order, regardless of the grid quality or folding in the (x,y,z) space. The equation reported in 4 - 6 is made quasi-linear by freezing before each iteration the variable coefficients Gij in order to increase the numerical stability of the method [6]. The central differentiation scheme involves the point position only during the discretization of the second derivative. Therefore, the construction of the explicit update formula is self-evident from the direct application of the finite-differencing scheme on equations 4 - 6. For the discretization of the source term, the procedure used in the current paper is the direct application of the methodology proposed by [6].
In order to accelerate the rate of convergence of the overall system, a Gauss-Seidel method is implemented. In particular, a Jacobi solution method for the solution of the PDE would require the calculation of the update of every grid point based on the position of the neighbouring points at the previous iteration of the domain. In a Gauss-Seidel approach, on the other hand, the position of the grid point is calculated from the actual position of the other neighbouring points. Since the G-S approach uses more updated information with respect to the Jacobi one, the spectral radius of convergence will be smaller, resulting in a faster convergence rate. For this reason, the G-S approach is preferred and implemented in the current framework.

6. Multiblock strategy

In order to be able to tackle complex domains with a structured mesh, it is necessary to be able to divide the mesh into several blocks. Therefore, the mesh generation procedure presented in the current paper is equipped with operators for the inter-block communication.
In particular, the first problems that arises during the development of a multiblock mesh is the identification of the neighbouring points across the block interfaces. For example, every point located on a block face, edge or vertex must be able to identify the position of the adjacent points in order to be able to apply the stencil of choice for the discretization of the elliptic equations. Therefore, as it will be presented in the following sections, the mesh generator in object is equipped with an automated procedure for the recognition of the block interfaces: the topology layer. After the presentation of the topology layer, the inter-block and intra-block operators will be presented.

6.1. Topology layer

The need of multi-block capabilities calls for the need for the ability to identify neighbouring points. In particular, during the construction of the finite-difference stencil, each point has to be able to access the adjacent point. From the point of view of the data storage, it is necessary to create a strategy to access the data of the neighbouring points. This is valid for points inside of the block, as well as for points located between two blocks, such as faces, edges and vertices. In order to achieve this objective different strategies are available. For example, one possibility is the usage of ghost points, which creates multiple copies of the same data in order to communicate the information between two respective blocks. Alternatively, it is possible to develop suitably-defined data-accessing functions without the need of data duplication. In the present paper, the latter approach of the data accessors has been chosen because it offers significant advantages. First of all, it allows to reduces the memory requirements of the executable which is particularly of interest for computationally intensive and complex domains. Additionally, the proposed approach does not require the step of copying the ghost data in order to share information between the blocks, with a consequent reduction of the computational time. Lastly, the proposed approach is much less error prone, since the programmer does not have to keep into account the continuous copy of redundant data in suitably-defined arrays.
The proposed approach is based on topology, which is a map of the connectivity between the various nodes of the domain. The construction of the topological map is made fully automatic and starts form the input data of the user, which mainly consists of the following steps:

- creation of the vertex array by providing a name
- creation of the edge array, by providing a name and the vertices each edge is attached to
- creation of the face array, by providing a name and the edges every face is attached to
- creation of the block array, by providing a name and the faces every block is attached to

Starting from the aforementioned very basic input parameter, the proposed mesh generator is able to build in a fully-automated way the complete map of connectivity for every grid point.
Thanks to the topological layer, every point in the

computational grid is stored in a separated memory array, depending on the topological role that the the point is subject to. For example, points in the same block will be stored together, but the points the edge will be stored separately. This provides an automatic marker for points in different topological configurations: for example, it is possible to use a first routine for the smoothing in the blocks and then a second routine for the edge and vertex points. The ability to differentiate points based on their topological role is used in the current paper to introduce routines of increasing level of complexity. The basic routine is the smoothing procedure for points inside the block. Then, a more specialized routine is used for the smoothing of edge points. Finally, the most complex routine is utilized for the smoothing of the vertices.

6.2. Block and face treatment

The most basic routine for the multi-block mesh smoothing is the block routine. The explicit update of a block point directly descends from the 2nd order central, finite-difference discretization. First of all, as a pre-processing step, it is necessary to calculate in the whole domain the so-called "metrics" Gij according to section 5. Then, the explicit update for the point in consideration is calculated for every point in the domain. The block routine provides the explicit update calculation for points located inside the blocks. The block then used as the basis for the other, more specialized routines in charge of providing a smooth solution in the connections between multiple blocks. In the following section the aforementioned inter-block routines are therefore presented.

6.3. Inter-block treatment

The inter-block treatment is the collective treatment of all the points that are located at the edges of the blocks. In figure 2 it is reported an example of 3 or 5 blocks meeting in a so-called singular point. The singular point is represented in red at the centre and consists in a point neighbouring more than two blocks at the same time and they are classified based on the number of concurring blocks. The peculiarity of these points consists in a non-self-evident choice of the stencil for the explicit update. Assuming indeed the discretization scheme presented in section 5, the singular point may have an incomplete stencil (as in the case of the 3-blocks) or be surrounded by more points than required in the stencil itself. Up to the knowledge of the author, there is no reference in literature about the proficient treatment of these points, despite their great importance for the local grid quality.
Similarly to the aforementioned case of the singular points on the edges, there is no reference in literature for the proficient treatment of the vertices. Therefore, for the development of the mesh generator object of the current paper a novel approach for the treatment of the 3D singularities has been developed. As an example, the treatment of the aforementioned singular point on the edge will be discussed in more details.

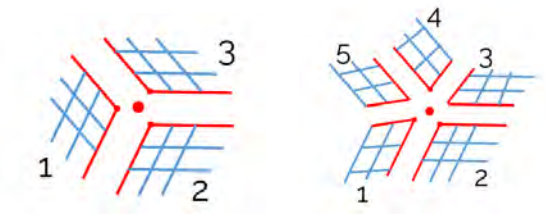

(a) 3 degrees of singularity (b) 5 degrees of singularity

Figure 2: Different degrees of singularity in singular points

The proficient treatment of singular points is based on a specialized regularizing procedure that involves all the neighbouring points around the singular point. Figure 3 represents the points that are involved in the newly-developed regularizing procedure. The procedure is based on the solution of a specialized Partial Differential Equation, applied on the complex stencil represented in figure 3. In particular, a key feature of this novel procedure is the central symmetry of the points involved in the procedure. The proposed procedure allows for the maximum generality: as represented in figure 3b, even non-singular points can be equally treated with the proposed regularization methodology.

The 3D vertex treatment follows a similar procedure with respect to the one presented for the singular points on the edge. For the easiness of representation, the points involved in the vertex regularizing procedure is not represented in the current paper. The treatment of the singular vertices follows the same rationale of the singular points on the edge: specific neighbouring points are considered in a suitably-defined Partial Differential Equation. The treatment of the singular vertices enjoys equally a high quality and general of treatment, as well as the capability to cover even non-singular cases.

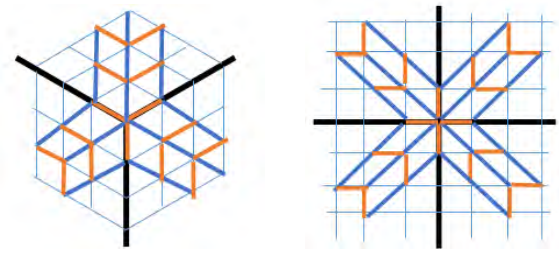

(a) 3 degrees of singularity (b) No singularity

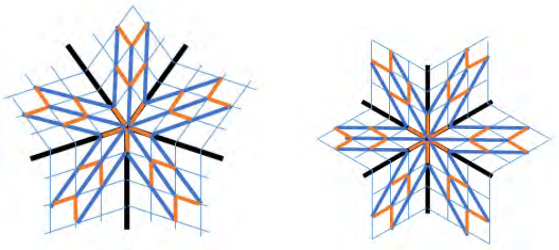

(c) 5 degrees of singularity (d) 6 degrees of singularity

Figure 3: Regularizing procedure in different configurations

7. Results

7.1. Transfinite interpolation

The TFI procedure used to generate the initial grid distribution is presented in figure 4. In figure 4, right, it is represented a 2D test case which features connections between several blocks. The points highlighted in the upper block have been selected in order to show the working principle of the TFI routine, as explained in section 3. It is possible to appreciate from figure 4 that the technique of TFI does not provide automatically a uniform and smooth distribution of grid lines. However, this is not a problem in terms of final mesh quality, since the internal mesh points will be moved by the mesh smoother as presented in the following section.

7.2. Grid smoothing and first cell thickness control

The result after the smoothing procedure for the section presented in figure 4 is presented in figure 5. It is possible to appreciate the higher quality of the mesh after the smoothing.

Additionally, from the closeup presented in 6, right, it is possible to observe the action of the wall refinement technique implemented in the current paper. It is possible to appreciate the clustering of the grid lines in the proximity of the wall.

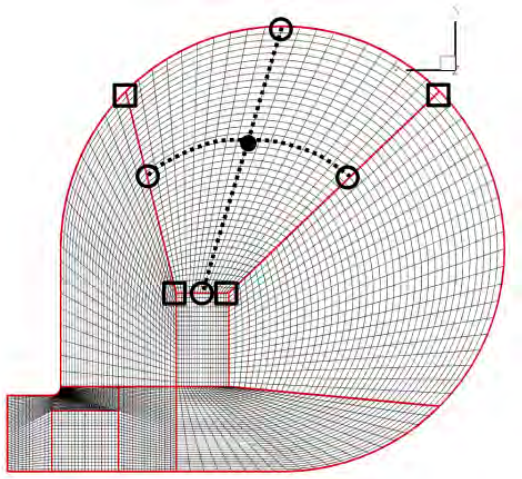

Figure 4: Initial mesh generation via TFI

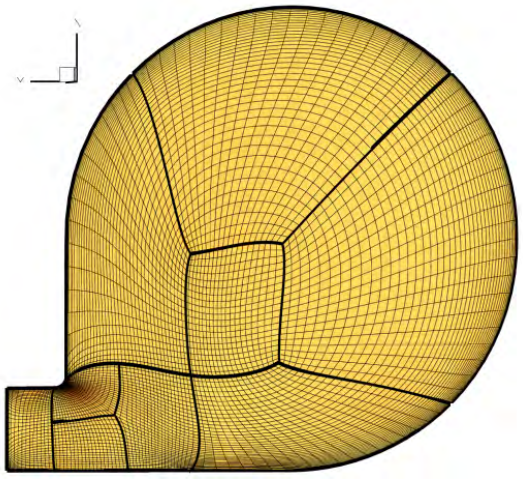

Figure 5: Smoothed mesh

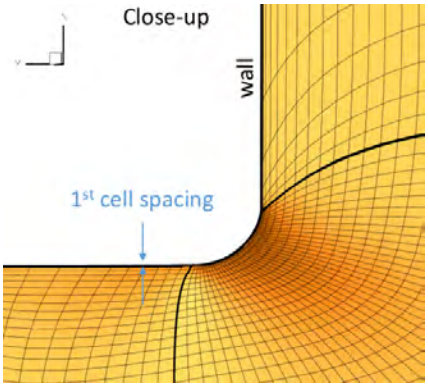

Figure 6: First cell spacing control

7.3. Singular edge treatment

The regularizing procedure presented in section 6.3 is presented in the followings. In figure 7 it is represented a test case with 3 degrees of singularity. For the sake of representation, the third dimension of the computational domain has been omitted, but it nonetheless present in the smoother computation. In figure 7a the result is obtained by direct application of the finite-difference, second-order central stencil presented in section 5. It is possible to observe a certain degree of non uniformity across the singular point, as the cell sizes are different. Additionally, the angle distribution of the cells surrounding the singular point is not optimal. The grid reported on top of figure 7a represents additionally the points interested by the regularization procedure of section 5. In figure 7b the same, 3-degree-of-singularity configuration is obtained by applying the regularizing procedure. The specialized treatment developed in the current paper is able to impose uniform mesh size and optimal angle distribution, counteracting the grid stretching.

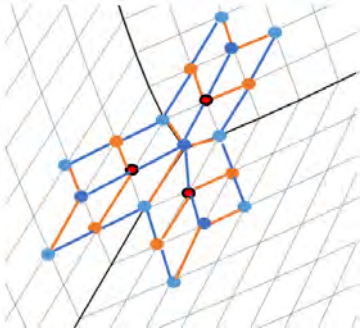

(a) Without regularization

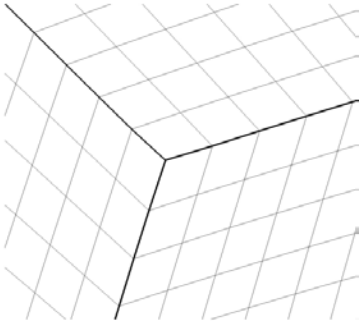

(b) With regularization

Figure 7: Regularization, 3 degrees of singularity

In figure 8 it is represented another test case with 5 degrees of singularity. The mesh size in figure 8b is not regular and, in particular, it is possible to appreciate a certain degree of mesh stretching. In particular, the non-orthogonality and the skewness of the cells is not acceptable. In figure 8b, on the other hand, it is presented the same test case, after the application of the regularizing procedure presented in section 6.3.

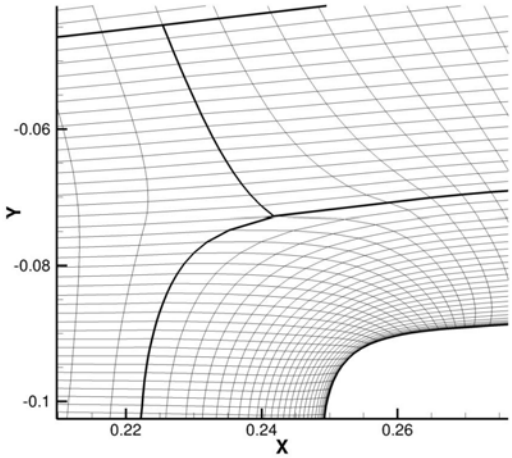

(a) Without regularization

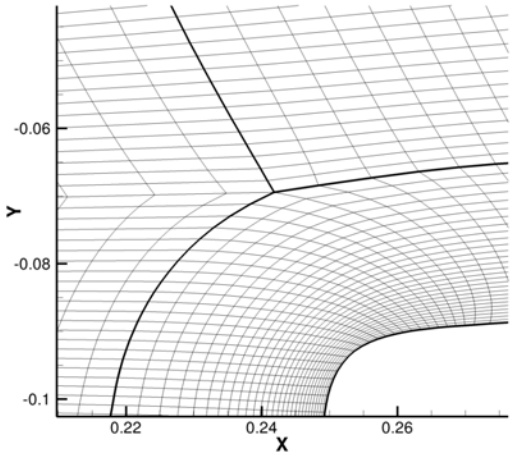

(b) With regularization

Figure 8: Regularization, 5 degrees of singularity

As a result, the specialized treatment developed in the current paper is able to overcome the mesh stretching and ensure a regular configuration in the neighbourhood of the singular point. Additionally, the proposed treatment is general as it can be applied suc-

cessfully to several, different configurations.

7.4. Multi-block configurations

The generality of the methodology presented in section 6.3 is presented in the followings. Figure 9 presents the external skin of a complex, 3D and multiblock test case. It is possible to appreciate the high number of blocks and different topological configurations that are required in order to proficiently tackle such a complex test case. In the current configuration of the mesh smoother, the external skin of the mesh is kept constant throughout the smoothing iterations and, therefore, the initial mesh generated via transfinite interpolation on the external skin corresponds also to the final mesh.
The action of the smoother is presented in figure 10, which presents the smoothed mesh in the internal section of the complex geometry. It is possible to notice two topological configurations in the foreground: a singular point with 3 and 5 degrees of singularity. From the observation of the mesh quality in these points, it is possible to appreciate the uniformity of the grid lines across the blocks meeting at the singular point. The provided example not only shows the generality and the effectiveness of the singular-point treatment, but it also proves the effectiveness of the developed mesh generation procedure for complex, 3D geometries.

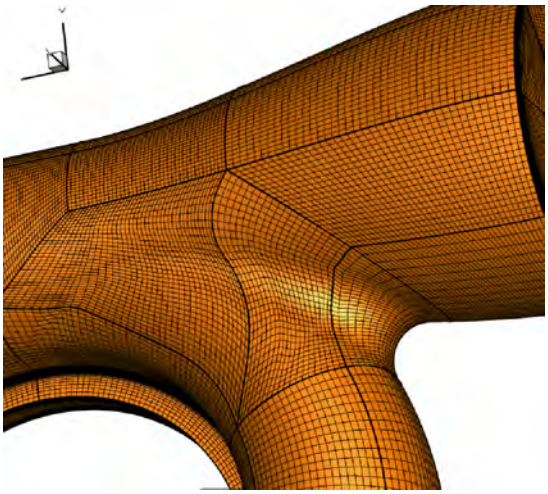

Figure 9: External skin of the complex geometry

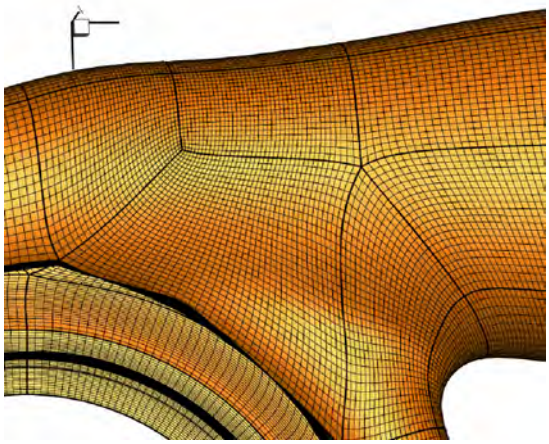

Figure 10: Internal, smoothed isp-surface

8. Future work

Further developments fort the mesh generator include:

- surface mesh generation capabilities, for the smoothing on the external skin of the domain
- acceleration of the solver, implementing a Newton method for the elliptic equations

9. Conclusion

A high quality and versatile mesh generation procedure has been developed, in order to provide the optimization platform CADO with the capability to tackle complex, 3D geometries. A novel procedure for the treatment of singular points has been presented and it shows great enhancements in terms of mesh quality at the interfaces between the blocks. Finally, the procedure has been successfully tested on a complex and multi-block test case, in order to prove the capabilities of the newly-developed, high quality meshing tool.

Acknowledgments

The author wishes to thanks the FNRS foundation for funding the project.

References

[1] F. Flager, J. Haymaker, A comparison of multidisciplinary design, analysis and optimization processes in the building construction and aerospace industries, Tech. rep.
URL `www.arup.com`

[2] L. Mueller, T. Verstraete, Adjoint-based multi-point and multi-objective optimization of a turbocharger radial turbine, in: 13th European Turbomachinery Conference on Turbomachinery Fluid Dynamics and Thermodynamics, ETC 2019, European Turbomachinery Society, 2019.
[3] T. Verstraete, L. Müller, J. D. Müller, Adjoint based design optimisation of an internal cooling channel u-bend for minimized pressure losses, in: 12th European Conference on Turbomachinery Fluid Dynamics and Thermodynamics, ETC 2017, KTH Royal Institute of Technology, 2017.
[4] W. J. Gordon, Transfinite Element Methods: Blending-Function Interpolation over Arbitrary Curved Element Domains, Numer. Math 21, 109-129.
[5] L. E. Eriksson, Generation of boundary-conforming grids around wing-body configurations using transfinite interpolation, AIAA Journal 20 (10) (1982) 1313–1320. doi:10.2514/3.7980.
[6] R. L. Sorenson, A Computer Program to Generate Two-Dimensional Grids About Airfoils and Other Shapes by the Use of Poisson's Equation, NASA Technical Memorandum 81198 (1980) 63.
[7] J. L. Steger, R. L. Sorenson, Automatic mesh-point clustering near a boundary in grid generation with elliptic partial differential equations, Journal of Computational Physics 33 (3) (1979) 405–410. doi:10.1016/0021-9991(79)90165-7.

Real-time optimization of bio-inspired wings using the deformable overset method and machine learning

Romain Poletti

Environmental and Applied Fluid Dynamics, von Karman Institute for Fluid Dynamics, Belgium, romain.poletti@vki.ac.be

Supervisor: Joris Degroote

Professor, Electromechanical, Systems and Metal Engineering Department, Ghent University, Belgium, Joris.Degroote@UGent.be

Supervisor: Jeroen van Beeck

Dean of Faculty, Environmental and Applied Fluid Dynamics Department, von Karman Institute for Fluid Dynamics, Belgium, vanbeeck@vki.ac.be

Supervisor: Miguel Mendez

Assistant Professor, Environmental and Applied Fluid Dynamics Department, von Karman Institute for Fluid Dynamics, Belgium, mendez@vki.ac.be

Supervisor: Lilla Koloszár

Research engineer, Environmental and Applied Fluid Dynamics Department, von Karman Institute for Fluid Dynamics, Belgium, lilla.koloszar@vki.ac.be

Abstract

Million years of evolution have shaped and optimized the outstanding flight capabilities of natural flyers. Birds and insects stably hover, catch preys in the blink of an eye and glide for hours continuously morphing their wings as a function of the flight requirements. Their unique features have inspired engineers throughout the centuries, and Flapping Wings Micro Air Vehicles (FWMAVs) are one of the latest examples. Hand-sized flapping drones require high maneuverability and are valuable for demanding tasks such as rescues in confined environments. Nevertheless, state-of-the-art FWMAVs are still far from extracting nature's full potential. A complete understanding and modeling of flapping aerodynamics, characterized by highly unsteady flows at low-Reynolds numbers, is missing and hinders the optimization of flapping flight.

This PhD thesis proposes a comprehensive numerical environment to learn from real birds and teach bio-inspired drones. Inspiration will be drawn from hummingbirds with a sound parametrization of the wing kinematic. The flapping motions will be evaluated and optimized leveraging on three interconnected disciplines.

First, a surrogate model of the wing aerodynamics will be developed based on fundamental theories, quasi-steady assumptions and calibrated empirical constants. The model will cheaply estimate the aerodynamic performance of given wing motions. The estimations will continuously feed a bio-inspired optimizer relying on reinforcement learning. The optimizer will learn, by trial and error and experience, the best flapping strategies driven by various objectives and constraints in different conditions. One test case will seek to achieve stable hovering in a gusty environment while minimizing energy consumption. Finally, high fidelity CFD simulations will verify and analyze few optimized flapping strategies. The deformable overset mesh technique along with Large Eddy Simulations will accurately reproduce the flow structures generated by flapping and morphing wings.

The multi-fidelity process will allow to learn flapping strategies driven by various optimization criteria (e.g., stability versus energy consumption), understand their key differences in flow field manipulation, and compare their aerodynamic performances with real birds. The proposed methodology aims to progressively close the gap between flapping machines and natural flyers and hence, open new avenues for the next generation of smart drones.

Keywords: Flapping Wings Micro Air Vehicles, unsteady aerodynamics, optimization, reinforcement learning, overset deformable method.

Inlet distortion mitigation through gradient-based optimization

Thanh-Son TRAN

Turbomachinery and Propulsion Department, von Karman Institute for Fluid Dynamics, Belgium, TTran@vki.ac.be

Supervisor: Tom VERSTRAETE

Professor, Turbomachinery and Propulsion Department, von Karman Institute for Fluid Dynamics, Belgium, Tom.Verstraete@vki.ac.be

University Supervisor: Grgory COUSSEMENT

Head of Department, Service Fluides-Machines, UMons, Belgium, Gregory.COUSSEMENT@umons.ac.be

Abstract

Aviation will face the challenges of the next decades given by climate change. The fuel consumption, emission, and noise of airbreathing jet engines can be improved by increasing the bypass ratio, as has been achieved with the recently introduced Geared High Bypass turbofan (GHB) and will be enabled further with the Ultra High Bypass turbofan (UHB), currently in conception. However, increased bypass ratio means as well a shorter nacelle to decrease weight and drag. GHB and UHB engines will face increasingly more distorted inlet flows. These non-uniformities now reach serious levels at the low-pressure compressor (LPC), which will result in loss in performance and operability. Especially the occurrence of flutter, an aero-elastic instability, is mostly feared. This feature represents a major challenge for the conception of LPC, which needs to be able to operate reliably at various conditions with much stronger inlet distortions compared to the past. This research aims at solving the engineering problem arising from the larger levels of inlet distortion on LPC using a multi-physics gradient-based optimization. This will be achieved through three key steps:

1) Development of a novel aero-elastic simulation tool which couples computational fluid dynamics and computational structural mechanics to predict flutter.

2) Development of a multidisciplinary gradient-based optimization framework combining the aerodynamic and structural domains.

3) Performing an aero-elastic optimization to mitigate the impact of inlet distortion on the low-pressure compressor.

The prediction of flutter requires a coupled approach between fluid dynamics and structural mechanics. The challenge and innovation proposed in this work lies in modelling this aspect and additionally computing the sensitivities of such calculations to changes made to the shape of the compressor blading that has so far not been successfully achieved and represents a breakthrough.

Keywords: Inlet Distortion, Optimization, Adjoint Method, Non-linear Harmonic method, Fluid-Structure Coupling

TURBINE AERODYNAMICS AND HEAT TRANSFER

Adaptation of a Transonic Linear Cascade to Investigate Purge and Secondary Flow Effects on the Aerodynamics of High-Speed Low-Pressure Turbines

Gustavo Lopes

Turbomachinery and Propulsion Department, von Karman Institute for Fluid Dynamics, Sint-Genesius-Rode, Belgium, gustavo.lopes@vki.ac.be

Supervisor: Sergio Lavagnoli

Turbomachinery and Propulsion Department, von Karman Institute for Fluid Dynamics, Sint-Genesius-Rode, Belgium, lavagnoli@vki.ac.be

University Supervisor: Koen Hillewaert

Dpartement d'aèrospatiale et mècanique, Universitè de Liège, Liège, Belgium, koen.hillewaert@uliege.be

Abstract

There is a shortage of experimental data to characterize the flow physics and loss mechanisms in high-speed low-pressure turbines at engine-relevant conditions. Linear cascade testing remains paramount in the development of high-performance blade geometries. This paper details the methodology employed to adapt a transonic linear cascade to house quasi-3D flow investigations.

Keywords: High-Speed Low-Pressure Turbine, Transonic Linear Cascade, Purge Flows, Secondary Flows, Unsteady Flows

1. Introduction

The increase in air traffic foreseen in the upcoming years has raised environmental, societal and governmental targets to reduce emissions and noise footprint of civil aircrafts. As presented by the Advisory Council for Aviation Research and Innovation in Europe ([1]ACARE), the [2]Flightpath 2050 initiative suggests a decrease of CO2, NOx and precepted noise by 75%, 90% and 65%, respectively (compared to a 2000 Turbofan engine). The Ultra-High By-Pass Ratio Geared Turbofan (GTF) has been identified as a key architecture with potential to achieve the targets proposed by ACARE. The latter makes use of a gearbox to decouple the fan and low-pressure turbine (LPT) speeds, allowing both to operate at their optimum point. As detailed by Kurzke [1], the geared turbofan becomes a more attractive solution for by-pass ratios higher than 10, enabling reduction of specific fuel consumption (SFC), LPT weight and stage count.

[1]http://www.acare4europe.com

[2]https://ec.europa.eu/transport/sites/transport/files/modes/air/doc/flightpath2050.pdf

The increase in rotational speed of the LPT enabled by the gearbox yields new aeromechanical challenges due to the increase in the centrifugal loads [2] and higher stage pressure ratio [3]. As a result of the latter, the LPT operates at transonic exit Mach numbers ($M_{out} > 0.8$) in combination with low-Reynolds numbers encountered during cruising regime. For these range of operating conditions, there is a lack of open literature on the combined impact of unsteady wakes and purge/leakage flows on the high-speed LPT secondary flow development and losses. Ultimately translating into a lack of experimental data under engine-scaled conditions to drive an informed design of compact and efficient high-speed LPTs.

In order to comprehend the flow physics and loss mechanisms of the three-dimensional (3D) highly unsteady flows encountered in high-speed LPTs, engine-scaled testing must be performed to provide relevant data to mature correlations as well as numerical transition models, and fine-tune direct numerical simulations. Linear cascade testing remains a critical step in the design of LPT blades, allowing researchers to vary different flow parameters of interest indepen-

dently Mach ($M_{out,is}$) and Reynolds numbers ($Re_{out,is}$), wake reduced frequency (St), inlet boundary layer state and thickness, free-stream turbulence intensity ($FSTI$), etc.). Consequently, a wide range of representative flow conditions from take-off to landing are achievable in a linear cascade environment.

Over the last decades, linear cascade testing has been fundamental to understand wake induced transition mechanisms in LPTs and design high-performance blades [4–14]. The majority of these studies were performed on the two-dimensional (2D) region of the cascade flow in low-speed conditions since the transition mechanisms are mainly dominated by Reynolds number effects. Similarly, endwall flows in linear cascade environment were also extensively studied by several authors in an attempt to understand the secondary flow structures and create descriptive models [15–21]. Similarly to the research performed on wake induced transition, the majority of the studies were performed at low-speed conditions. Nonetheless, there are studies performed in high-speed flow where the secondary flow structures identified in low-speed testing are present [22; 23]. Research on purge/leakage flow studies in linear cascade environment is more scarce than for the previous topics. The majority of work is also performed at low-speed conditions [24–26]. On top of this shortage of relevant studies at transonic flow conditions, open literature on the combined interaction of these effects is in short supply. Ciorciari et al. [27] investigated the effects of unsteady wakes on the secondary flows of a high-subsonic linear cascade. The later was performed in a linear cascade with capabilities to recreate unsteady wakes under engine-representative $Re_{out,is}$ and $M_{out,is}$. Apart from this facility, the author is not aware of any facility reported in open literature with capabilities to simultaneously study the interaction of unsteady wakes and purge flows with endwall flows in a transonic environment under low $Re_{out,is}$. The lack of facilities that allow to survey the aerodynamics of future high-speed LPT geometries at engine-relevant conditions reinforces the motivation to develop rigs with capabilities to test the impact of purge/leakage and unsteady flows on the 3D aerodynamics of LPT at engine-relevant conditions.

2. SPLEEN Project

2.1. Description

The current research aims at filling the gap of experimental data and understanding of the flow physics and loss mechanisms in high-speed LPTs and is part of a large EU-funded program named [3]SPLEEN (**S**econdary and Leakage Flow Effects in High-S**P**eed **L**ow-Pr**E**ssur**E** Turbi**N**es) led by the von Karman Institute in collaboration with Safran Aircraft Engines (SAE). The project SPLEEN envisages the adaptation of a transonic linear cascade to study the aerodynamics of high-speed LPT geometries under engine-relevant conditions. The interaction of the purge/leakage and unsteady flows with the cascade 3D aerodynamics will be investigated in the VKI S-1/C large-scale high-speed linear cascade, operating at engine-representative $M_{out,is}$ and $Re_{out,is}$, $FSTI$ and St. The target of the cascade measurements is to use high-resolution instrumentation to characterize the blade, endwall and flow field aerodynamics. The impact of purge/leakage streams on the unsteady LPT blade performance and endwall flows will be measured for various cavity geometries and different leakage/purge flow rates. The output of this project will be an open-access database of high-fidelity measurements under engine-scaled conditions that will contribute to develop and mature numerical transition models, provide boundary conditions and validation data for high-fidelity numerical simulations, and ultimately provide guidelines for the design of future high-speed LPTs.

2.2. Linear Cascade Testing

The need to test engine-representative blade-cavity configurations (Fig. 1-left) in a linear cascade environment requires the discretization of regions of interest within the LPT into 2D profiles (Fig. 1-center). Three airfoil-cavity arrangements will be investigated, representative of the purge flow emerging from the stator-rotor hub cavity and of those purge/leakage flows established between the casing and the tip of a shrouded rotor.

The airfoil-cavity arrangements are combinations of two airfoils geometries and three cavities with the following nomenclature:

I Airfoil 1 (rotor hub) - cavity A (stator-rotor hub cavity): Cavity purge investigation

II Airfoil 2 (rotor tip) - cavity B (shroud tip-casing cavity): Shroud leakage investigation

III Airfoil 1 (stator tip) - cavity C (shroud tip-casing): Shroud purge investigation

[3]https://www.h2020-spleen.eu/

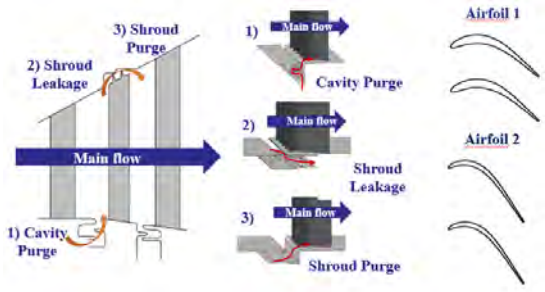

Figure 1: Engine airfoil-cavity arrangements (left), discretized geometries for linear cascade testing (center) and airfoil geometries (right).

The geometries of airfoil 1 and 2 are displayed in Fig. 1-right. The engine-representative operating conditions for the aforementioned airfoil-cavity arrangement are summarized in Table 1.

	I	II	III
$M_{out,is}$ [-]	0.90	0.85	0.90
$Re_{out,is}$ [-]		70k	
St [-]		~1.00	
$FSTI$ [%]		~2.50	
$\dot{m}_{purge}$ [% $\dot{m}_{mainflow}$]		0 ; 0.70 ; 1.40	

Table 1: Operating conditions for airfoil-cavity configurations.

3. The VKI S-1/C Transonic Linear Cascade

The experimental campaign will be performed in the VKI high-speed, low Reynolds facility S-1, showed in Fig. 2.

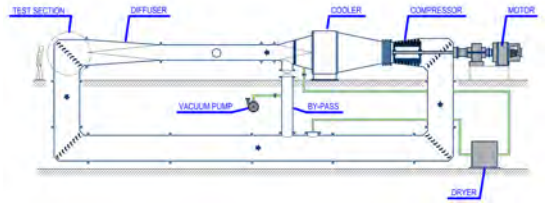

Figure 2: The VKI S-1 high speed, variable density wind tunnel.

This wind tunnel is a continuous closed-circuit facility driven by a 615 kW axial flow compressor. The mass flow is regulated via the adjustment of the compressor rotational speed and via a by-pass valve. The absolute pressure level inside the facility is regulated by means of a vacuum pump. The air inside the facility is maintained dry and at ambient temperature by means of a dryer and cooler, respectively. In order to test linear cascade configurations, one of the elbows of the facility is replaced with a test section capable of housing an array scaled airfoils (see Fig. 3-left). The facility allows to cover a wide range of operating conditions from sea-level take-off to high-altitude cruising at high subsonic and transonic exit flow regimes. The $FSTI$ can be adapted by means of a passive turbulence grid (TG). Lastly, a spoked-wheel type wake generator (WG) allows to recreate unsteady wakes. The latter offers the possibility to match a wide range of reduced frequencies and flow coefficients that can be adjusted by varying the rotational velocity and number of bars. For more in-depth descriptions of the facility in terms of operating ranges, the reader is referred to [28] and [29].

4. Configuration of the Test Section

To extend the VKI S-1/C capabilities to conduct research on endwall flows in a linear cascade arrangement, a thorough revamping of the facility was required. This involved the translation of one of the test section endwalls to house the purge/leakage flow system. The modification of the endwall gave rise to the introduction of an inlet bell mouth, the design of the purge/leakage flow system and the modification of the WG geometry. The relative location of the components can be seen in Fig. 3-right.

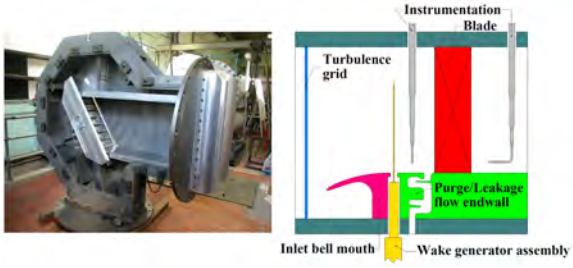

Figure 3: VKI S-1/C test section (left) and constituents to be modified/introduced (right).

The remainder of this work will detail the methodology employed to adapt/design the highlighted components. In addition, the trade-offs that arise due to the dependency between components (see Fig. 4) will be exploited.

4.1. Scaling of Experiments

The scaling of the airfoil-cavity configurations respected geometric, dynamic and kinematic similarity.

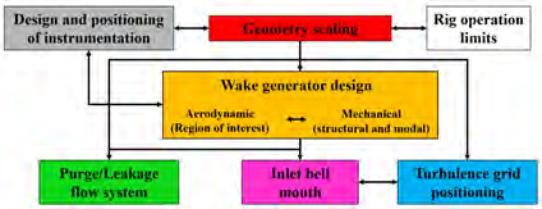

Figure 4: Dependencies between VKI S-1/C components.

The minimum outlet static pressure that ensures a stable and safe operation of the rig is close to 5 kPa. The scaling was maximized based on the desired flow conditions and the latter constraint (which impacts $M_{out,is}$ and $Re_{out,is}$). A maximum scaling factor of 1.60 and 1.46 was found for airfoil 1 and 2, respectively. For the given scaling factors, the cascade geometric characteristics are displayed in Table 2.

	Airfoil 1	**Airfoil 2**
Chord [mm]	52.280	56.600
Axial Chord [mm]	47.610	40.720
Pitch [mm]	32.950	44.620
Inlet Angle [deg]	37.300	18.200
Outlet Angle [deg]	53.800	63.900

Table 2: Airfoil 1 and 2 scaled geometric characteristics.

4.2. Design of Secondary Air Flow System

The need to recreate purge/leakage flows in a linear cascade environment required the design of a secondary air system. The VKI S-1/C operates at subatmospheric pressure levels. The pressure differential between the atmospheric pressure and the operating one can be used to drive flow inside the facility (purge flow for airfoil 1 cases). The mass flow rate can be controlled manually by means of a regulating valve and measured by means of an orifice plate (see Fig. 5-left). In the case of airfoil 2, the pressure drop across the cascade can be used to drive flow from the cascade inlet to the outlet using the same principle (see Fig. 5-right). The selection of the piping system and orifice plates was driven by the standard EN ISO, 5167-2 [30].

The translation of the engine-relevant geometries to a linear cascade setting also required the assessment of the purge flow periodicity and homogeneity. This was investigated by means 3D RANS computations of the cavity alone, using the commercial solver Numeca

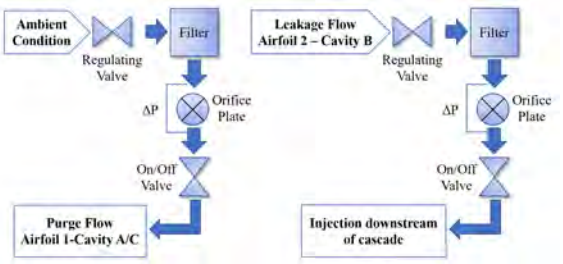

Figure 5: Geometries investigated for the BL control feature (left) velocity profiles (right).

FINE^{TM}/Open. In the case of cavity A (see Fig. 1), the cavity cross-section was extruded for nine blade passages and twelve ports were selected to inject the flow into the bottom of the cavity. The latter acts as a settling chamber for the purge flow. In addition, reinforcing elements were added to increase the structural integrity of the cavity shape. The latter were obtained from a NACA 0024 profile. In order to ensure the purge flow is mixed out prior to his injection in the test section, a buffer plate was introduced in the original cavity geometry. The latter ensures that the injected flow impinges on the buffer plate, aiding the mixing and homogeneity of the cavity flow [31]. The final design of cavity A for the linear cascade measurements is displayed in Fig. 6.

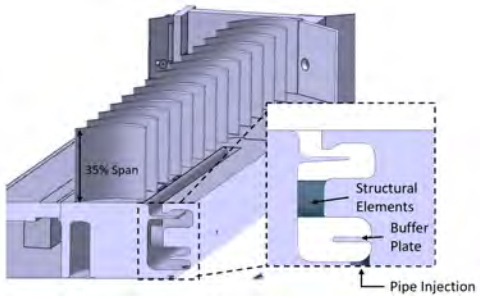

Figure 6: Test section and cavity cassette for purge flow injection.

4.3. Design of Inlet Bell Mouth

The inlet bell mouth is used to ensure a smooth flow transition from the original endwall to the raised one. Three different geometries were investigated with 2D RANS performed by means of Numeca FINE^{TM}/Open: flat plate, contoured lip and contoured lip with lower contoured endwall (see Fig. 7-left). A

[3]https://www.numeca.com/

super-elliptical leading edge [32] was used for all geometries to avoid possible separation on the LE of the profile and reduce the sensitivity to incidence angle.

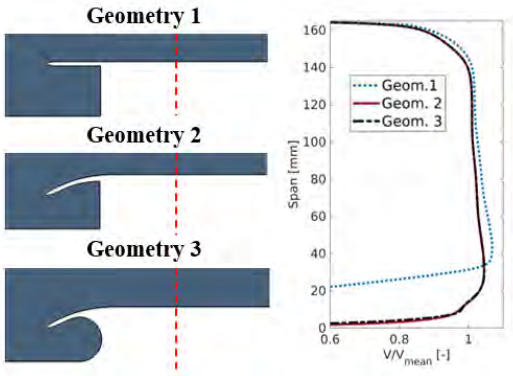

Figure 7: Geometries investigated for the inlet bell mouth (left) and resultant velocity profiles at inlet plane (right).

The velocity profiles were plotted at the cascade inlet (red dashed line in Fig. 7-right). A clear benefit in contouring the lip can be observed in the velocity profile displayed in Fig. 7-right. However, no added benefit was found from contouring the lower endwall. For this reason, the second geometry was selected.

4.4. Control of Free-Stream Turbulence Intensity

The natural FSTI inside the VKI S-1/C is around 0.9% [33]. A passive TG is used to increase the FSTI to desired levels by varying the axial distance to the central blade leading edge (LE). The passive TG present in the rig consists of an array of parallel cylindrical rods (see Fig. 8-left) and is angled relative to the cascade to avoid the introduction of a vertical pressure gradient upstream of the cascade. The grid is characterized by a rod diameter, d, of 3 mm and a mesh size, ms, of 12 mm (see Fig. 8 (right)). The same grid has been used in previous studies conducted in the VKI S-1/C by Michálek et al. [29], where the authors reported that the turbulence decay law proposed by Roach [34] predicted the current grid performance with a good agreement. To assess the suitability of the decay law ($FSTI = A[(x/d)]^n, A = 0.8, n = -5/7$) as a tool to estimate the passive grid position in the scope of the project SPLEEN, a comparison with experimental data from previous studies conducted in the VKI S-1/C was performed. In Fig. 8-right, the correlation of Roach [34] is presented against turbulence data obtained by Monaldi [35] and Paolucci [36]. The cascade inlet Mach number and Reynolds number based on the inlet conditions and bar diameter is reported for completeness.

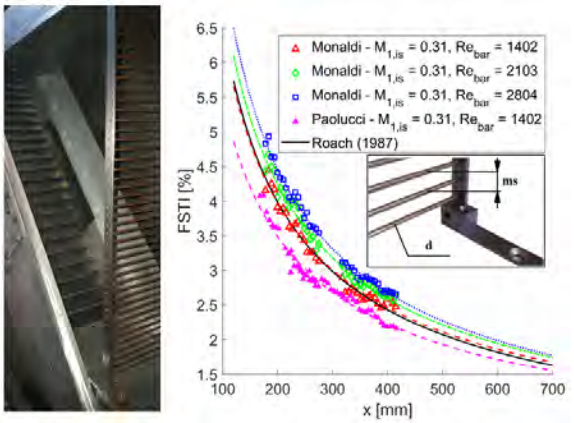

Figure 8: Passive TG present in the VKI S-1/C (left) and comparison between the correlation proposed by Roach [34] and previous experiments (right).

The correlation of Roach [34] and experimental data display good agreement over a wide range of flow conditions. The law was used to compute an axial distance from the central blade LE to the passive grid of 400 mm to match the required FSTI level of 2.5% in the scope of SPLEEN. The variation in FSTI between the two passages adjacent to the central blade in the plane containing the LE of the central blade has been estimated to be 0.19% and 0.15% for airfoil 1 and 2, respectively. Roach [34] also proposed a law for the Taylor and integral length scales. Based on the latter correlations, the Taylor length scale was estimated to be 2.7 mm and 3.6 mm for airfoil 1 and 2, respectively and the integral length scale was estimated to measure 6.72 mm and 6.92 mm for airfoil 1 and 2, respectively.

4.5. Wake Generator Design

The WG present in the VKI S-1/C test section consists of a set of cylindrical bars made of Molybdenum mounted on a brass disk with capability to rotate up to 3500 RPM. The spoked-wheel type WG can be mounted with 96, 48, 32, 24, 16, bars depending on the St and flow coefficient to achieve. A cutaway of the WG with its dimensions and an example of a WG mounted with 96 bars are displayed in Fig. 9. A thorough study detailing the WG capabilities can be found in [37].

The selection of bar length and diameter for SPLEEN are driven by physical, aerodynamic and mechanical constraints. Physically, the diameter should be of the same order of the TE thickness of

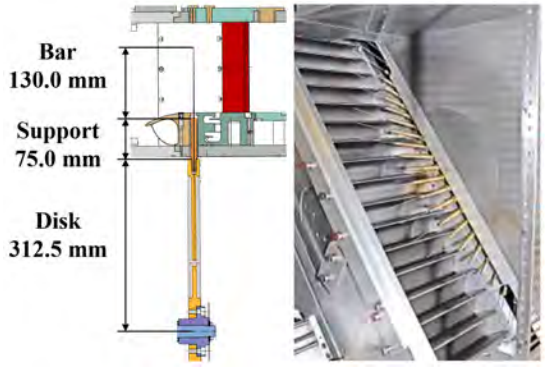

Figure 9: Rotating assembly (disk, support and bar) dimensions in the test section (left) and the position of the WG bars in the VKI S-1/C test section (right).

the scaled blade so its far wake resembles the one of an airfoil [38]. In addition, the bar should be long enough to promote a research region between the endwall flows and bar tip vortex. This region includes the endwall 3D flows and a portion of the cascade 2D flow. The extent of the research region was assessed by performing a RANS analysis to the cascade flow domain with static bars of different lengths. The aerodynamic analysis was performed using the commercial solver $FINE^{TM}/Open$. In addition to the aerodynamic impact, also modal and structural analyses were performed to assess the suitability of the bar geometry. A combination of four bar diameters ($d \in \{0.80, 1.00, 1.50, 2.00\}$ mm) and five lengths ($l \in \{110, 120, 130, 140, 150\}$ mm) were considered. The diameter of 1 mm was selected as it represented the best trade-off between wake similarity and mechanical robustness. As mentioned, the selection of the length was driven by the results of the numerical and modal analyses (see Subsection 4.6). Once a suitable bar geometry was identified based on the previous analyses, a non-linear static analysis was performed to assess the state of stress for that given geometry operating at the expected rotational velocity and flow conditions. Both the modal and structural analyses were performed using the $Code_Aster$ solver embedded in the $Salome - Meca$ platform. Furthermore, it was assumed that the portion of the bar inside the support cannot displace nor vibrate since is constrained. For this reason, both analyses only considered the portion of the bar outside of the bar support.

[3]https://code-aster.org/
[3]https://www.salome-platform.org/

4.6. Modal Analysis

The aim of the modal analysis was to obtain the Campbell diagram of the WG bar for its operation range. The latter is useful to determine critical speeds for which sources of excitation of the rig can interact with the bar natural frequencies and promote resonant behaviour. The sources of excitation identified as capable of energizing the bars are the WG engine harmonics, TG harmonics (upstream of bars) and cascade harmonics (downstream of bars). From these sources, the harmonics can be decomposed as:

- WG motor harmonics $\rightarrow 1N, 2N, 3N, 4N$ *and* $5N$
- TG harmonics $\rightarrow$ $(2\pi \times (diskradius + supportlength + l(i))) \times N / ms$
- Cascade harmonics $\rightarrow$ $(2\pi \times (diskradius + supportlength + l(i))) \times N / cascadepitch$

Where N is the rotational velocity in rad/s and $l(i)$ is the distance along the bar. Three $l(i)$ where considered to compute the harmonics: length associated with bar root, mid-length and bar tip. The Campbell diagrams for all the studied bar lengths and both airfoils were obtained. Only the first eight modes were considered to be energetic enough to excite the bar based on previous experimental campaigns performed in the rig. The critical speeds have been considered with a 5% safety margin. The Campbell diagrams for a bar length of 130 mm are displayed in Fig. 10.

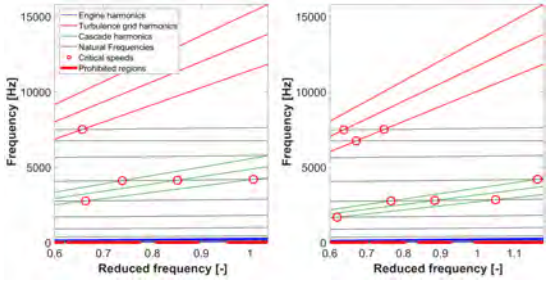

Figure 10: Cambpell diagram for bar length of 130 mm for airfoil 1 (left) and 2 (right).

From the modal analysis, the regions of safe operation for airfoil 1 and 2 in terms of reduced frequency are contained in Table 3.

From the studied geometries, the bar length of 130 mm displayed the best trade-off between length maximization and achievable Strouhal number, in addition to be compatible with both airfoils.

Bar length [mm]	Airfoil 1	Airfoil 2
110	[0.97, 1.02]	[-]
120	[0.93, 0.96]	[0.96, 1.00]
130	[0.90, 0.96]	[0.93, 0.99]
140	[0.93, 0.97]	[-]
150	[0.93, 0.97]	[0.88, 0.94]

Table 3: Range of applicability of Strouhal number for studied bar lengths for airfoil 1 and 2.

4.7. Non-Linear Static Analysis

A non-linear static analysis was performed to assess the state of stress of the bar with length of 130 mm and diameter of 1 mm under centrifugal and aerodynamic loads expected for airfoil 1 and 2. The centrifugal load was imposed by setting the distance from the bar root to the center of rotation as well as the rotational velocity required to match the St (found to be 3209 RPM and 2821 RPM for airfoil 1 and 2, respectively). The aerodynamic load was decomposed into two components: one perpendicular to the WG plane of rotation and one contained in the plane of rotation. In Fig. 11 (left), the decomposition of the aerodynamic loads resulting from the inlet flow velocity and angle is displayed.

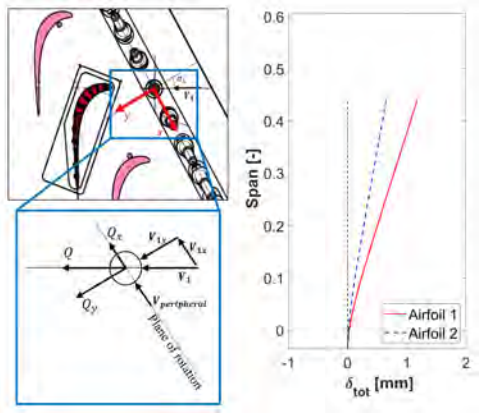

Figure 11: Decomposition of aerodynamic and centrifugal loads (left) and resulting bar total displacement (right).

Based on the imposed boundary conditions, a bar tip deflection of 1.178 mm and 0.653 mm were computed for airfoil 1 and airfoil 2, respectively (see Fig. 11 (right)). The maximum equivalent stresses of 162 MPa and 100 MPa are also found to be satisfactory since they are far below the yield strength of the Molybdenum (450 MPa).

4.8. Effect of Wake Generator on the Incoming Flow

The WG induces time-mean effects on the upcoming flow that must be considered when designing the cascade. The same control volume analysis used by Vera and Hodson [39] and Simoni et al. [40] was employed to quantify the flow deflection and total pressure loss coefficient ($\Delta P_{tot}/0.5\rho V_x^2$) induced by the bars. For the envisaged flow conditions, the effects introduced by the WG at mid-span of the cascade are presented in Table 4.

	Airfoil 1	Airfoil 2
Nominal inlet Angle [deg]	37.30	18.20
WG induced deflection [deg]	3.43	4.63
Pressure drop coefficient [-]	0.25	0.16

Table 4: Effect of WG on time-averaged inlet flow conditions for airfoil 1 and 2.

During the design phase of a new cascade, the latter must be turned by the WG induced deflection in order for the blade to experience nominal flow conditions when testing with a WG.

5. Instrumentation

5.1. Measurement Planes

The test matrix can be categorized into blade (Fig. 12-grey), endwall (Fig. 12-blue) and flow measurements (Fig. 12-red). These measurements are split into different planes as displayed in Fig. 12. Blade and endwall measurements are performed between plane 03 and 04 while flow field measurements are performed in plane 01, 02, 03, 05 and 06.

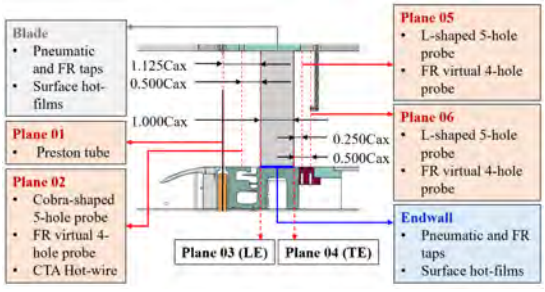

Figure 12: Cutaway of the VKI S-1/C test section with measurement planes and distance between planes normalized by axial chord.

5.2. Sliding Blade Measurements

In order to maximize the spatial resolution in the spanwise direction, the sliding blade mechanism was introduced (see Fig. 13-left). The latter consists of traversing the blade instrumentation, hence accomplishing very high spatial resolution along the span. The blade traversing mechanism was designed so the blade can be translated from the endwall to mid-span. In the scope of SPLEEN, different types of blade measurements are of interest: pneumatic taps, fast-response (FR) transducers and surface mounted hot-films (HF) (see Fig. 13-right).

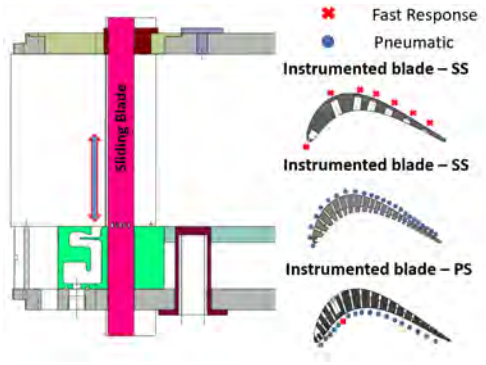

Figure 13: Sliding blade concept (left) and types of instrumented blades (right).

Selecting the location of the blade FR sensors and surface mounted HF was driven by transitional quasi-2D URANS and fully turbulent 3D RANS analyses. The former was conducted conducted with Numeca FINE^{TM}/Open while the later was performed with Numeca FINE^{TM}/Turbo. The pneumatic taps on the PS and SS were maximized to accurately characterize the blade distribution. The tap diameters range from 0.30 mm, close to the TE, to 0.80 mm. A total of 17 and 24 taps were placed on the pressure side (PS) and suction side (SS), respectively. Both the PS and SS are instrumented with commercially available Kulite LQ-062 5 psi that are recessed from the surface. The FR taps have a line diameter of 0.60 mm, while the length varies between 0.43 mm and 0.70 mm. The bandwidth of the line-cavity system was assessed with different models: Bergh and Tjideman [41], Helmholtz and Hougen et al. [42]. For the longest tap, a minimum natural frequency of 36.46 kHz was computed using the Helmholtz model with an end correction [43]. Lastly, in order to maximize the spatial resolution of the surface mounted hot-film sensors, a custom SENFLEX array of sensors was designed in-house and produced by Tao Systems. The copper leads and the gap between leads have a width of 0.60 mm and 0.40 mm, respectively. A total of 21 and 32 sensors along the PS and SS, respectively.

5.3. Endwall Measurements

Similar to the blade, the passage endwalls adjacent to the central blade are also instrumented with pneumatic and FR pressure taps, and surface mounted HF. The pneumatic and FR taps are combined in two inserts: insert 1 above and insert 2 bellow the instrumented blade (see Fig. 14-a). A total of 30(36) pneumatic taps and 6(2) FR taps are present in insert 1(2). The FR taps are mounted with Kulite XCQ-062 5 psi sensors. The two inserts can be seen in see Fig. 14-b. The location of pneumatic taps is selected based on the previously mentioned 3D RANS analysis. FR pressure sensors are mainly located near the leading-edge region. Similar to the design of blade surface mounted HF, the maximization of sensors on the endwall was sought. The flow is assumed to be periodic between the two blade passages adjacent to the central blade, allowing to distribute the sensors between them. As performed by Vera et al. [44], it was attempted to displace the sensors along the passage trajectory. A custom SENFLEX array was designed in-house and manufactured by Tao Systems. A total of 24 sensors per passage were placed. Fig. 14-c displays insert 1 mounted with the custom array.

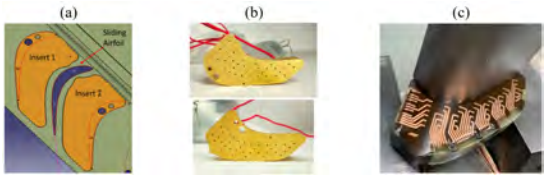

Figure 14: Endwall inserts relative to instrumented blade (a), pneumatic and FR pressure taps inserts 1 and 2 (b) and surface mounted HF insert 2 (c).

5.4. Flow Instrumentation

The highly unsteady and 3D flow field will be characterized by means of time-averaged and time-resolved measurements. A pneumatic cobra-shaped 5-hole (see Fig. 15-a) and virtual 4-hole (see Fig. 15-b) FR probes will be used to characterize inlet flow angles and total pressure. The cobra-shaped probe has a pyramidal-shaped head with 2 mm of diameter. The FR probe was designed with similar geometrical characteristics to the probes used by Lenherr et al. [45] and Pfau et al. [46]. This head shape was preferred to an hemispherical to minimize the line-cavity

system dimensions in addition to head diameter (2.65 mm). Both taps were instrumented with commercially available Kulite LQ-062 5 psi. The resulting tap diameter and distance between ports is 0.35 mm and 3.00 mm, respectively. The previously mentioned dynamic models were used to predict the bandwidth of the line-cavity system for both taps. The Hougen [42] model with end-correction [43] predicted the lowest natural frequency for both line-cavity systems: 27.79 kHz and 28.80 kHz for the lower and upper taps, respectively. The piezo-resistive transducers have a low absolute range (5 psi) that require a facility with capability to vary the density level to perform aerodynamic calibration. For this reason, a twin pneumatic probe head, based on the FR instrumented one, was designed for calibration and validation purposes (see Fig. 15-d).

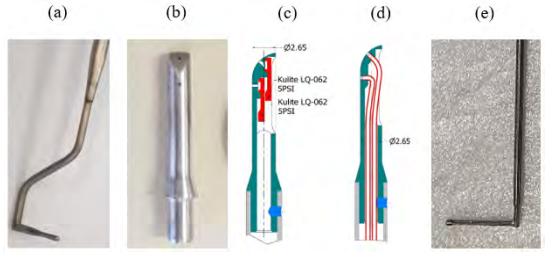

Figure 15: Cobra-shaped 5-hole probe (a), FR virtual 4-hole probe head (b), piezo-resistive sensor arrangement (c), pneumatic arrangement (d), L-shaped 5-hole probe (e).

A flattened Pitot tube, with head height and width of 1 mm and 2 mm, will be used to perform BL measurements. Analogous to the measurements upstream of the cascade, the same FR probe used at the inlet will be used downstream to complement measurements performed by a pneumatic L-shaped 5-hole probe. The latter is characterized by a hemispherical head with a diameter of 2.2 mm. Lastly, constant temperature hot-wire anemometry will be performed upstream to characterize the inlet field of turbulence intensity and flow length scales.

6. Conclusion

The present work details the adaptation of a transonic linear cascade to test high-speed LPTs geometries under engine-relevant conditions. The need to study the impact of purge/leakage flow and unsteady flows on the aerodynamics of transonic blades under low Reynolds numbers, required a thorough revamping of the facility components and instrumentation. The secondary air system for the linear cascade testing should be investigated with numerical methods to ensure flow homogeneity and periodicity. Similarly, CFD can be used to design the inlet bell mouth to promote smooth inlet flow. The preliminary design of the turbulence grid can be guided by an empirical correlation. The importance of designing the wake generator for minimum intrusiveness has been highlighted. The design of the bars should take into account the aerodynamic and mechanical constraints. Ultimately, the bar Cambpell diagram can be obtained to assess safety for the operating point. Aerodynamic wise, the time-averaged flow effects of the WG should also be taken into account when designing a cascade. Lastly, CFD should also inform the design of time-averaged and time-resolved instrumentation used to characterize the blade, endwall and flow field aerodynamics.

References

[1] J. Kurzke, Fundamental differences between conventional and geared turbofans, Vol. 1, 2009. doi:10.1115/GT2009-59745.

[2] M. Giovannini, F. Rubechini, M. Marconcini, A. Arnone, F. Bertini, Analysis of a lpt rotor blade for a geared engine. part i: Aero-mechanical design and validation, Vol. 2B-2016, 2016. doi:10.1115/GT2016-57746.

[3] F. J. Malzacher, J. Gier, F. Lippl, Aerodesign and testing of an aeromechanically highly loaded lp turbine, Journal of Turbomachinery 128. doi:10.1115/1.2172646.

[4] S. Brunner, L. Fottner, H. P. Schiffer, Comparison of two highly loaded low pressure turbine cascades under the influence of wake-induced transition, Vol. 3, 2000. doi:10.1115/2000-GT-0268.

[5] T. Coton, T. Arts, M. Lefebvre, N. Liamis, Unsteady and calming effects investigation on a very high-lift lp turbine blade - part i: Experimental analysis, Journal of Turbomachinery 125. doi:10.1115/1.1556013.

[6] H. P. Hodson, R. J. Howell, The role of transition in high-lift low-pressure turbines for aeroengines (2005). doi:10.1016/j.paerosci.2005.08.001.

[7] H. P. Hodson, R. J. Howell, Bladerow interactions, transition, and high-lift aerofoils in low-pressure turbines, Annual Review of Fluid Mechanics 37. doi:10.1146/annurev.fluid.37.061903.175511.

[8] R. J. Howell, O. N. Ramesh, H. P. Hodson, N. W. Harvey, V. Schulte, High lift and aft-loaded profiles for low-pressure turbines, Journal of Turbomachinery 123. doi:10.1115/1.1350409.

[9] M. T. Schobeiri, K. Pappu, Experimental study on the effect of unsteadiness on boundary layer development on a linear turbine cascade, Experiments in Fluids 23. doi:10.1007/s003480050115.

[10] V. Schulte, H. P. Hodson, Unsteady wake-induced boundary layer transition in high lift lp turbines, Journal of Turbomachinery 120. doi:10.1115/1.2841384.

[11] V. Schulte, H. P. Hodson, Prediction of the becalmed region for lp turbine profile design, Journal of Turbomachinery 120. doi:10.1115/1.2841797.

[12] R. D. Stieger, H. P. Hodson, The unsteady development of a turbulent wake through a downstream low-pressure

turbine blade passage, Journal of Turbomachinery 127. doi:10.1115/1.1811094.
[13] R. J. Volino, Effect of unsteady wakes on boundary layer separation on a very high lift low pressure turbine airfoil, Journal of Turbomachinery 134. doi:10.1115/1.4003232.
[14] X. F. Zhang, M. Vera, H. Hodson, N. Harvey, Separation and transition control on an aft-loaded ultra-high-lift lp turbine blade at low reynolds numbers: Low-speed investigation, Journal of Turbomachinery 128. doi:10.1115/1.2187524.
[15] L. S. Langston, Crossflows in a turbine cascade passage, Journal of Engineering for Gas Turbines and Power 102. doi:10.1115/1.3230352.
[16] C. H. Sieverding, P. V. D. Bosche, The use of coloured smoke to visualize secondary flows in a turbine-blade cascade, Journal of Fluid Mechanics 134. doi:10.1017/S0022112083003237.
[17] O. P. Sharma, T. L. Butler, Predictions of endwall losses and secondary flows in axial flow turbine cascades, Journal of Turbomachinery 109. doi:10.1115/1.3262089.
[18] R. J. Goldstein, H. P. Wang, M. Y. Jabbari, The influence of secondary flows near the endwall and boundary layer disturbance on convective transport from a turbine blade, Journal of Turbomachinery 117. doi:10.1115/1.2836585.
[19] H. P. Wang, S. J. Olson, R. J. Goldstein, E. R. Eckert, Flow visualization in a linear turbine cascade of high performance turbine blades, Journal of Turbomachinery 119. doi:10.1115/1.2841006.
[20] S. Harrison, Secondary loss generation in a linear cascade of high-turning turbine blades, Journal of Turbomachinery 112. doi:10.1115/1.2927702.
[21] J. Moore, R. Y. Adhye, Secondary flows and losses downstream of a turbine cascade, Journal of Engineering for Gas Turbines and Power 107. doi:10.1115/1.3239842.
[22] F. Taremi, S. A. Sjolander, T. J. Praisner, Application of endwall contouring to transonic turbine cascades: Experimental measurements at design conditions, Journal of Turbomachinery 135. doi:10.1115/1.4006565.
[23] F. Taremi, S. A. Sjolander, T. J. Praisner, Measurements of endwall flows in transonic linear turbine cascades: Part ii - high flow turning, Vol. 7, 2010. doi:10.1115/GT2010-22760.
[24] L. M. Wright, S. A. Blake, D. H. Rhee, J. C. Han, Effect of upstream wake with vortex on turbine blade platform film cooling with simulated stator-rotor purge flow, Journal of Turbomachinery 131. doi:10.1115/1.2952365.
[25] I. Popovc, H. P. Hodson, Aerothermal impact of the interaction between hub leakage and mainstream flows in highly-loaded high pressure turbine blades, Journal of Turbomachinery 135. doi:10.1115/1.4023621.
[26] G. Barigozzi, G. Franchini, A. Perdichizzi, M. Maritano, R. Abram, Purge flow and interface gap geometry influence on the aero-thermal performance of a rotor blade cascade, International Journal of Heat and Fluid Flow 44. doi:10.1016/j.ijheatfluidflow.2013.08.012.
[27] R. Ciorciari, I. Kirik, R. Niehuis, Effects of unsteady wakes on the secondary flows in the linear t106 turbine cascade, Journal of Turbomachinery 136. doi:10.1115/1.4027374.
[28] J. Clinckemaillie, L. Fattorini, T. Fontani, C. Nuyts, G. Wain, T. Arts, Aerodynamic performance of a very-high-lift low-pressure turbine airfoil (t106c) at low reynolds and high mach number including the effect of incoming periodic wakes, 2015.
[29] J. Michálek, M. Monaldi, T. Arts, Aerodynamic performance of a very high lift low pressure turbine airfoil (t106c) at low reynolds and high mach number with effect of free stream turbulence intensity, Journal of Turbomachinery 134. doi:10.1115/1.4006291.
[30] I. 5167-1, Measurement of fluid flow by means of pressure differential devices inserted in circular cross-section conduits running full part 1: General principles and requirements, International Standard Organisation.
[31] Effect of geometry of the plenum chamber on gas distribution in a fluidized bed, Industrial and Engineering Chemistry Research 48. doi:10.1021/ie9001684.
[32] C. Tropea, A. L. Yarin, Springer handbook of experimental fluid mechanics, Springer Science & Business Media, 2007.
[33] J. Michálek, M. Monaldi, T. Arts, Aerodynamic performance of a very high lift low pressure turbine airfoil (t106c) at low reynolds and high mach number with effect of free stream turbulence intensity, Vol. 7, 2010. doi:10.1115/GT2010-22884.
[34] P. E. Roach, The generation of nearly isotropic turbulence by means of grids, International Journal of Heat and Fluid Flow 8. doi:10.1016/0142-727X(87)90001-4.
[35] M. Monaldi, Aerodynamics of low pressure turbine blades, PR 2008-15, von Karman Institute for Fluid Dynamics (2008).
[36] D. Paolucci, Experimental study of separation and transition on very-high lift low pressure turbine blades at low re and high subsonic conditions, PR 2007-21, von Karman Institute for Fluid Dynamics (2007).
[37] J. Clinckemaillie, T. Arts, Characterization of periodic incoming wakes in a low-pressure turbine cascade test section by means of a fast-response single sensor virtual three-hole probe, International Journal of Turbomachinery, Propulsion and Power 4. doi:10.3390/ijtpp4030026.
[38] H. Pfeil, J. Eifler, Turbulenzverhltnisse hinter rotierenden zylindergittern, Forschung im Ingenieurwesen 42. doi:10.1007/BF02560822.
[39] M. Vera, H. P. Hodson, Low speed vs high speed testing of lp turbine blade-wake interaction, Symposium on Measuring Techniques.
[40] D. Simoni, M. Berrino, M. Ubaldi, P. Zunino, F. Bertini, Off-design performance of a highly loaded low pressure turbine cascade under steady and unsteady incoming flow conditions, Journal of Turbomachinery 137. doi:10.1115/1.4029200.
[41] H. Bergh, H. Tijdeman, Theoretical and experimental results for the dynamic response of pressure measuring systems.
[42] J. Hougen, O. Martin, R. Walsh, et al., Dynamics of pneumatic transmission lines, Control Engineering 10 (9) (1963) 114–117.
[43] E. O. Doebelin, D. N. Manik, Measurement systems: application and design.
[44] M. Vera, E. de la Rosa Blanco, H. Hodson, R. Vazquez, Endwall boundary layer development in an engine representative four-stage low pressure turbine rig, Journal of Turbomachinery 131. doi:10.1115/1.2952382.
[45] C. Lenherr, A. I. Kalfas, R. S. Abhari, High temperature fast response aerodynamic probe, Journal of Engineering for Gas Turbines and Power 133. doi:10.1115/1.4001824.
[46] A. Pfau, J. Schlienger, A. I. Kalfas, R. S. Abhari, Virtual four sensor fast response aerodynamic probe (frap), 2002.

Acknowledgments

The authors gratefully acknowledge funding of the SPLEEN project by the Clean Sky 2 Joint Undertaking under the European Unions Horizon 2020 research and innovation programme under the grant agreement 820883.

PIV Measurement of Rim Seal Flows in a High-Speed Turbine Rig

Mizuki Okada

Turbomachinery and Propulsion Department, von Karman Institute for Fluid Dynamics, Belgium, mizuki.okada@vki.ac.be

Supervisor: Sergio Lavagnoli

Associate Professor, Turbomachinery and Propulsion Department, von Karman Institute for Fluid Dynamics, Belgium, lavagnoli@vki.ac.be

Advisor: Jorge Pinho

Senior Research Engineer, Turbomachinery and Propulsion Department, von Karman Institute for Fluid Dynamics, Belgium, jorge.pinho@vki.ac.be

University Supervisor: Alessandro Parente

Associate Professor, Ecole polytechnique de Bruxelles, Universit libre de Bruxelles, Belgium, Alessandro.Parente@ulb.ac.be

Abstract

This study focuses on the implementation of Particle Image Velocimetry (PIV) technique into a high speed turbine test rig to evaluate the effect of purge flow emerging from the stator-rotor rim seal gap. A high speed short-duration rotating turbine test facility of the von Karman Institute will host new designed high-pressure turbine geometries on which PIV will be performed. Instantaneous spatial data acquisition with low-intrusiveness providing the possibility to analyze the complex three-dimensional flow structures present in turbine stages makes PIV a powerful tool for turbomachinery investigations. Installation of PIV equipment into the high speed turbine rig is challenging due to the packed hardware geometry with multiple design features and the transient operation of the rig itself. In order to get optical access through the turbine casings, endoscopes will be used for both camera sight and laser sheet introduction. The reliable data acquisition in the short-duration facility, in which blow down tests last only 0.3 seconds, is challenging due to reduced number of images, and limited period for in-situation system set up and tuning. The seeding will be carefully designed in order to guarantee the flow traceability and to enhance signal-to-noise ratio. The outcome of this research is not only the generation of experimental databases in a particular turbine stage, but also to provide further practical guidelines for the implementation of PIV into high-speed turbomachineries.

Keywords: PIV, turbine, cavity purge flow, rotation, high speed, short-duration test rig, fluorescent particle

1. Introduction

Recent interests in the development of advanced turbines include both the efficient use of purge flow and the reduction of energy loss attributed to secondary flows across the gas path. Purge flow is a flow emerges from the stator-rotor rim seal gap which is necessary to decouple rotating disk and stationary components (Fig. 1). In general, purge flow is directed from rim seal cavity to main flow path in order to prevent injection of hot gas into turbine disk cavity. The geometry of rim seal cavity and quantity of purge flow need to be carefully designed because interaction of purge flow and mainstream generates aerodynamics loss.

Computational Fluid Dynamics (CFD) is cost-efficient approach to predict behavior of fluid, but in the case of turbomachinery flows with complex geometry such as rim seal cavity, the prediction accuracy is still needs improvement to be used with confidence. Physical probe measurement such as multiple hole probe, hot-wire probe are widely used to provide reliable experimental database, but their measurements are spatially discretized and intrusive

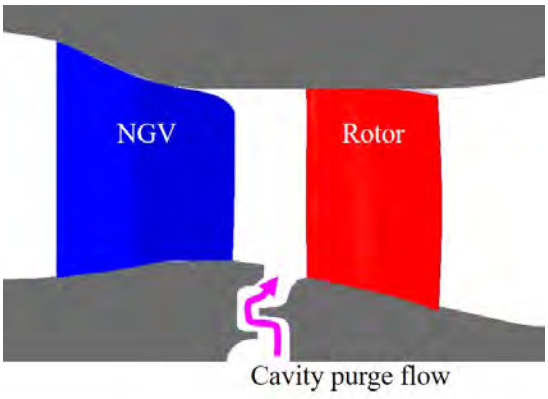

Figure 1: Turbine stage and cavity purge flow.

due to its finite geometry. Particle Image Velocimetry (PIV) can be used as low-intrusive spatial measurement technique. For turbomachinery investigations, instantaneous spatial data acquisition with low-intrusiveness provides great possibility to analyze the complex three-dimensional flow structures. Since PIV was invented in 80s [1], the technique has been developed by numerous researchers and implemented into various applications. For low/subsonic flow (vane exit Mach < 0.8), many authors presented successful implementation in both fixed linear cascade [2], [3], [4], and rotating cascade [5], [6], [7] facilities. In high speed turbomachinery (vane exit Mach > 0.8), there are less literature applied PIV measurements, and mostly they are in fixed cascade facilities [8] [9] [10]. Among rotating turbine rigs, PIV measurements has been performed in continuously running transonic test turbine facility in Graz university of Technology [11], [12] and transient transonic blow-down turbine rig in MIT [13]. Nevertheless, the available open literature is very scarce about PIV measurements of unsteady flow structures related to purge flow rates, rim seal and cavity geometries in high speed turbine wind tunnels.

The fundamental of PIV is to retrieve flow velocity from movement of particles seeded in flow. In modern digital PIV, movement of particles is calculated by displacement of particles recorded by two consecutive photo images with set separation time. In those images, position of particles at each time is frozen by short-period light sheet illumination. For 2D-PIV, the ideal orientation of optical system is to maintain light sheet perpendicular to optical axis of a camera [14]. That means, the application needs at least two optical accesses (for camera and laser sheet) to perform PIV. This requirement makes implementation of PIV into turbomachinery challenging due to packed hardware geometry with multiple design features. Besides, the image will suffer from strong light reflection because the components of turbine test rig are often made of metals which reflects illumination light significantly. Furthermore, the large velocity gradient present in high speed turbine flow will require carefully designed seeding method and adapted post-processing algorithm.

In the present study, PIV is going to be applied to a high speed short-duration rotational annular turbine test rig (CT3) in von Karman Institute.The test rig is equipped with a single-stage high pressure turbine (HPT) accompanied by rim seal cavity. The main subject of this paper is the design of custom equipment and evaluation for PIV implementation into CT3.

2. Development of Measurement Technique

2.1. Turbine Test Rig

The facility, high speed short-duration rotational annular turbine rig, operates on the principle of compression tube, and it allows HPT tests at engine representative condition in terms of pressure ratio, Mach number and Reynolds number [15]. Cavity purge flow is supplied from a pressure tank isolated from compression tube. For this particular test campaign, the test rig hosts single-stage HPT consists of 34 vanes and 48 rotors, and testing time is about 300ms.

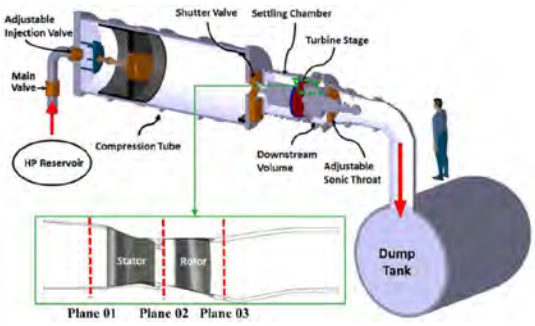

Figure 2: Short-duration compression tube turbine test facility (CT3) [16].

The nominal flow regime which is representative of engine cruise condition was considered for the present test campaign (Table 1). Suffix 01, 02, 03 are indicating the location of measurement locations as shown in Fig. 2. Plane 01 is located at half axial chord upstream of the nozzle guide vane (NGV) leading edge, plane

02 is in between NGV and rotor, and plane 03 is positioned downstream of rotor, approximately 2.5 axial chord downstream of NGV. Endwall pressure taps, mid-span pressure and temperature probes at plane 01 and 03 provide reference measurement values to monitor operating condition.

Table 1: Test conditions of Turbine Rig.

Parameter	Value	Units
P_{01}	$1040 \cdot 10^5$	mbar
T_{01}	436	K
$P_{01}/P_{s3,h}$	2.196	-
$P_{01}/P_{s3,t}$	2.222	-
$\mathrm{Re}_{02,NGV}$	$6.93 \cdot 10^5$	-
Re_{03,C_x}	$2.76 \cdot 10^5$	-
$\mathrm{Mach}_{03,rel}$	0.78	-
N_{rot}	5925	rpm
$\dot{m}_{purge}$	1.74% of $\dot{m}_{total}$	-



Figure 3: Rrainbow rotor setup (CT3).

Considering 100 images are used to obtain averaged flow field at each test (300ms testing time), the PIV acquisition frequency needs to be higher than 333Hz, which is much higher than standard PIV system (15Hz acquisition frequency). Furthermore, in present test campaign, various rotor profiles are tested simultaneously by adopting a "rainbow rotor" setup in order to minimize the test-to-test discrepancies caused by any variability in the operating conditions. The rotating cascade is divided into six different blade geometry sectors. Each sector consists of 8 blades of same geometry in order to ensure flow periodicity. The rainbow rotor strategy also saves the costs of the test campaign and highly time efficient, but at the same time it requires high frequency data acquisition. The sector passing frequency is about 700Hz at nominal test condition. Assuming at least 100 datasets at each sector at each test are required to obtain reasonable averaged flow data, the required acquisition rate for PIV measurement is estimated as:

$$f_{PIV} = \frac{100[datasets] \cdot 6[sectors]}{0.3[s]} = 2000[Hz] \quad (1)$$

In order to satisfy this requirement, a high speed laser system: Quantronix Darwin-Duo Nd:YLF Laser (Maximum double-pulses repetition frequency: 10kHz) and a high speed camera: Dantec Speedsense2012 (maximum flame rate: 22.5kfps @full resolution) are employed for PIV system. The laser pulse energy decreases as the repetition rate increases after exceeding 1kHz, therefore fully time resolved PIV in which data acquisition must be higher than blade passing frequency (5925[RPM]/60[s]×48[blades]=4.8kHz) is considered to be optional in present study.

2.2. Test Section and Optical Setup

The region of interest is set at intermediate flow passage between stator vanes and rotor blades where the rim seal cavity separates stationary parts and rotational parts. Fig. 4 shows the overview of the test section and accesses available for PIV measurement. The test section is covered by two layers of metallic casings, called internal and external casings. Moreover, the internal casings are divided into two part between stator and rotor side. Due to this complex geometry and mechanical features for the assembly such as threaded holes and pockets, the space that optical window can be installed is restricted, it only covers region of rotor blades and its vicinity. In addition, it was revealed that illumination of the area seen through optical widow is difficult due to limited accesses from both upstream and downstream. In order to fully investigate the flow interaction of mainstream and cavity purge flow, two measurement configurations, tangential and meridional 2D-PIV are planned as shown in Fig. 5.

In order to allow access for a light sheet to the intermediate flow passage, a laser sheet endoscope of 8mm diameter (Fig. 6 and a windowed NGV (Fig. 8) were designed and built. The laser sheet endoscope consists of Galilean type beam reducer, focusing lens, sheet forming cylindrical lens, and a prism mirror. The

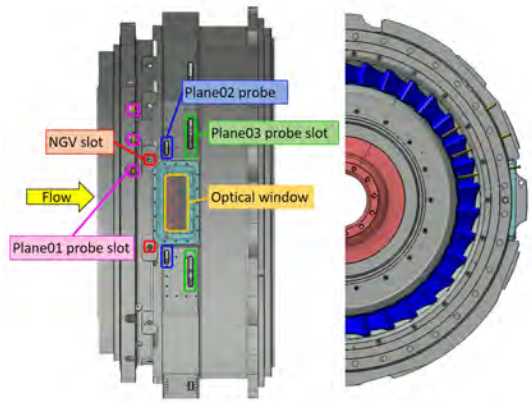

Figure 4: Test section of CT3.

prism mirror can be detached in case straight angle light sheet is desired. A windowed NGV was mainly made of metal, but a part of its suction side was partially replaced with transparent window made of polished Plexiglas window. The outer surface of transparent window matches the original three dimensional shape and inner surface has a constant curvature. The curvature of inner surface was determined by ray tracing simulation so that the light sheet can illuminate image capturing area with minimum light waste. For tangential plane PIV, the endoscope is inserted into the windowed vane through a hole made in external and internal casings. The rotation angle and depth (radial position) are adjusted by rotating probe and changing insertion depth.

For imaging optical access, the casings host an optical window on rotor blade shroud. The curvature of inner surface of the optical window matches shroud surface. This window is fairly large, however, as you can see in (Fig. 4 it was not extended to the area between NGV and rotor due to the complex geometry of entire facility. Therefore, in addition to the optical window, a camera borescope is employed to provide optical access. The advantage of borescope is that it only requires small hole to capture images. The counter part of employing a borescope is that the light transmission is much lower than standard objective lens.

Image calibration is a necessary process for PIV measurement. Especially in this study, it has a great importance because a borescope which has relatively large distortion effect will be used. Once the test rig is closed and optical probes are instrumented, the rig can not be opened. Therefore, positioning a calibration plate and removing it after taking calibration image has to be done through limited access. To allow this procedure, dedicated calibration equipment was designed and built for the application. It consists of calibration plates and supports of the plates. 3D-printed support parts have three dimensional shape so that it can sit on the rotor blade hub. Once 3D-printed support parts are fixed to the rotor blade, calibration plates are attached to the support. calibration plates have CNC-machined 2D profiles so that it can fit in between blade and blade or blade and NGV vane. After taking calibration image, the supports and plates will be taken away through an access on top of the annulus.

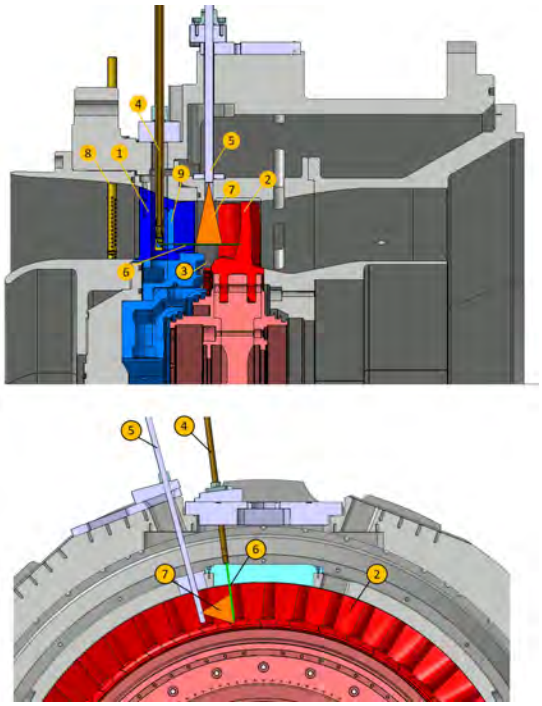

Figure 5: Tangential (top) and Meridional (bottom) PIV configuration. 1.NGV, 2.Rotor, 3.Cavity, 4.Laser endoscope window, 5.Camera borescope, 6.Laser sheet, 7.Field of view, 8.Seeding probe 9.transparent window.

2.3. Seeding

Implementing PIV into high-speed turbomachinery flow raises unique challenges for seeding method. The main challenge is to seed tracer particles satisfactorily in the flow. Besides, particle motion lag with respect to fluid motion must be minimized by the use of the particles that have small size and density. It also brings the difficulties of high-quality image acquisition because smaller particles scatter less light. As a consequence, a ground for compromise must

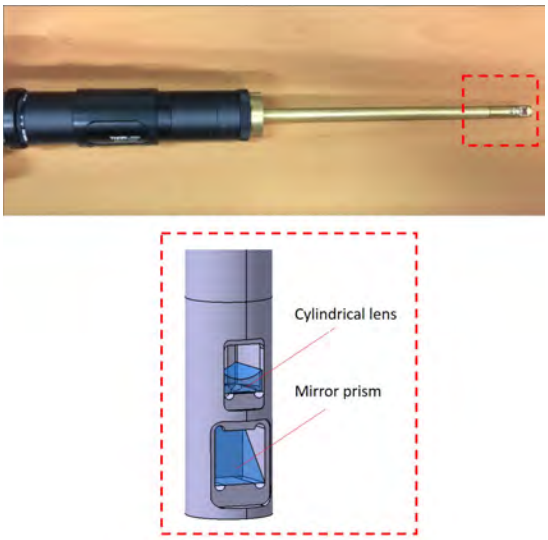

Figure 6: Top: Overview of laser sheet endoscope. Bottom: Detailed view of endoscope tip.

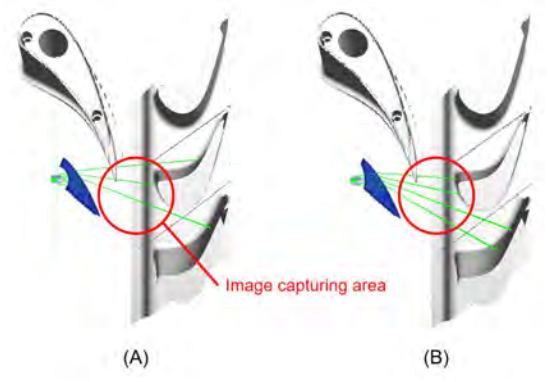

Figure 7: Laser sheet behavior by ray tracing simulation. (A) Inner hole radius: 8mm. (B) Inner hole radius; 19mm.

be found between traceability and light scattering efficiency. Commonly used particle for PIV in high speed turbomachinery is micro scale DEHS oil particles ($d_p = 0.3 - 1.0\ \mu$m) [17], [18]. Seeding probe is inserted through the slots in plane 01 as shown in Fig. 5. Also, purge flow is seeded upstream of cavity. Once particles are discharged in the flow path, they will be accelerated due to the drag force associated with velocity gap between particles and flow medium. The flow and particle are further accelerated while it travels NGV passage, approximately from 50m/s to 300m/s in absolute speed. The path length from plane01 to ROI is briefly estimated around 110mm. As a general rule, added mass and history effects are negligible for motion of particle in a gas flow, thus

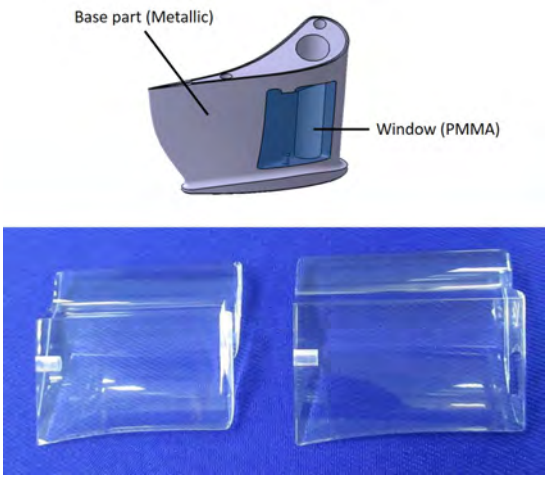

Figure 8: Design of windowed NGV (top) and manufactured transparent window made of PMMA (bottom).

particle trajectory is simply written as [19]:

$$\frac{\pi d_p^3 \rho_p}{6}\frac{du_p}{dt} = -\frac{\pi d_p^2 \rho}{8} C_D (u_p - u)|u_p - u| \tag{2}$$

where u, u_p, ρ, ρ_p are velocity and density of fluid and particle, respectively. Table 2 shows variation of drag coefficient C_D dependent on particle Reynolds number:

$$Re_p = \frac{\rho |u_p - u| d_p}{\mu} \tag{3}$$

Particle Reynolds number is calculated using local particle/fluid velocity and the range is in between 0 and 260.

Table 2: Recommended Drag Correlations: Standard Drag Curve. $w = log_{10} Re_p$ [19]

Range	C_D
$Re_p < 0.01$	$3/16 + 24/Re_p$
$0.01 < Re_p < 20$	$\frac{24}{Re_p}[1 + 0.1315 Re_p^{(0.82-0.05w)}]$
$20 < Re_p < 260$	$\frac{24}{Re_p}[1 + 0.1935 Re_p^{0.6305}]$

Figure. 10 shows particle velocity along with its trajectory. Velocity acceleration of medium (air, black solid line) is represented by 3rd order poly-nominal function. Two different diameter particles are subjected, with 1μm diameter particle (red dot line), the rising time to achieve 95% of medium velocity is less than 0.05mm, which is short enough for present study. Particles are also estimated to follow acceleration of

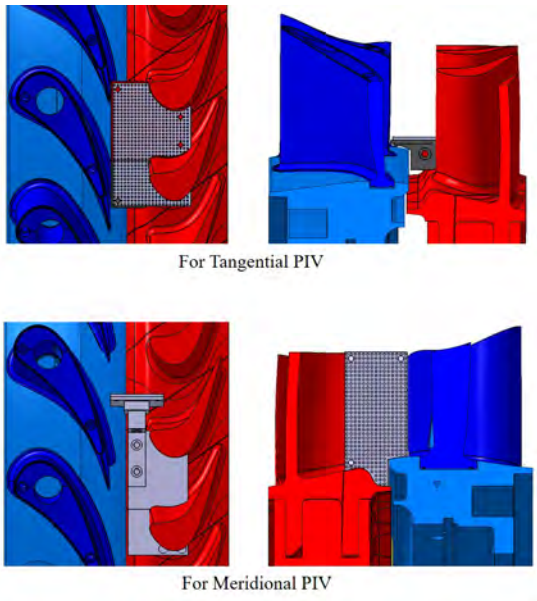

Figure 9: Design of calibration plate.

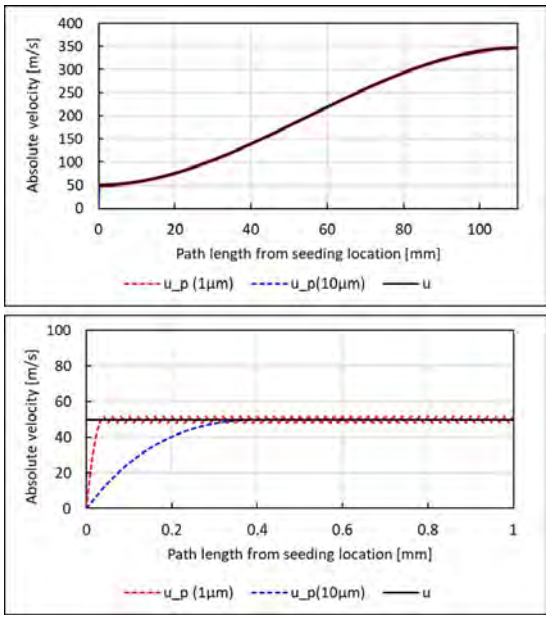

Figure 10: Trajectory of particle motion. Top: Global view. Bottom: Enlarged view at velocity rising period.

medium faithfully while they travel through NGV passage.

The light sheet illuminates not only particles but also other components near the region of interest, such as surfaces of casings, stator vanes, rotor blades, and rim seal cavity. The light reflections on these surfaces, most of the case they are metallic, generates much stronger background noise compared to scattering light from particles. As a result, particles in image becomes difficult to be recognized. The common approach to solve this problem is to paint these surfaces with light absorbing coating such as black paint. However, in the case of rotating annular turbine cascade, this is not favourable because all the rotor blades needs to be painted. Another solution to suppress the back ground illumination is using fluorescent-doped particles. When fluorescent doped particles are illuminated by light sheet, they not only scatter the light at same wavelength of incident light, but also emit light whose wavelength spectrum is shifted relative to the incident light. Thus, by cutting-off the incident light wavelength by optical filter, only fluorescent light, which shows presence of particles, can be acquired.

Thanks to availability of commercial products, fluorescent PIV is often used for liquid flow PIV [20]. However, in gas flow, there are very few studies tried to utilize fluorescent particle. Petrosky[21] performed PIV with Kiton Red 620 (KR620) doped Polystyrene Latex micro-sphere in free jet test facility. It was revealed that fluorescent particle images captured through 560nm long pass filter were 3 orders of magnitude less brighter than unfiltered Mie scattering images, still the velocity field was successfully obtained. In present study, Polystyrene latex microsphere is not ideal particle due to its cost (few hundred euros each gram for commercial product). In large-scale high speed test facility like CT3, large amount of particles are estimated to be consumed. Thus, as it was found to be commonly used, we plan to use DEHS as particle base. As fluorescent dyes, Rohodamine6G (R6G), Pyrromethene567 (P567), Pyrromethene597 (P597) were selected as candidates thanks to their adequate excitation wavelength range for Nd:YLF laser (527nm) and easy availability. Among three dye candidates, R6G is the only one which does not dissolve in DEHS. To dissolve R6G in DEHS, first it needs to be dissolved in Ethanol, then the solvent of Ethanol and R6G are dissolved in DEHS. After a couple of preliminary tests, P567 was chosen considering its fluorescent emission intensity and easiness of solvent preparation.

3. Preliminary Test

3.1. Mock-up chamber for preliminary test

In order to check the installation of all instruments for PIV measurements and to perform preliminary test in the same geometry, mock-up of the test section is designed and manufactured as shown in Fig. 11. The geometrical parts was 3D printed. Prior to test campaign in CT3 facility, the PIV tests was performed in this mock-up model to find any issue related to installation.

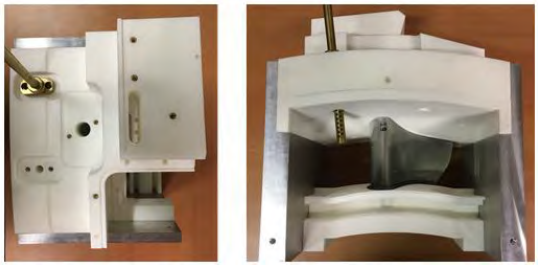

Figure 11: Mock-up chamber for preliminary test.

3.2. Reflection and background noise

Fig. 12 shows the images of test section in a mock-up chamber illuminated by a laser sheet aligned to tangential plane from upstream direction. Nikkor macro lens (f = 60mm) was attached to the camera for objective lens and subject distance was set to about 0.25m. The image was taken with and without notch-filter which cut-off light of $532+-10$nm wavelength. Without notch filter, strong reflection on the blade surface where pixels are saturated was observed. Moreover, the rotor hub and other surfaces of blades were also visible due to multiple reflections, which will significantly deteriorate particle image quality. Thus, some sort of method to eliminate strong reflection from particle image is necessary to perform PIV in this turbine test rig.



Figure 12: Comparison of background illumination noise. Left: WO filter. Right:W notch-filter

3.3. Fluorescent-PIV

Fluorescent-PIV image acquisition test was performed in mock-up chamber to investigate feasibility of fluorescent-PIV and dependency of fluorescent emission intensity on dye concentration. Initially, conventional spectroscopy measurement [22] was conducted to acquire fluorescent emission spectrum. However, considering the solvent (P567 dissolved in DEHS) is atomized, inner filter effect among dispersed particles was expected to be completely different from the one in liquid state specimen. Therefore, other method to find the optimum concentration of dye as a small particle needed to be conducted. As an alternative measurement, PIV tests with particles of solvent with different dye concentration were performed. The particles were generated by a single-action externally-mixing airbrush. The use of a seeding generator commonly used for PIV such as Laskin-nozzle type particle generator was avoided because of the large minimum quantity of solvent required to use the device. Four solvents with different dye concentrations ($A < B < C < D$) were tested. At fixed pulse repetition rate, laser pulse intensity was controlled only by input current. For these test cases laser current was set to 15A. Nikon Macro Lens (f = 60mm) equipped with notch filter was used as an objective lens of imaging system. Fig. 13 shows instantaneous particle images of each dye concentration. Image acquisition, hardware synchronization, and post-processing were done using Dantec Dynamic Studio 6.8. High image intensity area appeared on blade surface due to accumulation of particles, but overall the background illumination was well attenuated. In order to improve visibility, intensity scaling window of images A,B and C,D are adjusted separately (A, B: 100 to 1000, C, D: 100 to 3000, linear scaling). Fig. 14 shows histograms of pixel counts (intensity of pixel) of averaged particle images of each dye concentration. Each image used 50 images to obtain an averaged image. The clear difference can be seen between B and C while there no significant difference between A and B, C and D.

There are various method to evaluate the quality of image for particle image velocimetry [14]. Fig. 15 shows the number of valid vector at each interrogation window among 50 datasets at each test case. The vector is taken into account after it passes two step vector validation filters. The first vector filter is Signal-to-Noise ratio (SNR) filter. SNR is defined as quotient of correlation peak and noise level (Root Mean Square of the correlation values). If the SNR is above the specified value, then the calculated displacement is for-

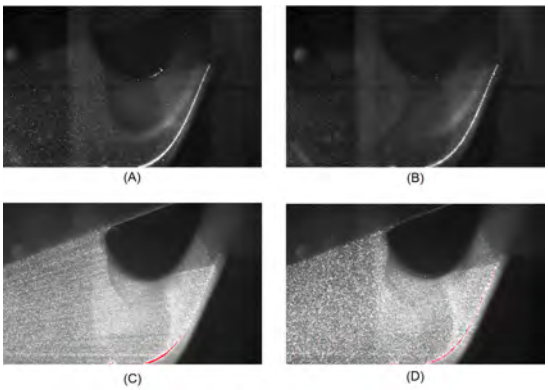

Figure 13: Comparison of particle images with different dye concentration. Dye concentration $(A) < (B) < (C) < (D)$.

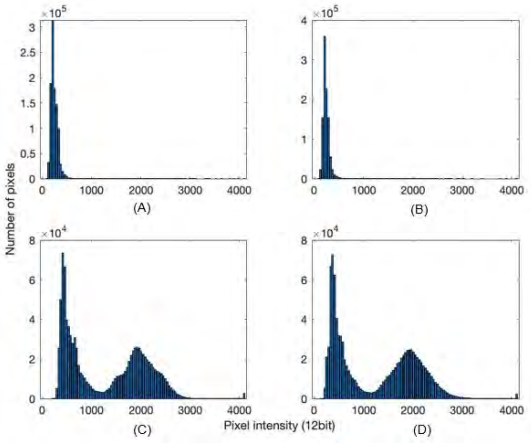

Figure 14: Pixel intensity histograms of instantaneous images. Dye concentration $(A) < (B) < (C) < (D)$.

warded to second filtering. For the results shown in this paper, the threshold of SNR was set to 2.5, which is twice as high as typical values (1.2-1.5) [23], to ensure the validity of correlation. Secondary filtering is normalized median test which compares the subject vector with neighbors [14]. 5×5 neighborhood vectors, minimum normalization factor of 0.10, and acceptance limit of 2.00 are used. The lower number of valid vectors were observed in a part of ROI at dye concentration case of A and B. Those areas correspond to the area where particle concentration is lower due to vortex structure in the mock-up chamber. This results indicate that to capture the flow velocity in the regions of lower particle concentration such as vortex cores, the higher dye concentration is preferable to obtain enough light intensity from limited number of particles.

Fluorescent PIV tests with camera borescope were

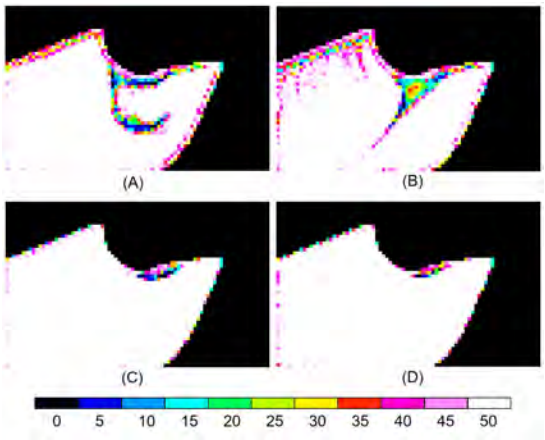

Figure 15: The number of valid vectors at each interrogation windows. Dye concentration $(A) < (B) < (C) < (D)$.

also carried out to examine the image quality through borescope. Due to low light transmission of the borescope, laser current was increased to 30A. Two different dye concentration, C and D were tested. The distance between borescope tip and laser sheet was set so that the size of field of view becomes approximately same as the one taken with macro lens. Fig. 16 shows instantaneous particle images. For better visualization, scaling of pixel intensity is adjusted in both images (0 to 200, linear scaling). Fig. 17 illustrates the histogram of pixel counts in particle images of 50 datasets average for each dye concentration. The pixel intensity dropped drastically compared to the results with Nikkor Macro objective lens, still, the post-processing of image was possible to retrieve velocity field from the images. Particularly with borescope, light intensity decreases significantly in the region distant from the image center. The effect associated with decline of intensity towards image edge is clearly observed in valid vectors counts map as shown in Fig. 18. Overall, the image of higher dye concentration showed better contrast and larger number of valid vector in the region of interest.

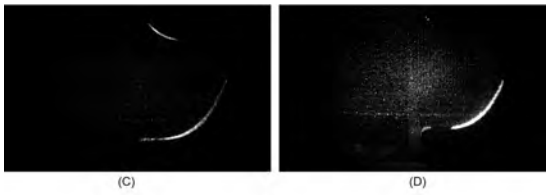

Figure 16: Comparison of particle images with different dye concentration. Images taken with camera borescope. Dye concentration: C, D

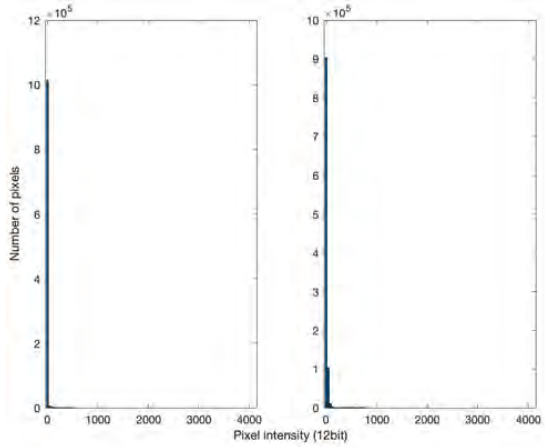

Figure 17: Pixel intensity histograms of an instantaneous images taken with camera borescope.

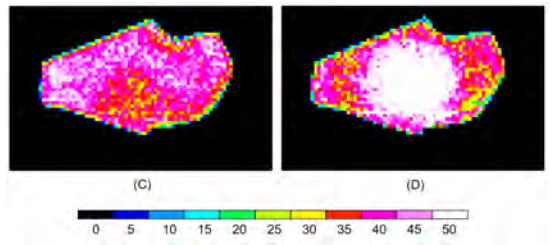

Figure 18: The number of valid vectors at each interrogation windows. Corresponding images were taken with camera borescope.

4. Conclusion

Implementation of PIV measurement technique into high speed short-duration annular turbine test rig was evaluated aiming at obtaining velocity field at intermediate flow passage where cavity purge flow interacts with mainstream. The main challenges were listed as: limited optical access due to complex geometry of facility, selection of tracer particle taking into account its traceability and cost, and strong reflection and background illumination on the metallic components. Dedicated equipment such as a laser endoscope and a windowed NGV were designed and built in order to provide an access for light sheet in the region of interest. Fluorescent particle was prepared in order to eliminate reflection and background illumination. A dependency of particle fluorescent emission on dye concentration was found by performing preliminary fluorescent-PIV test. A borescope was found to cause low light transmission and image distortion, but it still showed capability of image acquisition in which PIV post-processing can be performed and valid velocity fields were retrieved.

Acknowledgments

The support of the Yoshida Scholarship Foundation for execution of this PhD programme is greatly acknowledged.

References

[1] R. Meynart, Mesure de champs de vitesse dcoulements fluides par analyse de suites d'images obtenues par diffusion d'un feuillet lumineux, Ph.D. thesis, Universit Libre de Bruxelles (1983).

[2] J. Woisetschlager, N. Mayrhofer, B. Hampel, H. Lang, W. Sanz, Laser-optical Investigation of Turbine Wake Flow, Experiments in Fluids 34 (2003) 371–378.

[3] R. D. Stieger, D. Hollis, H. P. Hodson, Unsteady Surface Pressures Due to Wake-Induced Transition in a Laminar Separation Bubble on a Low-Pressure Cascade, Journal of Turbomachinery 126 (2004) 544–550.

[4] H. Rehder, A. Dannhauer, Experimental Investigation of Turbine Leakage Flows on the 3D Flow Field and end Wall Heat Transfer, no. ASME Turbo Expo GT2006-90173, 2006.

[5] K. D. Gallier, P. B. Lawless, S. Fleeter, Development of the unsteady flow on a Turbine Rotor Platform Downstream of a Rim Seal, no. ASME Turbo Expo GT2004-53899, 2004.

[6] M. Kegalj, H. Schiffer, Endoscopic PIV Measurement in a Low pressure Turbine Rig, no. 14th Int Symp on Applications of Laser Techniques to Fluid Mechanics, 2008.

[7] L. Porreca, Y. I. Yun, A. I. Kalfas, S. J. Song, R. S. Abhari, Investigation of 3D Unsteady Flows in a Two Stage Shrouded Axial Turbine Using Stereoscopic PIV and FRAP, no. ASME Turbo Expo GT2006-90752, 2006.

[8] P. Bryanston-Cross, C.E. Towers, The Application of Particle Image Veiocimetry (PIV) in a Short-Duration Transonic Annular Turbine Cascade, Journal of Turbomachinery 114 (1992) 504–509.

[9] S. Chemnitz, R. Niehuis, A Comparison of Turbulence Levels From Particle Image Velocimetry and Constant Temperature Anemometry Downstream of a Low-Pressure Turbine Cascade at High-Speed Flow Conditions, Journal of Turbomachinery 142 (2020) 071008.

[10] M. Boerner, On the Challenge of Five-hole-probe Measurements at High Subsonic Mach Numbers in the Wake of Transonic Turbine Cascades, Journal of the Global Power and Propulsion Society 2 (2018) 453–464.

[11] H. Lang, Stereoscopic Particle Image Velocimetry in a Transonic Turbine Stage, Experiments in Fluids 32 (2002) 700–709.

[12] E. Gttlich , J. Woisetschlger , P. Pieringer , B. Hampel , F. Heitmeir, Investigation of Vortex Shedding and Wake-Wake Interaction in a Transonic Turbine Stage Using Laser-Doppler-Velocimetry and Particle-Image-Velocimetry, Journal of Turbomachinery 128 (2006) 178–187.

[13] P. Bryanston-Cross, D.D. Udrea, Whole-Field Visualization and Velocity Measurement of an Instantaneous Transonic Turbine Flow, no. International Congress on Instrumentation in Aerospace Simulation Facilities, 1997.

[14] M. Raffel, Particle Image Velocimetry, Springer, Cham, 2018.

[15] G. Paniagua, C. Diverding, T. Arts, Review of the von Karman Institute Compression Tube Facility for Turbine Design, no. ASME Turbo Expo 2013: Turbine Technical Conference and Exposition, American Society of Mechanical Engineers, 2013.
[16] B. Cernat, On the Aerodynamics and Heat Transfer of a High-speed Turbine with Advanced Rotor Tip Geometries, Ph.D. thesis, Universit catholique de Louvain (2020).
[17] J. Woisetschlger, R. pecnik, E. Gttlich, Experimental and Numerical Flow Visualization in a Transonic Turbine, Journal of Visualization 11 (1) (2008) 95–102.
[18] S. Chemnitz*, R. Niehuis, A Comparison of Turbulence Levels from PIV and CTA Downstream of a Low-Pressure Turbine Cascade at High-speed Flow Conditions, no. ASME Turbo Expo, Phoenix, Arizona, 2019.
[19] R. Clift, Bubbles, Drops, and Particles, Academic Press, New York, 1978.
[20] J. Pinho, Experimental Investigation of Cavitation in a Safety Relief valve using Water. Extension to Cryogenic Fluids, Ph.D. thesis, Universite Libre de Bruxelles (2015).
[21] B. J. Petrosky, Particle Image Velocimetry Applications Using Fluorescent Dye-doped Particles, no. AIAA SciTech, Kissimmee, Florida, 2015.
[22] J. R. Lakowicz, Principles of Fluorescence Spectroscopy, Springer, New York, 2006.
[23] A. Masullo, R. Theunissen, On Dealing with Multiple Correlation Peaks in PIV, Experiments in Fluids 59 (2018) 89.

Experimental Investigation Of The Aerodynamics Of A Single-Stage High-Speed Low-Pressure Turbine

Antonino Federico Maria Torre

Turbomachinery and Propulsion Department, von Karman Institute for Fluid Dynamics, Belgium, antonino.torre@vki.ac.be

Supervisor: Sergio Lavagnoli

Associate Professor,Turbomachinery and Propulsion Department, von Karman Institute for Fluid Dynamics, Belgium, lavagnoli@vki.ac.be

University Supervisor: Koen Hillewaert

Dpartement darospatiale et mcanique, University of Liege, Belgium, koen.hillewaert@uliege.be

Abstract

The High-Speed Low-Pressure Turbine is a key component to enable modern Ultra High By-Pass Ratio Geared TurboFan. VKI undertakes an extensive experimental campaign to investigate in a rotating turbine rig the unsteady interaction of endwall and mainstream flows with purge and leakage flows in modern LPT. This paper introduces the preliminary design selections for the new LPT module testing.

Keywords: High-Speed Low-Pressure Turbine, Annular Rotating Rig, Purge flows, Tip leakage flows, Secondary flows, Unsteady flows

1. Introduction

According to the International Civil Aviation Organization (ICAO) forecast, a 4.2% annual growth of the revenue passenger per kilometer is expected for the next 30 years [1] . The European Commission directives for 2050 Europes vision for Aviation target a 75% reduction in CO2 emissions, 90% reduction of NOx and 65% reduction in perceived noise with respect to the levels of new 2000 aircrafts [2]. Greener and more efficient propulsive units are key factors to meet these objectives. The Ultra High By-Pass Ratio Geared TurboFan (GTF) is one of most promising innovative engine architecture that is leading the transition towards a greener air traffic. Its design incorporates a gearbox that decouples the fan and low-pressure turbine (LPT). The two comonents are now designed to operate at their optimal workspace. Kurzke [3] argues that, for by-pass ratios higher than 10, the GTF enables a substantial reduction of specific fuel consumption (SFC), weights and parts counts, while the turbine high circumferential velocity enables higher turbine efficiency levels. According to Torre et al. [4], the efficiency gains are to be attributed to reduction in profile losses because of higher pitch-to-chord ratios, and reduction of the secondary flows strength due to the lower blade turning characteristic of high-speed LPTs. On the contrary, the increase in rotational speed of the LPT yields new challenges that must be addressed at structural and an aerodynamic design levels. From a mechanical point of view, the increase in rotational speed of the LPT imposes critical aeromechanical constraints due to large centrifugal stresses, Giovannini et al. [5], and increased gas loads due to the higher pressure ratios, Malzacher et al. [6]. While conventional low pressure turbines are already subjected to low Reynolds number, its combination to Mach numbers close to the unity is the most challenging new aerodynamic feature of the new LPT module [6].

Rigorous and extensive testing is of primary importance to develop a detailed understanding of these operating conditions. Linear cascade testing is an attractive option to test in detail the aerodynamics of high aspect-ratio LPT airfoils in a controlled environment. This configuration have been widely used in 2D configuration, focusing on Reynolds number effects, blade-wake interaction and compressibility ef-

fects on the blade profile ([7] [8] [9]), and to assess the quasithree-dimensional (quasi-3D) blade-to-blade flow field. A large body of literature is available on subsonic turbine cascade investigations of end-wall flows rising from the development of boundary layer ([10], [11]) and on cavity purge flows interaction with secondary end-wall and main stream flows [12]. However, linear cascades found limits to reproduce truly periodic boundary blade-to-blade flow through a finite number of airfoils, and to simulate the radial pressure gradient, which effect is significant on secondary flow formation. Annular rotating rigs provide engine-realistic testing environment, multi-row configuration and versatile adaptability for testing at on and off-design conditions ([13]). Typical three-dimensional sources of losses are investigate such as the relevant impact cavity purge flows have on the stage efficiency. Jenny et Al. ([14]) study a 1.5 stage conventional LPT with profiled endwalls contouring at three purge injection rates. The impact of purge flow injection rates show the total-to-total efficiency decrease with increasing injection rate with an efficiency deficit of 1.3% per injected percent of purge flow. Although during the last years, High-Speed LPT have been gaining visibility there is a shortage in experimental data and knowledge of typical flow regimes experienced in the new module. A systematic research approach is needed to investigate in detail the unsteady interaction between purge flows and leakage flows with the mainstream in multi-row environment, representative of modern turbine modules.

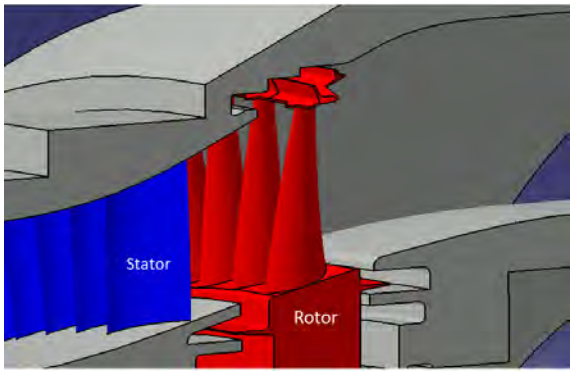

Figure 1: SPLEEN High-Speed Low-Pressure Turbine test section

2. SPLEEEN Project

The current research targets the investigation and understanding of the unsteady aerodynamics of the next-generation high-speed LPTs and is part of a large EU-funded program named SPLEEN (Secondary and Leakage Flow Effects in High-SPeed Low-PrEssurE TurbiNes) led by the von Karman Institute in collaboration with Safran Aircraft Engines (SAE). The project SPLEEN envisages the adaptation of the short-duration rotating turbine test rig of the von Karman Institute to study three-dimensional flows under engine realistic conditions. This facility will be used to conduct an extensive experimental campaign to detail the unsteady interaction between cavity purge, leakage and, secondary flows, as well the underlying loss mechanisms of high-speed LPT geometries. The cavity flow effects and the turbine unsteady 3D aerodynamics will be investigated in the Isentropic Compression Tube Annular Cascade Facility CT-3, operating at engine Mach and Reynolds numbers. The target of the measurements is to use high-resolution instrumentation to characterize the cavities aerodynamics, to quantify the stage loss and the unsteady interactions between the cavity and endwall flows. The impact of purge streams on the LPT rotor row will be measured for various purge flow rates and at off-design conditions. The output of this project will be an open-access database of high-fidelity measurements under that will contribute to develop and mature endwall models, provide boundary conditions and validation data for high-fidelity numerical simulations, and ultimately provide guidelines for the design and development of future high-speed LPTs.

3. Experimental Apparatus

3.1. Turbine Stage

The turbine module incorporates the one-to-one scale geometries of the first stage of the High Speed LP turbine (Fig. 1). Stator vanes ensure the aimed swirling flow and rotor inlet Mach number. The blade design was done to recreate the aerodynamic behavior of an intermediate stage High Speed LPT thus ensuring that the operating conditions meet the research interest. More details about the aerodynamic design of the stage are given in Table 1. The blade airfoil design features area taper form hub to tip, typically enabled to reduce the stress levels in fast spinning blades with high aspect ratios. A light interlocking shroud features the blade with two sealing teeth with a nominal tip clearance of 0.7 mm. Up and Downstream of the rotor, two hub cavities are included to perform purge flow injection, fed by discrete injecting points equally spaced over the annulus. The purge injection will allow investigating the effect of secondary air flows on

Table 1: Summary of rows geometries characteristics and flow quantities at midspan

Parameter	Value
Number of Vanes	96
Number of Blades	96
Vane outlet angle, a2 (deg.)	66.3
Blade relative inlet angle, 2 (deg.)	29.9
Blade relative angle change, (deg.)	94,8
Blade absolute exit angle, a3 (deg.)	-28.8
Vane Axial Chord $C_{ax,V}$ (mm)	32
Blade axial Chord$C_{ax,Bl}$(mm)	30
Vane aspect ratio, AR_V	3.49
Blade aspect ratio, AR_Bl	3.46
Stage Load at rotor inlet, Ψ	1.68
Flow Coefficient at rotor inlet, ϕ	0.59
Degree of reaction, DoR	45%
Specific Work (J/Kg K)	152.03

the LP blade aerodynamics. The operating conditions of the 1-stage LP test turbine can be seen in Table 2 alongside the operating conditions of the engine. As it can be seen all engine operating conditions are virtually matched with the test turbine.

3.2. Turbine Test Rig

The new module of the High-Speed Low Pressure Turbine is tested in the Von Karman Institute compression tube facility CT-3. The cross-section of the CT-3 experimental facility is represented in Fig. 2. This short duration facility can reproduce independently temperature ratios and Reynolds and Mach numbers of the actual engine conditions. The facility consists of two volumes, initially separated by a fast-acting shutter valve. The upstream compression tube contains a free piston while the downstream turbine stage is connected to the dump tank through a variable sonic throat. Prior to the experiments, the initial pressure in the tube is set and the test section (and dump tank) are evacuated to an absolute pressure of about 30 mbar. During the run-up, the rotor is accelerated by means of a small air turbine. Once the rotor nearly reaches its nominal rotational speed, air from the high-pressure reservoirs is injected at the back of the piston, which forces it to slide forward, quasi-isentropically compressing the fluid upstream of the shutter valve. When the target pressure and temperature are achieved inside the tube, the shutter valve opens. This allows the hot gas to be released into the turbine stage towards the dump tank during an actual testing time of about 400-500 ms. The operation cycle is described with further details by Sieverding and Arts [15].

Table 2: Operating Condition: Engine vs Rig

Parameter	Engine	Rig
Mass flow rate, (kg/s)	19.69	10.57
Rotational speed, rpm	7571	4466
Blade Tangential Velocity	288	170
Blade Exit Mach, M3r	0.774	0.776
Reynolds number, Re1	$1.95x10^5$	$2.10x10^5$
$U_m/\sqrt{\gamma RT_{01}}$	0.468	0.474
$\dot{m}\sqrt{RT_{01}}/D^2P_{01}\sqrt{\gamma}$	0.0701	0.0692

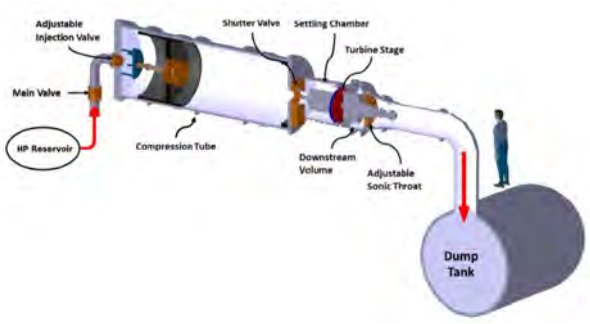

Figure 2: CT-3 compression tube facility overview

3.3. Measurement location and Instrumentation

To ensure a dense measurement matrix and high resolution data in our short duration facility, the test section will be heavily instrumented as represented in Fig. 3. A large number of time-averaged and time-resolved measurements will be taken across the turbine using a variety of stationary and traversable instrumentation. Within the gaspath, three measurement location are distinguished as stage entrance, rotor entrance and rotor outlet. Fixed measurement is envisaged at the two hub and rotor shroud cavities. In this section, every location point is discussed in detail.

3.3.1. Turbine inlet measurements Plane 1

Measurements at the inlet of the turbine are targeted to characterize total inlet flow conditions (total pressure and temperature) as well as the inlet boundary layer thickness, flow angles and turbulence intensity. These measurements will be used to obtain the status of the flow at the inlet to the stage and thus, for providing detailed inlet boundary conditions for accompanying CFD studies. The measurement plane is located approximately 2 axial chords upstream of the

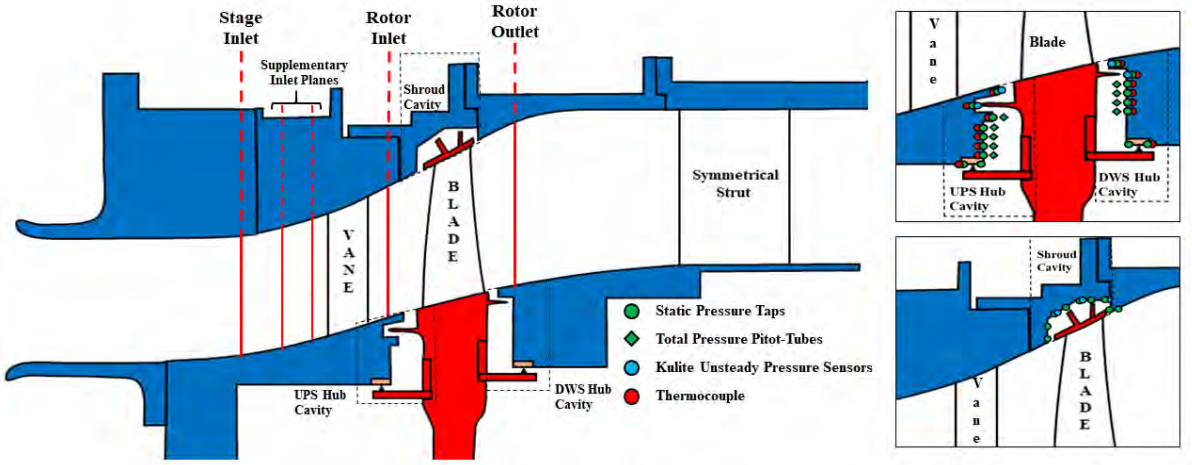

Figure 3: Stage meridional view and measurement planes (Left), Instrumentation on hub (Top-Right) and shroud cavities (Bottom-Right)

vane Leading edge. Only radial traverses are envisaged at this measurement points. The flow periodicity will be assessed by means of static pressure taps equally spaced around the annulus. Turbulence decay will be assessed by supplementary planes located further downstream between Plane 1 and Vane 1 LE.

3.3.2. Stator exit/Rotor inlet measurements Plane 2

Measurements between the stator vanes and rotor blades are primarily used to characterize the flow at the inlet of the rotor and be used as validation for the results of CFD studies in this region. The flow in this region is characterized by high Vane exit mach numbers that, with the reduced space available between Vane TE and Blade LE, makes the measurement in this region risky for the probe mechanical integrity and on the quality of the flow measurements, therefore the axial location of this plane will be set based on safety clearance assessed by structural analysis and numerical CFD investigations.The measurements will be taken traversing a multi-head Kiel probe and a single-head five-hole probe to determine total pressures and flow angles respectively. Continuous traverses will be performed by an actuated mechanism in the pitchwise direction during each blowdown. A refined measurement matrix is also achieved traversing the probe in the radial direction. In addition to the traverses, measurements of time-averaged and time-resolved static pressure will be taken on the hub and shroud endwalls at the same axial location as plane 2.

3.3.3. Stage exit measurements Plane 3

To fully characterize the flow downstream of the blade, measurements at the exit of the stage are to be taken by a numerous type of instrumentation. This region is characterized by unsteady, three-dimensional flow where the complex interactions between the hub and shroud leakage flows and the mainstream flow are not very well understood, posing challenges to the aerodynamic design of the hardware (blades, cavities, endwalls) and resulting in inefficiencies in the engine. The flow-field in this region will be characterized in terms of total pressure, flow-angle and total temperature. All of the above measurements will be made by traversing the probes in both the radial and circumferential directions along plane 3. Further to the measurements in the mainstream flow-path, a large number of measurements will also be taken at stationary endwalls downstream of the blades using pressure taps and unsteady static pressure sensors on the hub and tip endwalls. Higher number of fast-response pressure sensors is envisaged on the hub endwall to capture the higher instability expected at the hub and to relate the higher number of variances given by the test matrix, described later.

3.3.4. Hub upstream and downstream cavity measurements

Measurements in the upstream and downstream hub cavities are used to characterize the flow structure within the cavities and to determine the boundary conditions at the cavity-mainstream interface. Time-averaged and time-resolved static pressure measurements, total pressure and gas temperature at various

Table 3: Experimental campaign test matrix

Operating Conditions	**Configurations**	
	Nominal Tip Clearance	***High Tip Clearance***
Nominal Speed Nominal Purge Nominal Swirl	Test Case 1 Reference Case (All Measurements)	Test Case 2 (Plane 3 Measurements Only)
Nominal Speed Nominal Purge Low Swirl	Test Case 3 (Plane 3 Measurements Only)	-
Nominal Speed High Purge Nominal Swirl	Test Case 4 (Plane 3 Measurements Only)	-
High Speed Nominal Purge Nominal Swirl	Test Case 5 (All Measurements, No Plane 1)	Test Case 6 (Plane 3 Measurements Only)

radial and circumferential locations within the cavities are envisaged. Unsteady static pressure at the civity rim seals will be measured using eight Kulite transducers placed at eight different circumferential location around the wheels-space in order to enable a phase analysis of the unsteady signal and hence the determination of the number of unsteady flow structures that are known to form in these regions. Temperature measurements will be used to investigate the ingress/egress between the mainstream flow path and the cavity and the effectiveness of the rim-seals. Measurements of time-averaged static pressure and temperature will also be taken further inboard (Fig. 3), inside the wheel-space, at various radial locations. The total pressure will be measured using small pitot-tubes positioned at the same radial location as the pressure taps, at 5 mm off the surface of the stator walls. The pair of static and total temperature at each radial location will be used to determine the tangential velocity of the flow and hence the swirl ratio which in turn provides an indication of the flow structure inside the wheel-space. To determine the amount of purge flow leaking through the labyrinth seals and out of the cavities, measurements of static pressure will be taken on either side of the tooth of the upstream and downstream labyrinth seals.

3.3.5. Shroud cavity measurements

Measurements in the shroud cavity are used for characterizing the flow-field within this cavity and for determining the performance of the blade tip seals. Measurements of time-averaged static pressure will be taken at various axial and radial locations along the cavity using, as shown in Fig. 3. Measurements of time-resolved static pressure will be taken using Kulite sensors positioned in the three cavities formed between the lips of the blade tip-seal. At each of these locations two sensors will be used, placed at two different circumferential locations aligning with the vane leading edge and mid-pitch.

3.4. Test Matrix

The measurements mentioned in the preceding sections are to be taken for a number of combinations of operating conditions and geometric variations (referred to as configurations) involving two operating speeds, two purge flow rates and injection angles and two shroud cavity clearance variations. The resulting test matrix is given in Table 3.

Test case 1 represents the reference case. Comparison of the results of test case 1 and test case 2 aims at revealing the effect of the tip clearance variation on the flow-field downstream of the blades, near the tip region, and the subsequent effect on the efficiency of the rotor. Comparison of the results of test cases 1 and 3 aims at shedding light into the effect of hub purge flow swirl on the flow-field upstream of the blades, near the hub region, and on the subsequent effect on the efficiency of the rotor. Comparison of the results of test cases 1 and 4 aims at revealing the effect of hub purge flow increase on the flow-field upstream of the blades, near the hub region, and the on the subsequent effect on the efficiency of the rotor. Comparison of the results of test cases 1 and 5 will reveal the effect of under-speed operating conditions on the flow-field and efficiency or the rotor and lastly, comparison between test cases 5 and 6 will shed light into the effect of tip-clearance variation during under-speed operation of the turbine.

4. Prelinimary Design Of The SPLEEN 1-Stage LPT

To accommodate the flow-path geometry of the SPLEEN 1-stage LPT turbine, it was necessary a redefinition of the available-space region, based on facility hard constraints. The high aspect ratio of the

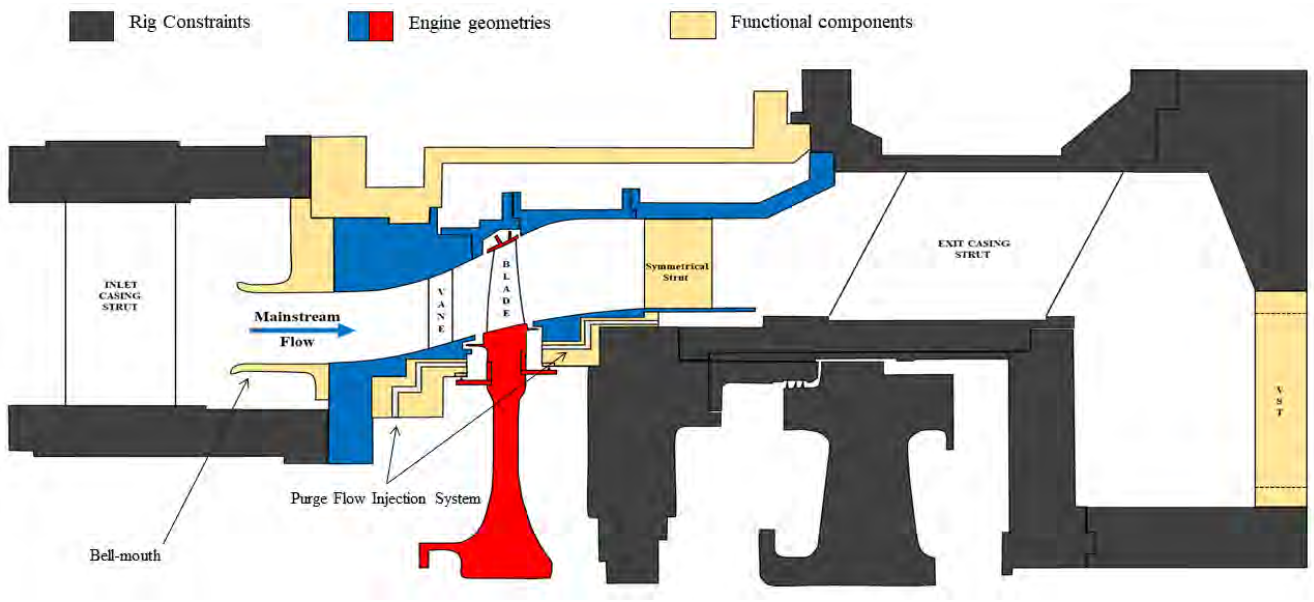

Figure 4: Overview of the preliminary facility redesign

new low pressure module, imposed a redesign of the rotating assembly (disk, lab seals and blades) as well as an extension of the radial geometrical envelop to include the new gaspath. The initial design phase of gaspath and stage was performed through an extensive coordination with the industrial partner Safran Aero Engines to embed the engine geometries within the hard constraint of the facility. An extensive revamping of the fixed facility modules is requested to ensure testing. Figure 4 shows the different modules of the facility underlining in grey the facility hard constraints. In blue and red are reported respectively the static and rotating engine geometries designed by SAE. In yellow the functional and auxiliary components designed by the research team of the Von Karman Isntitute. The latter are:

- Intake bell-mouth designed by means of numerical tools to ensure the smallest boundary layer thickness and to avoid risk of flow separation at the lip leading edge, given the available space envelope;
- Purge flow injection designed by means of 3D annular parametric CFD study intended to select the optimal swirling injecting angle and discrete injection parameters to ensures the target mass flow and velocity ratios (V_t/U) at the two hub cavities.
- The symmetrical exit struts embedded in the gas path, which geometrical characteristics are chosen to ensure the lowest intrusiveness in the upstream stage aerodynamics, serve the purpose to provide access for purge supply lines for the downstream wheel-space and instrumentation lead-out.
- Variable Sonic Throat (VST) - used to regulate the mass flow rate of the mainstream flow passing through the turbine. The maximum available cross-sectional area of the VST currently installed in CT-3 is not sufficient to ensure the high capacity requirements of the SPLEEN 1-stage LPT. A new VST is to be designed featuring openings with a larger area. The design of the new VST is to be aided by a CFD study that aims at validating the new area requirements.

4.1. Bellmouth

The intake assembly consists of the inner and outer intake lips and is used for setting the conditions of the flow at the inlet to the turbine, upstream of vane 1. The section of the intake lips is specifically designed so that the lips together form a bell-mouth inlet that accelerates the flow, keeping the boundary layer thickness within the required value and avoiding flow separation and distortion at the leading edge. A literature survey showed that the best design for the inlet bell-mouth is provided when an elliptical shape

is selected. Tawari et Al. [16] use numerical simulations to compare different intake design: 3-circle profiles, airfoil profiles and elliptical shapes. Both 3-circle and airfoil profiles require steeper inlet contraction to fulfill small inlet boundary layer thickness and to avoid separation, leading to increase the diameter at the entry. Blair and Cahoon [17] report an extensive experimental and numerical investigation of bell-mouth intakes with circular, airfoil-shaped and elliptical profiles, comparing the discharge coefficient of each design. Bell mouth with elliptical shapes show the highest discharge coefficient with the optimum results of ellipses with major-over-minor axis aspect-ratio = 1.8. A modified super elliptical (MSE) splitter plate ensures second derivative continuity on the transition from elliptical to planar shapes, therefore low susceptivity of the boundary layer from freestream flow perturbations ([18], [19], [20]). Planar 2D numerical RANS have been performed to validate the intake bellmouth design of the SPLEEN experimental apparatus, using the commercial software Numeca FINE/Open. Curvature continuity is ensured over the intake bell-mouth elliptical shape and at the junction with the gas path. A total of four different design have been investigated, differing from the elliptical lip aspect-ratio. The bottom lip is constrained by space, therefore a compact design shall be selected. Figure 5 shows an example of numerical 2D domain and the different geometries tested. ‘

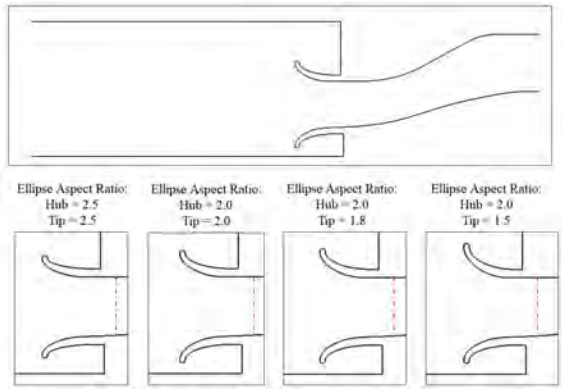

Figure 5: Intake bell-mouth numerical 2D domain (Top) and studied shapes (Bottom). Dash-dot red line indicates the evaluation plane

Fully turbulent numerical simulation have been performed using $k-\omega$ SST turbulence model. Stage Total inlet pressure and temperature, and outlet mass flow were imposed. The selected inlet turbulence intensity of 6% as measured from previous campaigns

Table 4: Boundary layer thickness at measurement plane

	δ_{99} **[mm]**	
Geometry	**Hub**	**Tip**
Symm AR =2.5	3.56	2.78
Symm AR =2.0	2.91	2.78
H AR = 2 — T AR = 1.8	2.91	2.14
H AR = 2 — T AR = 1.5	2.91	2.14

performed in CT-3. The investigation plane is located at the junction between gaspath and bell-mouth lips, indicated by the dash-dot red line in Figure 5. This plane was selected because provides the inlet of the test section. Table 4 reports the boundary layer thickness and shows that higher contraction ensures smaller boundary layer thickness. The selected design the design with symmetric lips at the top and at the bottom with aspect ratio. In this case a similar boundary layer thickness is measured both at the hub and tip lips, still displaying values below 3mm.

4.2. Symmetrical Struts

The main purpose of the symmetrical struts is to allow for access for purge lines and instrumentation cable/tube lead-out. The outlet flow delivered from the test section is swirling compressible flow (α = 30deg. , M = 0.38). The accurate design of the symmetrical strut is performed to reduce the potential flow effects on the upstream stage and instrumentation yet maintaining a simple design for manufacturing purposes. The selected airfoil shape is the NACA0024 selected to guarantee highest thickness and therefore the highest available space for piping and cabling. The airfoils axial chord is equal to 70 mm, maximum length constrained by the available space. A parametric analysis was undertaken to investigate the effect of 12, 18 or 24 struts located around the annulus. The evaluation of the design is performed by means of 2D numerical simulations with translational periodicity in accordance with the struts periodicity. The inlet boundary conditions are summarized in Table 5. Fully turbulent simulations have been performed using the $k-\omega$ turbulence model. The outlet static pressure imposed was selected iteratively to match the flow rate.

Figure 6 shows the static pressure contours of the test case with 24 struts around the annulus. In Figure 7 is reported the static pressure fluctuations along the pitch for the cases with 18 and 24 struts at different axial locations from the upstream Blade TE. An admissible fluctuation of static pressure below 0.1% $P_{0,in}$ (100 Pa) is targeted. 12 struts generate a fluctua-

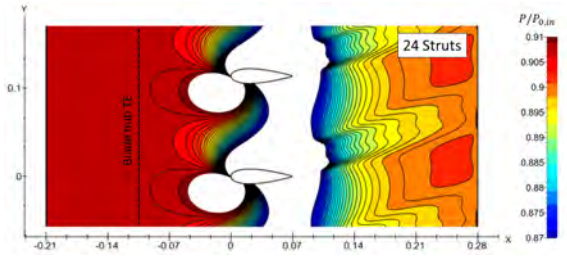

Figure 6: Static pressure contours prediction around the symmetrical strut. Case with 24 struts around the annulus

Table 5: Inlet boundary conditions of CFD simulations on the symmetrical struts aerodynamics

Quantity	Value
$P_{0,in}$ [Pa]	38926.97
$T_{0,in}$ [K]	271.6
Inlet Angle [$\circ$]	30.0
Tu [%]	2.5

tion over 0.1% at the blade TE, representing an unacceptable value and therefore not reported here. Considering the cavity opening and the space required for instrumentation, static pressure variation shall be kept within uncertainty up to at least 1 axial chord downstream the blade TE. This condition is respected when 18 or 24 struts are employed, although with noticeable improvement for 24 struts. In this case the available space can be extended over 1.5 axial chords and therefore represents the safest design. Furthermore, the total pressure losses ($(P_{0,in}$-$P_0)/P_{0,in}$) accounted for this design is of 1.14%, which represent an acceptable increment with respect to he case with 18 struts, accounting for a total pressure loss of 0.93%.

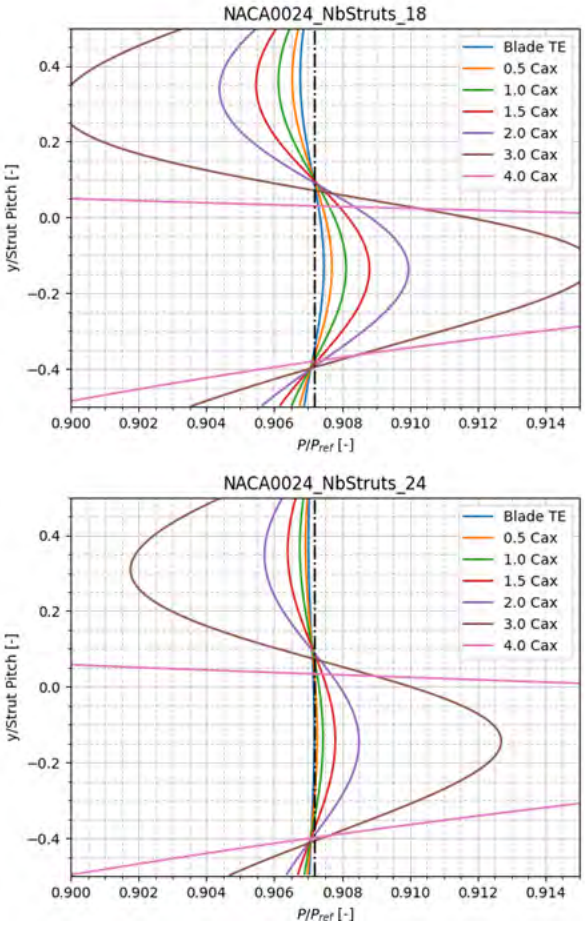

Figure 7: Pitch-wise static pressure variation at different axial position for the blade TE location. Static pressure normalized by the inlet total pressure. Case with 18 (Top) and 24 (Bottom) struts around the annulus

4.3. Variable Sonic Throat

The operative condition of the Variable Sonic Throat (VST) is examined by means of 3D RANS simulations. The study is performed to quantify the admissible mass flow rates flowing through the choked throat to identify the limitations of the facility. Two designs of the VST are investigated:

- Component currently installed in CT3 with maximal admissible cross sectional opening
- New VST design for testing turbines at higher capacities, increasing the cross-sectional opening of 35%.

These two designs have been tested with the inlet swirl angle and inlet total pressure measured downstream of the symmetric exit struts from the analysis described in the previous section. The analysis was run for testing condition with nominal Turbine Reynolds number with a target mass flow through the turbine of 10.57 [kg/s]. Table 6 reports inlet and outlet boundary conditions. The fluid domain includes the exit casing strut (Figure 4) and the variable sonic throat. The turbulence model $k-\omega$ was selected for the fully turbulent simulations. The maximum mass flow rate and discharge coefficient for the two VST designs are reported in Table 7. Both designs ensure the operating condition of the SPLEEN LPT, although the current design show a limited safety margin (< 25%) therefore the design with increased cross-sectional area was selected.

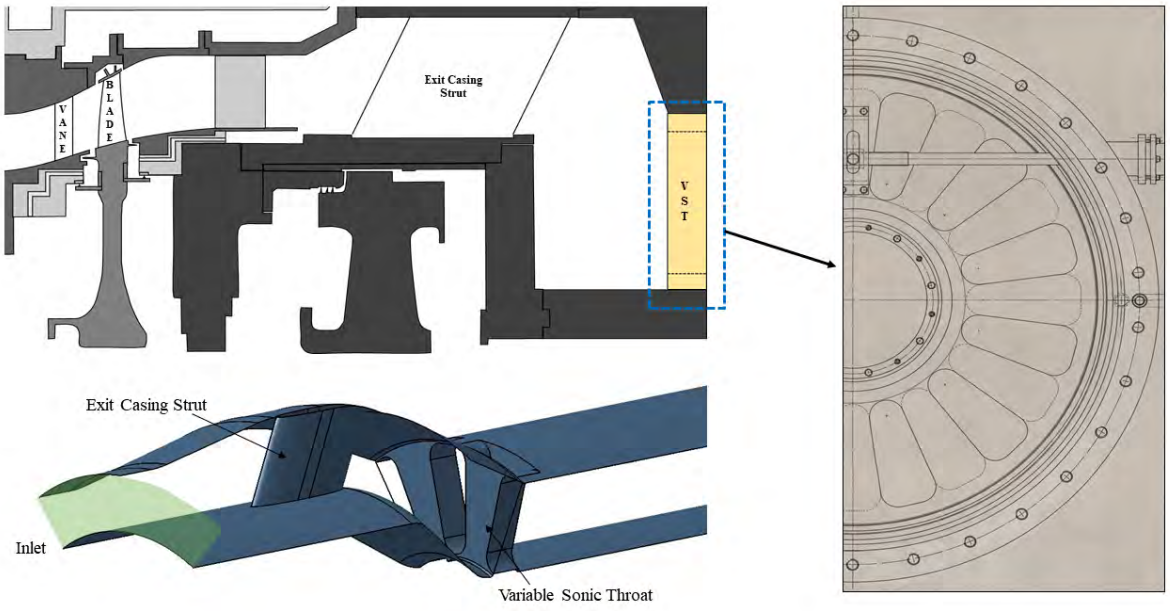

Figure 8: Variable sonic throat sketched in the rig (Top-Left). Current VST Design (Right) and CFD domain (Bottom-Left)

Table 6: VST numerical study - Boundary conditions

Quantity	Value
$P_{0,in}$ [Pa]	38460.32
$T_{0,in}$ [K]	271.56
Inlet Angle [$\circ$]	17.86
Pout [Pa]	15000
P0_in/Pout [-]	2.6

Table 7: VST Design Results

VST Size	$\dot{m}$ [Kg/s]	C_D [-]
Current Design	12.63	0.839
Enlarged Area +35%	16.78	0.832

5. Conclusion

This paper introduced the experimental apparatus of the Von Karman Institute to operate and test the new High-Speed Low Pressure Turbine module. The detailed test matrix will allow a decomposition of the different elements playing a role in the turbine efficiency and to retrieve the effect of each features. Meaningful data and useful information on the effect of cavity flows and purge variation in High-Speed LPT representative environment. The turbine efficiency will be measured, also evaluating the impact of the off-design velocity triangles on turbine losses and output work. As discussed, the facility will be heavily instrumented to capture the 3D flowfield both upstream and downstream of the rotor blade. Fast response pressure sensors will be used to measure the unsteady features rising in the turbine at the hub cavities location and on the shroud casing. Fast Response miniaturized probe will measure the unsteady flow angles at the rotor exit. In the paper is also presented the preliminary design selection for the revamping of the Von Karman Institute compression tube facility CT-3, to house the new High-Speed Low Pressure Turbine module. The redesign of the intake bell-mouth is discussed and the simulation performed predict boudary layer thickness about 10% of the blade axial chord. The new design of the variable sonic throat is discussed. It allows a safe operating conditions of the LPT module with a safety margin over 50% of the targeted mass flow rate. The auxiliary structural elements located dowsntream of the stage are also analysed. Their number around the annulus was optimised to reduce the potential effect upstream,and to limit the impact on the instrumentation. The numerical results show low effect on the static pressure fluctuation below 0.1% of the total inlet pressure on the measurement region located dowstream of the rotor TE.

Acknowledgments

The authors gratefully acknowledge funding of the SPLEEN project by the Clean Sky 2 Joint Undertaking under the European Unions Horizon 2020 research and innovation programme under the grant agreement 820883.

References

[1] Internation Civil Aviation Organization, Table of the traffic forecast, https://www.icao.int/sustainability/Documents/tables\%20of\%20the\%20traffic\%20forecasts_v2.pdf, (2018).

[2] EU, Flightpath 2050 europes vision for aviation, https://ec.europa.eu/transport/sites/transport/files/modes/air/doc/flightpath2050.pdf, (2011).

[3] J. Kurzke, Fundamental differences between conventional and geared turbofans, volume 1: Aircraft Engine; Ceramics; Coal, Biomass and Alternative Fuels; Controls, Diagnostics and Instrumentation; Education; Electric Power; Awards and Honors (Jun 2009). doi:10.1115/GT2009-59745.
URL https://doi.org/10.1115/GT2009-59745

[4] D. Torre, Design and testing of a multi-stage ip turbine for future geared turbofans, 2020.

[5] M. Giovannini, F. Rubechini, M. Marconcini, A. Arnone, F. Bertini, Analysis of a lpt rotor blade for a geared engine: Part i - aero-mechanical design and validation, 2016. doi:10.1115/GT2016-57746.

[6] F. Malzacher, J. Gier, F. Lippl, Aerodesign and testing of an aero-mechanically highly loaded lp turbine, Journal of Turbomachinery-transactions of The Asme - J TURBOMACH-T ASME 128. doi:10.1115/1.2172646.

[7] A. Mahallati, B. Mcauliffe, S. Sjolander, T. Praisner, Aerodynamics of a low-pressure turbine airfoil at low reynolds numbers-part i: Steady flow measurements, Journal of Turbomachinery 135 (2013) 011010–011010. doi:10.1115/1.4006319.

[8] A. Mahallati, S. Sjolander, Aerodynamics of a low-pressure turbine airfoil at low reynolds numbers-part ii: Blade-wake interaction, Journal of Turbomachinery 135 (2013) 011011–011011. doi:10.1115/1.4006320.

[9] M. Börner, R. Niehuis, Dynamics of shock waves interacting with laminar separated transonic turbine flow investigated by high-speed schlieren and surface hot-film sensors, volume 2B: Turbomachinery (Sep 2020). doi:10.1115/GT2020-14386.
URL https://doi.org/10.1115/GT2020-14386

[10] M. Giovannini, F. Rubechini, M. Marconcini, D. Simoni, Y. Vianney, F. Bertini, Secondary flows in lpt cascades: Numerical and experimental investigation of the impact of the inner part of the boundary layer, 2018. doi:10.1115/GT2018-76737.

[11] H.-P. Wang, S. J. Olson, R. J. Goldstein, E. R. G. Eckert, Flow visualization in a linear turbine cascade of high performance turbine blades, 1995. doi:10.1115/95-GT-007.

[12] M. Vera-Morales, E. Blanco, H. Hodson, R. Vazquez, Endwall boundary layer development in an engine representative four-stage low pressure turbine rig, Journal of Turbomachinery-transactions of The Asme - J TURBOMACH-T ASME 131. doi:10.1115/1.2952382.

[13] M. Lipfert, J. Habermann, M. Rose, S. Staudacher, Y. Guendogdu, Blade-row interactions in a low pressure turbine at design and strong off-design operation, Journal of Turbomachinery 136 (2014) 111002. doi:10.1115/1.4028213.

[14] P. Jenny, R. Abhari, M. Rose, M. Brettschneider, J. Gier, A low pressure turbine with profiled end walls and purge flow operating with a pressure side bubble, Journal of Turbomachinery 134.

[15] C. H. Sieverding, T. Arts, The vki compression tube annular cascade facility ct3, volume 5: Manufacturing Materials and Metallurgy; Ceramics; Structures and Dynamics; Controls, Diagnostics and Instrumentation; Education (Jun 1992). doi:10.1115/92-GT-336.
URL https://doi.org/10.1115/92-GT-336

[16] A. Tiwari, S. Patel, A. Lad, C. Mistry, Development of bell mouth for low speed axial flow compressor testing facility, 2016.

[17] Blair, G. P. and Cahoon, W. M., Design of an intake bellmouth, http://www.profblairandassociates.com/pdfs/RET_Bellmouth_Sept.pdf,.

[18] N. Lin, H. L. Reed, W. S. Saric, Effect of leading-edge geometry on boundary-layer receptivity to freestream sound, in: M. Y. Hussaini, A. Kumar, C. L. Streett (Eds.), Instability, Transition, and Turbulence, Springer New York, New York, NY, 1992, pp. 421–440.

[19] R. E. Hanson, H. P. Buckley, P. Lavoie, Aerodynamic optimization of the flat-plate leading edge for experimental studies of laminar and transitional boundary layers, 2012.

[20] C. Tropea, A. Yarin, J. Foss, Springer Handbook of Experimental Fluid Mechanics, 2007. doi:10.1007/978-3-540-30299-5.

Improvement of measurement accuracy using Bayesian inference - Application to low speed UHBR fan

Gonçalo G. Cruz

Turbomachinery and Propulsion Department, von Karman Institute for Fluid Dynamics, Belgium, goncalo.cruz@vki.ac.be

Supervisor: Fabrizio Fontaneto

Associate Professor, Turbomachinery and Propulsion Department, von Karman Institute for Fluid Dynamics, Belgium, fontaneto@vki.ac.be

University Supervisor: Xavier Ottavy

Professor, LMFA - Laboratoire de Mecanique des Fluides et d'Acoustique, École Centrale de Lyon, France, xavier.ottavy@ec-lyon.fr

Abstract

In the frame of the development of the next generation low-speed fans, to be employed in Ultra High Bypass Ratio engines (UHBR), the need for a leap forward in the typical testing procedures became more and more evident in the past few years. Low-speed fans, concerning the old direct drive configuration, provide a smaller pressure ratio, leading to a marked sensitivity to instrumentation accuracy and intrusiveness. First, decreasing the fan stage pressure ratio also reduces the change in the total temperature ratio. With the instrumentation used nowadays, this leads to a direct decrease in measurement accuracy, especially when assessing efficiency. Second, a reduction in the fan rotational speed shifts its characteristic curve, pronouncing probe throttling effects on the flow, imposing a variation on the fan operation point caused directly by instrumentation. This work aims at developing a novel methodology for the performance characterization of turbomachinery components sensitive to instrumentation limitations. The methodology will rely on a hybrid approach, coupling experimental techniques to modelling techniques within a Bayesian data assimilation framework. To ensure a direct beneficial impact on costs and implementation time, the methodology will lean on standard instrumentation technology. Additionally, being supported by a Bayesian framework, the methodology will provide a direct evaluation of the uncertainty budget linked to its usage. The methodology sensitivity must be assessed with respect to the modelling technique used, from low order modelling to high fidelity CFD. As a final goal, the technique must be applied in a design of experiments framework, ensuring a minimal uncertainty of a measurement campaign and a reduction in the intrusiveness of the probes in the flow. The proof of concept of the methodology was tested for a low aspect ratio axial compressor stage, showing a good prediction of the corrected compressor map, as well as a promising prediction of the inter-row radial pressure distribution and 2D flow field.

Keywords: bayesian data assimilation, low-speed fan, experimental measuring techniques, numerical modelling

COMPRESSOR AERODYNAMICS AND HEAT TRANSFER

Steady and Unsteady Numerical Characterization of the Stable Operating Range of a Highly-Loaded Low-Pressure Compressor Stage

Riccardo Toracchio

Turbomachinery and Propulsion Department, von Karman Institute for Fluid Dynamics, Belgium, riccardo.toracchio@vki.ac.be

Supervisor: Fabrizio Fontaneto

Associate Professor, Turbomachinery and Propulsion Department, von Karman Institute for Fluid Dynamics, Belgium, fontaneto@vki.ac.be

University Supervisor: Koen Hillewaert

Associate Professor, Aerospace and Mechanical Engineering Department, University of Lige, Belgium, koen.hillewaert@uliege.be

Abstract

Despite the improved propulsive performance induced by short-inlet and Boundary-Layer-Ingestion (BLI) aircraft architectures, the engine is forced to operate with non-homogeneous inlet flows. The low-pressure compressor is therefore subjected to the effects of the incoming distorted inlet flow at the outlet of the fan that can significantly affect its performance and stability. Before any characterization and description of the flow topology and performance is carried out under the effect of the distortion, clean conditions need to be analysed to allow a proper comparison with the distorted case and the available experimental results. On this purpose, steady and unsteady Reynolds-Averaged-Navier-Stokes (RANS) simulations of the VKI DREAM low-pressure compressor stage are performed.

Keywords: Distortion, CFD, unsteady, compressors

1. Introduction

Advanced aircraft technologies are currently in the focus of research to address the environmental goal of reducing aircraft emissions within the next decade and beyond [1]. Short-nacelle geared high bypass turbofans and BLI engines are among the most promising technologies to improve fuel and propulsive efficiency in the short and long term respectively, forcing nevertheless the engine to operate with a highly distorted inlet flow [2][3]. Although operability and performance deterioration of fans under distorted conditions has been the primary focus of research in last decades [4][5][6], given its strong impact in the definition of the overall propulsive efficiency, almost no information is currently available on the low-pressure compressor (booster), despite its crucial role in the forthcoming generation of engines. The complex flow distortion pattern observed behind the fan will indeed influence the underlying physical mechanisms taking place within the compressor stage, possibly jeopardizing performance and stability of the whole engine. Due to the impossibility of extending the results obtained for fans to the low-pressure compressor as a consequence of the marked aerodynamic and structural design differences, this research project aims at providing a complete characterization of the physical phenomena driving loss generation and stability deterioration in modern Low-Pressure Compressors (LPC) when distorted flow conditions set up.

However, before any investigation is carried out to understand the effects of inlet non-uniformities on the LPC, its characterization in clean conditions is needed in order to highlight the differences between the baseline and distorted configuration, and to add meaningful information to the available experimental results. To reach this goal, steady and unsteady RANS simulations are run on the highly-loaded low-pressure VKI DREAM compressor stage, which is representative of the first stage of a modern geared turbofan booster. The aim is to provide an overall assessment of the global performance of the machine, highlighting flow

mechanisms driving the loss generation.

In the first part of the paper the final configuration of the numerical domain and mesh is described, along with the numerical setup employed. In the second part, the results of the steady and unsteady simulations at design conditions are provided.

2. Test section and instrumentation

The test section considered in this work as reference to run the numerical simulations is the DREAM compressor stage. It is installed in the VKI R4 closed-loop high-speed test-rig, composed by a tank used as settling chamber (1), the test section (2), a discharging collector at the compressor outlet (3), a return channel to guide the air back to the reservoir (4), and a throttling valve to run the compressor at different operating conditions (5) (Figure 1). The tank is equipped with air/water heat exchanger to allow a temperature control at the test section inlet with an accuracy of +/- 1K. The temperature control and the closed-loop architecture allow an independent variation of Reynolds and Mach numbers, giving the chance to test in representative cruise and take-off aircraft conditions. The rotor is driven by a 450 kW DC motor with a continuous control of the rotational speed, and it is coupled to a 12:1 gearbox that increases the rotor speed up to 9000 RPM.

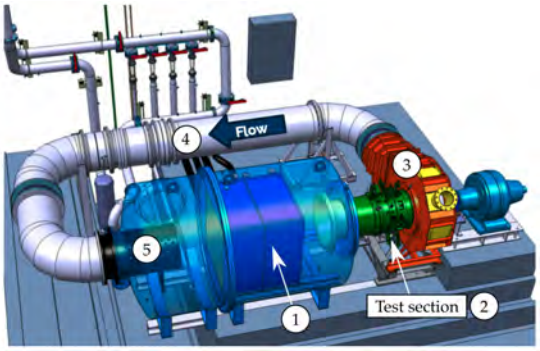

Figure 1: VKI-R4 closed-loop high-speed compressor rig.

The test section is a 1.5 stage characterized by 100 inlet guide vanes, to simulate the radial distribution of flow angle behind the fan, followed by 76 rotor blades and 100 stator blades. A smooth convergent bell-mouth guides the flow from the reservoir to the test section. Figure 2 shows a sectional view of the presented test section.

Total pressure, temperature, Mach number and flow angles are measured at four axial locations corresponding to the stage inlet (plane 1), IGV outlet (plane 2), rotor outlet (plane 3) and stage outlet (plane 4). Each axial location allows four circumferential positions of the instrumentation at 0°, 90°, 180° and 270°, and a span-wise variation of the probe location. Moreover, to avoid leaks for the presence of grooves, a circumferential traverse mechanism has been realized by rotating the stators instead of the probes. In plane 0, located upstream of plane 1, and in plane 4, 4 rakes are distributed circumferentially to compute the global performance. Every rake is composed by 6 Kiel heads, equipped with a pressure tap and a T-type thermocouple junction, to provide a proper area-averaging of total quantities. The performance map for the compressor is obtained by sistematically closing the throttling valve while keeping constant the corrected rotational speed of the compressor. A good-approximation of the mass-flow is possible by the only 6 inlet rakes. Moreover, at every measurement location, static pressure is acquired trough 5 static pressure holes at casing and other 5 in the hub walls distributed along the circumference . The static pressure along the span is retrieved by linear interpolation of the mean static pressure at hub and shroud. A pitot tube is traversed in plane 0 to assess the linearity of the radial distribution of the static pressure. To compute the efficiency and performance maps of the compressor, data have been acquired with a frequency of 2 Hz. The uncertainty associated to the measurements is calculated with the ASME method [7] and the values are presented in a 95% confidence interval. The uncertainty values are +/- 0.5 mbar and +/- 0.7K, resulting in a +/- 0.00053 uncertainty value for the pressure

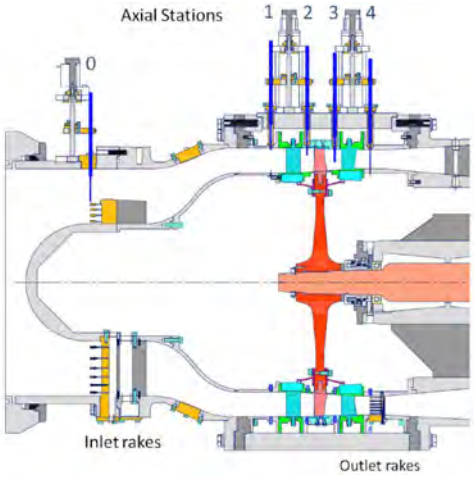

Figure 2: DREAM test section.

ratio.

For the unsteady instrumentation, 15 measurement points have been located at the casing for time-resolved static pressure measurements. These sensors have a resonance frequency higher than 200kHz, but the bandwidth is limited to 60 kHz due the metallic insert where they are contained. The sensors cover an arc of 42°, are equally spaced in one rotor pitch, and are axially displaced between plane 2 and 3. The static pressure at the hub is retrieved in plane 3 and 4 by using sensors located at 66°. Moreover, they are characterized by an uncertainty of +/- 1.2 mbar, again computed with the ASME method [7]. As last, a fast-response pressure probe, characterized by a resonance frequency of around 300 kHz and uncertainty calibration of +/- 1.8 mbar, is located at mid-span of the rotor outlet at 90°. The acquisition of the time-resolved data is carried out at a frequency of 1MHz for 10 s.

3. Numerical domain and setup

The numerical domain and setup employed in the simulations were chosen to provide as high as possible level of accuracy with respect to the experimental results, while keeping a limited computational cost. Hereafter a description of the procedure followed to assess the quality of the domain, mesh and numerical setup is presented.

3.1. Numerical domain

The numerical domain shown in Figure 3 is representative of the real geometry of the DREAM test section between Plane 1 (IGV inlet) and 4 (Outlet stage). The outlet section is imposed downstream of plane 4 to avoid any possible influence of the outlet boundary condition on the measurement plane.

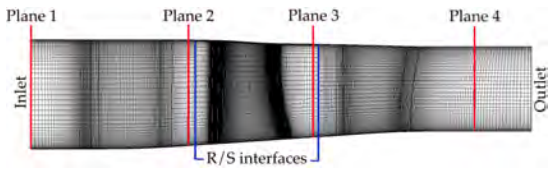

Figure 3: Numerical domain.

The process for the definition of the numerical domain went through the identification of real geometrical features playing a role in the assessment of global performance and flow field of the machine, which in this case are: fillets, tip gaps, hot geometries and cavities. Because of their significant impact on the definition of secondary flow structures at hub and casing respectively [8][9], along with the limited increase in mesh size determined, fillets and tip gaps have been directly implemented considering their averaged measured value. Hot geometries were also considered to take into account possible deformations of the machine when operating.

However, as highlighted by Babin et al. in [10] cavities can play an important role if looking to the performance of the machine and to the state of the boundary-layer at the rotor leading-edge. This can influence the axial component of the velocity and therefore the incidence at low span, forcing the flow to separate on the hub suction side wall. At the same time, the presence of cavities in the numerical domain impacts considerably the computational cost, especially if an unsteady RANS has to be performed. A study on the impact of rotor cavities was therefore undertaken to assess the quality of the results against the increased mesh size. Matching connections were used at the interface between cavities and main channel to allow an improved numerical accuracy of the leakage flow exchanged with the cavity. The same mesh topology was kept in both configurations to avoid any possible grid-dependent modification of the flow field (Figure 4), bringing the mesh size to reach 9.6 and 7.4 million cells for one passage in the cavity and no-cavity case respectively. The ratio between the grid points in the cavities and the rotor domain was chosen to be as close as possible to one to allow an improved balance of the solution quality in the two regions.

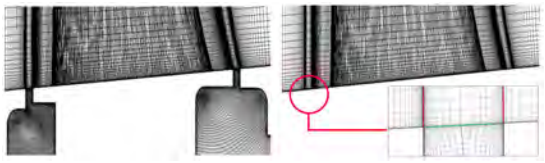

Figure 4: Mesh topology employed to study the effect of the cavity.

The comparison is hereafter presented in terms of global performance and rotor outlet total pressure difference, which is explicative of the losses generated at low span. The flow field over the outlet stator was not significantly affected by the presence of the cavities. As highlighted in Figure 5 a reduction of performance occurs when cavities are considered, and this is mainly due to the variation of flow topology at low span generated by the interaction with the cavity, as highlighted in Figure 6. A value of the mass flow equal to 1 is representative of the outlet boundary condition, that in this case was imposed equal to the experimental value. The averaged value of total

pressure for span lower than 30% is reduced by the flow ejected from the cavity (Figure 6, point 1), and the flow exchanged at the interface increases locally the incidence due to blockage effects, affecting size and intensity of the hub corner separation (Figure 6, point 2). Red regions are instead representative of low total pressure regions of the no-cavity configuration. The high values encountered on the hub wall at 0.25 and 1.25 were thought to be generated by the presence of a passage vortex, but no clear evidence of its presence can be detected from the experiments and the CFD simulations.

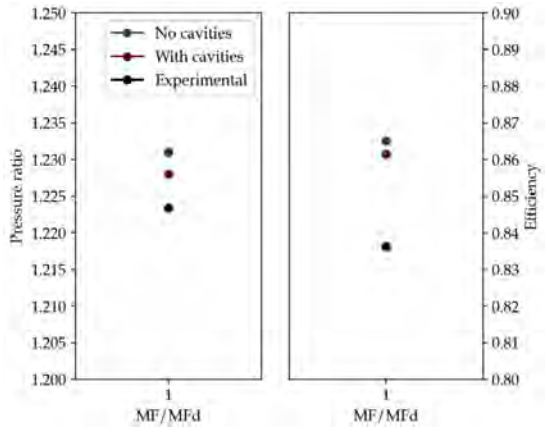

Figure 5: Comparison of cavity, no cavity case and experimental global performance.

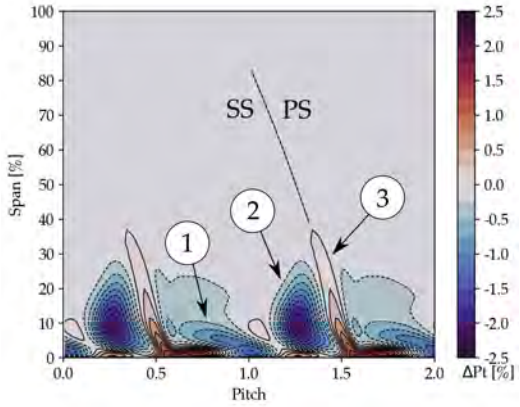

Figure 6: Difference of total pressure maps at rotor outlet between cavity and no cavity case.

As overall conclusion, despite the significative difference of the RANS simulations with respect to the experiments, the presence of the cavity does not seem to impact strongly the characterization of the global performance and flow field of the compressor, keeping the difference always limited to maximum 2.5%. Therefore, given the advantage of a reduced mesh size, the no-cavity configuration was selected for the steady and unsteady characterization of the machine.

3.2. Mesh and grid refinement study

For a better control of the grid quality, multi-block structured mesh was implemented with Autogrid5 and IGG softwares. An O4H symmetric blade-to-blade topology was considered for every blade row, and matching conditions were applied on the periodic boundaries. OH topology was used instead for the rotor tip gap region, with a number of cells equal to 30% of the rotor in the span-wise direction and 20% constant size cells in the mid-flow gap region. The B2B section offset method was selected for the geometry creation of the hub and shroud fillets. 20 span-wise points were used, along with a minimum angle of 25 to allow a good angular deviation and distribution of points on the wall. Mesh quality assessments showed minimum skewness level, maximum aspect and expansion ratio of the cells of 22, 2000 and 2.5 respectively, which are considered to provide good quality results. Expansion ratio and cell width at the wall were selected to guaranty uniform variation of the cells from the wall and a good interface with the main flow, allowing everywhere a value of the y+ lower than 3. Moreover, only for the present grid refinement study, radial equilibrium imposed on the static pressure was selected as outlet boundary condition.

A generalized Richardson extrapolation approach [11] [12] was adopted to quantify the uncertainty introduced by spatial discretization on the flow quantity of interest. At such extent, three mesh levels were considered with 0.64 (coarse), 5.12 (medium) and 40.96 (fine) million cells respectively, obtained from an isotropic refinement in the θ, R and Z directions by a factor of 2 (size ratio of 8 among the grid levels). The comparison is here proposed in terms of global performance (total pressure ratio and efficiency, Figure 7) and percentage difference of rotor outlet total pressure maps of the coarse, medium and fine solution with respect to the 2D Richardson extrapolation computed on the same plane (Figure 8).

No significant difference is present between medium and fine solutions for both global performance and rotor outlet maps, while the coarse solution shows discrepancies larger than 5% and 12% respectively when compared to the Richardson extrapolation. The latter is highlighted mainly in the shape

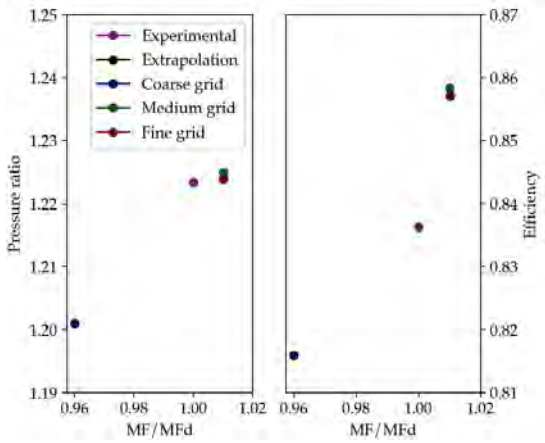

Figure 7: Comparison between mesh levels on the compressor and efficiency maps.

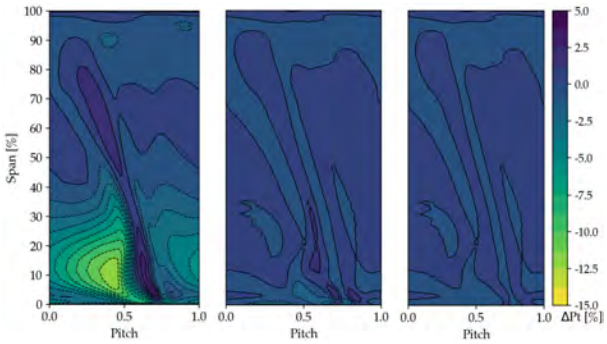

Figure 8: Comparison of the mesh levels with respect to the Richardson extrapolation.

and amplitude of the hub corner separated region, as shown in yellow in Figure 8. The increased numerical dissipation induced by the low refinement level of the coarse mesh can indeed influence the solution in the regions strongly affected by secondary-flows and losses, over-predicting the reduction of the total pressure. Moreover, the extrapolated point in the global performance map almost overlap the one computed from the fine mesh, becoming therefore not visible in the figure.

As a conclusion of the grid refinement procedure, given the good level of accuracy provided by the medium mesh when compared to the reduced computational cost with respect to the fine mesh, it was selected as best candidate to employ in the simulations.

3.3. Numerical setup

Numeca FineTurbo software was used to solve the fully-turbulent compressible Reynolds-Averaged-Navier-Stokes equations, spatially discretized with a cell-centered finite volume formulation on a multi-block structured grid. The eddy viscosity assumption was used to account for turbulent effects, and the two equations k-ω SST model was considered for the turbulence closure as consequence of the accuracy provided in both near-wall and free-stream regions. Inlet total pressure and temperature boundary conditions were imposed equal to the experimental pitch-average span-wise distributions, and the same was done for the mass-flow boundary condition imposed at the outlet. The outlet static pressure based on the radial equilibrium was used only in view of the simulations performed for the grid refinement study, but it appeared to be a very unstable boundary condition for the present case, forcing the machine to develop open hub corner separations which are not in line with experiments. Moreover, air was considered as a calorically perfect gas, and the walls of the numerical domain as adiabatic. Time integration to a steady-state solution was achieved with an explicit Runge-Kutta method combined with an implicit residual smoothing approach, while considering time discretization based on local and dual time stepping techniques for the steady and unsteady problem respectively.

For the steady computations a full non-matching mixing plane approach was used at the rotor/stator interfaces showed in Figure 3, while for the unsteady simulations a domain scaling approach was considered. The latter is based on the constraint that the pitch distance must be identical on both sides of the rotor/stator interface, implying either to increase the number of modelled passages or to scale the geometry accordingly. In the present study, the number of rotor passages was supposed to be 75 instead of 76, to allow therefore the applicability of the domain scaling approach by implementing only 4/3/4 passages for the IGV, rotor and outlet stator respectively. A preliminary evaluation of the span-wise diffusion factor computed in the case of 75 rotor blades confirmed that no significant variation with the respect to the original geometry should be expected. Moreover, the error in the computation of all time frequencies can be considered negligible being the scaling coefficient very close to 1. Moreover, the application of the explicit Runge-Kutta scheme on a sine wave confirmed that at least 30 points are required for a proper representation of every harmonic of interest. The experimental evidence of the appearance of physical phenomena with a frequency four time larger than the rotor Blade Passing Frequency (BPF) suggested the application of 120 time steps per passage. As last point, the unsteady computation was initialized with a steady simulation

employing frozen rotor approach at the domain interfaces.

4. Results

The main idea behind the characterization of DREAM in clean conditions was to provide a comparison against the available experimental results in the same operating conditions, and to further describe the most relevant flow phenomena taking place in the machine. The description of the global performance was already presented in the first part of the paper, therefore here an initial assessment, by means of low-order models applied to which appeared to be the highest source of losses in the machine is proposed, followed by the description of the span-wise distribution of flow quantities retrieved by the steady simulations. To conclude, the full 3D characterization of the flow by means of the unsteady simulations is presented.

In view of the comparison with the distorted case, design conditions at 100% speed were considered for this analysis. Despite the large value of efficiency, this operating point is considered one of the most interesting for the assessment of the distortion effects being representative of cruise aircraft conditions. Moreover, the limited variation of incidence and mass-flow allowed at high speed make this a critical operating point for the compressor under inlet distortions.

4.1. Low-order modeling

The stall indicator and the diffusion factor coefficients defined by Lei [13] were employed as a preliminary approach to quantify the extent of the reversed flow in the hub region and the diffusion limit conditions with respect to corner stall. Figure 9 shows the span-wise distribution of the diffusion factor in the rotor blade passage, which presents a closed corner structure for span values lower than 30%, as highlighted by the CFD simulations.

The diffusion factor is mainly affected by blade and incidence angles which are representative of the overall pressure rise, by the turning in the end-wall region (cross-flow) and solidity, that again influences the pressure gradient developed over the suction side of the blade. In the present case, the large blade turning at low-span combined with a local increase of the flow incidence at the rotor leading edge due to the high speed of the rotating platform appeared to be at the base of such high value of this parameter. Large values of the diffusion factor are present all over the blade height, determining a span-wise averaged value

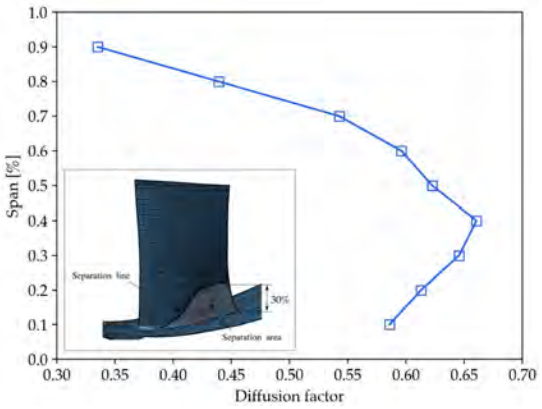

Figure 9: Span-wise diffusion factor distribution on the rotor blade.

of 0.56. The reduction visible in the tip region is mainly due to the low blade turning compared to low-span regions, still keeping values larger than 0.3. The maximum value is reached at 40% span being this location at the limit of the hub separation span-wise extent.

Figure 10 presents instead the position of the DREAM test section compared to the results provided by Lei [13]. The diffusion factor is here presented in terms of span-wise averaged value, while the stall indicator, representative of the blade loading reduction with respect to conditions outside of the separated region, is referred to mid-span, where the largest values of the diffusion factor appear. On this graph, DREAM is located in the region that exhibits open corner separations but lays almost on the line prolongation representative of closed separations, which is a condition not considered in the Lei's study. This situation could explain the experimentally and numerically evident presence of a closed separation, being nevertheless at limit of hub corner stall.

The corner shape factor criterion [14] was considered to further characterise the corner separation and its proximity to instability. This parameter is defined as the angle between co- (V1) and reversed flow vector (V2) identified on the peak streamline curvature, as highlighted in Figure 11, and can change between 0 and π, where the latter represents the limit condition to the hub stall. In the present case this angle reaches 162°, again confirming the tendency of DREAM to exhibit severe hub corner separations.

Finally, Bennington et al. [15] derived a simple model to quantify the location and movement of the mean flow/tip leakage interface as a consequence of the momentum balance between the approaching flow

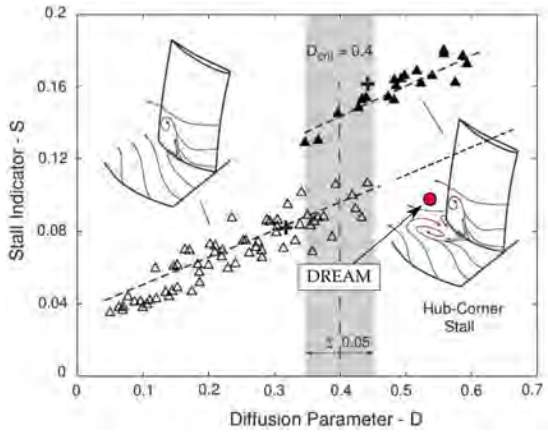

Figure 10: Location of the DREAM test section in the Lei's diagram.

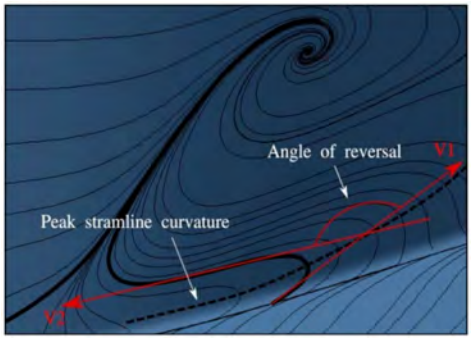

Figure 11: Angle of reversal in the DREAM stage.

and the tip gap reverse flow, and it is here proposed as a comparison with respect to steady RANS simulations (Figure 12). The interface distance with respect to the blade surface was computed on a blade location referred to the near-stall conditions. In the same figure a very good agreement is shown between CFD and model prediction.

4.2. Span-wise distributions

Pitch-wise mass-averaged distributions are retrieved from the steady simulations performed on the compressor and are hereafter shown for total pressure, temperature and flow angles respectively at plane 3 (rotor outlet) and 4 (stator outlet).

The total pressure was selected to identify the largest source of losses in the blade passage (Figure 13). In plane 3 two are the highest regions of discrepancy with respect to the experimental results, and these are the end wall regions. On the hub, the CFD over-predicts the reduction of total pressure, while on the tip region the opposite trend is visible. This will be

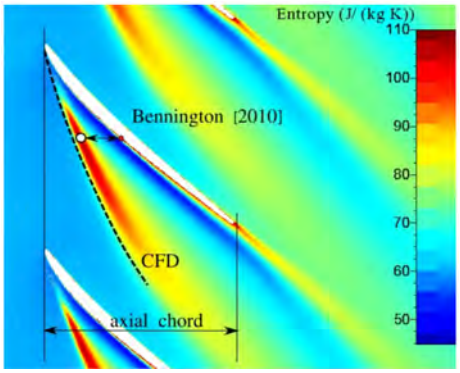

Figure 12: CFD at casing versus Bennington prediction.

shown also later in the outlet maps: the span-wise extent of the tip leakage flow is not clearly visible from the CFD, while it appears to have a strong impact on the experiments. The abrupt variation of total pressure at very low span for the experiments is the result of the cavity leakage flow which is not present in this configuration of the CFD domain. Less differences are instead visible from the total pressure distribution at plane 4. The total pressure losses in the experiments increase indeed with respect to the CFD for span lower than 50% and the flow tends to homogenise. Close to the tip region, again smaller value of the experimental total pressure are presents if compared to CFD. However, the reduction of total pressure visible at 70% is due to the span-wise propagation of the tip leakage flow coming from the rotor. Differences in the mid-span region between experiments and CFD could be addressed to a not perfect matching of the operating point in the two cases. The experimental uncertainty on the total pressure is too small to be visible from the figures. However, despite the difference in the end-wall regions, the results of the CFD simulations are considered in good agreement with experiments.

The most evident difference in the span-wise distribution of total temperature (Figure 14) is the mismatch in the tip region between CFD and experiments. The heat transfer through the casing walls of the facility from the external laboratory environment indeed impacts the value of total temperature, and therefore efficiency, at high span. This does not appear in the computations since adiabatic wall boundary conditions were employed. However, for most of the span height the CFD is within the experimental uncertainty, defining therefore good overall matching between the different distributions.

Figures 15 shows respectively the distribution of

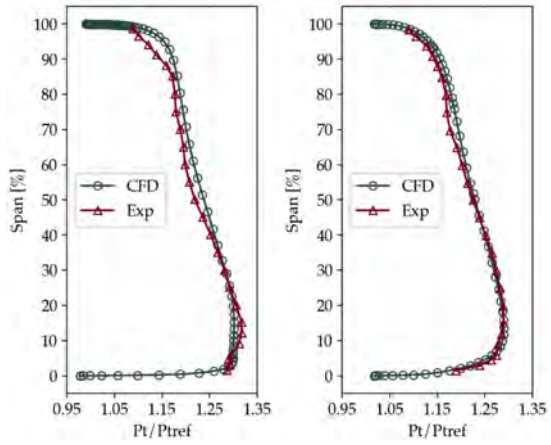

Figure 13: Total pressure span-wise distribution at rotor outlet (a) and stator outlet (b).

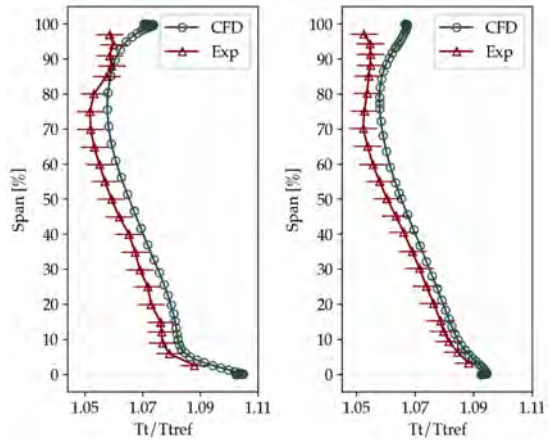

Figure 14: Total temperature span-wise distribution at rotor outlet (a) and stator outlet (b).

the flow angles (relative (a) and absolute (b)) and entropy at rotor outlet and stage outlet planes. The distribution of the relative flow angle in plane 3 is mainly determined by the outlet blade angle which increases with respect to the axial direction moving to higher span. It is worth to notice the local reduction for span lower than 10%. This effect is associated to a cross-flow motion into the blade passage. The flow indeed, after entering the rotating platform increases at very low span the incidence level, with subsequent generation of a sonic pocket due to the large values of relative velocity. However, after 20% of the chord, the flow that initially moved far from the blade starts to migrate toward the suction side on the second half of the blade, to arrive in plane 3 with reduced value of the relative flow angle. The span-wise variation of the flow angle in plane 4 is instead in the range -6, +2 the majority of which occurs into the boundary layer. For the rest of the span (10%-90% range) the variation of the absolute angle is kept lower than 1.5. For this case, no comparison is provided with respect to the experimental results.

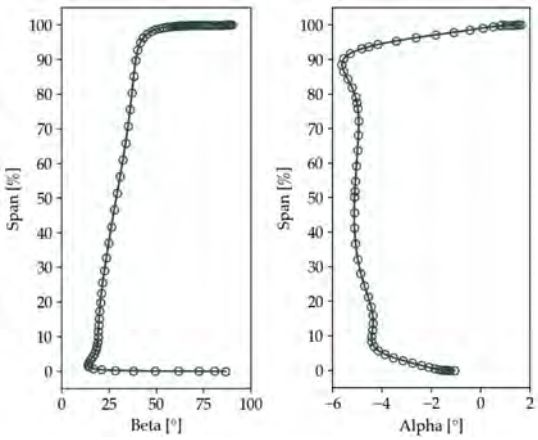

Figure 15: Flow angle span-wise distribution at rotor outlet (a) and stator outlet (b).

4.3. Detail flow characterization

4.3.1. Rotor outlet maps

Figures 16 and 17 show the total pressure distribution and the corresponding RMS computed from the flow fluctuations with respect to the Phase-Lock-Averaged (PLA) value at the rotor outlet plane, allowing the description of the flow field and distinguish the unsteady flow structures appearing in the blade passage. Since plane 3 (rotor outlet) belongs to the rotating frame of reference in the numerical domain, the PLA was computed to detect and isolate the fluctuations synchronous to the IGV/stator Blade-Passing-Frequency (BPF). The total pressure map highlights a general reduction of the total pressure in the rotor wake, with a thickening under 30% span due to the presence of the hub corner separation. This is clearly visible also from the RMS distribution, where a peak, reached in the same location, highlights that the hub corner separation represents one of the highest source of unsteadiness in the blade passage. Large values of RMS are also visible on the pressure side at low span. However, no clear secondary structure appears from the analysis of the flow in that region, meaning that rotor/stator interactions may be at the base of such fluctuations.

To provide a comparison with respect to the experimental results, the percentage difference between

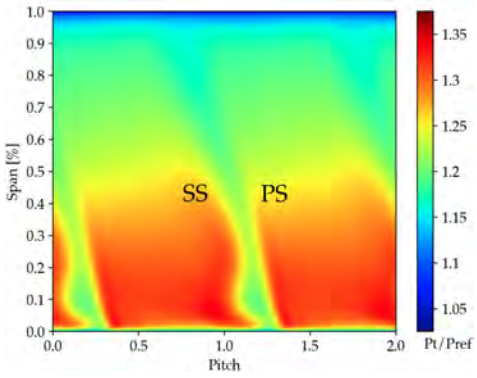

Figure 16: Total pressure map at rotor outlet.

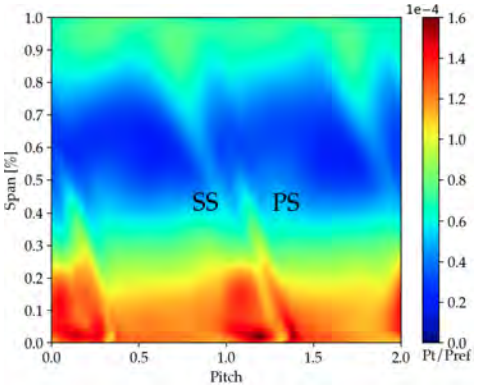

Figure 17: Total pressure RMS map at rotor outlet.

CFD and experimental total pressure maps is shown in Figure 18. The CFD over-predicts the total pressure level in the wake and in the hub corner region. Moreover, the intensity of the tip clearance flow is highly under-predicted in the CFD, and this is the reason why the structure of this vortex does not appear clearly on the outlet plane. This can not be linked with any issue of the mesh in the tip clearance, being the grid resolution in that region very high. Again, the high total pressure region at low span on the pressure side of the blade is visible.

The experimental and numerical RMS maps are not compared given the large difference in fluctuation amplitudes. Experimental signals contain indeed turbulence fluctuations which are not taken into account in unsteady RANS simulations, where only the statistical content of the fluctuations linked to the domain periodicity is visible.

4.3.2. Casing maps

Results are hereafter shown in terms of entropy distribution at casing. Entropy was selected as the quantity of interest given its capability to spot more in detail the unsteady features of the flow with respect to the static pressure.

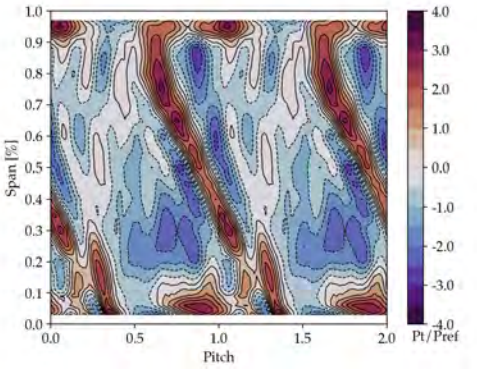

Figure 18: CFD vs experiments at rotor outlet.

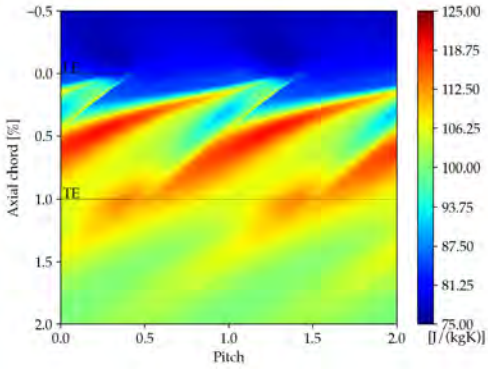

Figure 19: Entropy distribution at casing.

The entropy distribution at 100% span (Figure 19) shows an interface between mean flow and tip leakage flow inclined of almost 20° with respect to the line connecting two adjacent leading edges. The central core of the tip leakage is highlighted by a large value of the entropy and impacts on the pressure side of the adjacent blade from half of the axial chord until the trailing edge. An investigation of the instantaneous entropy pattern highlights that the tip leakage flow enters indeed the passage of the adjacent blade only in the second part of the blade, generating an high entropy region on the suction side trailing edge of the next blade. The flow is fully governed by the IGV wake, which estabilishes an oscillation of the entire structure of the tip leakage flow. The RMS highlights clearly a large value of the fluctuations at the interface

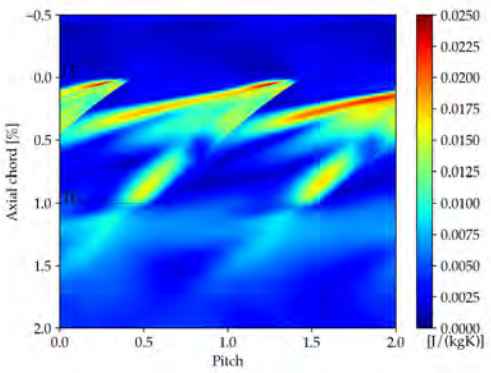

Figure 20: Entropy RMS distribution at casing.

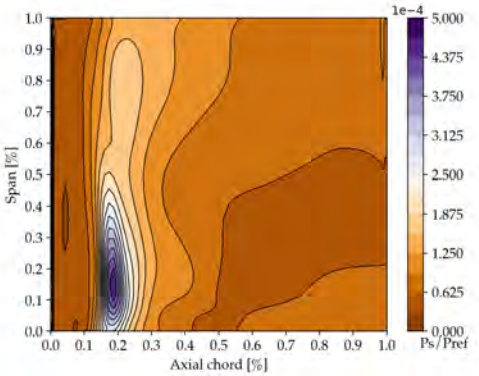

Figure 22: Static pressure RMS distribution over the suction side blade surface.

with the meanflow, while high peaks can be found also over the suction side of the blade.

4.3.3. Blade suction side

Also in this case, the unsteady behavior of the blade is shown in terms of static pressure and RMS distributions over the suction side of the blade as presented in Figures 21 and 22. The former shows the clear presence of a shock developing all along the span, which is mainly due to the high relative velocity reached by the flow just after the blade leading edge. The plateau of static pressure visible at span lower than 30%, in the downstream part of the blade (after 40% axial chord) is the clear presence of the hub corner separation, which is further confirmed by the high value of the RMS in the same region. Moreover, the largest source of unsteadiness on the suction side of the blade comes from the fluctuations of the supersonic pocket.

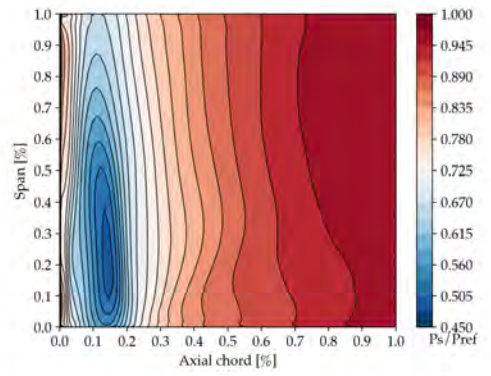

Figure 21: Static pressure distribution over the suction side blade surface.

5. Conclusion

Inlet distortions can considerably impact the performance and stability of a machine, altering localized regions of the flow field. The presented paper had the target to identify and characterize the most critical physical phenomena in a low-pressure compressor running in clean conditions to allow a proper assessment and quantification of the effects induced by the distortion. The provided numerical results showed good agreement with the experiments, and highlighted the presence of two main phenomena of interest: hub corner separations and tip leakage flows. The available literature confirms indeed that these are typical phenomena in axial compressors affected by the presence of the distortion.

The analysis of the numerical domain allowed to conclude that fillets and tip gaps should always be taken into account given their limited impact on the mesh size, while it is not worth in the present case to consider the presence of cavities due to the very small improvement of numerical results at the expense of a large increase of the computational cost.

Despite the mismatch of the total pressure reduction in the separated region with respect to experiments, the numerical results showed a span-wise extent of the rotor corner separation equal to 30% of the overall blade height and that it represents one of the largest source of unsteadiness in the blade passage. The same can be said about the evolution of the tip leakage flow, despite its span-wise extent is still not clearly visible from the simulations. As an overall conclusion, CFD determined a good prediction of the global performance and span-wise distribution of flow quantities against experiments, along with a proper descrip-

tion of the averaged unsteady flow features and corresponding fluctuations.

At the present state, further efforts are put to characterize the unsteady nature of the hub corner and tip leakage flows, meanly looking at the characterization of their frequencies. Moreover, as next step, the near-stall condition will be analysed, being this a very critical operating point for the compressor when inlet flow distortions appear.

References

[1] Sebastiampillai J., Rolt A., Nalianda D., Mastropierro F., Sethi V., "Technical and Economic Viability of an EIS 2050 Geared Open Rotor", ASME Turbo Expo GT2019-90290.

[2] Peters A., Spakovszky Z.S., Lord W.K., Rose B., Ultrashort Nacelles for Low Fan Pressure Ratio Propulsors, Journal of Turbomachinery 137(2) (021001).

[3] Gunn E.J., Hall C.A., Aerodynamics of Boundary Layer Ingesting Fans, ASME Turbo Expo GT2014-26142 (2014) pp. V01AT01A024.

[4] Giesecke D., Friedrichs J., Aerodynamic Comparison Between Circumferential and Wing- Embedded Inlet Distortion for an Ultra-High Bypass Ratio Fan Stage, ASME Turbo Expo GT2019-90425.

[5] Perovic D., Hall C.A., Gunn E.J., Stall Inception in a Boundary Layer Ingesting Fan, ASME Turbo Expo GT2015-43025 (2015) pp. V02AT37A031.

[6] Zhang W., Vahdati M., Stapelfeldt S., Stall and Recovery Process of a Transonic Fan in Presence of Inlet Distortion, 13th European Turbomachinery Conference ETC2019-371.

[7] Dieck R.H., Measurement uncertainties - methods and applications, USA: ISA 2007.

[8] Bae J., Kenneth S. B., Periodic unsteadiness of compressor tip clearance vortex, ASME Turbo Expo GT2004-53015.

[9] Goodhand M. N., Miller R. J., The impact of real geometries on three-dimensional separations in compressors, ASME Turbo Expo GT2010-22246.

[10] Babin C., Dumas M., Ottavy X., Fontaneto F., Numerical characterization of a HP compressor stage equipped with a closed shrouded stator cavity, ASME Turbo Expo GT2020-14908.

[11] Roache P.J., Perspective: A method for uniform reporting of grid refinement studies., Journal of fluid engineering 116 (3) (1994) : 405–413.

[12] Celik B.I., Ghia U., Roache P.J., freitas C. J., Coleman H., Raas P.E., Procedure for estimation and reporting of uncertainty due to discretization in CFD applications., Journal of fluid engineering 130 (078001-1).

[13] Lei V.M., Spakovszky Z.S., Greitzer E.M., A criterion for axial compressor hub-corner stall, ASME Turbo Expo GT2006-91332.

[14] Taylor J.V., Miller J.M., Competing three-dimensional machenisms in compressor flows, Journal of turbomachinery 139 (021009-1).

[15] Bennington ;.A., Ross M.H., Cameron J.D., Morris S.C., Du J., Lin F., Cehn J., An experimental and computational investigation of tip clearance flow and its impact on stall inception., ASME Turbo Expo GT2010-23516.

Measurement setup and strategy for shrouded stator cavity flow characterization in high speed axial compressor facility

Cedric Babin

Turbomachinery and Propulsion Department, von Karman Institute for Fluid Dynamics, Belgium, cedric.babin@vki.ac.be

Supervisor: Fabrizio Fontaneto

Associate Professor, Turbomachinery and Propulsion Department , von Karman Institute for Fluid Dynamics, Belgium, fontaneto@vki.ac.be

University Supervisor: Xavier Ottavy

Head of Turbomachinery Department - LMFA , Ecole Centrale Lyon, France

Abstract

In axial compressors, shrouded stator cavity flows are responsible for performance degradation due to their interaction with the power stream. The present paper introduces the experimental setup update of the VKI R4 H25 test section to characterize cavity flow in a realistic turbomachinery environment under controlled leakage. The measurement key points and strategy is discussed to collect data on cavity flow effect on axial compressor performance and stability. Elements are introduced such as cavity wall measurements, cavity main volume measurements, and H25 stator inlet hub boundary layer measurements.

Keywords: leakage flows, cavity flow, axial compressors, technological effects, shrouded stator,experiments.

1. Introduction

In order to improve blade design for low aspect ratio configurations, a better understanding of leakage flow induced loss mechanism is crucial. The following study framework is centered on the hub leakage flow in the case of shrouded stator hub platforms. The choice of such technology rely on the stage design parameters [1]. With shrouded stators the rotating assembly clear the stationary parts below the hub level. Leakage flow generated in a downstream to upstream flow recirculation under the hub platform, triggered by the static pressure increase in the main channel. The end of the leakage path is associated with the injection of the recirculated flow in the main channel. The leakage flow is defined by three components [2]: (1) the leakage fraction in the cavity (ratio between the recirculated mass flow and the main channel mass flow); (2) the swirl ratio or swirl factor (ratio of cavity flow tangential velocity to the one of the rotor assembly); (3) the windage heating (total temperature increase from shear work induced by the rotating assembly). A literature review on cavity flow experimental investigation and their effect on axial compressor reveal the two type of configuration used: blade cascades or rotating machine assemblies. Studies in cascades ([3], [4], [5]) allow to have an independent control on flow leakage parameters. Usually performed without representative cavity geometries but rather with injection slots, they allow flexibility in generating multiple leakage conditions without any mechanical modification of the test section. Furthermore, cascade configuration provides with an ease of access for visualization techniques such as ink-dye, oil-dye, PIV, and concentration measurements of gas mixtures (ethylene, carbon dioxide). The results obtained in rotating assemblies ([2], [6]) are supported by the use of engine-like configurations. The analysis of cavity flow effect on axial compressor rely on the measurement of flow quantities in the main channel. In all the aforementioned studies, probe traversing is at least performed downstream of the blade row under investigation. Eventually, probe traversing is done in both radial and azimuthal direction. The type of instrumentation used is either steady (3-hole pneumatic probe, 5-hole pneumatic probe) or unsteady (such as

Hot Wire Anemometry). The objectives of such channel measurement are: (1) To highlight the impact of leakage flow on the end wall secondary flow system; (2) To evaluate the span range of leakage flow contribution to local and propagated loss. Aside from main channel evaluation, some configuration ([4], [2]) proposes conclusion from inside cavity measurements made in the trench region (i.e. cavity to channel connection). Results from wall pressure taps, hot films, concentration measurements, as well as probe traversing are analyzed. To perform such measurements (especially probe traversing), bespoke trench configurations are used in which clearances are larger than the one found in out of production turbomachinery modules. The setup scale is mainly limited by probe intrusiveness. Such measurements are able to inform on rotationally induced cavity/main channel interactions. It is also a way to capture in the cavity trench, externally induced ingress and egress regions attributable to blade effects. In axial turbine literature, the author found more bespoke test sections for cavity flow analysis. If the objectives of cavity flow characterization differ from compression to expansion module, the experimental setup often uses the same means and philosophy. Two really interesting experimental setup are found in [7] and [8]. Experimental means used are such as: wall pressure taps (steady), wall pressure transducers (unsteady) in both cavity and main channel, concentration measurements, leakage injection control. Findings of these studies are eventually summarized in the review paper by [9] that covers the rotating flow induced perturbations generated in turbine rotor-stator cavities.

2. Context

Efforts made to predict and understand cavity leakage flow in turbomachinery through experimental investigation fulfilled the literature with test cases coming from either compressor or turbine applications. It results that a definition of the main flow structures generated in the rotor stator cavities is mandatory to draw conclusion on their impact inside and outside the cavity. From the author point of view, the design of a measurement setup eventually offers the possibility to propose validation data for CFD applications or low order modeling. Validation against existing experimental data is made on a regular basis. The update of the experimental data on existing test cases (thanks to the advancement in experimental means and post treatment strategies) is as important as the production of new challenge cases. For cavity leakage flows, the physics involved is highly unsteady and three dimensional. In the perspective of benchmarking numerical tools, the space time resolution of cavity modes is important. If unsteady data are highly valuable, time averaged radial gradients of cavity flow components are also key steps in the validation process (as done in the main channel). To the author knowledge no such measurement exists in the case of a rotating axial compressor test section. This study describes the experimental setup used to characterize cavity flow features in a high speed axial compressor research stage. The presented setup is set to be used to define the effect of cavity flows on axial compressor performance and stability. The measurement key points and strategy used are described. The guidelines for instrumentation design comes after the results obtained in [10] in a preliminary numerical investigation of the configuration.

3. Stage Configuration

The measurement setup presented here is designed for VKI high speed axial compressor test rig R4. The closed loop R4 facility is fully described in [10]. The main interest of the closed loop is that a complete flight envelope can be simulated in one rotation of the machine to address effects such as: Reynolds number effect; Rotational speed effect; Throttling transients...

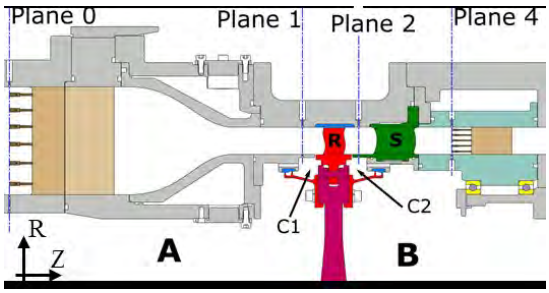

Figure 1: H25 test section, rotor(R) and stator(S) assembly. Plane 0 (bell mouth inlet); Plane 1 (Stage inlet); Plane 2 (Inter row plane); Plane 4 (Stage outlet). Identification of experimental planes, disk cavities A and B, and hub cavities C1 and C2

The test section investigated is the H25 high speed axial compressor stage (Figure 1). This stage is equipped with a shrouded stator configuration. Unlike multistage assemblies, the H25 stage do not present an under platform recirculation. The R4 loop being closed, the disk chambers (A and B) are closed to the atmosphere. In that extent, at fixed regime, the hub cavities (C1 and C2) behave as closed cavities. This

argument has eventually been verified through pressurization/depressurization cycles of the machine under rotation.

4. Objectives and Strategy

The instrumentation update of the H25 test section is made to assess the effect of cavity leakage flow on axial compressor performance and stability. To achieve such goal, focus is centered around the following items: Monitor the performance and stability of the stage, perform a deep investigation of the unsteady flow structures generated in the C2 cavity, identify the link between cavity flow structures and main channel flow through stator inlet boundary layer analysis, evaluate secondary flow system contribution of leakage flow in stator row. This analysis is performed at different operating conditions but also at different leakage conditions. The H25 test section is not a bespoke design for cavity flow investigation. The technical solutions retained are a compromise between the modification flexibility of the test section and the area of interest defined thanks to literature survey as well as preliminary studies results.

5. Performance and stability

The H25 stage performance and stability of the machine are evaluated for different leakage conditions. The performance, by means of pressure ratios, temperature ratios, efficiency, and mass flow are evaluated using rakes in measurement Plane 0 and Plane 4 (cf.Figure 1). In Plane 0, five spanwise rakes are equipped with both total pressure and total temperature kiel heads. In Plane 4, ten spanwise rakes are used for total pressure and total temperature measurements. In Plane 0, a 2.5 [Psi] pressure transducer is used whereas, in Plane 4, measurements are directed to a scanner with a full scale of 15 [Psi]. This choice is made to compromise between sensitivity, range and therefore uncertainty. The systematic uncertainty is of 0.08% of the full span, corresponding to 14 [Pa] and 82 [Pa] for the 2.5 [Psi] and 15 [Psi] transducers respectively. The inlet total pressure reference port is measured at the stagnation point of the test section inlet bell mouth by a high precision absolute pressure transducer, whose uncertainty is equal to 0,05% for a full span of 3[bar]. For the temperature measurements, Scanivalve DT3250 temperature scanners are used. The absolute temperature is reconstructed by means of four internal PT100 sensors. K-type thermocouples are used, leading to a systematic uncertainty value of 0.25 [K]. The dependency of the recovery factor to the yaw angle is evaluated following the calibration procedure in [11]. The typical fully propagated uncertainty level for the temperature recovery factor is in the order 0.02[K] for the corrected temperature. The total-to-total pressure ratio related uncertainty budget is estimated to be lower than 1% while the mass flow and the isentropic efficiency uncertainties are equal to 2.1% and 4% for a near-stall operating condition. The experimental campaign includes tests that purposely provoke machine failure (surge). Three high speed pressure transducers are inserted in the casing, upstream of the rotor leading edge at three different azimuthal positions. Their role is to track H25 pre stall and post stall behavior.

6. Cavity wall measurements

In the light of rotor-stator cavity literature, turbomachinery assemblies such as the one of H25-C2 produces complex flow regimes. The three dimensionality of the flow is such that instabilities propagate in the whole cavity volume. It is therefore easier to retrieve the cavity dynamics while measuring in one location only. However, with this approach it is more difficult to dissociate and identify the origin of the instabilities. Reader may refer to the study [12] as a good starting point on rotor stator cavity flows. In the aforementioned study, the preponderance of the instabilities born in the stator boundary layer (or Bdewadt layer) on the cavity dynamics is mentioned. The H25-C2 experimental setup update includes measurement at that location. The C2 cavity wall measurements are ensured by fast response pressure probes. The sensor used are Kulite XCQ-SL-062 pressure transducers. They are piezo resistive sensors of absolute range 25 [Psi]. The measurement device makes use of a membrane on which four strain gages are glued (silicium piezoresistors). When pressure is applied on the sensor diaphragm, the strain gages deform. It results in a variation of their electrical resistance. The equivalent circuit is a Wheatstone bridge in which the resistance unbalance maximize the voltage output of the circuit. The measured voltage output offset is then proportional to the pressure variation felt by the sensor. The sensors are mounted flush to the cavity wall thanks to special threaded brass inserts as shown by Figure 1.

Twelve inserts are distributed at several azimuthal positions as illustrated in Figure 3. Probe positioning

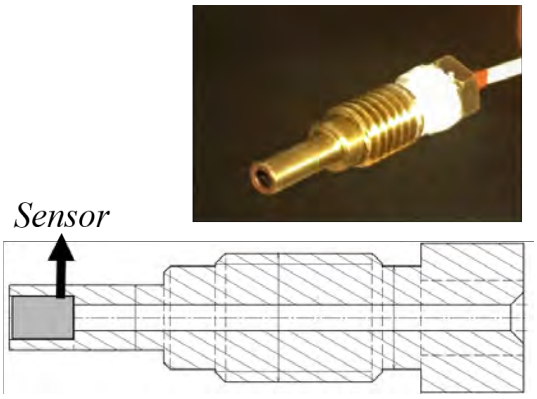

Figure 2: Sensor integration in brass insert

is selected such as cross correlation per sensor pair is done in the result analysis (see [8]). Spatial discretization is : the interval [5°:15°] is covered with steps of 5°; the interval [125°:60°] is covered in steps of 5°; [170°, 175°,180°] are covered. The rotor row is constituted of 65 blades, and so 65 platforms. The minimal spatial resolution of 5° is then chosen in order to cover a wide angle range as well as being smaller than one pitch (360/65 5.54[°]).

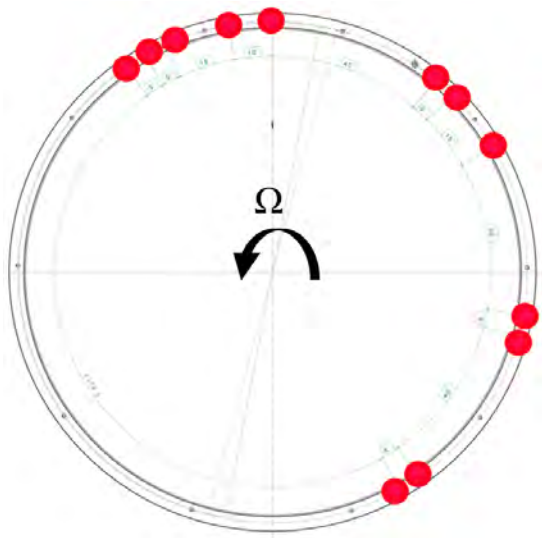

Figure 3: Fast response pressure inserts azimuthal positioning in stator hub cavity wall

The strain gages resistance variation is affected by the temperature changes of the media in which the sensor is immersed. The measurement chain includes an active compensation for the temperature. The principle described in [13] is that the sensor equivalent resistance is part of a Wheatstone bridge from whose voltage output is proportional to the temperature fluctuations. Figure 4 shows the two voltage output obtained from the measurement, Vp (function of pressure and temperature) and Vs (function of temperature only).

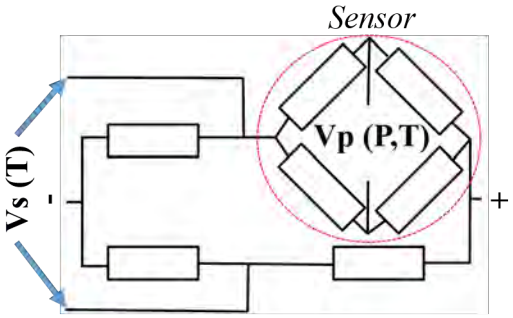

Figure 4: Active temperature compensation circuit for piezo-resistive transducers

Static calibration involves all the sensors. They are immersed simultaneously in a closed chamber where pressure and temperature are controlled. The calibration maps obtained for one of the probe are presented in Figure 5 and Figure 6. A fouth-order polynomial fitting is applied to retrieve the Vp and Vs contribution to pressure and temperature.

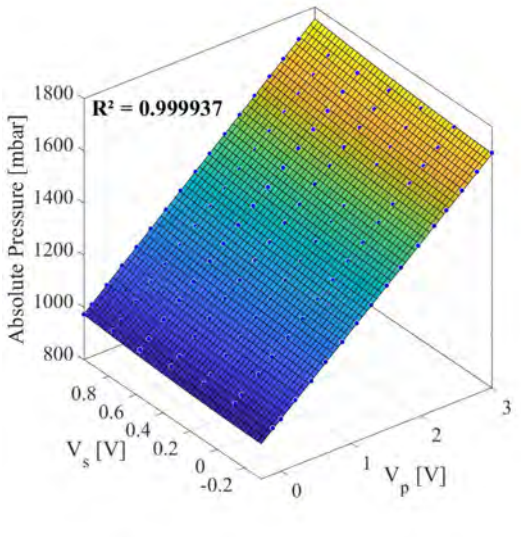

Figure 5: Pressure fitting for one piezo resistive sensor Fitting error is indicated by R^2

The calibration uncertainty computation is performed according to the procedure presented in [14]

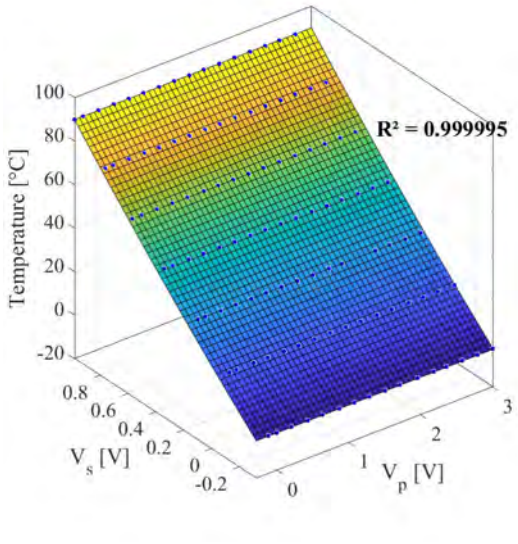

Figure 6: Temperature fitting for one piezo resistive sensor Fitting error is indicated by R^2

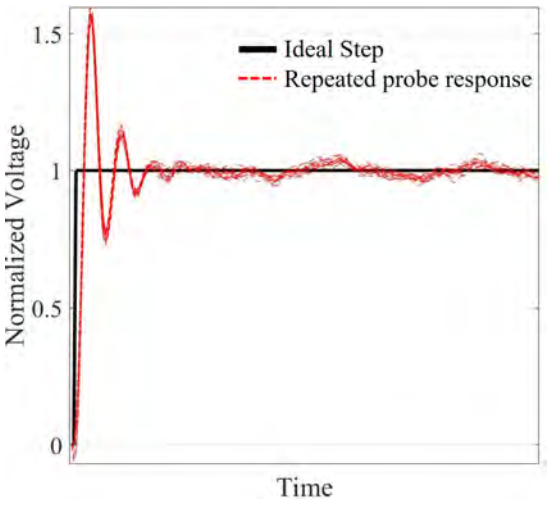

Figure 7: Kulite insert voltage output (Vp) response to fourteen pressure steps after filtering / normalisation/ windowing Sampling frequency of 1[MHz]

and [15]. For the twelve sensors, the maximal average fully propagated uncertainty (i.e. taking into account calibration uncertainty and measurement uncertainty) is of P = 4.3 [mbar]. The dynamic response of the inserts is evaluated to apply a correction on the measured raw signals. The natural frequency of the bare sensor used is of 240[kHz]. To estimate the response to a pressure step of the insert, the Von Karman Institute shock tube is used. More details of the facility and method are available in [16] and [17]. Sensors are positioned to mimic the final experimental setup, which implies a flush mount to the shock tube wall section. The response to one pressure step of 200[mbar] sampled at 1[MHz] is repeated

Figure 7 presents the repeated Vp response of one insert to fourteen pressure steps. From the raw signal, digital filtering is applied with a cut off frequency of 120[kHz] to damp perturbations linked to sensor resonance. The signal is normalized (0: value at test beginning; 1: value at test end). The signal is cut after the dynamics of the probe has been excited to remove traces of post shock disturbances in the spectral domain. To finish, signal is elongated with the mean voltage value to obtain the desired spectral resolution and a half Hamming window is applied at the elongation point to create a periodic signal. Averaging is performed in the frequency domain and sensor transfer function is established with respect to the ideal step visible in Figure 7. The experimental transfer function identification is performed with a linear second order system. The amplitude and phase from the experimental data as well as the model fitting are presented in Figure 8. The average estimated natural frequency of the cavity inserts is of 73[kHz] and the non-dimensional damping evaluated from half power is of 0.21.

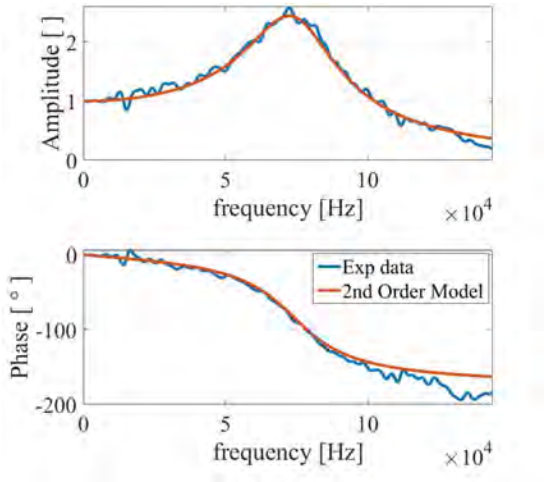

Figure 8: Three-hole virtual fast response pressure probe transfer function Second order linear model identification

7. Cavity wall measurements

The H25 stator platform is also modified to offer radial traversing measurements in the C2 cavity in three

azimuthal positions. The modification is illustrated in Figure 9 in which a probe is maintained in its lowest position in the stator shroud cavity. Cylindrical probes that are designed specifically for the test campaign are used. An example is given in Figure 10 in which the probe is traversed through the stator platform. The traversing system of the facility has been re-designed to allow yaw control of the probes on top of the existing radial traversing capabilities.

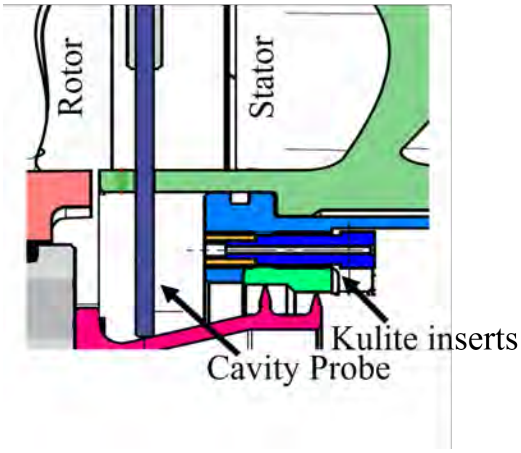

Figure 9: Instrumentation layout in C2 cavity



Figure 10: Cylindrical probe install through stator platform

Pressure and temperature measurements are used. Pressure measurements are performed by mean of an unsteady and a steady virtual three hole probes [14]. The fast response pressure probe is designed around a Kulite XCQ-SL-062 pressure transducer that has been introduced in the previous section cavity wall measurements. The sensor is mounted perpendicular to the flow in the probe stem as illustrated by Figure 11. With that design the author miniaturized the probe as much as possible. Nevertheless, when fully immersed in the cavity (cf. Figure 9), the probe still occupies 8.5% of the cavity cross section. The static calibration of the probe follows the same methodology as presented before. The maximal uncertainty of the pressure measurement is of P =4.8 [mbar]. Sensor integration is made to affect as less as possible the dynamic response of the probe. The line-cavity system presented in Figure 11 is designed to maximize the frequency response. The reader should refer at [18] to have an in depth view of the high impact of probe cavity design on one sensor fast response pressure probes.

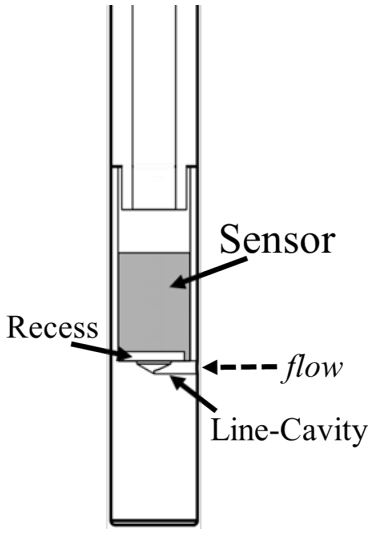

Figure 11: Fast response three-hole virtual probe side cut view sketch



Figure 12: Fast response three-hole virtual probe front view

The design chosen has been evaluated thanks to an-

alytical model predictions of the natural frequency. The model used are the model of Hougen [19] and the Bergh and Tijdemann model [20]. The model of Hougen considers the compressibility effects that arises from the line volume being comparable with the probe cavity volume. Since the presented probe has a line aspect ratio of 0.3 (<1) (line diameter over length), the Bergh and Tijdemann model is implemented to model the sinusoidal fluctuations in the line-cavity probe system. In Table 1, analytical model results are indicated. The effect of the probe recess is also referenced to indicate the important impact that probe manufacturing and assembly has on the system response. The target for the design is to guarantee a natural frequency response at zero recess of at least seven times the blade passing frequency that is at BPF=10.5[kHz]. Once manufactured, the probe undergoes pressure step response in VKI shock tube as described in [16]. After multiple testing, the identification of the probe transfer function fails at reproducing results in agreement with the analytical model used for its design. The evaluated natural frequency is of 9[kHz] which lies under the blade passing frequency of H25 at nominal speed. The author is still investigating the reason for such discrepancy.

Table 1: Analytical model prediction of three-hole virtual fast response pressure probe natural frequency Effect of membrane recess.

Recess Depth $[mm]$	$\Omega_n - Hougen$ [19] $[kHz]$	$\Omega_n - Bergh$[20] $[kHz]$
0	77.3	71.5
0.1	44.9	38.8
0.2	34.9	29.5
0.3	29.5	24.8

The pressure measurement also includes a pneumatic pressure probe whose design is directly taken the aforementioned fast response pressure probe. The pneumatic three-hole virtual probe is connected to a 5[Psi] pressure scanner whose systematic uncertainty is given for 0.08[%] of the full span. The use of virtual three hole probes allow flow angle measurements in the cavity. Angular calibration (Mach,Yaw) is performed using Dantec Streamline Pro Automatic Directional Calibrator. For the presented probes, the calibration ranges are the following ones: from M = 0.1 to M = 0.5 by steps of 0.1 for the Mach number; from -80[°] to +80[°] by steps of 1[°] for the yaw angle. On Figure 13 is showed the Vp voltage output obtained for the fast response pressure probe at a Mach number of M = 0.5. The voltage is maximal when the aerodynamic zero angle is reached between the jet and the probe hole. The central hole curve is duplicated and translated in order to generate the voltage output given by virtual left and right holes for a chosen hole spacing. Figure 13 illustrates for Mach 0.5 the output of the left, central, and right holes for a defined hole spacing of 30[°]. The reader may note that the left and right hole signals do not intersect perfectly on the 0[°] line. This is induced by the mechanical offset between the reference surface used in the probe positioning with the effective aerodynamic zero-degree angle.

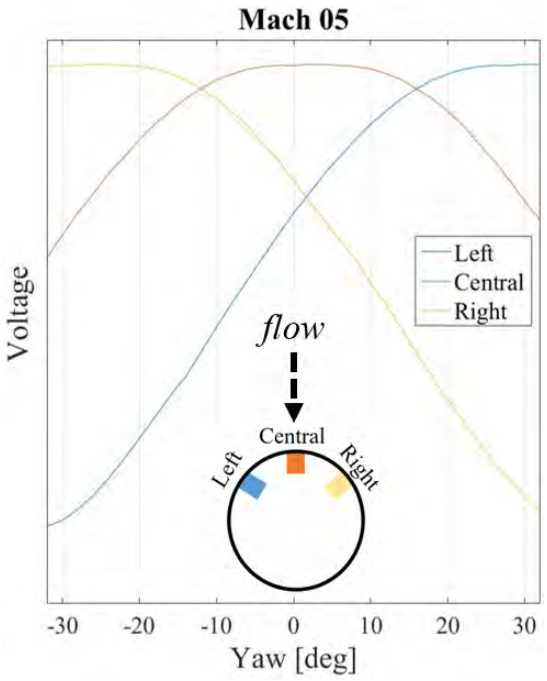

Figure 13: Left, central, and right hole voltage output for the three-hole virtual fast response probe at Mach = 0.5 hole spacing of 30[°]

Aerodynamic coefficients K_{Yaw}, K_{Pt}, K_{Ps} defined in equations 1, 2, and 3, are computed. Pleft, Pcentral, Pright, indicates the pressure measured by left, central, and right hole respectively. Ps and Pt are the static and total pressure of the calibration jet. In the experimental campaign these coefficients are used in an iterative procedure [17] to retrieve total pressure, static pressure, Mach number, and flow angle. The Figure 14 presents the K_{Yaw} aerodynamic coefficients for the three-hole virtual fast response pressure probe

for a hole spacing of 30[°].

$$K_{Yaw} = \frac{P_{Left} - P_{Right}}{P_t - P_s} \quad (1)$$

$$K_{Pt} = \frac{P_t - P_{Central}}{P_t - P_s} \quad (2)$$

$$K_{Ps} = \frac{P_s - 0.5*(P_{Right} + P_{Left})}{P_t - P_s} \quad (3)$$

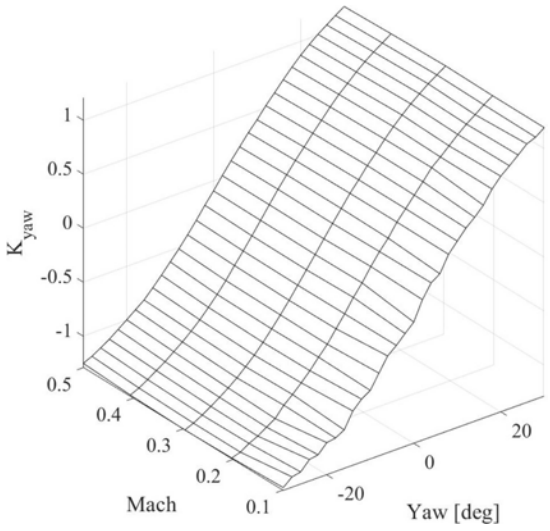

Figure 14: K_{Yaw} Aerodynamic coefficient for three-hole virtual fast response pressure probe

Temperature measurements are performed in the C2 cavity by means of a K-type thermocouple. The probe head built around the junction acts first as a shield to protect the junction in the traversing process but also isolate the sensor from the highly unsteady environment of the C2 cavity. The temperature probe presented in Figure 15 and Figure 16 is connected to the existing temperature scanner mentioned in the *Performance Stability section*.

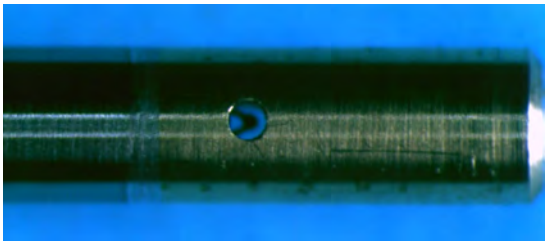

Figure 15: Shielded thermocouple front view

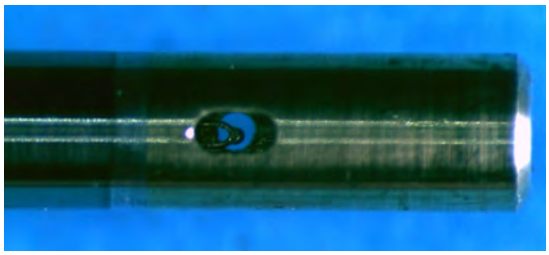

Figure 16: Shielded thermocouple back view

The use of directional probes is challenging in an environment such as the one of the C2 cavity. The measurement strategy for the test campaign consist in positioning the probes in the average flow angle direction for each operating condition. To find the average angle profile, the pneumatic pressure probe is used and measures along an azimuthal grid that ranges between ±60[°] at every radial position in the cavity. This operation is repeated for all the conditions investigated. The angular position that indicates the maximal voltage output is defined as aerodynamic zero-degree angle for the actual radius. Average angle profile are used to limit the number of points to be taken in the experimental campaign. The temperature measurements are performed in the average flow direction. The pressure measurements are then limited to three points per radius (to compute flow angle three hole virtual) whose central hole aligned with the average flow direction.

8. Stator hub inlet boundary layer measurements

The data that are collected in the H25-C2 cavity are put into perspective thanks to main channel measurements. The first location in which cavity flow effects are expected is the stator inlet hub boundary layer. One of the specificity of the H25 stage is that rotor-stator axial spacing is large. In Plane 2, the stator blade potential effect is limited. The preliminary numerical results even highlight no trace of stator potential effect in the C2 cavity trench. Limited stator potential effect is beneficial for results analysis since the azimuthal locations investigated are all clocked at the same position with respect to the stator row. The instrumentation presented in section *Cavity main volume measurements* is used for the boundary layer measurements. As visible in Figure 12 and Figure 15, the specific shape of each probe head allows to perform measurement in the main channel while ensuring sealing of the stator hub platform. The distance from the probe measurement point to the bottom

of the probe head is selected to overlap with existing traversing data from previous experimental campaign. The overlapping interval ranges between 2% and 12% span. To remove totally the traversing probes from the C2 cavity is also interesting to remove probe induced effects in cavity wall measurements. The objectives are to identify traces of the C2 unsteady cavity flow in the main channel as well as evaluate the effect of cavity leakage flow on boundary layer skewness.

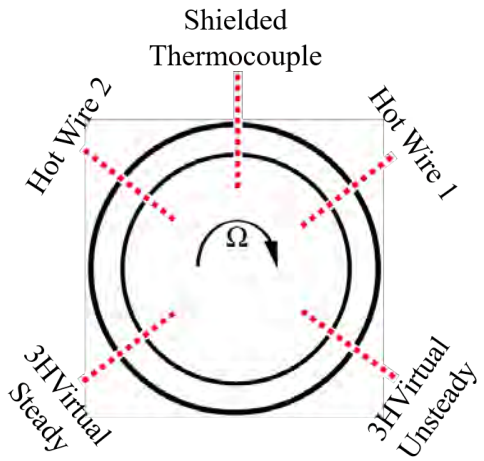

Figure 17: Experimental Plane 2 traversing probe disposition around H25 test section annulus

The remaining two azimuthal positions available for probe traversing are used to perform hot wire anemometry (Figure 17). Single wire, one straight needles and one L-shaped needles with an active sensor length of 1[mm] are used. In the present experimental campaign, constant temperature anemometry (CTA) is used. The use of CTA removes thermal inertia on the measurement but fluctuations of the flow temperature affect flow velocity estimation. Computed flow turbulence statistics are then biased by temperature effects. To reduce temperature effects the wire temperature is kept as high as possible within the oxidation limit of the material used. To account for temperature effects in the measurements, non-dimensional calibration approach described in [21] is used. It links the bridge voltage ouput to the wire Nusselt number (Nu) that is then expressed as a function of Reynolds number (Re) and Mach number of the flow. The calibration is performed using Dantec Streamline Pro Automatic Directional Calibrator. The calibration curves for different jet temperature and Mach number (from M = 0.1 to M = 0.55) at reference angular position are presented in Figure 18. In the (Re,Nu) system, all the curves collapse on one fitting line. With the non-dimensional approach, the calibration is performed in the operational Reynolds number range. To use the fitting from the calibration, total temperature and total pressure of the flow as well as static pressure and wire voltage must be recorded in the experimental campaign. These variable allow to retrieve local Nusselt and Reynolds number.

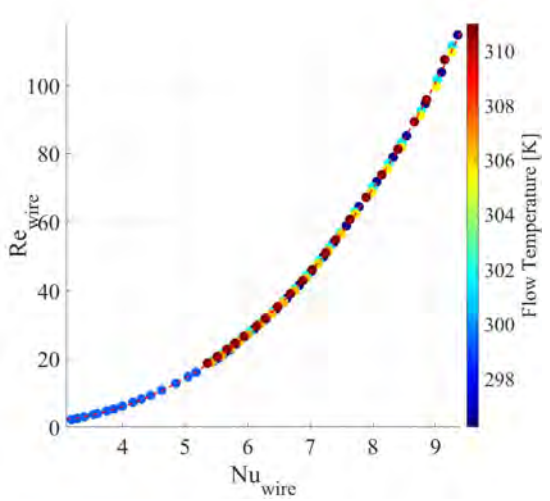

Figure 18: Nu-Re calibration for one sensor straight hot wire Flow temperature and Mach number dependency Temperature effects

The hot wires are aligned with the average flow angle following the method presented in the last section *Cavity main volume measurements*. It is also possible to deduce flow angle information from the hot wire measurement by extracting the effective Reynolds number. The effective Reynolds number is the one that give the same Nusselt number when the sensor is orthogonal to the flow in the case of the single sensor hot wire presented. The probe is calibrated for the angle in a range of ±80[°]. The angular calibration map is created such as the wire behaves like a virtual 2 wire probe. As an example, Figure 19 indicates the angular dependency of effective Reynolds number for virtual wires at plus ±30[°] from the reference angle direction. R_{eff1} and R_{eff2} are the effective Reynolds number for each angular direction. The ratio R_{eff1}/R_{eff2} is plotted on Figure 20 and allows to retrieve the flow angle from the experimental data independently from the Mach and Reynolds number.

The investigation of the boundary layer with CTA is also limited by conduction induced effects and probe blockage induced effect when the hot wire gets closer

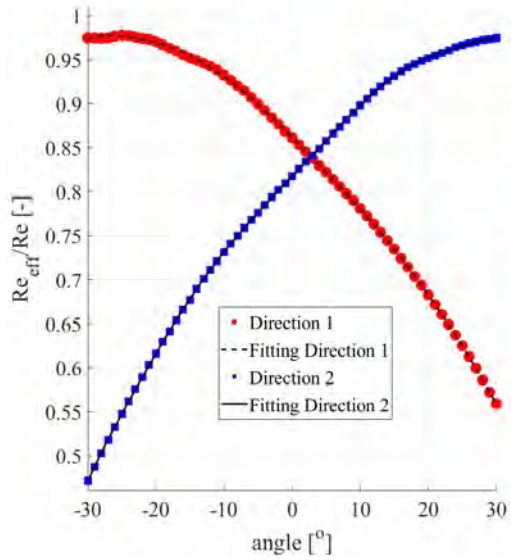

Figure 19: Angular calibration for virtual two sensors hot wire probe with angular clocking of 30[°] Effective Reynolds number at Mach = 0.4

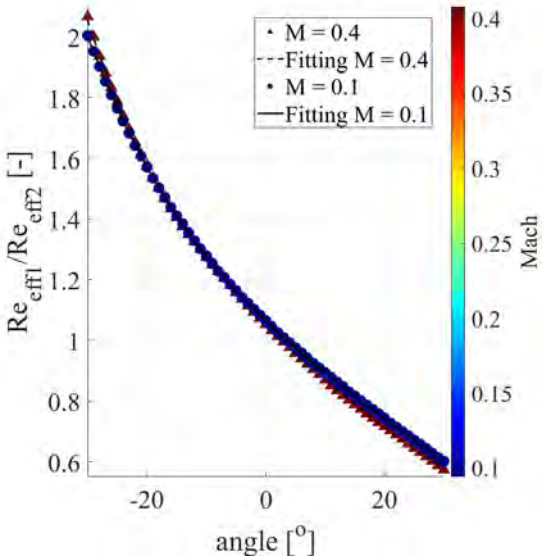

Figure 20: Angular dependency of effective Reynolds number ratio at varying Mach number

to the wall. The minimal span wise value measured is set at the non dimensional wall distance (y^+) where the turbulent boundary layer profile departs from the log law or from the viscous sublayer law.

9. Leakage flow control

An injection port is added at the back of the test section as illustrated by Figure 21. Pressurization of the adjacent disk volume (cavity B in Figure 1) generates leakage flow through the C2 labyrinth seal. The injection line prior to the port is composed with two sonic orifices in parallel. Multiple diameter orifices combined with maximal pressure supply of 40 [bar] allow to tune the mass flow injected in the disk cavity and pressurize it without exceeding the maximal axial load accepted by the disk bearings. From the compressed air supply to the main channel, 2[Hz] sampled instrumentation is present to compute the mass flow injected. Figure 21 informs on the measurement available along the injection line.

Section restrictions along the injection flow path determine the mass flow injected in the C2 cavity. Aside from sonic orifice and injection line section, the labyrinth seal gap is also a parameter to consider. The labyrinth seal gap is varying as a function of the operating conditions of the machine. The original design, made to avoid leakage flow, uses abradable tracks in which labyrinth teeth rub to generate as less clearance as possible. The abradable tracks are measured thanks to sections molding at two azimuthal positions. Sections of abradable molding are presented in Figure 23. The molding present two traces from the labyrinth seal. This is due to multiple dismount and assembly of the rotor ring. Labyrinth teeth displacement are summarized in Table 2 for the sections investigated. The data from the double tracks are averaged since the maximal difference in track height is of 0.05[mm].

The labyrinth seal opening is a function of the centrifugal force on the disk, the temperature of the material and the pressure forces acting on the disk wall. A Finite Element Method computation of the disk ring is performed to establish the link between labyrinth opening and disk cavity pressure at running conditions. Open source Calculix software is used at such extent. The operating condition for the rotor is the design point at nominal speed. The H25 stage never rotated above nominal speed. That is why, the results are also compared with the molding measurements that indicates the maximal labyrinth radial displacement. The boundary condition used are presented in Figure 24. The temperature condition is the temperature obtained in the disk cavity (cf Figure 21 station 4) after thermal stabilization of the stage. The pressure 1 condition is imposed equal to the static pressure measured at hub between rotor and stator row. Pressure 2 (Ps2) condition is changed between the static pres-

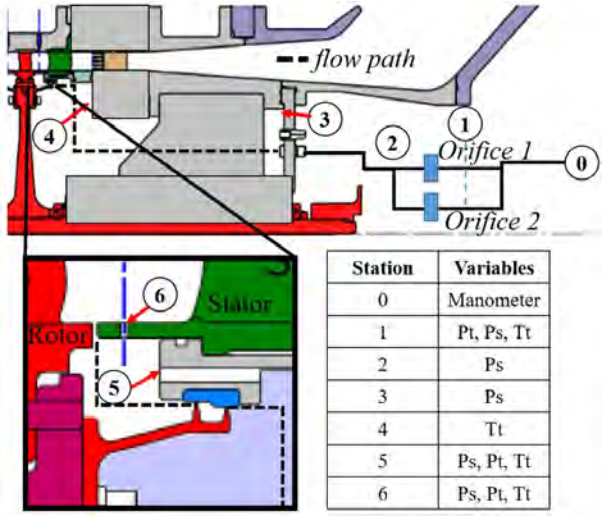

Station	Variables
0	Manometer
1	Pt, Ps, Tt
2	Ps
3	Ps
4	Tt
5	Ps, Pt, Tt
6	Ps, Pt, Tt

Figure 21: H25 injection line and measurement stations for leakage flow quantities evaluation

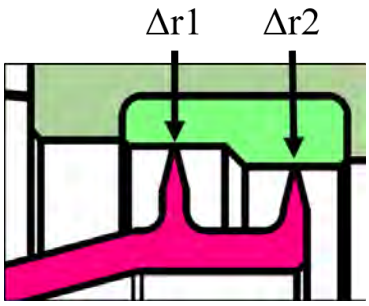

Figure 22: H25 labyrinth seal configuration

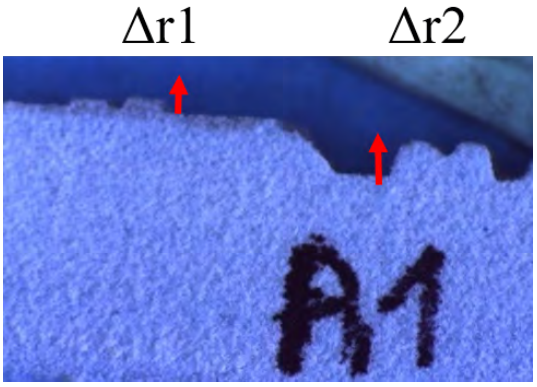

Figure 23: Example of abradable molding section cut

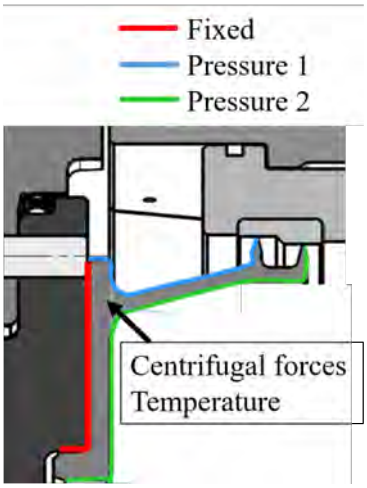

Figure 24: Boundary conditions applied in the FEM analysis

sure measured in the stage outlet at design condition (baseline) and a pressure ratio of 3.5 with respect to the stage inlet total pressure (Pt0). As indicated by Table 2 for the baseline case, the r1 value is comparable with the molding measurements with an error of 0.04[mm] when the r2 value is underestimated by 45%. This can be explained with the computation not including teeth/abradable rubbing effects on temperature and material integrity. Nevertheless, the results on the trend of labyrinth closing with the disk cavity pressure increase are presented in Figure 25.

10. Conclusions

This paper objective is to present the experimental setup for shrouded stator cavity flow characterization in high speed axial compressor facility. The VKI H25 test section received an instrumentation upgrade in order to draw conclusions on the effect of cavity leakage flow on axial compressor performance and stability. The H25-C2 cavity combination has not been designed on purpose to study cavity leakage flow. However, stage performance evaluation by means of 0D parameters is possible with the already existing instrumentation. Efforts has then been put into selecting and developing instrumentation to fully characterize H25-C2 cavity average and unsteady flow features. Fast response pressure transducers in stator wall as well as pressure and temperature probe traversing in the cavity main volume at three azimuthal positions serve such purpose. H25 stator inlet hub boundary layer is also investigated to identify (or not) traces of the leakage flow average and unsteady contribution to the main channel stream. This data are meant to justify the performance and stability impact of cavity leak-

Table 2: Labyrinth teeth displacement contribution of centrifugal forces, temperature and pressure at H25 design operating conditions, nominal rotor speed

Test Conditions	$Ps2/Pt0$	$\Delta r1$ [mm]	$\Delta r2$ [mm]
Moldings	x	0.308	0.700
FEM-Baseline	1.20	0.262	0.380

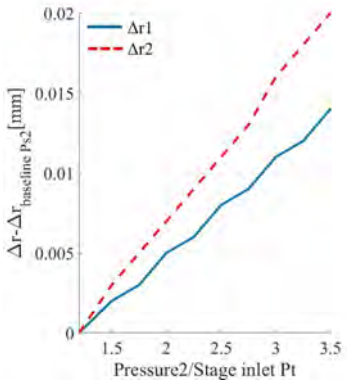

Figure 25: Labyrinth teeth displacement from baseline pressure case in function of disk cavity pressure- design operating condition, rotor nominal speed

age flow in axial compressors. A controlled injection system has been added to the facility in order to pressurize the disk adjacent cavity. The generated pressure difference across the labyrinth seal produces controlled leakage flow conditions. The leakage flow conditions are tuned from the information retrieved from the instrumentation along the injected flow path.

References

[1] S. Yoon, R. Selmeier, P. Cargill and P. Wood, Effect of the Stator Hub Confguration and Stage Design Parameters on Aerodynamic Loss in Axial Compressor, *ASME Turbo Expo GT2014-26095*.

[2] S. R. Wellborn, T. H. Okiishi, Effects of Shrouded Stator Cavity Flows on Multistge Axial Compressors Aerodynamic Performance, Tech. Rep. NASA CR 135391, NASA Lewis Research Center (1996).

[3] D. W. Sohn, T. Kim, and S. J. Song, Influence of the Leakage Flow Tangential Velocity on the Loss Generation and Leakage Flow Kinematics in Shrouded Axial Compressor Cascade, *ASME Turbo Expo GT2006-90979*.

[4] A. A. J. Demargne and J. P. Longley, The Aerodynamic Interaction of Stator Shroud Leakage and Mainstream Flows in Compressors, *ASME Turbo Expo* $2000_G T_5 70$.

[5] Taylor, D. J., Longley, J. P., Effects of Stator Platform Geometry Features on Blade Row Performance, *Journal of the Global Power and Propulsion Society, 3, 609-629*.

[6] Auchoybur, K., Miller, R. , The sensitivity of 3D separations in multi-stage compressors, *Journal of the Global Power and Propulsion Society, 2, 329-343*.

[7] S. S. Savov, N. R. Atkins, and S. Uchide, Comparison of Single and Double Lip Rim Seal Geometry, *ASME Turbo Expo GT2016-56317*.

[8] P. F. Beard, F. Gao, K. S. Chana, J. Chew , Unsteady Flow Phenomena in Turbine Rim Seals, *Journal of of Engineering for Gas Turbines and Power, Vol. 139, 032501-1:10*.

[9] J. W. Chew, F. Gao, D. M. Palermo, Flow Mechanisms in Axial Turbine Rim Sealing, *Journal of Mechanical Engineering Science, Vol. 233(23-24) 7637-7657*.

[10] C. Babin, M. Dumas, X. Ottavy, F. Fontaneto, Numerical Characterization of a HP Compressor Stage Equipped with a Closed Shrouded Stator Cavity, *Journal of Turbomachinery,*.

[11] Fontaneto F. and Lahalle A., Highly Reliable Aerodynamic Calibration For Ground And Flight Testing Total Temperature Probes, *XXIII Biannual Symposium on Measuring Techniques in Turbomachinery Transonic and Supersonic Flow in Cascades and Turbomachines*.

[12] E. Serre, E. Crespo del Arco, P. Bontoux, Annular and Spiral Patterns in Flows Between Rotating and Stationary Discs, *Journal of Fluid Mechanics, vol. 434, pp. 65-100*.

[13] J. F. Brouckaert, Development of fast response pressure probes for time resolved measurements in turbomachines., *Diss. Ph. D. thesis Von Karman Institute of Fluid Dynamics*.

[14] G. Dell'Era, M. Mersinligil, J. F. Brouckaert, Assessment of Unsteady Pressure Measurement UncertaintyPart II: Virtual Three-Hole Probe., *Journal of Engineering for Gas Turbines and Power 138.4*.

[15] Test Uncertainty, Tech. Rep. ASME PTC 19.1-2005, The American Society of Mechanical Engineers (2005).

[16] E. Boufidi, M. Alati, F. Fontaneto, S. Lavagnoli, Design and Testing of a Miniaturized Five-Hole Fast Response Pressure Probe with a Large Frequency Bandwidth and High Angular Sensitivity., *ASME Turbo Expo GT2019-90470*.

[17] P. Gaetani, G. Persico, Technology Development of Fast-Response Aerodynamic Pressure Probes., *International Journal of Turbomachinery Propulsion and Power 2020, 5, 6*.

[18] G. Persico, P. Gaetani, A. Guardone, Design and Analysis of New Concept Fast-Response Pressure Probes., *Measurement Science and Technology. 16(2005) 1741-1750*.

[19] J. O. Hougen, O. R. Martin, R. A. Walsh, Dynamics of Pneumatic Transmission Lines, *Control Engineering, 10, pp. 114-117*.

[20] Bergh, H., and Tijdeman, H, Theoretical and experimental results for the dynamic response of pressure measuring systems., Tech. Rep. F.238, NLR-TR (1965).

[21] B. Cukurel, S. Acarer, T. Arts, A novel perspective to high-speed cross-hot-wire calibration methodology., *Exp Fluids (2012) 53:1073-1085*.

The Role of Turbulence Length Scales on the Aerodynamics of Internal Flow Passages

Federico Bertelli

Turbomachinery and Propulsion Department, von Karman Institute for Fluid Dynamics, Belgium, federico.bertelli@vki.ac.be

Supervisor: Sergio Lavagnoli

Associate Professor, Turbomachinery and Propulsion Department, von Karman Institute for Fluid Dynamics, Belgium, lavagnoli@vki.ac.be

University Supervisor: Koen Hillewaert

Associated Professor, Aerospace & Mechanical Department, University of Lige, Belgium, koen.hillewaert@uliege.be

Abstract

The continuous demand for improving performance and efficiency of modern turbomachinery still motivates research communities to intensify the aerodynamics research efforts. One prominent factor that limits the current knowledge is the role of turbulence. While relevant numerical and experimental evidences have demonstrated the strong influence of the freestream turbulence intensity, the role of length (and time) scales on the flow physics of blade-passage flows, is still scarcely documented in the open literature. Much has been learned from the work to date, but the complex spatio-temporal nature of the turbulence length scales interactions with the flow dynamic mechanisms are still not completely clear, and existing models are still not as robust as needed for accurate flow predictions. Presently, the individual role of turbulence scales is far from being fully comprehended and it is recognized to represent one of the main sources of uncertainty and impediment to properly characterize, model and predict the fluid dynamic mechanisms in blade-passage flows.

The current research aims at filling this critical shortage, seeking to answer the question: how does turbulence length scale variation affect the aerodynamics of blade-passage flows, and ultimately, does it play a crucial role in loss generating mechanisms? A combination of experiments and CFD simulations is used to investigate the 2D/3D fluid dynamic mechanisms arising in bladed internal flows exposed to a wide set of both freestream turbulence levels and inflow operative conditions. Linear turbine cascade, representative of modern low-pressure turbines, is tested in the VKI low-speed C-1 test rig, heavily instrumented to allow a full-field space- and time-resolved characterization of aerodynamic fields. A new modular turbulence generator is firstly designed and implemented in the C-1 test facility, allowing to generate turbulent flows able to discern the individual role of length scales from that of free-stream turbulence intensity. In support of experimental investigation, CFD computations (RANS, URANS, ILES and DNS) are performed on few selected test cases, providing in-depth analysis of physical mechanisms to benefit the development of physically-based predictive models that account for turbulence scale effects to predict the flow mechanisms. The experimental and numerical data serve to create an unprecedented database essential for advancing turbulence modeling, CFD practices and design methods.

Keywords: Turbulence Generator, Internal flows, Turbulence Length Scale, Turbulence, Low-Speed Linear Cascade, Low-Pressure Turbine, CFD, Fluid Dynamics

INSTRUMENTATION AND MEASUREMENT TECHNIQUES

Monitoring of flow mechanics in cohesive sediment layers

Bart Brouwers

Flanders Hydraulics Research (FHR), Belgium, Bart.brouwers@mow.vlaanderen.be

Supervisor: Jeroen van Beeck

Professor, Environmental and Applied Fluid Dynamics Department, von Karman Institute for Fluid Dynamics, Belgium, vanbeeck@vki.ac.be

University Supervisor: Evert Lataire

Professor, Department of Civil Engineering, Maritime Technology Division, Ghent University, Belgium, Evert.Lataire@UGent.be

Abstract

Evaluation of fluid dynamics in cohesive sediment (mud) is currently a challenge. Applicable visualization techniques are unknown and reproduction of tests is problematic due to the changing properties of mud over time. This research has the objective to customize known visualization techniques for use in mud and establish a procedure to condition mud to enhance reproduction of experimental tests.

Keywords: cohesive sediment, flow visualization, mud, opaque, reproduction, velocimetry

1. Introduction

The nautical bottom is a term used in the nautical community to define the critical water depth for ships in navigation areas. In 1997 the concept was introduced by PIANC (The World Association for Waterborne Transport Infrastructure) as "the level where physical characteristics of the bottom reach a critical limit beyond which contact with a ships keel causes either damage or unacceptable effects on controllability and manoeuvrability". In case of sand or rock bottoms the depth of the nautical bottom level is straightforward. When cohesive sediment layers (mud) form on the bottom of the navigation areas, there is however no clear physical limit which determines the applicable nautical bottom. Nonetheless, the presence of such muddy layers can influence the maneuverability and controllability of ships, even when the keel of the ship does not penetrate these layers [1].

Due to the complex interactions between ship, mud and water layers, the use of Computational Fluid Dynamics (CFD) models is preferred by nautical researchers to facilitate research on the influence of a mud layer on a ships' maneuvering behavior [2]. Development of such CFD models requires validation data, preferably generated by physical laboratory tests using natural mud. The complexity here is the lack of techniques capable of visualizing flow mechanics and measuring velocities within the range of 0–2m/s, in real natural mud layers. Furthermore it is the experience at Flanders Hydraulics Research (FHR) that due to the changing properties of mud in time, the use of natural mud, even in controlled conditions of a laboratory environment, proofs to be a challenge with regard to reproduction of the generated data. In search of confirmation of this experience, a literature survey was conducted [3], concluding that the reproducibility of similar consolidation tests of mud is hardly discussed. In most literature only an affirmation of the reproducibility of the tests is mentioned without further substantiation. Only [4] presented results indicating the reproducibility of tests and confirmed reproducibility issues for mud with a density greater than 1.08 g/cm^3. These results are however solely based on visual observation of the tests and not quantified.

The objective of this research is to make physical laboratory tests using natural mud a valuable tool for other research by finding the means to overcome these two major deficiencies.

Nowadays, Particle Image Velocimetry (PIV) is considered to be the state-of-the-art technique for flow visualization and flow velocity measurement in laboratory experiments [5]. The ability of PIV to ana-

lyze the fluid dynamics over an entire area simultaneously and without intrusive probing is a great advantage with regards to efficiency and quality compared to classic point measurements. Conventionally a laser is used to visualize (seeded) particles in the fluid, enabling the recording of their movement over time [5]. However, even at low densities, mud is highly opaque which renders the use of lasers or any other optical illumination sources useless. Hence an alternative method needs to be found which enables the visualization of particles in the mud, on which PIV algorithms can be applied, resulting in the visualization of flows and determination of flow velocities. By means of a literature survey, different promising visualization techniques were identified and evaluated using small-scale experiments. This resulted in the selection of a technique which showed great potential. A more in depth study of this technique was performed to stipulate future experiments enabling customization for the intended application on mud.

To improve the reproducibility, a procedure will be developed describing how to condition natural mud. Like for all other fluids, the behavior of mud depends on characteristics like density and viscosity. The challenge with natural mud is however that these characteristics change over time due to settlement and consolidation [6]. Assuming that the changes of these properties over time are reproducible when these properties are initially equal, the ability of the conditioning procedure should be to create such a reference point of the mud properties. A note should be made here that the behavior of mud depends on more properties than only density and viscosity, as discussed in [6]. However, like with the determination of the nautical bottom on site [7], due to practical reasons the focus during this research is on density only. With regards to the conditioning of mud, emphasis is mainly on the applied mixing technique. From a literature survey, different mixing techniques were selected and their influence on the reproducibility of the mud consolidation process evaluated by conducting several small-scale consolidation tests.

2. Flow visualization in mud

2.1. Potential techniques

In search of potential techniques for the visualization of flows in mud, inspiration was particularly found in the medical sector because of similar implications as opacity of human tissue and the preferred avoidance of probing. After a first high level evaluation concerning applicability in a typical hydraulic research setup and costs, radiography and ultrasonography were retained as potential techniques. The main difference between both techniques is related to the propagation path of the applied energy through the mud layer, as illustrated in Fig. 1.

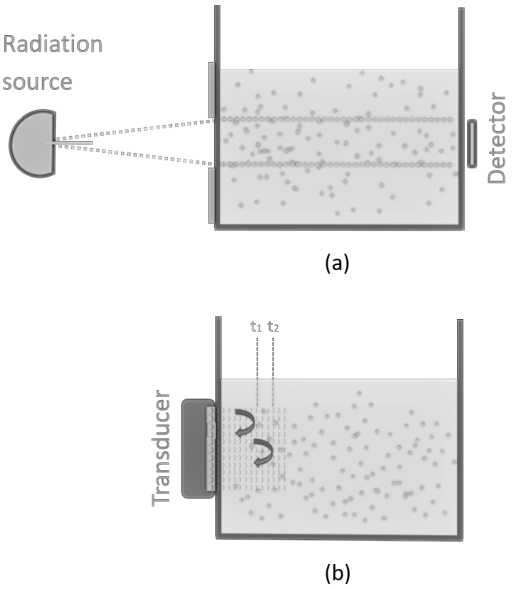

Figure 1: (a) setup for radiography requiring full penetration; (b) setup for ultrasonography based on reflection of signals

Visualization with radiography is based on a difference in absorption of the radiation. When the particles in the fluid absorb more radiation compared to the surrounding fluid, they will appear as shadows on the image. As a consequence, full penetration of the mud layer by the radiation is required. Visualization using ultrasonography on the other hand is based on the difference in acoustic impedance of particles compared to that of the fluid. This difference will cause reflection of the transmitted ultrasound waves by the insonified particles. These reflection signals are recorded back by the transducer and represented as a function of brightness on the screen. The stronger the echo signal the brighter the reflecting particle will appear on the screen. Hence, full penetration of the mud layer is not required allowing minimization of the propagation path of the waves and intensity loss.

A first more detailed evaluation of these two potential techniques concerned the attenuation of the transmitted energy by mud. The physics of attenuation for both can be expressed with the Beer - Lambert law:

$$I_L = I_0.e^{(-\mu.l)} \tag{1}$$

With

I_L: intensity after propagation over distance l
I_0: initial intensity
l: propagation distance through the medium
μ: attenuation coefficient of the radiated medium

The attenuation coefficient is obviously different for each type of radiation. In case of electromagnetic waves the attenuation coefficients are more or less stable resulting in extensive databases in which the attenuation coefficient of chemical elements, compounds or common mixtures can be found in function of the energy of the electromagnetic waves. The attenuation of ultrasound however, is highly dependent on the origin of the medium, [8]. It is therefore recommended that attenuation coefficients for ultrasound are determined experimentally for each case. Consequently available values of ultrasound attenuation coefficients of materials in literature are rather sparse.

2.2. Radiography

By means of a chemical element analysis using the Inductive Coupled Plasma - Optical Emission Spectrometry technique (ICP-OES), the different compounds and their weight fractions have been determined for 3 mud densities: 1.035 g/cm^3, 1.100 g/cm^3 and 1.200 g/cm^3. The attenuation coefficients for high energetic electromagnetic waves of each of these compounds can be found in databases such as that from the National Institute of Standards and Technology (NIST) which is freely accessible. With this input the attenuation coefficient of mixtures, such as mud, at different densities and in function of the energy of the radiated electromagnetic waves can be determined using the so-called "mixture rule" as presented in [9]:

$$\left(\frac{\mu}{\rho}\right)_{mix} = \sum_{i=1}^{N} \omega_i . \left(\frac{\mu}{\rho}\right)_i \tag{2}$$

With
i : reference to elements of the mixture
μ: attenuation coefficient $\left[\frac{cm^2}{g}\right]$
ρ: density $\left[\frac{g}{cm^3}\right]$
ω: weight fraction [%]

The resulting attenuation coefficients are hardly influenced by the mud density. This correlates with the observation during consolidation tests, where a clear interface between mud and water is always present. This indicates that mud at densities almost equal to water is already highly opaque. With the attenuation coefficient known, the transmission coefficient T can be determined using the Beer Lambert law (Eq. 1):

$$T = \frac{I_L}{I_0} \tag{3}$$

The resulting transmission coefficient for mud confirmed the opacity of mud for optical light, as even a 1 mm thick mud layer results in negligibly low transmission coefficients even for low energetic x-rays, which are still a factor 10^3 more energetic compared to optical light rays. Therefore further focus was on the use of x- and γ-rays.

Looking at the electromagnetic spectrum it would be expected that γ-rays will show higher potential as they are higher in energy, and therefore result in greater penetration rates. Nonetheless, in practice the opposite holds true because of the difference in activity of the radiation sources. The activity of a radiation source is a measure of the number of photons emitted in function of time and is far greater for x-ray generators compared to γ-ray sources. In the end, it is the objective of transmitting as much photons (energy) as possible through the mud layer. So even though the transmission coefficient for x-rays might be lower, more photons will be able to transmit through the mud layer as they are greater in number.

In order to determine the required radiation dose rate (amount of radiation in function of time) emitted by the source, the required minimum dose rate, after penetration of the mud layer, to create adequate images needs to be known. Although probably on the conservative side, the minimal dose rate for medical diagnostic imaging is used, as medical applications are always subject to the ALARA principle. ALARA is an acronym for "As Low As Reasonably Achievable", hence is an indication of the minimum dose rate required to create images of sufficient quality for diagnostic use.

This evaluation of the use of high energy electromagnetic waves concludes that x-ray generators are the best option to visualize flows in mud. Nonetheless, for the intended application with a minimal mud layer thickness of 560 mm and maximal flow velocities of 2m/s, even the most powerful x-ray generator "freely" available on the market is insufficient. Furthermore this range of x-ray generators and the accompanying HSE measures require a budget far beyond the budget of a common hydraulic research setup.

2.3. Ultrasonography

Without the availability of any values for attenuation of ultrasound waves by chemical elements, com-

pounds or mixtures, the attenuation by mud can not be estimated. In addition, other research related to the acoustic properties of mud [10], mention the lack of any available trustworthy data from measurement campaigns.

In the Port of Zeebrugge a device called the Admodus USP pro is however used to measure the density of the mud layers, based on ultrasound transmission measurements. As density is the product of the speed of sound and the acoustic impedance (Eq. 6) the values of these parameters should also be known or measured by the device. Reviewing the measuring principles confirmed this assumption as it is actually the speed of sound and acoustic impedance which are measured by the device and from which the density is deduced. In addition, the Admodus USP pro also measures the attenuation of mud over a frequency spectrum of 1.0 MHz to 3.5 MHz. From the data of a survey campaign performed in February 2019 in the Port of Zeebrugge, these acoustic properties were retrieved in function of mud densities from 1.0 g/cm^3 to 1.3 g/cm^3. The speed of sound through mud shows small variation in this density spectrum, from 1460 to 1485 m/s. Consequently, so does the acoustic impedance, ranging from 1500 to 1900 $\frac{kg}{(m^2.s)}$. The measured attenuation values are presented in Fig. 2.

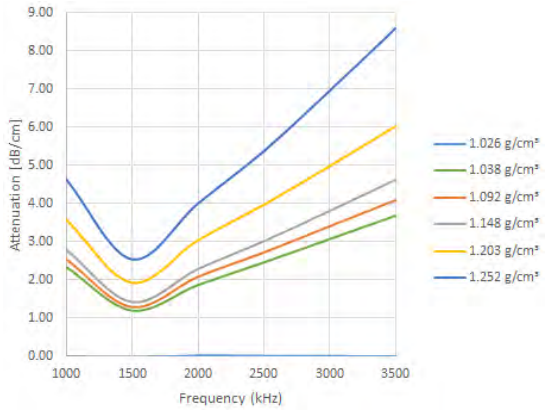

Figure 2: Attenuation values $\alpha_{(f)}$ (Eq. 7) of mud measured on site using the Admodus USP pro

Despite the knowledge of these values for attenuation and speed of sound, it can not yet be estimated whether or not the use of ultrasound waves would allow for sufficient penetration and energy conservation to create images of adequate quality for a PIV application. Like for all medical applications, an optimal compromise between penetration depth, field of view and the different types of resolution (axial, lateral and time) will need to be determined ([11]), which requires the knowledge of attenuation values over a greater range of frequency. Nonetheless, the fact that the speed of sound and attenuation of human tissue and organs as specified in [12], are in the same order as the aforementioned values for mud, gives confidence that such a compromise can be found with standard acoustic medical equipment.

2.3.1. Ultrasound properties of mud

In search of this optimal compromise for the application on mud, the acoustic properties of mud need to be known over a wider spectrum of frequencies compared to the data obtained from the Admodus USP pro measurements. Laboratory experiments will therefore be conducted during this research. In literature different methods (e.g. [13], [8],[14],[15]) can be found to determine the acoustic properties of materials or media. Because of the suitability on a medium of interest with changing properties, the method presented in [14] is preferred. This method allows to determine all acoustic properties with one single acquisition, hence excluding the changing behavior of mud over time.

The intended setup for this experiments is illustrated in Fig. 3. The medium of interest (referred to as sample) is placed in a plastic cup with a rectangular cross section and placed perpendicular to the ultrasound transducers' transmitting direction. To allow for optimal propagation of the ultrasound waves, both the transducer and the cup are submerged in water. For optimal results, the recommendations as presented in [15] are taken into account, resulting in minimal dimensions for d_w, d_p, d_s and the lateral dimensions of the cup. The experiments will be performed using broadband acoustic transducers with a center frequency ranging from 1 MHz to 10 MHz. The proposed method is based on the so-called "Pulse Echo principle" whereby acoustic parameters are determined based on the analysis of the transmitted ultrasound waves and the different echo signals received back by the same transducer. When a change in acoustic impedance, e.g. at the interface between water and plastic, is encountered along the propagation path of the ultrasound wave, a part of the ultrasound wave is reflected while the remaining part continues transmission through the new medium. The reflection coefficient r_{ij} hereby represents the part of the signal that is reflected, while the transmitting part of the signal is represented by the transmission coefficient t_{ij}. Hence both coefficients are closely related (Eq. 5) and determined solely by the acoustic impedance Z_i and Z_j of

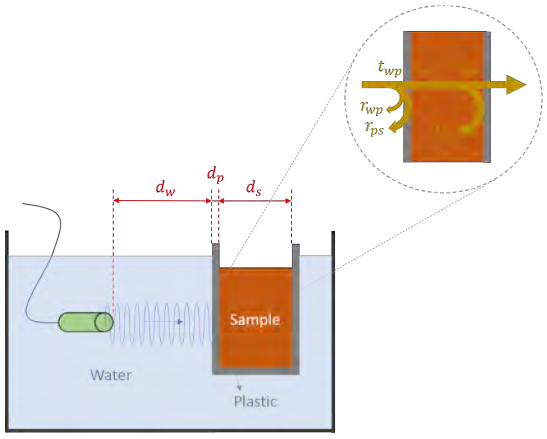

Figure 3: Intended setup to determine acoustic parameters of mud

the two media creating the interface, (Eq. 4).

$$r_{ij} = \frac{Z_i - Z_j}{Z_i + Z_j} \tag{4}$$

$$t_{ij} = 1 + r_{ij} \tag{5}$$

When the densities of the two media are known, the respective speed of sound c_i can be determined with Eq. 6

$$c_i = \frac{Z_i}{\rho_i} \tag{6}$$

Knowing the acoustic impedance of the present media, the signal loss due to propagation P_i through a single medium can be determined from the ratio of the two echo signals reflected at the two interfaces of this medium. In turn, the propagation loss is related to the attenuation α_i and propagation distance d_i through the medium (Eq. 7).

$$P_i = e^{(-\alpha_{i(f)}.d_i)} \tag{7}$$

Using these relations, all acoustic parameters of mud can be determined by recording the times of receipt t_1, t_2, t_3 and the amplitudes of the three echo signals A_{R1}, A_{R2} and A_{R3} reflected respectively at the interfaces *water/plastic*, *plastic/mud* and *mud/plastic* as illustrated in Fig. 3. In preparation of these measurements, the density and acoustic parameters of the plastic material need to be determined in advance. This is done by using water as the sample medium in the plastic cup.

While the minimum required signal strength of the received echo signals is limited by the gain capacity of the ultrasound evaluation unit (typically around 100 dB), attention should be paid to the choice of plastic material and the dimensions of the plastic cup. The choice of plastic and the wall thickness should result in minimal signal losses. This is however in contradiction with the recommendations presented in [15] and might cause issues which require intermediate change(s) in dimensions of the plastic cup, to enable measurements over a greater frequency range. For the intended tests with mud, this results in the choice of Polymethylmethacrylate, more commonly known as "acrylic", and one conversion of dimensions to cover the intended frequency range as presented in Table 1.

Table 1: Test setup configurations

Step	Frequency range MHz	d_w mm	d_p mm	d_s mm
1	1–6	70	28	18
2	7–10	70	5	11

With this two-step procedure the maximal signal loss will be limited to 80 dB while still complying with the recommendations from [15]. These measurements will be performed at the NDT experimental facilities of the Materials, Textiles and Chemical Engineering Department of Ghent University with the continuation of this research.

2.3.2. *Ultrasound B-scan of mud*

An ultrasound B-scan, or brightness scan is the most familiar mode of ultrasound imaging for medical purposes. A good example is a fetal scan during pregnancies. The images are typically in grayscale, where the brightness of a pixel is a measure for the amplitude of the reflected signal at the corresponding position in the insonified area. Therefore strong reflectors such as muscle tissue will appear bright while fluids will appear dark. In order to see any distinction in an image created with a B-scan some variety in acoustic impedance is thus required. To evaluate whether or not mud complies with this requirement the results of the chemical element analysis can be used again. The result of the chemical element analysis shows the different compounds or oxides and their weight fraction for different mud densities. For some of these oxides, the acoustic impedance can be found in literature while in accordance with Eq. 4, the strength of a reflected signal is related to the difference in acoustic impedance. Acoustic properties found in literature should always be used carefully as these values are very variable in function of the origin of the medium [8]. The values found and presented in Table 2 illustrate however a great difference in acoustic impedance

between the oxides which represent almost 74 % of mud. This allows to conclude that reflections are expected to occur when an ultrasound wave is transmitted through mud.

Table 2: Acoustic impedance and weight fractions of chemical elements present in mud with density 1.10 g/cm^3

Element	Weight fraction %	Acoustic impedance $.10^6 \frac{kg}{(m^2.s)}$
Al_2O_3	7.84	39.1
SiO_2	36.02	13.1
H_2O	29.68	1.5

In wave physics there are however different degrees of reflection depending on the ratio of the wavelength towards the size of the reflecting object. While specular reflections are created by objects larger in size than the wavelength of the incident sound wave, smaller objects will scatter omni-directional, resulting in much weaker reflection signals.

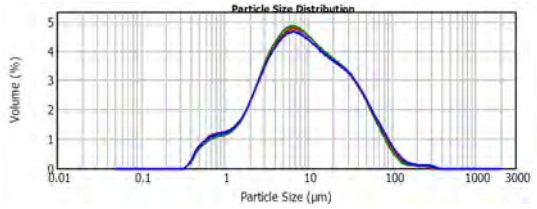

Figure 4: Particle size distribution of mud from the Port of Zeebrugge - Performed by FHR using a Mastersizer 2000

The frequency range of interest for this application is expected to be similar to that of medical imaging, from 1 MHz to 10 MHz. With a speed of sound through mud of 1460 m/s this results in wavelengths ranging from respectively 1460 μm to 146 μm. The particle size distribution of mud from the Port of Zeebrugge as presented in Fig. 4 shows a range of particle sizes ranging from 0.3 μm to 120 μm with a D50 around 6.5 μm. It can thus be concluded that the reflecting particles in mud will always be smaller compared to the applied ultrasound wavelengths, which results in scattering of the ultrasound waves.

There are however different scattering regimes which differentiate in properties and are again determined by the size of the scatterer with respect to the wavelength. Scatterers smaller in size than the wavelength of the incident soundwave act as point scatterers. This scattering regime is referred to as diffusive or Rayleigh scattering. In case of a high concentration of point scatterers, a speckle like signal will be created, as the scattered signals of each point scatterer will reach the transducer over slightly different path lengths. This results in a so-called "Speckle Pattern" ([16]), which is typically created when scanning muscle tissue. This ratio between the size of the scatterer and the wavelength is expressed with the factor $k.a$ where a is the radius of the scatterer and k the so-called "wavenumber" (Eq. 8).

$$k = \frac{2.\pi}{\lambda} \tag{8}$$

According to [17] diffusive scattering starts to occur when $k.a = 0.35$. A lower limit is not mentioned. However, as scattering is a major contributor to the attenuation of sound waves, a lower limit for $k.a$ must exist from which the scattered intensity is so small that it becomes negligible. In search of confirmation of this conclusion, a small-scale test was performed using A GE Vivid 7 ultrasound scanner equipped with a 10L linear probe. For protection against the seawater present in mud, the probe was inserted in a medical glove injected with acoustic gel to ensure good transmission of the ultrasound waves. This assembly was inserted in a bucket of mud with a density of 1.13 g/cm^3 as illustrated in Fig. 5. The resulting image is presented in Fig. 6.

2.3.3. Speckle pattern and Speckle tracking

As elaborated in [17], a speckle pattern arises from the constructive and destructive interference of a great amount of scatterers, which appears as a light and dark mottled grainy pattern. For many years users of ultrasound systems assigned a diagnostic value to the appearance of speckle and assumed it was tissue microstructure. Speckle is however an illusion and despite its deceiving appearance as a tissue texture it is more dependent on the measuring system than on the tissue itself. It is actually an unwanted effect for medical imaging as it reduces both image contrast as the distinction of subtle gradations and boundaries in tissue structure. A classic imaging problem is quantifying the ability to define a cyst object against a speckle background. On the other hand, there is medical application which makes use of speckle patterns to track tissue movement or blood flow. This technique is relatively new and called "Speckle Tracking". It is actually very similar to the PIV technique used in fluid dynamic research setups. Although the intention of the small-scale test as illustrated in Fig. 5 was only the creation of a B-scan image of mud, the appearance of



Figure 5: Setup of B-scan on mud, similar to figure 1b: (1) mud sample; (2) ultrasound probe; (3) scanner



Figure 6: B-scan of mud resulting in a clear speckle pattern due to scattering. Depth scale in cm.

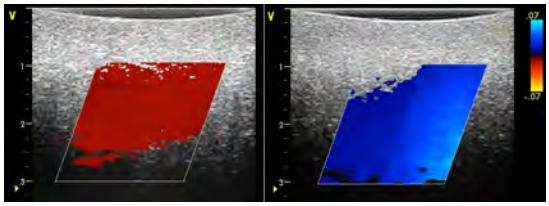

Figure 7: Snapshots during recording of induced flows with speckle tracking feature. Depth scale in cm. Velocity scale in m/s

speckle was of such good quality, that an attempt was made to use the speckle tracking feature of the scanner as well. A flow was induced by moving a spoon back and forth in the mud at sufficient depth below the probe to ensure it was out of reach of the ultrasound image. The result of this attempt was satisfying as the speckle tracking feature was able to record the induced flows as illustrated in Fig. 7. The blue and red color indicate the more or less equal flow velocities with opposite signs, indicating the back and forth induced flow in the mud.

Unlike for medical applications, visualization of flows in mud does not require a clear distinction between different tissues or revealing tissue boundaries. Minimal requirements on lateral resolution are therefore not required, which allows to lower the ultrasound frequency in order to increase the penetration depth. Lowering the frequency however lowers the wavenumber, and as mentioned earlier, there will be a minimum value for the factor $k.a$, from where the scattering intensity becomes too low to be of any further use. Assuming the scatterers can be considered as rigid spheres, [17] presents Eq. 9 for the Rayleigh scattering regime, showing the great influence of the frequency (4th power) and the scatterer radius (6th power) on the scattering intensity. This clearly shows the requirement to find a new compromise between penetration depth and frequency while considering the minimal scattering intensity as an additional restriction. Because of the origin of speckle, the minimal scattering intensity is however depending on the amount of scatterers present. As the latter is impossible to determine this ideal compromise will need to be determined experimentally.

$$\frac{I_s}{I_i} = \frac{k^4.a^6}{9.r^2}.\left[1 - \frac{3.cos\phi}{2}\right]^2 \tag{9}$$

with:

I_s : scattering intensity
I_i : incoming intensity
k: wavenumber = $\frac{2.\pi}{\lambda}$
a: scatterer radius
r: distance to the scatterer
ϕ: scattering angle

The relation between the scattering angle ϕ and the scattering intensity I_s might also allow for alternative setups. Eq. 9 shows the bi-polar scattering pattern with maximal intensities at $\phi = 0$ (forward scattering) and $\phi = \pi$ (backscattering). For medical applications this is of course an advantage as it allows the use and

flexibility of only one transducer without loss in intensity. For a stationary setup this flexibility is of no use while working in an angle by means of a second transducer is perfectly feasible. This would allow for a great increase in frame rate when one transducer is used as transmitter and the other as receiver instead of one transducer switching continuously between transmitting and receiving. In addition, working in an angle can allow optimization of the propagation path, decreasing the required penetration depth. According to Eq. 9, the intensity will decrease with a factor 6.25 when working in an angle $\phi = \pi/2$. Such a decrease in intensity can be compensated with an increase in frequency, e.g. 1MHz to 1.58MHz. This will however lead again to higher attenuation and a decrease in penetration depth. Knowing the attenuation values of mud over the entire frequency range of interest will therefore be of great use to in order to evaluate whether or not the benefits of working in an angle are worth the decrease in penetration depth.

3. Reproducibility of experiments using mud

At FHR numerous consolidation tests of mud, originating from different rivers and ports in Europe, have been conducted over the past decade. The setup used for these tests is similar to the setup described in [6] and is presented in Fig. 8. In brief, the mud prepared at a predefined density is pumped into a transparent column and left at rest to consolidate for a period up to 12 weeks or even more. The consolidation process is monitored by recording the height of the water-mud interface, measuring the density profile and the pore pressure at different heights at regular time intervals. Despite the uniformity applied in the handling of the mud and the preparations of the tests, the repeatability of these tests is an issue. For hydraulic test setups the ability to reproduce results is of great importance. When the behavior of the fluid of interest is out of control this can however not be guaranteed, which undermines the credibility of the results. Therefore the consolidation process of mud should at least be better controlled when mud is intended to be used in a hydraulic test setup.

3.1. Conditioning of mud

As discussed in [6], mud must be properly homogenized to ensure repeatability of consolidation tests. This homogeneity is to be achieved by mixing the mud prior to pumping it into the column. Different effects can however be achieved with mixing, depending on

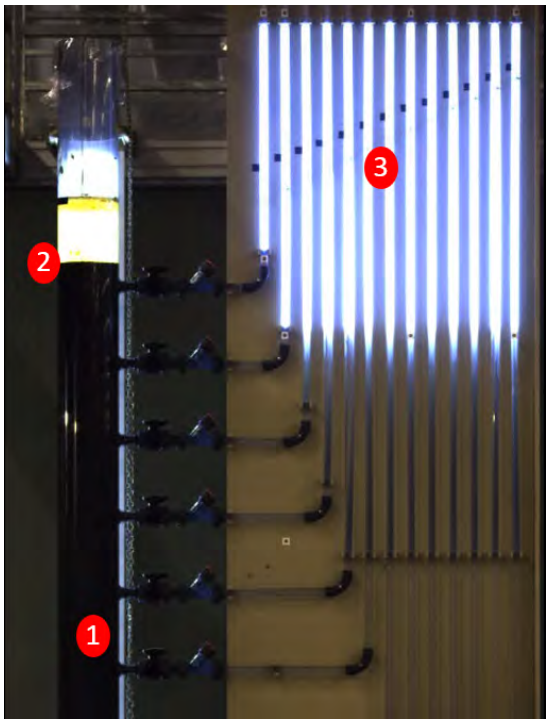

Figure 8: Consolidation test as performed at FHR: (1) transparent plastic column filled with mud; (2) water-mud interface; (3) pore pressure measurement at different heights in column

the used mixing impellers and the associated induced flows [18]. In preparation of the consolidation tests performed at FHR, a handheld mixer with a helical-ribbon impeller was used to prepare the mud. According to [19], this type of impeller is intended for mixing liquids with a high viscosity of 100 Pa.s and even more, such as mortar. Measured values of mud viscosity after 8 weeks of consolidation are however in the range of 3 Pa.s. Hence, it is clear that a helical-ribbon mixing impeller is not the best option for the mixing of mud. To determine which type of impeller should be used, a closer look at the consolidation process is required. According to [20], consolidation of mud happens in different steps. While heavy particles settle almost instantly, lighter particles will first merge and form larger flocs until they are sufficient in weight to settle. When settled on the bottom they will form new sediments which can concentrate and consolidate. As the formation of flocs and their settlement is a relative fast phase in the entire consolidation process, the behavior of the mud during this phase is the most susceptible to any variety in the initial condition of the mud. When mud is not properly homogenized, heavier flocs can already be at the bot-

tom, causing an earlier initiation of the consolidation. If the amount of heavier flocs present in mud differentiates, more or less flocs need to be formed which influences the time of transition from settlement towards consolidation. Although both inconsistencies have a similar result, they require different types of mixing flows to be avoided. According to [18], good homogenization requires dispersion of the mixing energy over the entire mixing volume for which an axial flow is recommended. In case the amount of remaining flocs prevail, the creation of shear forces by means of radial flows is more required. Both type of flows are illustrated in Fig. 9. Axial flows are created by so-called "marine blade impellers" while radial flows require impellers with vertical paddles or blades. When a combination of both flows is required, an impeller with pitched blades can be used, where the angle in which the blades are pitched determines the dominant flow type. These different mixing impellers are presented in Fig. 10.

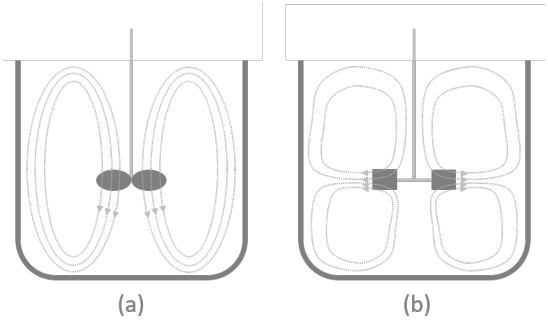

Figure 9: (a) axial flow; (b) radial flow



Figure 10: (a) marine blade impeller; (b) pitched blade impeller; (c) paddle impeller

3.2. Small-scale consolidation tests

To evaluate different mud conditioning procedures with regards to mixing method and duration, small-scale consolidation tests are being conducted. Mixing is performed using the three impellers presented in Fig. 10, during 15, 30 and 45 minutes. After every 15 minutes mud is pumped in three small transparent columns (height 2 m; diameter 63 mm), resulting in 9 mud columns per mud batch. These tests are performed at least three times per impeller and left to consolidate over a period of 1 week. During the consolidation process, the level of the water-mud interface is recorded to assess the relative decrease of the water-mud interface level over time. In the end it is the objective to have similar evolution of the water-mud interface levels over time between mud columns created with the same procedure but in different batches. During mixing the density of the mud is continuously measured using an Anton Paar DPRN 427 device, installed in a closed pumping circuit as illustrated in Fig. 11. This setup allows to evaluate the homogeneity of the mud batch with regards to density. When the density measurements are stable, the mud batch is considered to be homogeneous. To evaluate the amount of large flocs present in the mud, a grain size distribution analysis is performed on mud samples using a Mastersizer 2000.

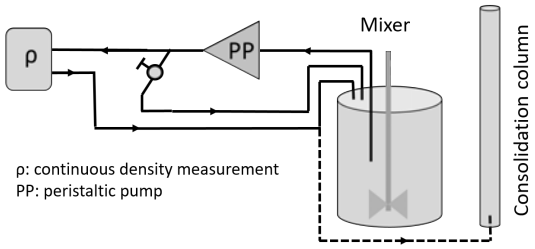

Figure 11: Schematic illustration of the mud conditioning setup

3.3. Preliminary results

So far three series with both the marine and the pitched blade impeller have been conducted, resulting in a total of 54 consolidation tests. In general it can be concluded that the performed mud conditioning procedures already result in an improvement of the repeatability of the consolidation process. A difference between the two impeller types can however not yet be evaluated as some practical issues occurred during some tests, which disrupted the consolidation process and thus need to be repeated. Secondly it can be concluded that repeatability improves with increasing mixing duration. This is illustrated in Fig. 12 where the graphs for mud conditioned over 45 minutes are closer to each other compared to those with mud conditioned over 15 minutes. In case further improvement is possible even a longer mixing duration

might thus be considered, although this tends to be rather marginal.

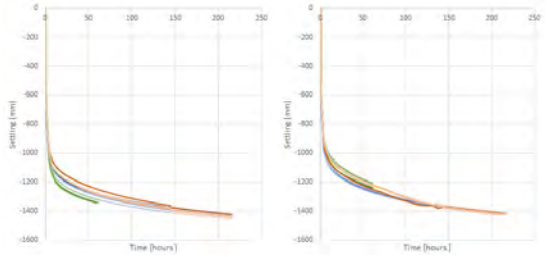

Figure 12: Curves illustrating the evolution of water-mud interface level over time. Left: 9 curves representing the 9 tests conducted with mud conditioned over 15 minutes. Right: 9 curves representing the 9 tests conducted with mud conditioned over 45 minutes.

From a practical point of view, the use of the Anton Paar DPRN 427 device for continuous monitoring of the density during mixing in this setup is not the best option, as the measurements are influenced by the rotating velocity of the mixer. This device is therefore considered to be too sensitive for the current setup and application. A derivative of the setup presented in Fig. 3 can however provide a more robust density measurement system, similar to the measuring principles of the Admodus USP pro. This will require some in-house development of which the feasibility is under discussion.

4. Conclusion

The objective of this research is twofold with first the search for a technique able to visualize flows in mud and customize it to allow the application of PIV. Because of some essential resemblances, inspiration was found in the medical sector, resulting in radiography and sonography on the shortlist of potential techniques. Review of the application of radiography on mud showed however that the technique is not efficient enough to be used on typical hydraulic research facilities. Even with the use of the most powerful radiation sources freely available on the market, either the mud layer thickness or flow velocities should be limited in such a way that they are no longer relevant for the intended hydraulic research. As sonography does not require full penetration of the mud layer the focus to evaluate the potential of this technique is more in finding a compromise between the penetration depth, frame rate and image quality. With a small-scale test it was shown that a common ultrasound scan of mud results in a so-called ”speckle pattern”. Although speckle patterns are an unwanted feature for medical diagnostics, they are also used to track tissue movement or blood flow. This technique is known as ”speckle tracking” and is much alike PIV. With the same small-scale setup speckle tracking was applied on mud, demonstrating its ability to visualize the induced flows and determine flow velocities. The continuation of this research will therefore focus on the application of speckle tracking with experiments to determine the attenuation values of mud within the applicable frequency range and the optimal compromise between penetration depth, frame rate and image quality.

The second objective is to develop a procedure for the conditioning of mud resulting in an improvement of the repeatability of the mud consolidation process. The first experiments showed that an increased mixing duration and a substantiated choice of mixing equipment are already beneficial. With further experiments the influence of other mixing equipment will be evaluated which will provide a better understanding on the requirements to enable reproduction of consolidation tests. During conditioning of the mud it was found that the application requires robust equipment. While still being practical and adequate for use in a laboratory environment, suitable equipment can not always be found on the market. In this case an in-house development of a continuous density measurement device using ultrasound is hoped to provide a solution.

Acknowledgments

This research is promoted by Flanders Hydraulics Research (FHR) and supported by the Maritime Technology Division of Ghent University in collaboration with the von Karman Institute for Fluid Dynamics (VKI). The author is grateful to these institutions for the opportunity to conduct this research. This paper was reviewed by Tom Lauriks, collaborative PhD student at the von Karman Institute and University of Antwerp.

References

[1] Delefortrie, Guillaume and Vantorre, Marc, Prediction of the forces acting on container carriers in muddy navigation areas using a fluidization parameter, Journal of Marine Science and Technology 14 (1) (2009) 51–68.

[2] G. Delefortrie, M. Vantorre, Ship manoeuvring behaviour in muddy navigation areas : state of the art, Bundesanstalt fr Wasserbau, 2016, pp. 26–36.
URL http://dx.doi.org/10.18451/978-3-939230-38-04

[3] M. D. M. F. Ibanez M., Claeys S., (in prep) Literature study on consolidation experiments, Tech. Rep. 19_114_4, Flanders Hydraulics Research.

[4] R.K. Bowden, Compression Behaviour and Shear Strength Characteristics of a Natural Silty Clay Sedimented in the Laboratory , Ph.D. thesis, University of Oxford (1998).
[5] S. T. W. Markus Raffel, Christian E. Willert, J. Kompenhans, Particle Image Velocimetry: A Practical Guide (2nd edition), Springer, New York, 2007.
[6] J. Berlamont,M. Ockenden, E. Toorman, J. Winterwerp, The characterisation of cohesive sediment properties, Coastal Engineering 21 (1-3) (1993) 105–128.
[7] Delefortrie, Guillaume and Vantorre, Marc and Laforce, E and De Brauwer, D, A new approach for defining the nautical bottom in the harbour of Zeebrugge, no. IHMA Congress Matla 2006 Proceedings, Malta, 2006.
[8] Edward Ginzel and Ben Turnbull, Determining approximate acoustic properties of materials, e-Journal of Nondestructive testing (NDT) 12.
[9] Burcu Aka, Salih Z. Erzeneolu, The Mass Attenuation Coefficients, Electronic, Atomic, and Molecular Cross Sections, Effective Atomic Numbers, and Electron Densities for Compounds of Some Biomedically Important Elements at 59,5 keV, Science and Technology of Nuclear Installations 2014 (901465) (2014) 8.
[10] Pierce,Allan D. and Siegmann,William L. and Brown,Elisabeth, Analytical discussion of past measurements of acoustic attenuation in mud sediments and of possible future experimental approaches, The Journal of the Acoustical Society of America 138 (3) (2015) 1933–1933.
[11] Ng, Alexander and Swanevelder, Justiaan, Resolution in ultrasound imaging, Continuing Education in Anaesthesia Critical Care Pain 11 (5) (2011) 1743–1816.
[12] E. R. R. P. William R. Hendee Ph.D., Medical Imaging Physics, John Wiley Sons, Ltd, 2002.
[13] Rui Zheng and Lawrence H Le and Mauricio D Sacchi and Dean Ta and Edmond Lou, Spectral ratio method to estimate broadband ultrasound attenuation of cortical bones in vitro using multiple reflections., Physics in Medicine and Biology 52 (19) (2007) 5855–5869.
[14] Tomohisa Norisuye and Satoshi Sasa and Kohsuke Takeda and Mariko Kohyama and Qui Tran-Cong-Miyata, Simultaneous evaluation of ultrasound velocity, attenuation and density of polymer solutions observed by multi-echo ultrasound spectroscopy, Ultrasonics 51 (2) (2011) 215–222.
[15] A. R. Selfridge, Approximate Material Properties in Isotropic Materials, IEEE Transactions on Sonics and Ultrasonics 32 (3) (1985) 381–394.
[16] Poelma, Christian, Ultrasound Imaging Velocimetry: a review, Experiments in Fluids 58.
[17] T. L. Szabo, Diagnostic Ultrasound Imaging: Inside Out, Elsevier Academic Press, 2004.
[18] Chapter 8 - mixing of liquids in stirred tanks, in: M. F. E. N Harnby, J. C. Godfrey (Eds.), Mixing in the Process Industries, Butterworth-Heinemann, Oxford, 1992, pp. 137–158.
[19] Chapter 7 - a review of liquid mixing equipment, in: M. F. Edwards, M. R. Baker (Eds.), Mixing in the Process Industries, Butterworth-Heinemann, Oxford, 1992, pp. 118–136.
[20] Teisson, C. and Ockenden, Mary and Hir, P. and Kranenburg, C. and Hamm, Luc, Cohesive sediment transport processes, Coastal Engineering 21 (1993) 129–162.

Ray-Tracing Based PIV of Turbulent Flows in Roughened Circular Channels

Muhsin Can Akkurt

Environmental and Applied Fluid Dynamics, von Karman Institute for Fluid Dynamics, Belgium, muhsin.can.akkurt@vki.ac.be

Supervisor: Delphine Laboureur

Associate Professor, Environmental and Applied Fluid Dynamics Department, von Karman Institute for Fluid Dynamics, Belgium, delphine.laboureur@vki.ac.be

University Supervisor: Kevin M. Van Geem

Professor, Department of Materials, Textiles and Chemical Engineering, Ghent University, Belgium, Kevin.VanGeem@UGent.be

Abstract

Recently, complex geometries such as various indentations and cavities are successfully applied to the surfaces to improve the heat transfer in the channel flows. Particle Image Velocimetry (PIV) measurements have been widely used to measure the velocity field and turbulence behaviour in the channels. However, some geometries on the surfaces are optically too complex to properly investigate the particle displacements, and therefore use PIV since they cause high distortions on the PIV images. Therefore, a raytracing-based image correction method providing pixel by pixel mapping can be applied in such cases where the conventional methods (3rd order polynomial and pinhole model) are not sufficient to have acceptable corrections. In this work, PIV measurements have been performed with ray tracing-based image correction to provide the flow field inside heart-shaped cavities of a dimpled pipe which induces high levels of image distortions.Because the method is based on creating a synthetic image of calibration grid in an experimental setup with a rendering software, an optimization algorithm has been developed to reduce the deviation between the real and synthetic images. In the calibration process, the ray tracing-based correction method provided a standard deviation of 0.32 pixels from the reference grid while 3rd order polynomial had provided 9.6 pixels. Measurements were acquired on the center plane of the 9th cavity from the inlet in the streamwise direction. 2D velocity field and turbulent kinetic energy are collected to validate Large Eddy Simulations which are to be carried out for the same geometry. In the present work, the flow is set to Reynolds number of around 20000, which corresponds to a fully turbulent state.

Keywords: Enhanced tubes, Dimples, PIV, Image distortions, Image mapping

1. Introduction

Steam cracking of hydrocarbons has been widely used in the chemical industry to produce light olefins such as ethylene, propylene and butadiene. The formation of coke layer on the internal walls of the cracking reactors leads to a decrease in heat transfer from furnace to the process gas and an increase in pressure drop since the flow area is reduced [1]. The operations need to be halted for decoking of the reactor when one of these effects becomes too big. The duration of this interruption can be decreased by an improvement in heat transfer which reduces the inner wall temperature of the reactor and therefore the coking formation [2].

A variety of heat transfer augmentation techniques, as for example rib turbulators, pin fins, dimpled surfaces, are recently employed in channel flows. The wall heat transfer is improved by roughness elements promoting turbulence and disturbing the boundary layer to be separated and reattached downstream the element. On the other hand, the utilization of these techniques contributes to the rise in the pressure losses which has to be kept at a minimum level while augmenting the turbulence intensity and the local heat transfer. Dimples, which are the cavities that can have various types of shapes such as spherical, rectangular

and teardrop, augment the heat transfer rates without significant pressure drops. They have lower friction factors compared to other methods since they do not block the flow field and produce remarkable form drag in the channel [3]. The augmentation of the convective heat transfer coefficient is provided by creating multiple vortex pairs behind the dimples. Afanasyev et al. [4] investigated spherical cavities on flat plates and described the heat transfer and pressure loss phenomena for the cavities. It is found that the heat transfer is increased by 30-40% without a significant increase in skin friction.

Griffth et al. [5] mentioned the flow structures explaining the secondary flow induced by the dimples. According to this study, a flow separation takes place in this region after the flow reaches the edge of the dimple. Then, the flow arrives in the upstream portion of the dimple where low heat transfer coefficients exist due to the recirculation zone. However, in the downstream portion of the cavity, flow reattachment occurs, which results in the enhancement of the heat transfer coefficient. Zhou et al. [6] also investigated the flow structures on dimpled surfaces. They used PIV for determining not only the characteristics of the turbulent boundary layer over the dimpled flat surface but also the evolution of the vortex structures in the dimple. They found that much stronger Reynolds stresses and improved turbulence kinetic energy levels exist on dimpled surfaces. They also noted that friction factors changing with Reynolds number are higher than that of the flat surfaces. Virgilio et al. [7] studied turbulent flow structures in a pipe with spherical dimples by using PIV and Stereo PIV for Re=20000. With the PIV measurements, they found a significant flow separation/reattachment is formed, and secondary flows are generated by spherical cavities. The vorticity level is higher, and the wall heat transfer is increased by convection compared to smooth pipes.

There are many studies on the effects of the dimple geometry on the flow structure and therefore the effectiveness of the surfaces. Chyu [8] et al. studied the effects of two different shapes of dimples, spherical and teardrop, on heat transfer and skin friction. It is stated that, although both induce 2.5 times more heat transfer compared to smooth surfaces, tear-shaped dimples provide higher heat transfer coefficients. Moreover, it is found that the pressure drops for the cases are nearly half the values obtained by the conventional obstacles. Burgess and Ligrani [9] investigated the effect of the depth of dimples on heat transfer and flow structure for Reynolds numbers ranging from 9540 to 74800. Experimental results including three different ratios of dimple depth to dimple print diameter showed that the augmentations of Nusselt numbers and friction factor increase as the dimple depth increase at all Reynolds numbers considered. These results were attributed to two main reasons. The vortices and ejected secondary flows become stronger and more intense (i) whereas magnitudes of turbulence production and turbulence transport increase (ii) as the dimple depth increases. Dedeyne et al. [10] carried out an optimization study with multiple design parameters such as width, height and curvature to obtain a dimple geometry that maximizes the heat transfer and while keeps the pressure drop at minimum. In the study, enhanced heat transfer, more uniform radial temperature profile and low-pressure drop were aimed and it is found that heart-shaped dimples have better performance compared to spherical dimples. Next to this, they stated that the optimized shape can increase the TEF by more than 15% and decrease pressure drop by 20%.

In the presence of complex geometries such as dimples, ray-tracing image correction was used by several researchers to overcome the high distortions for which conventional image correction techniques are not sufficient to determine the particle displacements correctly. Kang et al. [11] used two different ray tracing based correction methods, i.e., an image and a velocity mapping methods, to eliminate the effects of the strong refraction of the light for the case of liquid droplet surfaces. Zha et al. [12] applied a correction method, which is a combination of the ray-tracing and the polynomial methods, to correct optical distortions changing with time and space. The main issue is related to the fact that, these methods were used to correct only moderate optical distortions given by axisymmetric geometries. For this reason, Martins et al. [13] proposed a novel ray tracing-based image correction method for applications of gaseous flows inside packed beds, which computes the correspondence between the pixels of the image plane and the spatial coordinates of the points inside the object plane using an open-source rendering software, pbrt. The authors managed to perform PIV of a gas flow, by correcting the high optical distortions given by a sequence of glass spheres placed in front of the camera.

This study aims at applying the ray tracing method [13] to a real scenario, where the spatially resolved experiments have been provided to investigate the velocity field of the turbulent flow inside a tube with heart-shaped dimples, which are obtained by Dedeyne et al. [10], on its inner wall. The high-level of image distortions caused by the complexity of the heart-shaped dimple have been removed during the calibration pro-

cess. On the other hand, to reduce the errors in the calibration, an optimization loop, which is a combination of evolutionary algorithm and simulated annealing, has been developed to create the synthetic image required in the application of the correction. The time-averaged velocity components and the fields of turbulent kinetic energy are presented for a streamwise plane at the center of the cavity at Re=20000.

2. Experimental Setup

2.1. Test facility

The PIV measurements were performed by using the low-speed facility that was designed to investigate the flow field in circular channels in the von Karman Institute. This facility, consist in a closed water circuit with five main sections: settling chamber, development duct, test section, outlet channel and discharge chamber, as shown in Fig. 1. [14].

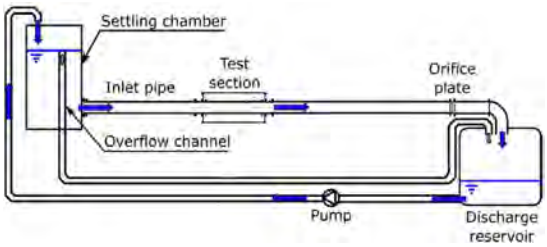

Figure 1: Experimental setup [14].

The main aims of the circuit are to obtain a required Reynolds number and a constant total pressure at the inlet of the channel. Therefore, the height of the water column in the settling chamber is kept at a constant level by using an adjustable overflow channel as in the Fig. 1. In this way, the inlet total pressure, as well as the mass flow and Reynolds number, can be set to desired values by preventing the unsteadiness coming from the water pump. Before the fluid enters the discharge reservoir, an orifice plate is placed in the outlet duct for defining the mass flow by measuring the pressure drop between upstream and downstream of the diaphragm. Defining the mass flow rate, which will be defined later, allows calculating the bulk velocity. Subsequently, the fluid is collected in the liquid tank from where it goes to the piping system again to close the water circuit.

The test section, where the PIV images are taken, is located downstream of the inlet pipe where the flow is supposed to be fully developed. In this study a circular channel with inner diameter 150mm, was mounted and the flow fields were investigated. To minimize the optical distortions resulting from the curved surface of the channel, a transparent rectangular box (test box), made of Plexiglas, is placed in the test section as shown in Fig. 2. So that, a straight surface between ambient air and the Plexiglas can be provided. Finally, filling the test box with the working fluid, whose refractive index is closer to that of Plexiglas, assures better refractive index matching and the errors are minimized.

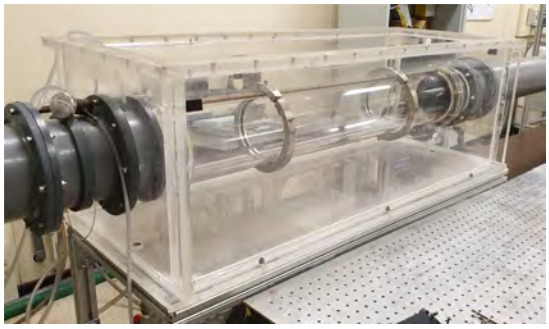

Figure 2: Test section.

As a property of fluorescent tracer particles, they scatter both the laser light and also re-emit the absorbed laser light with a longer wavelength. By using a proper optical filter, the light with the wavelength of the laser sheet can be blocked and the light emitted from the fluorescent particles would pass. So that, undesirable lights scattered from the other objects such as the wall and, air bubbles, and other causes can be banned. Therefore, more accurate measurements can be provided especially for near-wall measurements. For this reason, fluorescent particles were chosen to be used as tracers and a Notch Filter was mounted to the CCD Camera. By using the Notch Filter, the laser wavelength (523 nm) was kept in the blocking range so that acquired images become much cleaner from the background noises.

2.2. PIV Configuration

The measurements were carried out in a circular test tube which consists of one smooth half (with) made of acrylic glass and one transparent, heart-shaped dimpled half. Ten evenly spaced rows, each containing five heart-shaped dimples at the circumference, are placed on the dimpled half. The smooth half provides optical access for both the laser sheet and field of interest for the cases when the heart-shaped refracts the laser sheet or blocks the field of view. Planar PIV was performed with one camera where the

axis of the camera is perpendicular to the wall of the test box and parallel to the horizontal (Fig. 3). In this configuration, the field of view is investigated through the heart shape.

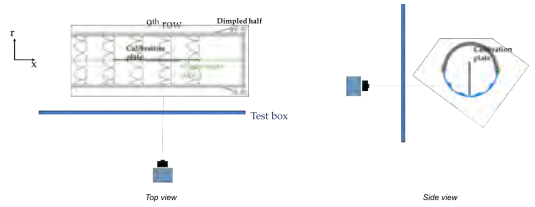

Figure 3: Planar PIV configuration.

The laser sheet was generated by using optical lenses displaced after the laser head. The generated laser sheet is turned of 90 by a mirror (Gimbal mount Edmund optics) and is aligned with the investigation area where the calibration plate is located. A10x10cm plate which has 2500 black dots with a diameter of 1mm is used to calibrate the field of view on the PIV images. Since the configuration is used for the measurement of the center plane in a streamwise direction, the calibration plate was located on the centerline of the pipe in a manner that it was slightly touching the wall of the dimpled half (Fig. 3). At this point, high-level irregular distortions occur on the calibration image due to the complexity of the heart shape and the difference between the refractive indexes of the water and dimpled tube. A ray tracing-based correction method, which was proposed by Martins et al., was used because the conventional methods, such as 3rd order polynomial and pinhole model, fails to remove strong irregular image distortions. The correction method, which will be explained in detail later, uses pixel-pixel dependence between the image and the calibration plate whereas the other method uses one mapping function to correct the entire image.

Each experiment consists of 1000 PIV image pairs, acquired at a frequency of 1 Hz. The acquisition frequency has been selected such that the time between realizations is long enough with respect to the flow characteristic time. The separation time between two consecutive PIV images was determined during the experiment such that the particle displacements would be around 10 pixels. The background image was generated by averaging all the intensities of each pixel. The correction has been applied to the images after the background subtraction. Finally, the images are processed by Davis 8.4.0 software. The cross-correlation algorithm has been run by dividing the images in the final interrogation windows of 32x32 pix2 with overlaps of 50%. Related to the distance between the camera and investigation plane, the field of view, and the interrogation window, the final resolutions are obtained as 1x1mm2. More details of the devices and the tools have been summarized in Table 1.

Table 1: Main properties of the devices.

Flow	Liquid	Water
Laser sheet	Laser model	Quantel Evergreen
	Type	Nd:YAG
	Pulse Rep. Rate	1 Hz
	Pulse energy	60 mJ
	Wavelength	532 nm
	Pulse duration	$\leq$ 10 ns
PIV Images	Model	LaVision SX 4M
	Type	CCD
	Resolution	2360 x 1776 pix^2
	Pixel size	5.5 x 5x5 μm^2
	Digital output	12 bit
	Lens	50 mm
PIV Setup	Software	Davis 8.4.0

3. Mapping Methodology

3.1. Image Correction Method

The image correction method, based on a ray-tracing algorithm, was applied to remove the optical distortions coming from the heart-shaped dimples. The main procedure of the method depends on correcting the distorted image by using the relation between the computer-generated image and the real image. As Martins et al. [13] suggested, the method mainly consists in three steps:

i) Creating the 3D experimental setup that represents the experimental scene where the rays to be traced.

ii) Creating a computer-rendered image by tracing the rays in the experimental scene.

iii) Determining the correspondence between the pixel coordinates (i, j) in the created image and the position coordinates (x, y) in the investigation plane which exists in the experimental scene.

The software pbrt [15] is used to create the computer-generated image which is to be as close as possible to the real one and to find the correspondence. The first step is introducing a 3D model of the experimental facility consisting of all the objects, their optical properties and camera model, to the pbrt.

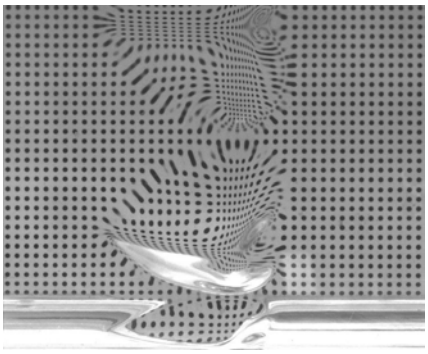

(a) Real image

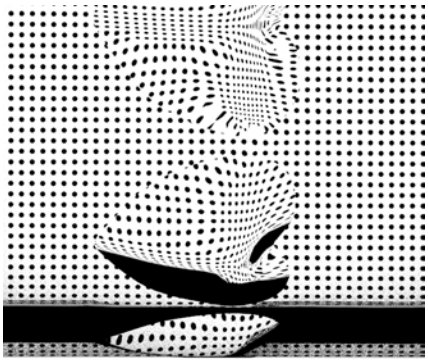

(b) Generated image

Figure 4: Real and computer-generated image images

For this purpose, 3D CAD models of the material in the test section were inserted into the pbrt as triangle meshes so that they can be rendered by the software. To minimize the uncertainties, result from manufacturing, the CAD models have been obtained by 3D scanning of the heart-shaped dimpled pipe. The distorted calibration image taken by CCD camera and rendered synthetic image for PIV configuration (one-camera layout) are presented in Fig. 4. These images are desired to match each other so that both can be corrected with the same correspondence. An optimization algorithm explained in the next chapter, has been used for the matching process.

A ray in the scene intersects a point of the investigation plane after some refractions and/or reflections throughout its path as it can be seen in the schematic view of the experimental facility (Fig. 5).

The intersections between the rays and points on the investigation object are to be found for the final step of the method. According to the study of Martins et al. [8], an output file, which records the information of the pixel element where the rays are generated from and the position coordinates where the rays intersect with the object (that is made of triangle meshes in this study) was created during the rendering process.

However, in this study, only the bounces of rays which had only refractions along their ray-path were recorded as all the object are submitted into software from CAD models. Specific to the configuration in Fig. 5, the recording file included the rays that hit the calibration plate with the number of bounces, 5. In such a way, the points on the calibration plate with which all the rays in the scene intersect were found.

To obtain image correction, the average of all intensity values on each particular pixel element is calculated considering that the one-pixel element has been intersected with more than one ray and therefore it has more than one intensity value.

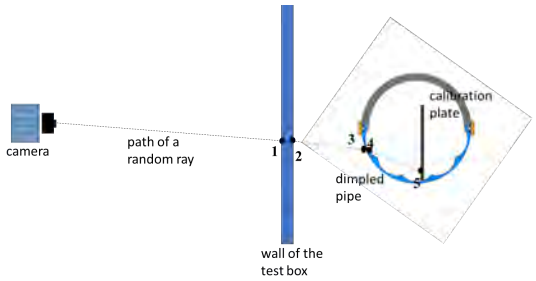

Figure 5: Schematic view of the PIV setup.

The correction based on extracted correspondence was applied to both images of the calibration plate, acquired in the actual facility, and generated. The corrected are presented in Fig. 6.

The same image correction is to be implemented for PIV image frames besides the calibration plate since they are affected by the same refractions as in the calibration. The cross-correlation of the corrected frames was performed by Davis 8.4.0 after having the calibration for the corrected calibration image.

3.2. Optimization Algorithm

It is necessary for a perfect calibration that the distortions rendered by using the pbrt software are ”the same” as the distortions on the images taken from the actual facility. The deviation in the match between the images leads to a deviation of the corrected image from the reference grid. Therefore, at this point, the deviation between the correction of the calibration image and the reference grid becomes an indicator of the uncertainty in the calibration process. To render the same image, all the spatial properties in the experimental environment should be inserted into pbrt.

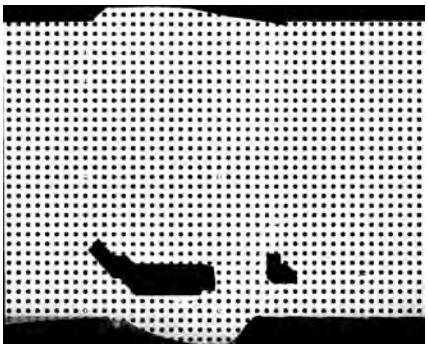

(a) Correction of generated image

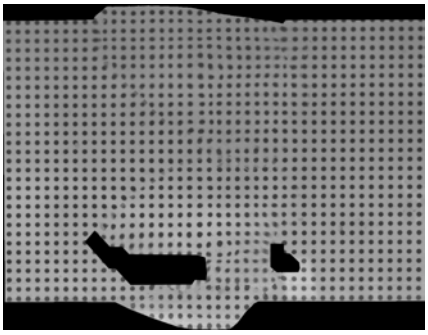

(b) Correction of real image

Figure 6: Corrected images.

For rendering process, pbrt requires an input file consists of numerous properties of experimental scene such as positions of the geometries, settings of the camera, etc. to create a synthetic image. As it is not always possible to measure all the dimensions accurately in the experimental facility, there is always a difference/deviation between the synthetic image and the real image. Therefore, a genetic algorithm is used to find the best setup, that is, generate an image with minimum deviation.

Genetic algorithms are commonly used for the optimization of designs in global search algorithms with a wide parameter range. In the algorithm, there is a fixed number of individuals of which all parameters are represented by a binary string. The binary string representation allows a new population to be created by crossing over the operation. Two new individuals, children, are generated from selected two individuals, parents, whose binary strings are exchanged randomly [16].

The individuals with higher fitness, higher objective values, have a higher probability to be selected as parents. Mutation is another operation that plays a role in generating new individuals. After crossing over,

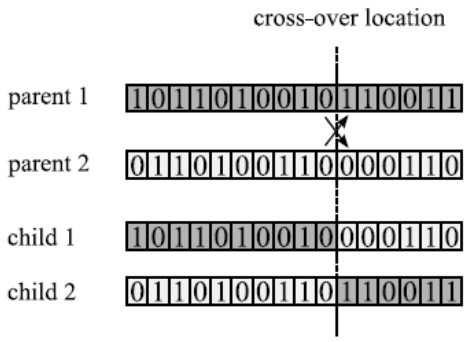

Figure 7: Crossing over operation [16].

the mutation leads to a change in the binary sequence of an individual randomly. This process is mainly to avoid converging to a local minimum rather than a global minimum. However, the higher probability of mutation may lead to divergence.

All properties, affecting the positions of each dot on the image, in the input file have been taken as design parameters. The properties have been described by 14 parameters including the position with three spatial coordinates (x, y, z) and the rotation of the camera (β), the position of the calibration grid (x_2, y_2, z_2), the focal length of the camera (f), the rotation (θ) and the position of the related half tube (x_3, y_3, z_3) and refractive index of the tube and the test box $(n1, n2)$. Measured values have been taken as the initial values of the parameters whereas their respective ranges are defined by the uncertainties in the corresponding measurement.

The objective function has been defined as the standard deviation between the centers of the dots on the rendered and the real image. Using the information of the pixel coordinates (x, y) of the centers, the deviation is defined as the distance between the corresponding dots.

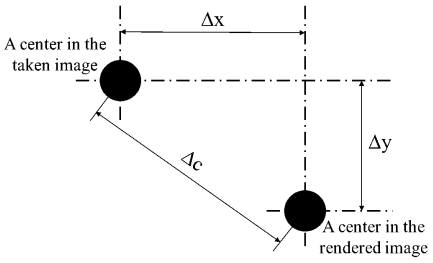

Figure 8: Deviation between centers in the pixel domain.

The standard deviation is calculated as a quantitative comparison of the images and expressed as

$$deviation = \frac{\sqrt{\sum_{i=1}^{n} \Delta c_i}}{N} \quad (1)$$

where N is the total number of the dots.

First of all, the design variables in the population have been proposed by the optimization algorithm developed in MATLAB. The individuals are prepared as an input file to be inserted into the pbrt. After the rendering process is completed, the output image is read by another code and compared with the real image. After this evaluation of the objective function, the standard deviation for this study, a new generation is generated, and the loop closes as presented in Fig. 9.

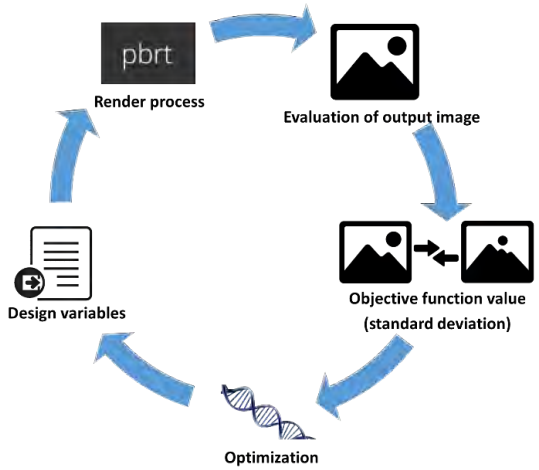

Figure 9: Optimization loop which is run with three tools (optimization algorithm, pbrt, std calculation).

4. Results and Discussion

4.1. Image rendering quality

The optimization algorithm has been used to generate an image (Fig. 6a) for the PIV where very-high level distortions exist on the calibration image (Fig. 6b). The calibration image has been corrected using the correction matrix that was created in the rendering process (see Section 3). Fig. 10 shows the maps of the deviation of the corrected images which were obtained from both the images generated using an optimization algorithm and manually (without optimization). It can simply be noticed that the deviation values have been significantly reduced using the algorithm. The overall deviation has been calculated as

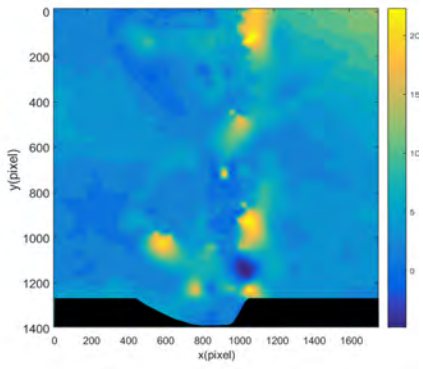

(a) The map of the image manually generated

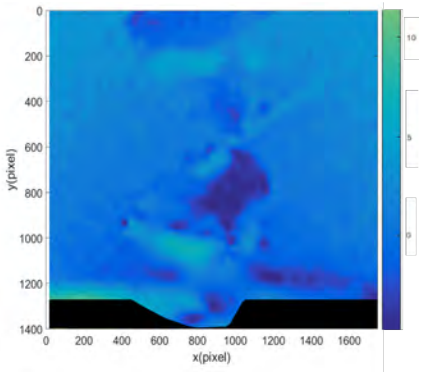

(b) The map of the image generated with the algorithm

Figure 10: Pixel-pixel deviations between the corrected image and reference grid.

0.52 for the manual case (Fig. 10a) while the case with the algorithm provided 0.32 pixels of standard deviation. The maximum deviation in Fig. 10b is obtained as 8.4 pixels on the bottom left corner. Minimum levels of deviation take place in the middle of the map, where high distortions exist on the calibration image. Just below this region, there is another part where the values are higher compared to the whole map.

The measurement has been calibrated with ray tracing-based correction. Other correction methods, based on a mapping function, were also checked in Davis8.4 software and the results are presented in Table 2.

4.2. Turbulent flow structures in the half-dimpled tube

PIV measurements were performed for the center dimple at the 9th row. The flow field results represent time-averaged velocity fields in this chapter. Fig. 11a

Table 2: Standard deviation values based on correction methods.

Correction Method	RMS fit [pix]
Pinhole	13.7
3rd order polynomial	9.6
Ray tracing	0.32

and Fig. 11b shows the average axial and radial velocity fields respectively on the symmetry plane of the center dimple. There is a recirculation zone captured inside the dimple can be seen in both figures. The flow separation starts at the leading edge of the cavity and it reattaches to the wall in the final section of the shape. Far away from the wall of the dimple, the streamlines are parallel to each other and not affected by the cavity. It is to be noted that flame-shaped fluctuations in the axial velocity field are not representative of the real flow. They are mainly due to the movements of the test section after the measurements, which lead to a change in the calibration, that is, an increase in the deviation between the final corrected image and reference grid because heart-shaped distortions are quite sensitive to the position. It is illustrated in Fig. 11b that the positive components of the radial velocity located are in the final part of the dimple while the negative components are at the leading edge part and located in a wider area explains the asymmetrical circulation zone inside the dimple. Furthermore, positive values of radial velocity downstream of the dimple show that the flow pushed to the ending edge exits from the dimple and mixes with the core flow.

The Turbulent Kinetic Energy generated by the turbulent flow at the center of the dimple in Fig. 12, where the quantity of the Turbulent kinetic energy is expressed as:

$$TKE = \frac{3}{4}\frac{[(V_x - \overline{V_x})^2 + (V_r - \overline{V_r})^2]}{U_b^2} \qquad (2)$$

where U_b is the bulk velocity. Since the planar PIV contains two components of the velocity in this case, V_x and V_r, the third component is assumed to have similar turbulent contribution as the others. In the upper part of the cavity, where velocity gradients are bigger, larger values of TKE takes place.The highest values (around 4% of bulk kinetic energy) is located in the leading edge of the dimple. In general, the heat transfer is expected to be improved near wall region due to relatively high turbulent kinetic energy.

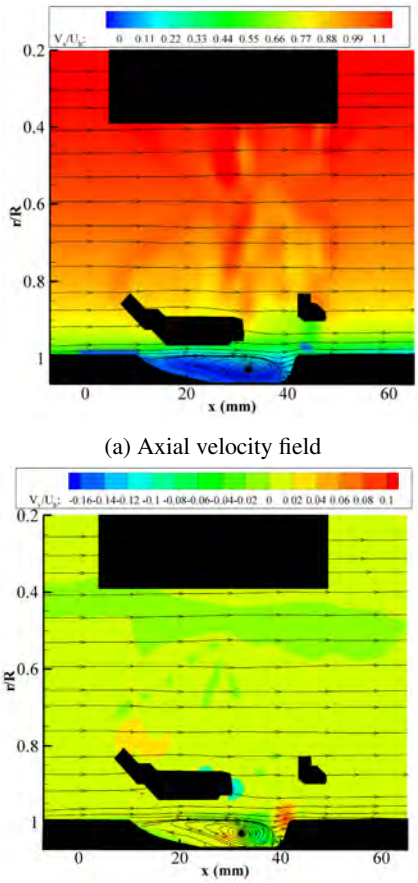

(a) Axial velocity field

(b) Radial velocity field

Figure 11: Axial and radial velocity fields in the streamwise center plane.

5. Conclusions

During the production of light olefins in steam cracking reactors, improvements in heat transfer with low pressure penalties are desired. It is known that dimples have less pressure drop compared to other heat transfer enhancement wall modifications. Therefore, for maximum dimple geometry performance, Jens et al. conducted an optimization study and found that heart-shaped dimples provide a significant increase in thermal enhancement factor. In this study, the flow field in a channel, with one half of which has heart-shaped dimples and the other half is smooth, has been experimentally investigated. The flow structures around a dimple in the 9th row were provided by using planar PIV at around Re=20000. To be able to carry out PIV through the heart-shaped cavity, a ray tracing-based image correction method has been used

and an optimization algorithm has been developed to minimize the uncertainty in this correction.

Time-averaged averaged flow field and turbulent statistics in stream-wise center plane, were presented. The experimental data show that the flow is separated as it approaches the leading edge of the dimple. It reattaches to the wall at the end of the shape, where a local heat transfer may appear, while the recirculation zone occurs inside the dimple. It is observed that streamlines remain parallel to each other above the dimple. Maximum turbulent kinetic energy level has been recorded as %4 of bulk kinetic energy close to the wall where the heat transfer is expected to be improved.

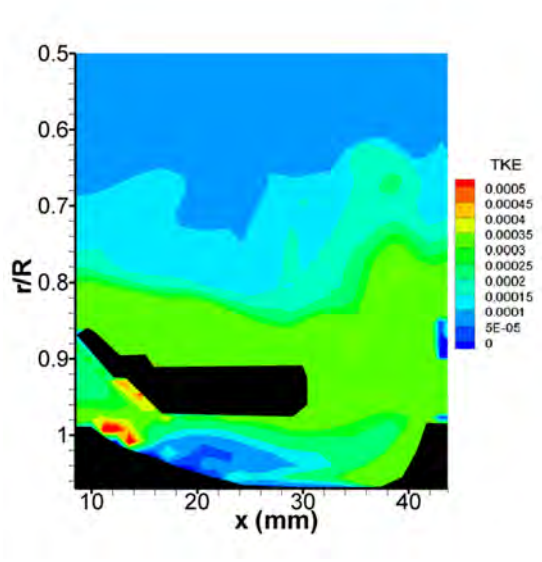

Figure 12: TKE fields in the streamwise center plane.

References

[1] J. N. Dedeyne, D. J. Van Cauwenberge, P. A. Reyniers, K. M. Van Geem, G. B. Marin, Large eddy simulation of tubular reactors with spherical dimples, Chemical Engineering Journal 380.

[2] L.A. Vandewalle, D.J. Van Cauwenberge, J.N. Dedeyne, K.M. Van Geem, G.B. Marin, Dynamic simulation of fouling in steam cracking reactors using CFD, Chemical Engineering Journal.

[3] P. M. Ligrani, M. M. Oliveira, T. Blaskovich, Comparison of Heat Transfer Augmentation Techniques, AIAA Journal 41 (3).

[4] V. N. Afanasyev, Y. P. Chudnovsky, A. I. Leontiev, P. S. Roganov, Turbulent Flow Friction and Heat Transfer Characteristics for Spherical Cavities on a Flat Plate, Experimental Thermal and Fluid Science 7 (1993) 1–8.

[5] T. S. Griffith, L. Al-Hadhrami and J. Han, Heat Transfer in Rotating Rectangular Cooling Channels (AR=4) With Dimples, Journal of Turbomachinery 125 (2003) 555–564.

[6] W. Zhou, Y. Rao, and H. Hu, An experimental investigation on the characteristics of turbulent boundary layer flows over a dimpled surface, Journal of Fluids Engineering 138 (2016) 021204021217.

[7] M. Virgilio, J.N. Dedeyne, K.M. Van Geem, G.B. Marin, T. Arts, Dimples in turbulent pipe flows: experimental aerothermal investigation, International Journal of Heat and Mass Transfer 157.

[8] M. K. Chyu, Y. Yu, H. Ding, J. P. Downs, and F. O. Soechting, Concavity enhanced heat transfer in an internal cooling passage, no. ASME 1997 International Gas Turbine and Aeroengine Congress and Exhibition, 1997.

[9] N. K. Burgess and P. M. Ligrani, Effects of dimple depth on channel nusselt numbers and friction factors, Journal of Heat Transfer 127 (2005) 839–847.

[10] J. N. Dedeyne, M. Geerts, P. Reyniers, F. Wry, K. Van Geem and G. Marin, Computational fluid dynamics-based optimization of dimpled steam cracking reactors for reduced CO_2 emissions, Transport Phenomena and Fluid Mechanics 66 (2020) 071702.

[11] 17. K. Kang, S. Lee, C. Lee, I. Kang, Quantitative visualization of flow inside an evaporating droplet using the ray tracing method, Measurement Science and Technology 15 (6) (2004) 1104–1112.

[12] 18. K. Zha, S. Busch, C. Park, and P. Miles, A novel method for correction of temporally- and spatially-variant optical distortion in planar particle image velocimetry, Measurement Science and Technology 27 (2016) 085201.

[13] F. J. W. A. Martins, C. Carvalho da Silva, C. Lessig, K. Zhringer, Ray-tracing based image correction of optical distortion for piv measurements in packed beds, Journal of Advanced Optics and Photonics 1 (2018) 71–94.

[14] I. Mayo, B. C. Cernat, M. Virgilio, A. Pappa, and T. Arts, Experimental investigation of the flow and heat transfer in a helically corrugated cooling channel, Journal of Heat Transfer 140 (7) (2018) 071702.

[15] M. Pharr, W. Jakob, G. Humphreyss, Physically Based Rendering: From Theory to Implementation. Morgan Kaufmann, 2016.

[16] T. Verstraete, . Introduction to Optimization and Multidisciplinary Design, Course note, Rhode-St- Genese, Belgium, The von Karman Institute for Fluid Dynamics (2018-2019).